

Influence of complex environments on the photophysical properties of organic chromophores



Inaugural dissertation

for the attainment of the title of doctor in the
Faculty of Mathematics and Natural Sciences at the
Heinrich Heine University Düsseldorf

presented by

Simon HÉDÉ

from: Laval (France)

Düsseldorf, September 2024

From the institute for Theoretical and Computational Chemistry
at the Heinrich Heine University Düsseldorf

Published by permission of the
Faculty of Mathematics and Natural Sciences at
Heinrich Heine University Düsseldorf

Supervisor: PD Dr. Oliver Weingart
Co-supervisor: Univ.-Prof. Dr. Christoph Janiak

Date of the oral examination __/__/2024

Affidavit

I declare under oath that I have produced my thesis independently and without any undue assistance by third parties under consideration of the ‘Principles for the Safeguarding of Good Scientific Practice at Heinrich Heine University Düsseldorf’. The dissertation has not been submitted in this form or in a similar form to any other examination authority. No previous unsuccessful PhD attempts were made.

Düsseldorf, 30/09/2024

Abstract

In this thesis, a protocol to compute the photophysical properties of chromophores within complex solid state embedding was established and validated. The protocol involves plane wave calculation of experimentally obtained crystal structures and subsequent QM/MM calculations centred on one or multiple chromophores. The use of a QM/MM scheme allows the inclusion of explicit surroundings that would be impossible to study solely relying on quantum mechanical based methods.

The first study was conducted on the effect of three different environments on the MIA chromophore, involving the MIA organic single crystal and two MOFs. This experiment illustrated the significance of including inter-molecular interactions to describe electronic properties in a condensed medium. In the MIA single crystal, the first excited state corresponds to a charge transfer between neighbouring MIA molecules, while both MOF structures basically prevent aggregation and interaction of chromophores by isolating them.

A second study was conducted on three different (co-)crystals based on a flavin derivative. The co-crystals modify the emission wavelength of the flavine. The performed QM/MM computations could explain the reasons behind experimentally observed blue-shifts in emission. The distance between the molecules involved in the charge transfer has a major effect: the larger the distance, the more the emission shifts to smaller wavelengths. The type of in-plane neighbours also weakly affects the emission.

In the third study, three phenazine derivatives were investigated as potential TADF emitters in solvent and in their own single crystal. Calculations on these models were at first performed using standard methods but led to inadequate results. By introducing vibrational effects into the calculation, I was able to identify TADF in two of the three molecules, matching the experimental observations. The difference between solvent and crystalline medium on the TADF properties could also be assessed.

The last study presented in this thesis aimed at investigating singlet fission in pentacene and TIPS-pentacene in their single crystal environment. The application of the here established protocol helped in identifying the mechanism of the singlet fission process, which was only achievable due to detailed description of the crystal embedding.

Thanks

My first thanks go to Oliver Weingart for being my doctorate supervisor and having taught me through the strange world of QM/MM. I wish to thanks all the people from the institute for Theoretical and Computational Chemistry for their kindness. I also want to thank all people from the ModISC training group, PhDs and professor with a particular shout-out to Martina Holz.

I wish to give special thanks to Timo Shulz for existing, no more. Lastly, I want to thanks my family and friends who have been there for me over those 5 years, either online or in a bar!

I dedicate this work to my grand parents, Hélène et Roger Hédé.

Contents

Chapter 1: Introduction	1
Chapter 2: Theory	5
2.1 QM, MM and QM/MM.....	5
2.1.1 Quantum Mechanics: The DFT model.....	5
2.1.2 Quantum Mechanics: Hybrid functionals.....	7
2.1.3 Molecular Mechanics: Principle.....	8
2.1.4 Combining QM and MM.....	9
2.2 Plane wave and pseudopotentials.....	10
2.3 Configuration interaction.....	11
2.4 DFT/MRCI.....	12
Chapter 3: Computational protocol	13
3.1 Infinite solids and plane wave calculations.....	13
3.2 Properties with PW structures.....	15
3.3 QM/MM setup.....	18
3.3.1 Expansion of the unit cell.....	18
3.3.2 x2p.py.....	18
3.3.3 Calculation of atomic charges.....	19
3.3.4 Force field setup.....	20
3.3.5 Preparation of QM/MM inputs.....	21
3.4 QM/MM: Cobramm, Gaussian, Amber, Turbomole.....	22
3.5 Properties: DFT-MRCI, Vibes, Gradienator.....	23
Chapter 4: The MIA chromophore	25
4.1 MIA in its organic crystal.....	26
4.2 Structural optimisation of MIA@MOFs.....	29
4.2.1 MIA@MOF-5.....	29
4.2.2 MIA@MIL-53(Al).....	30
4.3 DFT/MRCI computations of MIA@MOFs.....	32

Chapter 5: Co-crystals of roseolumiflavin	35
5.1 R single crystal.....	37
5.2 R-D co-crystal.....	41
5.3 R-DE co-crystal.....	42
5.4 Conclusions.....	44
Chapter 6: Phenazine derivatives	45
6.1 Static model calculations.....	46
6.2 Beyond the static model.....	48
6.3 Crystal structure calculations.....	50
6.3.1 mBN organic crystal.....	50
6.3.2 pBN organic crystal.....	53
6.4 Conclusions.....	55
Chapter 7: (TIPS-)Pentacene	57
7.1 Pentacene crystal.....	58
7.2 Results of the pentacene study.....	60
7.3 TIPS-pentacene crystal.....	61
7.4 Conclusion.....	63
Chapter 8: Conclusion and outlook	65
Appendix 1: File types	69
Appendix 2: Python3	71
Appendix 3: Results in R (co-)crystals	81
References	85
Included papers	96

List of publications

Multiexcitonic and optically bright states in subunits of pentacene crystals: A hybrid DFT/MRCI and molecular mechanics study.

American Institute of Physics, The Journal of Chemical Physics, 2024, 160 (14), 144114

Timo Schulz, Simon Hédé, Oliver Weingart, Christel M. Marian

Contribution: Modelling and calculation of ground and excited state structures of pentacene in solid-state embedding. Manuscript preparation.

Molecular design of phenazine-5,10-diyl-dibenzonitriles and the impact on their thermally activated delayed fluorescence properties.

Royal Society of Chemistry, Journal of Materials Chemistry C, 2023, 11 (26), 8982-8991

Dietrich Püschel, Julia Wiefermann, Simon Hédé, Tobias Heinen, Leo Pfeifer, Oliver Weingart, Markus Suta, Thomas J. J. Müller, Christoph Janiak

Contribution: Calculation of ground and excited state structures of the three molecules (BPN, mBN, pBN) in solvent. Calculation of electronic properties. Manuscript preparation.

Enhanced Solid-State Fluorescence of Flavin Derivatives by Incorporation in the Metal-Organic Frameworks MIL-53(Al) and MOF-5.

Multidisciplinary Digital Publishing Institute, Molecules, 2023, 28 (6), 2877

Dietrich Püschel, Simon Hédé, Iván Maisuls, Simon-Patrick Höfert, Dennis Woschko, Ralf Kühnemuth, Suren Felekyan, Claus A. M. Seidel, Constantin Czekelius, Oliver Weingart, Cristian A. Strassert, Christoph Janiak

Contribution: Modelling and calculation of ground and excited state structures of MIA in the crystalline state. Determination of optimised number of molecules in the QM layer. Modelling and inclusion of MIA into the MOF crystal structures. Calculation of electronic properties of the MIA and characterisation of the effect of the MOF surrounding. Manuscript preparation.

List of abbreviations

BH-LYP	Becke Half and half Lee Yang Parr hybrid functional
BPN	Bi-phenylnitrile
CASPT2	Complete active space perturbation theory
CASSCF	Complete Active Space Self Consistant Field
CI	Configuration Interaction
CIF	Crystallographic Information File
CT	Charge Transfert
D	2,4,6 triaminopyrimidin
DFT	Density Functional Theory
DL	Delocalised
DSCF	Direct Self Consistant Field
E	Acetic Acid
FFTK	Force Field Tool Kit
GAFF	Generalised Amber Force Field
GGA	Generalised Gradient Approximation
HF	Hartree-Fock
HL	High Layer
HOMO	Highest Occupied Molecular Orbital
ISC	Inter System Crossing
LE	Local Excitation
LL	Low Layer
LSDA	Local Spin Density Approximation
LUMO	Lowest Unoccupied Molecular Orbital
LYP	Lee Yang Parr
mBN	meta-benzonitrile
MFIS	Multi-parameter Fluorescence Image Spectroscopie
MIA	10-methyl-isoalloxazine
ML	Medium Layer
MM	Molecular Mechanics
MO	Molecular Orbitals
MOFs	Metal Organic Frameworks
MRCI	Multi Reference Configuration Interaction
OLED	Organic Light Emitting Diode

PBE0	Perdew Burke Ernzerhof hybrid functional
pBN	para-benzonitrile
pdb	Protein Data Bank file format
PP	PseudoPotential
PW	Plane Wave
QM	Quantum Mechanics
R	Roseolumiflavin
rISC	Reverse Inter System Crossing
RMSD	Root Mean Square Deviation
Ry	Rydberg, energy unit. $1 \text{ Ry} = 13.606 \text{ eV}$
TADF	Thermally Activated Delayed Fluorescence
TD	Time Dependent
TDA	Tamm-Dancoff Approximation
TFD	Thomas Fermi Dirac
TIPS	Triisopropylsilylethynyl

List of figures

- 3.1 Schematic representation of the complete procedure to study a chromophoric system within a complex environment.
- 3.2 MIL-53(Al) derived subsystem used to compute aluminium parameters.
- 4.1 The MIA chromophore on the left and the experimental emission spectra of MIA (F1) in crystal or embedded into different MOFs on the right.
- 4.2 π - π stacking of MIA in crystal, distance are given in Ångstrom
- 4.3 Electronic density difference at S_1 geometry for S_1 to S_0 transition for (a) 2 MIA in the small stacking configuration (1-2), (b) 2 MIA in the large stacking configuration (2-3) and (c) 3 MIA. Density loss is pictured in red, density gain is yellow.
- 4.4 The two MOF-5 cavities, INWARD on the left (orange sphere) and OUTWARD on the right (green sphere).
- 4.5 Representation of one MIL-53(Al) channel, empty (left) and filled with a MIA chromophore (right).
- 4.6 Optimised MIA embedded in MIL-53(Al) at the ground state (up) and the first excited state (down).
- 4.7 Computed absorption (full line) and emission (dot line) spectra of MIA in Vacuum (black), three MIA in crystal (red), MIA in MIL-53(Al) (blue) and MIA in MOF-5 in the INWARD (orange) and the OUTWARD (green) pore.
- 4.8 Electronic density difference between S_1 and S_0 for MIA in Vacuum (a), MIL53 (b), INWARD (c), OUTWARD (d). Red is density loss, yellow is density gain.

- 5.1** a) Roseolumiflavin R, b) 2,4,6-Triaminopyrimidin D and c) acetic acid E.
- 5.2** Experimental normalised emission wavelength of R, R-D and R-DE (co-)crystals. Excitation wavelengths are 423 nm for R and R-D, 400 nm for R-DE.
- 5.3** Crystal arrangement of R in single crystal. Distances are given in Ångstrom.
- 5.4** R-D co-crystal arrangement, planar (upper) and stacking (lower) views. The stacking distance is 3.681 Å (at the ground state). In the planar view, the four molecular fragments correspond to four other R molecules.
- 5.5** R-DE co-crystal arrangement. A) Planar view of the crystal arrangement. Fragments visible on the left are from other R molecules. B) Stacking view along R short axis. C) Stacking view along the long axis of R, co-crystallites D and E are omitted.
- 6.1** The three phenazines derivative studied in this work, a) BPN, b) mBN and c) pBN.
- 6.2** Change of oscillator strength by rotation of dihedral angles of pBN (left) and mBN (right). Modified dihedrals are pictured in green (vertical parameters in the table) and yellow (horizontal parameters).
- 6.3** Combined computed absorption and emission of mBN and pBN in toluene.
- 6.4** Comparison of mBN ground state structure in vacuum (left) and in its organic crystal (right).
- 6.5** HOMO (left) and LUMO (right) of mBN in crystal. Isosurface were plotted with a cutoff of 0.03.
- 6.6** Computed normalised absorption (full line) and emission (dotted line) spectra of mBN, vertical (black) and after sampling treatment (red). Static emission oscillator strength is 0.003 and average emission oscillator strength with zpve sampling is 0.004.
- 6.7** pBN-lin (left) and pBN-ben (right) structures extracted from the crystal structure, viewed along the long (top) and short (bot) axis of the phenazine.

- 6.8** Computed absorption (full lines) and emission (dotted lines) spectra of pBN-lin (black and red) and pBN-ben (blue and green) from static and ZPE-sampling methods.
- 7.1** Simplified direct and indirect mechanism of singlet fission.
- 7.2** (a) Pentacene trimer in blue, green molecules are in the low layer. (b) Definition of the three dimer subunits, distances between centroids are given in Ångstrom.
- 7.3** Visualisation of experimental structure of one TIPS-pentacene in the organic crystal structure. Before (left) and after (right) refinement.
- 7.4** Packing arrangement of TIPS-pentacene. TIPS groups have been shortened for clarity. Distances are given in Ångstrom.

List of tables

- 3.1** Computed absorption wavelength and corresponding oscillator strength of MIA crystal with 1, 2, 3 and 4 MIA molecules embedded into point charges. Experimental excitation: 440 nm
- 3.2** Emission wavelength and associated oscillator strength for one to four MIA in QM and the number of S1 structure inserted. Experimental emission is 562 nm.
- 4.1** Absorption and emission wavelength and emission rate constant of a single molecule of MIA in vacuum, models including a medium layer contain “ML” in the first row. Experimental excitation wavelength is 440 nm and emission is 545 nm.
- 5.1** Experimental and computed theoretical cell parameters of R, RD and RDE (co-)crystals
- 5.2** Computed first bright absorption properties, corresponding density differences are shown in supplementary information of the associated paper. H= HOMO, L= LUMO, LE= Local Excitation, DL= Delocalised.
- 5.3** Computed emission properties for 1, 2, 3 or 4 R molecules (MOs localisation is shown under brackets wrt. figure 5.3 number attribution) in R, R-D and R-DE (co-)crystals. Exp. emissions are 733 nm, 668 nm and 585 nm.
- 6.1** TD-DFT and DFT/MRCI results of excited states properties for BPN, mBN and pBN in vacuum or in toluene medium. Experimental emission wavelengths are noted in brackets under molecule name.
- 6.2** mBN/pBN in vacuum rate constants (s⁻¹)
- 6.3** Rate constants of mBN
- 6.4** Rate constant for the pBN-lin and pBN-ben molecules in the β -pBN crystal environment.

- 7.1** RMSD of QM geometry computed by the PBE0 and CAM-B3LYP functional. Values are in Ångstrom.
- 7.2** RMSD of QM geometry computed by the PBE0 and CAM-B3LYP functional. For one or two TIPS-pentacene in the QM region. Values are in Ångstrom.

Chapter 1

Introduction

Organic chromophores are light absorbing and emitting compounds. Light absorption involves an excitation from the electronic ground state towards an excited state, changing the distribution of electrons within the molecule [1]. The stored photon energy can then be released via different pathways, eventually carrying the molecule back towards the ground state. These pathways include radiative and non-radiative deactivation processes which may either leave the molecular structure unaltered or subsequently induce a chemical reaction [2]. Organic light emitting materials play an important role in Nature and in technical applications [3]. In the last decades, they became more and more present in devices of every-day life like e.g. in OLED displays of television sets, mobile phones or other small electronic devices. They are also used as biological sensors [4]. The demand for efficient and stable emitters is steadily increasing, the same is true for the experimental complexity in finding such emitters. Computational chemistry can be an ideal tool for revealing possible target systems, provided the envisaged methods are accurate and applicable within reasonable time. In this thesis, the focus lies on the emissive nature of organic chromophores and how the latter can be influenced by its chemical surroundings. This surrounding can either involve a solvent, a solid environment like e.g. a crystalline state, a protein or a molecular framework.

For chromophore target systems, the plethora of natural organic chromophores may serve as a guideline. Flavines e.g. are prototypical examples for chromophores with various functions in Nature, found as co-enzymes or photoreceptors [5]. Their functionalities strongly depend on their environment, which makes them ideal targets for the investigation of tunable light emission properties.

The 10-methyl-isoalloxazine core (MIA) is one of the target molecules within the graduate college GRK 2482, which investigates the modulation of intersystem crossing in OLED emitters. It was explored in recent computational and experimental studies [6]. In the crystalline state, MIA yields only weak emission [7], while in solution MIA shows a strong emission band at 524 nm [8]. Employing vacuum- as well as implicit and explicit solvent computational models, Bracker et al. [6] were able to tune the emission properties of MIA by mono-fluorine substitution and to predict how di-fluorination

may further enhance fluorescence emission. Investigations of MIA embedded in metal-organic frameworks (MOFs) indicate a severe enhancement of fluorescence with only little effect on the emission wavelength. Sohi et al. [9] were able to influence the luminescence properties of roseolumiflavin by producing co-crystals with acetylenedicarboxylic acid, diiodotetrafluorobenzene and 2,4-diaminopyrimidine, shifting the emission wavelength from 733 nm down to 628 nm in the solid state.

Another chromophore target system investigated within this study involves phenazine derivatives. These electron-rich compounds can be combined with electron acceptor moieties like benzonitrile, forming tunable emitters that show thermally activated delayed fluorescence (TADF) [10]. In 2015, Adachi et al. reported TADF in phenazine derivatives [11]. One of these compounds, DHPZ-2BN, was the base of our investigations on three derivatives that helped us to enlighten the importance of vibrational analysis to properly describe TADF processes in different environments.

The last target system investigated in this work was pentacene and one of its derivatives, TIPS-pentacene. This compound has been studied both experimentally and theoretically by many groups for its singlet fission properties that may pave the way towards third generation solar cells [12] [13]. Previous investigations by Nagami et al. have shown that the process of interest mainly occurs in condensed media, i.e. either in highly concentrated solution or crystalline environment [14]. However, although there is experimental evidence of singlet fission occurring in such systems, the exact mechanism is still not fully understood.

As stated above, crystalline solid-state environments provide an interesting surrounding for the modification of luminescence properties due to their periodicity, which allows the design of defined chromophore-substrate interactions. In this regard, metal organic frameworks (MOFs) will form another target environment. MOFs are a class of crystalline materials consisting of organic linkers and metal nodes, forming a regular alternating network. The diversity of linker and node combinations gives rise to millions of theoretically possible structures, with unique properties like porosity, contact surface or rigidity. The large contact surface and porosity of MOFs make them perfect materials for gas adsorption, separation and/or storage for molecules like CO₂, NO_x, SO₂, C_xH_y [15] [16]. The computational description of a chromophoric system within such an environment imposes numerous challenges, starting with the computational description of the chromophoric system itself. Methods like e.g. CASPT2 [17] employ accurate multistate configuration interaction schemes, which are often too costly to be applied for high-throughput analyses. There is no generally applicable standard scheme, especially for the earlier mentioned MOFs. The targeted approaches range from simple electrostatic solvation descriptions towards explicit solvation, periodic plane wave methods and QM/MM embed-

ding with a focus towards combinations of the latter two. Excited state structures can reliably be obtained with modern DFT functionals applying the time-dependent DFT formalism [18] or within the Tamm-Dancoff [19] approach. Excitation energies are refined through the DFT/MRCI formalism [20]. The aim of this work is to provide a general workflow for the investigation of organic chromophoric systems within regular solid state environments like organic crystals or (metal-) organic frameworks. The principal theory behind the methods used in this work is presented in the first chapter. A second chapter will display the overall workflow established during my PhD. Further chapters show the work performed on the previously presented target system, i.e. the MIA crystal and MIA@MOFs, co-crystals of MIA derivatives, phenazine in solution and in crystal phase and finally crystals of pentacene and TIPS-pentacene.

Chapter 2

Theory

2.1 QM, MM and QM/MM

In the overall study of a chromophore embedded into a complex environment, which will be detailed later in this thesis, the combination of quantum mechanical (QM) and molecular mechanics (MM) methods, QM/MM, play a major role. We will first explain how both work independently and then how they are combined within Cobramm2.0 [21].

2.1.1 Quantum Mechanics: The DFT model

One of the roots of density functional theory (DFT) is the Thomas-Fermi model first introduced in the 1920's by Llewellyn Thomas and Enrico Fermi [22]. This model allows the calculation of system properties by solely using its electron density, thus reducing the problem of describing a molecule with $3n$ atomic coordinates to just three for volume elements of density. The model was later improved by Paul Dirac with the addition of an exchange part K_D to become the Thomas-Fermi-Dirac model (TFD) (1)[23].

$$E_{TF}(p) = T_{TF}(p) + E_{ne}(p) + J(p) + K_D(p) \quad (1)$$

It is when Carl von Weizsäcker introduced the variation of the density through space in the expression of the kinetic term that this model was complete [24], yet insufficient to be as widely used as the density functional theory is nowadays. Walter Kohns and Pierre Hohenbergs contributions to the TFD model led to the basis of DFT thanks to two theorems [25]:

The first theorem states that the minimum energy of a system can be written in terms of a unique function of the electron density (giving the name of the method), which means in principle that only

the density over all space needs to be known to determine all properties of a system. An explanation of that theorem and its implication was given by Edgar Bright Wilson Jr. [26] stating that:

- The integral of the density over all space gives the number of electrons.
- The density shows a cusp where nuclei are located.
- The cusp's height defines the charge of the nucleus.

The second theorem is the proof that the functional of energy follows the variational principle; meaning that whatever external potential is applied to the electrons, there exists one functional minimizing the energy which represents the exact solution.

A major problem with the so far discussed models was the description of the kinetic energy of the electrons. Kohn and Sham therefore introduced orbitals into the equation of DFT through the introduction of kinetic energy T_{tot} , hence increasing the complexity. The kinetic energy is split into two parts, one that can be approximated with an independent electrons model (T_s) and a correction term T_{xc} . In formula (2) the electron and nuclei attraction energies are denoted as E_{ne} , the Coulomb potential is J and the exchange correlation term is E_{xc} :

$$E_{DFT} = T_s + E_{ne} + J + E_{xc} \quad (2)$$

The exchange correlation term E_{xc} includes components describing the electron-electron interaction (3). Those are the terms that cannot be computed exactly.

$$E_{xc} = T_{xc} + (E_{ee} - J) \quad (3)$$

As E_{xc} is small in comparison to the rest of the equation, which can be computed exactly within the given method, the mean error of DFT is solely depending on how good the approximation of E_{xc} is. Improvements of DFT based methods are related to the improvement of the determination of E_{xc} . So far, DFT is still limited to the study of the electronic ground state. The addition of time dependency to the external potential thanks to the Runge and Gross theorem [27] also enabled calculation of electronically excited states.

2.1.2 Quantum Mechanics: Hybrid functionals

One method to calculate the exchange correlation term of the DFT equation, proposed by Enrico Clementi in 1974 [28], is to use the exchange from the Hartree-Fock (HF) method which can be computed exactly. Correlation contributions are calculated with the Generalized Gradient Approximation (GGA) using the first derivative of the density. This idea was not accurate enough but led to Axel Beckes hybrid functional combining HF and GGA exchange to obtain an exchange correlation term [29]. In most of the work done during my PhD, the hybrid functional used was PBE0. This functional was created by Carlo Adamo and Vincenzo Barone [30] from the PBE functional by John Perdew, Kieron Burke and Matthias Ernzerhof [31]. It uses one fourth of HF exchange, the rest comes from the PBE exchange and correlation terms (4).

$$E_{xc}^{PBE0} = 0.25 \times E_x^{HF} + E_x^{PBE-GGA} + E_c^{PBE-GGA} \quad (4)$$

Every DFT/MRCI calculation uses the BH-LYP hybrid functional. Its exchange part consists of HF exchange, exchange through the local spin density approximation (LSDA) [32] [33] and B88 exchange [34] on the same ratio and the LYP correlation functional. (5)

$$E_{xc}^{BH-LYP} = 0.50 \times (E_x^{HF} + E_x^{LSDA} + E_x^{B88}) + E_c^{LYP} \quad (5)$$

The original formula of B3LYP [35] includes a combination of HF, LSDA and B88 exchanges similar to BH-LYP, and the LYP and VWN correlation functional (6). DFT methods tend to underestimate excitation energies for charge transfers. A solution to that is to partition the exchange term depending on the range of the interaction. The CAM-B3LYP [36] functional adds a range separation to the B3LYP functional.

$$E_{xc}^{B3LYP} = 0.20 \times E_x^{HF} + 0.80 \times E_x^{LSDA} + 0.72 \times E_x^{B88} + 0.81 \times E_c^{LYP} + 0.19 \times E_c^{VWN} \quad (6)$$

With the implementation of a variable factor for the exchange, the CAM-B3LYP exchange correlation term is written as follows, with α varying from 0.19 in very short range to 0.65 in long range (7):

$$E_{xc}^{CAM-B3LYP} = \alpha \times E_x^{HF} + (1 - \alpha) \times E_x^{B88} + 0.81 \times E_c^{LYP} + 0.19 \times E_c^{VWN} \quad (7)$$

2.1.3 Molecular Mechanics: Principle

One disadvantage of quantum mechanical methods is their computational cost. Molecular mechanics is based on classical physics, it does not include subatomic particles or orbitals; an atom is described as a particle with mass and charge. An essential characteristic in molecular mechanics is the atom type. This property not only defines its position in the periodic table, but also specifies its covalent surrounding, oxidation level or any other distinguishable property. In the Generalized AMBER Force Field (GAFF) [37] that I used, carbon atoms may be labelled, for example, as *Ca* if aromatic or *Co* if involved in a double bond with oxygen. For each possible covalent and non-covalent combination of atom types there exists a sets of parameters to generate the associated potential.

There are four types of potentials involving covalently bound atoms:

- Binding potential
- Angle strength
- Torsion angle strength
- Improper dihedral strength

At least two parameters define the non-bonded interactions between pairs of atoms:

- Van der Waals interaction represented by e.g. Lennard-Jones potentials
- Electrostatic interaction (Coulomb potential)

In the end the calculus of the MM potential is done as follows by AMBER (8) [38] [39] [40]:

$$V_{AMBER} = \sum_{bonds} k_b (r - r_0)^2 + \sum_{angles} k_\theta (\theta - \theta_0)^2 + \sum_{dihedrals} V_n [1 + \cos(n\phi - \gamma)] + \sum_{i=1}^{N-1} \sum_{j=i+1}^N \left[\frac{A_{ij}}{R_{ij}^{12}} - \frac{B_{ij}}{R_{ij}^6} + \frac{q_i q_j}{\epsilon R_{ij}} \right] \quad (8)$$

2.1.4 Combining QM and MM

The QM/MM scheme used by Cobramm splits the system into three parts. The inner part of the system containing the studied chromophore(s) is labelled as high layer (HL), it is computed with QM methods. The outer part can be split into two parts called medium layer (ML) and low layer (LL). Both are described at the MM level of theory. The ML part is allowed to move during geometry optimizations or molecular dynamics computations, while the LL part is kept fixed. In all cases studied in this thesis the boundary region between QM and MM does not pass through a covalent bond, which simplifies the approach. The overall QM/MM energy computed by Cobramm2.0 [16] without link atoms is not just the sum of the QM and MM energies but also involves the interaction energy between HL and the surrounding layer (9a). The total MM energy is the sum of the MM internal energies ($E_{MM}(HL)$, $E_{MM}(ML)$, $E_{MM}(LL)$) and the interaction energy between all three layers ($E_{MM}(HL/ML)$, $E_{MM}(HL/LL)$, $E_{MM}(ML/LL)$) (9b) [21].

$$E_{QM/MM} = E_{QM}(HL) + E_{MM}(All) - E_{MM}(HL) \quad (9a)$$

$$E_{MM}(All) = [E_{MM}(HL) + E_{MM}(ML) + E_{MM}(LL)] + [E_{MM}(HL/ML) + E_{MM}(HL/LL) + E_{MM}(ML/LL)] \quad (9b)$$

2.2 Plane wave and pseudopotentials

The complexity of solving the Schrödinger equation increases with the number of particles in the studied system. A full crystalline system contains thousands of atoms, which is impossible to compute explicitly. However, the structural properties of a symmetric crystal are defined by its unit cell, the smallest volume that can be repeated by translation in three dimensions. To compute such a periodic system we can apply the Bloch theorems [41], stating that a periodic system can be described by a periodic wave function with the same periodicity as the crystal (10).

$$\Psi_r = e^{ik \cdot r} \times u(r) \quad (10)$$

With u being a periodic function and r the spatial position with a periodicity of r_0 (11) such that:

$$u(r) = u(r + n \times r_0) \quad (11)$$

Due to the symmetry properties of crystals and the Bloch theorems, we can define a finite system that can be infinitely reproduced to theoretically describe a perfect crystal. Computations, however, need to consider only the elemental cell. This method has proven to be very efficient for describing delocalized electron density, however the complexity of the interactions involving core electrons and nucleus requires a large number of functionals causing the methods to be “effective” but inefficient. To counter this inefficiency of plane wave they are combined with pseudopotentials (PP). Pseudopotentials combine all potentials involving the nucleus and the core electrons into one simpler effective potential. The limit between core electrons (localized) and valence electrons (delocalized) is defined during the creation of the PP, for example with silver (^{47}Ag) one can define two different core sizes (electrons not replaced by pseudopotential are in bold) [42]:

- Small core PP: $(1s)^2 (2s)^2 (2p)^6 (3s)^2 (3p)^6$ **$(4s)^2 (3d)^{10} (4p)^6 (4d)^{10} (5s)^1$**
- Large core PP: $(1s)^2 (2s)^2 (2p)^6 (3s)^2 (3p)^6$ $(4s)^2 (3d)^{10} (4p)^6$ **$(4d)^{10} (5s)^1$**

In a plane wave calculation, pseudopotentials are required for all atom types to model the potential near the nucleus.

2.3 Configuration interaction

In the Hartree-Fock method each electron experiences an averaged potential created by all other electrons. This method accounts for ca. 99% of the exact solution for the total energy. The difference to the true energy is the so-called correlation energy. This correlation energy can be obtained by “Post-HF methods”, like CI, MP2 etc [43]. The CI wavefunction is written as a linear combination of the HF Slater determinant and excited Slater determinants. In a singly excited determinant, one formerly occupied orbital from the ground state HF description is replaced by a virtual orbital. A doubly excited determinant exchanged two occupied orbitals by virtual etc. Determinants Φ are combined with expansion coefficients a_i (12) which values are determined variationally.

$$\Psi^{CI} = a_0 \Phi^{HF} + \sum_{i=1} a_i \Phi^i \quad (12)$$

There are several restrictions on the Slater determinants to limit the computational cost. One is to limit the number of simultaneous excitations to only single, double, etc. Another restriction could be to just use a defined set of orbitals to create excitations, this Ansatz is e.g. followed in the CASSCF approach [36]. The basis set choice also influences the cost as more orbitals means more determinants to calculate. Sometimes, CI methods based on only one reference Slater determinant for the ground state (i.e. the Hartree-Fock Slater determinant) do not yield satisfying results. Then, a multireference configuration interaction (MRCI) scheme [44] can be adopted, which also includes excited configurations as references for further expansion.

2.4 DFT/MRCI

The DFT/MRCI method proposed by Grimme and Waletzke in 1999 is a combination of density functional theory and multireference configuration interaction [45] [46]. The principle is to build a multi-reference space using DFT-computed orbitals. As DFT already includes dynamical correlation, DFT/MRCI uses a scheme that, according to the classification of Hamiltonian elements, shifts and/or scales diagonal elements while off-diagonal elements are damped by a function [47]. This avoids double counting of dynamic electron correlation from both MRCI- and DFT-approaches. The method uses empirical parameters in the damping function and is therefore semi-empirical. The damping function in the original Hamiltonian is written as follows (13):

$$f_{damp}^{orig} = p_1 \cdot e^{-p_2 \cdot \Delta E} \quad (13)$$

The work of Lyskov et al. led to the re-parametrized R2016 Hamiltonian [48] in which the calculation of diagonal elements was improved. Furthermore, the exponential dependency in the damping function was changed to an *arctan* dependency (14):

$$f_{damp}^{2016} = \frac{p_1}{1 + (p_2 \Delta E^5) \cdot \arctan(p_2 \Delta E^5)} \quad (14)$$

Dombrowski et al. parametrized the R2022 Hamiltonian to further improve results on doubly and degenerate excited states by modifying the original Hamiltonian [49]. They changed the parameter $p1$ to be a function of two other parameters (15).

$$f_{damp}^{2022} = [1 - 2 \cdot p_{1.1} + p_{1.2}] \cdot e^{-p_2 \Delta E^4} \quad (15)$$

Chapter 3

Computational protocol

The first task in my PhD was to establish a protocol to compute the properties of a chromophore embedded into a crystalline environment, with the crystallographic structure provided by experimentalists. As mentioned in the introduction “there is no generally applicable standard scheme”. The protocol established in this thesis consists of four main parts:

1. Plane wave computation of the crystal structure.
2. Preparation to run QM/MM computations
3. Executing QM/MM computations
4. Electronic property computations

Figure 3.1 depicts the complete protocol that is described in this chapter.

3.1 Infinite solids and plane wave calculations

Input structures for optimisations with plane wave methods were taken from experimentally obtained *cif* files. If necessary, the *cif* files were modified to delete duplicate atoms resulting from different possible orientations of rotatable groups. Computations were performed with the Quantum Espresso suite [50] of programs using the pwscf module. The pseudopotentials applied were all generated using Andrea Dal Corso’s codes [51]. These utilise the PBE exchange correlation functional [31] and include small core pseudopotentials (cf. part 2.2). The wave function cutoff was set to 70 Ry and the charge density cutoff to 700 Ry. Grimme’s dispersion correction (D3) [52] was used, grid computation was only performed using the Γ point. For some of the systems, relaxation of the unit cell was deactivated after notifying larger deformations of the unit cell with respect to the experimental structure.

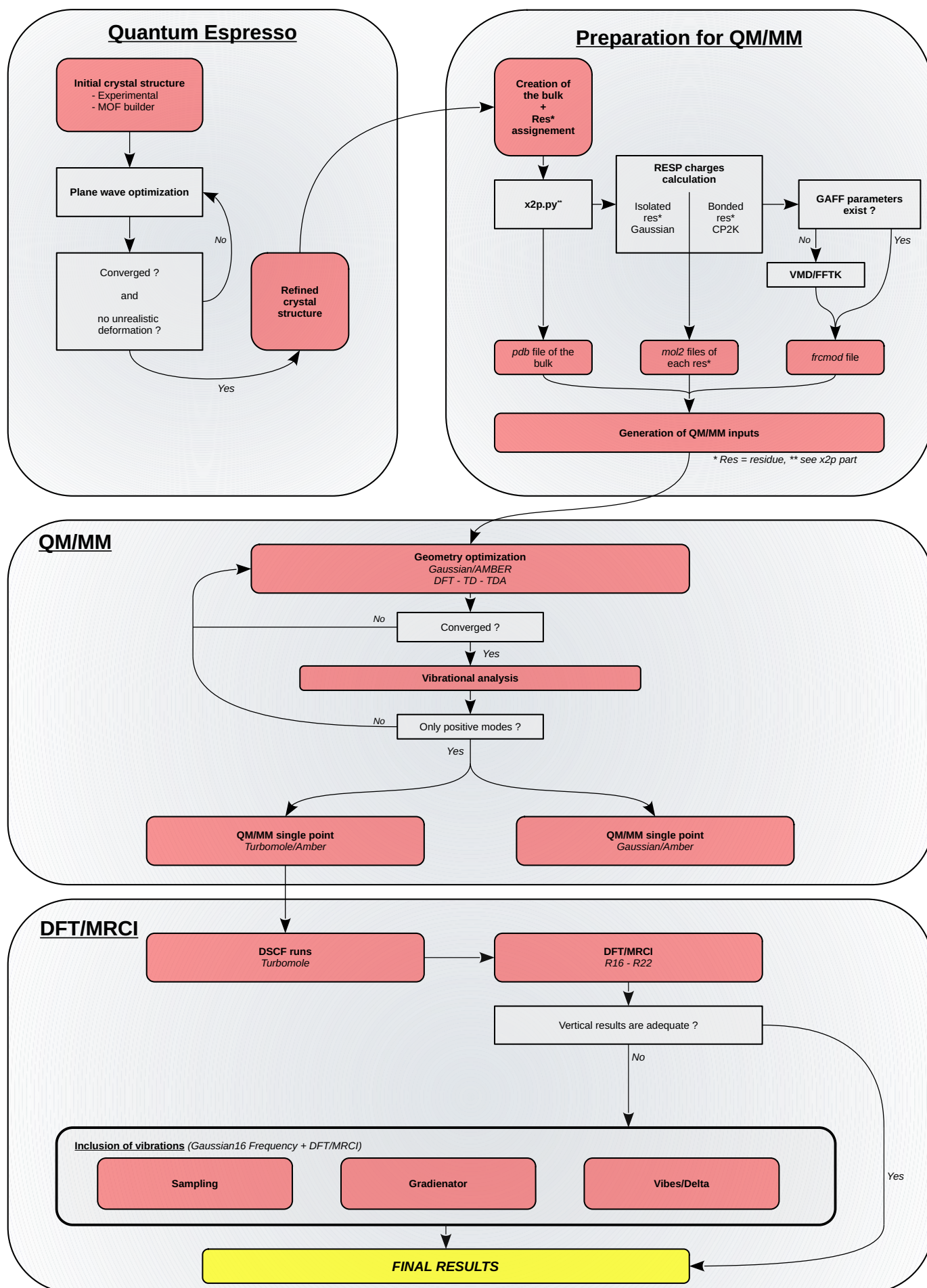


Figure 3.1: Schematic representation of the complete procedure to study a chromophoric system within a complex environment.

In these cases, the cell parameters were frozen to the experimental values, while the rest of the system was fully relaxed using the BFGS-algorithm [53]. No experimental structures for chromophores embedded into MOFs are available, hence for these calculations the chromophore was manually inserted into the MOF after optimising its unit cell and then the combination of both was again optimised. If necessary, an expanded supercell was used to fit the chromophore. Special care was taken to cover all possible positions of the chromophore within the cavity.

3.2 Properties with PW structures

In a first attempt, electronic properties were calculated using the plane wave optimised structure, i.e. without further QM/MM optimisation. From the optimised plane wave geometry of the MIA organic crystal, an 8x8x8 supercell including 1024 MIA molecules was created. For a single point energy calculation, one, two, three or four neighbouring MIA molecules in the centre of the supercell were computed at the BH-LYP/TZVP level of theory, the remaining MIA molecules were represented as point charges. The charge-polarised orbitals were subjected to a DFT/MRCI computation including 20 roots and the R2016 Hamiltonian.

Results of these calculations are summarised in table 3.1, showing lowest energy absorption wavelengths of bright states and their associated oscillator strengths as well as the experimental absorption corresponding to the reported excitation wavelength. Ground state electronic properties were matching experimental data, but with this strategy, no information is available on the excited state emission, as the PW computations provide only ground state structures.

Table 3.1: Computed absorption wavelengths and corresponding oscillator strengths of MIA crystal with 1, 2, 3 and 4 MIA molecules embedded into point charges. Experimental excitation: 440 nm.

Number of MIA in QM	Absorption wavelength (nm)	Oscillator strength
1	433 (S ₁)	0.30
2	454 (S ₂)	0.55
3	469 (S ₁)	0.12
	459 (S ₂)	0.52
	452 (S ₃)	0.19
4	471 (S ₁)	0.13
	461 (S ₂)	0.63
	454 (S ₃)	0.10
	447 (S ₄)	0.39

In a second attempt, ground state structures of the previously discussed model were subsequently replaced by freely optimised S₁-TD-DFT structures using PBE0/def2-TZVP. This strategy led to a total of 26 configurations with different combinations of ground- and excited state structures (see table 3.2). The closest value to the experimental emission was obtained with a model including two or more excited state geometries. Contrary to the experiment, which shows only a weak emission in the crystalline state, the computed oscillator strength was significantly higher. Consequently, this simple model with only charges and up to four MIA molecules cannot fully explain the excited state properties of MIA in its organic crystal. The effect of the embedding, especially the van der Waals interactions of the neighbouring molecules, has to be included in further computations. This is performed within a combined QM/MM scheme and is the topic of the following chapters.

Table 3.2: Emission wavelengths and associated oscillator strengths for one to four MIA molecules in the QM part and the number of S_1 structures inserted. Experimental emission is 562 nm.

Total number of MIA in QM	Number of S_1 geometries	Wavelength (nm)	Oscillator Strength
1	1	512	0.19
2	1	540	0.16
	2	548	0.32
3	1	546	0.16
	2	552	0.13
	3	569	0.32
4	1	542	0.19
	2	555	0.13
	3	556	0.21
	4	557	0.42

3.3 QM/MM setup

Once PW calculations are performed, a series of steps are necessary to produce the QM/MM input files required to conduct the QM/MM calculations as depicted in figure 3.1. Some of these steps require a specific order while others can be executed independently.

3.3.1 Expansion of the unit cell

PW calculations result in a theoretically perfect unit cell defining an infinite system without any borders. Our QM/MM protocol, however, requires a finite system. Therefore the system needs to be extended by adding unit cells around the central unit, thus creating multiple layers of embedding, simulating a crystal surrounding to the chromophore(s) that will be described at the QM level. Currently there are technical restrictions to this expansion in the utilised Amber version. All atom/atom interactions are computed at the MM level without any cutoff, the size of the expanded system therefore can not be larger as ca. 60 000 atoms. In the case of chromophore@MOFs, the loading percentage can be determined experimentally. This value is used to model the chromophore distribution within the expanded system.

To finalise the expanded system, further adaptations may be necessary. For a single organic crystal, incomplete molecules at the system edges are removed. For frameworks, system edges need to be saturated with hydrogens to obtain an electronic neutral system.

3.3.2 x2p.py

x2p.py is a *python3* script (full script can be found in annex 2) that I wrote to convert a randomly ordered xyz file into a structured pdb format, which lists each molecule within the structure as a separate residue. A residue defines a specific atom or group of atoms, each residue of the same name shares the same ordering and internal bonding between its components. The definition of a residue is provided through template files. The script loops over all atoms and compares the distance to the atom under examination, defining if a specific atom is bonded to the latter. If this is the case and the atom matches the residue template file, the atom will be added to the residue. After all residues are identi-

fied, the atoms of each residue are sorted accordingly and a formatted pdb is created. Detailed information on the programming of the script and file formats specifications can be found in annex 1. `x2p.py` needs three inputs files:

- **Molecule.xyz**: A standard xyz coordinate file of the full cluster.
- **Groups.txt**: Names of the residue (three characters by residue).
- **List.txt**: Indices of all atoms with the same residue type in one line. Line ordering is the same as the name order of residues in Groups.txt.

The script will then produce three different files:

- **Out.pdb**: Contains the complete system in pdb format.
- **RES.pdb**: For each residue type there will be one pdb file containing only one set of atoms of the named residue.
- **Bonds.txt**: Each bond between residues will be noted inside. It is useful for chromophore@MOF cases as these bonds need to be properly assigned. They are defined by the residue index and atom names of both atoms of the bonds.

3.3.3 Calculation of atomic charges

A crucial step in producing the QM/MM input files is the calculation of atomic charges. This is performed differently for a single molecule or for a framework. Atomic charges in single molecules are computed following a two-step procedure. A first calculation uses restricted HF and the 6-31G* basis set to compute the electrostatic potential of the molecule. In a second computation, the antechamber package [54] is used to compute the restrained electrostatic potential (RESP) [55] by using the Merz-Singh-Kollman scheme [56] [57]. Herein, the charges are constrained to be equal for all atoms of the same atom type. Framework charges are computed using the CP2K program [58]. It uses plane wave and the REPEAT method [59] on the optimised unit cell from PW optimisation; this strategy is similar to the computation of RESP charges but applied to periodic systems.

3.3.4 Force field setup

One essential component in MM calculation is the force field. Cobramm [21] uses the AMBER suite of programs [40] to deal with the MM part of its QM/MM scheme. Upon the preparation of the files, atom types have been attributed to atoms according to the GAFF definitions and written into mol2 files, obtained through the charge calculation step for each residue. The antechamber routine then creates the force field files that will contain all necessary parameters to describe the system. GAFF is used to describe organic molecules, for this purpose it contains parameters for C, N, O, H, S, P, F, Cl, Br and I. However, some of our systems involve atoms not implemented into GAFF, e.g. metals. To complete the force field description for such cases there are two options: Parameters can be taken from literature or they have to be created computationally. Numerous methods or programs exist to perform the latter task, the force field toolkit (FFTK) [60] is one of them. FFTK is a plugin for the VMD program. To produce parameters for MOFs, a subsystem that mimics the MOF environment including the atoms with missing parameters has to be created. During the MIL-53(Al) study, parameters for aluminium were missing. In this case, the subsystem from the work of Vanduyfhus et al. [61] was used (see figure 3.2).

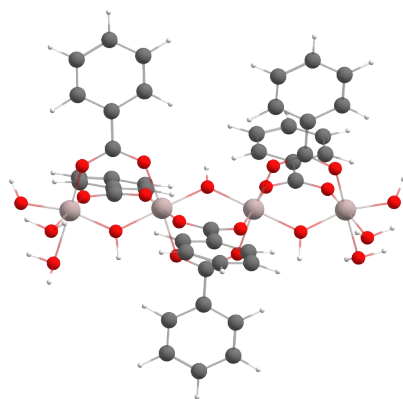


Figure 3.2: MIL-53(Al) derived subsystem used to compute aluminium parameters.

The creation of force field parameters is achieved through several steps. Each kind of parameter is created separately. In a first step, a geometry optimisation and charge computation is performed if necessary. Then, scans over bond lengths, angles and dihedral angles are conducted to obtain the corresponding potentials. From this data, force constants and equilibrium values for each structural component are derived.

3.3.5 Preparation of QM/MM inputs

The final step before starting a QM/MM calculation involves the generation of specific input files:

- One or multiple files containing the force field parameters.
- One mol2 file for each residue of the system, containing the previously computed charges and atom types.
- The pdb file of the complete system provided by the x2p.py script.
- A command file defining parameters for the QM- and MM-sub-systems.

The command file named “cobram_parm” contains information on QM and MM subsystems. Herein, the division into QM and MM parts is specified, as well as the location of parameter files from the previously described steps. The QM system is selected by either providing a list of atom indices or by choosing a specific residue. The QM region can be extended by including atoms or residues within a given distance from the initial choice. The same strategy can be applied to choose the mobile region of the MM subsystem; this region is then allowed to move during geometry optimisations or MD-simulations. Four files are obtained after execution of the cobram_prepare script: Topology files for the full system and for the high layer in amber top-format, an xyz file defining the division into high, medium and low layers and a coordinate file for the whole system in amber crd-format. To start a QM/MM computation, another file is required which contains execution parameters for the QM, MM and combined QM/MM routines. Its contents will be detailed later (section 3.5).

3.4 QM/MM: Cobramm, Gaussian, Amber, Turbomole

The third step of the protocol (see figure 3.2) focuses on the chromophore. A QM/MM scheme is used to perform geometry optimisation. As mentioned before, QM/MM input files generated previously will be used in combination with a command file named “cobram.command”, controlling the three programs involved in the QM/MM scheme (QM, MM and QM/MM). The file is divided into three main blocks defined by a very specific first and last line; the order of these blocks is not important. The block that controls Cobramm is used to specify the type of calculation to be executed (geometry optimisation, frequency calculation, single point, ...) and which program will handle the QM part as several programs are available. There is no program choice for MM as currently, only AMBER is implemented into Cobramm. This part is also used to specify the necessary computing resources. Another block will be used to supply commands to the AMBER program steering MM computations. This part will also contain specifications such as distance threshold for atomic interactions and number of cycles for the minimization algorithm. The input for the QM program depends on the program used. In this thesis, mainly two programs have been used, Gaussian and Turbomole. Gaussian’s command section is very similar to a Gaussian input file without resource specific commands. It mentions the pair functional/basis set but also if the calculation will include the ground state (DFT) or excited states (TD-DFT). Classical verifications like confirming convergence criteria or performing frequency calculations to ensure the absence of negative frequency modes can be utilised to verify the correctness of a geometry optimisation. To perform QM/MM with Turbomole the setup is different, as Turbomole uses its own input files stored in a subdirectory. This directory contains a coordinate file of the QM region only and information of its molecular orbitals. Another file stores basis set data. The main use of Turbomole in our QM/MM scheme was to generate orbitals embedded into point charges with the necessary BH-LYP functional to perform the DSCF and DFT/MRCI computations.

3.5 Properties: DFT-MRCI, Vibes, Gradienator

Geometry optimisation provides, as the name suggests, an optimised geometry of the chromophore and its close surroundings, either by PW at the very beginning of the process or also with QM/MM if a ML is included in the calculation. The outputs of a QM/MM calculation with Turbomole as the QM program are used to perform DSCF runs to generate orbitals and thus reference states for DFT/MRCI. These runs must be performed with BH-LYP, the basis choice depends on the user and the system under investigation. Grimme dispersion correction can also be included in this step. DFT/MRCI calculations are performed using the tight parameter set and a selection threshold of 0.8 eV. In standard computations, twenty roots, i.e. the ground state and nineteen excited states, were computed within a reference space including 8 electrons and 8 orbitals, allowing only singly and doubly excited configurations. In order to improve the results, the calculation is performed twice, the resulting configuration of the first run being the reference configuration of the second. The results obtained after a DFT/MRCI calculation are the state energies at the given geometry. Results for all transitions from ground state to excited states include energies, rate constants, oscillator strengths as well as the molecular orbitals (MOs) involved in the transitions. The oscillator strength of a transition is an indicator of its probability. It is directly linked to the spatial overlap of MOs. A small overlap between initial and final MOs will lead to a small oscillator strength and thus small probability for the phenomenon to occur. Charge transfer between two different molecules is mostly associated with a low oscillator strength. To explain why charge transfer transitions can be visible experimentally, a new component has to be included, the vibrational states.

Gradienator [62] is a tool developed by Fabian Meitza. Its purpose is to include vibrational effects on top of DFT/MRCI computed properties. This is achieved by combining a frequency calculation on the optimised state of interest with the results of the DFT/MRCI computation. The user can choose the number of normal modes to include as well as the number of generated sampling points along these modes. The program will then perform single point DFT/MRCI computations on the generated structures, providing combined spectral properties for the computed ensemble. Out of these calculations, Gradienator will extract results that will be used by the Vibes program [63] [64] [65] in a second step to derive radiative and non-radiative rate constants for transitions between different states.

Chapter 4

The MIA chromophore

This chapter will present the works that document how the surrounding affects the properties of the MIA chromophore. The group of Prof. Janiak performed experiments (figure 4.1) measuring the emission intensity of MIA (F1 in figure 4.1) in different crystalline media. They found that the emission intensity was modified by the medium. The chromophore embedded into the MOF MIL-53(Al) has the most intense emission, while the organic crystal of MIA has the lowest intensity.

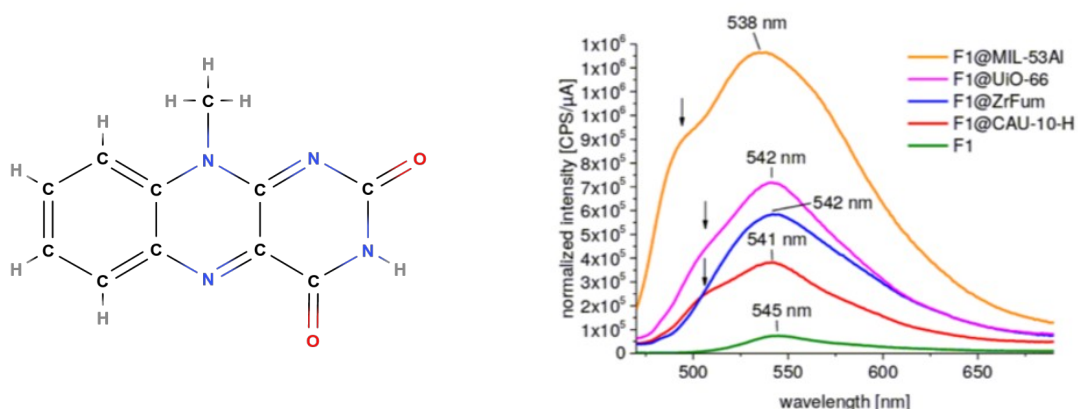


Figure 4.1: The MIA chromophore on the left and the experimental emission spectra of MIA (F1) in crystal or embedded into different MOFs on the right.

After further discussions with the experimentalists, the focus was set on three systems:

- The organic crystal of MIA
- MIA embedded into MIL-53(Al)
- MIA embedded into MOF-5

4.1 MIA in its organic crystal

The unit cell of the MIA crystal is composed of two molecules. It was optimised with Quantum Espresso using the described procedure with cell parameters constrained to the experimental value, as a non-realistic deformation occurred upon free optimization. A bulk of 1024 individual molecules, i.e. 8 replicas of the unit cell in x, y and z direction, was created for further investigations with QM/MM methods.

All calculations were performed with the PBE0 hybrid functional and the 6-31G* basis set using Gaussian16 for the QM-part and AMBER for the MM-part. Up to three molecules were included in the QM part. To study the effect of a partially mobile environment, calculations with and without mobile MM layers have been conducted.

As apparent from figure 4.2, there are two different π - π -stacking modes for the MIA molecule in its organic crystal: One which includes π - π -interactions between terminal phenyl rings (1-2 in fig 4.2) and another mode including interactions of one terminal phenyl and the middle ring with terminal and middle phenyl rings of the neighbouring molecules (2-3 in fig. 4.2).

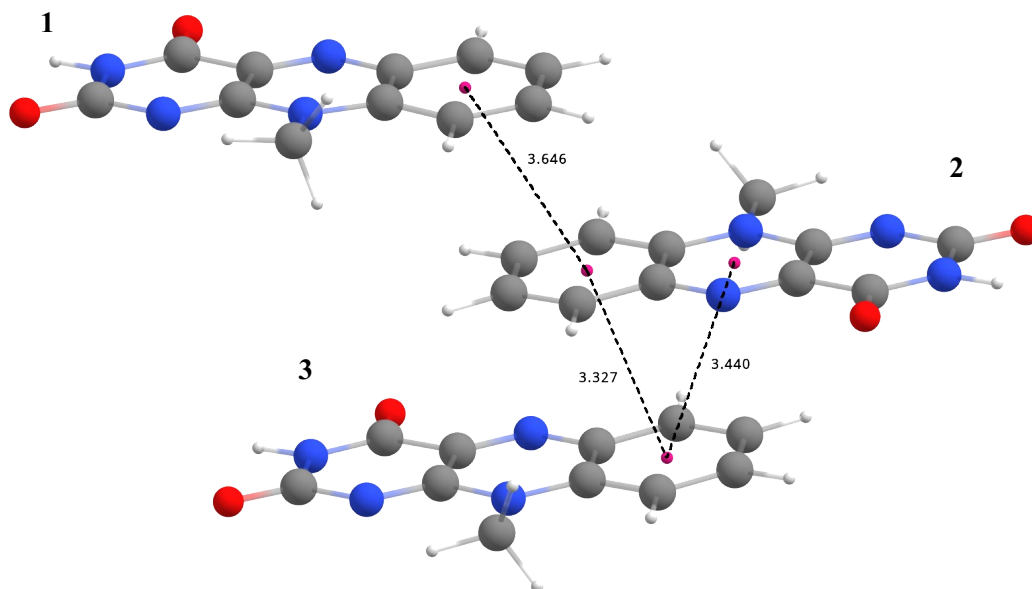


Figure 4.2: π - π stacking of MIA in crystal, distances are given in Ångstrom.

Among the six possible setups that were explored, convergence could not be obtained in the setup with two MIA molecules and a medium layer (ML). Results for the vacuum computation and setups including one to three MIA molecules with and without ML are presented in table 4.1.

Table 4.1: Spectral properties of one MIA in vacuum and 1, 2 or 3 molecules embedded into the organic single crystal. Models including a medium layer contain “ML” in the first row. Experimental excitation wavelength and maximum emission of the crystal are 440 nm is 545 nm.

	Vacuum	1 MIA	1 MIA ML	2 MIA (1-2)	2 MIA (2-3)	3 MIA	3 MIA ML
Absorption (nm)	412.0	418.6	419.0	443.7	447.8	449.8	457.6
Emission (nm)	527.5	510.8	517.0	534.2	531.7	540.0	560.1
Rate constants (s ⁻¹)	5.22 x 10 ⁷	5.36 x 10 ⁷	5.14 x 10 ⁷	5.95 x 10 ⁷	1.95 x 10 ³	5.6 x 10 ⁶	1.60 x 10 ⁷

At first, clusters with one QM molecule in the centre are compared to single molecule computations in vacuum (1st to 3rd column in table 4.1). Computed wavelengths for absorption and emission as well as rate constants were similar for all three cases with only one MIA molecule. These computations could not give any explanation for the weak emission intensity in the crystal, the computed rate constants are comparably large and all in the same range (51-54 x 10⁶).

For two MIA molecules the results largely differ, depending on the orientation of the included MIA chromophores. For the 1-2 configuration with small π overlap, a rate constant with the same order of magnitude as in the one MIA case is obtained. The 2-3 model with larger π -overlap generates a rate constant that is 3 orders of magnitude smaller. In both models, emission wavelengths are blue-shifted by ca. 10 nm and therefore closer to the experimental value as in the one MIA case.

The difference in the emission rate constant results from the MOs involved in the transition. Figure 4.3 shows the electronic density difference between the S₁ and S₀ states. The 1-2 stacking on the left corresponds to a local π - π^* transition occurring on a single molecule. The 2-3 stacking with more π -overlap on the right constitutes a charge transfer from one molecule to the other resulting in a non-radiative transition.

The absorption and emission results for three MIA molecules yield the closest match to the experimental findings. In the model including a movable medium layer, the geometrical changes upon excitation are larger than without the ML, causing the difference in the fluorescence rate constant. It is ten or five times smaller than the vacuum rate constant. By looking at the electron density difference for the model including three molecules (fig 4.3c) it is still visible that the emission process involves is a charge transfer, but it also has a local contribution.

As a conclusion, the lowering of the emission intensity of MIA in its molecular crystal environment can be reproduced by considering at least three π -stacked molecules. Herein, the transition from the first singlet excited state to the ground state has both, charge transfer but also a π - π^* local transition character.

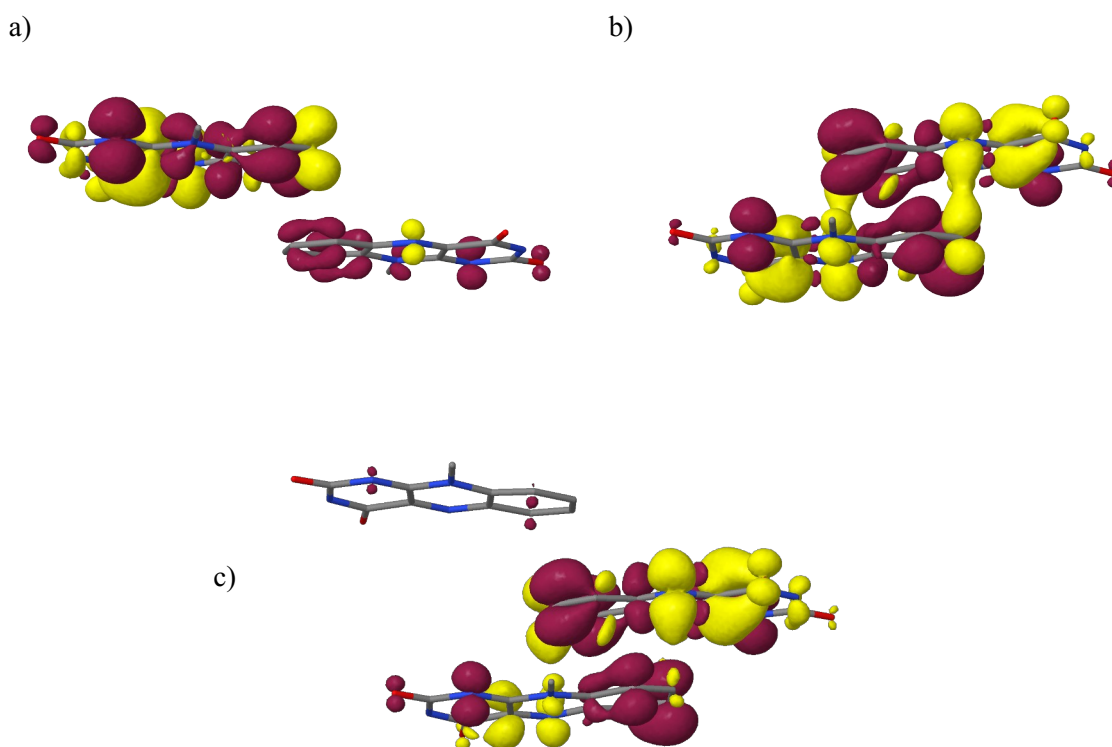


Figure 4.3: Electronic density difference at S_1 geometry for S_1 to S_0 transition for (a) 2 MIA in the small stacking configuration (1-2), (b) 2 MIA in the large stacking configuration (2-3) and (c) 3 MIA. Density loss is pictured in red, density gain is yellow.

4.2 Structural optimisation of MIA@MOFs

4.2.1 MIA@MOF-5

The metal-organic framework MOF-5 was built from the organic linker benzene-1,4-dicarboxylic (bdc) acid and a metallic core Zn_4O [66] [67]. The MOF-5 structure shows two different possible cages for MIA, one named INWARD where the hydrogen atoms of bdc linkers point inward the cage and the other named OUTWARD where the hydrogen atoms of bdc linkers point outward the cage (see figure 4.4).

In each cage, multiple QE optimisations have been performed to identify a possible most favourable position but none could be identified. This result was comforted by confocal multi-parameter fluorescence image spectroscopy (MFIS) (figure 6 in publication) showing that no specific orientation of the transition dipole moment could be detected, i.e. there is no specific orientation of MIA in MOF-5.

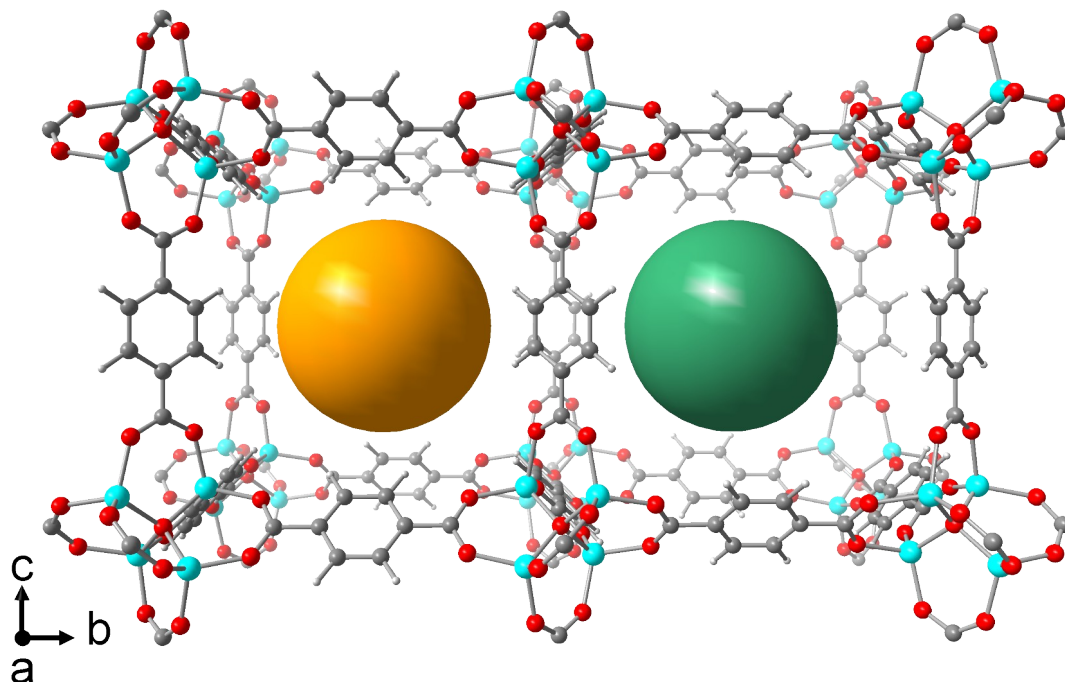


Figure 4.4: The two MOF-5 cavities, INWARD on the left (orange sphere) and OUTWARD on the right (green sphere).

Force field parameters were adapted from the work of Vanduyfhuys et al.[56] QM/MM optimisations were performed with the inclusion of a medium layer composed of bdc linkers, Zn₄O metal cores had to be excluded from the latter as artificial distortions of the metal bonds occurred upon optimisation.

4.2.2 MIA@MIL-53(Al)

The second MOF studied filled with MIA molecules was MIL-53(Al). Its structure is made of chains of Al and OH linked to four other chains by the bdc linker (same as in MOF-5). The MIL-53 MOFs can reversibly change its pore size through a “breathing effect” in response to external stimuli [68]. Pores of MIL-53 MOF are of channel type, i.e. the theoretical length in one direction is infinite.

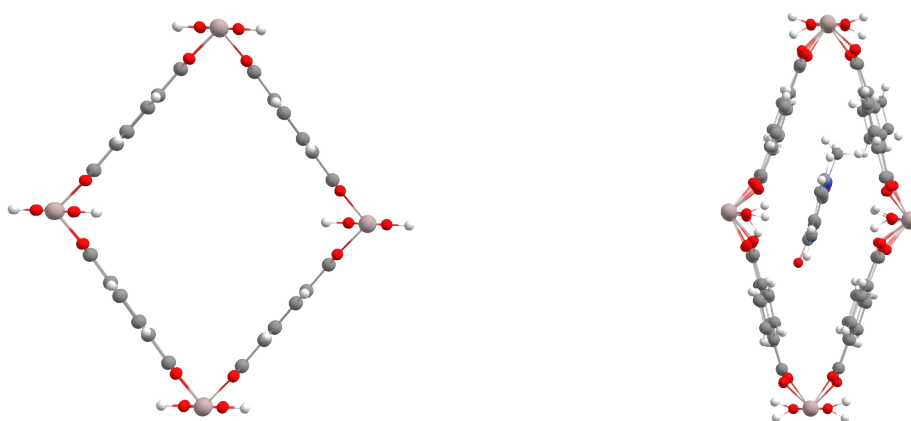


Figure 4.5: Representation of one MIL-53(Al) channel, empty (left) and filled with a MIA chromophore (right).

Characterisation of the “breathing effect” and its reversibility was performed through PW-SCF calculations (see figure 4.5). The unit cell of MIL-53(Al) was expanded to a 3x1x1 supercell (alongside the channel direction), large enough to hold a MIA molecule inside. Structural parameters from the experiment were reproduced by PW calculations of MIL-53(Al) with and without MIA (table S3 supporting information). The ideal position of MIA within the channel was also investigated. The long axis of MIA was found to be always in alignment with the channel direction. This finding was also confirmed through MFIS analyses of MIA@MIL-53(Al) (figure 6a panel 3 of Paper). No favourite location of MIA could be identified when translating the chromophore along the channel. A position where the

MIA molecule is held by weak polar interaction with the MOF was used for later calculation (figure 8 of associated paper).

To perform QM/MM calculations, a bulk was created incorporating nine channels (60x30x30 Ångstrom size) with one MIA located in the middle channel. Geometry optimisation for the ground and first single excited state were carried out using the PBE0 functional and the 6-31G* basis set for the QM part and AMBER for the MM part. Force field parameters related to aluminium were obtained using FFTK on a cluster model created by Vanduyfhuys et al. (see figure 3.3) [61]. A MM mobile layer was defined containing residues within a distance of 7.5 Å around the MIA chromophore. The remaining atoms were frozen to their positions after QE optimisation. Optimised ground and excited state geometries of MIA are distorted wrt. to the vacuum structure, as the MIL-53(Al) channels narrow upon geometry relaxation. (figure 4.6)

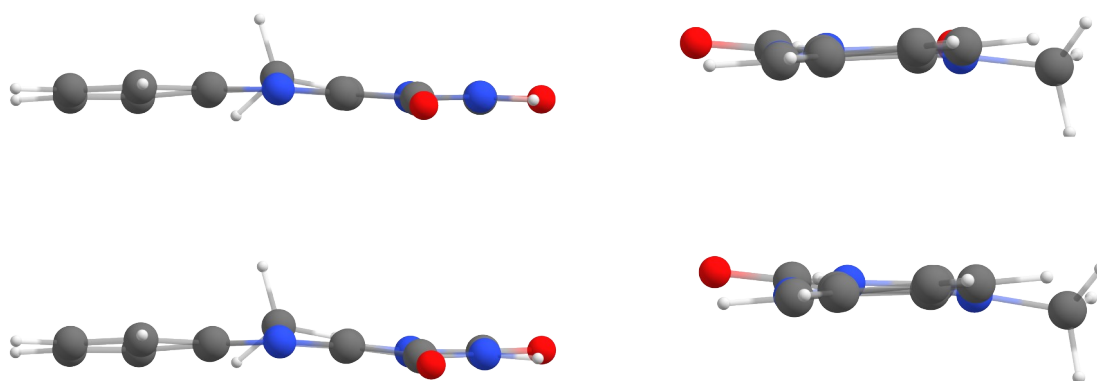


Figure 4.6: Optimised MIA embedded in MIL-53(Al) at the ground state (up) and the first excited state (down).

4.3 DFT/MRCI computations of MIA@MOFs

DFT/MRCI calculations of MIA in the IN- or OUTWARD cages of MOF-5 and inside a channel of MIL-53(Al) were performed using the same parameters as for the organic crystal of MIA. The computed absorption and emission spectra in the two MOF-5 cages are, compared to vacuum calculations, very similar in wavelength and in oscillator strength (see figure 4.7).

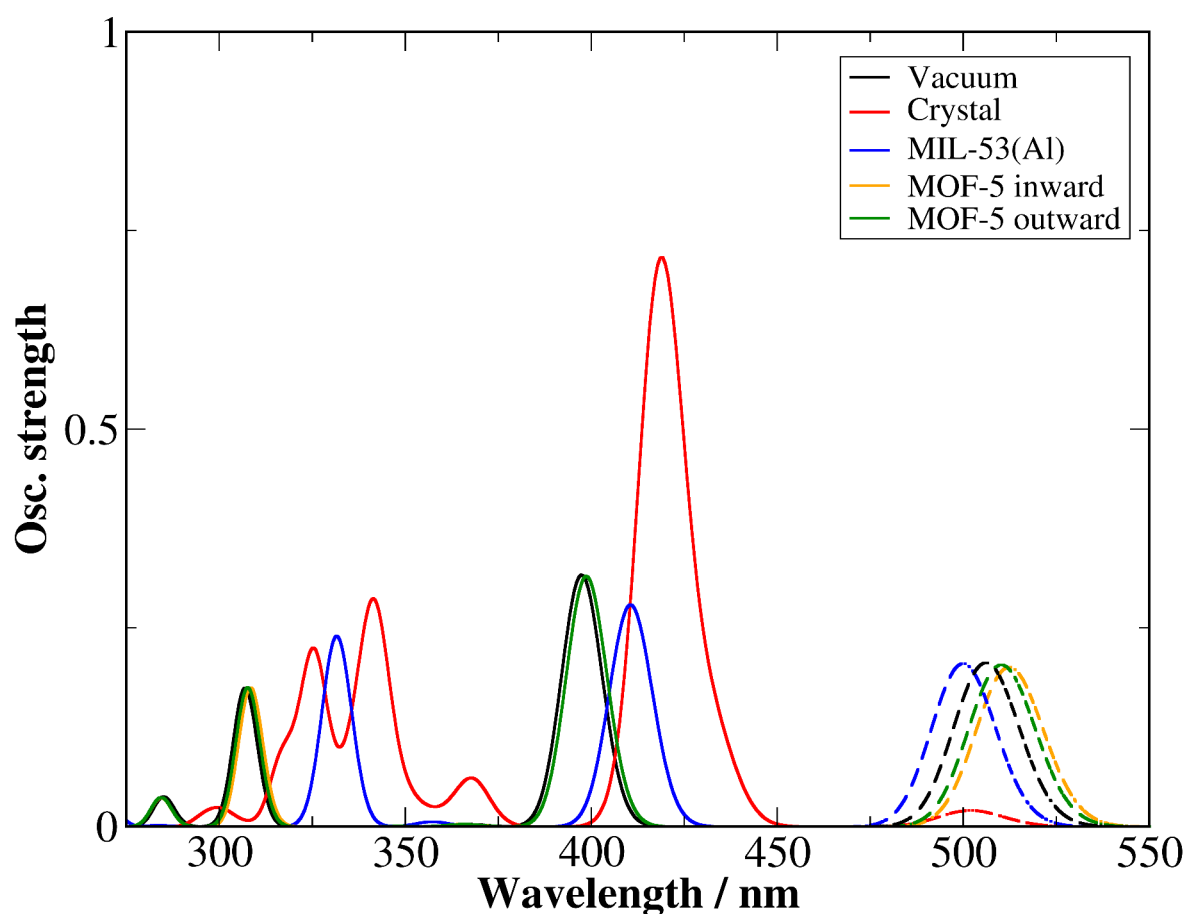


Figure 4.7: Computed absorption (full line) and emission (dot line) spectra of MIA in vacuum (black), three MIA in crystal (red), MIA in MIL-53(Al) (blue) and MIA in MOF-5 in the INWARD (orange) and the OUTWARD (green) pore.

The electronic structure of MIA is not largely influenced by both MOFs (figure 4.8), this is true for ground and excited states. In MIL-53(Al), a red shift in absorption can be noticed, apparently a result of its slightly distorted geometry.

Electronic studies of the emission phenomenon show that the transition of MIA has the same character in vacuum, in MIL-53(Al), and in the MOF-5 INWARD and OUTWARD configurations (see figure 4.8). The emission is a π - π^* transition, involving the HOMO and LUMO MOs of MIA.

The charge transfer transition found in the crystal cannot be observed here as the formation of MIA π - π aggregates is unfavourable due to the narrowness of the MOF environment.

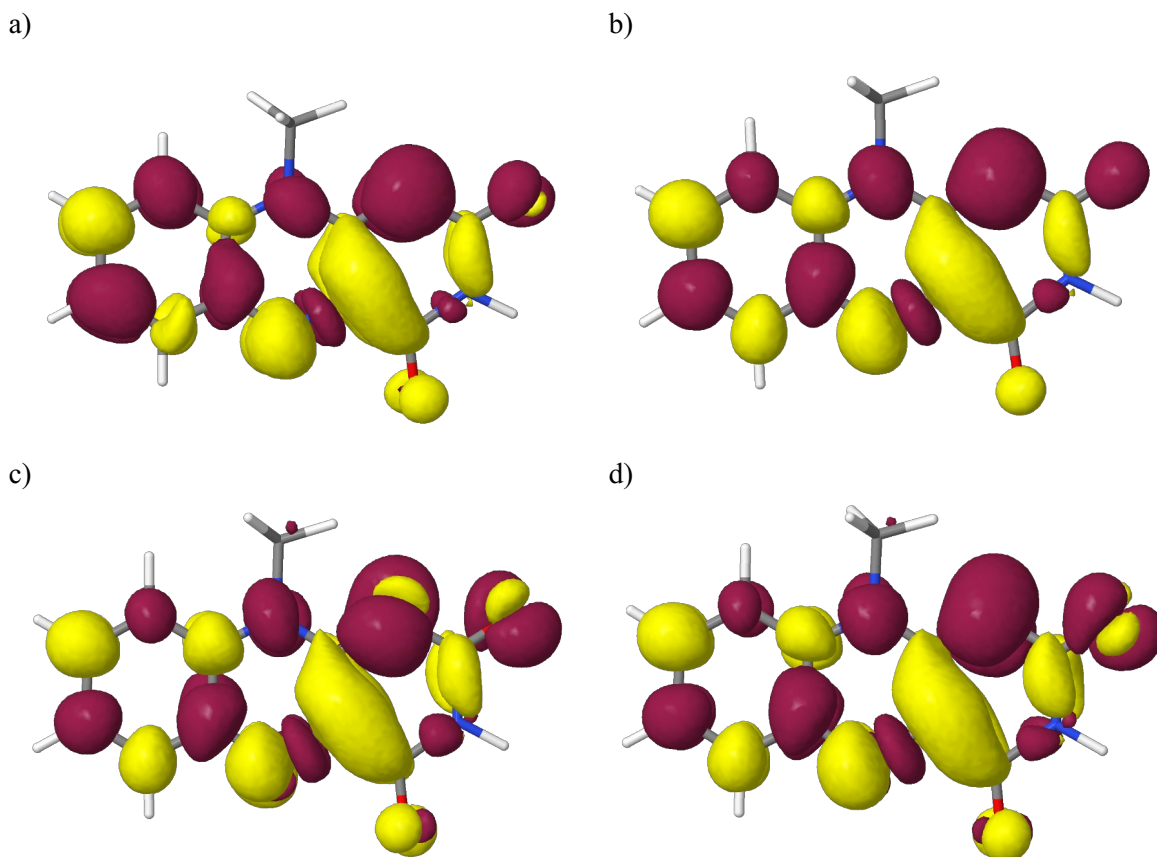


Figure 4.8: Electronic density difference between S_1 and S_0 for MIA in vacuum (a), MIL53 (b), INWARD (c), OUTWARD (d). Red is density loss, yellow is density gain.

Chapter 5

Co-crystals of roseolumiflavin

In 2022, Vasylyeva-Shor et al.[9] reported about the tuning of roseolumiflavin (R) photophysical properties by crystallising it with three different co-crystalites: acetylenedicarboxylic acid, diiodotetrafluorobenzene and 2,4 diaminopyrimidine. A second series of co-crystals were produced, the R-D and R-DE co-crystals (see figure 5.1). Photophysical measurements revealed a blue shift of the emission wrt. the roseolumiflavin single crystal upon addition of co-crystallites (visible in figure 5.2).

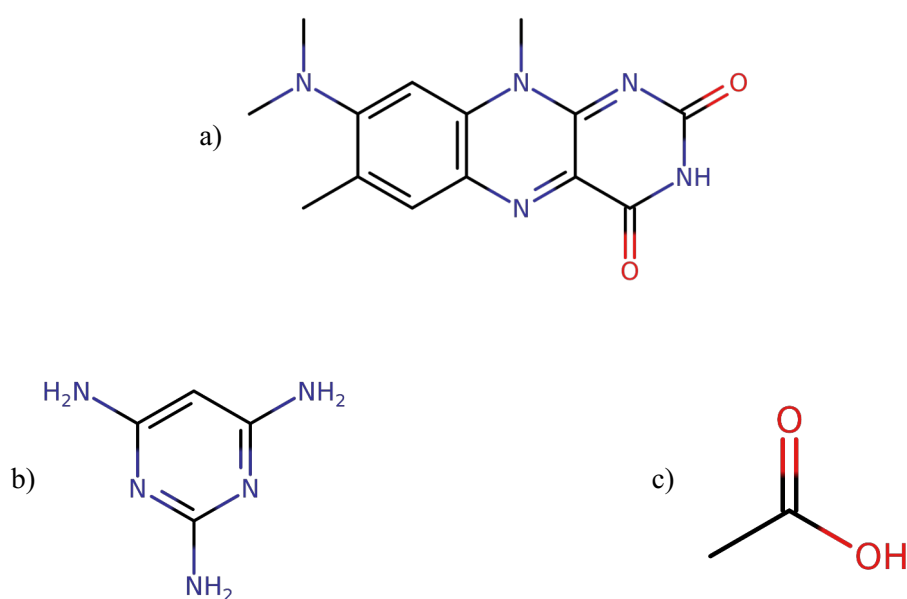


Figure 5.1: a) Roseolumiflavin R, b) 2,4,6-Triaminopyrimidin D and c) acetic acid E.

The aim of the theoretical calculations was to explain the reason for the observed blue shifts that occurred in the co-crystallites by excitation with the same wavelengths. The R, R-D and R-DE unit cell structures were provided by the group of Dr. Vasylyeva-Shor. They were refined through PW calculation. The changes of the three unit cells upon PW treatment are collected in table 5.1. Overall, an expansion along the a, b and c axes by ca. 2.3%, 0.5% and 1.4% were observed in the R, R-D and R-DE

structures. In order to perform QM/MM computations, clusters with 18000, 14080 and 13600 atoms were generated. QM/MM input files were created following the same procedure as with the MIA crystal discussed in chapter 4.

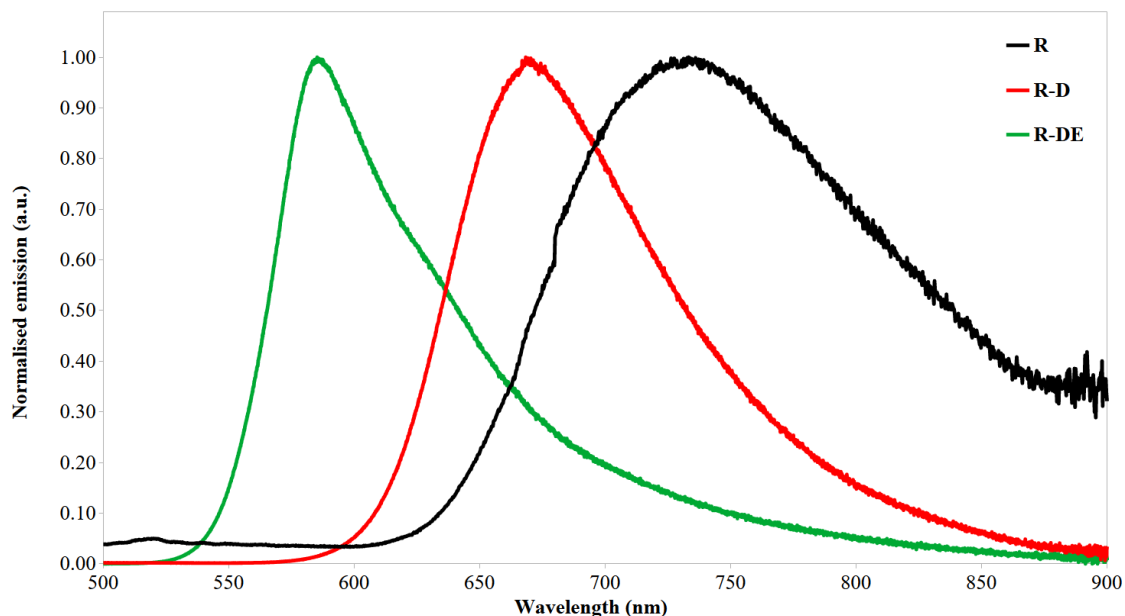


Figure 5.2: Experimental normalised emission wavelength of R, R-D and R-DE (co-)crystals. Excitation wavelengths are 423 nm for R and R-D, 400 nm for R-DE.

QM/MM computations were performed using the PBE0 hybrid functional with the def2SVP basis set and Grimme-D3 dispersion correction. TD-DFT was used to compute excited state geometries. Following the results of the MIA crystal investigations, no medium layer (i.e. no movable MM part) was used in the calculations.

Prior investigations with DFT/MRCI lead to strongly blue-shifted emission wavelengths and spurious description of excitations. Also, the application of the DFT/MRCI method would limit the model to only three molecules within the QM layer. TD-DFT on the other hand performed well in the description of the expected charge transfer states and emissions, hence the study was continued using this method.

A second set of QM/MM computations using the CAM-B3LYP functional instead of PBE0 was performed in parallel. A similar strategy was also applied by Karasulu and Thiel [69] [70] in a previous study on the R molecule in vacuum/solvent. For the current system, CAM-B3LYP however generated

similar problems in the description of the excited states as in the DFT/MRCI computations. For an overview, results generated with CAM-B3LYP, DFT/MRCI and PBE0 are collected in appendix 3. Hence, only PBE0 based results were considered in the following.

Table 5.1: Experimental and computed cell parameters of R, RD and RDE (co-)crystals

Cell param.	a	b	c	α	β	γ
R exp	12.75	7.03	14.33	90.00	99.14	90.00
R theo	12.63	7.58	14.34	90.00	99.32	90.00
diff _{theo-exp}	-0.12	0.55	0.01	0.00	0.18	0.00
R-D exp	8.20	13.78	14.56	78.89	83.19	75.89
R-D theo	8.16	14.00	14.63	77.88	83.35	75.81
diff _{theo-exp}	-0.04	0.22	0.07	-1.01	0.16	-0.08
R-DE exp	7.38	8.23	22.26	92.70	93.06	115.50
R-DE theo	7.69	8.26	22.18	92.48	92.81	118.80
diff _{theo-exp}	0.31	0.03	-0.08	-0.22	-0.25	3.30

5.1 R single crystal

In the previous part, the importance of a proper definition of the QM part has been emphasised. QM parts were created with different arrangements including molecule **1** in figure 5.3 and up to three of its direct neighbours, resulting in eight multimers:

- The monomer: 1R
- Three dimers: 2R-12, 2R-13 and 2R-14
- Three trimers: 3R-123, 3R-124 and 3R-134
- One quadrimer: 4R-1234

Table 5.2: Computed properties for the first bright absorption, corresponding density differences are shown in supplementary information of the associated paper. H = HOMO, L = LUMO, LE= Local Excitation, DL= Delocalised.

Model	Transition	Character	Wavelength (nm)	Oscillator strength
1R	$S_0 \rightarrow S_1$			
	$H \rightarrow L$	LE	403.5	0.5674
2R-12	$S_0 \rightarrow S_4$			
	$H-1 \rightarrow L$	LE	406.0	0.7220
	$H \rightarrow L+1$	LE		
2R-13	$S_0 \rightarrow S_4$			
	$H-1 \rightarrow L$	LE	405.6	0.6720
	$H \rightarrow L+1$	LE		
2R-14	$S_0 \rightarrow S_2$			
	$H-1 \rightarrow L$	LE	410.1	1.3906
	$H \rightarrow L+1$	LE		
3R-123	$S_0 \rightarrow S_9$			
	$H-1 \rightarrow L+1$	LE	404.8	0.7100
3R-124	$S_0 \rightarrow S_6$			
	$H-2 \rightarrow L$	LE	410.4	1.4945
	$H-1 \rightarrow L+1$	LE		
	$H \rightarrow L+2$	LE		
3R-134	$S_0 \rightarrow S_6$			
	$H-2 \rightarrow L$	LE	411.1	1.5975
	$H-1 \rightarrow L+1$	LE		
	$H \rightarrow L+2$	LE		
4R-1234	$S_0 \rightarrow S_{12}$			
	$H-3 \rightarrow L$	LE	409.8	1.6511
	$H-1 \rightarrow L+2$	LE		
2R-D	$S_0 \rightarrow S_4$			
	$H-1 \rightarrow L$	DL	420.3	0.6610
	$H \rightarrow L+1$	DL		
2R-DE	$S_0 \rightarrow S_1$			
	$H \rightarrow L$	DL	465.9	0.4336
	$S_0 \rightarrow S_4$			
	$H-1 \rightarrow L+1$	DL	413.0	0.8568

Molecules number **2** and **3** differ to **1** by their π -stacking, defined by the distance between the centres of their middle rings. Molecule **4** is located near the O-terminal of the first molecule (**1**) molecule creating two hydrogen bonds (fig 5.3).

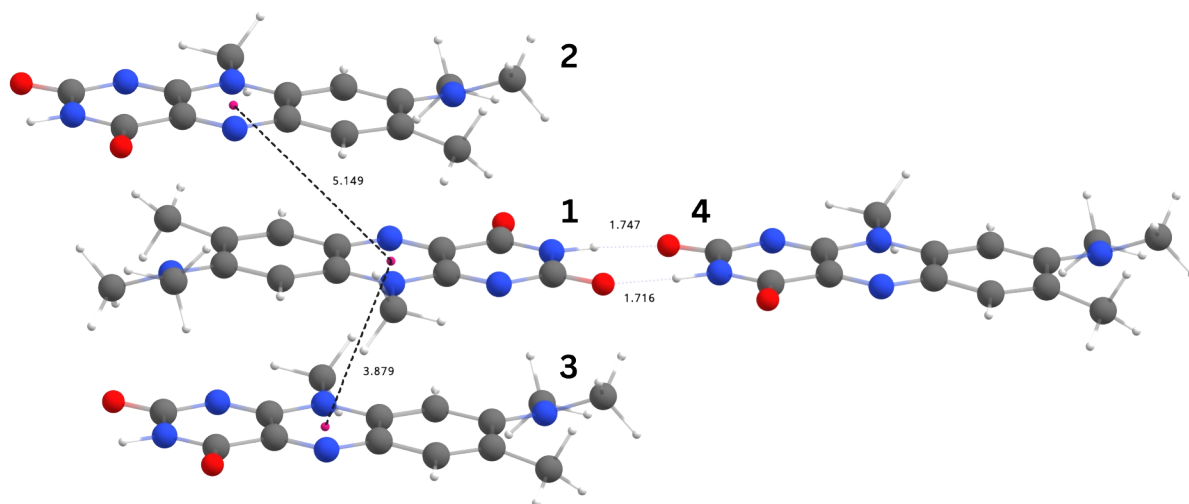


Figure 5.3: Crystal arrangement of R in single crystal. Distances are given in Ångstrom.

Investigations on the ground state absorption of all models, summarised in table 5.2, revealed that for all models the first bright singlet transition is a local excitation (LE) in one or several molecules at wavelengths between 400 and 410 nm (the experimental excitation wavelength is 423 nm).

Computed emission properties for the eight models of R in their crystal environments are collected in table 5.3. In the first excited state of the 2R-14 model, a proton transfer occurs creating an emission in the infra-red range, hence rendering the results for this model unusable. TD-DFT calculations on the S_1 state geometries all converge to the same emission process with charge transfer (CT) character. In the trimer and quadrimer models, where molecule **1** has the central position, the HOMO is always located on the upper (**2**) or the bottom (**3**) molecule while the LUMO is on **1**. The energy of the emission is mainly influenced by one parameter: The stacking distance (see fig.5.3) between the two molecules involved in the CT. When the CT is between **1** and **3** (in 2R-13 and 2R-134) with smaller stacking distance, the emission wavelength is red shifted compared to CT between **1** and **2** (see 2R-12 and 3R-124). Addition of molecule **4** leads to a weak red shift (see 2R-12 vs. 3R-124, 2R-13 vs. 3R-134 and 3R-123 vs. 4R-1234).

Table 5.3: Computed emission properties for 1, 2, 3 or 4 R molecules (MO localisation is shown under brackets wrt. figure 5.3 number attribution) in R, R-D and R-DE (co-)crystals. Exp. emissions are 733 nm, 668 nm and 585 nm.

	Wavelength (nm)	Oscillator strength	MOs	Characters
1R	427.62	0.5158	H \rightarrow L	LE
2R-12	672.29	0.0018	H \rightarrow L	CT
2R-13	698.35	0.0018	H \rightarrow L	CT
2R-14	3700.22	0.0001	H \rightarrow L	CT
3R-123	693.34	0.0012	H(2) \rightarrow L(1)	CT
3R-124	688.39	0.0020	H(2) \rightarrow L(1)	CT
3R-134	729.20	0.0011	H(3) \rightarrow L(1)	CT
4R-1234	700.49	0.0014	H(2) \rightarrow L(1)	CT
2R-D	691.97	0.0010	H \rightarrow L	CT
2R-DE	663.51	0.0465	H \rightarrow L	CT

Except for 1R, all computed emissions have a CT character. In the trimer and quadrimer models, emission is due to a CT from **2** to **1**. These results must however be interpreted with caution, as the description of MOs of the middle molecule **1** is certainly more complete than those of **2**, **3** and **4**, which only have one direct interaction with the neighbouring molecule **1**. This is specifically true for **2**, which is more spatially isolated than **3** in our model. The charge transfer from molecule **3** to **1** has the lowest energy and thus likely corresponds to the emission observed experimentally, hence emission in single crystal R occurs between two species with the largest π -overlap.

5.2 R-D co-crystal

In the binary co-crystal R-D, the D molecule prevents hydrogen bonded interactions between R molecules (fig 5.4-A). The inter layer distance between R molecules is ca. 3.7 Å (fig 5.4-B). Two R molecules were included into the QM layer, the rest of the R-D co-crystal is inside the low layer (non movable MM layer), the model is named 2R-D in tables 5.2 and 5.3.

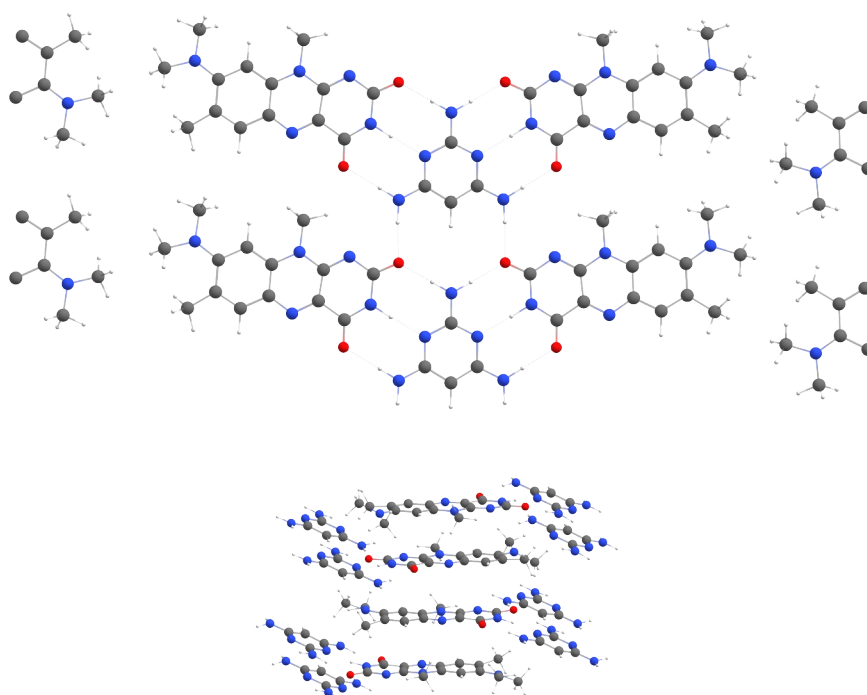


Figure 5.4: R-D co-crystal arrangement, planar (upper) and stacking (lower) views. The stacking distance is 3.681 Å (in the ground state). In the planar view, the four molecular fragments correspond to four other R molecules.

TD-DFT calculation on the ground state geometry (see table 5.2) revealed that the excitation process is a LE with high oscillator strength (ca. 0.66) involving both molecules (see appendix 3 figure A3.1). The excitation stays local, because each of the QM molecules has essentially the same environment and description of the latter, thus the energy levels of the molecules are the same: HOMO and LUMO of both R molecules are almost degenerate, resulting in HOMO-1, HOMO, LUMO and LUMO+1 of the dimer being delocalised over the full system.

In this case, the 2R-D model is sufficient. Unlike in the R single crystal, where at least three molecules were needed to cover the most important interactions, all molecules in this system share equivalent π -stacking contributions toward the upper and lower molecule. Adding a third or fourth molecule to the QM layer would create unequivalent descriptions of the electronic environment between side and centred molecule, hence yielding artefacts that may lead to misinterpretation.

Computed emissions for 2R-D are comparable to 2R-13 (single crystal) (see table 5.3). The emission is the result of a charge transfer with a similar wavelength as in 2R-13. It is blue-shifted by ca. 40 nm wrt. the 3R-134 model. This was expected, as the stacking distance is similar and no side-R molecules are present which would induce the aforementioned weak red-shift.

5.3 R-DE co-crystal

In the ternary co-crystal R-DE, the addition of the acid E induces a protonation of the D molecule, the corresponding hydrogen-bonded network is visible in figure 5.5.A. Similarly to the R-D co-crystal, direct interactions between R molecules are excluded due to the presence of the co-crystallite. The parallel alignment of R molecules differs from R-D. By looking along the short axis of R, a displacement along the long axis is visible between all molecules of different layers (see fig. 5.5.B). Layers of R are arranged by pairs, these bi-layers are shifted to the next bi-layer along the short axis of R (see fig. 5.5.C). Distance between two R molecules of the same bi-layer is ca. 5.7 Å and ca. 7.1 Å for molecules of different pairs of layer. The QM/MM computation was performed with 2 R molecules in the QM layer and no movable MM layer; the model is referred as 2R-DE.

The computed excitation process of the R-DE co-crystal is similar to R-D. In 2R-DE, two possible excitations of the same kind were identified, both involving delocalised MOs over the two molecules with an oscillator strength of ca. 0.4 and 0.8 for S_0 to S_1 and S_0 to S_4 (see table 5.2). The 2R-DE emis-

sion characteristics presented in table 5.3 show a large blue-shift wrt. the single crystal. Also this was expected due to the long stacking distance between the molecules directly involved in the charge transfer. Other models containing up to four molecules have been investigated but the error created by asymmetrical modelling of the electronic surrounding lead to spurious and finally unusable results.

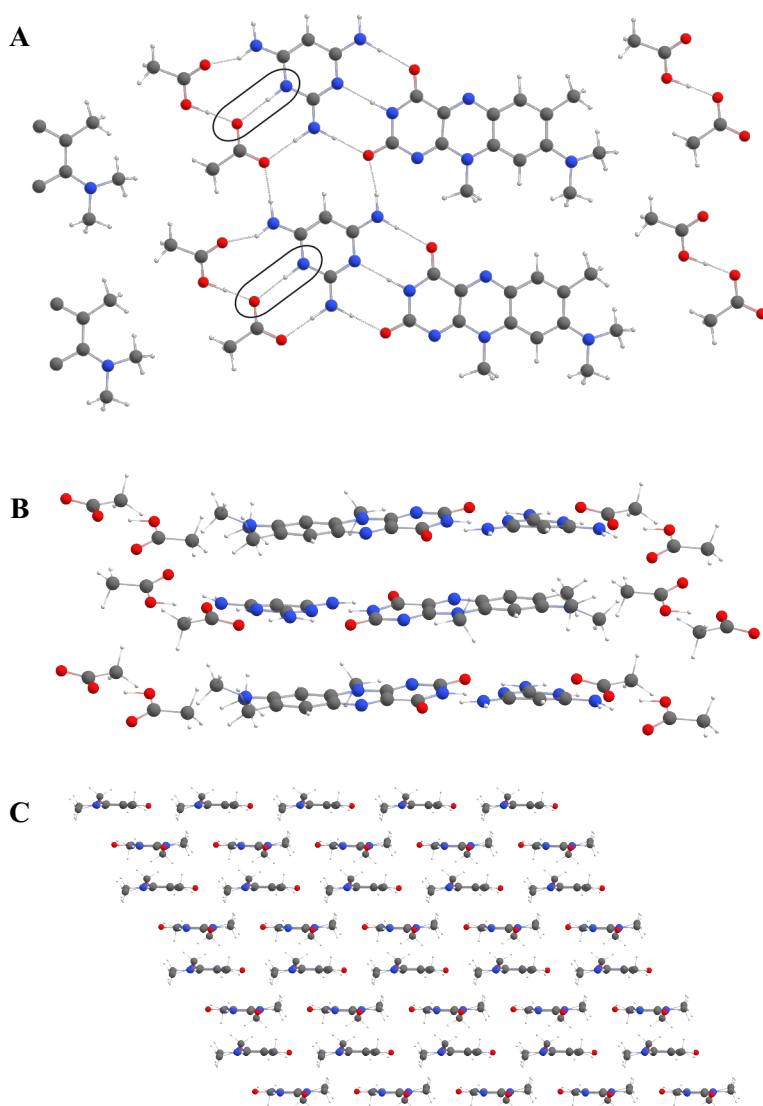


Figure 5.5: R-DE co-crystal arrangement. A) Planar view of the crystal arrangement. Fragments visible on the left are from other R molecules. B) Stacking view along R short axis. C) Stacking view along the long axis of R, co-crystallites D and E are omitted.

5.4 Conclusions

TD-DFT calculations were performed on three crystal structures containing the R chromophore. Numerous QM/MM models were derived from the structures to analyse the different interactions between one R molecule and its surrounding.

All calculations on electronic properties in the ground state show that the excitation occurs as a local phenomenon involving the respective HOMO and LUMO orbitals of the separate molecules. The energy difference between the frontier MOs in the ground state is unaffected by the surrounding environment. This leads to very similar excitation energies in all three (co-)crystals. Emission processes have CT character in all models that contain at least two R molecules. Through the investigations on the R single crystal, two parameters were found that influence the energy of the CT emission. The stacking distance is the stronger effect, the longer the distance between the two molecules participating in the charge transfer, the higher the transition energy. A second effect observed is the inclusion of side molecules in the QM layer which cause a weak red-shift of the emission wavelength. However, the exact characteristics of this interaction could not be unveiled and would require more extensive investigations.

R-D and R-DE co-crystal arrangement prevent linear contacts between R molecules that were causing the latter effect. Thus, the emission wavelength in the co-crystals only depends on the π -stacking distance of R molecules. In R-D, a small stacking distance makes the emission weakly blue-shifted whereas in the R-DE case the long stacking distance creates a strong blue-shift. It would, however, require more specific computations to assert this hypothesis.

Chapter 6

Phenazine derivatives

In light emitting devices, spin statistics lead to 25% of molecules ending up in an excited singlet state, 75% will reach a triplet state. In the latest generation of LED emitters, the latter 75% are converted into singlet states via thermally activated delayed fluorescence (TADF), leading to a theoretical efficiency of ~100 %. A “good” TADF emitter is a chromophore with a small energy difference ($\Delta E_{st} < 100$ meV [71]) between S_1 and T_1 , allowing a transition at room temperature. The reverse process (reverse intersystem crossing, rISC) describing the transition from T_1 to S_1 is also a major factor. The group of Prof. Janiak investigated three phenazine derivatives in solvents and in organic crystals, biphenylnitrile (BPN), meta-benzonitrile (mBN) and para-benzonitrile (pBN). The latter is already known in literature for its TADF properties [10]. In this study the three molecules, BPN, mBN and pBN, have been investigated in vacuum and in implicit toluene solvent. Crystals of mBN and pBN have undergone deeper investigations as TADF behaviour was reported by experimentalists (see figure 4 of associated publication).

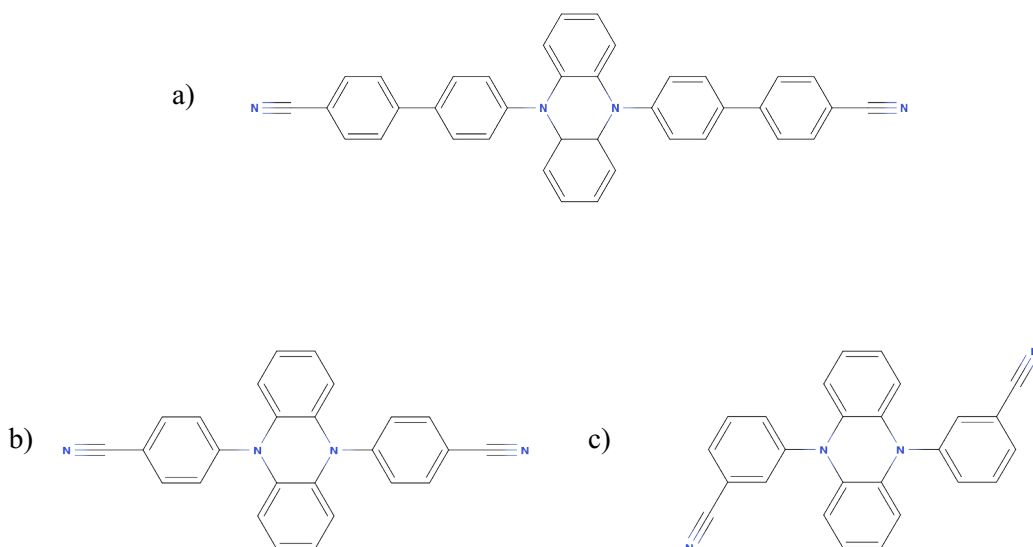


Figure 6.1: The three phenazine derivative studied in this work, a) BPN, b) mBN and c) pBN.

6.1 Static model calculations

The first investigations on the three phenazine derivatives were carried out using Gaussian16 for geometry optimisations with the PBE0 functional, the TZVP basis set and Grimme-D3 dispersion corrections. For computation of the excited states, TD-DFT was used for singlets and TDA was employed for triplets. The Polarizable Continuum Model (PCM) was used to simulate an implicit toluene environment. A single point calculation using Turbomole at the BH-LYP/TZVP level of theory was employed with COSMO for solvation. DFT/MRCI calculations with the R2022 Hamiltonian were performed using the standard parameters described in part 3.6. Computation of the excited states revealed that the inclusion of toluene environments does not notably affect the results as visible in table 6.1. However, the computed emission wavelengths are not in accordance with the experimental results, also the oscillator strength points toward a lack of emission, which does not agree with experimental observations.

Table 6.1: TD-DFT and DFT/MRCI results of excited states properties for BPN, mBN and pBN in vacuum or in toluene medium. Experimental emission wavelengths are noted in brackets under molecule name.

		TD-DFT		DFT/MRCI		
		Emission (nm)	Osc. Str.	Emission (nm)	Osc. Str.	ΔE_{st} (eV)
BPN (604 nm)	Vacuum	807	0.000	544	0.000	0.046
	Toluene	772	0.000	526	0.000	0.047
mBN (572 nm)	Vacuum	719	0.000	497	0.003	0.093
	Toluene	701	0.001	491	0.003	0.098
pBN (562 nm)	Vacuum	690	0.000	482	0.000	0.034
	Toluene	682	0.000	479	0.000	0.033

The influence of the torsion angle between the side groups to the phenazine central group has been studied by scanning the corresponding potential energy surfaces (figure 6.2). Both dihedral angles were varied from ca. 90° in 15° steps in +/- direction. The ΔE_{st} values are modulated by changing the described dihedrals, reaching values up to 177 meV for mBN and 279 meV for pBN (see fig. SI S30), minimal ΔE_{st} values are obtained for a rotation of maximally 15° in opposite directions. Generally, the oscillator strength (f) increases when moving away from the equilibrium value of 90°. Values tend to be larger when both side groups rotate in the same direction. The highest oscillator strengths are achieved when one angle is rotated to +/- 45° and the other one stays at its initial value, then f increases to 0.279 for pBN and reaches 0.032 for mBN (figure 6.2).

pBN	-45°	-30°	-15°	89.97°	+15°	+30°	+45°
-45°	0.235	0.127	0.041	0.001	0.024	0.088	0.165
-30°	0.238	0.131	0.041	0.000	0.027	0.098	0.175
-15°	0.275	0.146	0.043	0.000	0.036	0.128	0.233
89.97°	0.279	0.148	0.043	0.000	0.042	0.147	0.279
+15°	0.235	0.129	0.037	0.000	0.043	0.145	0.273
+30°	0.175	0.099	0.028	0.000	0.040	0.130	0.236
+45°	0.166	0.089	0.024	0.000	0.040	0.126	0.233

mBN	-45°	-30°	-15°	90.42°	+15°	+30°	+45°
-45°	0.031	0.017	0.008	0.003	0.004	0.011	0.026
-30°	0.032	0.018	0.007	0.003	0.004	0.012	0.027
-15°	0.032	0.018	0.007	0.003	0.005	0.014	0.029
90.42°	0.032	0.018	0.007	0.003	0.005	0.015	0.032
+15°	0.030	0.017	0.007	0.003	0.005	0.016	0.032
+30°	0.027	0.015	0.006	0.003	0.005	0.015	0.032
+45°	0.026	0.014	0.006	0.003	0.005	0.014	0.031

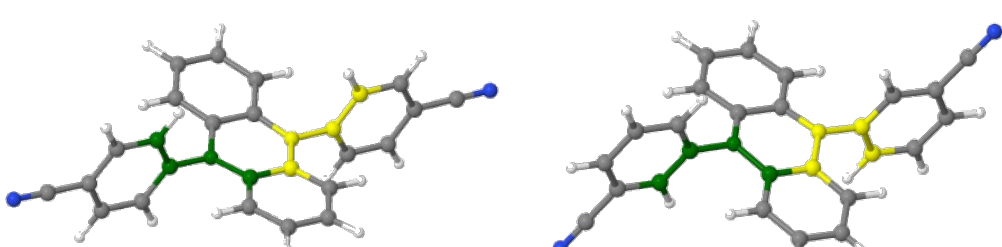


Figure 6.2: Change of oscillator strength by rotation of dihedral angles in pBN (left) and mBN (right). Modified dihedrals are pictured in green (vertical parameters in the table) and yellow (horizontal parameters).

6.2 Beyond the static model

Static calculations could not deliver clear conclusions for the experimentally obtained emission intensities or emission wavelengths; the computed oscillator strengths all indicate an absence of radiative emission. In order to improve our model, vibrational modes have been included into the description. Two hundred geometries were generated by zero-point-energy (ZPE) sampling for the optimised ground- and S_1 -state, obtaining distorted structures along their vibrational modes. DFT/MRCI computations with the R2016 Hamiltonian yielded a combined absorption and emission spectrum (see figure 6.3) with emission maxima at 547 nm for mBN and 573 nm for pBN, the average oscillator strength for mBN is ca. 0.004 and ca. 0.003 for pBN.

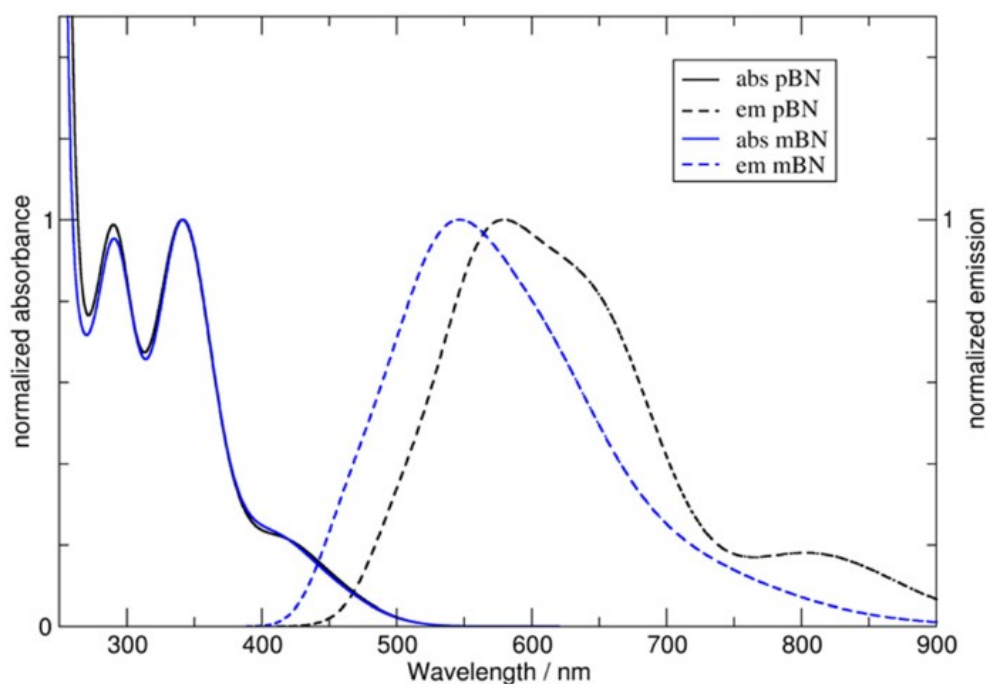


Figure 6.3: Combined computed absorption and emission of mBN and pBN in toluene

Rate constants for fluorescence, ISC and rISC have been computed with the Vibes program. Computations were performed using the static model and with sampling generated by the Gradienator program. The results of both computations are presented in table 6.2. The static rate constants for pBN are very small (~ 1.0), i.e. the decay to the ground state is not a radiative process according to this model. By including vibrational contributions, not only the fluorescence rates but also ISC and rISC rise in value. In this scenario, a TADF mechanism is plausible. Also, as mentioned by the experiment-

alists, the calculated rate constants for rISC point toward the fact that pBN is a more potent TADF emitter than mBN.

As apparent from figure 6.2, the phenyl groups are in perpendicular orientation wrt. the phenazine core. Vibrations will distort the molecule away from this perpendicular position, generating a non zero oscillator strength and a more realistic emission wavelength. Embedding the pBN and mBN molecules into their own organic single crystal environments may force the molecules into different configurations, possibly enhancing TADF.

Table 6.2: mBN/pBN in vacuum rate constants (s^{-1}).

		Fluorescence ($S_1 \rightarrow S_0$)	ISC ($S_1 \rightarrow T_1$)	rISC ($T_1 \rightarrow S_1$)
mBN	Static	8.30×10^5	1.18×10^5	3.20×10^3
	Gradienator	1.05×10^6	1.31×10^7	5.19×10^5
pBN	Static	1.28×10^0	1.46×10^0	7.88×10^{-1}
	Gradienator	1.01×10^6	7.82×10^7	2.28×10^7

6.3 Crystal structure calculations

In their experimental investigations, Dietrich et al. found that:

- The BPN crystal showed no TADF
- The mBN crystal “shows weak TADF”
- The pBN crystal “is a potent TADF emitter”

Computational investigations on pBN and mBN crystals have been conducted to elucidate these observations.

After PW treatment, a bulk of 1160 molecules for mBN and 840 molecules for pBN was created. QM/MM calculations were performed using the PBE0 functional and the TZVP basis set; the Grimme-D3 dispersion correction has been used with the Gaussian16 program. TD-DFT and TDA were used for computation of excited singlet and triplet states, respectively. Frequency calculations have been conducted to validate the structure and to be later used in combination with DFT/MRCI within the Gradienator and Vibes programs. One molecule located in the middle of the bulk was included into the QM part, the rest was described with MM parameters and frozen to its initial position. Static Turbomole and DFT/MRCI calculations were performed using the R2022 Hamiltonian and the standard parameters.

The Vibes program was used to calculate the rate constants for fluorescence ($S_1 \rightarrow S_0$), ISC ($S_1 \rightarrow T_1$) and rISC ($T_1 \rightarrow S_1$). Two rate constants for each process were generated. The first was derived from static computation, the second one after sampling performed by the Gradienator program. This latter method was used to evaluate the influence of the sampling methods.

6.3.1 mBN organic crystal

The ground state structure of mBN in vacuum and embedded in the crystalline environment differ, as apparent from figure 6.4. The phenazine core, which is bent in vacuum, becomes planar in the crystal. The angle between the side groups and the phenazine moiety is also slightly modified. In vacuum, the benzonitrile is perpendicular to the phenazine. In the crystal, the dihedral angles are tilted toward the

same direction by $\sim 5^\circ$. Upon excitation, this value is reduced to $\sim 3^\circ$. Without inclusion of vibrational contributions, the DFT/MRCI result yields blue-shifted emission wavelengths compared to the experiment and almost null oscillator strength. This is similar to the observations in vacuum. The computed emission corresponds to a charge transfer, as visible from figure 6.5, the spatial overlap between the MOs is practically zero.

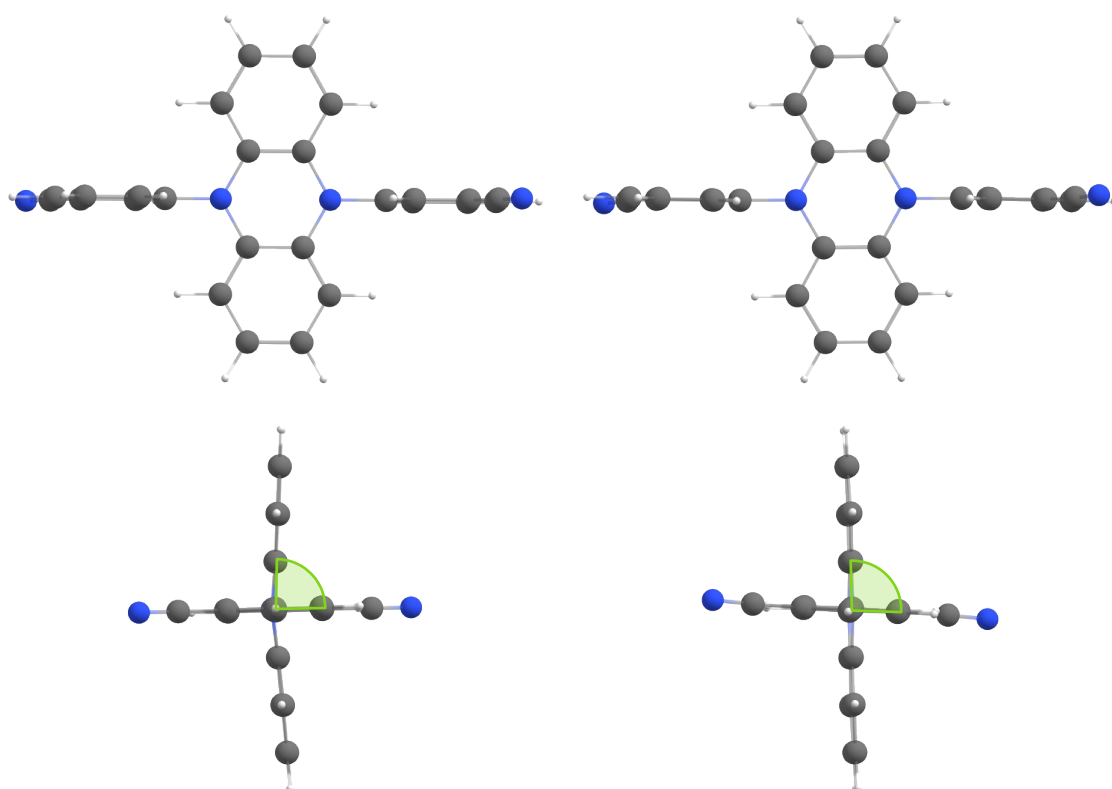


Figure 6.4: Comparison of mBN ground state structure in vacuum (left) and in its organic crystal (right).

A ZPE-sampling similar to the vacuum methodology was performed to obtain new values for emission and oscillator strength, this time taking into account vibrationally distorted structures. The absorption and emission spectra of mBN in the crystal are presented in figure 6.6. The maximum emission wavelength obtained with the sampling method is 503 nm (experiment: 537 nm).

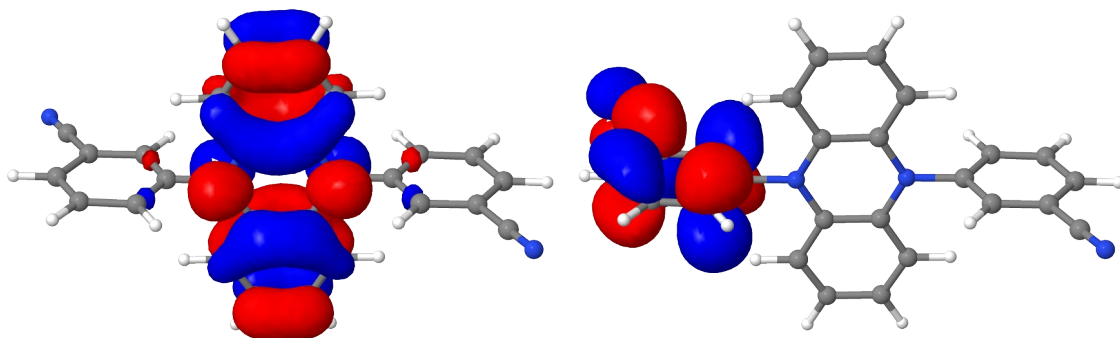


Figure 6.5: HOMO (left) and LUMO (right) of mBN in crystal. Isosurface were plotted with a cutoff of 0.03.

Rate constant calculations are summarised in table 6.3. The two methods point toward the same conclusion about the ability of mBN to perform TADF. It is possible to reach S_1 from the T_1 state, i.e. TADF would theoretically be possible. However, the rISC rate constant is relatively small, matching the experimental observation of weak TADF.

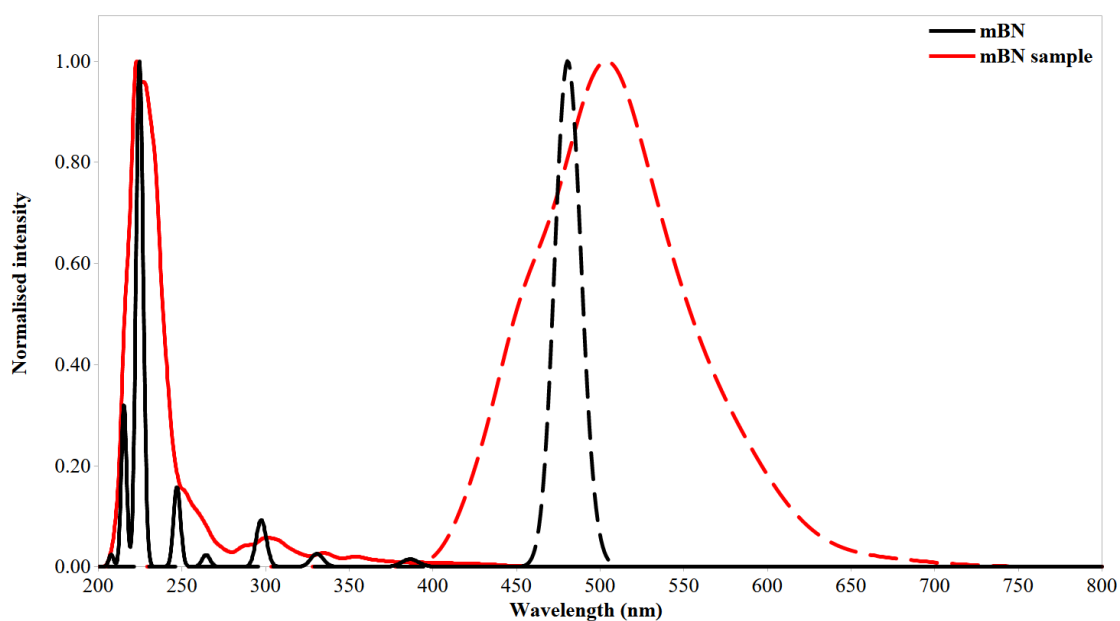


Figure 6.6: Computed normalised absorption (full line) and emission (dotted line) spectra of mBN, vertical (black) and after sampling treatment (red). Static emission oscillator strength is 0.003 and average emission oscillator strength with ZPE sampling is 0.004.

Table 6.3: Rate constants of mBN

Transitions	Fluorescence ($S_1 \rightarrow S_0$)	ISC ($S_1 \rightarrow T_1$)	rISC ($T_1 \rightarrow S_1$)
Static	1.11×10^6	4.47×10^6	4.57×10^4
Gradienator	1.96×10^6	8.71×10^6	1.01×10^5

6.3.2 pBN organic crystal

In the pBN crystal two forms of pBN can be found, a linear form named pBN-lin and a bent forme named pBN-ben. Two crystal structures of pBN have been reported, composed of a different ratios of pBN-lin:pBN-ben, the α -pBN [72] with a 1:1 ratio and β -pBN with a 2:1 ratio. Both pBN structures have been studied in the environment of β -pBN provided by the experimentalists.

Both side groups are tilted in the same direction, forming a dihedral angle of 70° (highlighted in lime in figure 6.7) with the phenazine core (see left and right bottom structures of fig 6.7). In the bent form, the long axis of the side groups (red line) is not aligned with the short axis of the phenazine (green line) as visible in the upper right structure of figure 6.7. The phenazine core is non-planar in vacuum but planar in the crystalline environment for both pBN-lin and pBN-ben.

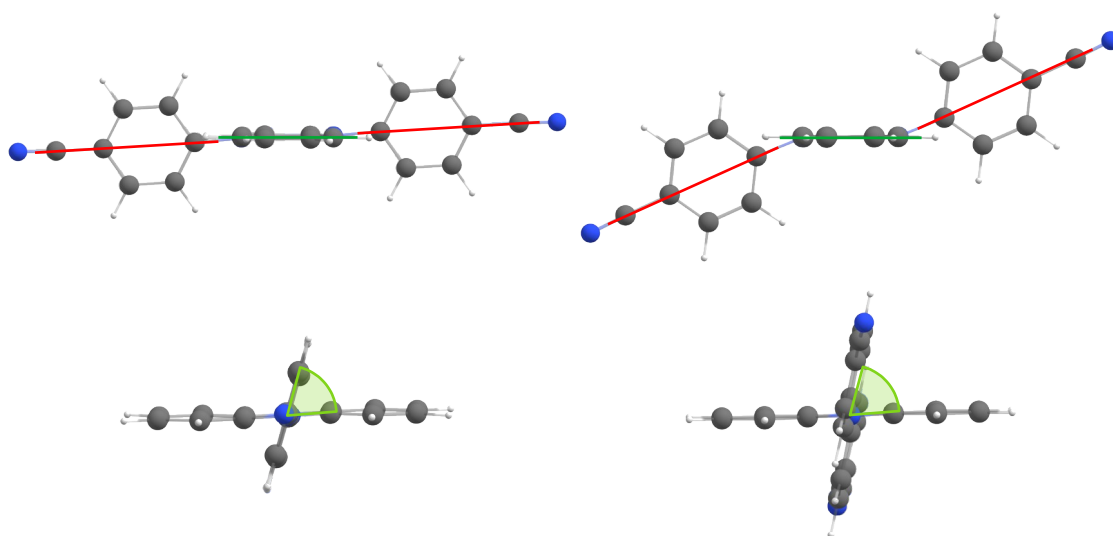


Figure 6.7: pBN-lin (left) and pBN-ben (right) structures extracted from the crystal structure, viewed along the long (top) and short (bot) axis of the phenazine.

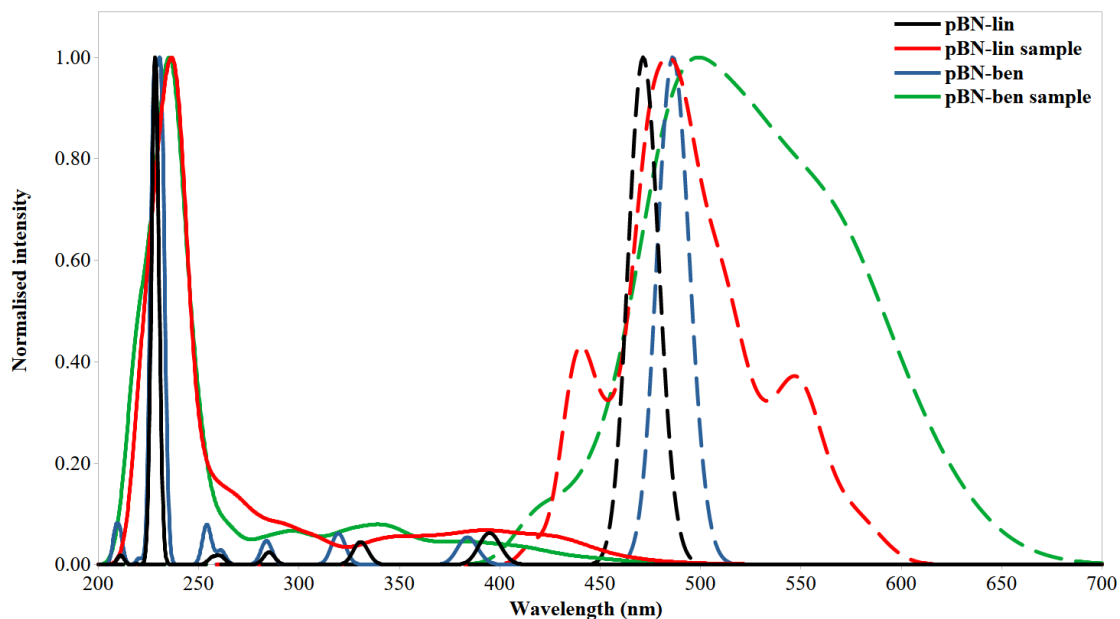


Figure 6.8: Computed absorption (full lines) and emission (dotted lines) spectra of pBN-lin (black and red) and pBN-ben (blue and green) from static and ZPE-sampling methods.

Static DFT/MRCI calculations on the β -pBN crystal yielded a blue-shifted emission of approx. 80 nm (~ 0.38 eV). The weak oscillator strength of 0.013 and 0.006 for the linear and bent form does not explain the fluorescence visible in the experiment. A sampling has been performed on both pBN forms to obtain absorption and emission spectra including the vibrational motion of the molecules, all computed normalised spectra are shown in figure 6.8. Sampling of pBN-lin and pBN-ben results in emissions with notable oscillator strength (0.023 for pBN-lin and 0.011 for pBN-ben) and wavelengths that corresponds to the experimental emission maximum of 565 nm. The combination of the Gradienator and the Vibes programs produced rate constants summarised in table 6.4. The linear and bent form of pBN present similar results with a higher probability to perform rISC rather than fluorescence. Also, the influence of sampling with Gradienator is more important in the pBN models than within mBN; here, the ISC and rISC rates are three times higher (two times in the mBN model).

Table 6.4: Rate constant for the pBN-lin and pBN-ben molecules in the β -pBN crystal environment.

		Fluorescence ($S_1 \rightarrow S_0$)	ISC ($S_1 \rightarrow T_1$)	rISC ($T_1 \rightarrow S_1$)
pBN-lin	Static	4.16×10^6	1.51×10^8	8.16×10^6
	Gradienator	4.31×10^6	3.00×10^8	1.64×10^7
pBN-ben	Static	1.61×10^6	8.03×10^7	3.92×10^6
	Gradienator	1.92×10^6	2.37×10^8	1.48×10^7

6.4 Conclusions

Calculations on the three phenazine derivatives BPN, mBN and pBN in different media revealed the importance of including vibrational contributions in the computation of transition rates and emission energies. The study of mBN and β -pBN crystals unveiled the role of solid state embedding on their TADF properties. By constraining the molecule into a different form than in solvent, the crystal environment enhances the rISC rates for both, mBN and pBN. Inclusion of vibration throughout ZPE sampling within the complex embedding provided an accurate description of complex mechanism occurring in mBN and pBN.

Chapter 7

(TIPS-)Pentacene

Singlet fission is a phenomenon that occurs in the excited state. The first singlet excited state can evolve into two lower energy triplet states. A simple version of the two main mechanisms of singlet fission is pictured in figure 7.1. An electron from fragment **A** is photoexcited to a higher energy level, in the indirect mechanism, the same electron will then be transferred to fragment **B**. Later, on a time scale of picoseconds to nanoseconds [73] [74], an electron from fragment **B** is promoted to fragment **A**, creating two triplet state configurations. In the direct mechanism, the transfers from **A** to **B** and the promotion of the electron of **B** to **A** occur simultaneously. Singlet fission was first observed in 1965 [75]. Anthracene and oligocene molecules are known to be prominent candidates for this process [76] [77].

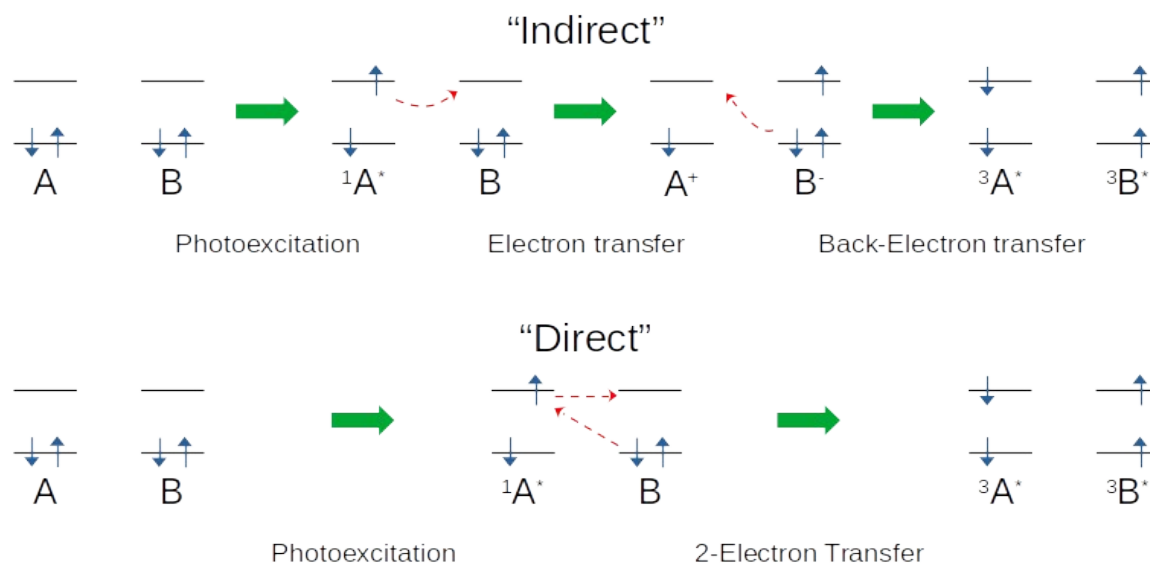


Figure 7.1: Simplified direct and indirect mechanism of singlet fission [78] [79].

In the context of his PhD thesis, Timo Shulz [80] aimed to study pentacene and TIPS-pentacene in their organic crystal phase to determine the mechanism associated with the singlet fission process.

To explore the interactions between the different electronic states, the production of different geometries of pentacene and TIPS-pentacene sub-units, embedded into crystalline environment, were carried out in the singlet ground state (S_0) as well as in the first excited singlet (S_1), triplet (T_1) and quintet (Q_1) states.

7.1 Pentacene crystal

The crystal structure of pentacene was taken from the Cambridge Crystallographic Data Centre [81]. It was refined through the previously defined Quantum Espresso procedure with the unit cell parameters fixed to experimental values to prevent unrealistic distortions. The preparation to perform QM/MM calculations also followed the standard procedure. A bulk of 205 molecules was created. Similar to other single crystal embedding computations, calculations were performed without a medium layer. The QM part was composed of one, two or three pentacene units. Three different dimer arrangements were identified by Nagami et al. [82], namely the **u**, **v** and **w** patterns shown in figure 7.2. The trimer of pentacene consists of a combination of the three dimer patterns.

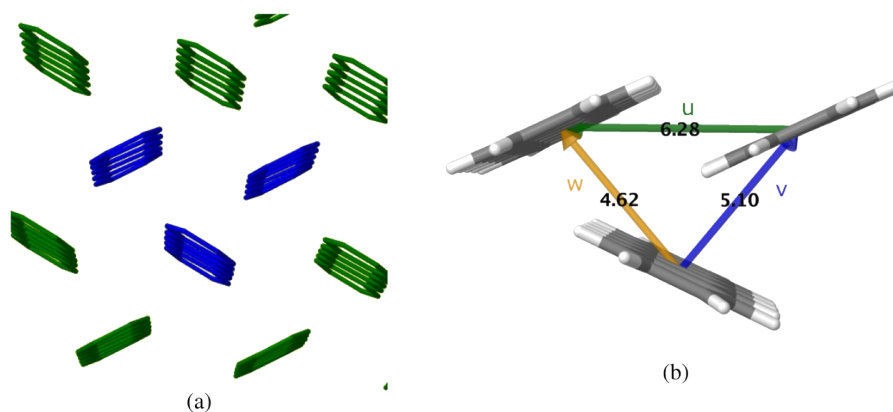


Figure 7.2: (a) Pentacene trimer in blue, green molecules are in the low layer. (b) Definition of the three dimer subunits, distances between centroids are given in Ångstrom.

QM/MM calculations were performed using the SV(P) basis set and Grimme-D3-BJ dispersion corrections. TD-DFT and TDA were used for the calculation of singlet and triplet excited states. The reported results were computed on geometries obtained with the hybrid functional PBE0. The geometries have also been computed using the long range corrected hybrid functional CAM-B3LYP in order to compare the performance of both geometry optimisation methods.

Table 7.1: RMSD of QM geometries computed by the PBE0 and CAM-B3LYP functional. Values are given in Ångstrom.

States	1	2-u	2-v	2-w	3
S ₀	3.57 x 10 ⁻³	3.34 x 10 ⁻³	9.76 x 10 ⁻³	1.04 x 10 ⁻²	1.36 x 10 ⁻²
S ₁	4.23 x 10 ⁻³	4.72 x 10 ⁻²	3.85 x 10 ⁻²	3.12 x 10 ⁻²	2.71 x 10 ⁻²
T ₁	3.34 x 10 ⁻³	5.82 x 10 ⁻³	3.86 x 10 ⁻²	1.38 x 10 ⁻²	1.71 x 10 ⁻²
Q ₁	3.34 x 10 ⁻³	4.72 x 10 ⁻²	8.94 x 10 ⁻³	9.69 x 10 ⁻³	1.67 x 10 ⁻²

The RMSD between the geometries of the five QM configurations at S₀, S₁, T₁ and Q₁ states are reported in table 7.1. The values therein indicate a very small difference between the two methods. The CAM-B3LYP functional has been developed to perform well for computation of charge transfer states. For this reason, the RMSD values for one pentacene are expectedly small as the charge transfer characters of the S₁, T₁ and Q₁ states are very weak if not absent. Also, in dimer or trimer cases, the differences in geometries are small. The higher values of RMSD are mainly attributed to the fact that the number of atoms increases with the number of pentacenes (one pentacene contains 36 atoms). The comparison shows that explicit consideration of charge transfer does not significantly influence the geometries, hence PBE0 yields adequate structures for these types of calculations.

Another outcome of the TD-DFT calculations concerns the MOs involved in the corresponding transitions. DFT/MRCI calculations revealed that the S₀ to S₁ transition includes the HOMO and LUMO orbitals. TD-DFT with PBE0 and CAM-B3LYP attributed the same MOs to this transition.

7.2 Results of the pentacene study

A first set of calculations on one single pentacene molecule in the crystal was carried out. To confirm the validity of the methods, they were compared to other reported computations and to experimental results. In table I of the associated paper, the S_0 to T_1 transition (line $1^3B_{2u} T_h^1$) and the S_0 to S_1 transition (line $1^1B_{2u} S_h^1$) as well as other states are properly described by our methods.

Calculation on the u-dimer of pentacene revealed a direct mechanism involving a conical intersection, followed by singlet fission leading to two antiferromagnetic triplets, i.e. two local triplets with different spins. Neef et al. [77] postulated that the singlet fission mechanism in the pentacene crystal was initiated by a charge transfer. Our investigations on the w-dimer and the trimer of pentacene led to the same conclusion.

7.3 TIPS-pentacene crystal

The 6,13-Bis(triisopropylsilyl)ethynyl)pentacene (TIPS-pentacene) in its organic crystal [83] was also computed with PW and QM/MM under the same conditions as for pentacene. To prepare the PW calculation, the experimental cif file had to be cleaned up. As visible on the left side of figure 7.3, some methyl groups of the TIPS were duplicated due to free rotation. The resulting TIPS-pentacene structure is shown on the right side.

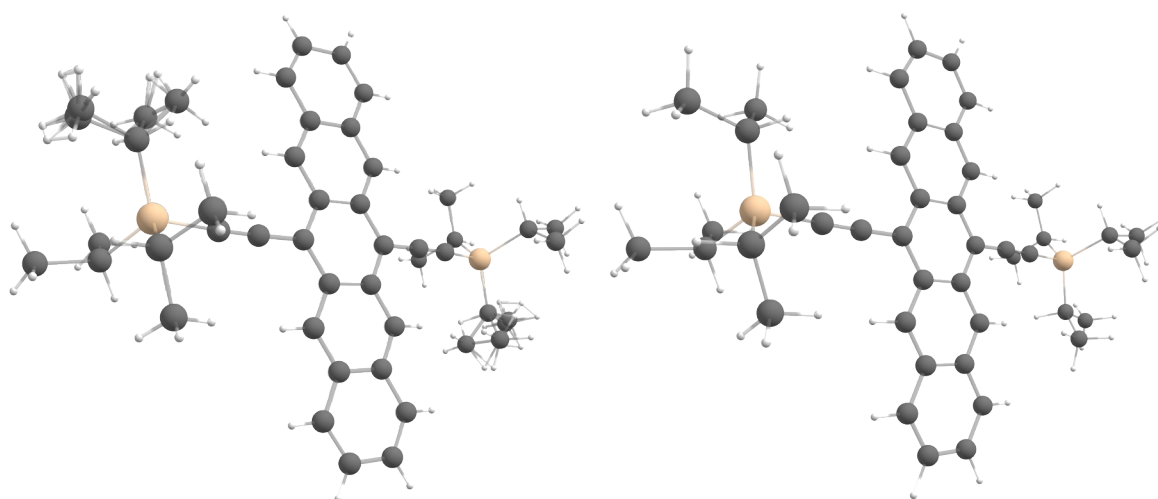


Figure 7.3: Visualisation of experimental structure of one TIPS-pentacene in the organic crystal structure before (left) and after (right) refinement.

Three QM computations were performed, one with the monomer and two including dimers. These two dimers are combined in figure 7.4. The short stacking is composed of the upper and right molecule and the long stacking includes the upper and left molecule. Like for the pentacene crystal, the TIPS-pentacene geometries were computed with the PBE0 and the CAM-B3LYP functionals.

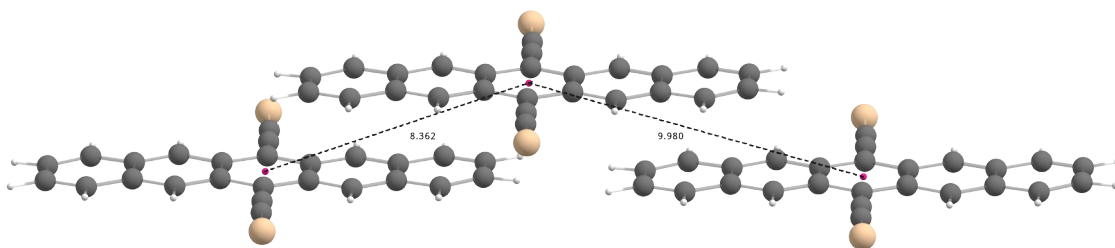


Figure 7.4: Packing arrangement of TIPS-pentacene. TIPS groups have been shortened for clarity. Distances are given in Ångstrom.

The RMSD of computed geometries of the TIPS-pentacene monomer, the short- and the long-dimer are reported in table 7.2, the same conclusion as for pentacene can be drawn as all RMSD values are under 0.1. Using the PBE0 or the CAM-B3LYP functionals also provides very similar results wrt. the MOs involved in the transitions to excited states.

Table 7.2: RMSD of QM geometries computed with the PBE0 and CAM-B3LYP functionals for one or two TIPS-pentacene in the QM region. Values are given in Ångstrom.

States	1	2-Short	2-Long
S_0	1.99×10^{-2}	2.34×10^{-2}	2.23×10^{-2}
S_1	9.07×10^{-3}	5.09×10^{-2}	3.81×10^{-2}
T_1	8.77×10^{-3}	5.51×10^{-2}	2.43×10^{-2}
Q_1	9.31×10^{-3}	2.35×10^{-2}	2.10×10^{-2}

7.4 Conclusion

A total of eight models has been computed, five for the pentacene crystal and three for the TIPS-pentacene crystal. Comparison between PBE0 and CAM-B3LYP methodologies for geometry optimisation yielded no significant differences in the structures and electronic state compositions, both methods therefore appear adequate for describing the investigated systems. The resulting pentacene geometries and exploration of their electronic structures could provide a better understanding of the singlet fission process in this crystal. For the organic crystal of pentacene the indirect mechanism was identified in the **w** dimer as well as in the trimer. The **u** dimer arrangement is similar to TIPS-pentacene. Thus, the hypothesis of having a similar direct mechanism occurring in TIPS-pentacene crystal was formulated and will be the subject of further studies.

Chapter 8

Conclusion and outlook

Within this thesis, a protocol to compute electronic properties of chromophores embedded into explicit complex environments has been established. The procedure begins with the refinement of experimental crystal unit cells through plane wave calculations. This step is followed by the production of QM/MM input files. The atomic charges are computed and the system is expanded to form a supercell of adequate size. Force field parameters are taken from existing libraries or are created individually. The division of the system into residues is another fundamental step to obtain QM/MM input files. The QM/MM scheme is used to perform geometry optimisations and frequency calculations using (TD-)DFT based methods for the QM part and the AMBER program suite for the MM part. Ultimately, electronic investigations are performed with QM/MM or with the DFT/MRCI program. Inclusion of vibrational modes may be necessary to improve the statically obtained results, consequently obtaining the corresponding rate constants for singlet to singlet or singlet to triplet and reverse transitions. Based on this protocol, several studies have been performed.

The first system under study was the flavin derivative MIA in three different solid environments, in the single crystal, in MOF-5 and in MIL-53(Al). These three cases were used to establish for the first time a full protocol allowing the investigation of MIA within different solid surroundings. The computations could show that only optimization of MIA within the explicit surroundings lead to viable results, especially for the excited states. Sole placement of vacuum-optimised MIA into the corresponding charge field turned out to be inadequate.

In the experiment, MIA shows weak emission in its own crystal environment. Light emission intensity increases when MIA is inserted into a MOF. The latter can be explained by the ability of MOFs to prevent the dimer formation, which upon creating charge-transfer states would diminish emission. The different models used to investigate MIA in the single crystal revealed the importance of a careful QM-layer definition. QM/MM setups with only two molecules led to underestimation or overestimation of the emission intensity, depending on the choice of π -stacked molecules. A minimum of three MIA molecules was needed to obtain accurate data.

A second study on a flavin derivative was conducted using a crystal structure (R) with only one flavin and two different co-crystal structures (R-D, R-D-E). In the single crystal, two effects were identified that influence the emission energy. One is related to the distance of neighbouring, π -stacked molecules, the second effect concerns the presence of a neighbouring R molecule within the same plane. Longer π -stacking distances lead to a blue-shift in emission. Inclusion of an in-plane neighbour into the QM calculation led to a red-shift. Similar effects occur in the two co-crystals. R-D had a small stacking distance and no in-plane R-neighbour, resulting in a small blue-shift compared to the single crystal. On the other hand, the R-DE co-crystal shows a strong blue-shift of emission mainly due to the long stacking distance between the R molecules.

Thermally activated delayed fluorescence was a central aspect in the third study. The TADF capabilities of phenazine derivatives were investigated in vacuum and embedded in their crystal structure. In these computations, the static model yielded only unsatisfactory results. Computed wavelengths of emission within the static model were blue-shifted compared to experimental values, this shift was corrected by the inclusion of vibrations into the model. The use of vibrational sampling to calculate emission, fluorescence, ISC and rISC rate constants was mandatory to obtain reliable values, evidencing the importance of including these effects.

The last study on pentacene and TIPS-pentacene provided insight into the mechanism of singlet fission that occurs in the excited pentacene crystal. This was achieved by computing the geometries of dimers and trimers of pentacene within the crystal environment in ground and excited states of different multiplicities. Three dimeric configurations have been studied, two of them, the u and the w forms, showed potential singlet fission with different mechanisms. Calculations on the trimer showed that a similar mechanism of singlet fission occurred as in the w-dimer, supporting experimental observations. Similar structures of TIPS-pentacene have been computed and are still under investigation.

The studied cases exemplify that the environment plays a fundamental role in the description of crystal-embedded systems. Furthermore, a suitable choice has to be taken on the inclusion of molecules in the QM part. This requires careful investigation of the possible interactions between neighbouring molecules prior to performing productive calculations. The limit of the provided protocol naturally depends on the complexity of the system and the available computational resources. Currently, the protocol developed during this thesis is being used to study zinc complexes and other molecules embedded into complex environments. Further studies with different force fields developed specifically to describe solid states and including parameters for metal atoms would increase the range of complex environments that could be described, such as e.g. flexible MOFs (see Part 4.2.2: MIL-53(Al) breath-

ing effect). The variety of existing DFT hybrid functionals as well as basis sets could also be explored to further improve the performance and accuracy of electronic property computations of embedded chromophores.

Appendix 1

File types

Crystallographic Information File

Crystallographic Information File (CIF), firstly introduced in 1990 by Sydney R. Hall, Frank H. Allen and I. David Brown [84] and lastly updated by I. David Brown and Brian McMahon [85], is a file format used to store crystallographic information. The main information inside are the cell parameters (symmetry operation, axes length, angles, etc.) and atom positions inside the cell either in cartesian or fractional coordinates (percentage of axis length). Only the minimum number of atoms are listed in the cif file, the others can be obtained by applying symmetry operations.

Protein Data Bank

The **Protein Data Bank** was created in 1971 by Edgar Meyer, Gerson Cohen and Helen M. Berman [86], it aims to collect structures from simple organic molecules to biological ensembles like viruses. The associated file store information as follow:

Each line corresponds to one atom and its information, they are stored into 11 columns.

- In our case always the same list of characters “ATOM”
- Atomic index (number) in the full system.
- Atom name in the residue, made with atomic symbol and its rank in the residue, if the second atom is a hydrogen its name will be “H2”.
- The residue name, composed of 3 characters.
- Residue index.
- X cartesian coordinate.
- Y cartesian coordinate.

- Z cartesian coordinate.
- Fix value of “1.00”, it is used for biological systems, in our cases it never changes.
- Fix value of “0.00”, it is used for biological systems, in our cases it never changes.
- Atomic symbol.

A number of atoms can be combined to a residue, which is a subsystem of the full system. In our applications it consists of a single molecule, or linkers/metal for MOFs. For practical reasons the less residue type there is the better.

XYZ

The xyz format in its basic form is the most common coordinate format, the first line of the file is the number of atom in the system archived into the document, after a blank line each line will be filled with 4 columns:

- Atomic symbol
- X cartesian coordinate.
- Y cartesian coordinate.
- Z cartesian coordinate.

More information can be stored into it like vectors to display dipole moment or cell axis.

Mol2

If the xyz format explained later is one of the simplest, the mol2 format tends to be storing a complete description of a molecular system. The file is split into multiple parts having “@<TRIPOS>XXX” as the first line, XXX being one of the 32 category names possible. An important category is ATOM which holds cartesian coordinates, charges, atomic name, atom type (like in pdb) are saved; another one is BOND which contains all bond information between atoms, atom index of those involved in the bond and the bond type, single, aromatic, etc.

Appendix 2

Python3

Generality

Python is a programming language created in 1991, its main use is to automatize simple but tedious tasks. Every object in python has a type on which different operation can be applied, the most common among them are:

- STRING (STR): list of characters defining a text
- INTEGER (INT): Integer number without decimals (1, -1, ...)
- FLOAT: Number with decimals (1.00..., 1.333..., 3.14...,)
- BOOLEAN (BOOL): Either True or False

Among these types are multiple compound data (MCD) types that can be used to store and interact with objects, one of them is the list (which is also a type). A list is a collection of separated objects of various types separated and indexed (starting from index 0). More complicated MCD exist but the x2p script only uses lists and strings. The advantage of the list type is its ability to store every type of object together where a string consists of only string type objects. Every object can be manipulated with operators like '+' or '-'.

FOR and WHILE

The FOR loop is used when the user knows in advance the number of iterations required to fulfil the task, it is very convenient to go through a list and perform operation on each element once. The WHILE loop can be translated in human language as “do it until you reach the condition”, it is mostly used when the complexity of the condition is not known and/or depends on the studied case.

Bucket sort

In the x2p.py script one of the main tasks is to sort the atoms following a specific order, the function used for that case is called a recursive bucket sort. The bucket sort is one of many ways to sort a pool of objects, the main idea is to split the pool under conditions and regroup the object into different buckets, then re-iterating the function over the new and smaller buckets until there are only buckets containing one object. The action to call a function inside itself is what makes it recursive, it implies to have a stopping condition which is in our case to not reiterate the sorting if called with a bucket that is empty or only containing one element. In x2p.py the splitting is done by taking the first atom of the tested list of atoms, placing it in a bucket and creating two other buckets, one will take all atoms with smaller coordinates and one with bigger coordinates. Smaller and Bigger coordinates are defined by comparing first the x coordinate, if the number is smaller or bigger than the first atom then it will be placed into the respective bucket, if it is equal or the difference between reference coordinate and tested coordinate is smaller than a threshold then the y coordinate will be tested following the same procedure, then if needed the z coordinate.

Library

In programming languages a library is a pool of resources that can be directly used in programs. Their use varies from simple mathematical operation to complex specific sorting. In the x2p.py script the Numpy library has been employed. It has been developed to work on matrices and tables but also contain mathematical functions, like square root (sqrt), that are not directly available in python.

X2P.py script

```
import numpy as np

# Open Molecule.xyz file and put atomic type/coordinate into lists

f = open("./Molecule.xyz", "r")
fr = f.read()
fl = len(fr)

a0 = 1
frl = list(fr)
while (frl[a0-1], frl[a0]) != ('\n', '\n'):
    a0 += 1
del frl[0:a0+1]
fr = "".join(frl)
fl = len(fr)

del frl
del a0

# Open List.txt file

g = open("./List.txt", "r")
gr = g.read()
gl = len(gr)

# Open Groups.txt file

h = open("./Groups.txt", "r")
hr = h.read()
hl = len(hr)

# Creation of the 3 functions used in the main function x2p

def distance(a1,a2,a3,b1,b2,b3):
    d = 0
    x = (float(b1)-float(a1))**2
    y = (float(b2)-float(a2))**2
    z = (float(b3)-float(a3))**2
    d = np.sqrt(x+y+z)
    return d

def voisin(La,Lb,Nb):
```

```

a = distance(float(La[2]),float(La[4]),float(La[6]),float(Lb[2]),float(Lb[4]),float(Lb[6]))
if La[0] == 'H' and Lb[0] == 'H':
    return False
else:
    if a < Nb:
        return True
    else:
        return False

def voisinblock(La,Lb,Nb):
    for i in range(0,len(La)):
        if La[i][0] == 'H':
            return False
        else:
            for j in range(0,len(Lb)):
                if Lb[j][0] == 'H':
                    return False
                else:
                    if distance(float(La[i][2]),float(La[i][4]),float(La[i][6]),float(Lb[j][2]),float(Lb[j]
[4]),float(Lb[j][6])) < Nb:
                        return True
            return False

    return False

def Triblock(L):
    if L == []:
        return []
    xx = 0
    yy = 0
    zz = 0
    a = L[0]
    Smaller = []
    Bigger = []
    for x in L[1:]:
        xx = abs(float(x[2]) - float(a[2]))
        yy = abs(float(x[4]) - float(a[4]))
        zz = abs(float(x[6]) - float(a[6]))
        if len(x[0]) > len(a[0]):
            Bigger.append(x)
        if len(x[0]) < len(a[0]):
            Smaller.append(x)
        if len(x[0]) == len(a[0]):
            if x[0] < a[0] :
                Smaller.append(x)
            if x[0] > a[0] :
                Bigger.append(x)
            if x[0] == a[0]:

```

```

        if float(x[2]) < float(a[2]) and xx > 0.030:
            Smaller.append(x)
        if float(x[2]) > float(a[2]) and xx > 0.030:
            Biggers.append(x)
        if float(x[2]) == float(a[2]) or xx <= 0.030:
            if float(x[4]) < float(a[4]) and yy > 0.030:
                Smaller.append(x)
            if float(x[4]) > float(a[4]) and yy > 0.030:
                Biggers.append(x)
            if float(x[4]) == float(a[4]) or yy <= 0.030:
                if float(x[6]) < float(a[6]) and zz > 0.030:
                    Smaller.append(x)
                if float(x[6]) > float(a[6]) and zz > 0.030:
                    Biggers.append(x)
    return Triblock(Biggers) + [a] + Triblock(Smaller)

```

NombreStr = ['0','1','2','3','4','5','6','7','8','9']

NombreInt = [0,1,2,3,4,5,6,7,8,9]

The main function of the script: x2p

```

def x2p():
    m = open("./part1.txt", "w")
    a1 = 0
    a2 = 0
    a3 = 0
    a4 = 0
    a5 = 0
    a6 = 0
    s1 = ""
    s2 = ""
    s3 = ""
    L0 = []
    L1 = []
    L2 = []
    L3 = []
    L4 = []
    L5 = []
    L6 = []
    L7 = []
    L8 = []
    L9 = []
    L10 = []
    print('It is only the beginning (it can take many minutes)')
    for i in range(0,gl):
        #L1, number index of atom
        if gr[i] == ' ':

```

```

        L1.append(int(s1))
        s1 = ""
    if gr[i] in NombreStr:
        s1 += gr[i]
    if gr[i] == ':':
        j = i+1
        while gr[j] != ' ':
            if gr[j] in NombreStr:
                s3 += gr[j]
                j += 1
        for k in range (int(s1),int(s3)):
            L1.append(k)
            s1 = ""
            s3 = ""
    if gr[i] == '\n':
        L1.append('Switch')
    print('L1 setup done')
for i in range (0,fl):
    if fr[i] != '\n':
        s2 += fr[i]
    else:
        L2.append(str.split(s2))
        s2 = ""
    print('L2 setup done')
for i in range (0,hl):
    if hr[i] != ' ':
        s1 += hr[i]
    if hr[i] == ' ':
        L3.append(s1)
        s1 = ""
    print('L3 setup done')
for i in range (0,len(L2)):
    a1 = 0
    a2 = 0
    a3 = 0
    j = 0
    while L1[j] != i:
        if L1[j] == 'Switch':
            a1 += 1
        j += 1
    L0.append([L2[i][0], ' ',f'{float(L2[i][1]):.6f}', ' ',f'{float(L2[i][2]):.6f}', ' ',f'{float(L2[i][3]):.6f}', '
',L3[a1],'\n'])
    print('Sorting of the blocks')
while L0 != []:
    print (len(L0))
    L4.append(L0[0])

```

#end L1

#L2, List of all atoms (from xyz file)

#end L2

#L3, Name of the blocks

#end L3

#Go through L2 to give block name to each atom

All atom have their block name, so now we will regroup them by block

```

while L4 != []:
    if L0 == []:
        L6.append(L4[0])
        del(L4[0])
        for i in range (0,len(L5)):
            L0.append(L5[i])
        L5 = []
    else:
        if L4[0][8] == L0[0][8]:
            if voisin(L4[0],L0[0],2.000) == True:
                if L4[0] != L0[0]:
                    L4.append(L0[0])
            else:
                L5.append(L0[0])
                del(L0[0])
        else:
            L5.append(L0[0])
            del(L0[0])
    L7.append(L6)
    L6 = []
for i in range (0,len(L7)):
    if type(L7[i]) == list:
        for j in range(0,len(L7[i])):
            for k in range (0,len(L7[i][j])):
                m.write(str(L7[i][j][k]))

m.close()
print('Blocks Sorted')
print('Generation of neighbours')
while L7 != []:
    L8.append(L7[0])
    while L8 != []:
        if L7 == []:
            L10.append(L8[0])
            del(L8[0])
            for i in range (0,len(L9)):
                L7.append(L9[i])
            L9 = []
        else:
            if L7[0] in L8:
                del(L7[0])
            else:
                if voisinblock(L8[0],L7[0],2.00) == True:
                    L8.append(L7[0])
                else:
                    L9.append(L7[0])
                    del(L7[0])

```

```

L0 = []
for i in range(0,len(L10)):
    if type(L10[i]) == list:
        L0.append(Triblock(L10[i]))
    else:
        L0.append(L10[i])
n = open("./part2.txt","w")
for i in range(0,len(L0)):
    if type(L0[i]) == list:
        for j in range(0,len(L0[i])):
            for k in range(0,len(L0[i][j])):
                n.write(str(L0[i][j][k]))
    else:
        n.write(str(L0[i]))
n.close()
print('Generation of neighbours done')
a1 = 0
a2 = 0
a3 = 0
a4 = 0
a5 = 0
a6 = 0
L1 = [[],[]] #L1 contains [[Atome types in the block], [associated number]]
L2 = []
L3 = []
L4 = []
L5 = []
L6 = []
L7 = []
L8 = []
L9 = []
print('Creation of the pdb')
L0.append('END')
o = open("./Out.pdb","w")
for i in range(0,len(L0)):
    if type(L0[i]) == list:
        for j in range(0,len(L0[i])):
            L3.append(float(L0[i][j][2]))
            L4.append(float(L0[i][j][4]))
            L5.append(float(L0[i][j][6]))
a31 = max(L3)-min(L3)+0.3
a41 = max(L4)-min(L4)+0.3
a51 = max(L5)-min(L5)+0.3
a3 = f'{a31:.3f}'
a4 = f'{a41:.3f}'
a5 = f'{a51:.3f}'

```



```

o.write('CRYST1')
o.write(f'{a3:>9}')
o.write(f'{a4:>9}')
o.write(f'{a5:>9}')
o.write(' 90.00 90.00 90.00                1\n')
a3 = 0
a4 = 0
a5 = 0
for i in range(0,len(L0)):
    if type(L0[i]) == list:
        for j in range(0,len(L0[i])):
            a1 += 1
            del(L0[i][j][-1:])
            L0[i][j].append(' ')
            L0[i][j].append(str(a1))
            L0[i][j].append('\n')
        a1 = 0
for i in range(0,len(L0)):
    if type(L0[i]) == list:
        a6 += 1
        for j in range(0,len(L0[i])):
            a2 += 1
            o.write('ATOM')
            o.write(f'{a2:7d}')
            o.write(f'{str(L0[i][j][0]):>3}')
            o.write(f'{str(L0[i][j][10]):<3}')
            o.write(f'{str(L0[i][j][8]):3}')
            o.write(f'{a6:6d}')
            o.write(' ')
            a3 = f'{float(L0[i][j][2]):.3f}'
            o.write(f'{a3:>8}')
            a4 = f'{float(L0[i][j][4]):.3f}'
            o.write(f'{a4:>8}')
            a5 = f'{float(L0[i][j][6]):.3f}'
            o.write(f'{a5:>8}')
            o.write('  1.00  0.00                ')
            o.write(f'{str(L0[i][j][0]).upper():>2}')
            o.write('\n')
        else:
            o.write(str(L0[i]))
hrr = hr.split()
o.close()
p = open("./Out.pdb","r")
pl = p.readlines()
pll = []
for i in range (1,len(pl)):

```

```

        pll.append(pl[i].split())
    for i in range(0,len(hrr)):
        w = open(hrr[i]+'pdb','w')
        j = 0
        k = 0
        while pll[j][3] != hrr[i]:
            j += 1
        while pll[k+j][4] == pll[j][4] or pll[k+j][0] == 'TER' or pll[k+j][0] == 'END':
            w.write(pl[k+j+1])
            k += 1
        j = 0
        k = 0
    print('Work is finished, good night Zzz')
    print('Oh wait, let me check for the bonds')
    q = open("./Bond.txt", "w")
    qll = []
    for i in range(1,len(pl)):
        if len(pl[i]) > 8:
            qll.append(str.split(pl[i]))
    for i in range(0,len(qll)):
        for j in range(i,len(qll)):
            if qll[i][4] != qll[j][4]:
                if qll[i][10] != 'H':
                    if qll[j][10] != 'H':
                        x = distance(float(qll[i][5]),float(qll[i][6]),float(qll[i][7]),float(qll[j]
[5]),float(qll[j][6]),float(qll[j][7]))
                        if x < 2.10 and x > 0.50:
                            q.write('bond model.{} model.{} \n'.format(qll[i][4],qll[i]
[2],qll[j][4],qll[j][2]))
    print('Now I can sleep, turn off the lights please Zzz')

```

Next line is needed to run the script

x2p()

Depending of the MOFs you may need to change some values

Line 165: To set the max distance between two neighbour atoms of the same residue

Line 197: To set the distance between two neighbour residue

Line 324: To define the distance between two atome of different residue number

For MIL53: 2,000 | 2.600 | 0,500 - 2.90

For DMOF: 2,801 | 2.600 | 0,500 - 2.55

Appendix 3

Results in R (co-)crystals

Table A1: Computed emission for the model 3R-134 in the R single crystal embedding. Experimental maximum emission wavelength is measured at 733nm.

Method	Emission character	MOs transition	Wavelength (nm)
TD-DFT PBE0	CT	Homo \rightarrow Lumo	729.2
TD-DFT CAM-B3LYP	CT	Homo \rightarrow Lumo	523.29
DFT-MRCI	CT	Homo \rightarrow Lumo	539.0

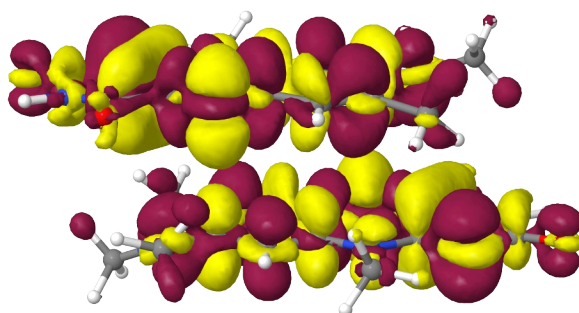
Table A2: Computed emission properties using TD-DFT and the CAM-B3LYP functional for R molecules (MOs localisation is shown under brackets wrt. figure 5.3 number attribution) in R, R-D and R-DE (co-)crystals.

	Wavelength (nm)	Oscillator strength	MOs	Characters
3R-123	528.14	0.0026	H(2) \rightarrow L(1)	CT
3R-124	523.29	0.0118	H(2) \rightarrow L(1)	CT
3R-134	534.38	0.0028	H(3) \rightarrow L(1)	CT
4R-1234	534.05	0.0071	H(2) \rightarrow L(1)	CT
2R-D	458.84	0.0000	H \rightarrow L	CT
2R-DE	670.75	0.0351	H \rightarrow L	CT

Figure A3.1: Density difference for excitation at S_0 geometry, cutoff = 0.0003, red = density loss, yellow = density gain.

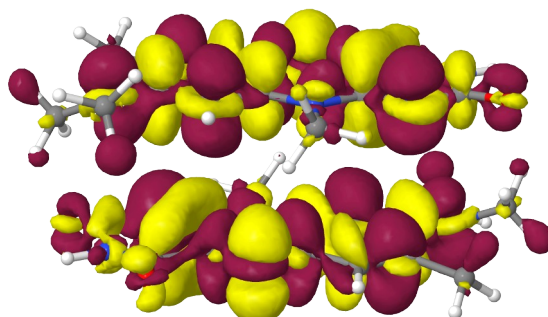
2R – 12:

$S_0 \rightarrow S_4$



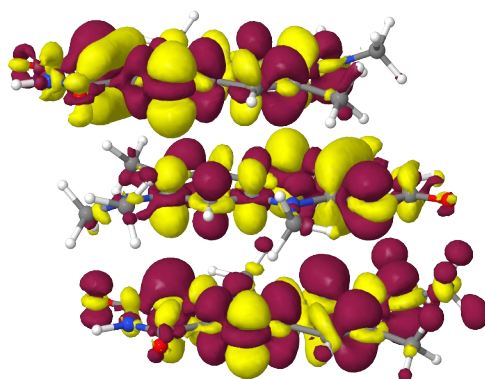
2R – 13:

$S_0 \rightarrow S_4$



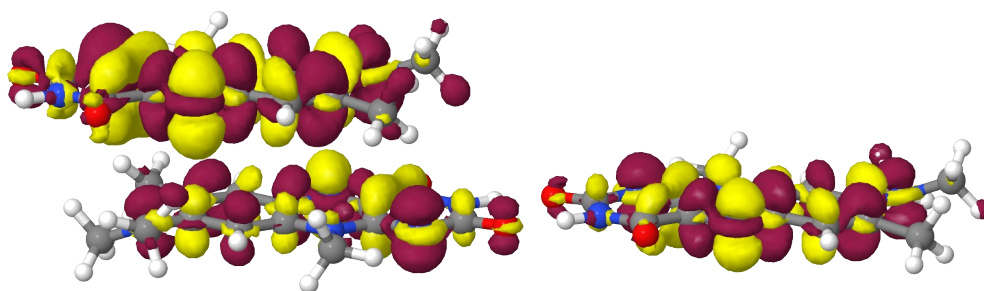
3R – 123:

$S_0 \rightarrow S_9$



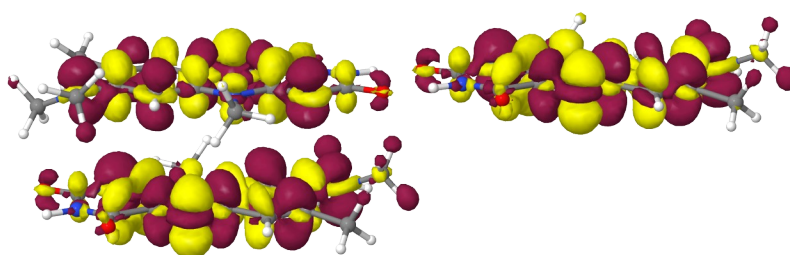
3R – 124:

$S_0 \rightarrow S_6$



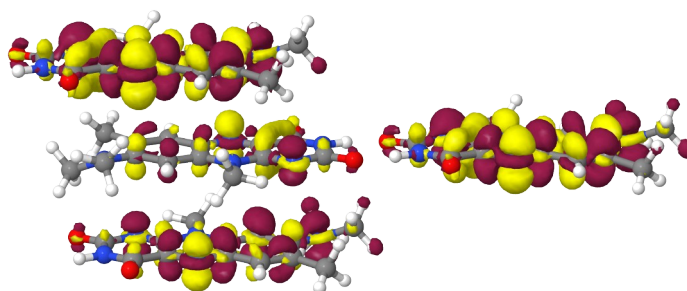
3R-134:

$S_0 \rightarrow S_6$



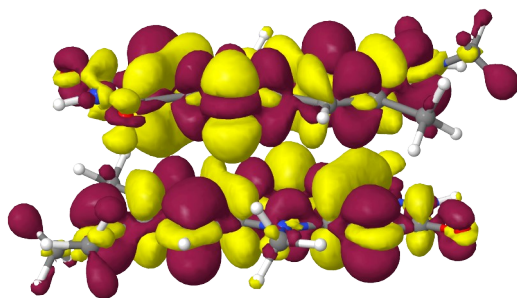
4R – 1234:

$S_0 \rightarrow S_{12}$



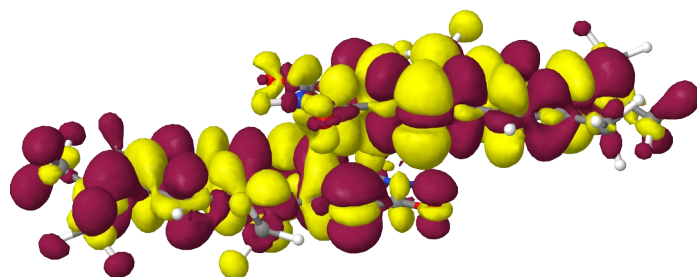
$2R - D:$

$S_0 \rightarrow S_4$

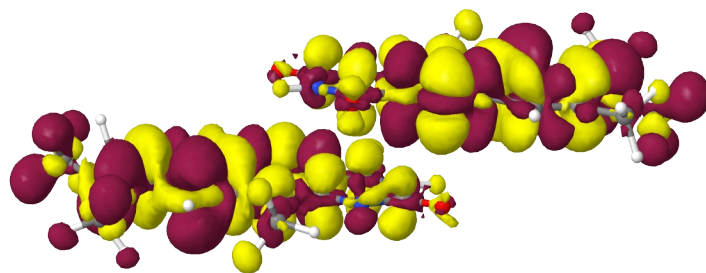


$2R - DE:$

$S_0 \rightarrow S_1$



$S_0 \rightarrow S_4$



References

- [1] J. W. Verhoeven, « Glossary of terms used in photochemistry (IUPAC Recommendations 1996) », *Pure and Applied Chemistry*, vol. 68, n° 12, p. 2223-2286, janv. 1996, doi: 10.1351/pac199668122223.
- [2] J.-P. Launay et M. Verdaguer, *Electrons in molecules: from basic principles to molecular electronics*, Revised edition. Oxford, United Kingdom: Oxford University Press, 2018.
- [3] N. T. Kalyani, *Principles and applications of organic light emitting diodes (OLEDs)*. in Woodhead Publishing series in electronic and optical materials. Duxford, United Kingdom: Elsevier, 2017.
- [4] S. Prasad, « OLED-based biochemical sensors », in *Organic Light-Emitting Diodes (OLEDs)*, Elsevier, 2013, p. 548-571. doi: 10.1533/9780857098948.3.548.
- [5] A. M. Edwards, « Structure and General Properties of Flavins », in *Flavins and Flavoproteins*, vol. 1146, S. Weber et E. Schleicher, Éd., in *Methods in Molecular Biology*, vol. 1146, New York, NY: Springer New York, 2014, p. 3-13. doi: 10.1007/978-1-4939-0452-5_1.
- [6] M. Bracker, F. Dinkelbach, O. Weingart, et M. Kleinschmidt, « Impact of fluorination on the photophysics of the flavin chromophore: a quantum chemical perspective », *Phys. Chem. Chem. Phys.*, vol. 21, n° 19, p. 9912-9923, 2019, doi: 10.1039/C9CP00805E.
- [7] J. Daďová, S. Kümmel, C. Feldmeier, J. Cibulková, R. Pažout, J. Maixner, R. M. Gschwind, B. König, et R. Cibulka, « Aggregation Effects in Visible-Light Flavin Photocatalysts: Synthesis, Structure, and Catalytic Activity of 10-Arylflavins », *Chemistry A European J*, vol. 19, n° 3, p. 1066-1075, janv. 2013, doi: 10.1002/chem.201202488.
- [8] A. Reiffers, C. Torres Ziegenbein, A. Engelhardt, R. Kühnemuth, P. Gilch, et C. Czekelius, « Impact of Mono-Fluorination on the Photophysics of the Flavin Chromophore », *Photochem & Photobiology*, vol. 94, n° 4, p. 667-676, juill. 2018, doi: 10.1111/php.12921.

- [9] T. Haj Hassani Sohi, F. Maass, C. Czekelius, M. Suta, et V. Vasylyeva, « Co-crystallization of organic chromophore roseolumiflavin and effect on its optical characteristics », *CrystEngComm*, vol. 24, n° 41, p. 7315-7325, 2022, doi: 10.1039/D2CE00589A.
- [10] H. Zhang, Q. Guo, H. Cheng, C. Ran, D. Wu, et J. Lan, « An umpolung strategy for rapid access to thermally activated delayed fluorescence (TADF) materials based on phenazine », *Chem. Commun.*, vol. 58, n° 10, p. 1581-1584, 2022, doi: 10.1039/D1CC06705B.
- [11] J. Lee, K. Shizu, H. Tanaka, H. Nakanotani, T. Yasuda, H. Kaji, et C. Adachi, « Controlled emission colors and singlet–triplet energy gaps of dihydrophenazine-based thermally activated delayed fluorescence emitters », *J. Mater. Chem. C*, vol. 3, n° 10, p. 2175-2181, 2015, doi: 10.1039/C4TC02530J.
- [12] M. Mamada, R. Nakamura, et C. Adachi, « Synthesis, crystal structure and charge transport characteristics of stable *peri*-tetracene analogues », *Chem. Sci.*, vol. 12, n° 2, p. 552-558, 2021, doi: 10.1039/D0SC04699J.
- [13] N. Shah, A. A. Shah, P. K. Leung, S. Khan, K. Sun, X. Zhu, et Q. Liao, « A Review of Third Generation Solar Cells », *Processes*, vol. 11, n° 6, p. 1852, juin 2023, doi: 10.3390/pr11061852.
- [14] T. Nagami, H. Miyamoto, R. Sakai, et M. Nakano, « Stabilization of Charge-Transfer States in Pentacene Crystals and Its Role in Singlet Fission », *J. Phys. Chem. C*, vol. 125, n° 4, p. 2264-2275, févr. 2021, doi: 10.1021/acs.jpcc.0c10029.
- [15] P. Brandt, S.-H. Xing, J. Liang, G. Kurt, A. Nuhnen, O. Weingart, et C. Janiak, « Zirconium and Aluminum MOFs for Low-Pressure SO₂ Adsorption and Potential Separation: Elucidating the Effect of Small Pores and NH₂ Groups », *ACS Appl. Mater. Interfaces*, vol. 13, n° 24, p. 29137-29149, juin 2021, doi: 10.1021/acsami.1c06003.

- [16] S. Xing, J. Liang, P. Brandt, F. Schäfer, A. Nuhnen, T. Heinen, I. Boldog, J. Möllmer, M. Lange, O. Weingart, et C. Janiak, « Capture and Separation of SO₂ Traces in Metal–Organic Frameworks via Pre-Synthetic Pore Environment Tailoring by Methyl Groups », *Angew Chem Int Ed*, vol. 60, n° 33, p. 17998-18005, août 2021, doi: 10.1002/anie.202105229.
- [17] B. O. Roos, P. R. Taylor, et P. E. M. Sigbahn, « A complete active space SCF method (CASSCF) using a density matrix formulated super-CI approach », *Chemical Physics*, vol. 48, n° 2, p. 157-173, mai 1980, doi: 10.1016/0301-0104(80)80045-0.
- [18] E. Runge et E. K. U. Gross, « Density-Functional Theory for Time-Dependent Systems », *Phys. Rev. Lett.*, vol. 52, n° 12, p. 997-1000, mars 1984, doi: 10.1103/PhysRevLett.52.997.
- [19] S. Hirata et M. Head-Gordon, « Time-dependent density functional theory within the Tamm–Dancoff approximation », *Chemical Physics Letters*, vol. 314, n° 3-4, p. 291-299, déc. 1999, doi: 10.1016/S0009-2614(99)01149-5.
- [20] C. M. Marian, A. Heil, et M. Kleinschmidt, « The DFT/MRCI method », *WIREs Comput Mol Sci*, vol. 9, n° 2, p. e1394, mars 2019, doi: 10.1002/wcms.1394.
- [21] O. Weingart, A. Nenov, P. Altoè, I. Rivalta, J. Segarra-Martí, I. Dokukina, et M. Garavelli, « COBRAMM 2.0 — A software interface for tailoring molecular electronic structure calculations and running nanoscale (QM/MM) simulations », *J Mol Model*, vol. 24, n° 9, p. 271, sept. 2018, doi: 10.1007/s00894-018-3769-6.
- [22] L. H. Thomas, « The calculation of atomic fields », *Math. Proc. Camb. Phil. Soc.*, vol. 23, n° 5, p. 542-548, janv. 1927, doi: 10.1017/S0305004100011683.
- [23] P. A. M. Dirac, « Note on Exchange Phenomena in the Thomas Atom », *Math. Proc. Camb. Phil. Soc.*, vol. 26, n° 3, p. 376-385, juill. 1930, doi: 10.1017/S0305004100016108.
- [24] C. F. V. Weizsäcker, « Zur Theorie der Kernmassen », *Z. Physik*, vol. 96, n° 7-8, p. 431-458, juill. 1935, doi: 10.1007/BF01337700.

- [25] P. Hohenberg et W. Kohn, « Inhomogeneous Electron Gas », *Phys. Rev.*, vol. 136, n° 3B, p. B864-B871, nov. 1964, doi: 10.1103/PhysRev.136.B864.
- [26] D. J. Tozer, N. C. Handy, et W. H. Green, « Exchange-correlation functionals from ab initio electron densities », *Chemical Physics Letters*, vol. 273, n° 3-4, p. 183-194, juill. 1997, doi: 10.1016/S0009-2614(97)00586-1.
- [27] E. Runge et E. K. U. Gross, « Density-Functional Theory for Time-Dependent Systems », *Phys. Rev. Lett.*, vol. 52, n° 12, p. 997-1000, mars 1984, doi: 10.1103/PhysRevLett.52.997.
- [28] E. Clementi et C. Roetti, « Roothaan-Hartree-Fock atomic wavefunctions », *Atomic Data and Nuclear Data Tables*, vol. 14, n° 3-4, p. 177-478, sept. 1974, doi: 10.1016/S0092-640X(74)80016-1.
- [29] A. D. Becke, « A new mixing of Hartree-Fock and local density-functional theories », *The Journal of Chemical Physics*, vol. 98, n° 2, p. 1372-1377, janv. 1993, doi: 10.1063/1.464304.
- [30] C. Adamo, G. E. Scuseria, et V. Barone, « Accurate excitation energies from time-dependent density functional theory: Assessing the PBE0 model », *The Journal of Chemical Physics*, vol. 111, n° 7, p. 2889-2899, août 1999, doi: 10.1063/1.479571.
- [31] J. P. Perdew, M. Ernzerhof, et K. Burke, « Rationale for mixing exact exchange with density functional approximations », *The Journal of Chemical Physics*, vol. 105, n° 22, p. 9982-9985, déc. 1996, doi: 10.1063/1.472933.
- [32] J. C. Slater, « A Simplification of the Hartree-Fock Method », *Phys. Rev.*, vol. 81, n° 3, p. 385-390, févr. 1951, doi: 10.1103/PhysRev.81.385.
- [33] P. A. M. Dirac, « Quantum mechanics of many-electron systems », *Proc. R. Soc. Lond. A*, vol. 123, n° 792, p. 714-733, avr. 1929, doi: 10.1098/rspa.1929.0094.

- [34] A. D. Becke, « Density-functional exchange-energy approximation with correct asymptotic behavior », *Phys. Rev. A*, vol. 38, n° 6, p. 3098-3100, sept. 1988, doi: 10.1103/PhysRevA.38.3098.
- [35] P. J. Stephens, F. J. Devlin, C. F. Chabalowski, et M. J. Frisch, « Ab Initio Calculation of Vibrational Absorption and Circular Dichroism Spectra Using Density Functional Force Fields », *J. Phys. Chem.*, vol. 98, n° 45, p. 11623-11627, nov. 1994, doi: 10.1021/j100096a001.
- [36] T. Yanai, D. P. Tew, et N. C. Handy, « A new hybrid exchange–correlation functional using the Coulomb-attenuating method (CAM-B3LYP) », *Chemical Physics Letters*, vol. 393, n° 1-3, p. 51-57, juill. 2004, doi: 10.1016/j.cplett.2004.06.011.
- [37] J. Wang, R. M. Wolf, J. W. Caldwell, P. A. Kollman, et D. A. Case, « Development and testing of a general amber force field », *J Comput Chem*, vol. 25, n° 9, p. 1157-1174, juill. 2004, doi: 10.1002/jcc.20035.
- [38] D. A. Case, T. E. Cheatham, T. Darden, H. Gohlke, R. Luo, K. M. Merz, A. Onufriev, C. Simmerling, B. Wang, et R. J. Woods, « The Amber biomolecular simulation programs », *J Comput Chem*, vol. 26, n° 16, p. 1668-1688, déc. 2005, doi: 10.1002/jcc.20290.
- [39] R. Salomon-Ferrer, D. A. Case, et R. C. Walker, « An overview of the Amber biomolecular simulation package », *WIREs Comput Mol Sci*, vol. 3, n° 2, p. 198-210, mars 2013, doi: 10.1002/wcms.1121.
- [40] D. A. Case, H. M. Aktulga, K. Belfon, D. S. Cerutti, G. A. Cisneros, V. W. D. Cruzeiro, N. Forouzeshe, T. J. Giese, A. W. Götz, H. Gohlke, S. Izadi, K. Kasavajhala, M. C. Kaymak, E. King, T. Kurtzman, T.-S. Lee, P. Li, J. Liu, T. Luchko, R. Luo, M. Manathunga, M. R. Machado, H. M. Nguyen, K. A. O’Hearn, A. V. Onufriev, F. Pan, S. Pantano, R. Qi, A. Rahnamoun, A. Risheh, S. Schott-Verdugo, A. Shajan, J. Swails, J. Wang, H. Wei, X. Wu, Y. Wu, S. Zhang, S. Zhao, Q. Zhu, T. E. Cheatham, D. R. Roe, A. Roitberg, C. Simmerling, D. M. York, M. C. Nagan, et K. M. Merz, « AmberTools », *J. Chem. Inf. Model.*, vol. 63, n° 20, p. 6183-6191, oct. 2023, doi: 10.1021/acs.jcim.3c01153.

- [41] F. Bloch, « Über die Quantenmechanik der Elektronen in Kristallgittern », *Z. Physik*, vol. 52, n° 7-8, p. 555-600, juill. 1929, doi: 10.1007/BF01339455.
- [42] F. Jensen, *Introduction to computational chemistry*, Third edition. Chichester, West Sussex Hoboken, NJ Oxford: Wiley, 2017.
- [43] A. Szabo et N. S. Ostlund, *Modern quantum chemistry: introduction to advanced electronic structure theory*, 1. publ., Unabr., Unaltered republ. of the 1. ed., New York 1989. Mineola, New York: Dover Publications, 1996.
- [44] P. G. Szalay, T. Müller, G. Gidofalvi, H. Lischka, et R. Shepard, « Multiconfiguration Self-Consistent Field and Multireference Configuration Interaction Methods and Applications », *Chem. Rev.*, vol. 112, n° 1, p. 108-181, janv. 2012, doi: 10.1021/cr200137a.
- [45] S. Grimme et M. Waletzke, « A combination of Kohn–Sham density functional theory and multi-reference configuration interaction methods », *The Journal of Chemical Physics*, vol. 111, n° 13, p. 5645-5655, oct. 1999, doi: 10.1063/1.479866.
- [46] A. Heil et C. M. Marian, « DFT/MRCI Hamiltonian for odd and even numbers of electrons », *The Journal of Chemical Physics*, vol. 147, n° 19, p. 194104, nov. 2017, doi: 10.1063/1.5003246.
- [47] A. Heil, M. Kleinschmidt, et C. M. Marian, « On the performance of DFT/MRCI Hamiltonians for electronic excitations in transition metal complexes: The role of the damping function », *The Journal of Chemical Physics*, vol. 149, n° 16, p. 164106, oct. 2018, doi: 10.1063/1.5050476.
- [48] I. Lyskov, M. Kleinschmidt, et C. M. Marian, « Redesign of the DFT/MRCI Hamiltonian », *The Journal of Chemical Physics*, vol. 144, n° 3, p. 034104, janv. 2016, doi: 10.1063/1.4940036.
- [49] D. R. Dombrowski, T. Schulz, M. Kleinschmidt, et C. M. Marian, « R2022: A DFT/MRCI Ansatz with Improved Performance for Double Excitations », *J. Phys. Chem. A*, vol. 127, n° 8, p. 2011-2025, mars 2023, doi: 10.1021/acs.jpca.2c07951.

- [50] P. Giannozzi, S. Baroni, N. Bonini, M. Calandra, R. Car, C. Cavazzoni, D. Ceresoli, G. L. Chiarotti, M. Cococcioni, I. Dabo, A. Dal Corso, S. De Gironcoli, S. Fabris, G. Fratesi, R. Gebauer, U. Gerstmann, C. Gougoussis, A. Kokalj, M. Lazzeri, L. Martin-Samos, N. Marzari, F. Mauri, R. Mazzarello, S. Paolini, A. Pasquarello, L. Paulatto, C. Sbraccia, S. Scandolo, G. Sclauzero, A. P. Seitsonen, A. Smogunov, P. Umari, et R. M. Wentzcovitch, « QUANTUM ESPRESSO: a modular and open-source software project for quantum simulations of materials », *J. Phys.: Condens. Matter*, vol. 21, n° 39, p. 395502, sept. 2009, doi: 10.1088/0953-8984/21/39/395502.
- [51] A. M. Rappe, K. M. Rabe, E. Kaxiras, et J. D. Joannopoulos, « Optimized pseudopotentials », *Phys. Rev. B*, vol. 41, n° 2, p. 1227-1230, janv. 1990, doi: 10.1103/PhysRevB.41.1227.
- [52] S. Grimme, J. Antony, S. Ehrlich, et H. Krieg, « A consistent and accurate *ab initio* parametrization of density functional dispersion correction (DFT-D) for the 94 elements H-Pu », *The Journal of Chemical Physics*, vol. 132, n° 15, p. 154104, avr. 2010, doi: 10.1063/1.3382344.
- [53] R. Fletcher, *Practical methods of optimization*, 2nd ed. Chichester ; New York: Wiley, 1987.
- [54] J. Wang, wang Wei, P. A. Kollman, et D. A. Case, « Antechamber: an accessory software package for molecular mechanical calculations ».
- [55] C. I. Bayly, P. Cieplak, W. Cornell, et P. A. Kollman, « A well-behaved electrostatic potential based method using charge restraints for deriving atomic charges: the RESP model », *J. Phys. Chem.*, vol. 97, n° 40, p. 10269-10280, oct. 1993, doi: 10.1021/j100142a004.
- [56] U. C. Singh et P. A. Kollman, « An approach to computing electrostatic charges for molecules », *J Comput Chem*, vol. 5, n° 2, p. 129-145, avr. 1984, doi: 10.1002/jcc.540050204.
- [57] B. H. Besler, K. M. Merz, et P. A. Kollman, « Atomic charges derived from semiempirical methods », *J Comput Chem*, vol. 11, n° 4, p. 431-439, mai 1990, doi: 10.1002/jcc.540110404.

- [58] T. D. Kühne, M. Iannuzzi, M. Del Ben, V. V. Rybkin, P. Seewald, F. Stein, T. Laino, R. Z. Khaliullin, O. Schütt, F. Schiffmann, D. Golze, J. Wilhelm, S. Chulkov, M. H. Bani-Hashemian, V. Weber, U. Borštnik, M. TAILLEFUMIER, A. S. Jakobovits, A. Lazzaro, H. Pabst, T. Müller, R. Schade, M. Guidon, S. Andermatt, N. Holmberg, G. K. Schenter, A. Hehn, A. Bussy, F. Belleflamme, G. Tabacchi, A. Glöß, M. Lass, I. Bethune, C. J. Mundy, C. Plessl, M. Watkins, J. VandeVondele, M. Krack, et J. Hutter, « CP2K: An electronic structure and molecular dynamics software package - Quickstep: Efficient and accurate electronic structure calculations », *The Journal of Chemical Physics*, vol. 152, n° 19, p. 194103, mai 2020, doi: 10.1063/5.0007045.
- [59] C. Campaña, B. Mussard, et T. K. Woo, « Electrostatic Potential Derived Atomic Charges for Periodic Systems Using a Modified Error Functional », *J. Chem. Theory Comput.*, vol. 5, n° 10, p. 2866-2878, oct. 2009, doi: 10.1021/ct9003405.
- [60] C. G. Mayne, J. Saam, K. Schulten, E. Tajkhorshid, et J. C. Gumbart, « Rapid parameterization of small molecules using the force field toolkit », *J. Comput. Chem.*, vol. 34, n° 32, p. 2757-2770, déc. 2013, doi: 10.1002/jcc.23422.
- [61] L. Vanduyfhuys, S. Vandenbrande, T. Verstraelen, R. Schmid, M. Waroquier, et V. Van Speybroeck, « QuickFF: A program for a quick and easy derivation of force fields for metal-organic frameworks from *ab initio* input », *J Comput Chem*, vol. 36, n° 13, p. 1015-1027, mai 2015, doi: 10.1002/jcc.23877.
- [62] F. Dinkelbach, « Electronic Matrix Elements and Their Derivatives for Radiative and Non-Radiative Rate Constants: Development and Applications », Heinrich Heine Universität, Düsseldorf, 2023.
- [63] M. Etinski, J. Tatchen, et C. M. Marian, « Time-dependent approaches for the calculation of intersystem crossing rates », *The Journal of Chemical Physics*, vol. 134, n° 15, p. 154105, avr. 2011, doi: 10.1063/1.3575582.
- [64] M. Etinski, « The role of Duschinsky rotation in intersystem crossing: A case study of uracil », *J Serb Chem Soc*, vol. 76, n° 12, p. 1649-1660, 2011, doi: 10.2298/JSC110713147E.

- [65] M. Etinski, J. Tatchen, et C. M. Marian, « Thermal and solvent effects on the triplet formation in cinnoline », *Phys. Chem. Chem. Phys.*, vol. 16, n° 10, p. 4740, 2014, doi: 10.1039/c3cp53247j.
- [66] N. L. Rosi, J. Eckert, M. Eddaoudi, D. T. Vodak, J. Kim, M. O’Keeffe, et O. M. Yaghi, « Hydrogen Storage in Microporous Metal-Organic Frameworks », *Science*, vol. 300, n° 5622, p. 1127-1129, mai 2003, doi: 10.1126/science.1083440.
- [67] H. Furukawa, K. E. Cordova, M. O’Keeffe, et O. M. Yaghi, « The Chemistry and Applications of Metal-Organic Frameworks », *Science*, vol. 341, n° 6149, p. 1230444, août 2013, doi: 10.1126/science.1230444.
- [68] F. Millange et R. I. Walton, « MIL-53 and its Isorecticular Analogues: a Review of the Chemistry and Structure of a Prototypical Flexible Metal-Organic Framework », *Israel Journal of Chemistry*, vol. 58, n° 9-10, p. 1019-1035, oct. 2018, doi: 10.1002/ijch.201800084.
- [69] J. P. Götze, B. Karasulu, et W. Thiel, « Computing UV/vis spectra from the adiabatic and vertical Franck-Condon schemes with the use of Cartesian and internal coordinates », *The Journal of Chemical Physics*, vol. 139, n° 23, p. 234108, déc. 2013, doi: 10.1063/1.4844055.
- [70] B. Karasulu et W. Thiel, « Photoinduced Intramolecular Charge Transfer in an Electronically Modified Flavin Derivative: Roseoflavin », *J. Phys. Chem. B*, vol. 119, n° 3, p. 928-943, janv. 2015, doi: 10.1021/jp506101x.
- [71] F. B. Dias, T. J. Penfold, et A. P. Monkman, « Photophysics of thermally activated delayed fluorescence molecules », *Methods Appl. Fluoresc.*, vol. 5, n° 1, p. 012001, mars 2017, doi: 10.1088/2050-6120/aa537e.
- [72] Q. Wan, Y. Li, K. Ding, Y. Xie, J. Fan, J. Tong, Z. Zeng, Y. Li, C. Zhao, Z. Wang, et B. Z. Tang, « Aggregation Effect on Multiperformance Improvement in Aryl-Armed Phenazine-Based Emitters », *J. Am. Chem. Soc.*, vol. 145, n° 3, p. 1607-1616, janv. 2023, doi: 10.1021/jacs.2c09210.

- [73] C. K. Yong, A. J. Musser, S. L. Bayliss, S. Lukman, H. Tamura, O. Bubnova, R. K. Hallani, A. Meneau, R. Resel, M. Maruyama, S. Hotta, L. M. Herz, D. Beljonne, J. E. Anthony, J. Clark, et H. Sirringhaus, « The entangled triplet pair state in acene and heteroacene materials », *Nat Commun*, vol. 8, n° 1, p. 15953, juill. 2017, doi: 10.1038/ncomms15953.
- [74] J. C. Johnson, « Open questions on the photophysics of ultrafast singlet fission », *Commun Chem*, vol. 4, n° 1, p. 85, juin 2021, doi: 10.1038/s42004-021-00527-w.
- [75] S. Singh, W. J. Jones, W. Siebrand, B. P. Stoicheff, et W. G. Schneider, « Laser Generation of Excitons and Fluorescence in Anthracene Crystals », *The Journal of Chemical Physics*, vol. 42, n° 1, p. 330-342, janv. 1965, doi: 10.1063/1.1695695.
- [76] A. Neef, S. Beaulieu, S. Hammer, S. Dong, J. Maklar, T. Pincelli, R. P. Xian, M. Wolf, L. Rettig, J. Pflaum, et R. Ernstorfer, « Orbital-resolved observation of singlet fission », *Nature*, vol. 616, n° 7956, p. 275-279, avr. 2023, doi: 10.1038/s41586-023-05814-1.
- [77] A. Neef, M. Rossi, M. Wolf, R. Ernstorfer, et H. Seiler, « On the Role of Nuclear Motion in Singlet Exciton Fission: The Case of Single-Crystal Pentacene », *Physica Status Solidi (a)*, vol. 221, n° 1, p. 2300304, janv. 2024, doi: 10.1002/pssa.202300304.
- [78] E. G. Fuemmeler, S. N. Sanders, A. B. Pun, E. Kumarasamy, T. Zeng, K. Miyata, M. L. Steigerwald, X.-Y. Zhu, M. Y. Sfeir, L. M. Campos, et N. Ananth, « A Direct Mechanism of Ultrafast Intramolecular Singlet Fission in Pentacene Dimers », *ACS Cent. Sci.*, vol. 2, n° 5, p. 316-324, mai 2016, doi: 10.1021/acscentsci.6b00063.
- [79] R. D. Pensack, E. E. Ostroumov, A. J. Tilley, S. Mazza, C. Grieco, K. J. Thorley, J. B. Asbury, D. S. Seferos, J. E. Anthony, et G. D. Scholes, « Observation of Two Triplet-Pair Intermediates in Singlet Exciton Fission », *J. Phys. Chem. Lett.*, vol. 7, n° 13, p. 2370-2375, juill. 2016, doi: 10.1021/acs.jpcllett.6b00947.
- [80] T. Schulz, « Evaluation of the DFT/MRCI Method in the contexts of Singlet Fission and Photodetachment-Photoelectron spectroscopy », Heinrich Heine Universitat, Dusseldorf, 2024.

- [81] C. C. Mattheus, A. B. Dros, J. Baas, A. Meetsma, J. L. D. Boer, et T. T. M. Palstra, « Polymorphism in pentacene », *Acta Crystallogr C Cryst Struct Commun*, vol. 57, n° 8, p. 939-941, août 2001, doi: 10.1107/S010827010100703X.
- [82] T. Nagami, H. Miyamoto, R. Sakai, et M. Nakano, « Stabilization of Charge-Transfer States in Pentacene Crystals and Its Role in Singlet Fission », *J. Phys. Chem. C*, vol. 125, n° 4, p. 2264-2275, févr. 2021, doi: 10.1021/acs.jpcc.0c10029.
- [83] J. E. Anthony, J. S. Brooks, D. L. Eaton, et S. R. Parkin, « CCDC 172476: Experimental Crystal Structure Determination ». Cambridge Crystallographic Data Centre, 2001. doi: 10.5517/CC5SGR4.
- [84] S. R. Hall, F. H. Allen, et I. D. Brown, « The crystallographic information file (CIF): a new standard archive file for crystallography », *Acta Crystallogr A Found Crystallogr*, vol. 47, n° 6, p. 655-685, nov. 1991, doi: 10.1107/S010876739101067X.
- [85] I. D. Brown et B. McMahon, « CIF: the computer language of crystallography », *Acta Crystallogr B Struct Sci*, vol. 58, n° 3, p. 317-324, juin 2002, doi: 10.1107/S0108768102003464.
- [86] wwPDB consortium, S. K. Burley, H. M. Berman, C. Bhikadiya, C. Bi, L. Chen, L. D. Costanzo, C. Christie, J. M. Duarte, S. Dutta, Z. Feng, S. Ghosh, D. S. Goodsell, R. K. Green, V. Guranovic, D. Guzenko, B. P. Hudson, Y. Liang, R. Lowe, E. Peisach, I. Periskova, C. Randle, A. Rose, M. Sekharan, C. Shao, Y.-P. Tao, Y. Valasatava, M. Voigt, J. Westbrook, J. Young, C. Zardecki, M. Zhuravleva, G. Kurisu, H. Nakamura, Y. Kengaku, H. Cho, J. Sato, J. Y. Kim, Y. Ikegawa, A. Nakagawa, R. Yamashita, T. Kudou, G.-J. Bekker, H. Suzuki, T. Iwata, M. Yokochi, N. Kobayashi, T. Fujiwara, S. Velankar, G. J. Kleywegt, S. Anyango, D. R. Armstrong, J. M. Berrisford, M. J. Conroy, J. M. Dana, M. Deshpande, P. Gane, R. Gáborová, D. Gupta, A. Gutmanas, J. Koča, L. Mak, S. Mir, A. Mukhopadhyay, N. Nadzirin, S. Nair, A. Patwardhan, T. Paysan-Lafosse, L. Pravda, O. Salih, D. Sehnal, M. Varadi, R. Vařeková, J. L. Markley, J. C. Hoch, P. R. Romero, K. Baskaran, D. Maziuk, E. L. Ulrich, J. R. Wedell, H. Yao, M. Livny, et Y. E. Ioannidis, « Protein Data Bank: the single global archive for 3D macromolecular structure data », *Nucleic Acids Research*, vol. 47, n° D1, p. D520-D528, janv. 2019, doi: 10.1093/nar/gky949.

Included papers

Article

Enhanced Solid-State Fluorescence of Flavin Derivatives by Incorporation in the Metal-Organic Frameworks MIL-53(Al) and MOF-5

Dietrich Püschel ¹, Simon Hédé ², Iván Maisuls ³, Simon-Patrick Höfert ¹, Dennis Woschko ¹, Ralf Kühnemuth ⁴, Suren Felekyan ⁴, Claus A. M. Seidel ^{4,*} , Constantin Czekelius ⁵, Oliver Weingart ^{2,*} , Cristian A. Strassert ^{3,*} and Christoph Janiak ^{1,*} 

¹ Institut für Anorganische Chemie und Strukturchemie, Heinrich-Heine-Universität Düsseldorf, Universitätsstraße 1, D-40225 Düsseldorf, Germany

² Institut für Theoretische Chemie und Computerchemie, Heinrich-Heine-Universität Düsseldorf, Universitätsstraße 1, D-40225 Düsseldorf, Germany

³ Institut für Anorganische und Analytische Chemie, CeNTech, CiMIC, SoN, Westfälische Wilhelms-Universität Münster, Heisenbergstraße 11, D-48149 Münster, Germany

⁴ Institut für Physikalische Chemie, Heinrich-Heine-Universität Düsseldorf, Universitätsstraße 1, D-40225 Düsseldorf, Germany

⁵ Institut für Organische Chemie und Makromolekulare Chemie, Heinrich-Heine-Universität Düsseldorf, Universitätsstraße 1, D-40225 Düsseldorf, Germany

* Correspondence: cseidel@hhu.de (C.A.M.S.); oliver.weingart@hhu.de (O.W.); ca.s@wwu.de (C.A.S.); janiak@uni-duesseldorf.de (C.J.); Tel.: +49-2118-112-286

Abstract: The flavin derivatives 10-methyl-isoalloxazine (MIA) and 6-fluoro-10-methyl-isoalloxazine (6F-MIA) were incorporated in two alternative metal-organic frameworks, (MOFs) MIL-53(Al) and MOF-5. We used a post-synthetic, diffusion-based incorporation into microcrystalline MIL-53 powders with one-dimensional (1D) pores and an in-situ approach during the synthesis of MOF-5 with its 3D channel network. The maximum amount of flavin dye incorporation is 3.9 wt% for MIA@MIL-53(Al) and 1.5 wt% for 6F-MIA@MIL-53(Al), 0.85 wt% for MIA@MOF-5 and 5.2 wt% for 6F-MIA@MOF-5. For the high incorporation yields the probability to have more than one dye molecule in a pore volume is significant. As compared to the flavins in solution, the fluorescence spectrum of these flavin@MOF composites is broadened at the bathochromic side especially for MIA. Time-resolved spectroscopy showed that multi-exponential fluorescence lifetimes were needed to describe the decays. The fluorescence-weighted lifetime of flavin@MOF of 4 ± 1 ns also corresponds to those in solution but is significantly prolonged compared to the solid flavin dyes with less than 1 ns, thereby confirming the concept of “solid solutions” for dye@MOF composites. The fluorescence quantum yield (Φ_F) of the flavin@MOF composites is about half of the solution but is significantly higher compared to the solid flavin dyes. Both the fluorescence lifetime and quantum yield of flavin@MOF decrease with the flavin loading in MIL-53 due to the formation of various J-aggregates. Theoretical calculations using plane-wave and QM/MM methods are in good correspondence with the experimental results and explain the electronic structures as well as the photophysical properties of crystalline MIA and the flavin@MOF composites. In the solid flavins, π -stacking interactions of the molecules lead to a charge transfer state with low oscillator strength resulting in aggregation-caused quenching (ACQ) with low lifetimes and quantum yields. In the MOF pores, single flavin molecules represent a major population and the computed MIA@MOF structures do not find π -stacking interactions with the pore walls but only weak van-der-Waals contacts which reasons the enhanced fluorescence lifetime and quantum yield of the flavins in the composites compared to their neat solid state. To analyze the orientation of flavins in MOFs, we measured fluorescence anisotropy images of single flavin@MOF-5 crystals and a static ensemble flavin@MIL53 microcrystals, respectively. Based on image information, anisotropy distributions and overall curve of the time-resolved anisotropy curves combined with theoretical calculations, we can prove that all fluorescent flavins species have a defined and rather homogeneous orientation in the MOF framework. In MIL-53, the transition dipole moments of flavins are orientated along the 1D channel axis, whereas in MOF-5 we resolved an



Citation: Püschel, D.; Hédé, S.; Maisuls, I.; Höfert, S.-P.; Woschko, D.; Kühnemuth, R.; Felekyan, S.; Seidel, C.A.M.; Czekelius, C.; Weingart, O.; et al. Enhanced Solid-State Fluorescence of Flavin Derivatives by Incorporation in the Metal-Organic Frameworks MIL-53(Al) and MOF-5. *Molecules* **2023**, *28*, 2877. <https://doi.org/10.3390/molecules28062877>

Academic Editors: Mei Hong and Guangchao Zheng

Received: 25 January 2023

Revised: 14 March 2023

Accepted: 17 March 2023

Published: 22 March 2023



Copyright: © 2023 by the authors. Licensee MDPI, Basel, Switzerland. This article is an open access article distributed under the terms and conditions of the Creative Commons Attribution (CC BY) license (<https://creativecommons.org/licenses/by/4.0/>).

cence anisotropy images of single flavin@MOF-5 crystals and a static ensemble flavin@MIL53 microcrystals, respectively. Based on image information, anisotropy distributions and overall curve of the time-resolved anisotropy curves combined with theoretical calculations, we can prove that all fluorescent flavins species have a defined and rather homogeneous orientation in the MOF framework. In MIL-53, the transition dipole moments of flavins are orientated along the 1D channel axis, whereas in MOF-5 we resolved an average orientation that is tilted with respect to the cubic crystal lattice. Notably, the more hydrophobic 6F-MIA exhibits a higher degree order than MIA. The flexible MOF MIL-53(AI) was optimized essentially to the experimental large-pore form in the guest-free state with QuantumEspresso (QE) and with MIA molecules in the pores the structure contracted essentially to the experimental narrow-pore form in the guest-free state with QuantumEspresso (QE) and with MIA molecules in the pores the structure contracted to close to the experimental narrow-pore form which was also confirmed by PXRD. In summary, the incorporation of flavins in MOFs yields solid-state materials with enhanced rigidity, stabilized conformation, defined orientation and reduced aggregations of the flavins, leading to increased fluorescence lifetime and quantum yield as controllable photo-luminescent and photo-physical properties.

Keywords: flavins; 10-methyl-isoalloxazine; metal-organic framework (MOF); MIL-53; MOF-5; fluorescence; flavin@MOF; solid solution; dye anisotropy; fluorescence lifetime; multiparametric fluorescence microscopy

1. Introduction

Flavins represent a ubiquitous group of compounds in nature [1–4]. The basic structure consists of an isoalloxazine ring system (Figure 1) that has strong fluorescent properties [4,5]. Besides the well-known vitamin B₂, flavins or riboflavins occur predominantly in combination with proteins as the so-called flavoproteins [1,6,7]. Flavoproteins play an important role in the respiratory chain of cells [1]. In addition, light-dependent biological processes such as flowering and circadian rhythm often employ this class of chromophore [8,9]. Flavins that are not bound to proteins are of great interest due to their photochemical and photophysical properties [10]. As in nature, flavins are used as photo-redox catalysts due to their redox properties [11,12]. In aqueous solution, all flavins exhibit strong absorptions in the ultraviolet and visible range. The absorption spectra typically show two bands with high molar absorptivities ($>10^4$ L mol⁻¹ cm⁻¹) which are attributed to $\pi \rightarrow \pi^*$ excitations [12,14]. The exact position of the absorption maxima, the absorptivity, the absorption and the photoluminescence yield depend significantly on the chemical structure of the flavine derivative and the chemical-physical environment, including solvation effects [15,16].

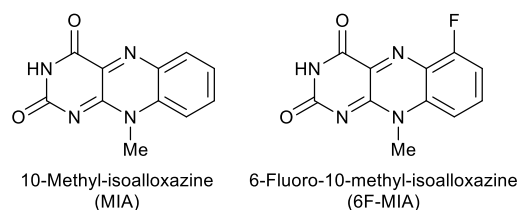


Figure 1. 10-Methyl-isoalloxazine (MIA) and the mono-fluorinated derivative 6-fluoro-10-methyl-isoalloxazine (6F-MIA) [17].

In their neat solid state, the photoluminescence of dye molecules is often quenched by nonradiative processes. The incorporation of luminescent dye molecules into metal-organic frameworks (MOFs) as a dye@MOF composite tries to exploit the photophysical properties of single molecules in a well-defined solid-state environment for applications such as white-light emission, upconversion, non-linear optics, biological fluorescent imaging, chemical sensing, optical thermometry and others [18–23]. The structure and pore environment of MOF compounds can be designed by the selection of organic linkers and the metal cluster secondary building units (SBUs) [24–31]. Through incorporation into MOFs, the dye molecules could be protected from dynamic quenching, e.g., by O₂ or solvent interactions. Aggregation-caused quenching (ACQ) of the dye in the solid-state is also effectively prevented by the confinement of separated single molecules in the pore system [18,32]. This protection could ensure consistent luminescence even under harsh environmental conditions. Conversely, targeted quenching of dyes by the selective addi-

environment of MOF compounds can be designed by the selection of organic linkers and the metal cluster secondary building units (SBUs) [24–31]. Through incorporation into MOFs, the dye molecules could be protected from dynamic quenching, e.g., by O₂ or solvent interactions. Aggregation-caused quenching (ACQ) of the dye in the solid-state is also effectively prevented by the confinement of separated single molecules in the pore system [18,32]. This protection could ensure consistent luminescence even under harsh environmental conditions. Conversely, targeted quenching of dyes by the selective additional adsorption of analyte species in dye@MOF composites could be interesting in sensor technologies [18,33–40].

A prerequisite for the MOF as a host for a dye guest with unchanged fluorescence is a minimal interference of MOF and dye. If the MOF should just act as a host matrix, then ideally the MOF should show no fluorescence and color. Accordingly, aluminum-based MIL-53, [Al(OH)(hdc)] (hdc = benzene-1,4-dicarboxylate) [41–50] and zinc-based MOF-5, [Zn₄O(O₂)₆] [51–53] are promising host networks (see Section S3, Supplementary materials for structure details).

The crystalline MOF host structures are often seen to give also a highly ordered packing of the dye molecule guests. Such an optimal alignment in host guest MOF hybrids and materials would be needed for polarized nonlinear optical responses [20,53] to tune the exciton coupling [54] [34]. Yet, a correlation between photoreponses and anisotropy of dye guest molecules in ordered host matrices appears to be seldom done, e.g., in dyes [55,56]. Here we chose the prototypical and well characterized MOFs MIL-53(Al) with its periodic one-dimensional channels and MOF-5 with its three-dimensional orthogonal channel structure (Fig. (Fig. 2) and 2) for a proof of principle analysis of the anisotropy of encapsulated dye molecules in these MOFs.

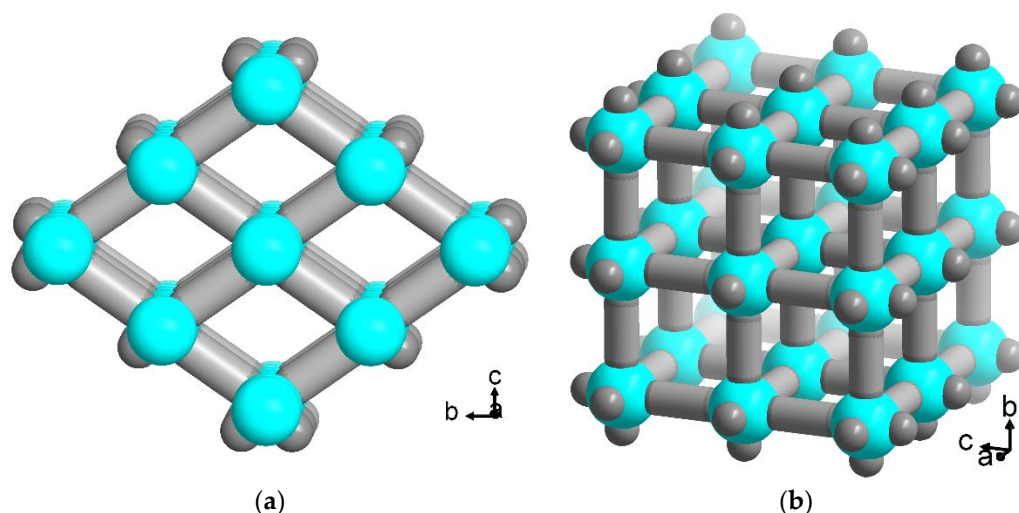


Figure 2. Schematic presentation of the periodic channel structures in (a) MIL-53, [Al(OH)(hdc)] and (b) MOF-5, [Zn₄O(O₂)₆] (hdc = benzene-1,4-dicarboxylate). The inorganic building units {Al(OH)} and {Zn₄O(O₂)₆}, respectively, are represented in cyan and the hdc linker schematically as a grey rod; see Section S3, Supplementary materials for structure details). (Structure images were drawn with Diamond [57] from the deposited cif files under CCDC-no./Refcode 220476/SABVUN [41] and 256966/SAHYOQ [52,58]).

Furthermore, single crystals with an average diameter of 100 µm can be obtained for MOF-5 which allow the imaging of the embedded flavin with confocal laser scanning microscopy (CLSM) [59].

To the best of our knowledge we are not aware of flavin@MOF composites. Here, we report the incorporation of the flavin derivatives 10-methyl-isoalloxazine (MIA) and 6-fluoro-10-methyl-isoalloxazine (6F-MIA) (Figure 1) in the prototypical MOFs MIL-53 and MOF-5 and analyze the effects of the flavin@MOF composites on emission wavelength, the fluorescence lifetimes and photoluminescence quantum yields in comparison to the neat solid state and solution. The electronic structures of crystalline MIA, MIA@MIL-53 and MIA@MOF-5 and the resulting luminescent properties were calculated with plane-wave and QM/MM methods and compared with the experimental data.

2. Results and Discussion

The incorporation of the flavin derivatives 10-methyl-isoalloxazine (MIA) and 6-fluoro-10-methyl-isoalloxazine (6F-MIA) into MIL-53 and MOF-5 was carried out using a post-synthetic, diffusion-based incorporation into microcrystalline MIL-53 powders and an in situ embedding during MOF-5 synthesis.

2.1. Flavin@MIL-53 Synthesis

For the post-synthetic wet infiltration of MIL-53, different quantities of a saturated MIA or 6F-MIA solution in chloroform were added to the activated MOF MIL-53-lp and the suspension stored on an orbital shaker until all the solvent had been evaporated. The flavin@MIL-53 composites were washed with chloroform and then dried at 60 °C under dynamic vacuum. The MIA@MIL-53 composites contained 0.4 to 2.7 wt% of the flavin in the MOF and the 6F-MIA@MIL-53 composites between 0.1 to 1.5 wt% (see Supplementary Materials for details).

To further verify the incorporation of the flavins in the MOFs, nitrogen adsorption isotherms were recorded at 77 K (Figure S16). For very small amounts of incorporated flavin in MIL-53 (<1 wt% for MIA and 0.1 wt% for 6F-MIA), a slight increase in the internal surface area may occur (Table 1), which can be attributed to an additional washing effect exerted by shaking in the flavin solution. The proportional decrease in BET surface area and pore volume (Table 1) with an increase in flavin amount indicates successful incorporation into the network. The initial S_{BET} value of 1130–1150 m²/g for MIL-53 decreases to 80 m²/g (MIA@MIL-53) and 40 m²/g (6F-MIA@MIL-53), corresponding to a nearly nonporous structure which is due to pore blocking by occupation of the pore mouths with the flavin molecules. For the small wt% of the flavin the pore volume of the large-pore form of MIL-53 cannot be completely filled. Based on the crystallographic density ρ in the crystal structure of MIA of $\rho = 1.6 \text{ g/cm}^3$ [60] and $1/\rho = 0.63 \text{ cm}^3/\text{g}$, the maximum flavin loading of ~4 wt%, that is 0.04 g(flavin)/g(composite), would only occupy a volume of 0.025 cm³/g or about 6% of the determined total pore volume of ~0.5 cm³/g in neat MIL-53.

Table 1. Results of nitrogen sorption measurements for MIL-53 and flavin@MIL-53.

Compound	Flavin Loading [wt%] ^a	S_{BET} [m ² /g]	$V_{\text{pore(total)}}$ [cm ³ /g] ^b	$V_{\text{pore(micro;NLDFT)}}$ [cm ³ /g] ^c
MIL-53-lp literature	-	1150 [61]	0.53	0.53
	-	1140 [41]	n.a.	n.a.
MIL-53-lp synthesized	-	1130	0.45	0.43
MIA@MIL-53	0.4	1290	0.52	0.50
	0.8	1130	0.47	0.46
	1.6	1000	0.43	0.43
	2.0	890	0.41	0.42
	2.7	340	0.17	0.20
	3.9	80	0.05	0.09
6F-MIA@MIL-53	0.1	1150	0.49	0.49
	0.5	890	0.41	0.42
	1.0	600	0.28	0.30
	1.5	40	0.02	0.04

^a Calculated by UV-VIS from initial flavin concentration. ^b Total pore volume at $p/p_0 = 0.50$ for pores $\leq 2 \text{ nm}$.

^c Micropore volume calculated from NLDFT for pores $\leq 2 \text{ nm}$.

When we consider the MIL-53 formula unit of $[\text{Al}(\text{OH})\text{bdc}]$ ($M = 208.11 \text{ g/mol}$), then there is one channel segment of 13 Å (which is about the length of a MIA molecule) for 8 formula units. At a loading of 4 wt% MIA@MIL-53 we have 0.04 g MIA (0.175 mmol) in 0.96 g MIL-53 (4.6 mmol). Thus, the molar ratio of MIA molecules to the channel segments of 13 Å is $0.175:(4.6/8) = 0.3$ or ~3.3 channel segments per MIA molecule. In other words, on average at this loading the MIA molecules can be $\sim 2 \times 13 \text{ Å} = 26 \text{ Å}$ apart, that is separated

by 26 Å. At a loading of 1.5 wt% 6F-MIA@MIL-53, we have 0.015 g MIA (0.06 mmol) in 0.985 g MIL-53 (4.7 mmol). Thus, the molar ratio of 6F-MIA molecules to the channel segments of 13 Å is $0.06:(4.7/8) = 0.1$ or ~ 10 channel segments per 6F-MIA molecule. On average at this loading the 6F-MIA molecules can be $\sim 9 \times 13 \text{ Å} = 117 \text{ Å}$ separated along a channel. Other diffusion-based incorporations into MOFs have shown that in such a post-synthetic modification the molecules remain trapped close to the pore mouths [59]. For MIL-53 with its flexibility and breathing mode, formation of the narrow-pore form can also occur upon activation, which precedes the nitrogen sorption measurement.

The phase analysis of the flexible MIL-53 network structure after flavin insertion and before activation by powder X-ray diffraction (PXRD) shows a superposition of the three MIL-53 phases from the comparison of the MIA@MIL-53 composites with the simulated MIL-53-as, MIL-53-np and MIL-53-lp diffractograms (Figure S17a). The samples with the two highest loadings (2.7 wt% and 3.9 wt% for MIA, 1.0 wt% and 1.5 wt% for 6F-MIA) were measured before and after activation (Figure S17b). The incorporated flavin affects the phase which the flexible MIL-53 network assumes. A loading of up to 2.7 wt% MIA gives only the narrow-pore form after activation which is understandable if the flavin molecules would occupy little of the inner pore volume and do not penetrate deep into the channels. At a loading of 3.9 wt% MIA, a superposition of the large- and narrow-pore form remains (Figure S17b). The comparison of the 6F-MIA@MIL-53 composites with the simulated MIL-53 PXRDs patterns show good matches with the MIL-53-lp form, independently of incorporated flavin amounts (Figure S18a). For 1.0 wt% 6F-MIA@MIL-53 after activation the PXRD is also a superposition of the large- and narrow-pore phases (Figure S18b). At the maximum loading of 1.5 wt% of 6F-MIA, almost no change in the diffractogram is evident upon activation, indicating retention of the large-pore form with just a trace formation of the narrow-pore phase (Figure S18b).

2.2. Flavin@MOF-5 Synthesis

The flavins were incorporated in situ into MOF-5, that is during the MOF formation, in order to achieve a uniform distribution and pore filling of the flavins throughout the network [51,59]. From a comparison of the dimensions of MIA and 6F-MIA ($4 \times 8.5 \times 12 \text{ Å}$) (Figure S12) with the pore diameter of 15 Å in MOF-5, which is larger than its pore window size ($8 \times 8 \text{ Å}$) (Figure S15), the flavin molecules can be very well incorporated during the crystal formation. By using concentrated solutions of the flavins in dimethylformamide (DMF), cubic single crystals with an edge length up to 1 mm were synthesized according to a protocol by Han et al. [62].

The incorporated flavin amounts were determined to 0.85 wt% for MIA@MOF-5 by UV/Vis spectroscopy from the supernatant solution (Section S1.2) and to 5.2 wt% for 6F-MIA@MOF-5 by postsynthetic digestion ^1H NMR (Section S1.2). The higher amount of 6F-MIA is explained by the very good solubility of 6F-MIA in DMF for a saturated solution of $c_{6\text{F-MIA}} = 2640 \text{ mg}\cdot\text{L}^{-1}$ whereas MIA was much less soluble, giving only $c_{\text{MIA}} = 272 \text{ mg}\cdot\text{L}^{-1}$ as a saturated solution (Section S2). From the crystallographic density of MIA of $\rho = 1.6 \text{ g}/\text{cm}^3$ [60] and $1/\rho = 0.63 \text{ cm}^3/\text{g}$, the 6F-MIA loading of 0.052 g(6F-MIA)/g(composite) would still occupy only a volume of $0.03 \text{ cm}^3/\text{g}$ or about 3% of the total pore volume of $\sim 1.0 \text{ cm}^3/\text{g}$ in neat MOF-5 [52]. The MOF-5 formula unit is $[\text{Zn}_4\text{O}(\text{bdc})_3]$ ($M = 769.87 \text{ g}/\text{mol}$). There is 1 “pore” per formula unit. At a loading of 0.85 wt% MIA@MOF-5 we have 0.0085 g MIA (37 μmol) in 0.9915 g MOF-5 (1.3 mmol). Thus, the molar ratio of MIA molecules to pores is 0.037:1.3 or 0.029 (MIA per pore), or ~ 34 pores for each MIA molecule. At a loading of 5.2 wt% 6F-MIA@MOF-5 we have 0.052 g MIA (0.21 mmol) in 0.95 g MOF-5 (1.2 mmol). Thus, the molar ratio of 6F-MIA molecules to pores is 0.21:1.2 or 0.18 (6F-MIA per pore), that is on average 5.7 pores for each MIA molecule.

Powder X-ray diffraction shows a good match between the flavin@MOF-5 composites, synthesized MOF-5 crystals and the simulated MOF-5 diffractogram (Figure S19).

(1.2 mmol). Thus, the molar ratio of 6F-MIA molecules to pores is 0.21:1.2 or 0.18 (6F-MIA (1.2 mmol). Thus, the molar ratio of 6F-MIA molecules to pores is 0.21:1.2 or 0.18 (6F-MIA per pore), that is on average 5.7 pores for each MIA molecule.

Powder X-ray diffraction shows a good match between the flavin@MOF-5 composites, synthesized MOF-5 crystals and the simulated MOF-5 diffractogram (Figure S19). The large flavin@MOF-5 crystals were analyzed by confocal laser scanning microscopy (CLSM) for the distribution of MIA (Figure 3) and 6F-MIA (Figure 4) in the MOF. The fluorescence images of the sectional planes support an even incorporation of the dyes. The fluorescence images of the sectional planes support an even incorporation of the flavin dyes throughout the whole MOF crystals during the in situ synthesis.

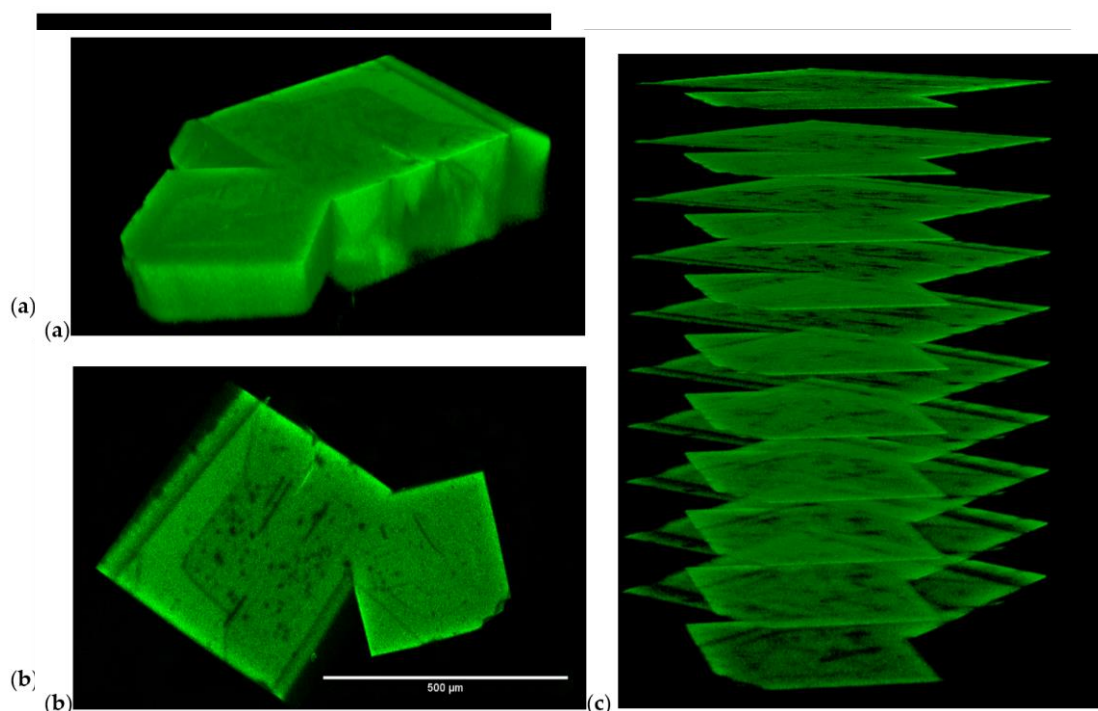


Figure 3. Confocal images of MIA@MOF-5. (a) Confocal laser scanning microscopy 3D profile. (b) Confocal laser scanning microscopy 3D profile. (c) Stack of sectional planes of MIA@MOF-5. (b) sectional plane at 200 μm from top, and (c) stack of sectional planes of MIA@MOF-5. Excitation at $\lambda_{exc} = 458 \text{ nm}$, $\lambda_{em} = 530–555 \text{ nm}$. Every sectional plane corresponds to a measurement thickness of 4 μm, which corresponds to the optical resolution of the used objective (UPSAPO10X/0.4NA).

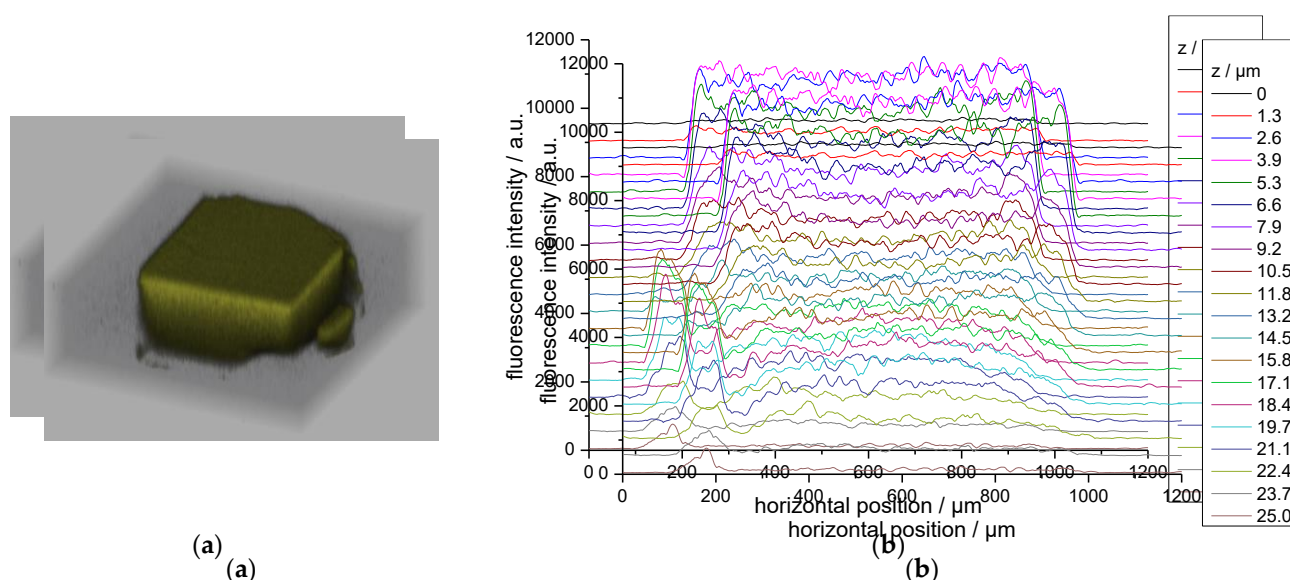


Figure 4. (a) Confocal laser scanning microscopy 3D profile for a height z of 25 μm. (b) line profile of 6F-MIA@MOF-5. The fluorescence intensity decreases with the depth due to the inner filter effect. (UPSAPO10X/0.4NA). The fluorescence intensity decreases with the depth due to the inner filter effect. (UPSAPO10X/0.4NA). The fluorescence intensity decreases with the depth due to the inner filter effect.

2.3. Fluorescence Spectroscopy and Photophysics

Before discussing the fluorescence properties of the flavin@MOF composites in detail, it is important to consider which fluorescent species can be expected upon incorporation in MOFs. Since we varied the loading rate of incorporated flavins, we computed the probability p that a certain occupation number of flavins per site could be incorporated in MOFs assuming a random distribution of dyes. Using the average numbers of flavins per site $n_{av}(\text{flavins/site})$ approximated in Sections 2.1 and 2.2, our computation shows that the probability $p(> one)$ that more than one flavin is incorporated per site can be significant for our conditions (Table 2). The probability $p(> one)$ is higher in MIL-53 already at low loading as compared to MOF-5. In this context, it is important to take into account that organic chromophores with an extended π system can stack in solution with increasing concentration so that H- or J-aggregates of variable composition and structural arrangements can be formed. Due to the affinity of these chromophores to associate, the computed probabilities $p(> one)$ represent only lower limits that will be even higher in reality. Thus, flavin confinement in MOF composites could lead to J- or H-aggregates of variable stoichiometry. Notably, the emission properties of the chromophore aggregates critically depend on the strength of the excitonic coupling and on charge transfer interactions which can be influenced by their orientation stoichiometry and chemical structure. Therefore, we can expect variable fluorescent species for flavin@MOFs. Accordingly, we investigated in the following, whether the measured fluorescence spectra, lifetimes and anisotropies indicate the presence of multiple fluorescent species that could be related to aggregates.

Table 2. Probability p that a certain occupation number of flavins per site is confined in MOFs assuming a random distribution of flavins ^a.

	MIA@MOF-5 0.85 wt%	6F MIA@MOF-5 5.2 wt%	MIA@MIL-53 3.9 wt%	6F MIA@MIL-53 1.5 wt%
$n_{av}(\text{flavins/site})$	0.029	0.18	0.3	0.1
$p(one)$	98.7%	92.0%	86.9%	95.5%
$p(two)$	1.3%	7.6%	12.1%	4.3%
$p(\geq three)$	0.0%	0.4%	1.0%	0.1%

^a: Site corresponds to a pore in MOF-5 and to a channel segment in MIL-53, respectively. Since the channel in MIL-53 is infinite, we cannot speak of “pores” as in MOF-5. Therefore, we define the length of a channel segment that is needed to host a MIA via the length of MIA molecule of ≈ 13 Å.

The fluorescence spectra at room temperature of both flavins, in a solution of 1:1 DCM/MeOH and in solid amorphous powder, are compared with their composites (bold lines) in Figure 5 for measurements at room temperature. Additional fluorescence spectra at 77 K were measured for all compounds and are compared with the corresponding spectra at room temperature in the supplementary materials Section S5, Figures S20–S23. The fluorescence spectrum of solid MIA is strongly red shifted with respect to the solution in 1:1 DCM/MeOH, while this shift is much weaker for 6F-MIA where a shoulder appears around 650 nm. The fluorescence spectra of flavin@MOF composites reveal a broadening at the bathochromic side that is stronger for higher loadings. We conclude that a mixture of emitters (flavin monomers and aggregates) exists. Due to the bathochromic shift of the spectra and the presence of shoulders for lower emission energies, we identify fluorescent J-aggregates as additional emitters. Consistently, the presence of bathochromically shifted emitters was enhanced for high flavin loadings at 77 K.

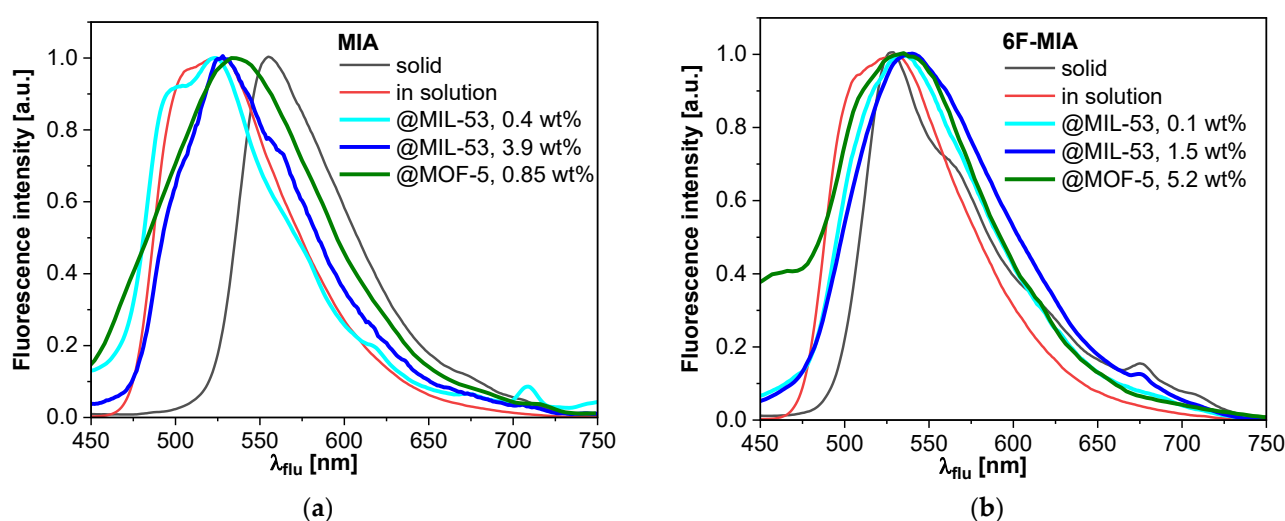


Figure 5. Normalized fluorescence spectra at room temperature of (a) MIA and (b) 6F-MIA in their neat solid state, in 1:1 DCM/MeOH solution and for the flavin@MOF composites; wt% refers to the flavin loading. Since the fluorescence signal of flavin@MOF composites with low loading is weak, the contributions of scattered excitation light at short emission wavelengths becomes relevant, which causes additional shoulders in the spectra at short wavelengths.

Next, we analyzed the fluorescence lifetimes and quantum yields. Table 3 summarizes fluorescence lifetimes (τ), quantum yields (Φ_F) and the wavelengths of the fluorescence maxima ($\lambda_{F,max}$) of the flavin dyes MIA, 6F-MIA and the flavin@MOF composites, which were measured with a time-resolved fluorescence spectrometer front-face sample holder (fluorescence spectra in Figure 3 and Figures S20–S23) and multiparameter fluorescence image spectroscopy (MFIS) with polarization resolved detection, both using single photon timing electronics. All measured time-resolved fluorescence decays of both instruments are displayed in Figures S23–S33. The time-resolved fluorescence measurements in the fluorescence spectrometer and the confocal microscope with multiparameter fluorescence detection (see Section 3) gave consistent results. All fluorescence decays of flavin@MOF composites are multi-exponential. In addition to three fluorescence lifetimes in the ns range, polarisation-resolved MFIS detected a significant fraction of depolarized signal (i.e. fluorescence and not scattered excitation light) with a lifetime of 30 ps, which indicates the presence of strongly quenched fluorescent species. This agrees with the drop of the fluorescence quantum yields, Φ_F , observed for flavin@MOF composites. Notably, the fluorescence lifetimes of solid flavins are all in low picosecond time ranges, too. This finding agrees also with the quantum-chemical calculations presented in Section 2.4 below and in supplementary material section S6. Although the fluorescence quantum yields, Φ_F , in flavin@MOF composites indicate partially quenched fluorescence species, the Φ_F values are up to 8 times higher than for solid flavins. Moreover, in agreement with Table 2, we observe a qualitative correlation between lower fractions of quenched species for the loading and the $\lambda_{F,max}$ (or λ_{exc}). The flavin tendency of forming aggregates is already visible in solution. While measurements of pure dyes (most likely fluorescent species) are most likely a small fraction of defective or aggregated species, the detectable species in the DCM/MeOH dissolving flavin@MOF composites are significantly more species, is detectable in the solid state, while the flavin@MOF composites are dissolved while the flavin@MOF composites are dissolved. The longest DCM/MeOH species' lifetime with 10 and 20% is in the range 10 and 20 ns in this range of $\lambda_{F,max}$ and λ_{exc} is longer than the lifetime of the measurement and solid state measurements and suggest that weakly aggregated species can coexist.

We applied confocal multi-parameter fluorescence image spectroscopy (MFIS) to map also the spatial and orientation dependence of the fluorescence properties for the microcrystalline sample of flavin@MIL-53 and large single crystals of flavin@MOF-5.

Table 3. Photophysical data for MIA, 6F-MIA and the flavin@MOF composites with $\lambda_{exc} = 405$ nm (TCSPC) or 440 nm (confocal MFIS) at room temperature (RT) unless indicated otherwise.

Compound	$\lambda_{F,max}$ [nm] ^a	τ_1 (x_1), τ_2 (x_2), τ_3 (x_3) [ns] ^b	τ_F [ns] ^b	τ_x [ns] ^b	x_{sq} ^g	Φ_F [%] ^c
MIA in solution:						
DCM/MeOH (RT)	527 ^d	10.2 (0.20), 6.1 (0.62), 2.9 (0.19)	7.1	6.3 ^d		28 ^d
DCM/MeOH (77 K) ^h	487/513	7.5 (1)	7.5	7.5		54
water	524 ^e	5.0 (1)	5.0	5.0 ^e		22
MIA solid	555, theo: 540 ^f	3.5 (0.01), 0.8 (0.12), 0.2 (0.87)	0.8	0.3		<2
0.4 wt% MIA@MIL-53	523	7.2 (0.22), 4.0 (0.51), 1.7 (0.27)	5.0	4.1		15
3.9 wt% MIA@MIL-53	527, theo: 509 ^f	7.6 (0.17), 4.0 (0.51), 1.3 (0.32)	4.9	3.7		11
		6.2 (0.13), 2.5 (0.33), 0.7 (0.53) ^g	3.6 ^g	2.1 ^g	0.87 ^g	
0.85 wt% MIA@MOF-5	533, theo: 528 ^f	9.5 (0.10), 4.2 (0.55), 1.3 (0.35)	5.1	3.7		6
		8.6 (0.10), 3.2 (0.65), 1.3 (0.24) ^g	4.7 ^g	3.3 ^g	0.79 ^g	
6F-MIA in solution:						
DCM/MeOH (RT)	530 ^d		3.6	3.6 ^d		13 ^d
DCM/MeOH (77 K) ^h	486/514	4.6 (0.17), 3.4 (0.83), 6.0 (0.41), 3.1 (0.59)	4.7	4.3		26
water	533 ^e	3.6 (1) ^e	3.6	3.6 ^e		12 ^e
6F-MIA solid	527	0.5 (0.01), 0.2 (0.05), 0.05 (0.94)	0.1	0.06		<2
0.1 wt% 6F-MIA@MIL-53	534	5.9 (0.13), 2.6 (0.46), 0.8 (0.41)	3.4	2.3		5
1.5 wt% 6F-MIA@MIL-53	538	6.7 (0.09), 2.5 (0.36), 0.6 (0.55)	3.5	1.9		
		6.7 (0.07), 2.4 (0.39), 0.8 (0.53) ^g	3.2 ^g	1.9 ^g	0.87 ^g	3
5.2 wt% 6F-MIA@MOF-5	510	7.0 (0.12), 3.2 (0.59), 0.8 (0.29)	4.1	3.0		
		6.2 (0.21), 2.6 (0.70), 1.1 (0.09) ^g	4.0 ^g	3.2 ^g	0.79 ^g	8

^a: Maximum of the fluorescence wavelength. ^b: Fluorescence lifetimes: $\tau(x_i)$ lifetime of species i (fraction), τ_F fluorescence-weighted average lifetime, τ_x species-weighted average lifetime. Raw time-resolved fluorescence decays with fits and obtained parameters are shown in the supplementary materials Section S5 Figures S24–S33 except for the MFIS data marked by ^g. ^c: Fluorescence quantum yield. Precision $\pm 2\%$. ^d: In DCM/MeOH 1:1 (DCM = dichloromethane). ^e: Mono-exponential fits from time-correlated single photon counting by Reiffers et al. [17]. ^f: Computations in this work. ^g: From confocal multi-parameter fluorescence image spectroscopy (MFIS) with pulsed excitation at 440 nm and $\lambda_{em} = 502$ –538 nm. Global fits to p- and s-polarized decays required 4 fluorescence lifetime components. The shortest lifetime component (<30 ps, close to the instrumental resolution but distinct from scatter due to its smaller anisotropy) was not considered in the calculation of the average lifetimes and amplitudes were rescaled to the bright species with $\tau >$ instrument response function (FWHM ≈ 0.5 ns). The non-rescaled amplitude fractions x_{sq} of the lifetime component with $\tau_{sq} < 30$ ps amount to 87% (dye@MIL-53) and 79% (dye@MOF-5) of all species, indicating a significant amount of strongly quenched dyes in both matrices. Raw time- and polarization-resolved fluorescence decays with fits and obtained parameters are shown in the supplementary materials Section S5 Figure S34. ^h: Measured in a 1:1 DCM/MeOH glassy matrix at 77 K.

We applied confocal multi-parameter fluorescence image spectroscopy (MFIS) to map also the spatial and orientation dependence of the fluorescence properties for the microcrystalline sample of flavin@MIL-53 and large single crystals of flavin@MOF-5.

The average fluorescence lifetime $\langle \tau \rangle_F$ of MIA@MIL-53 (3.9 wt%) (Figure 6a, panel 1) and a crystal of MIA@MOF-5 (Figure 6b panel 1) yielded 4.5 and 4.7 ns, respectively. For 6F-MIA@MIL-53 (1.5 wt%) and 6F-MIA@MOF-5 the values of $\langle \tau \rangle_F$ are 3.5 and 4.5 ns (Figure 6c,d panel 1), respectively. These results are consistent with the lifetimes measured in the fluorescence spectrometer. The average fluorescence lifetime values of the chromophores in flavin@MOF composites are similar to the values in aqueous solution (Table 3). Interestingly, the fluorescence lifetime of MIA is affected by the location in the crystal. The lifetime of MIA is slightly but significantly longer in the center of the MOF-5 crystal (Figure 6b—the false colors for lifetime values are darker in the middle (5.5 ns)). This positional effect explains the surprising result that the fluorescence lifetime distribution of MIA is broader in MOF-5 than in MIL-53 crystals (Figure 6b vs. a). Being aware that deactivation processes of MIA and 6F-MIA in solution include fluorescence, intersystem crossing and internal conversion with different relative efficiencies [17], we note that both methods for lifetime analysis indicate that MIA is the less sensitive derivative as compared to 6F-MIA.



Figure 6. Images of MIL-53 and 6f-MIL-53 with two MOFs obtained by confocal multiplane fluorescence image spectroscopy (MPFIS) method. (Panel 1) Image of fluorescence-weighted average lifetime; (Panel 2) Image of experimental steady state fluorescence anisotropy; (Panel 3), Interrelation (t_f/r) in the 2D diagram of the parameter images in panels 1 and 2 with a full horizontal line for the average anisotropy \bar{r} of the sample and second dashed line of other MOF composite as reference; and (Panel 4) Time-resolved fluorescence anisotropy curves and second dashed line of other MOF composite as reference and (Panel 4) Time-resolved fluorescence anisotropy curves in the circular polarized light and linearly polarized light. (a) MIL-53 MOF; (b) MIL-53 MOF; (c) 6f-MIL-53 MOF; (d) 6f-MIL-53 MOF. The acquisition conditions were $\lambda_{ex} = 440$ nm, pulsed@32MHz objective UPLSAPO10X/0.4NA for MIL-53 and objective UPLSAPO10X/0.75NA for MOF-5; $\lambda_F = 502\text{--}538$ nm, under air.

With higher loading of the flavins into MIL-53, $\lambda_{F,max}$ shifts to slightly longer wavelengths (Table 3). A similar shift is seen for MIA when going from an aqueous to a DCM/MeOH solution and oppositely for 6F-MIA between a DCM/MeOH and water solution. In general, conditions where the flavin molecules come closer together enable charge transfer processes and self-quenching between them, resulting in spectral shifts and broadening of the emission bands with loss of fine structure and reduction of the fluorescence quantum yield. It is known that the photophysical properties of a chromophore in a MOF are influenced by the geometric restrictions imposed by the framework structure [18]. In all flavin@MOF composites, a strong increase in both lifetimes and quantum yields compared to the neat solid flavin is observed. In the case of MIA@MIL-53 and MIA@MOF-5 a ~10-fold increase in lifetime and a 3 to 5-fold increase in quantum yield can be observed compared to solid MIA. For the 6F-MIA@MOF composites, these increases are even more evident, with a ~50-fold increase in lifetime and ~3-fold increase in quantum yield. Compared to the neat solid flavins the incorporation of the molecules within the MOFs reduces the nonradiative decay rates, leading to increased fluorescence intensities, lifetimes, and quantum yields. This effect is especially prominent in MFIS. The photophysical parameters of the flavin@MOF composites correspond to the data of the flavins in solution (Table 3) fostering the concept of “solid solutions” for dye@MOF composites.

From the MFIS analysis, it is evident that microcrystals of flavin@MIL-53 vary significantly in both size and polarization properties (Figure 6a,c panel 2). The orientational distributions of both flavin chromophores is indicated by a broad distribution of the fluorescence anisotropies r due to varying size and orientation of the flavin@MIL-53 microcrystallites (Figure 6a,c). The anisotropies are calculated according to Schaffer et al. [63]. For this discussion of the r -distributions, it is important to consider the broadening of the distributions due to shot noise caused by the relatively small average number of photons per pixel ($\overline{N}_p(\text{MIA}) = 35$) and $\overline{N}_p(6\text{F-MIA}) = 200$). 6F-MIA@MIL-53 exhibits the broadest r -distribution reaching its upper limit ($r = 1$) and lower limit ($r = 0$). To reduce shot noise, we integrated the signal of the whole image to compute time-resolved anisotropy curves $r(t)$ (Figure 6a,c panel 4). This was accomplished by global fits with iterative deconvolution of the instrumental function (grey curves in Figure S34) to p- and s-polarized decays as described in ref. [63,64]. The fits required 4 fluorescence lifetime components (lifetimes and species fractions are compiled in Table 3) and one (two for MIA@MIL-53) depolarization correlation time.

It is especially remarkable, that $r(t)$ of 6F-MIA@MIL-53 starts at a fundamental anisotropy $r_0 = 0.4$ and exhibits no decay. This is direct proof the MFIS images resolve the distribution of particles whose orientation on the surface is static and random so that the isotropic average of r is obtained, which is usually mathematically derived in text books [65] considering the case of fluorophores in solution. Three arguments (the anisotropy of pixels of some MIA and 6F-MIA@MIL-53 microcrystals reaches one (see Figure 6a,c, panels 2 and 3 and Figure S35), geometric constraints of available space in MIL-53 and quantum-chemical calculations (see below)) allow us to conclude that transition dipole moments for absorption and fluorescence (TDM) (see supplementary materials Section S6.5 Figure S42) of the various fluorescent MIA and 6F-MIA species must be oriented along the one-dimensional channel of MIL-53 with no large deviation among each other. Considering MIA@MIL-53, the fundamental anisotropy $r_0 = 0.364$ is slightly smaller and an additional decay term with a depolarization time of 3.1 ns is observed. From this it is evident that the order of the MIA TDMs is slightly lower, but nevertheless quite similar for all fluorescent species. The TDMs are preferentially orientated along the channel axis.

In contrast to MIL-53, MOF-5 provides a very well defined and ordered porous framework with large flavin@MOF-5 crystals (Figures 3, 4 and 6b,d) as indicated by a narrow distribution of fluorescence anisotropies r , which are centered around mean anisotropy values: $\bar{r}(\text{MIA}) = 0.6$ (full blue line in Figure 6b, panel 3) and $\bar{r}(6\text{F-MIA}) = 0.56$ (full magenta line in Figure 6d, panel 3). Both flavin@MOF-5 samples show high anisotropies that indicate distinct oriented binding sites, excluding random orientation of the dye molecules in the

In contrast to MIL-53, MOF-5 provides a very well defined and ordered porous framework with large flavin@MOF-5 crystals (Figure 3, Figure 4 and Figure 6b,d) as indicated by a narrow distribution of fluorescence anisotropies r , which are centered around mean anisotropy values: $\bar{r}(\text{MIA}) = 0.6$ (full blue line in Figure 6b, panel 3) and $\bar{r}(6\text{F-MIA}) = 0.56$ (full magenta line in Figure 6d, panel 3). Both flavin@MOF-5 samples show high anisotropies that indicate distinct oriented binding sites, excluding random orientation of the dye molecules in the crystal. As for 6F-MIA@MIL53, no time-dependence of the anisotropy $r(t)$ was observed for 6F-MIA@MOF-5. MIA embedded in either of the two MOFs shows limited depolarization on the ns to us scale, which could have one or several of the following reasons: (i) constrained rotational motion, (ii) resonance energy transfer to chromophores in close vicinity and/or (iii) slightly differing orientations of fluorescent species with distinct lifetimes.

Due to the high symmetry of the cubic MOF-5 crystal for the x , y , z directions defined in the crystal parameters, it is feasible and appropriate to assume an identical rotation of the transition dipole moment of the MIA chromophore using the normalized rotation vector of the crystal u_{CA} in an angle axis representation that rotates the $S_0 \rightarrow S_1$ absorption transition dipole moment A of the chromophore with respect to the crystal axis c by an angle ω_{CA} . For a cube, the directions of the four potential rotation vectors correspond to the respective body diagonals. Since the body diagonals are equivalent, we consider in the following only one rotation vector. Using the experimental observables for 6F-MIA@MOF-5 ($\bar{r}(6\text{F-MIA}) = 0.56$ (Figure 6d panel 3) and $\alpha = 8.2^\circ$ (Figure 6d panel 2)) and for MIA@MOF-5 ($\bar{r}(\text{MIA}) = 0.6$ (Figure 6b panel 3) and $\alpha = 65^\circ$ (Figure 6b panel 2)), a unique solution with an angle of the normalized rotation vector $\omega_{CA} = 13^\circ$ (for MIA) and $\omega_{CA} = 16^\circ$ (for 6F-MIA) is obtained that describes the average orientation of the TDM for absorption of all fluorescent species defined by the Euler angles relative to the crystal lattice $\theta_{CA} = 12.1 \pm 1$ and $\phi_{CA} = 40.5 \pm 1$, i.e., the TDM is not oriented along one of the crystal axes. This confirms that MOF-5 provides a suitable frame to incorporate flavins in a defined average orientation regardless of their aggregation.

2.4. QM/MM Excited State Computations

In the neat MIA crystal [60], we can identify two orientations of stacked neighboring molecules (Figure 7). In one orientation, π -stacking interactions occur between the terminal phenyl and the central lateral terminal ring of two adjacent MIA molecules (ruler 1 and 2 in Figure 7) with a centroid-centroid separation of 3.518 and 3.589 Å. The other π -stacking orientation involves only the terminal phenyl rings of two adjacent MIA molecules (ruler 2 and 3) at a centroid-centroid distance of 3.561 Å.

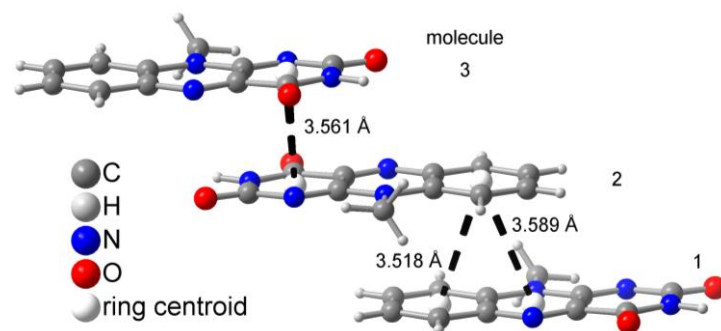


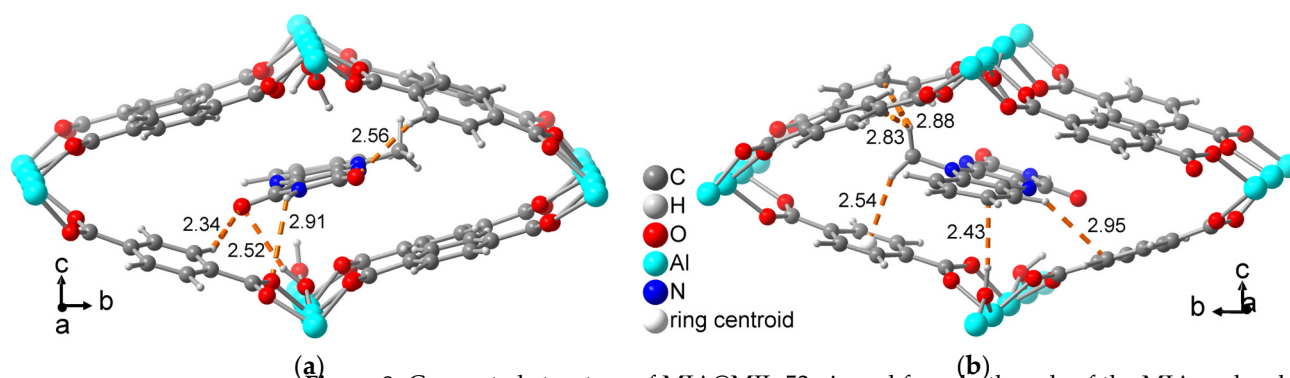
Figure 7. π - π stacking modes in crystalline MIA with centroid-centroid distances (graphics were drawn from the deposited file with CSD Refcode ISMEX160 [60]) the numbers 1, 2 and 3 indicate the molecules for their different stacking interactions (see text).

Due to the different π -stacking modes in the crystal of neat MIA, QM/MM geometry optimizations of ground and excited state structures had to include at least three MIA molecules for a sensible description of interactions with all direct neighbors (see Section S6.1). Compared to the single MIA chromophore in vacuum ($\lambda_{\text{abs, max}} = 401$ nm), the calculated maximum absorption value in the crystal is 441 nm, thus significantly red-shifted. The calculated emission from S_1 state in the crystal occurs at ca. 540 nm, compared to ca. 555 nm in the solid-state experiment and 505 nm for MIA calculated in vacuum (Table 3) with a calculated small oscillator strength ($f = 0.025$) and an emission rate constant of $5.87 \cdot 10^6 \text{ s}^{-1}$. While for the single MIA molecule S_1 corresponds to a locally π -excited state, orbital analysis for the three-molecule MIA complex reveals a dominating charge-

S6.1). Compared to the single MIA chromophore in vacuum ($\lambda_{\text{abs, max}} = 401 \text{ nm}$), the calculated maximum absorption value in the crystal is 441 nm, thus significantly red-shifted. The calculated emission from S₁ state in the crystal occurs at ca. 540 nm, compared to ca. 555 nm in the solid-state experiment and 505 nm for MIA calculated in vacuum (Table 3) with a calculated small oscillator strength ($f = 0.025$) and an emission rate constant of $5.87 \cdot 10^6 \text{ s}^{-1}$. While for the single MIA molecule S₁ corresponds to a locally π -excited state, orbital analysis for the three-molecule MIA complex reveals a dominating charge-transfer character. Here, electron density is relocated between the two molecules that overlap with two aromatic rings (number 1 and 2 in Figure 7). This is the main reason for the loss in fluorescence emission intensity in the crystalline state.

Optimization of MIL-53(Al) with Quantum Espresso (QE) revealed essentially the same results as the experimental structural data (Table S3). Compared to the reported orthorhombic large-pore form MIL-53(Al) (CCDC 2204204 [46]), the computed guest-free MIL-53(Al) structure after optimization has nearly the same cell-edge lengths within $\sim 1\%$ (Figure S4B, Table S3). With one molecule per unit cell, the structure becomes similar to the reported narrow-pore form (Figure S3a, Table S3). A variation of lattice parameters and space group description of MIL-53(Al) was also suggested with xy interchange [66], kinetic annealing [67] or frame change [68].

The position of the MEA molecule is optimized with its nitrogen atom being placed in the center and close to the center of the channel (Fig. 8). There are no evident steric hindrance and strong supramolecular interactions that MEA molecule is placed by weak C-H...O, C-H...F, C-H...C, C-H...N, O-H...O, and O-H...F interactions. Even the N-H...O and O-H...O contacts that have shorter N-H...O distances (2.5 Å) (Fig. 8).



(a) **Figure 8.** Computed structure of MIA@MIL-53 viewed from both ends of the MIA molecule with indication of the weak C-H...O, C-H... π , C-H...C, N-H...O, O-H...O and O-H...C interactions (H...X distances in Å, distances above 3 Å are not shown).

[illegible]

except for two C-H...H-C contacts in the *inward*-cage position (Figure 9b) with an H...H distance of 2.5–2.6 Å. The next-nearest distances are four C-H...O contacts of ~3.2 Å in the *inward*-cage position.

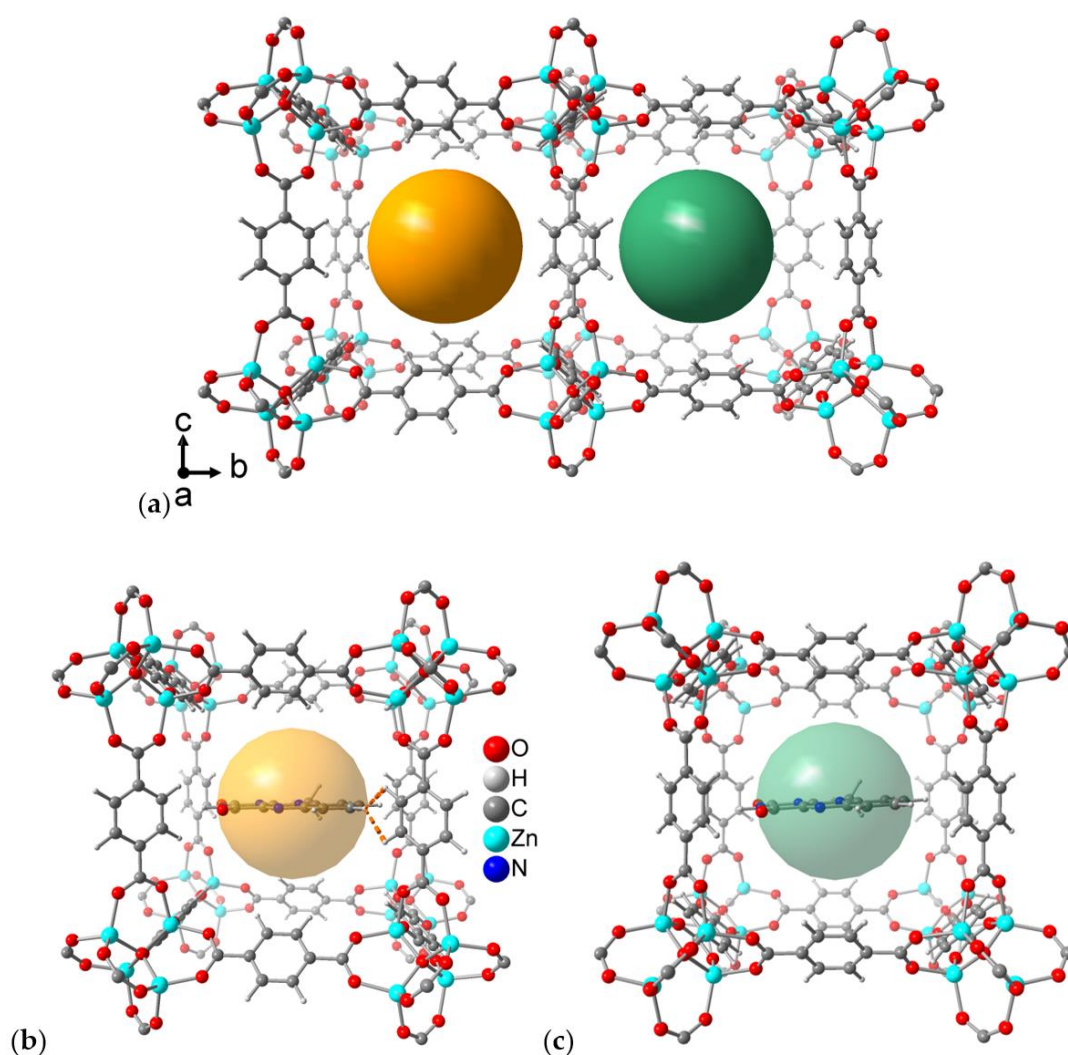


Figure 9. (a) Alternating neighboring pores in MOF-5 with different cages for binding MIA. Orange pore at left: linker phenyl hydrogens face *inward* toward the center of the pore. Green pore at right: outward position of linker phenyls. (b) Computed MIA molecule in the *inward*-cage in MOF-5 with the only two supramolecular contacts below 3.0 Å (two C-H...H-C contacts) indicated as dashed orange lines. (c) Computed MIA molecule in the *outward*-cage for which there are no supramolecular contacts below 3.0 Å.

In the MIA@MOF-53 complex, the ground state QM/MM optimization converges to essentially the same structure as with plane wave methods. The lowest excitation wavelength is 414 nm with an oscillator strength of 0.2656 and local excitation character, corresponding to HOMO-LUMO excitation. The computed emission wavelength from the S_1 state is 509 nm ($f = 0.209$) (Figure 10) with an emission rate constant of $6.539 \times 10^7 \text{ s}^{-1}$, about ten times larger than in the neat MIA crystal. The absorption and emission wavelength values are slightly blue-shifted with respect to the experimental measurements (523 (52326–527, depending on the MIA:MOF) with the oscillator strength compares well with the value for neat MIA in vacuum (from 0.243 to 0.248), demonstrating that the MOF environment efficiently increases fluorescence emission by preventing quenching due to stacking.

For MOF-5, we find no significant change in absorption and emission wavelength values depending on the mode of complexation. In the more stable *inward* form, maximum wavelength absorption occurs at 402 nm ($f = 0.305$), while emission from S_1 is at 502 nm ($f = 0.238$) with a rate constant of $6.30 \cdot 10^7 \text{ s}^{-1}$. Similar to MIL-53, the S_1 -excitation shows the same characteristics as in vacuum.

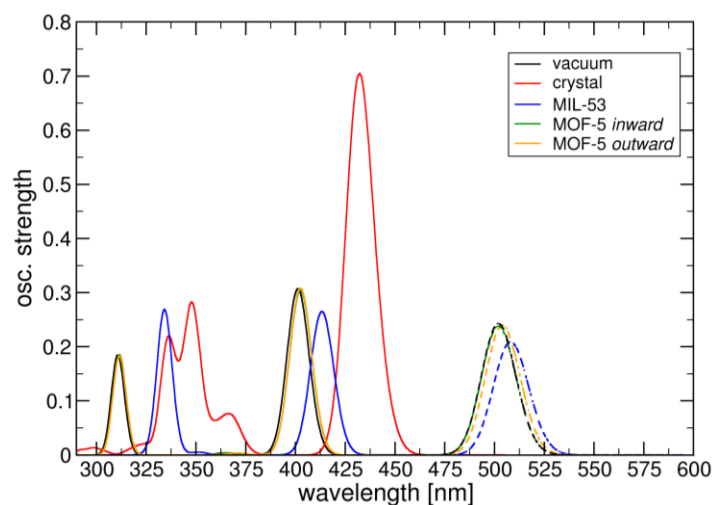


Figure 10. DFT/MRCI-computed absorption (full lines) and emission (dashed lines) signatures of MIA in vacuum, neat crystal and MOF environments.

3. Materials and Methods

3.1. Chemicals and Equipment

Reagents were obtained from commercial sources (Table S1) and used without further purification. All flavin derivatives [17,69,70] and metal-organic frameworks [41,62,66,71] were synthesized and purified according to the literature.

3.2. Powder X-Ray Diffraction

Powder X-Ray diffractograms (PXRD) were measured on a Bruker D2 phaser bench-

top diffractometer (Bruker, Ettlingen/Karlsruhe, Germany, 300 W, 30 kV, 10 mA) at ambient temperature using Cu-K α radiation ($\lambda = 1.5418 \text{ \AA}$) at a scan rate of $0.0125^\circ/\text{s}$. The measurements were performed with a flat silicon, low-background sample holder. This Bragg-Brentano geometry broadens the beam spot at low angles so that only a fraction of the diffraction radiation reaches the detector with reflections measured at $2\theta < 7^\circ$ have lower than expected intensity.

Powder X-Ray diffractograms (PXRD) were measured on a Bruker D2 phaser bench-top diffractometer (Bruker, Ettlingen/Karlsruhe, Germany, 300 W, 30 kV, 10 mA) at ambient temperature using Cu-K α radiation ($\lambda = 1.5418 \text{ \AA}$) at a scan rate of $0.0125^\circ/\text{s}$. The measurements were performed with a flat silicon, low-background sample holder. This Bragg-Brentano geometry broadens the beam spot at low angles so that only a fraction of the diffraction radiation reaches the detector with reflections measured at $2\theta < 7^\circ$ have lower than expected intensity.

Nitrogen physisorption isotherms were obtained at 77 K on a Nova 4200e S/N volumetric gas sorption analyzer from Quantachrome (Boynton Beach, FL, USA), equipped with degassing and three analyses stations. Before the gas sorption experiment, the sample was weighed into a glass tube capped with a septum. The tube was connected to the degassing port of the Nova instrument and degassed under dynamic vacuum of $1 \cdot 10^{-2}$ mbar at a temperature of 120°C for 3 h, then weighed again and transferred to an analysis

port of the Nova device. The Brunauer-Emmett-Teller (BET) surface areas were calculated from the nitrogen adsorption isotherms in the p/p_0 range from 0.017 to 0.07. Total pore volumes were calculated from the nitrogen sorption isotherm at $p/p_0 = 0.95$.

Fluorescence microscopy. Characterization of the incorporated fluorophores by confocal laser scanning and multi-parameter fluorescence image spectroscopy (CLSM and MFIS [72]) (condition g in Table 3) was carried out with a modified Olympus Fluoview 1000 inverse confocal microscope system (Olympus, Hamburg, Germany) with an internal 405 nm laser and a 6-channel single photon detector on dye@MIL-53 ($20 \times$ objective) and dye@MOF-5 ($10 \times$ objective). For the excitation of CLSM a cw argon laser with a wavelength of 458 nm was used. For MFIS, the acquisition conditions were $\lambda_{\text{ex}} = 440$ nm (pulsed@32MHz, objective UPLSAPO10X/0.4NA for MIL-53 and objec-

tion of the Nova device. The Brunauer-Emmett-Teller (BET) surface areas were calculated from the nitrogen adsorption isotherms in the p/p_0 range from 0.017 to 0.07. Total pore volumes were calculated from the nitrogen sorption isotherm at $p/p_0 = 0.95$.

Fluorescence microscopy. Characterization of the incorporated fluorophores by confocal laser scanning and multi-parameter fluorescence image spectroscopy (CLSM and MFIS [72]) (condition g in Table 3) was carried out with a modified Olympus Fluoview 1000 inverse confocal microscope system (Olympus, Hamburg, Germany) with an internal 405 nm laser and a 6-channel single photon detector on dye@MIL-53 ($20 \times$ objective) and dye@MOF-5 ($10 \times$ objective). For the excitation of CLSM a cw argon laser with a wavelength of 458 nm was used. For MFIS, the acquisition conditions were $\lambda_{\text{ex}} = 440$ nm (pulsed@32MHz, objective UPLSAPO10X/0.4NA for MIL-53 and objec-

tion of the Nova device. The Brunauer-Emmett-Teller (BET) surface areas were calculated from the nitrogen adsorption isotherms in the p/p_0 range from 0.017 to 0.07. Total pore volumes were calculated from the nitrogen sorption isotherm at $p/p_0 = 0.95$.

Fluorescence microscopy. Characterization of the incorporated fluorophores by confocal laser scanning and multi-parameter fluorescence image spectroscopy (CLSM and MFIS [72]) (condition g in Table 3) was carried out with a modified Olympus Fluoview 1000 inverse confocal microscope system (Olympus, Hamburg, Germany) with an internal 405 nm laser and a 6-channel single photon detector on dye@MIL-53 ($20 \times$ objective) and dye@MOF-5 ($10 \times$ objective). For the excitation of CLSM a cw argon laser with a wavelength of 458 nm was used. For MFIS, the acquisition conditions were $\lambda_{\text{ex}} = 440$ nm (pulsed@32MHz, objective UPLSAPO10X/0.4NA for MIL-53 and objec-

tion of the Nova device. The Brunauer-Emmett-Teller (BET) surface areas were calculated from the nitrogen adsorption isotherms in the p/p_0 range from 0.017 to 0.07. Total pore volumes were calculated from the nitrogen sorption isotherm at $p/p_0 = 0.95$.

Fluorescence microscopy. Characterization of the incorporated fluorophores by confocal laser scanning and multi-parameter fluorescence image spectroscopy (CLSM and MFIS [72]) (condition g in Table 3) was carried out with a modified Olympus Fluoview 1000 inverse confocal microscope system (Olympus, Hamburg, Germany) with an internal 405 nm laser and a 6-channel single photon detector on dye@MIL-53 ($20 \times$ objective) and dye@MOF-5 ($10 \times$ objective). For the excitation of CLSM a cw argon laser with a wavelength of 458 nm was used. For MFIS, the acquisition conditions were $\lambda_{\text{ex}} = 440$ nm (pulsed@32MHz, objective UPLSAPO10X/0.4NA for MIL-53 and objec-

tion of the Nova device. The Brunauer-Emmett-Teller (BET) surface areas were calculated from the nitrogen adsorption isotherms in the p/p_0 range from 0.017 to 0.07. Total pore volumes were calculated from the nitrogen sorption isotherm at $p/p_0 = 0.95$.

Fluorescence microscopy. Characterization of the incorporated fluorophores by confocal laser scanning and multi-parameter fluorescence image spectroscopy (CLSM and MFIS [72]) (condition g in Table 3) was carried out with a modified Olympus Fluoview 1000 inverse confocal microscope system (Olympus, Hamburg, Germany) with an internal 405 nm laser and a 6-channel single photon detector on dye@MIL-53 ($20 \times$ objective) and dye@MOF-5 ($10 \times$ objective). For the excitation of CLSM a cw argon laser with a wavelength of 458 nm was used. For MFIS, the acquisition conditions were $\lambda_{\text{ex}} = 440$ nm (pulsed@32MHz, objective UPLSAPO10X/0.4NA for MIL-53 and objec-

tion of the Nova device. The Brunauer-Emmett-Teller (BET) surface areas were calculated from the nitrogen adsorption isotherms in the p/p_0 range from 0.017 to 0.07. Total pore volumes were calculated from the nitrogen sorption isotherm at $p/p_0 = 0.95$.

Fluorescence microscopy. Characterization of the incorporated fluorophores by confocal laser scanning and multi-parameter fluorescence image spectroscopy (CLSM and MFIS [72]) (condition g in Table 3) was carried out with a modified Olympus Fluoview 1000 inverse confocal microscope system (Olympus, Hamburg, Germany) with an internal 405 nm laser and a 6-channel single photon detector on dye@MIL-53 ($20 \times$ objective) and dye@MOF-5 ($10 \times$ objective). For the excitation of CLSM a cw argon laser with a wavelength of 458 nm was used. For MFIS, the acquisition conditions were $\lambda_{\text{ex}} = 440$ nm (pulsed@32MHz, objective UPLSAPO10X/0.4NA for MIL-53 and objec-

tion of the Nova device. The Brunauer-Emmett-Teller (BET) surface areas were calculated from the nitrogen adsorption isotherms in the p/p_0 range from 0.017 to 0.07. Total pore volumes were calculated from the nitrogen sorption isotherm at $p/p_0 = 0.95$.

Fluorescence microscopy. Characterization of the incorporated fluorophores by confocal laser scanning and multi-parameter fluorescence image spectroscopy (CLSM and MFIS [72]) (condition g in Table 3) was carried out with a modified Olympus Fluoview 1000 inverse confocal microscope system (Olympus, Hamburg, Germany) with an internal 405 nm laser and a 6-channel single photon detector on dye@MIL-53 ($20 \times$ objective) and dye@MOF-5 ($10 \times$ objective). For the excitation of CLSM a cw argon laser with a wavelength of 458 nm was used. For MFIS, the acquisition conditions were $\lambda_{\text{ex}} = 440$ nm (pulsed@32MHz, objective UPLSAPO10X/0.4NA for MIL-53 and objec-

tive UPLSAPO20X/0.75NA for MOF-5), $\lambda_{em} = 502\text{--}538\text{ nm}$, under air. Experimental anisotropy decays in Figure 6 were calculated from the measured p- and s-polarized fluorescence decays (Figure S34) after subtracting the observed background according to: $r = (GF_{\parallel} - F_{\perp}) / ((1 - 3l_1)GF_{\parallel} + (2 - 3l_2)F_{\perp})$. The correction factors, taking into account polarization mixing in high-NA objectives were $l_1 = 0.0308$ and $l_2 = 0.0368$ [73]. The model curves (red lines in Figure 6) are constructed in the same way from the fits to the decays. Global fits by iterative deconvolution of the instrumental function (grey curves) to p- and s-polarized decays required 4 fluorescence lifetime components (Table 3 main document) and one (two for MIA@MIL-53) rotational correlation time. The offsets in the decays are caused by afterpulsing of the detectors and taken into account by the fitting routine. The G-factor, compensating differences in the detection efficiencies in the two polarization channels, of $G = 0.97$ was determined by fitting polarized fluorescence decays of an aqueous solution of Rhodamine 110. The doped MOFs were studied under air.

Steady-state excitation and emission spectra were recorded on a FluoTime 300 spectrometer from PicoQuant (Berlin, Germany) equipped with a 300 W ozone-free Xe lamp (250–900 nm), a 10 W Xe flash-lamp (250–900 nm, pulse width <10 μ s) with repetition rates of 0.1–300 Hz, an excitation monochromator (Czerny-Turner 2.7 nm/mm dispersion, 1200 grooves/mm, blazed at 350 nm and 600 g/mm), diode lasers (pulse width <80 ps) operated by a computer-controlled laser driver PDL-820 (repetition rate up to 80 MHz, burst mode for slow and weak decays), two emission monochromators (Czerny-Turner, selectable gratings blazed at 500 nm with 2.7 nm/mm dispersion and 1200 grooves/mm, or blazed at 1250 nm with 5.4 nm/mm dispersion and 600 grooves/mm) with adjustable slit width between 0 mm and 10 mm, Glan-Thompson polarizers for excitation (Xe-lamps) and emission, a Peltier-thermostated sample holder (−40–105 °C), and two detectors, namely a PMA Hybrid 40 (transit time spread FWHM <120 ps, 200–900 nm) and a R5509-42 NIR-photomultiplier tube (transit time spread FWHM 1.5 ns, 300–1400 nm) from Hamamatsu. The signal-to-noise ratio (optical noise) is typically better than 29000:1, as measured with double monochromators in the excitation and emission light path. Steady-state photoluminescence spectra and fluorescence lifetimes were recorded in TCSPC mode by a PicoHarp 300 (minimum base resolution 4 ps), whereas phosphorescence was measured in the MCS mode by a TimeHarp 300, where up to several ms can be detected. Emission spectra were corrected for source intensity (lamp and grating) by standard correction curves. For samples with lifetime in the ns order, an instrument response function calibration (IRF) was performed using a diluted Ludox[®] solution. The lifetime analysis was performed using the commercial EasyTau 2.2 software. The quality of the fit was assessed by minimizing the reduced chi squared function (χ^2) and visual inspection of the weighted residuals and their autocorrelation. Absolute photoluminescence quantum yields were measured with a Hamamatsu Photonics measurement system (C9920-02) equipped with a L9799-01 CW Xenon light source (150 W), a monochromator, a C7473 photonic multi-channel analyzer, an integrating sphere and employing the U6039-05 PLQY measurement software (Hamamatsu Photonics, Ltd., Shizuoka, Japan). All solvents used were of spectrometric grade (Uvasol[®]).

3.2. Flavin@MIL-53 Synthesis

Post synthetic wet infiltration was performed by adding different quantities (1 to 15 mL) of saturated solutions of the flavins in chloroform ($c_{MIA} = 69.5\text{ mg}\cdot\text{L}^{-1}$, $c_{6F-MIA} = 20.25\text{ mg}\cdot\text{L}^{-1}$) to activated microcrystalline MIL-53 powders (20 mg) in 25 mL glass vials. The different suspensions were stored on an orbital shaker until all the solvent had been evaporated. The flavin@MIL-53 composites were washed three times with chloroform for 5 min at each washing step and then dried at 60 °C under dynamic vacuum. Since the filtrate was already colorless after the first washing process, all of the dye from the initial solution was incorporated in the solid MIL-53 sample. The MIA@MIL-53 composites contained 0.4 to 2.7 wt% of the flavin in the MOF and the 6F-MIA@MIL-53 composites between 0.1 to 1.5 wt% (see also Section S1.2).

3.3. Flavin@MOF-5 Synthesis

In situ MOF-5 crystallization was performed by synthesizing the host network in saturated solutions of the flavins in dimethylformamide, DMF ($c_{\text{MIA}} = 272 \text{ mg}\cdot\text{L}^{-1}$, $c_{6\text{F-MIA}} = 2640 \text{ mg}\cdot\text{L}^{-1}$). The amount of incorporated flavin was then quantified using UV/Vis or postsynthetic digestions ^1H NMR. The MIA@MOF-5 composites contained 0.85 wt% (UV/Vis) and 6F-MIA@MOF-5 composites contained 5.2 wt% (^1H NMR) of the flavin (see also Section S1.2).

3.4. Computational Methods

Crystal structures of MIA (CCDC Refcode MISALX [60]), MIL-53(Al) (CCDC no./Refcode 220476/SABVUN for -MIL-53-lp [41]) and MOF-5 (CCDC-no./Refcode 256966/SAHYOQ [52,58]) were extracted from experimental data. The geometries were optimized with Quantum Espresso (QE) [74] using RRKJ-pseudopotentials [75], the generalized gradient approximation (GGA) with PBE-exchange correlation [76], Grimme-type D3-dispersion corrections [77] and a kinetic energy cutoff of 40 eV. SCF computations were performed including only the gamma point. For the optimization of the MIA crystal the cell parameters were frozen to the experimental values. MIL-53(Al) and MOF-5 were optimized without any constraints. To obtain the MOF-MIA complexes, one MIA molecule was placed into the center of the unit cell. To fit the MIA chromophore, the MIL53 the unit cell was replicated three times in a-direction, comprising a $3 \times 1 \times 1$ supercell. The resulting geometries were then fully relaxed using the aforementioned methodologies. These structures were used as input structures for QM/MM cluster model computations.

Atomic partial charges for the MIA chromophore were computed with Gaussian16 [78] using RHF, the 6-31G* basis set and the Merz–Kollmann scheme [79]. Periodic charges for the frameworks were generated with the REPEAT method [80] implemented in CP2K [81]. Atoms herein were described with DZVP-MOLOPT-GTH basis sets and corresponding GTH-PBE pseudopotentials [82]. Force field parameters for MIA were obtained from the Generalized Amber Force Field (GAFF). MOF-5 force field parameters were adapted from a previous work by Vanduyfhuys et al. [83]. MIL-53(Al) parameters were computed with the FFTK program suite [84] using cluster models optimized with Gaussian16 (see Section S6.2 for details).

Finite cluster models were generated for each structure using the previously optimized geometries. The MOF structures were saturated accordingly (see Sections S6.2 and S6.3 for details). The MIA crystal cluster was prepared by replicating the unit cell eight times in each direction, thus including 1024 individual MIA molecules with a cell size of ca. $40 \times 50 \times 60 \text{ \AA}^3$. The size of the MIL-53 cluster was ca. $60 \times 30 \times 30 \text{ \AA}^3$, the MOF-5 cluster had ca. $98 \times 98 \times 98 \text{ \AA}^3$.

For QM/MM geometry optimizations, the COBRAMM2.0 package [85] was employed, choosing Gaussian16 [78] for the computation of the QM part (MIA) and AMBER16 [86] for the MM part (i.e., the surrounding). The QM-part was described with the PBE0 functional. The MIA crystal model was computed with different sizes for the central QM part, including 1, 2 and 3 stacked MIA molecules (see Section S6.1) and the 6-31G* basis set. The QM part was allowed to fully relax while the remaining atoms were frozen to their initial positions. MOF structures were calculated with one MIA molecule as the QM part in the center of the clusters using the TZVP basis set. MIA and direct neighbors in the MM part were movable during optimization, while the rest of the cluster was kept fixed. In the case of MOF-5, the metal centers positions were additionally kept frozen.

Spectral properties were computed with the DFT/MRCI [87] program using the R2016 Hamiltonian [88]. Orbitals for MRCI were computed at the B3LYP/TZVP level using Turbomole [89]. The initial reference space was chosen by computing single and double excitations from eight electrons in eight orbitals. An energy selector of $0.8 E_h$ and the *tight* parameter set were chosen. A second run was performed with the same parameters to obtain an updated reference space and the final values for energies and oscillator strengths.

4. Conclusions

The flavin derivatives 10-methyl-isoalloxazine (MIA) and 6-fluoro-10-methyl-isoalloxazine (6F-MIA) were successfully encapsulated in the metal-organic frameworks (MOFs) MIL-53 and MOF-5. The incorporation of flavin@MOF composites was verified by BET surface measurements and powder X-ray diffraction. In the case of the flavin@MOF-5 composites, the incorporation was also demonstrated spectroscopically by homogeneous images obtained by confocal laser scanning microscopy (Figures 3 and 4). The photophysical properties of the flavin@MOF composites are significantly dependent on the specific molecular environment. Compared to the neat dyes in their solid states, the lifetime and quantum yield increase significantly in solution and in the dye@MOF composite. At least four fluorescent MIA species are present in the MOF composites. The lower lifetimes and quantum yield in the solid state of the dyes can be attributed to aggregation-caused quenching (ACQ). The fluorescence lifetimes and quantum yields of the flavins in liquid solution and in the “solid MOF solution” are of comparable orders. The electronic structures of MIA in its crystal environment, of MIA in MIL-53 and MIA in MOF-5 were investigated with plane-wave and QM/MM methods. In the crystalline state, π -stacking interactions of neighboring MIA chromophores change the nature of the first excited state from a local π - π (HOMO-LUMO) electronic excitation with high fluorescence intensity to a charge transfer state with low oscillator strength. The channels in the investigated metal-organic frameworks provide an environment for the incorporation of MIA as separated molecules, thus preventing π -stacking interactions between MIA molecules. The strong reduction of ACQ explains the enhanced fluorescence lifetime and quantum yield compared to the neat MIA crystal. The MIL-53 framework adapts towards the narrow-pore form when the MIA chromophore binds, thereby enhancing van-der-Waals contacts between the chromophore and the framework walls. Together with fluorescence anisotropy images and decays in Figure 6a,c, we can conclude that the transition dipole moments of the MIA derivatives are preferentially oriented along the one-dimensional channel axis. MOF-5 is a rather rigid framework but offers a narrower and wider pore environment for MIA with similar absorption and emission characteristics. In the preferred MIA position in the narrower pore, the hydrogen atoms of the phenyl linkers point towards the MIA-chromophore, thus enhancing host-guest van-der-Waals interactions. Together with fluorescence anisotropy images and decays in Figure 6b,d, we can conclude that the transition dipole moments of the MIA derivatives are not preferentially oriented along the three-dimensional cubic lattices but tilted in a similar manner (see Euler angles as described in Section 2.3).

The MOF environment influences the photophysical properties of the host chromophores. For 6F-MIA the non-radiative processes are significantly reduced. For MIA the location within the crystal becomes relevant. Further studies by fluorescence correlation spectroscopy (FCS) and transient state imaging microscopy (TRAST) will unravel the nature of these processes (internal conversion, IC or intersystem crossing, ISC). Moreover, we will also study the influence of the MOF environment on the photostability of the chromophores.

Supplementary Materials: The following supporting information can be downloaded at <https://www.mdpi.com/article/10.3390/molecules28062877/s1>. Section S1: Materials and methods; Section S2: MIA and 6F-MIA absorption spectra and calibration curves (Figures S4–S11); Section S3: Structure descriptions (Figures S12–S15); Section S4: Nitrogen adsorption isotherms and powder X-ray diffractograms (Figures S16–S19); Section S5: Photophysical characterization of the dyes and dye@MOF (Figures S20–S35); Section S6: Theoretical calculations (Figures S36–S42). References [90–93] are cited in the supplementary materials.

Author Contributions: Conceptualization: C.J. and S.-P.H.; methodology: D.P., O.W. and S.-P.H.; validation: S.-P.H., S.H. and D.P.; formal analysis: D.P., S.H., I.M., S.-P.H., R.K. and C.J.; investigation: D.P., S.H., I.M., S.-P.H., D.W. and R.K.; resources: C.A.M.S., C.C., O.W., C.A.S. and C.J.; data curation: D.P., S.H., I.M., S.-P.H. and R.K.; writing—original draft preparation: S.-P.H., S.H., C.A.M.S., O.W., D.P. and C.J.; writing—review and editing: C.J., R.K., O.W., C.A.M.S., C.C. and C.A.S.; visualization:

D.P., S.H., S.-P.H., R.K., S.F., C.A.M.S. and C.J.; supervision: C.A.M.S., C.C., O.W., C.A.S. and C.J.; project administration: O.W. and C.J.; funding acquisition: I.M., C.A.M.S., C.C., O.W., C.A.S. and C.J. All authors have read and agreed to the published version of the manuscript.

Funding: We thank the Deutsche Forschungsgemeinschaft (DFG, German Research Foundation) for grant 396890929/GRK 2482 (Research Training Group Modulation of Intersystem Crossing, ModISC). I.M. gratefully acknowledges the post-doctoral fellowship from the Alexander von Humboldt Foundation.

Institutional Review Board Statement: Not applicable.

Informed Consent Statement: Not applicable.

Data Availability Statement: The data presented in this study are available on request from the corresponding author.

Acknowledgments: We thank the Center for Molecular and Structural Analytics at Heinrich Heine University (CeMSA@HHU) for recording the mass spectrometric and NMR-spectrometric data. We thank Oleg Opanasyuk for discussing and computing the features of polarized fluorescence of flavins@MOFs and Dragana Sretenović for providing reference spectra of MIA and 6F-MIA.

Conflicts of Interest: The authors declare that they have no known competing financial interest or personal relationship that could have appeared to influence the work reported in this paper.

Sample Availability: Samples of the compounds will not be available.

References

1. Van Berkel, W.J.H. Special Issue: Flavoenzymes. *Molecules* **2018**, *23*, 1957. [CrossRef]
2. Romero, E.; Gómez Castellanos, J.R.; Gadda, G.; Fraaije, M.W.; Mattevi, A. Same Substrate, Many Reactions: Oxygen Activation in Flavoenzymes. *Chem. Rev.* **2018**, *118*, 1742–1769. [CrossRef]
3. Edwards, A.M. Structure and general properties of flavins. In *Flavins and Flavoproteins: Methods in Molecular Biology*; Weber, S., Schleicher, E., Eds.; Humana Press: New York, NY, USA, 2014; Volume 1146, pp. 3–13. [CrossRef]
4. Penzer, G.R.; Radda, G.K. The chemistry and biological function of isoalloxazines (flavines). *Q. Rev. Chem. Soc.* **1967**, *21*, 43–65. [CrossRef]
5. Penzkofer, A. Absorption and emission spectroscopic investigation of alloxazine in aqueous solutions and comparison with lumichrome. *J. Photochem. Photobiol. A Chem.* **2016**, *314*, 114–124. [CrossRef]
6. Ramírez-Gamboa, D.; Díaz-Zamorano, A.L.; Meléndez-Sánchez, E.R.; Reyes-Pardo, H.; Villaseñor-Zepeda, K.R.; López-Arellanes, M.E.; Sosa-Hernández, J.E.; Coronado-Apodaca, K.G.; Gámez-Méndez, A.; Afewerki, S.; et al. Photolyase Production and Current Applications: A Review. *Molecules* **2022**, *27*, 5998. [CrossRef]
7. Powers, H.J. Riboflavin (vitamin B-2) and health. *Am. J. Clin. Nutr.* **2003**, *77*, 1352–1360. [CrossRef] [PubMed]
8. Liscum, E.; Hodgson, D.W.; Campbell, T.J. Blue Light Signaling through the Cryptochromes and Phototropins. So That's What the Blues Is All About. *Plant Physiol.* **2003**, *133*, 1429–1436. [CrossRef] [PubMed]
9. Van der Horst, M.A.; Hellingwerf, K.J. Photoreceptor Proteins, “Star Actors of Modern Times”: A Review of the Functional Dynamics in the Structure of Representative Members of Six Different Photoreceptor Families. *Acc. Chem. Res.* **2004**, *37*, 13–20. [CrossRef]
10. Silva, E.; Edwards, A.M. (Eds.) *Flavins: Photochemistry and Photobiology*; Comprehensive Series in Photochemical & Photobiological Sciences; Royal Society of Chemistry: Cambridge, UK, 2006; pp. 1–338. [CrossRef]
11. Mansoorabadi, S.O.; Thibodeaux, C.J.; Liu, H.-W. The diverse roles of flavin coenzymes—Nature's most versatile thespians. *J. Org. Chem.* **2007**, *72*, 6329–6342. [CrossRef]
12. Galbán, J.; Sanz-Vicente, I.; Navarro, J.; de Marcos, S. The intrinsic fluorescence of FAD and its application in analytical chemistry: A review. *Methods Appl. Fluoresc.* **2016**, *4*, 042005. [CrossRef] [PubMed]
13. Ahmad, I.; Vaid, F.H. Photochemistry of Flavins in Aqueous and Organic Solvents. In *Flavins: Photochemistry and Photobiology*; Comprehensive Series in Photochemical & Photobiological, Sciences; Silva, E., Edwards, A.M., Eds.; Royal Society of Chemistry: Cambridge, UK, 2006; pp. 13–40. Available online: <http://books.rsc.org/books/chapter-pdf/1150045/bk9780854043316-00013.pdf> (accessed on 15 January 2023).
14. Kotaki, A.; Yagi, K. Fluorescence Properties of Flavins in Various Solvents. *J. Biochem.* **1970**, *68*, 509–516. [CrossRef]
15. Bracker, M.; Kubitz, M.K.; Czekelius, C.; Marian, C.M.; Kleinschmidt, M. Computer-Aided Design of Fluorinated Flavin Derivatives by Modulation of Intersystem Crossing and Fluorescence. *ChemPhotoChem* **2022**, *6*, e202200040. [CrossRef]
16. Mukherjee, A.; Walker, J.; Weyant, K.B.; Schroeder, C.M. Characterization of flavin-based fluorescent proteins: An emerging class of fluorescent reporters. *PLoS ONE* **2013**, *8*, e64753. [CrossRef] [PubMed]
17. Reiffers, A.; Ziegenbein, C.T.; Engelhardt, A.; Kühnemuth, R.; Gilch, P.; Czekelius, C. Impact of Mono-Fluorination on the Photophysics of the Flavin Chromophore. *Photochem. Photobiol.* **2018**, *94*, 667–676. [CrossRef] [PubMed]

18. Ryu, U.; Lee, H.S.; Park, K.S.; Choi, K.M. The rules and roles of metal–organic framework in combination with molecular dyes. *Polyhedron* **2018**, *154*, 275–294. [\[CrossRef\]](#)
19. Nguyen, T.N.; Ebrahim, F.M.; Stylianou, K.C. Photoluminescent, upconversion luminescent and nonlinear optical metal-organic frameworks: From fundamental photophysics to potential applications. *Coord. Chem. Rev.* **2018**, *377*, 259–306. [\[CrossRef\]](#)
20. Li, H.; Zhang, L.; He, H.; Yang, Y.; Cui, Y.; Qian, G. Tunable nonlinear optical responses based on hostguest MOF hybrid materials. *Sci. China Mater.* **2020**, *64*, 698–705. [\[CrossRef\]](#)
21. Xing, S.; Janiak, C. Design and properties of multiple-emitter luminescent metal-organic frameworks. *Chem. Commun.* **2020**, *56*, 12290–12306. [\[CrossRef\]](#)
22. Wan, Y.; Li, Y.; Yue, D. Dye-Encapsulated Metal–Organic Frameworks for the Multi-Parameter Detection of Temperature. *Molecules* **2023**, *28*, 729. [\[CrossRef\]](#)
23. Sun, Z.; Khurshid, A.; Sohail, M.; Qiu, W.; Cao, D.; Su, S.-J. Encapsulation of Dyes in Luminescent Metal-Organic Frameworks for White Light Emitting Diodes. *Nanomaterials* **2021**, *11*, 2761. [\[CrossRef\]](#)
24. Janiak, C.; Vieth, J.K. MOFs, MILs and more: Concepts, properties and applications for porous coordination networks (PCNs). *New J. Chem.* **2010**, *34*, 2366–2388. [\[CrossRef\]](#)
25. Yuan, S.; Feng, L.; Wang, K.; Pang, J.; Bosch, M.; Lollar, C.; Sun, Y.; Qin, J.; Yang, X.; Zhang, P.; et al. Stable Metal-Organic Frameworks: Design, Synthesis, and Applications. *Adv. Mater.* **2018**, *30*, e1704303. [\[CrossRef\]](#) [\[PubMed\]](#)
26. Lu, W.; Wei, Z.; Gu, Z.-Y.; Liu, T.-F.; Park, J.; Tian, J.; Zhang, M.; Zhang, Q.; Gentle, T.; et al. Tuning the structure and function of metal-organic frameworks via linker design. *Chem. Soc. Rev.* **2014**, *43*, 55615593. [\[CrossRef\]](#) [\[PubMed\]](#)
27. Ebrahimi, A.; Krivosudský, L. Metalloporphyrin Metal–Organic Frameworks: Eminent Synthetic Strategies and Recent Practical Exploitations. *Molecules* **2022**, *27*, 4917. [\[CrossRef\]](#) [\[PubMed\]](#)
28. Woschko, D.; Millan, S.; Ceyran, M.-A.; Oestreich, R.; Janiak, C. Synthesis of a Chiral 3,6T22-Zn-MOF with a T-Shaped Bifunctional Pyrazole-Isophthalate Ligand Following the Principles of the Supramolecular Building Layer Approach. *Molecules* **2022**, *27*, 5374. [\[CrossRef\]](#) [\[PubMed\]](#)
29. Qin, L.; Liang, F.; Li, Y.; Wu, J.; Guan, S.; Wu, M.; Xie, S.; Luo, M.; Ma, D. A 2D Porous Zinc-Organic Framework Platform for Loading of 5-Fluorouracil. *Inorganics* **2022**, *10*, 202. [\[CrossRef\]](#)
30. Zheng, M.; Chen, J.; Zhang, L.; Cheng, Y.; Lu, C.; Liu, Y.; Singh, A.; Trivedi, M.; Kumar, A.; Liu, J. Metal organic frameworks as efficient adsorbents for drugs from wastewater. *Mater. Today Commun.* **2022**, *31*, 103514. [\[CrossRef\]](#)
31. Dong, X.; Li, Y.; Li, D.; Liao, D.; Qin, T.; Prakash, O.; Kumar, A.; Liu, J. A new 3D 8-connected Cd(II) MOF as a potent photocatalyst for oxytetracycline antibiotic degradation. *CrystEngComm* **2022**, *24*, 6933–6943. [\[CrossRef\]](#)
32. Chen, Y.; Yu, B.; Cui, Y.; Xu, S.; Gong, J. Core–Shell Structured Cyclodextrin Metal–Organic Frameworks with Hierarchical Dye Encapsulation for Tunable Light Emission. *Chem. Mater.* **2019**, *31*, 1289–1295. [\[CrossRef\]](#)
33. Pramanik, S.; Zheng, C.; Zhang, X.; Emge, T.J.; Li, J. New microporous metal-organic framework demonstrating unique selectivity for detection of high explosives and aromatic compounds. *J. Am. Chem. Soc.* **2011**, *133*, 4153–4155. [\[CrossRef\]](#)
34. Pramanik, S.; Hu, Z.; Zhang, X.; Zheng, C.; Kelly, S.; Li, J. A Systematic Study of Fluorescence-Based Detection of Nitroexplosives and Other Aromatics in the Vapor Phase by Microporous Metal–Organic Frameworks. *Chem. Eur. J.* **2013**, *19*, 15964–15971. [\[CrossRef\]](#)
35. Hu, Z.; Pramanik, S.; Tan, K.; Zheng, C.; Liu, W.; Zhang, X.; Chabal, Y.J.; Li, J. Selective, Sensitive, and Reversible Detection of Vapor-Phase High Explosives via Two-Dimensional Mapping: A New Strategy for MOF-Based Sensors. *Cryst. Growth Des.* **2013**, *13*, 4204–4207. [\[CrossRef\]](#)
36. Hu, Z.; Deibert, B.J.; Li, J. Luminescent metal–organic frameworks for chemical sensing and explosive detection. *Chem. Soc. Rev.* **2014**, *43*, 5815–5840. [\[CrossRef\]](#)
37. Zheng, J.-P.; Ou, S.; Zhao, M.; Wu, C.-D. A Highly Sensitive Luminescent Dye@MOF Composite for Probing Different Volatile Organic Compounds. *ChemPlusChem* **2016**, *81*, 758–763. [\[CrossRef\]](#)
38. Miller, S.E.; Teplensky, M.H.; Moghadam, P.Z.; Fairen-Jimenez, D. Metal-organic frameworks as biosensors for luminescence-based detection and imaging. *Interface Focus* **2016**, *6*, 20160027. [\[CrossRef\]](#) [\[PubMed\]](#)
39. Zhao, D.; Yu, S.; Jiang, W.-J.; Cai, Z.-H.; Li, D.-L.; Liu, Y.-L.; Chen, Z.-Z. Recent Progress in Metal-Organic Framework Based Fluorescent Sensors for Hazardous Materials Detection. *Molecules* **2022**, *27*, 2226. [\[CrossRef\]](#) [\[PubMed\]](#)
40. Li, L.; Zou, J.; Han, Y.; Liao, Z.; Lu, P.; Nezamzadeh-Ejhieh, A.; Liu, J.; Peng, Y. Recent advances in Al(III)/In(III)-based MOFs for the detection of pollutants. *New J. Chem.* **2022**, *46*, 19577–19592. [\[CrossRef\]](#)
41. Loiseau, T.; Serre, C.; Huguenard, C.; Fink, G.; Taulelle, F.; Henry, M.; Bataille, T.; Férey, G. A Rationale for the Large Breathing of the Porous Aluminum Terephthalate (MIL-53) Upon Hydration. *Chem. Eur. J.* **2004**, *10*, 1373–1382. [\[CrossRef\]](#)
42. Ashling, C.W.; Johnstone, D.N.; Widmer, R.N.; Hou, J.; Collins, S.M.; Sapnik, A.F.; Bumstead, A.M.; Midgley, P.A.; Chater, P.A.; Keen, D.A.; et al. Synthesis and Properties of a Compositional Series of MIL-53(Al) Metal–Organic Framework Crystal-Glass Composites. *J. Am. Chem. Soc.* **2019**, *141*, 15641–15648. [\[CrossRef\]](#) [\[PubMed\]](#)
43. Millange, F.; Walton, R.I. MIL-53 and its Isoreticular Analogues: A Review of the Chemistry and Structure of a Prototypical Flexible Metal-Organic Framework. *Isr. J. Chem.* **2018**, *58*, 1019–1035. [\[CrossRef\]](#)
44. Meilikhov, M.; Yusenkov, K.; Fischer, R.A. The adsorbate structure of ferrocene inside [Al(OH)(bdc)]_x (MIL-53): A powder X-ray diffraction study. *Dalton Trans.* **2009**, *4*, 600–602. [\[CrossRef\]](#) [\[PubMed\]](#)

45. Millange, F.; Serre, C.; Férey, G. Synthesis, structure determination and properties of MIL-53as and MIL-53ht: The first Cr^{III} hybrid inorganic–organic microporous solids: Cr^{III}(OH)·{O₂C–C₆H₄–CO₂}·{HO₂C–C₆H₄–CO₂H}_x. *Chem. Commun.* **2002**, *8*, 822–823. [CrossRef] [PubMed]
46. Millange, F.; Guillou, N.; Walton, R.I.; Grenèche, J.-M.; Margiolaki, I.; Férey, G. Effect of the nature of the metal on the breathing steps in MOFs with dynamic frameworks. *Chem. Commun.* **2008**, *39*, 4732–4734. [CrossRef] [PubMed]
47. Serre, C.; Millange, F.; Thouvenot, C.; Noguès, M.; Marsolier, G.; Louër, D.; Férey, G. Very Large Breathing Effect in the First Nanoporous Chromium(III)-Based Solids: MIL-53 or Cr^{III}(OH)·{O₂C–C₆H₄–CO₂}·{HO₂C–C₆H₄–CO₂H}_x·H₂O_y. *J. Am. Chem. Soc.* **2002**, *124*, 13519–13526. [CrossRef]
48. Millange, F.; Serre, C.; Guillou, N.; Férey, G.; Walton, R.I. Structural Effects of Solvents on the Breathing of Metal–Organic Frameworks: An In Situ Diffraction Study. *Angew. Chem. Int. Ed.* **2008**, *47*, 4100–4105. [CrossRef]
49. Couck, S.; Gobechiya, E.; Kirschhock, C.E.A.; Serra-Crespo, P.; Juan-Alcañiz, J.; Martinez Joaristi, A.; Stavitski, E.; Gascon, J.; Kapteijn, F.; Baron, G.V.; et al. Adsorption and Separation of Light Gases on an Amino-Functionalized Metal–Organic Framework: An Adsorption and In Situ XRD Study. *ChemSusChem* **2012**, *5*, 740–750. [CrossRef]
50. Salles, F.; Bourrelly, S.; Jobic, H.; Devic, T.; Guillermin, V.; Llewellyn, P.; Serre, C.; Férey, G.; Maurin, G. Molecular Insight into the Adsorption and Diffusion of Water in the Versatile Hydrophilic/Hydrophobic Flexible MIL-53(Cr) MOF. *J. Phys. Chem. C* **2011**, *115*, 10764–10776. [CrossRef]
51. Kaye, S.S.; Dailly, A.; Yaghi, O.M.; Long, J.R. Impact of Preparation and Handling on the Hydrogen Storage Properties of Zn₄O(1,4-benzenedicarboxylate)₃ (MOF-5). *J. Am. Chem. Soc.* **2007**, *129*, 14176–14177. [CrossRef]
52. Li, H.; Eddaoudi, M.; O’Keeffe, M.; Yaghi, O.M. Design and synthesis of an exceptionally stable and highly porous metal-organic framework. *Nature* **1999**, *402*, 276–279. [CrossRef]
53. Zhang, L.; Li, H.; Yang, Y.; Yang, D.; Cui, Y.; Quia, G. Aligned chromophores in a host–guest MOF crystal for switchable polarized nonlinear optical response. *J. Mater. Chem. C* **2022**, *10*, 14915–14920. [CrossRef]
54. Haldar, R.; Mazel, A.; Krstić, M.; Zhang, Q.; Jakoby, M.; Howard, I.A.; Richards, B.S.; Jung, N.; Jacquemin, D.; Diring, S.; et al. A de novo strategy for predictive crystal engineering to tune excitonic coupling. *Nat. Commun.* **2019**, *10*, 2048. [CrossRef]
55. López Arbeloa, F.; Martínez Martínez, V.; Arbeloa, T.; López Arbeloa, I. Photoresponse and anisotropy of rhodamine dye intercalated in ordered clay layered films. *J. Photochem. Photobiol. C Photochem. Rev.* **2007**, *8*, 85–108. [CrossRef]
56. Martínez Martínez, V.; López Arbeloa, F.; Bañuelos Prieto, J.; López Arbeloa, I. Orientation of Adsorbed Dyes in the Interlayer Space of Clays. 1. Anisotropy of Rhodamine 6G in Laponite Films by Vis-Absorption with Polarized Light. *Chem. Mater.* **2005**, *17*, 4134–4141. [CrossRef]
57. Brandenburg, K. *Diamond (Version 4.6), Crystal and Molecular Structure Visualization, Crystal Impact*; K. Brandenburg & H. Putz Gbr: Bonn, Germany, 2009–2022.
58. Li, H.; Eddaoudi, M.; O’Keeffe, M.; Yaghi, O.M. CCDC 256966: *Experimental Crystal Structure Determination*; Cambridge Crystallographic Data Centre: Cambridge, UK, 2005. [CrossRef]
59. Ma, M.; Gross, A.; Zacher, D.; Pinto, A.; Noei, H.; Wang, Y.; Fischer, R.A.; Metzler-Nolte, N. Use of confocal fluorescence microscopy to compare different methods of modifying metal–organic framework (MOF) crystals with dyes. *CrystEngComm* **2011**, *13*, 2828–2832. [CrossRef]
60. Wang, M.; Fritch, C.J., Jr. Geometry of the Unperturbed Flavin Nucleus. The Crystal Structure of 10-Methylisoalloxazine. *Acta Crystallogr.* **1973**, *29*, 2040–2045. [CrossRef]
61. Taheri, A.; Babakhani, E.G.; Towfighi, J. Study of synthesis parameters of MIL-53(Al) using experimental design methodology for CO₂/CH₄ separation. *Adsorpt. Sci. Technol.* **2018**, *36*, 247–269. [CrossRef]
62. Han, S.; Wei, Y.; Valente, C.; Lagzi, I.; Gassensmith, J.J.; Coskun, A.; Stoddart, J.F.; Grzybowski, B.A. Chromatography in a Single Metal–Organic Framework (MOF) Crystal. *J. Am. Chem. Soc.* **2010**, *132*, 16358–16361. [CrossRef]
63. Schaffer, J.; Volkmer, A.; Eggeling, C.; Subramaniam, V.; Striker, G.; Seidel, C.A.M. Identification of single molecules in aqueous solution by time-resolved fluorescence anisotropy. *J. Phys. Chem. A* **1999**, *103*, 331–336. [CrossRef]
64. Möckel, C.; Kubiak, J.; Schillinger, O.; Kühnemuth, R.; Della Corte, D.; Schröder, G.F.; Willbold, D.; Strodel, B.; Seidel, C.A.M.; Neudecker, P. Integrated NMR, fluorescence and MD benchmark study of protein mechanics and hydrodynamics. *J. Phys. Chem. B* **2019**, *123*, 1453–1480. [CrossRef] [PubMed]
65. Lakowicz, J.R. *Principles of Fluorescence Spectroscopy*, 3rd ed.; Springer: Berlin/Heidelberg, Germany, 2006; Chapter 10; pp. 356–358.
66. Alaerts, L.; Maes, M.; Giebler, L.; Jacobs, P.A.; Martens, J.A.; Denayer, J.F.M.; Kirschhock, C.E.A.; De Vos, D.E. Selective Adsorption and Separation of ortho-Substituted Alkylaromatics with the Microporous Aluminum Terephthalate MIL-53. *J. Am. Chem. Soc.* **2008**, *130*, 14170–14178. [CrossRef]
67. Llewellyn, P.L.; Horcjada, P.; Maurin, G.; Devic, T.; Rosenbach, N.; Bourrelly, S.; Serre, C.; Vincent, D.; Loera-Serna, S.; Filinchuk, Y.; et al. Complex Adsorption of Short Linear Alkanes in the Flexible Metal–Organic–Framework MIL-53(Fe). *J. Am. Chem. Soc.* **2009**, *131*, 13002–13008. [CrossRef] [PubMed]
68. Rosenbach, N.J.; Jobic, H.; Ghoufi, A.; Salles, F.; Maurin, G.; Bourrelly, S.; Llewellyn, P.L.; Devic, T.; Serre, C.; Férey, G. Quasi-Elastic Neutron Scattering and Molecular Dynamics Study of Methane Diffusion in Metal Organic Frameworks MIL-47(V) and MIL-53(Cr). *Angew. Chem. Int. Ed.* **2008**, *47*, 6611–6615. [CrossRef] [PubMed]
69. Brown, S.A.; Rizzo, C.J. A “One-Pot” Phase Transfer Alkylation/Hydrolysis of o-Nitrotrifluoroacetanilides. A Convenient Route to N-Alkyl o-Phenylenediamines. *Synth. Commun.* **1996**, *26*, 4065–4080. [CrossRef]

70. Imada, Y.; Iida, H.; Ono, S.; Masui, Y.; Murahashi, S.-I. Flavin-Catalyzed Oxidation of Amines and Sulfides with Molecular Oxygen: Biomimetic Green Oxidation. *Chem. Asian J.* **2006**, *1*, 136–147. [CrossRef] [PubMed]
71. Eddaoudi, M.; Kim, J.; Rosi, N.; Vodak, D.; Wachter, J.; O’Keeffe, M.; Yaghi, O.M. Systematic Design of Pore Size and Functionality in Isoreticular MOFs and Their Application in Methane Storage. *Science* **2002**, *295*, 469–472. [CrossRef]
72. Weidtkamp-Peters, S.; Felekyan, S.; Bleckmann, A.; Simon, R.; Becker, W.; Kühnemuth, R.; Seidel, C.A.M. Multiparameter Fluorescence Image Spectroscopy to study molecular interactions. *Photochem. Photobiol. Sci.* **2009**, *8*, 470–480. [CrossRef]
73. Koshioka, M.; Sasaki, K.; Masuhara, H. Time-Dependent Fluorescence Depolarization Analysis in Three-Dimensional Microspectroscopy. *Appl. Spectrosc.* **1995**, *49*, 224–228. Available online: <https://opg.optica.org/as/abstract.cfm?URI=as-49-2-224> (accessed on 24 January 2023). [CrossRef]
74. Giannozzi, P.; Baroni, S.; Bonini, N.; Calandra, M.; Car, R.; Cavazzoni, C.; Ceresoli, D.; Chiarotti, G.L.; Cococcioni, M.; Dabo, I.; et al. QUANTUM ESPRESSO: A modular and open-source software project for quantum simulations of materials. *J. Phys. Condens. Matter* **2009**, *21*, 395502. [CrossRef]
75. Rappe, A.M.; Rabe, K.M.; Kaxiras, E.; Joannopoulos, J.D. Optimized pseudopotentials. *Phys. Rev. B* **1990**, *41*, 1227–1230. [CrossRef]
76. Perdew, J.P.; Ernzerhof, M. Rationale for mixing exact exchange with density functional approximations. *J. Chem. Phys.* **1996**, *105*, 9982–9985. [CrossRef]
77. Grimme, S.; Antony, J.; Ehrlich, S.; Krieg, H. A consistent and accurate ab initio parametrization of density functional dispersion correction (DFT-D) for the 94 elements H–Pu. *J. Chem. Phys.* **2010**, *132*, 154104. [CrossRef] [PubMed]
78. Frisch, M.J.; Trucks, G.W.; Schlegel, H.B.; Scuseria, G.E.; Robb, M.A.; Cheeseman, J.R.; Scalmani, G.; Barone, V.; Petersson, G.A.; Nakatsuji, H.; et al. *Gaussian, 16, Revision C.01*; Gaussian, Inc.: Wallingford, CT, USA, 2016.
79. Singh, U.C.; Kollman, P.A. An approach to computing electrostatic charges for molecules. *J. Comput. Chem.* **1984**, *5*, 129–145. [CrossRef]
80. Campaña, C.; Mussard, B.; Woo, T.K. Electrostatic Potential Derived Atomic Charges for Periodic Systems Using a Modified Error Functional. *J. Chem. Theory Comput.* **2009**, *5*, 2866–2878. [CrossRef] [PubMed]
81. Kühne, T.D.; Iannuzzi, M.; Del Ben, M.; Rybkin, V.V.; Seewald, P.; Stein, F.; Laino, T.; Khaliullin, R.Z.; Schütt, O.; Schiffmann, F.; et al. CP2K: An electronic structure and molecular dynamics software package—Quickstep: Efficient and accurate electronic structure calculations. *J. Chem. Phys.* **2020**, *152*, 194103. [CrossRef] [PubMed]
82. Goedecker, S.; Teter, M.; Hutter, J. Separable dual-space Gaussian pseudopotentials. *Phys. Rev. B* **1996**, *54*, 1703–1710. [CrossRef] [PubMed]
83. Vanduyfhuys, L.; Vandenbrande, S.; Verstraelen, T.; Schmid, R.; Waroquier, M.; Van Speybroeck, V. QuickFF: A program for a quick and easy derivation of force fields for metal-organic frameworks from ab initio input. *J. Comput. Chem.* **2015**, *36*, 1015–1027. [CrossRef]
84. Mayne, C.G.; Saam, J.; Schulten, K.; Tajkhorshid, E.; Gumbart, J.C. Rapid parameterization of small molecules using the force field toolkit. *J. Comput. Chem.* **2013**, *34*, 2757–2770. [CrossRef]
85. Weingart, O.; Nenov, A.; Altoè, P.; Rivalta, I.; Segarra-Martí, J.; Dokukina, I.; Garavelli, M. COBRAMM 2.0—A software interface for tailoring molecular electronic structure calculations and running nanoscale (QM/MM) simulations. *J. Mol. Model.* **2018**, *24*, 271. [CrossRef]
86. Case, D.A.; Cheatham, T.E., III; Darden, T.; Gohlke, H.; Luo, R.; Merz, K.M., Jr.; Onufriev, A.; Simmerling, C.; Wang, B.; Woods, R. The Amber biomolecular simulation programs. *J. Comput. Chem.* **2005**, *26*, 1668–1688. [CrossRef]
87. Grimme, S.; Waletzke, M. A combination of Kohn–Sham density functional theory and multi-reference configuration interaction methods. *J. Chem. Phys.* **1999**, *111*, 5645–5655. [CrossRef]
88. Lyskov, I.; Kleinschmidt, M.; Marian, C.M. Redesign of the DFT/MRCI Hamiltonian. *J. Chem. Phys.* **2016**, *144*, 034104. [CrossRef] [PubMed]
89. Balasubramani, S.G.; Chen, G.P.; Coriani, S.; Diedenhofen, M.; Frank, M.S.; Franzke, Y.J.; Furche, F.; Grotjahn, R.; Harding, M.E.; Hättig, C.; et al. TURBOMOLE: Modular program suite for ab initio quantum-chemical and condensed-matter simulations. *J. Chem. Phys.* **2020**, *152*, 184107. [CrossRef] [PubMed]
90. Kumar, V.; Bode, K.A.; Bryan, R.F.; Averill, B.A. Evidence for a competing condensation reaction in the alloxan synthesis of flavins: Synthesis and crystal and molecular structures of 7-chloro-8-methylalloxazine and 7,10-dimethyl-8-[(2-hydroxyethyl)thio]isoalloxazine. *J. Am. Chem. Soc.* **1986**, *108*, 490–496. [CrossRef] [PubMed]
91. Bauer, S.; Serre, C.; Devic, T.; Horcajada, P.; Marrot, J.; Férey, G.; Stock, N. High-Throughput Assisted Rationalization of the Formation of Metal Organic Frameworks in the Iron(III) Aminoterephthalate Solvothermal System. *Inorg. Chem.* **2008**, *47*, 7568–7576. [CrossRef]
92. Bailey, M.; Brown, C.J. The crystal structure of terephthalic acid. *Acta Crystallogr.* **1967**, *22*, 387–391. [CrossRef]
93. Lock, N.; Wu, Y.; Christensen, M.; Cameron, L.J.; Peterson, V.K.; Bridgeman, A.J.; Kepert, C.J.; Iversen, B.B. Elucidating Negative Thermal Expansion in MOF-5. *J. Phys. Chem. C* **2010**, *114*, 16181–16186. [CrossRef]

Disclaimer/Publisher’s Note: The statements, opinions and data contained in all publications are solely those of the individual author(s) and contributor(s) and not of MDPI and/or the editor(s). MDPI and/or the editor(s) disclaim responsibility for any injury to people or property resulting from any ideas, methods, instructions or products referred to in the content.

Supplementary Material

Enhanced solid-state fluorescence of flavin derivatives by incorporation in the metal-organic frameworks MIL-53(Al) and MOF-5

Dietrich Püschel ¹, Simon Hédé ², Iván Maisuls ³, Simon-Patrick Höfert ¹, Dennis Woschko ¹, Ralf Kühnemuth ⁴, Suren Felekyan ⁴, Claus A. M. Seidel ^{4,*}, Constantin Czekelius ⁵, Oliver Weingart ^{2,*}, Cristian A. Strassert ^{3,*} and Christoph Janiak ^{1,*}

1 Institut für Anorganische Chemie und Strukturchemie, Heinrich-Heine-Universität Düsseldorf, Universitätsstraße 1, D-40225 Düsseldorf, Germany

2 Institut für Theoretische Chemie und Computerchemie, Heinrich-Heine-Universität Düsseldorf, Universitätsstraße 1, D-40225 Düsseldorf, Germany

3 Institut für Anorganische und Analytische Chemie, CeNTech, CiMIC, SoN, Westfälische Wilhelms-Universität Münster, Heisenbergstraße 11, D-48149 Münster, Germany

4 Institut für Physikalische Chemie, Heinrich-Heine-Universität Düsseldorf, Universitätsstraße 1, D-40225 Düsseldorf, Germany

5 Institut für Organische Chemie und Makromolekulare Chemie, Heinrich-Heine-Universität Düsseldorf, Universitätsstraße 1, D-40225 Düsseldorf, Germany

Corresponding authors:

E-mails: Cseidel@hhu.de, Oliver.Weingart@hhu.de, ca.s@wwu.de, janiak@uni-duesseldorf.de;

Tel: +49-211-81-12286

Additional E-mail addresses:

Dietrich.Pueschel@hhu.de; Simon.Hede@hhu.de; Maisuls@uni-muenster.de;

Simon.patrick.hoefert@googlemail.com; Dennis.Woschko@hhu.de; Ralf.Kuehnemuth@hhu.de;

Suren.Felekyan@uni-duesseldorf.de, Cseidel@hhu.de ; Oliver.Weingart@hhu.de;

Constantin.Czekelius@hhu.de; ca.s@wwu.de

Table of Contents

Section S1: Materials and methods	3
Section S1.1: Synthesis of flavins.....	3
Section S1.2: MOF syntheses and flavin incorporation	3
Section S2: MIA and 6F-MIA absorption spectra and calibration curves (Figure S4-Figure S11)	11
Section S3: Structure descriptions (Figure S12 - Figure S15).....	15
Section S3.1: Structure of 10-methyl-isoalloxazine (MIA) (Figure S12)	15
Section S3.2: Additional structure description of MIL-53(Al) (Figure S13 and Figure S14)	15
Section S3.3: Additional structure description of MOF-5 (Figure S15)	17
Section S4: Nitrogen adsorption isotherms and powder X-ray diffractograms (Figure S16 - Figure S19)	19
Section S5: Photophysical characterization of the dyes and dye@MOF (Figure S20 - Figure S35)	24
Section S6: Theoretical calculations (Figure S36 - Figure S42)	33
Section S6.1: Force Field MIA	33
Section S6.2: Force Field MIL-53(Al).....	36
Section S6.3: Force Field MOF-5	39
Section S6.4: QM part, MM part	42
Section S6.5: Transition dipole moments of MIA.....	47

Section S1: Materials and methods

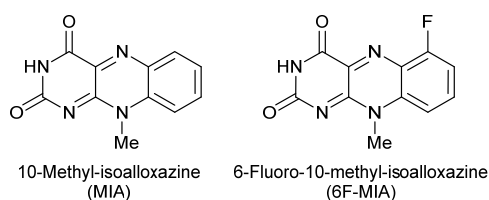
Commercially available reagents (Table S1) were used without further purification. All reagents were used in reagent grade without further purification. The solvents were purchased in reagent grade or purified by conventional methods. For reactions requiring an inert atmosphere the glassware was dried in a compartment dryer at 120 °C and standard Schlenk techniques were used to work under a dry nitrogen atmosphere. Degassing of solvents was done by purging with dry nitrogen for 30 minutes.

Table S1. Sources for starting materials and solvents.

Reagent	Manufacturer
Zinc nitrate hexahydrate	ACROS Organics
Terephthalic acid	Alfa Aesar
Ethanol	CHEMSOLUTE
<i>N,N</i> -dimethylformamide	Honeywell
<i>N,N</i> -diethylformamide	Honeywell
Aluminum nitrate nonahydrate	CARL ROTH

Section S1.1: Synthesis of flavins

Flavins were prepared from the corresponding 2-methylamino-anilines by condensation with alloxan hydrate. *N*-Methylation of 2-nitro-anilines was performed by alkylation of the corresponding trifluoroacetamides with dimethylsulfate following a procedure by Brown and Rizzo [1]. 10-Methyl-isoalloxazine (MIA) (Scheme S1) was prepared following a protocol reported by Imada, Murahashi and coworkers [2]. 6-Fluoro-10-methyl-isoalloxazine (6F-MIA) (Scheme S1) [3] was prepared following a modified protocol reported by Averill and co-workers [4].



Scheme S1. 10-Methyl-isoalloxazine (MIA) and 6-fluoro-10-methyl-isoalloxazine (6F-MIA).

Section S1.2: MOF syntheses and flavin incorporation

Preparation of saturated MIA and 6F-MIA dye solutions

The MIA or 6F-MIA dye was mixed in chloroform or DMF and dissolved for 30 min at 40 °C using ultrasound. When a clear homogeneous solution was obtained, this process was repeated until no more dye could be dissolved. The saturated chloroform solutions ($c_{\text{MIA}} = 69.5 \text{ mg}\cdot\text{L}^{-1}$, $c_{6\text{F-MIA}} = 20.25 \text{ mg}\cdot\text{L}^{-1}$; see Section S2) or DMF solutions ($c_{\text{MIA}} = 272 \text{ mg}\cdot\text{L}^{-1}$, $c_{6\text{F-MIA}} = 2640 \text{ mg}\cdot\text{L}^{-1}$; see Section S2) were then filtered at room temperature and used for the syntheses.

Synthesis of MIL-53(Al) according to Alaerts et al. and Loiseau et al. [5,6]

Aluminum nitrate nonahydrate (3.75 g, 10.0 mmol), terephthalic acid (0.83 g, 5.0 mmol) and dist. water (7.16 mL) were mixed in a 60 mL Teflon-lined stainless-steel autoclave, which was heated at 220 °C for 72 h including a 3 h heating ramp and 3 h cooling ramp. After cooling to room temperature, the white raw product was washed three times with water (10 mL). The white solid was dispersed in DMF and heated under reflux to 160 °C for 48 h to remove the incorporated terephthalic acid from the pores. The product was finally washed three times with hot ethanol (10 mL each). Yield 46 %.

10-Methyl-isoalloxazine (MIA) and 6-fluoro-10-methyl-isoalloxazine (6F-MIA) incorporation into MIL-53

Post-synthetic wet infiltration was performed by adding 1 to 15 mL from the concentrated solutions of the dyes in chloroform to 20 mg activated powders of the microcrystalline MIL-53. After brief mixing, slow evaporation at room temperature was used to promote diffusion of the dyes into the MOF pores.

MOF-5 single crystal synthesis according to Han et al. and Eddaoudi et al. [7,8]

Zinc nitrate hexahydrate (511 mg, 1.72 mmol) and terephthalic acid (96 mg, 0.58 mmol) were dissolved in dimethylformamide, DMF (5 mL). The solution was transferred to Pyrex tubes, which were placed in a programmable oven at 85 °C for 72 h including a 2.5 h heating ramp and 3.5 h cooling ramp. The colorless crystals obtained were washed with DMF (5 mL each) twice daily for three days and with ethanol (5 mL each) twice daily for another three days. After washing, the MOF-5 crystals were filtered and dried under vacuum (15 h at 120 °C). Yield 58 %. The MOF-5 were stored under nitrogen until further investigations.

MOF-5 single crystal synthesis with 10-methyl-isoalloxazine (MIA)

MIA (5.0 mg, 0.022 mmol) was added to DMF (5 mL) and sonicated at 60 °C for 30 min. The solution was then filtered to obtain a homogeneous MIA-saturated DMF solution with $c_{\text{MIA}} = 272 \text{ mg}\cdot\text{L}^{-1}$ (Section S2). Zinc nitrate hexahydrate (175.5 mg, 0.59 mmol) and terephthalic acid (31.0 mg, 0.19 mmol) were dissolved in the MIA-DMF solution (5 mL). The solution was then placed in a programmable oven at 85 °C for 72 h including a 2.5 h heating ramp and 3.5 h cooling ramp. Yellow discolored cubic crystals were obtained. The crystals were washed three times with DMF (5 mL), filtered and dried under vacuum (15 h at 120 °C). Yield 42.3 mg (MIA@MOF-5), 39.9 mg MOF-5 after deduction of MIA content (see below), ~90% MOF-5 based on terephthalic acid. The dry MIA@MOF-5 composites were stored under nitrogen until further investigations. For longer storage (> 4 weeks), the non-washed crystals were stored in the mother liquor at 4 °C. When needed, the crystals were then worked up as described above.

The 10-fold diluted supernatant DMF solution gave an absorption at 436 nm of 0.892 from which a residual MIA concentration of $0.892/0.04467 = 19.97 \text{ mg L}^{-1}$ (Figure S5), thus 199.7 mg L^{-1} for the original supernatant could be obtained. Hence, from 1.36 mg of MIA in 5 mL of the saturated MIA-DMF solution 1.00 mg of MIA was still present in the supernatant after MOF-5 formation or 0.36 mg MIA were incorporated in 39.94 mg MOF-5 ($42.3 \text{ mg} - 0.36 \text{ mg}$), representing $0.36 / (0.36 + 39.94) = 0.85 \text{ wt\%}$.

MOF-5 single crystal synthesis with 6-fluoro-10-methyl-isoalloxazine (6F-MIA)

6F-MIA (20 mg, 0.081 mmol) was added to DMF (5 mL) and sonicated at 60 °C for 30 min. The solution was then filtered to obtain a homogeneous 6F-MIA-saturated DMF solution with $C_{6F-MIA} = 2640 \text{ mg}\cdot\text{L}^{-1}$ (Section S2). Zinc nitrate hexahydrate (175.5 mg, 0.59 mmol) and terephthalic acid (31.0 mg, 0.19 mmol) were dissolved in the 6F-MIA-DMF solution (5 mL). The solution was then placed in a programmable oven at 85 °C for 72 h including a 2.5 h heating ramp and 3.5 h cooling ramp. Yellow discolored cubic crystals were obtained. The crystals were washed three times with DMF (5 mL each), filtered and dried under vacuum (15 h at 120 °C). Yield 40.5 mg (6F-MIA@MOF-5), 29.3 mg MOF-5 after deduction of 6F-MIA, ~57% MOF-5 based on terephthalic acid.

The dry 6F-MIA@MOF-5 composites were stored under nitrogen until further investigations. For longer storage (> 4 weeks), the non-washed crystals were stored in the mother liquor at 4 °C. When needed, the crystals were then worked up as described above.

The 20-fold diluted supernatant DMF solution gave an absorption at 425 nm of 0.544 from which a residual 6F-MIA concentration of $0.544/0.0272 = 20.0 \text{ mg L}^{-1}$ (Figure S9), thus 400 mg L^{-1} for the original supernatant could be obtained. Hence, from 13.2 mg of 6F-MIA in 5 mL of the saturated MIA-DMF solution 2.0 mg of 6F-MIA was still present in the supernatant after MOF-5 formation or 11.2 mg MIA were adsorbed onto or incorporated in 29.3 mg MOF-5 ($40.5 \text{ mg} - 11.2 \text{ mg}$), representing $11.2 / (11.2 + 29.3) = 27.6 \text{ wt\%}$, albeit before the washing process three times with DMF (5 mL each).

However, digestive dissolution in DMSO- d_6 /DCI of 6F-MIA@MOF-5 gave a loading of 5.2 wt%.

The MIA@MOF-5 and 6F-MIA@MOF-5 composites were dissolved in 0.8-0.9 mL DMSO- d_6 upon addition of ~0.1 mL 35% DCI/D₂O. The solution ¹H NMR spectra were recorded on a Bruker Avance III-300 MHz spectrometer. Chemical shifts are referenced to the residual proton solvent signal (2.50 ppm for DMSO- d_6).

The digestion ¹H NMR spectrum of 6F-MIA@MOF-5 (Figure S1a) shows a small signal for the N-methyl group of 6F-MIA (cf. Scheme S1).

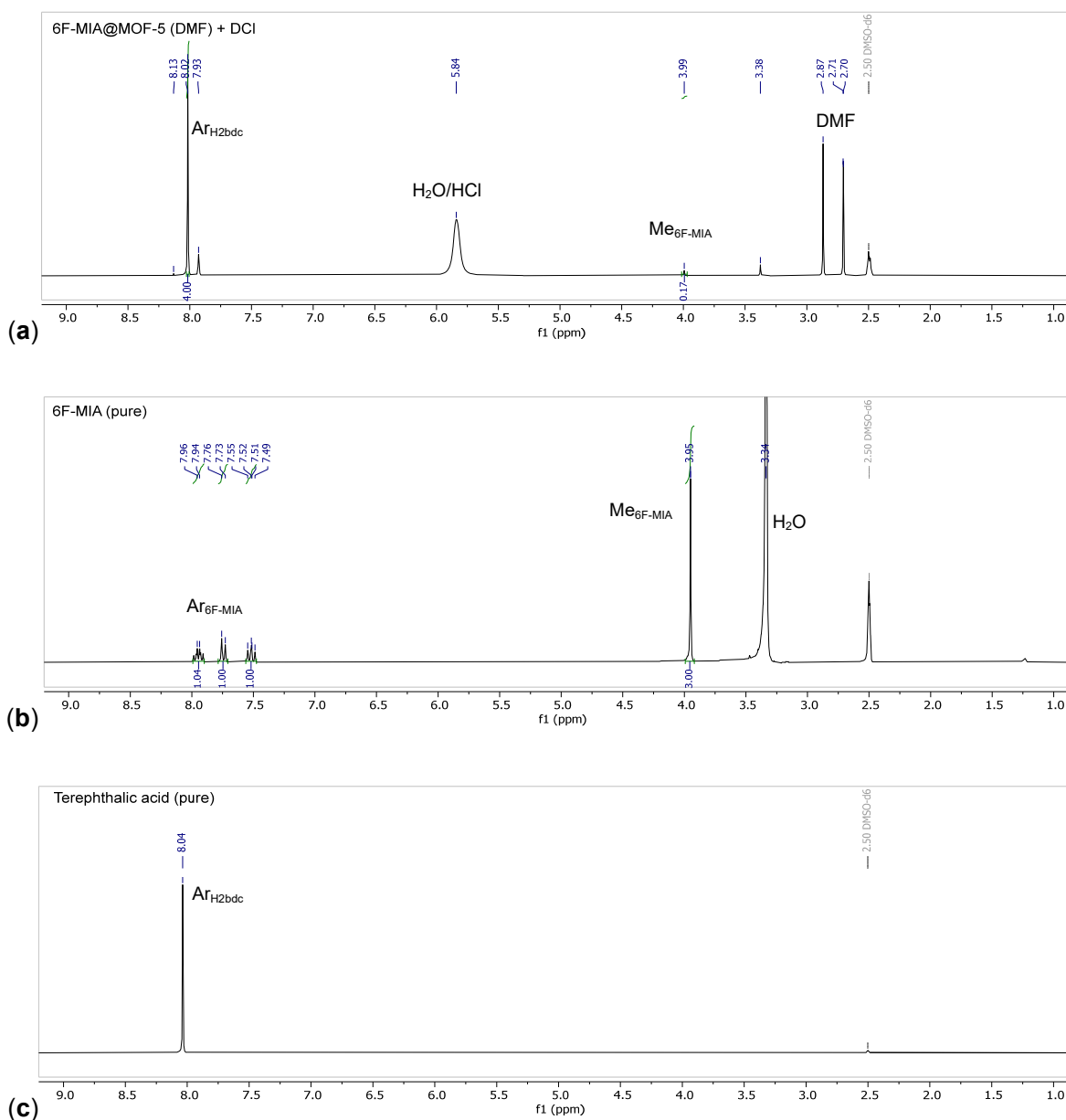


Figure S1. ^1H NMR spectra in DMSO-d_6 at 300 MHz of (a) 6F-MIA@MOF-5 upon digestive dissolution with DCI/D $_2$ O, (b) 6F-MIA and (c) terephthalic acid.

The integral of 4.00 for the terephthalic acid signal (4 aromatic protons) has to be divided by 12 as there are three terephthalate (bdc) linkers in the $[\text{Zn}_4\text{O}(\text{bdc})_3]$ formula unit of MOF-5. The integral of 0.17 for the N-methyl group (3 protons) of 6F-MIA has to be divided by 3. This normalization then gives the molar ratio of MOF-5 formula units to 6F-MIA molecules:

$$4/12 : 0.17/3 = 1:0.17 = 5.88 \text{ mol } [\text{Zn}_4\text{O}(\text{bdc})_3] \text{ for each mol of 6F-MIA.}$$

With $M = 769.87 \text{ g/mol}$ for $[\text{Zn}_4\text{O}(\text{bdc})_3]$ and $M = 246.20 \text{ g/mol}$ for 6F-MIA

there are $246.20 \text{ g 6F-MIA per } 5.88 \text{ mol} \times 769.87 \text{ g/mol} = 4528.6 \text{ g MOF-5.}$

This gives a 6F-MIA@MOF-5 loading of $246.20 / (246.20 + 4528.6) \times 100\% = 5.2 \text{ wt\%}.$

In view of the much smaller content of MIA@MOF-5 of at most 0.85 wt% from UV/Vis difference measurements no N-methyl signal is seen in the digestion ^1H NMR spectra of MIA@MOF-5.

As an explanation of the obtained large loading of 6F-MIA from the UV/Vis absorption difference measurement we suggest that a sizeable amount of 6F-MIA from the concentrated solution was adsorbed on the outer surface or in the pore mouths. This 6F-MIA content could easily be removed when the crystals were washed three times with DMF (5 mL). The much better solubility of 6F-MIA with $c_{6\text{F-MIA}} = 2640 \text{ mg}\cdot\text{L}^{-1}$ compared to MIA with only $c_{\text{MIA}} = 272 \text{ mg}\cdot\text{L}^{-1}$, both for saturated solutions, will also lead to a more facile postsynthetic removal of 6F-MIA through the washing cycles.

Infrared (IR) spectra of flavin@MOF

The Fourier transform infrared (FT-IR) spectra were collected with a Bruker Tensor 37 instrument with KBr or attenuated total reflection (ATR) technique. The spectra are collected in Figure S2 and Figure S3.

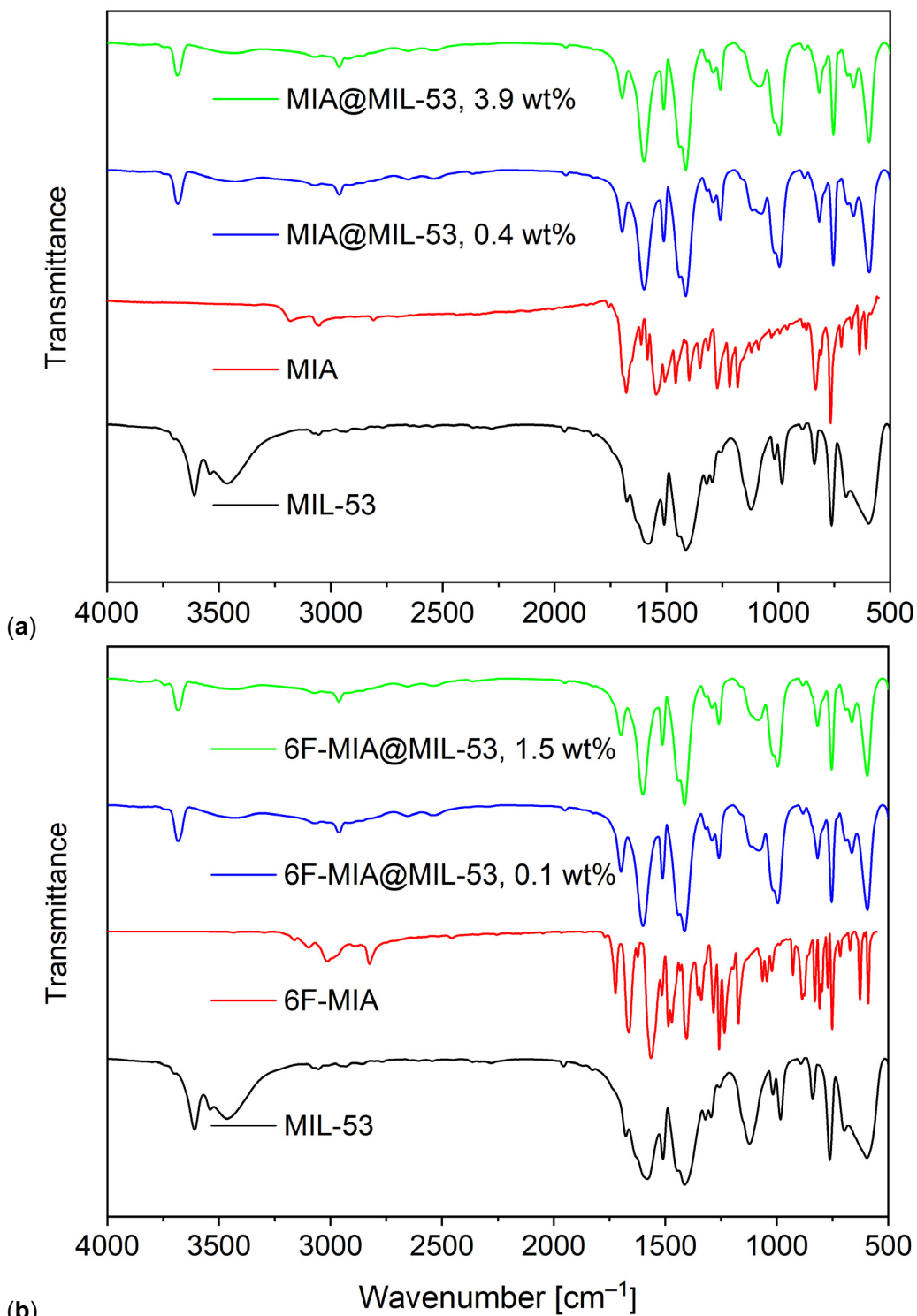


Figure S2. IR spectra of (a) MIL-53 (KBr), MIA (ATR) and MIA@MIL-53 (KBr) and (b) MIL-53 (KBr), 6F-MIA (ATR) and 6F-MIA@MIL-53 (KBr).

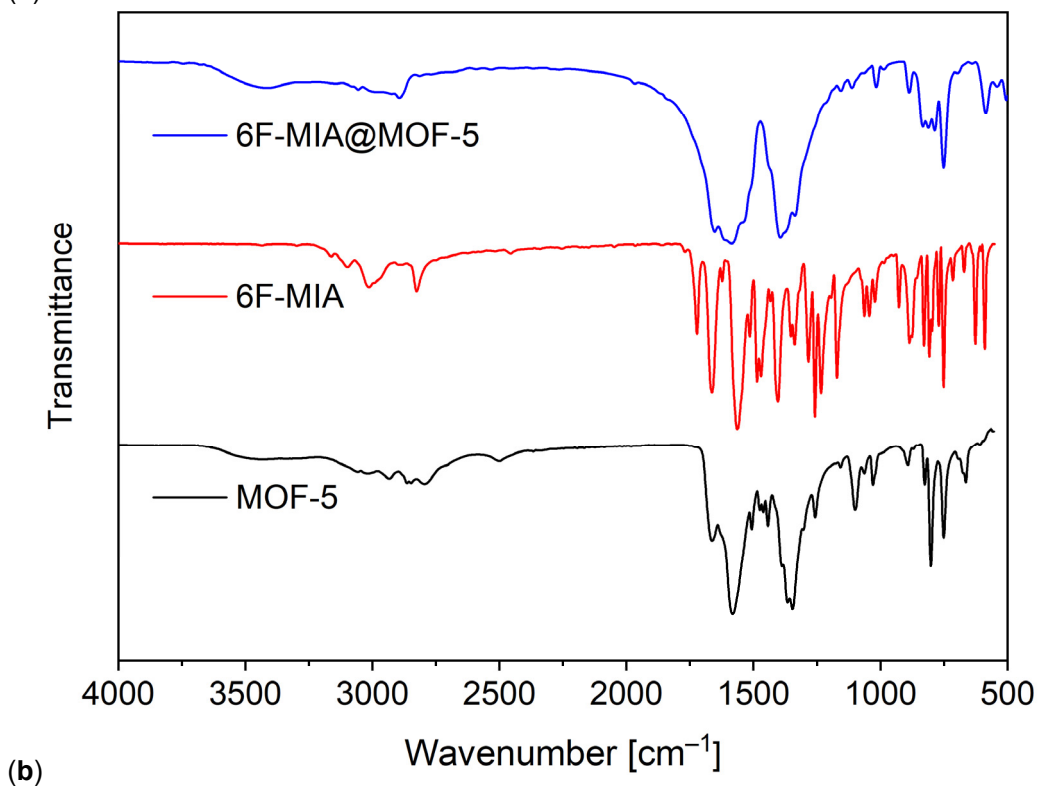
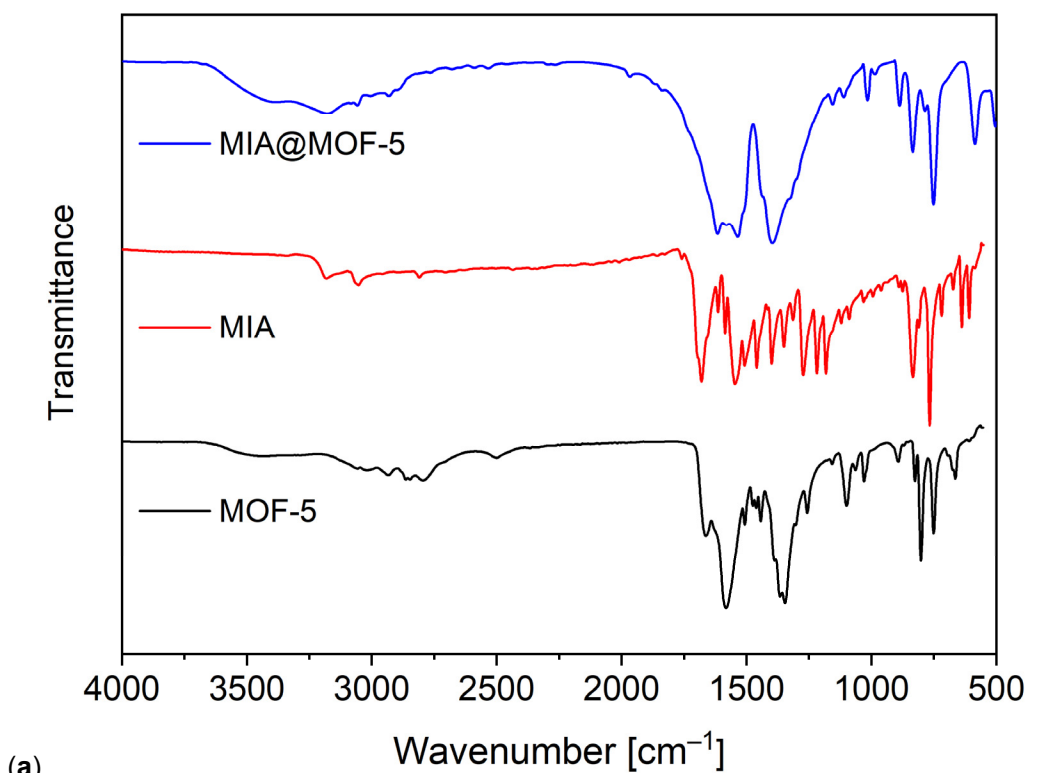


Figure S3. IR spectra of (a) MOF-5 (KBr), MIA (ATR) and MIA@MOF-5 (KBr) and (b) MOF-5 (KBr), 6F-MIA (ATR) and 6F-MIA@MOF-5 (KBr).

Neat MIL-53 features broad signals which we see as evidence for the superposition of the three MIL-53 phases MIL-53-as, MIL-53-np and MIL-53-lp (and intermediate phases) as is also evident from

the powder X-ray diffractograms (cf. Figure S14a). In the flavin@MIL-53 composites the bands sharpen and become more distinct with all composites giving nearly identical spectra (Figure S2). This is due to the formation of the same phase from the sample preparation as KBr pellets. The superposition of the flavin bands and the low amounts of flavins in MIL-53 do not allow a detection of flavin bands in the composites.

MOF-5 on the other hand has more distinct bands in its neat form whereas in the composites the band between 1000 and 1750 cm^{-1} have considerably broadened (Figure S3). Distinct bands remain only in the region between 750 to 1000 cm^{-1} where C=C- and C-H-bending vibrations occur. Also, MIA and 6F-MIA have bands in the same region. Upon close inspection the flavin-only bands at 606 and 833 cm^{-1} (MIA) and 588 and 828 cm^{-1} (6F-MIA) are also localized in the composites (Table S2).

Table S2. Listing of IR wavenumbers of MOF-5, MIA, 6F-MIA and flavin@MOF-5 composites.

Wavenumber [cm^{-1}]	MOF-5 (KBr)	MIA (ATR)	MIA@MOF-5 (KBr)	6F-MIA (ATR)	6F-MIA@MOF-5 (KBr)
C=C bending, C-H bending		606 ++	590 ++	588 ++	586 ++
	660 +	636 ++		625 ++	
	750 ++	765 +++	751 +++	750 +++	750 +++
	800 +++			808 ++	810 ++
				828 ++	835 ++
		833 ++	837 ++		
	892 +		889 +	885 ++	887 +
	1025 +		1012 +		1014 +
	1096 ++				
C-H stretching, O-H bending	1250-1450 +++, b (1343)	1216 ++	1230-1470 +++, b (1390)	1257 +++	1250-1470 +++, b (1390)
C-H/O-H stretching	1450-1670 +++, b (1578)	1454 +++	1470-1750 +++, b (1531,1616)	1564 +++	1480-1750 +++, b (1585)
		1680 ++		1722 ++	
	2495 +				
C-H/O-H stretching	2790-3100 +, b	2800-3180 +, b	2925-3530 +, b (3175)	2823 +	2900-3400 +, b
				3010 +	

Section S2: MIA and 6F-MIA absorption spectra and calibration curves (Figure S4-Figure S11)

For the concentration determination of the saturated solution of MIA in DMF, a stock solution with a concentration of $100 \text{ mg}\cdot\text{L}^{-1}$ MIA in DMF was prepared, diluted to lower concentrations and measured by UV/Vis spectroscopy (Figure S4).

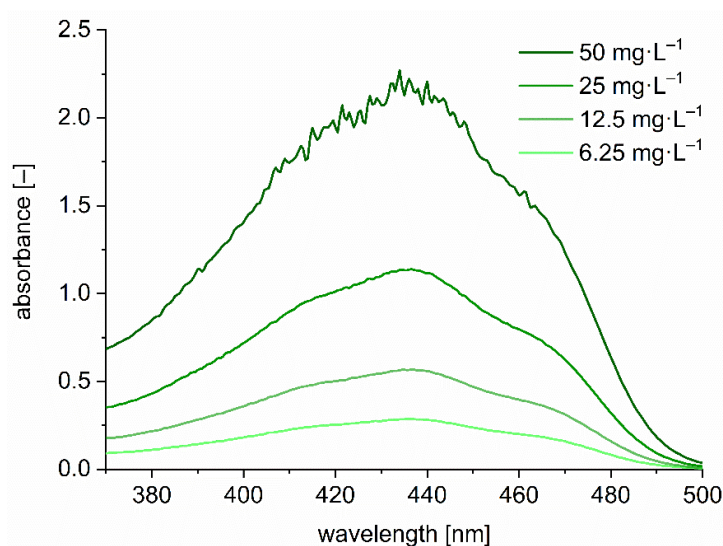


Figure S4. UV/Vis spectra of differently concentrated solutions of MIA in DMF in the range from 370 to 500 nm.

Using the maxima of the absorption spectra at 436 nm, a calibration curve was derived (Figure S5).

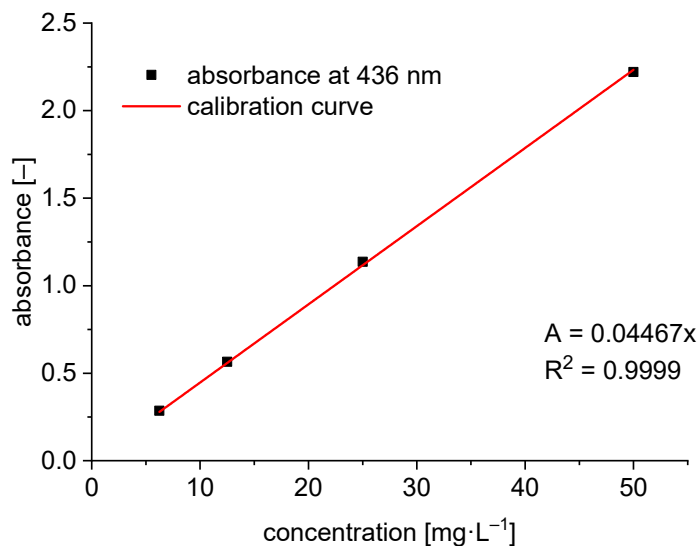


Figure S5. Calibration line for MIA in DMF from the absorbance at 436 nm.

The concentration of the **saturated MIA-DMF solution** was determined as follows: The saturated MIA-DMF solution was diluted by a factor of 1:10 to obtain an absorbance at 436 nm of 1.214 within the calibration range giving a concentration of 27.2 mg L^{-1} for the tenfold-diluted solution. Taking this dilution into account, a concentration of $272 \text{ mg}\cdot\text{L}^{-1}$ was calculated for the saturated MIA-DMF solution.

For the concentration determination of the saturated solution of MIA in chloroform, a stock solution of $4 \text{ mg}\cdot\text{L}^{-1}$ of MIA in chloroform was prepared and diluted. This was followed by the recording of the UV/Vis spectra of the solution series (Figure S6).

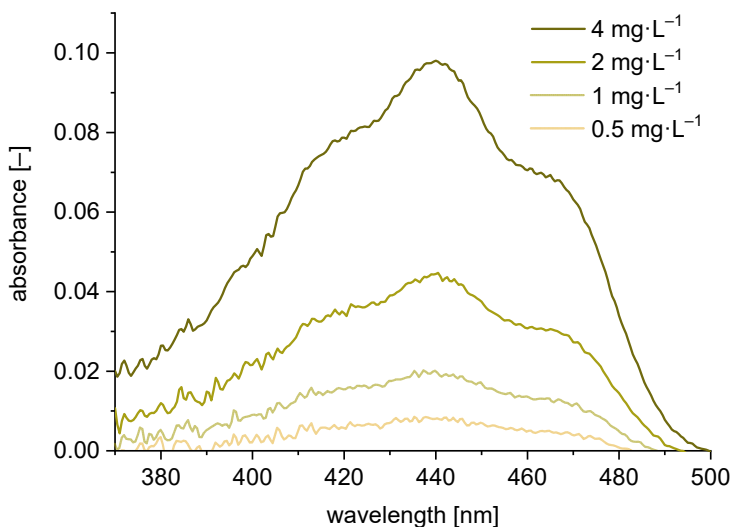


Figure S6. UV/Vis spectra of differently concentrated solutions of MIA in chloroform in the range from 370 to 500 nm.

From the absorbance maxima at 440 nm the calibration curve was obtained (Figure S7).

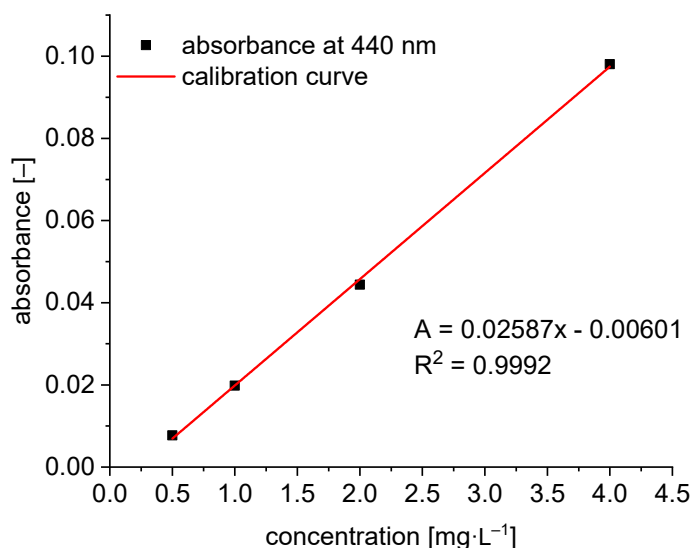


Figure S7. Calibration line for MIA in chloroform from the absorbance at 440 nm.

Subsequently, the concentration of the **saturated MIA-CHCl₃ solution** was determined as follows: The saturated MIA-CHCl₃ solution was diluted by a factor of 1:25 to obtain an absorbance at 440 nm of 0.078 within the calibration range giving a concentration of 2.78 mg L^{-1} for the 25-fold-diluted solution. Taking this dilution into account, a concentration of $69.5 \text{ mg}\cdot\text{L}^{-1}$ was calculated for the saturated MIA-CHCl₃ solution.

To determine the concentration of the saturated solution of 6F-MIA in DMF, a stock solution with a concentration of $100 \text{ mg}\cdot\text{L}^{-1}$ of 6F MIA in DMF was prepared and the UV/Vis-spectra were recorded for the dilution series (Figure S8).

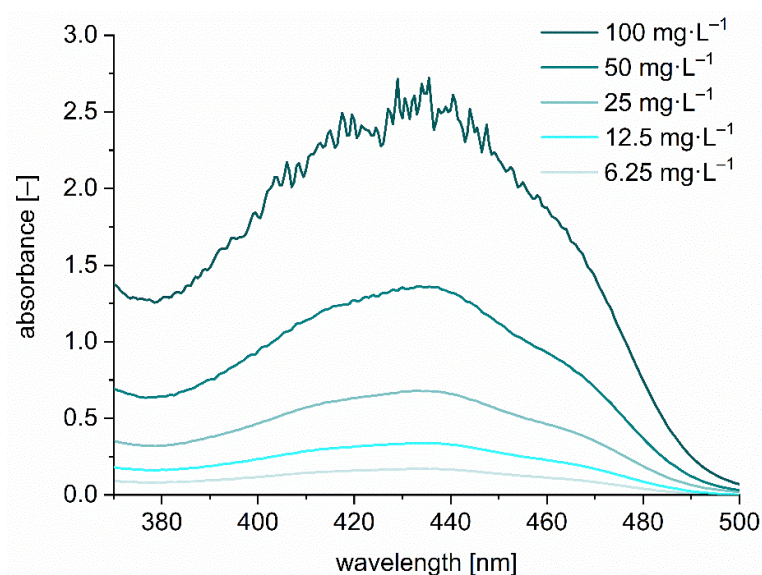


Figure S8. UV/Vis spectra of different concentrated solutions of 6F-MIA in DMF in the range from 370 to 500 nm.

From the absorbance maxima at 435.5 nm the calibration curve was obtained (Figure S9).

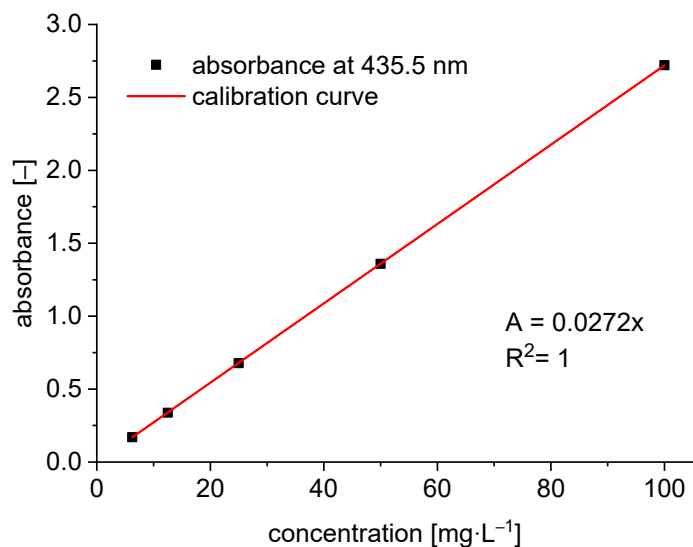


Figure S9. Calibration line for 6F-MIA in DMF from the absorbance at 435.5 nm.

The concentration of the **saturated 6F-MIA-DMF solution** was determined as follows: The saturated 6F-MIA-DMF solution was diluted by a factor of 1:50 to obtain an absorbance at 435.5 nm of 1.436 within the calibration range giving a concentration of 52.8 mg L^{-1} for the 50-fold-diluted solution. Taking this dilution into account, a concentration of $2640 \text{ mg}\cdot\text{L}^{-1}$ was calculated for the saturated 6F-MIA-DMF solution.

The concentration of the saturated solution of 6F-MIA in chloroform was determined by starting from a solution with a concentration of $2.4 \text{ mg}\cdot\text{L}^{-1}$ 6F MIA in chloroform, from which a dilution series was prepared and the UV/Vis spectra were recorded (Figure S10).

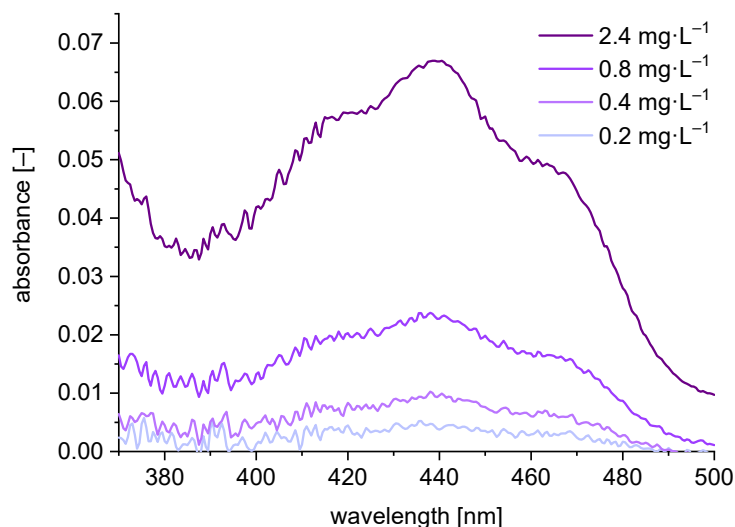


Figure S10. UV/Vis spectra of differently concentrated solutions of 6F-MIA in chloroform in the range from 370 to 500 nm.

The calibration line was derived from the maxima of the absorption at 440 nm (Figure S11).

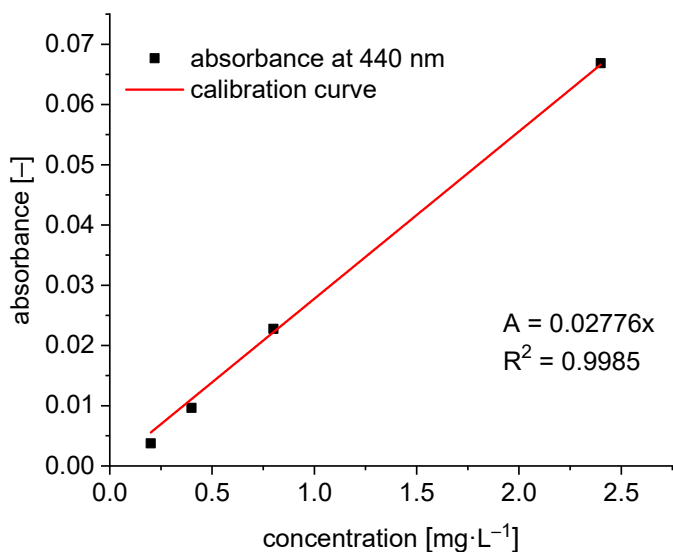


Figure S11 Calibration line for 6F-MIA in chloroform from the absorbance at 440 nm.

Subsequently, the **saturated 6F-MIA-CHCl₃ solution** was diluted by a factor of 1:12.5 to obtain an absorbance at 440 nm of 0.045 within the calibration range giving a concentration of 1.62 mg L^{-1} for the 12.5-fold-diluted solution. Taking this dilution into account, a concentration of $20.25 \text{ mg}\cdot\text{L}^{-1}$ was determined for the saturated 6F-MIA-CHCl₃ solution.

Section S3: Structure descriptions (Figure S12 - Figure S15)

Section S3.1: Structure of 10-methyl-isoalloxazine (MIA) (Figure S12)

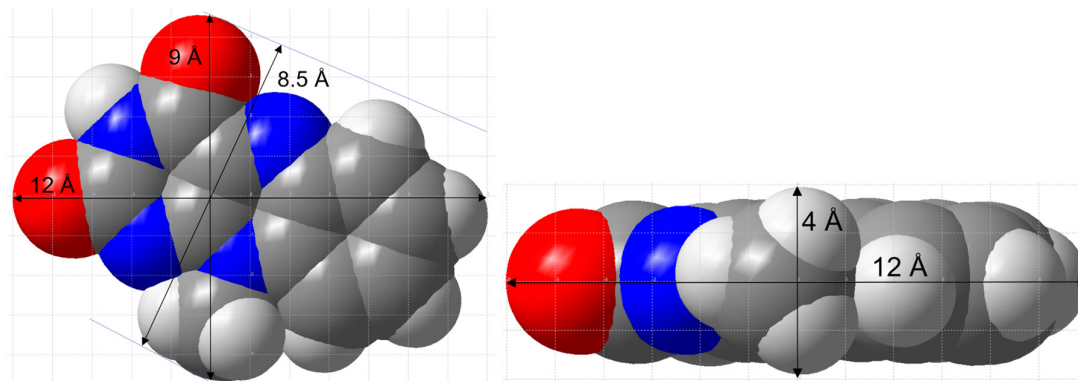


Figure S12. Top view and side view of a 10-methyl-isoalloxazine (MIA) molecule in space-filling presentation with the molecular dimensions indicated (the grid unit is 1 Å). (Structures were drawn with Diamond [9] from the deposited cif file under CCDC-no./Refcode MISALX [10]).

Section S3.2: Additional structure description of MIL-53(Al) (Figure S13 and Figure S14)

The MIL-53(Al) structure with the formula unit $[\text{Al}(\text{OH})(\text{bdc})]$ (bdc = benzene-1,4-dicarboxylate, terephthalate) is a very flexible, 'breathing'-type network, that is, it can assume different shapes and porosities depending on the presence or absence of host-guest interactions (Figure S13) [5,11]. The secondary or here infinite building unit (SBU, IBU) in MIL-53 is a linear chain of $\{\text{MO}_6\}$ octahedra ($\text{M} = \text{Al}, \text{In}, \text{Ga}, \text{Cr}, \text{Fe}$) The Al^{3+} centers are octahedrally coordinated by terephthalate linkers and bridging $\mu\text{-OH}$ groups, giving chains of trans- $\mu\text{-OH}$ -connected vertex-bridged $\{\text{AlO}_6\}$ octahedra. The hydroxido-bridging and carboxylate-bridging occurs along the direction of the metal chains (Figure S13a). These chains are connected perpendicular to the chain direction through the ditopic terephthalate linkers to a three-dimensional network with channels running parallel to the $\{\text{MO}_6\}$ chains (Figure S13b). Each benzene-1,4-dicarboxylate ligand bridges between four Al atoms. This forms a three dimensional network consisting of rhombic-shaped channels with a significant breathing effect [5,11,12,13,14,15,16,17,18].

MIL-53 can be found in three different crystalline forms which are usually differentiated as MIL-53_{as}, MIL-53_{ht} = MIL-53_{lp} and MIL-53_{lt} = MIL-53_{np} with *as* = *as synthesized*, *ht* = *high temperature* *lp* = *large pore*, *lt* = *low temperature* and *np* = *narrow pore* (Figure S13). After the hydrothermal synthesis as-synthesized MIL-53-as is obtained. By heating to a temperature between 275 °C and 420 °C (without vacuum), MIL-53 can be activated by the removal of guest molecules. This leads to the large-pore (lp) structure MIL-53-lp. Upon the uptake of water molecules from the air at ambient conditions, the narrow-pore (np) MIL-53-np is formed (Figure S13). The transformation between MIL-53-lp to MIL-53-np is reversible and is commonly referred to as the 'breathing effect'. For the large-pore (lp) form the diagonals for the rhombohedral channel cross section are 8.4 x 12 Å (Figure S14).

When incorporating the flavin derivatives, the MIL-53-lp form can be used as the van-der-Waals dimensions of MIA molecules are approximately $4 \times 8.5 \times 12$ Å (Figure S12) with the width of 8.5 Å being the critical dimension for the diffusion through the rhombohedral MIL-53 channels.

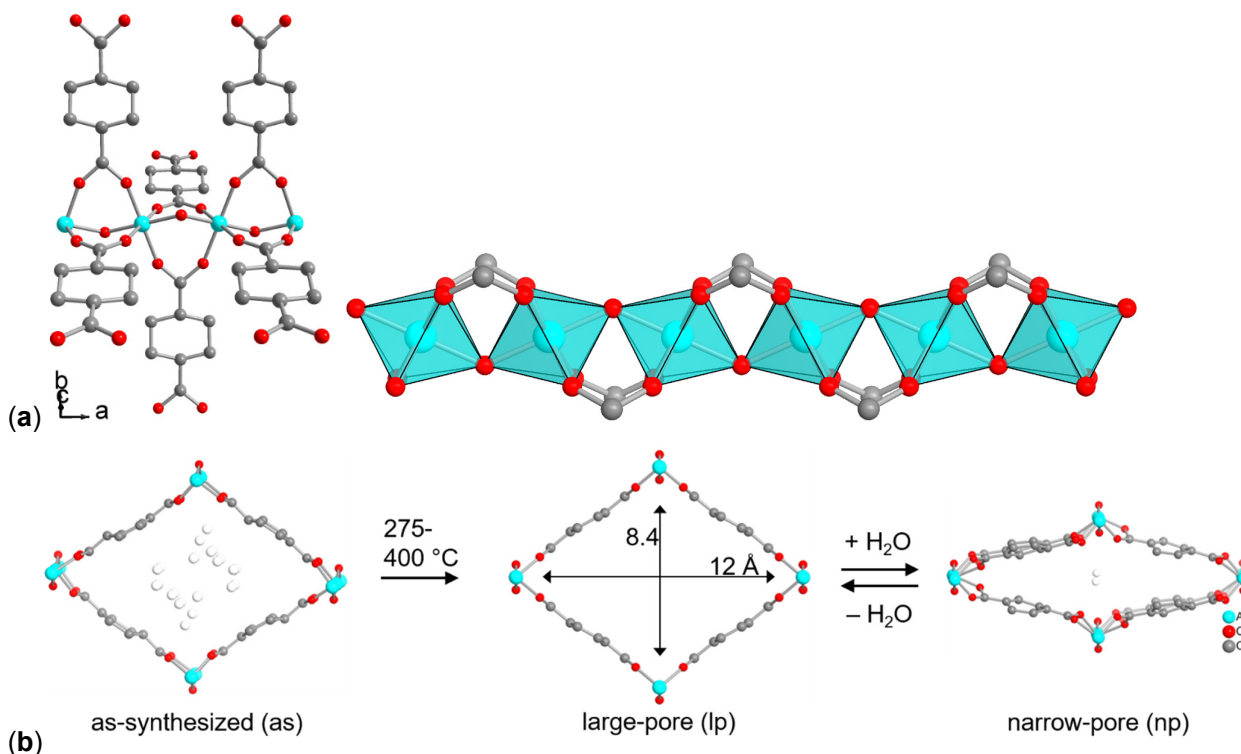


Figure S13. (a) Terephthalato- and hydroxido-bridged metal strand of $[\text{Al}(\text{OH})(\text{bdc})]$ as an infinite subunit. (b) Sections of the packing diagram with a flexible, 'breathing' network adapting to guest molecules. The pore structures of MIL-53(Al) are viewed along the channel direction. The channels can contain guest molecules in the as-synthesized or narrow-pore form or be empty in the similar large-pore structure. The as-synthesized, and the narrow-pore form also indicate the (disordered) guest molecules (hydrogen atoms are not shown). The high temperature for the transition from as-synthesized to large-pore form is due to the removal of residual terephthalic acid. The dimensions along the diagonals of the rhombic opening include the van-der-Waals radii of the atoms (see also Figure S14). Adsorption of water from air at room temperature transforms the structure into the narrow-pore / low-temperature form (right). Hydrogen atoms are not shown. (Structure images were drawn with Diamond [9] from the deposited cif files under CCDC-no./CSD-Refcodes 220475/SABVOH for MIL-53-as, 220476/SABVUN for -MIL-53-lp and 220477/SABWAU for MIL-53-np [6]).

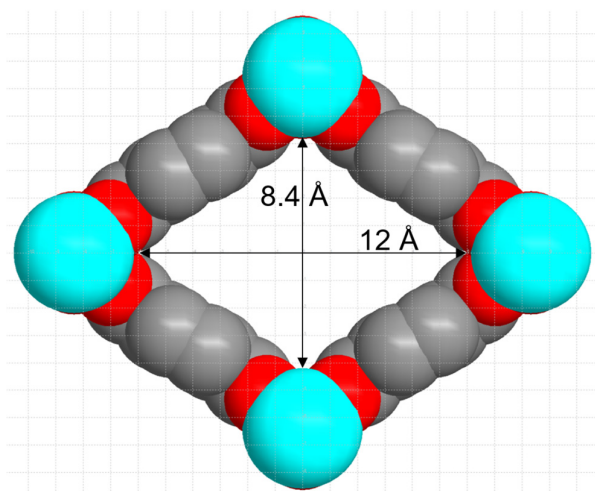
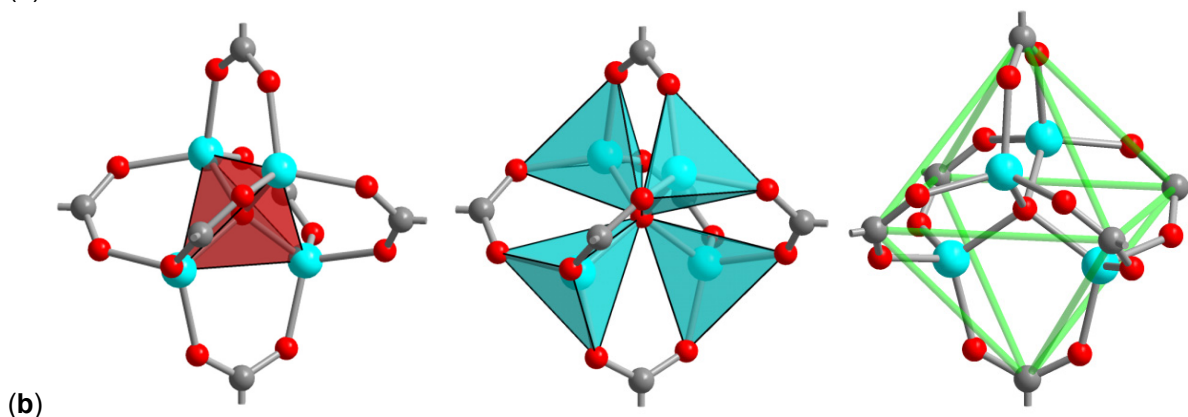
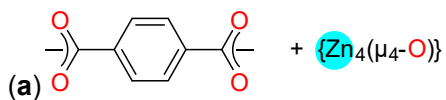


Figure S14. MIL-53(Al)-lp (large pore) in space-filling mode viewed along the channel direction. The dimensions along the diagonals of the rhombic opening include the van-der-Waals radii of the atoms (the grid unit is 1 Å).

Section S3.3: Additional structure description of MOF-5 (Figure S15)

MOF-5 (also named IRMOF-1), $[\text{Zn}_4\text{O}(\text{bdc})_3]$ with bdc = benzene-1,4-dicarboxylate, terephthalate) is one of the best known and prototypical MOFs [19]. The structure of MOF-5 is constructed of tetrahedral $\{\text{Zn}_4\text{O}\}$ secondary building units where six carboxylate groups of the terephthalate linkers span the six edges of the $\{\text{Zn}_4\text{O}\}$ tetrahedron in an octahedral fashion to give a 3D primitive cubic (**pcu**) structure with orthogonal channels along each axis of a cartesian coordinate system with channel cross-sections (window size) of 8×8 Å and a pore diameter of 15 Å (Figure S15) [8]. Activated MOF-5 has a high surface area ($3000 \text{ m}^2/\text{g}$) and high thermal stability (up to 400°C) [19].



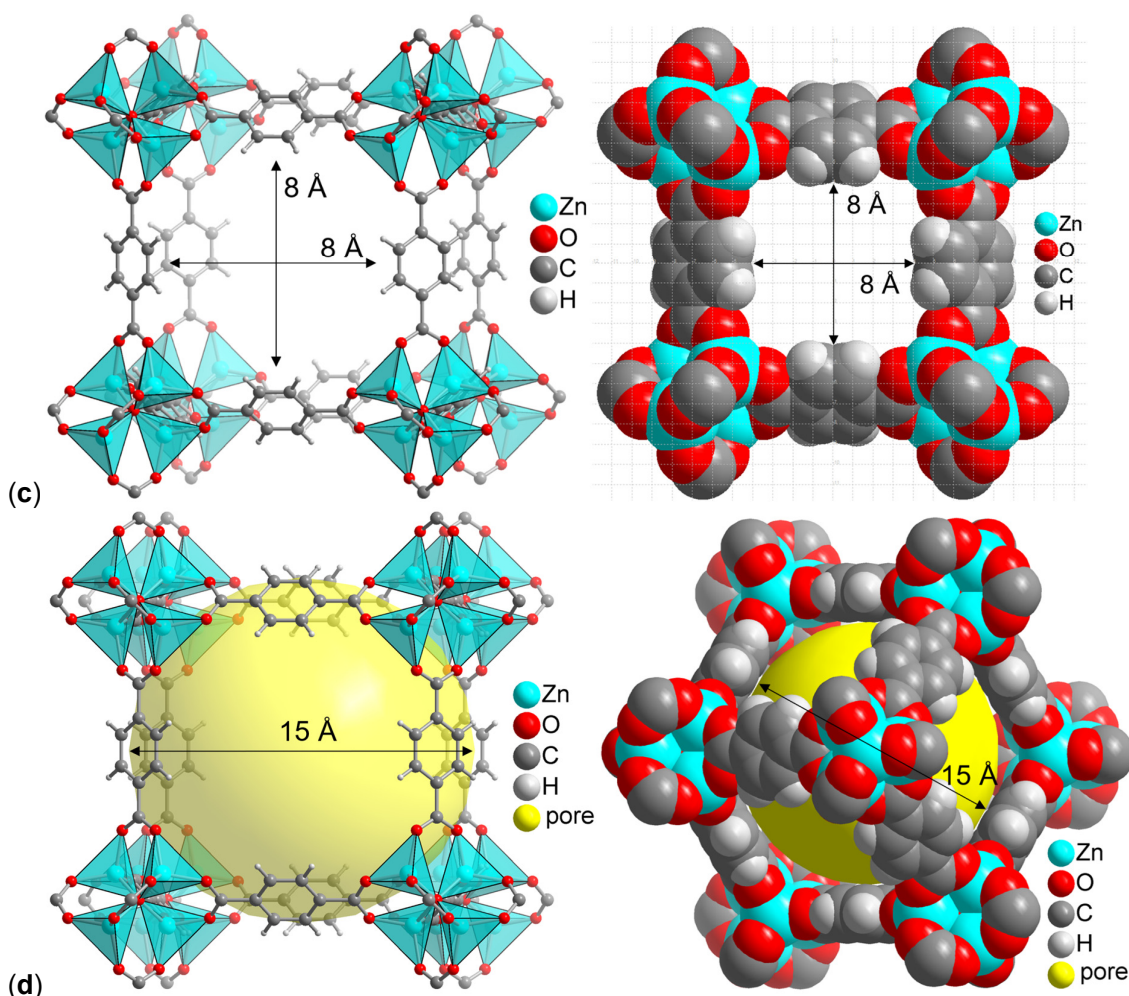


Figure S15. (a) Benzene-1,4-dicarboxylate, terephthalate, bdc and μ_4 -oxido bridged tetranuclear zinc cluster as building blocks for MOF-5 (IRMOF-1), 3D-[Zn₄O(bdc)₃].

(b) {Zn₄O} SBU with six carboxylate groups in MOF-5, emphasizing the tetrahedral environment of the central μ -oxido atom, the tetrahedral Zn coordination and the carboxylate carbon atom positions at the vertices of an octahedron.

(c) Section of the MOF-5 **pcu** framework in ball-and-stick and space-filling mode viewed along one of channel directions. The edge-to-edge dimensions of the square opening (cross-section) of 8 × 8 Å extend to the van-der-Waals radii of the atoms (the grid unit is 1 Å). (d) The pore diameter of 15 Å extends to the van-der-Waals surface of the framework atoms. At right, view along the cube diagonal. The objects in (b) to (d) are not drawn to scale. (Structure images were drawn with Diamond [9] from the deposited cif file under CCDC-no./Refcode 256966/SAHYOQ [19,20].)

Section S4: Nitrogen adsorption isotherms and powder X-ray diffractograms (Figure S16 - Figure S19)

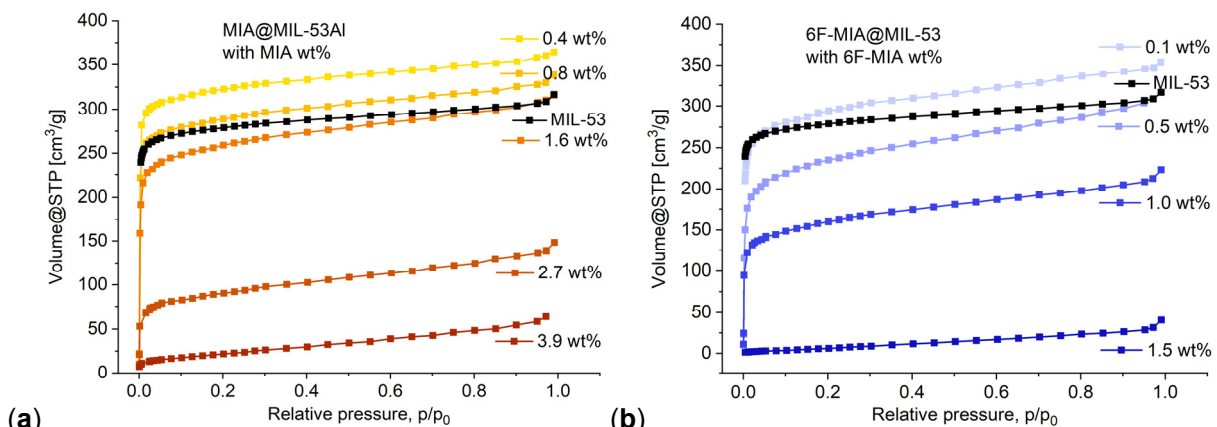
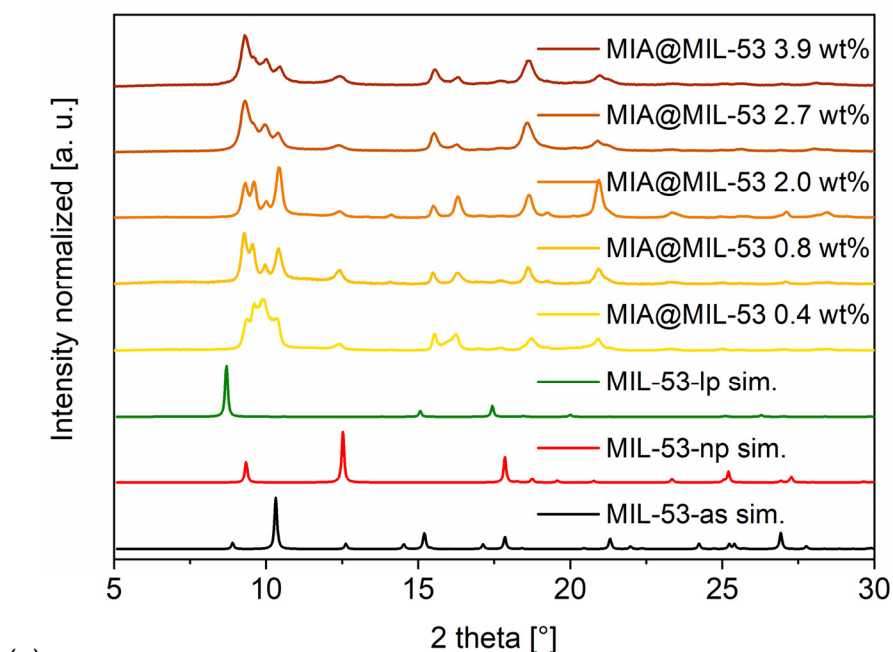
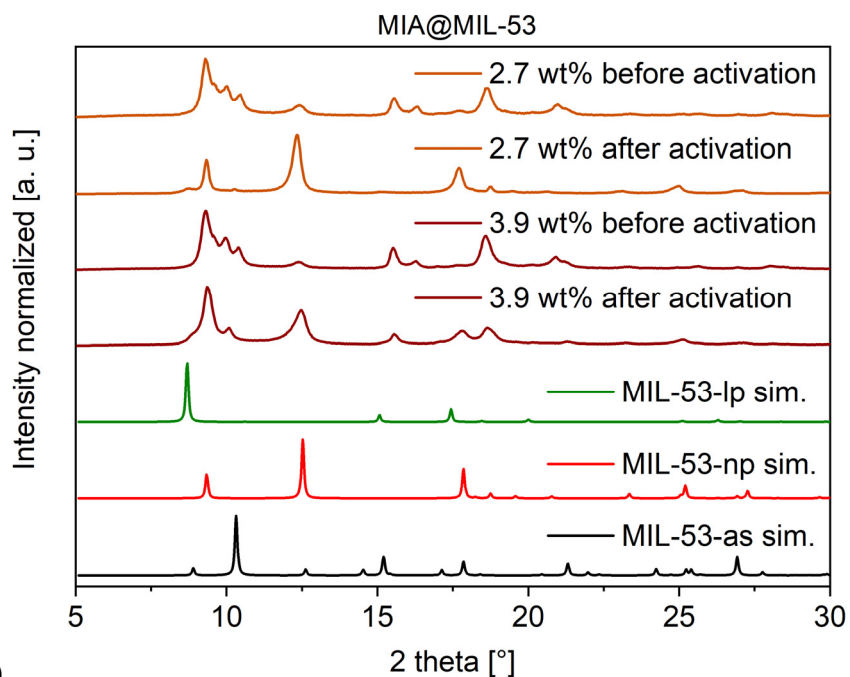


Figure S16. Nitrogen adsorption isotherms (77 K) of (a) MIA@MIL-53 and (b) 6F-MIA@MIL-53 with different flavin amounts.



(a)



(b)

Figure S17. Comparison of the PXRD patterns of MIA@MIL-53 with varying flavin amounts (a) *before* activation and (b) *before and after* activation for 2.7 wt% and 3.9 wt% with the simulated PXRDs for MIL-53-as, -np and -lp based on the deposited cif files under CCDC-no./Refcode 220475/SABVOH for MIL-53-as, 220476/SABVUN for MIL-53-lp and 220477/ SABWAU for MIL-53-np [6].

The slight shift in the corresponding peak positions between the experimental and simulated diffractograms in Figure S17 is due to different cell constants from the formation of the experimental MIA@MIL-53 phases which only approximate the published MIL-53-as, -lp and -np phases. The simulated patterns from these published MIL-53-as, -lp and -np phases are based on Rietveld

refinements of PXRDs from a specific sample treatment protocol [6], which understandably differs from our treatment of the composite samples. An X-ray thermodiffractogram of MIL-53-as in ref. [6] illustrates the peak shift in the diffractograms with temperature. Hence, the experimental diffractograms of flavin@MIL-53 reflect 'breathing' phases which can only approximate the literature phases obtained at different conditions. Yet, the peak pattern allows for an unequivocal phase assignment.

The transition from as-synthesized to large-pore form required high temperature (cf. Figure S13), due to the removal of residual terephthalic acid. When the terephthalic acid is already removed through the washing steps concomitant with the flavin insertion, then there is only volatile solvent remaining in the as-synthesized form. Subsequently, the transition from as-synthesized to large-pore and further to narrow-pore form can occur upon sample storage and preparation under ambient air conditions. The reflections indicate a phase mixture that additionally varies with the different amounts of flavin incorporated.

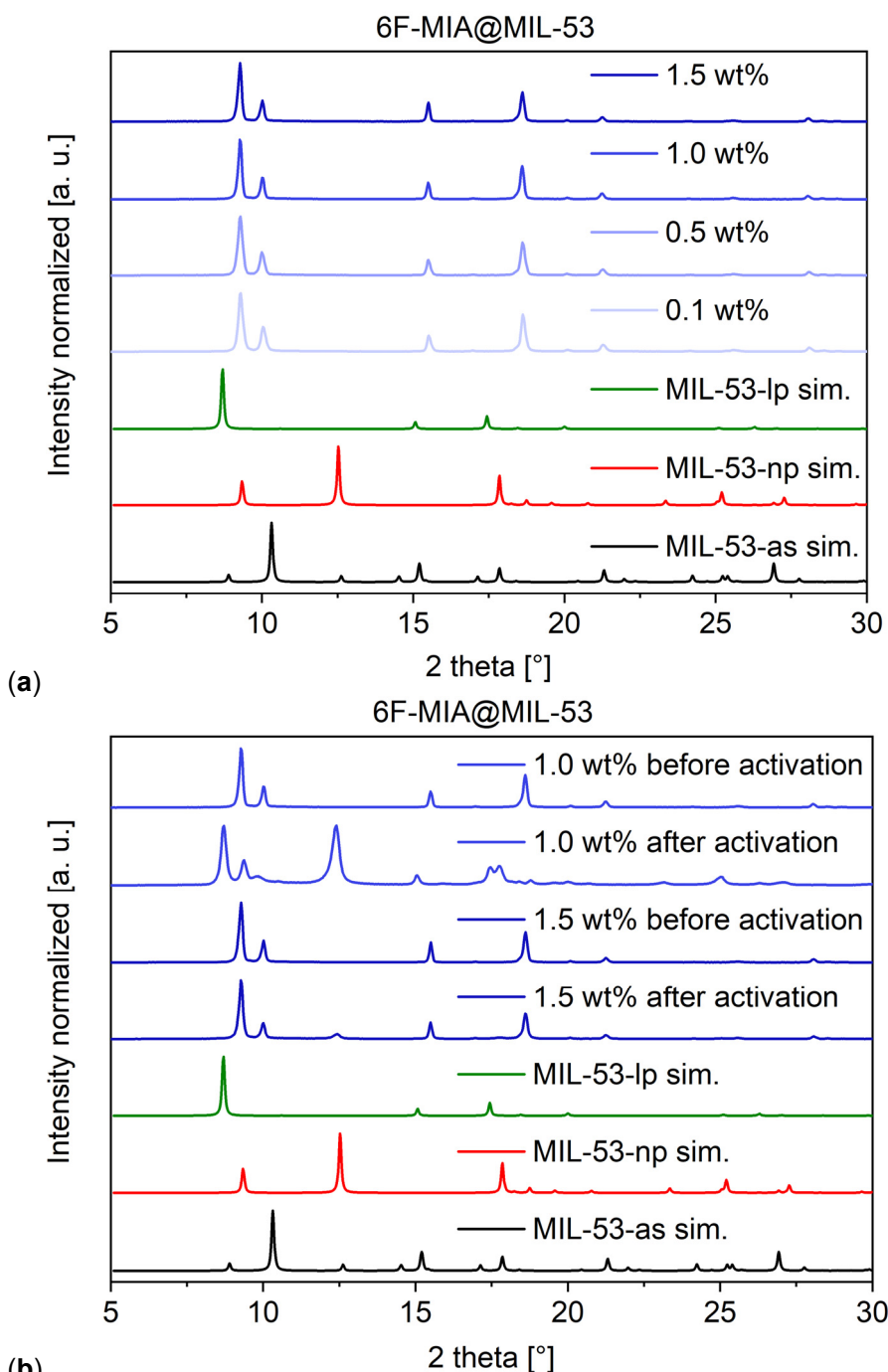


Figure S18. Comparison of the PXRD patterns of 6F-MIA@MIL-53 with varying flavin amounts (a) *before* activation and (b) *before and after* activation for 1.0 wt% and 1.5 wt%. The simulated PXRDs are based on the deposited cif files under CCDC-no./Refcode 220475/SABVOH for MIL-53-as, 220476/SABVUN for MIL-53-lp and 220477/ SABWAU for MIL-53-np [6].

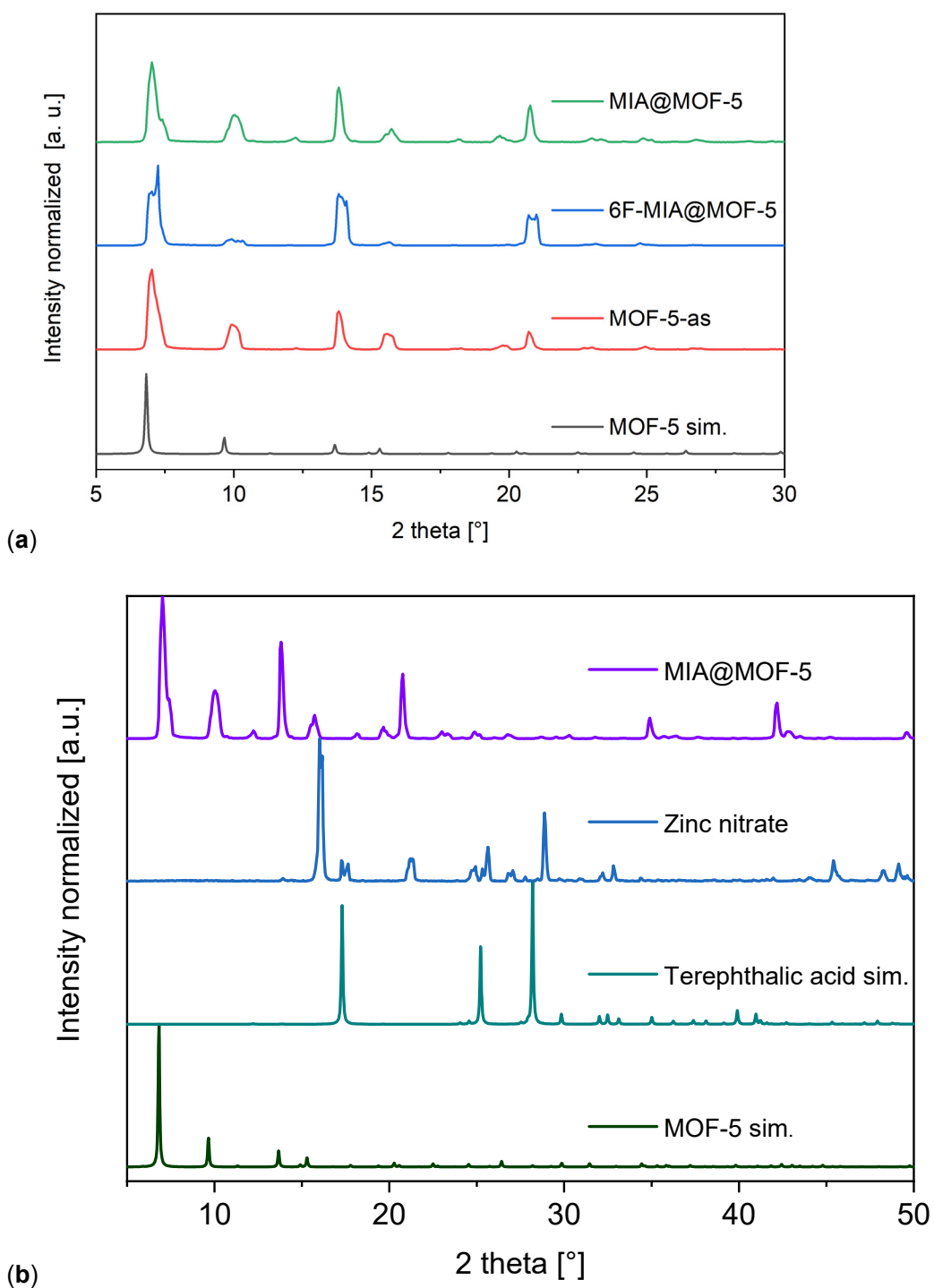


Figure S19. Comparison of the PXRD patterns of (a) MIA@MOF-5 and 6F-MIA@MOF-5 with simulated MOF-5; (b) MIA@MOF-5 with the measured patterns of zinc nitrate hexahydrate and simulated terephthalic acid and MOF-5. (Note the different 2theta range in (a) and (b). The simulated PXRDs are based on the deposited cif files under CCDC-no./Refcode 1269122/TEPHTH for terephthalic acid [21] and CCDC-no./Refcode 256966/SAHYOQ for MOF-5 [20,22].

Section S5: Photophysical characterization of the dyes and dye@MOF (Figure S20 - Figure S35)

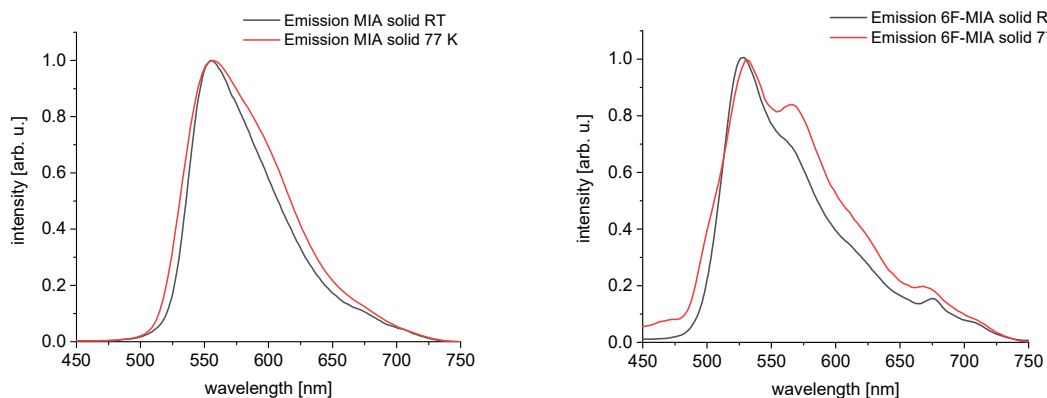


Figure S20. Photoluminescence spectra of MIA (left) and 6F-MIA (right) ($\lambda_{\text{exc}} = 440$ nm) at room temperature, RT, (black) and at 77 K (red).

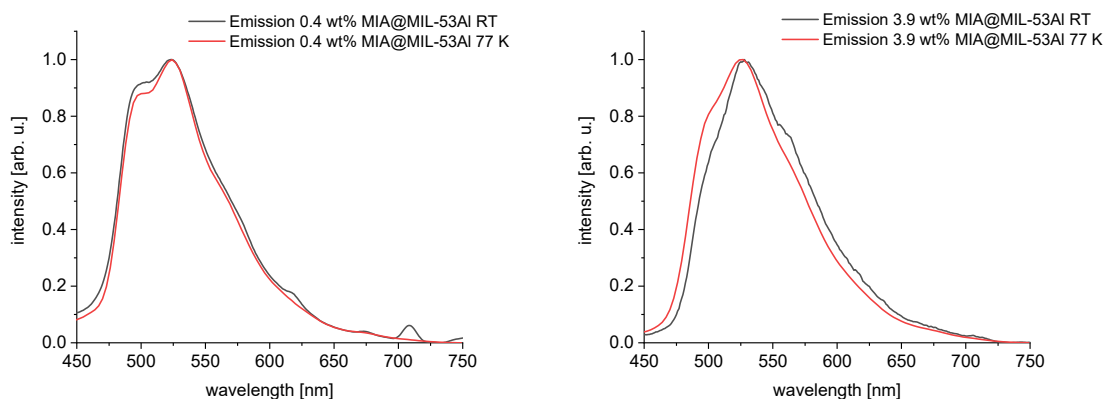


Figure S21. Photoluminescence spectra of MIA@MIL53Al with 0.4 wt % loading (left) and 3.9 wt % loading (right) ($\lambda_{\text{exc}} = 440$ nm) at room temperature, RT, (black) and at 77 K (red).

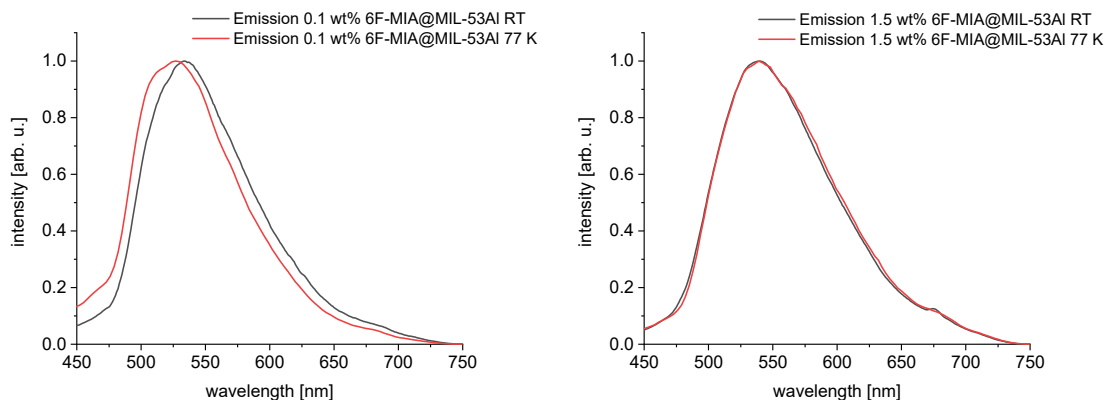


Figure S22. Photoluminescence spectra of 6F-MIA@MIL53Al with 0.1 wt % loading (left) and 1.5 wt % loading (right) ($\lambda_{\text{exc}} = 440$ nm) at room temperature, RT, (black) and at 77 K (red).

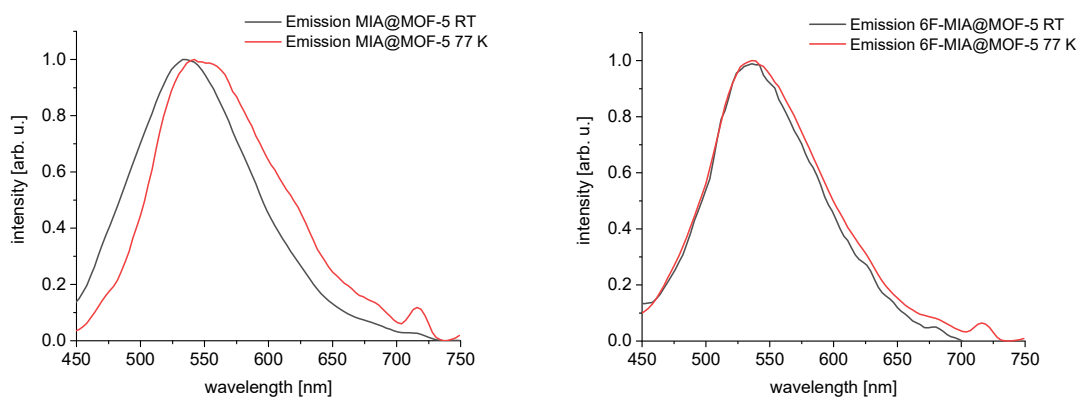


Figure S23. Photoluminescence spectra of MIA@MOF-5 (left) and 6F-MIA@MOF-5 (right) ($\lambda_{\text{exc}} = 440$ nm) at room temperature, RT, (black) and at 77 K (red).

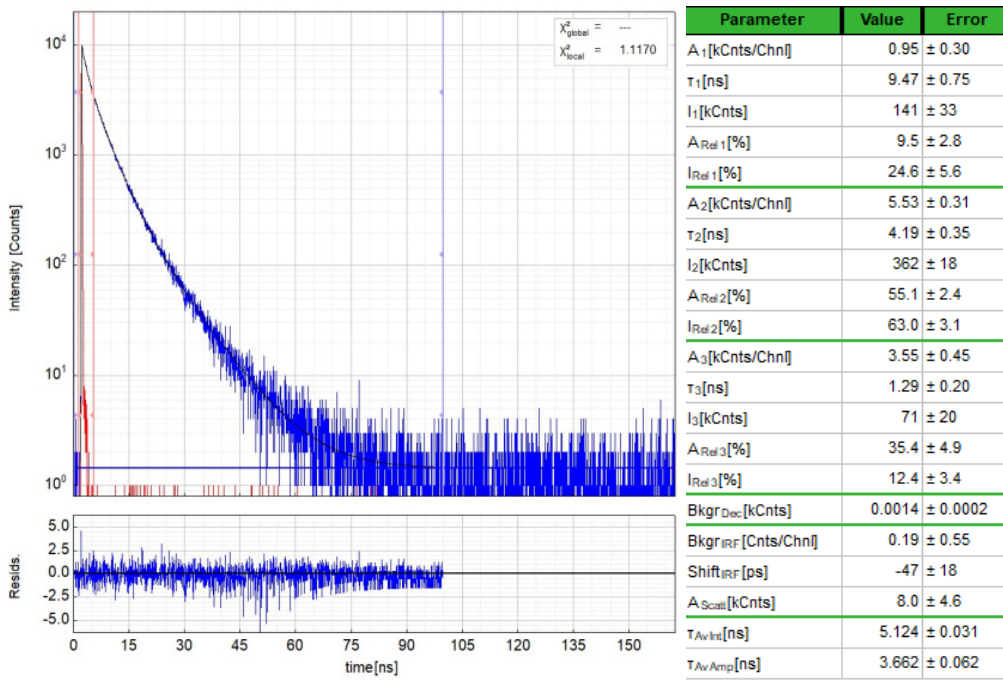


Figure S24. Left: Raw time-resolved photoluminescence decay (blue) of MIA@MOF-5 in the solid state at 298 K and the instrument response function (red), including the residuals ($\lambda_{ex} = 405$ nm, $\lambda_{em} = 530$ nm). Right: Fitting parameters including pre-exponential factors and confidence limits. Here, τ_{av_int} is the intensity-weighted average lifetime (τ_F) and τ_{av_amp} is amplitude-weighted average lifetime (τ_x).

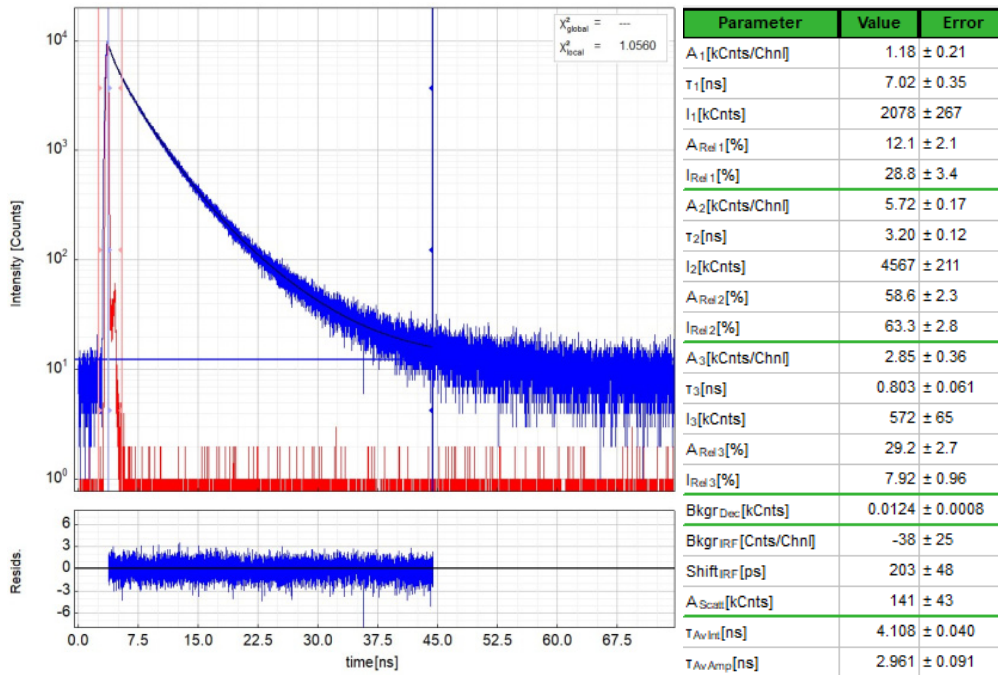


Figure S25. Left: Raw time-resolved photoluminescence decay (blue) of 6F-MIA@MOF-5 in the solid state at 298 K and the instrument response function (red), including the residuals ($\lambda_{ex} = 405$ nm, $\lambda_{em} = 510$ nm). Right: Fitting parameters including pre-exponential factors and confidence limits. Here, τ_{av_int} is the intensity-weighted average lifetime (τ_F) and τ_{av_amp} is amplitude-weighted average lifetime (τ_x).

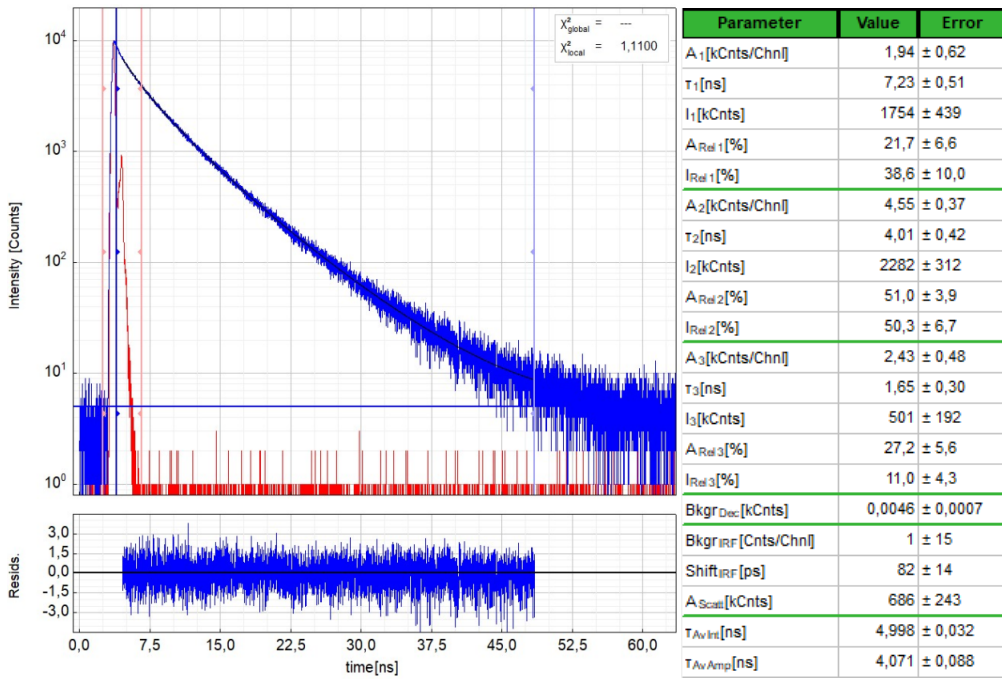


Figure S26. Left: Raw time-resolved photoluminescence decay (blue) of 0.4 wt% MIA@MIL-53 in the solid state at 298 K and the instrument response function (red), including the residuals ($\lambda_{ex} = 405$ nm, $\lambda_{em} = 520$ nm). Right: Fitting parameters including pre-exponential factors and confidence limits. Here, τ_{av_int} is the intensity-weighted average lifetime (τ_f) and τ_{av_amp} is amplitude-weighted average lifetime (τ_x).

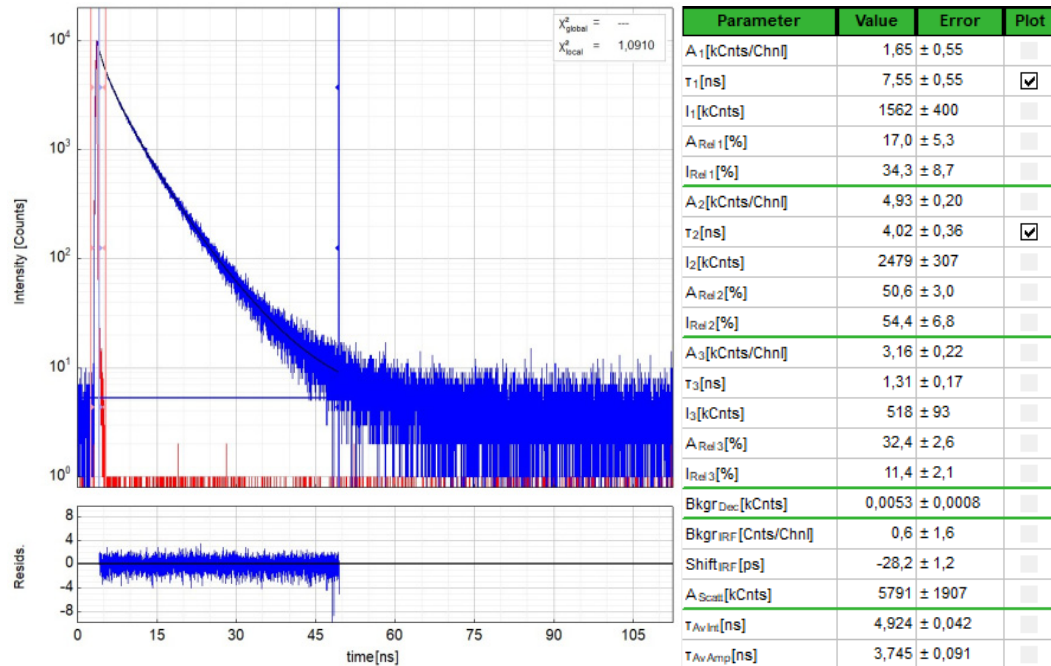


Figure S27. Left: Raw time-resolved photoluminescence decay (blue) of 3.9 wt% MIA@MIL-53 in the solid state at 298 K and the instrument response function (red), including the residuals ($\lambda_{ex} = 405$ nm, $\lambda_{em} = 525$ nm). Right: Fitting parameters including pre-exponential factors and confidence limits. Here, τ_{av_int} is the intensity-weighted average lifetime (τ_f) and τ_{av_amp} is amplitude-weighted average lifetime (τ_x).

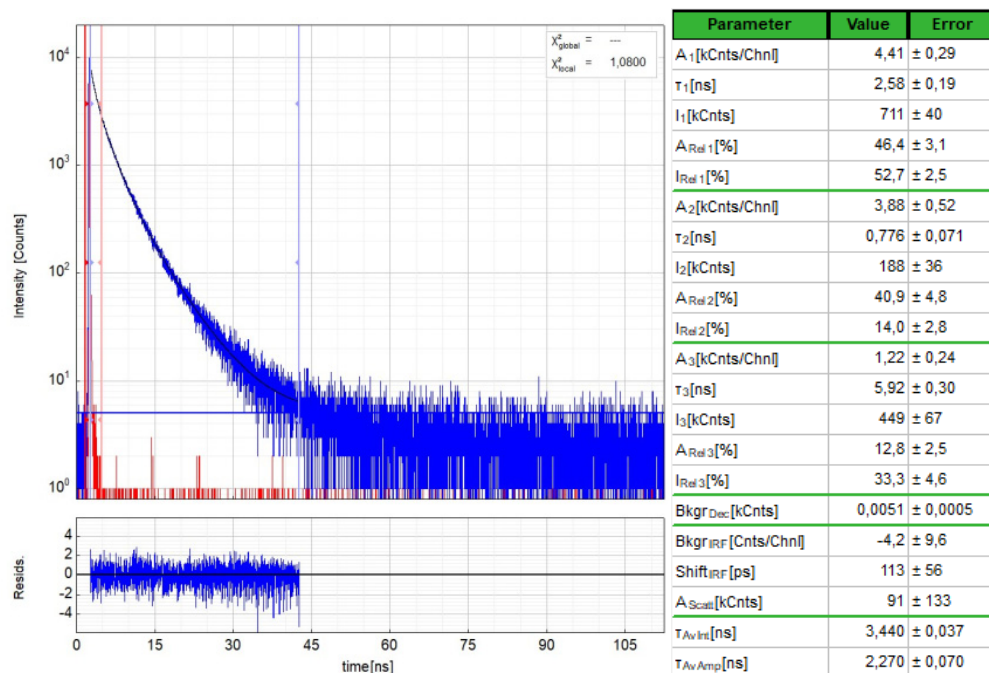


Figure S28. Left: Raw time-resolved photoluminescence decay (blue) of 0.1 wt% 6F-MIA@MIL-53 in the solid state at 298 K and the instrument response function (red), including the residuals ($\lambda_{ex} = 405$ nm, $\lambda_{em} = 535$ nm). Right: Fitting parameters including pre-exponential factors and confidence limits. Here, τ_{av_int} is the intensity-weighted average lifetime (τ_F) and τ_{av_amp} is amplitude-weighted average lifetime (τ_x).

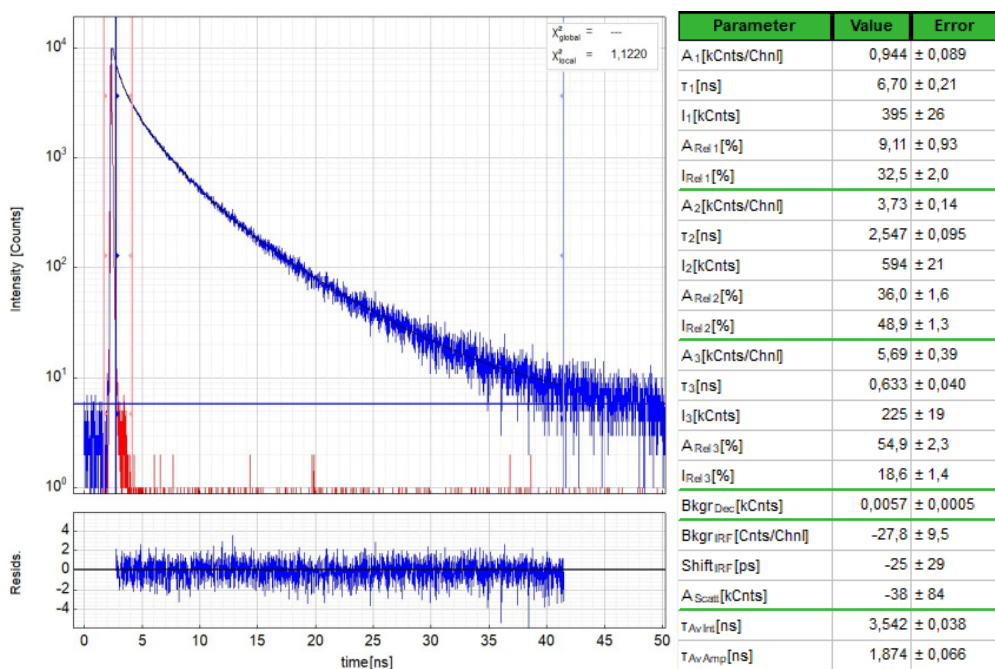


Figure S29. Left: Raw time-resolved photoluminescence decay (blue) of 1.5 wt% 6F-MIA@MIL-53 in the solid state at 298 K and the instrument response function (red), including the residuals ($\lambda_{ex} = 405$ nm, $\lambda_{em} = 535$ nm). Right: Fitting parameters including pre-exponential factors and confidence limits. Here, τ_{av_int} is the intensity-weighted average lifetime (τ_F) and τ_{av_amp} is amplitude-weighted average lifetime (τ_x).

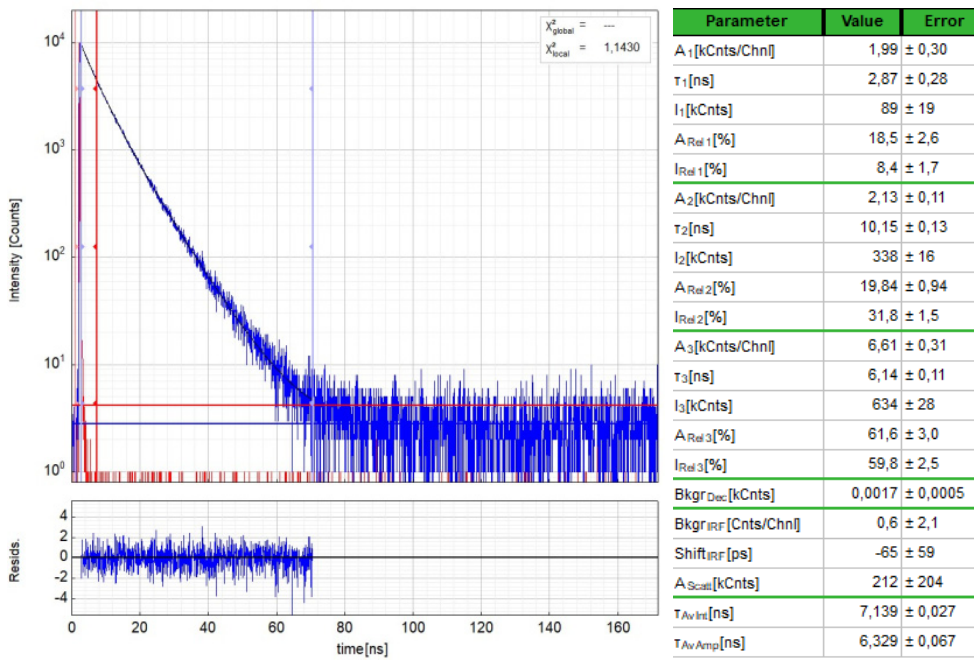


Figure S30. Left: Raw time-resolved photoluminescence decay (blue) of MIA in a DCM/MeOH 1:1 fluid solution at 298 K and the instrument response function (red), including the residuals ($\lambda_{ex} = 405$ nm, $\lambda_{em} = 525$ nm). Right: Fitting parameters including pre-exponential factors and confidence limits. Here, τ_{av_int} is the intensity-weighted average lifetime (τ_F) and τ_{av_amp} is amplitude-weighted average lifetime (τ_x).

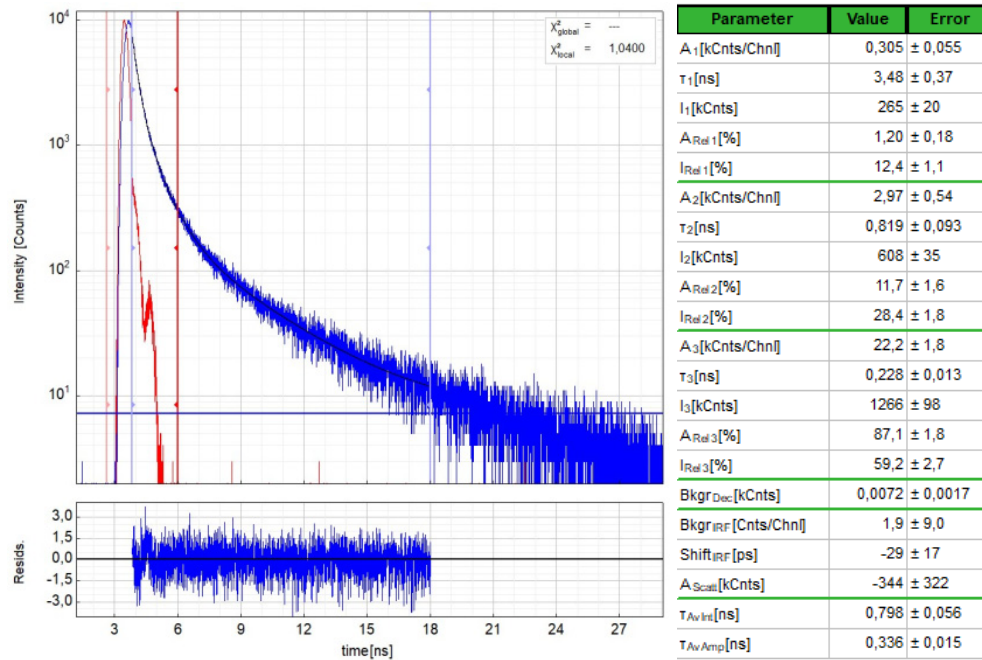


Figure S31. Left: Raw time-resolved photoluminescence decay (blue) of MIA in the solid state at 298 K and the instrument response function (red), including the residuals ($\lambda_{ex} = 405$ nm, $\lambda_{em} = 550$ nm). Right: Fitting parameters including pre-exponential factors and confidence limits. Here, τ_{av_int} is the intensity-weighted average lifetime (τ_F) and τ_{av_amp} is amplitude-weighted average lifetime (τ_x).

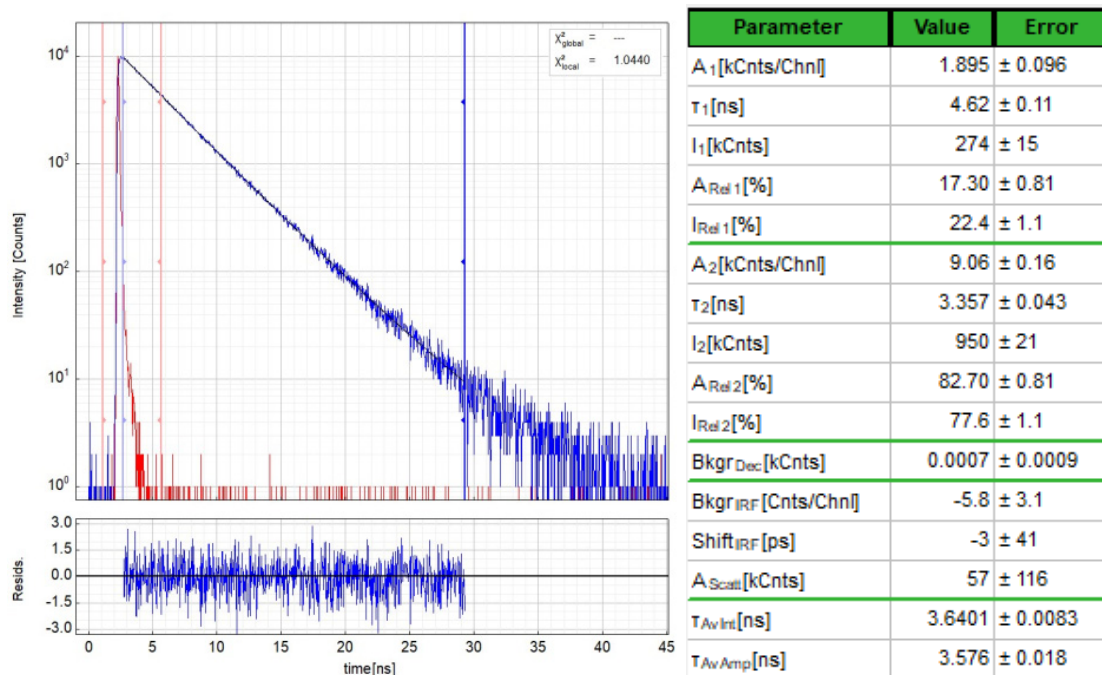


Figure S32. Left: Raw time-resolved photoluminescence decay (blue) of 6F-MIA in a DCM/MeOH 1:1 fluid solution at 298 K and the instrument response function (red), including the residuals ($\lambda_{ex} = 405$ nm, $\lambda_{em} = 525$ nm). Right: Fitting parameters including pre-exponential factors and confidence limits. Here, τ_{av_int} is the intensity-weighted average lifetime (τ_F) and τ_{av_amp} is amplitude-weighted average lifetime (τ_x).

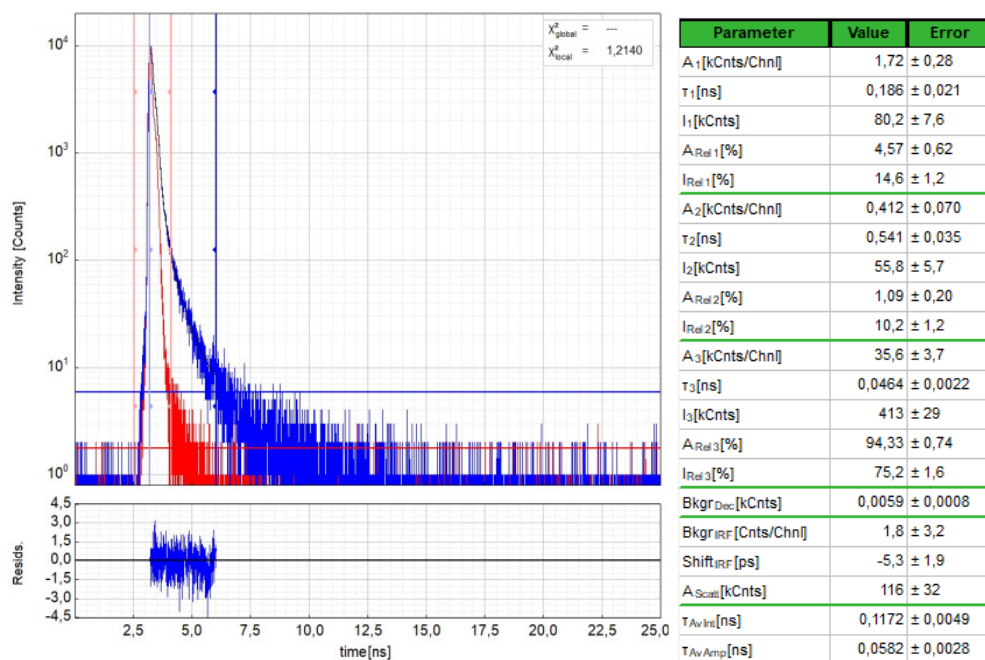


Figure S33. Left: Raw time-resolved photoluminescence decay (blue) of 6F-MIA in the solid state at 298 K and the instrument response function (red), including the residuals ($\lambda_{ex} = 405$ nm, $\lambda_{em} = 550$ nm). Right: Fitting parameters including pre-exponential factors and confidence limits. Here, τ_{av_int} is the intensity-weighted average lifetime (τ_F) and τ_{av_amp} is amplitude-weighted average lifetime (τ_x).

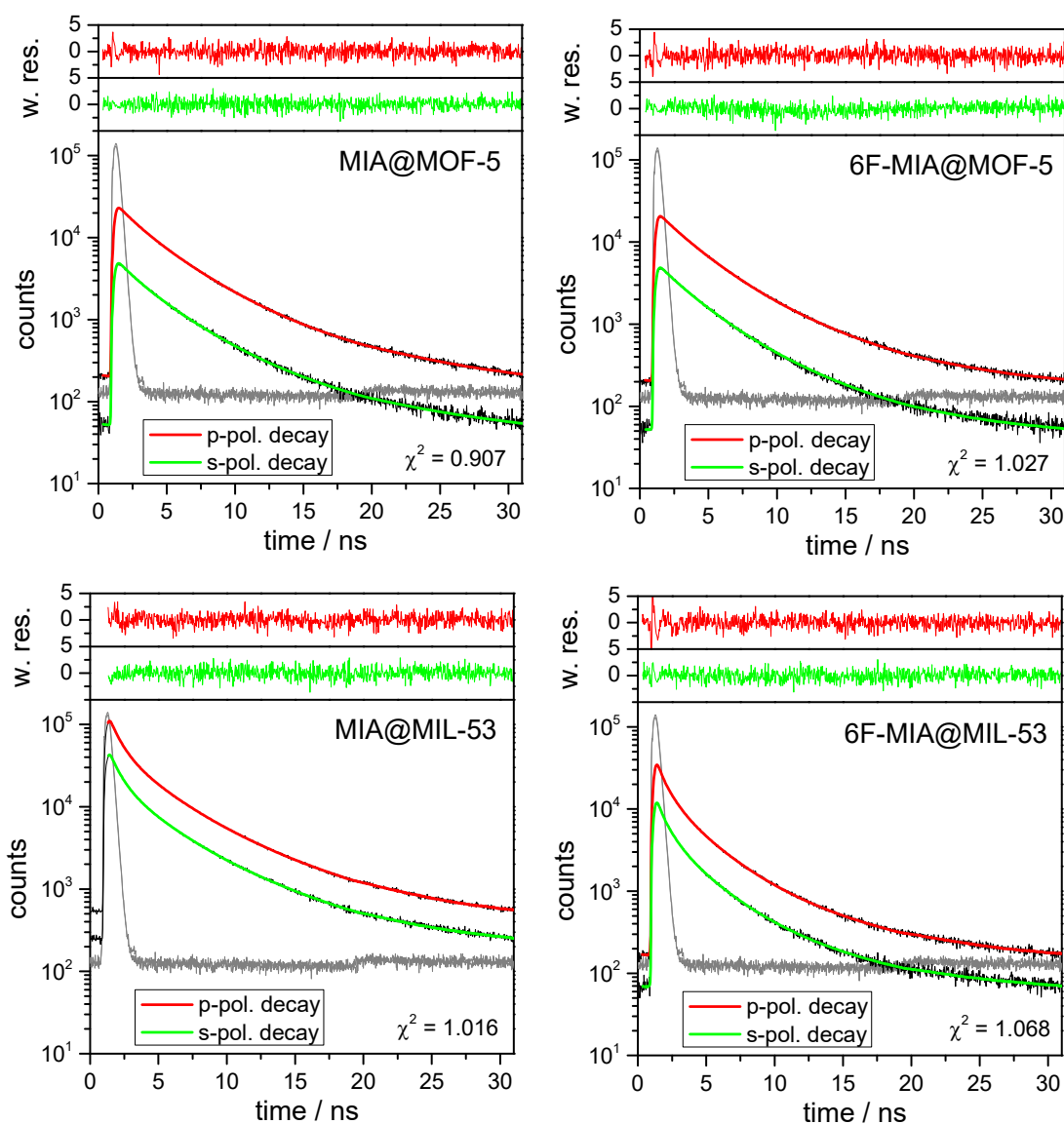


Figure S34. Time-correlated polarization-resolved single-photon data of the flavin@MOF composites imaged by confocal multi-parameter fluorescence image spectroscopy (MFIS) with pulsed excitation at 440 nm and $\lambda_{\text{em}} = 502\text{-}538$ nm (Figure 6, main document). Global fits by iterative reconvolution of the instrumental function (grey curves) to p- and s-polarized decays required 4 fluorescence lifetime components (lifetimes and species fractions are compiled in Table 3 of the main document) and one (two for MIA@MIL-53) rotational correlation time. The corresponding equations are described in ref. [23]. The offsets in the decays are caused by afterpulsing of the detectors and taken into account by the fitting routine. The G-factor, compensating differences in the detection efficiencies in the two polarization channels, of $G = 0.97$ was determined by fitting polarized fluorescence decays of an aqueous solution of Rhodamine 110. For flavin@MOF-5 five slices in the center of the z-stack were selected to generate the decay histograms, for flavin@MIL53 all photons from the images were used.

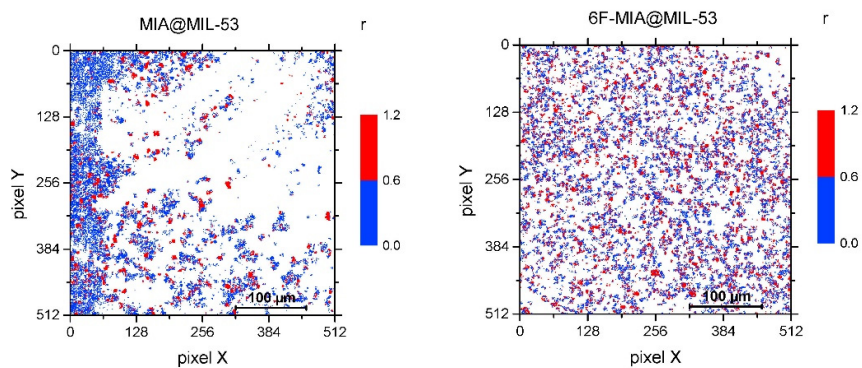


Figure S35. MFIS images of flavin@MIL-53 displaying experimental steady state fluorescence anisotropy r of Figure 6 with a distinct color scheme to highlight that one microcrystal has a unique anisotropy, i.e. r is a unique feature for each crystal that is related to its orientation. For further information, see discussion of Figure 6 in the main text section 2.3.

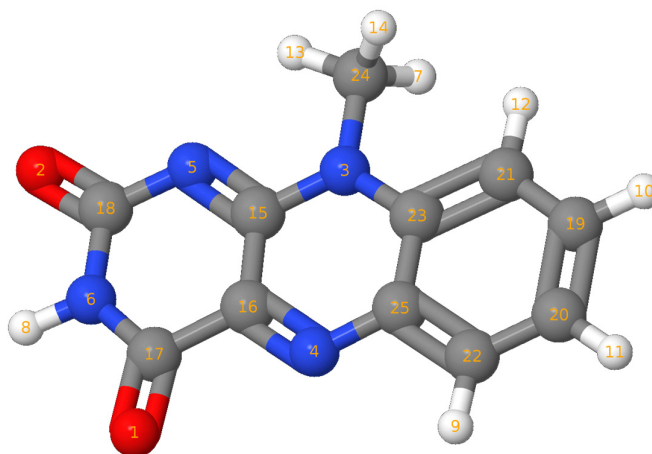
Section S6: Theoretical calculations (Figure S36 - Figure S42)

Force Field parameters are in the AMBER20 format and units.

Section S6.1: Force Field MIA

Atom number FF atom type

O	1	Oc
O	2	Oc
N	3	Na
N	4	Nc
N	5	Nc
N	6	N
H	7	H1
H	8	Hn
H	9	Hm
H	10	Hm
H	11	Hm
H	12	Hm
H	13	H1
H	14	H1
C	15	Cd
C	16	Cd
C	17	Co
C	18	Co
C	19	Cm
C	20	Cm
C	21	Cm
C	22	Cm
C	23	Cm
C	24	C3
C	25	Cm



MASS

om	16.0000.434
n	14.0100.530
nc	14.0100.530
na	14.0100.530
hn	1.0080.161
h1	1.0080.135
hm	1.0080.135
c2	12.0100.616
cd	12.0100.360
c3	12.0100.878
cm	12.0100.360

BOND STRETCHING

om-c2	637.70	1.218
n -hn	403.20	1.013

n -c2	427.60	1.379
nc-c2	416.90	1.387
nc-cd	525.40	1.317
nc-cm	467.70	1.352
na-cd	425.80	1.380
na-c3	327.70	1.463
na-cm	420.50	1.384
h1-c3	330.60	1.097
hm-cm	345.80	1.086
c2-cd	371.00	1.468
cd-cd	419.80	1.428
cm-cm	461.10	1.398

ANGLE BENDING

om-c2-n	74.220	123.050
om-c2-nc	73.910	123.180
om-c2-cd	69.140	123.930
n -c2-nc	71.580	117.110
n -c2-cd	69.070	112.700
nc-cd-na	74.900	112.220
nc-cd-cd	71.570	112.560
nc-cd-c2	67.620	121.880
nc-cm-cm	69.460	119.720
na-cd-cd	68.580	117.770
na-c3-h1	49.830	108.780
na-cm-cm	69.080	118.340
hn-n -c2	48.330	117.550
h1-c3-h1	39.240	108.460
hm-cm-cm	48.180	119.880
c2-n -c2	63.740	127.080
c2-nc-cd	66.680	120.490
c2-cd-cd	63.620	122.690
cd-nc-cm	72.480	104.880
cd-na-c3	61.880	126.460
cd-na-cm	67.400	113.150
c3-na-cm	62.320	124.360
cm-cm-cm	66.620	120.020

TORSION

om-c2-n -hn	1	2.500	180.000	-2.000
om-c2-n -hn	1	2.000	0.000	1.000
om-c2-n -c2	1	2.500	180.000	2.000
om-c2-nc-cd	1	4.000	180.000	2.000
om-c2-cd-nc	1	2.875	180.000	2.000
om-c2-cd-cd	1	2.875	180.000	2.000
n -c2-nc-cd	1	4.000	180.000	2.000
n -c2-cd-nc	1	2.875	180.000	2.000

n -c2-cd-cd	1	2.875	180.000	2.000
nc-c2-n -hn	1	2.500	180.000	2.000
nc-c2-n -c2	1	2.500	180.000	2.000
nc-cd-na-c3	1	1.700	180.000	2.000
nc-cd-na-cm	1	1.700	180.000	2.000
nc-cd-cd-nc	1	4.000	180.000	2.000
nc-cd-cd-c2	1	4.000	180.000	2.000
nc-cd-cd-na	1	4.000	180.000	2.000
nc-cm-cm-na	1	3.625	180.000	2.000
nc-cm-cm-cm	1	3.625	180.000	2.000
nc-cm-cm-hm	1	3.625	180.000	2.000
na-cd-nc-c2	1	4.750	180.000	2.000
na-cd-cd-c2	1	4.000	180.000	2.000
na-cm-cm-cm	1	3.625	180.000	2.000
na-cm-cm-hm	1	3.625	180.000	2.000
hn-n -c2-cd	1	2.500	180.000	2.000
h1-c3-na-cd	1	0.000	0.000	2.000
h1-c3-na-cm	1	0.000	0.000	2.000
hm-cm-cm-cm	1	3.625	180.000	2.000
hm-cm-cm-hm	1	3.625	180.000	2.000
c2-n -c2-cd	1	2.500	180.000	2.000
c2-nc-cd-cd	1	4.750	180.000	2.000
c2-cd-nc-cm	1	4.750	180.000	2.000
cd-nc-cm-cm	1	4.800	180.000	2.000
cd-cd-na-c3	1	1.700	180.000	2.000
cd-cd-na-cm	1	1.700	180.000	2.000
cd-na-cm-cm	1	0.300	180.000	2.000
cd-cd-nc-cm	1	4.750	180.000	2.000
c3-na-cm-cm	1	0.300	180.000	2.000
cm-cm-cm-cm	1	3.625	180.000	2.000

OUT-OF-PLANE

c2-c2-n -hn	1.1	180.0	2.0
c3-cm-na-cd	1.1	180.0	2.0
n -nc-c2-om	10.5	180.0	2.0
cd-n -c2-om	10.5	180.0	2.0
c2-cd-cd-nc	1.1	180.0	2.0
cd-na-cd-nc	1.1	180.0	2.0
cm-cm-cm-nc	1.1	180.0	2.0
cm-cm-cm-na	1.1	180.0	2.0
cm-cm-cm-hm	1.1	180.0	2.0

NON-BONDED

om	1.6612	0.2100
n	1.8240	0.1700
nc	1.8240	0.1700
na	1.8240	0.1700

hn	0.6000	0.0157
h1	1.3870	0.0157
hm	1.4590	0.0150
c2	1.9080	0.0860
cd	1.9080	0.0860
c3	1.9080	0.1094
cm	1.9080	0.0860

Section S6.2: Force Field MIL-53(Al)

-Metal residue (Al):

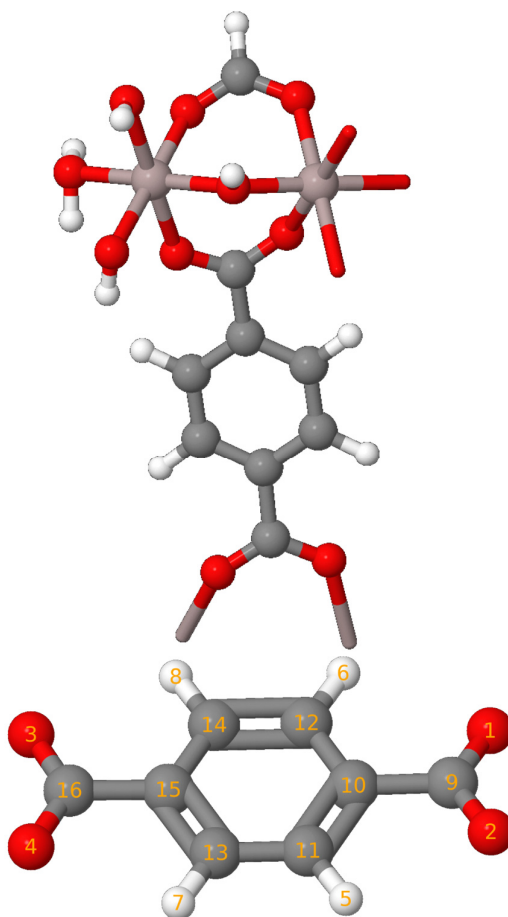
Atom number FF atom type

Al	1	Al
----	---	----

-Linker (C₈O₄H₄):

Atom number FF atom type

O	1	Oc
O	2	Oc
O	3	Oc
O	4	Oc
H	5	Ha
H	6	Ha
H	7	Ha
H	8	Ha
C	9	Co
C	10	Cp
C	11	Ca
C	12	Ca
C	13	Ca
C	14	Ca
C	15	Cp
C	16	Co



-Hydroxy bridge (OH):

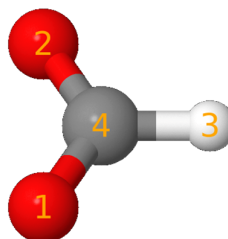
Atom number FF atom type

O	1	Oh
H	2	Ho

-Border residue (CO₂H):

Atom number FF atom type

O	1	Oc
O	2	Oc
H	3	H5
C	4	Co



- Border Hydroxy (OH):

Atom number FF atom type

O	1	Oy
H	2	Hy

- Border water (OH₂):

Atom number FF atom type

O	1	Ow
H	2	Hw
H	3	Hw

MASS

al	26.982	0.520
oh	16.000	0.465
oc	16.000	0.465
od	16.000	0.465
ow	16.000	0.465
oy	16.000	0.465
co	12.010	0.360
cp	12.010	0.360
ca	12.010	0.360
ho	1.008	0.135
ha	1.008	0.135
h5	1.008	0.135
hw	1.008	0.135
hy	1.008	0.135

BOND STRETCHING

al-oh	226.383	1.807
al-oc	191.193	1.905
al-od	185.625	1.910
al-oy	179.614	1.802
oh-ho	483.767	0.948
oy-hy	619.790	0.958
oc-co	532.656	1.264
od-co	515.050	1.268
co-cp	323.272	1.482
cp-ca	394.916	1.397
ca-ca	394.916	1.397
ca-ha	271.310	1.200
co-h5	319.400	1.115
al-ow	226.383	1.807

ANGLE BENDING

al-oh-al	267.297	125.491
----------	---------	---------

al-oh-ho	88.822	114.648
al-oy-hy	17.242	122.255
al-oc-co	94.016	133.962
al-od-co	94.016	133.962
oc-al-oc	56.898	179.890
od-al-od	55.952	179.789
oh-al-oh	61.380	179.487
oc-al-od	180.099	91.440
od-al-oh	9.883	90.324
oh-al-oc	221.271	90.942
oy-al-oy	46.500	90.000
oy-al-oh	63.653	90.000
oy-al-oc	63.653	90.000
oy-al-od	63.653	90.000
oy-al-ow	46.500	90.000
oc-co-oc	290.609	124.241
od-co-od	287.813	123.089
oc-co-cp	290.848	117.674
od-co-cp	290.848	117.674
co-cp-ca	284.293	120.197
cp-ca-ca	136.436	120.261
cp-ca-ha	82.144	121.174
ca-cp-ca	136.436	120.261
ca-ca-ha	82.144	121.174
oc-co-h5	55.501	123.760
od-co-h5	55.501	123.760
ow-al-oc	221.271	90.942
ow-al-od	221.271	90.942
ow-al-oh	221.271	90.942
ow-al-ow	55.952	179.789
al-ow-hw	88.822	114.648

TORSION

al-oc-co-cp	1	1.516	180.000	2.000
al-od-co-cp	1	1.516	180.000	2.000
al-oc-co-h5	1	1.516	180.000	2.000
oc-co-cp-ca	1	2.175	180.000	-2.000
oc-co-cp-ca	1	0.300	0.000	3.000
od-co-cp-ca	1	2.175	180.000	-2.000
od-co-cp-ca	1	0.300	0.000	3.000
co-cp-ca-ca	1	6.650	180.000	2.000
co-cp-ca-ha	1	6.650	180.000	2.000
cp-ca-ca-ha	1	6.650	180.000	2.000
ca-cp-ca-ha	1	6.650	180.000	2.000
ha-ca-ca-ha	1	6.650	180.000	2.000

OUT-OF-PLANE

cp-oc-oc-co	1.100	180.0000	2.000
co-ca-ca-cp	1.100	180.0000	2.000
ca-cp-ha-ca	1.100	180.0000	2.000
ca-ca-ca-ha	1.100	180.0000	2.000
co-ca-cp-ca	1.100	180.0000	2.000
ca-ca-cp-co	1.100	180.0000	2.000

NON-BONDED

al	2.36	0.115918
oh	1.82	0.059034
oc	1.82	0.059034
od	1.82	0.059034
oy	1.82	0.059034
ow	1.82	0.059034
co	1.94	0.055927
cp	1.94	0.055927
ca	1.94	0.055927
ho	1.60	0.016013
ha	1.60	0.016013
hw	1.60	0.016013
h5	1.60	0.016013
hy	1.60	0.016013

Section S6.3: Force Field MOF-5

-Metal residue (Zn_4O):

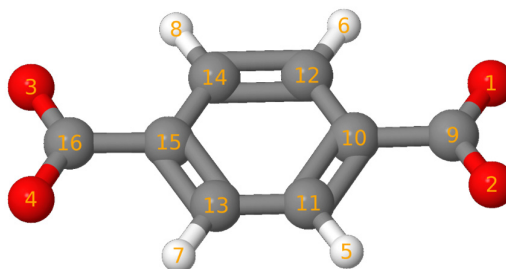
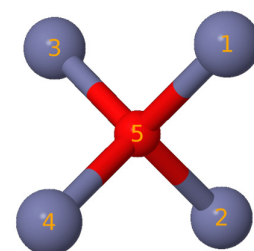
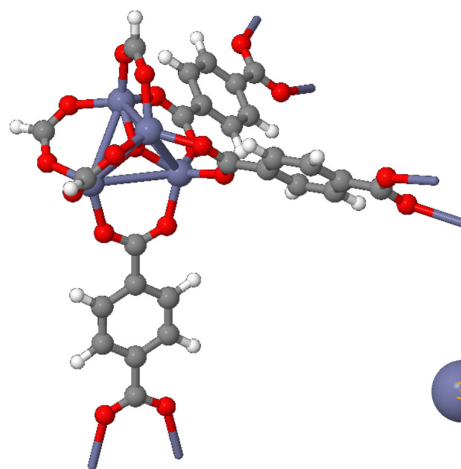
Atom number FF atom type

Zn	1	Zn
Zn	2	Zn
Zn	3	Zn
Zn	4	Zn
O	1	Os

-Linker ($\text{C}_8\text{O}_4\text{H}_4$):

Atom number FF atom type

O	1	O
O	2	O
O	3	O
O	4	O
H	5	Ha
H	6	Ha
H	7	Ha
H	8	Ha
C	9	C
C	10	Ca

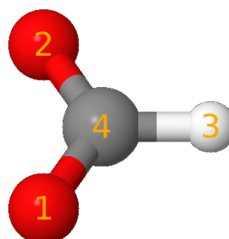


C	11	Ca
C	12	Ca
C	13	Ca
C	14	Ca
C	15	Ca
C	16	C

-Border residue (CO₂H):

Atom number FF atom type

O	1	O
O	2	O
H	3	H5
C	4	C



MASS

zn	65.38	0.999
o	16.00	0.434
os	16.00	0.465
c	12.01	0.616
ca	12.01	0.360
ha	1.008	0.135
h5	1.008	0.135

BOND STRETCHING

c -o	637.70000	1.2183
o -zn	61.13030	2.0150
zn-os	61.13030	2.0750
ca-o	542.26172	1.2850
ca-ca	471.78208	1.3800
c -ca	348.08312	1.4800
h5-c	319.40000	1.1150

ANGLE BENDING

zn-os-zn	28.76720	109.471
o -zn-os	21.57540	111.300
o -zn-o	15.82196	107.600
c -o -zn	30.92474	131.200
o -c - o	46.02752	125.500
ca-ca- c	52.50014	120.000
o - c-ca	56.09604	117.000
h5-c -o	55.50125	123.760

TORSION

ca-ca- c- o	1	1.0	180.0	2.0
os-zn- o- c	1	5.0	180.0	2.0

zn-os-zn- o	1	5.0	180.0	2.0
zn- o- c- c	1	5.0	180.0	2.0
zn -o- c-ca	1	5.0	180.0	2.0
zn-o -c -h5	1	1.6	180.0	2.0

OUT-OF-PLANE

o -o -c -ca	16.54	180.0	2.0
ca-ca-ca-ha	1.1	180.0	2.0
c -ca-ca-ca	1.1	180.0	2.0
ca-o -c -o	1.1	180.0	2.0

NON-BONDED

zn	2.29	0.276
os	1.82	0.059
o	1.82	0.059
c	1.94	0.056
ca	1.94	0.056
ha	1.62	0.020

Section S6.4: QM part, MM part

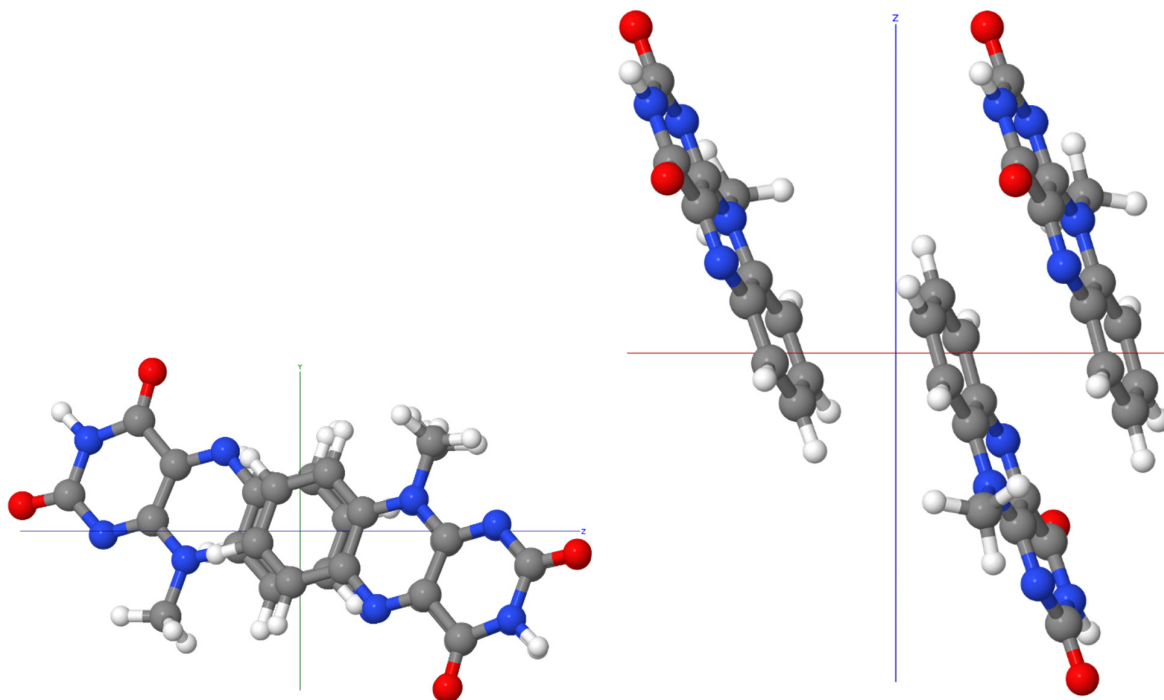


Figure S36. QM-Layer including three MIA molecules. During QM/MM-optimization only QM atoms were allowed to move (mobile layer), the remaining atom position were fixed at their optimized values from the corresponding plane-wave calculation with QuantumEspresso [24]. (left: view along X axis, right: view along Y axis).

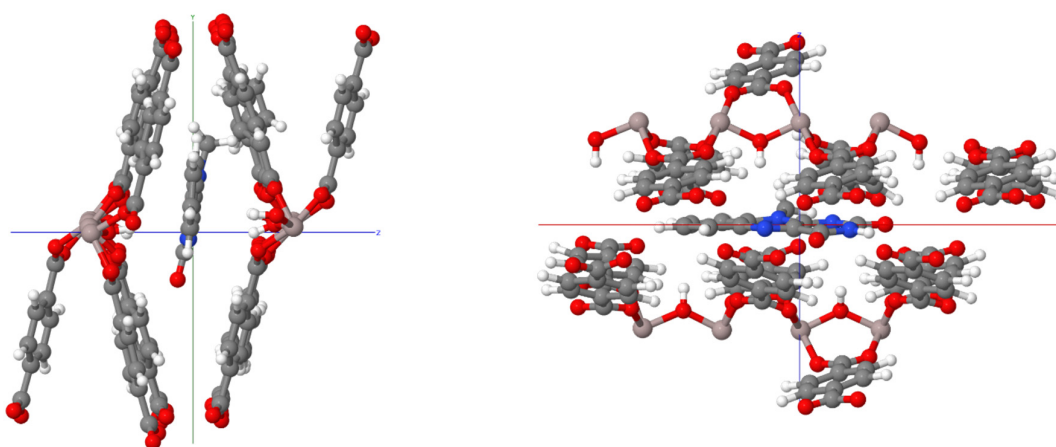


Figure S37. The mobile layer in MIL-53(Al) contains MIA and all residues that have at least 1 atom in a radius of 7.5 Å around the MIA chromophore (QM layer (MIA) and movable MM portion (MOF), left: view along X axis, right: view along Y axis). The remaining atoms (not shown) were fixed at their optimized positions from the plane-wave computation with QuantumEspresso [24].

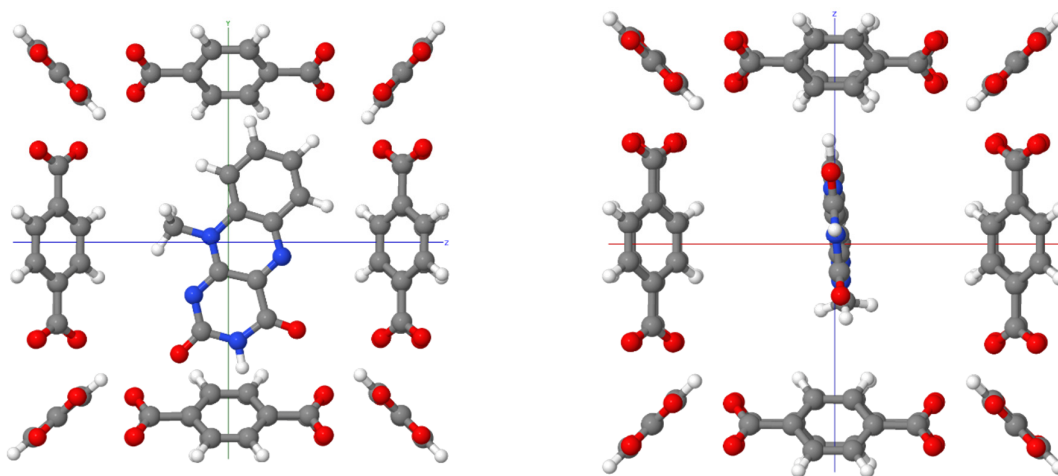


Figure S38. The mobile layer in both *inward* and *outward* pores of MOF-5, containing MIA and all residues that have at least one atom within a radius of 5.0 Å around the MIA chromophore. Zn₄O residues and the remaining portion of the MOF were kept fixed at their plane-wave optimized positions. (QM layer (MIA) and medium layer (MOF), left: view along X axis, right: view along Y axis).

Cluster for MIL-53(Al) Force Field generation:

The same cluster as presented in the work of Vanduyfhuys et al. [25] was used to generate the MIL-53(Al) force field (Figure S39). The total charge was -1 . It was first geometry-optimized with the B3LYP hybrid functional and the 6-311++G(d,p) basis set, followed by vibrational analysis using the Gaussian16 package [26].

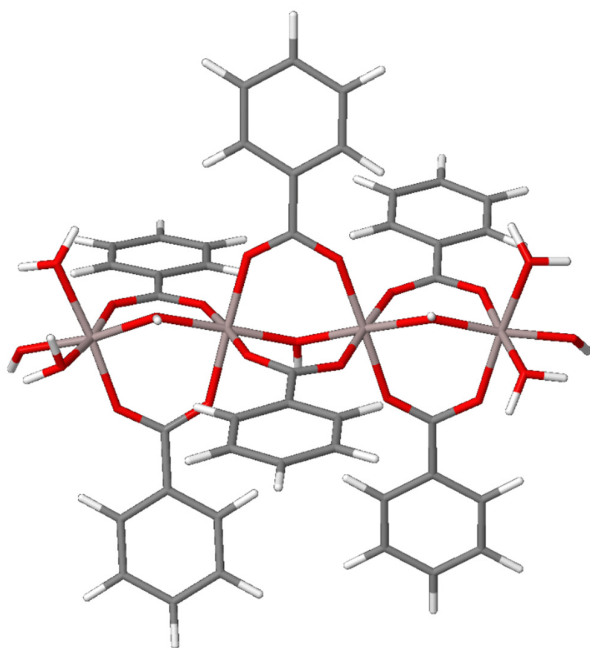


Figure S39. Cluster model of Vanduyfhuys et al. [25] used for generating the MIL-53(Al) force field used in this work.

Table S3. Crystallographic data for MIL-53 phases (powder data with Rietveld refinement from literature) and MIL-53 (computed).

Compound	experiment. MIL-53-lp ^a	computed MIL-53-lp ^b	experiment. MIL-53-np ^{a,c}	computed MIA@MIL-53 ^b
Crystal system	orthorhombic	unconstrained (triclinic)	monoclinic	unconstrained (triclinic)
Space group	<i>Imma</i>	unconstrained (<i>P1</i>)	<i>Cc</i>	unconstrained (<i>P1</i>)
a [Å]	6.6085(9)	6.8904	19.513(2)	20.1698 ^d
b [Å]	16.675(3)	16.4224	7.612(1)	18.8673
c [Å]	12.813(2)	13.5000	6.576(1)	8.9399
α [°]	90	90	90	89.92
β [°]	90	90	104.24(1)	90.31
γ [°]	90	90	90	87.29
V [Å ³]	1411.95(40)	1527.62	946.74(10)	3398.21

^a CCDC no. 220476 (lp), 220477 (np) [6]. ^b Cell parameters refined through Quantum Espresso.

^c The cell setting/orientation of the coordinate system in the experimental structure of MIL-53-np is different from those of the other three (exp. and comput.) structures. To facilitate a comparison of the axes lengths, matching directions are given in the same color. ^d Note that in computed MIA@MIL-53 the *a* axis (channel direction) was extended to about three times the corresponding axis length in experimental MIL-53-lp or -np (ca. 6.6 Å) to accommodate separated MIA molecules with their length of 12 Å (cf. Figure S12).

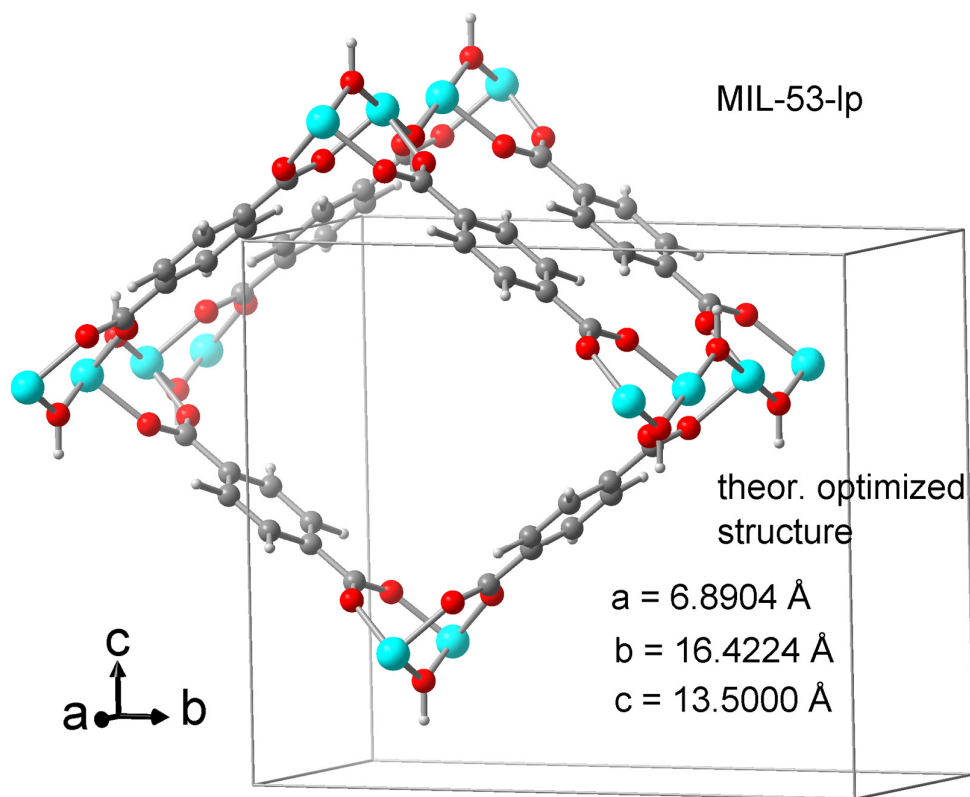
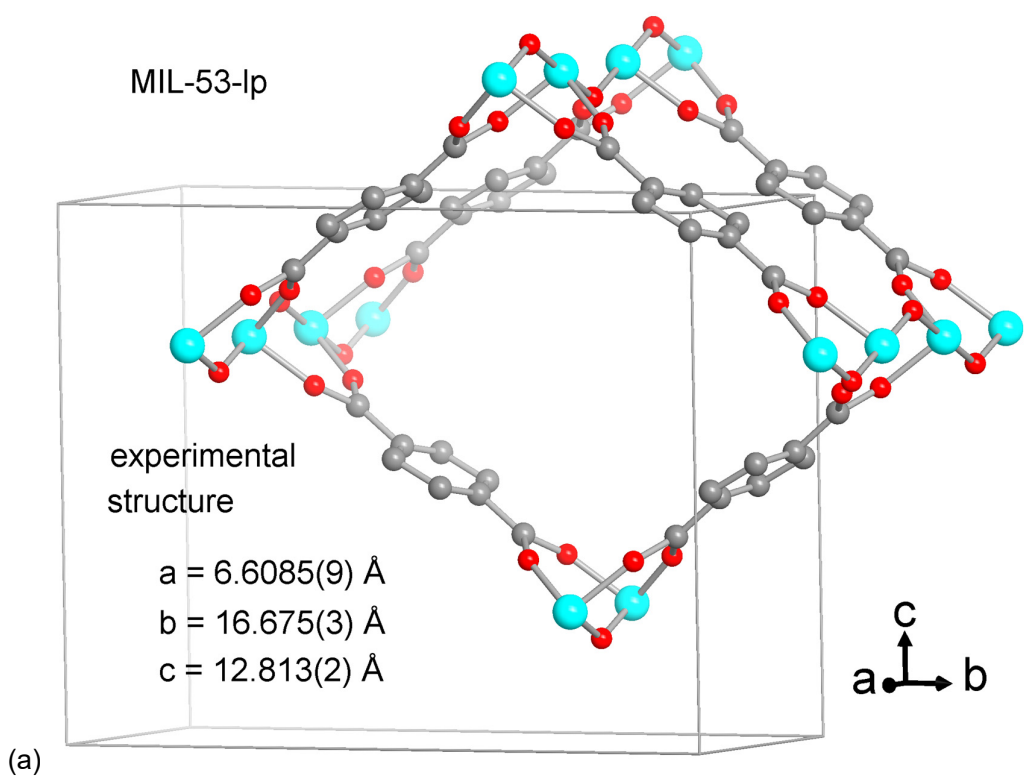


Figure S40. Sections of the structures with the cell edges and cell constants of MIL-53-lp from (a) experimental Rietveld refinement (CCDC no./Refcode 220476/SABVUN) [6] and (b) from theoretical optimization with QuantumEspresso (see also Table S3). Compared to the experimental orthorhombic large-pore form MIL-53-lp the computed guest-free MIL-53-lp structure after optimization widens by ca. 0.3 Å and 0.7 Å in a- and c-directions, respectively, while it shrinks by ca. 0.25 Å in the b-direction, with the cell angles remaining at 90°

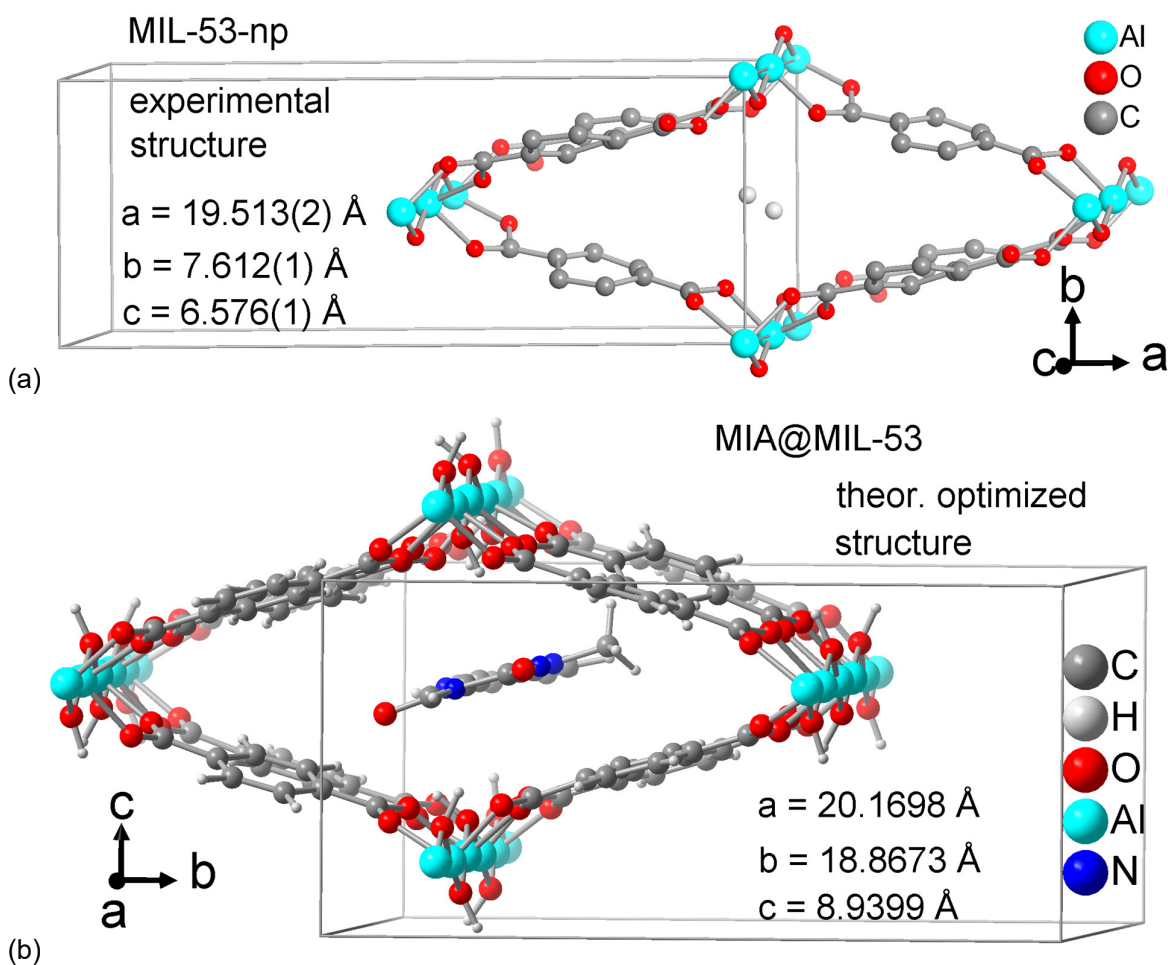


Figure S41. Sections of the structures with the cell edges and cell constants of (a) MIL-53-np from experimental Rietveld refinement (CCDC no./Refcode 220477/SABWAU) [6] and of (b) MIA@MIL-53 from theoretical optimization with QuantumEspresso. The theoretical cell setting/orientation of the coordinate system in (b) is the same as in the MIL-53-lp structures in Figure S40 but different to the MIL-53-np structure in (a). However, the axis parallel to the channel direction in MIA@MIL-53 (*a* axis, ca. 20 Å) was extended to about three times the corresponding axis length in experimental MIL-53-lp or -np (ca. 6.6 Å) to accommodate separated MIA molecules in the channels (cf. MIA length of 12 Å in Figure S12) (see also Table S3).

Section S6.5: Transition dipole moments of MIA

The orientations of the transition dipole moment vector (TDM) were obtained from the quantum-chemical calculations for $S_0 \rightarrow S_1$ (absorption) and for $S_1 \rightarrow S_0$ (fluorescence) (see example in Figure S42). The vector coordinates are as follows:

MIA in vacuum			
TDM	x	y	z
Absorption ($S_0 \rightarrow S_1$)	1.8176223	-0.4546537	0.7971484
Emission ($S_1 \rightarrow S_0$)	1.6719799	-0.3554352	0.7142668
Difference ($S_0 \rightarrow S_1$)	0.1456424	-0.0992185	0.0828816
Angle = 1.9°			

MIA@MIL-53			
TDM	x	y	z
Absorption ($S_0 \rightarrow S_1$)	1.7076416	0.9172188	-0.1371604
Emission ($S_1 \rightarrow S_0$)	1.5876942	-0.9185493	-0.1183539
Difference ($S_0 \rightarrow S_1$)	0.1199474	0.0013305	-0.0188065
Angle = 1.8°			

MIA@MOF-5			
TDM	x	y	z
Absorption ($S_0 \rightarrow S_1$)	0.0462862	-2.0319814	-0.0827332
Emission ($S_1 \rightarrow S_0$)	-0.0345843	-1.8358583	-0.1126006
Difference ($S_0 \rightarrow S_1$)	0.0808705	-0.1961231	
Angle = 2.7°			

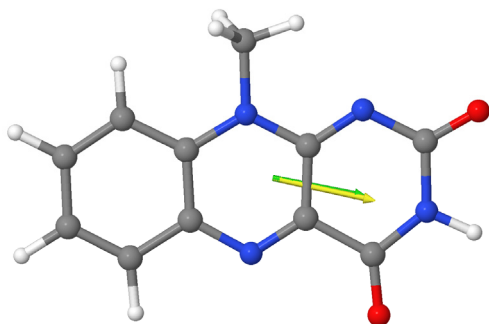


Figure S42. Transition dipole moments of MIA@MIL-53. Yellow arrow for $S_0 \rightarrow S_1$ (absorption) and green arrow for $S_1 \rightarrow S_0$ (fluorescence).

References

- 1 Brown, S.A.; Rizzo, C.J. A “One-Pot” Phase Transfer Alkylation/Hydrolysis of *o*-Nitrotrifluoroacetanilides. A Convenient Route to *N*-Alkyl *o*-Phenylenediamines. *Synth. Commun.* **1996**, *26*, 4065-4080. <https://doi.org/10.1080/00397919608003827>
- 2 Imada, Y.; Iida, H.; Ono, S.; Masui, Y.; Murahashi, S.-I. Flavin-Catalyzed Oxidation of Amines and Sulfides with Molecular Oxygen: Biomimetic Green Oxidation. *Chem. Asian J.* **2006**, 136-147. <https://doi.org/10.1002/asia.200600080>
- 3 Reiffers, A.; Ziegenbein, C.T.; Engelhardt, A.; Kühnemuth, R.; Gilch, P.; Czekelius, C. Impact of Mono-Fluorination on the Photophysics of the Flavin Chromophore. *Photochem. Photobiol.* **2018**, *94*, 667-676. <https://doi.org/10.1111/php.12921>
- 4 Kumar, V.; Bode, K.A.; Bryan, R.F.; Averill, B.A. Evidence for a competing condensation reaction in the alloxan synthesis of flavins: synthesis and crystal and molecular structures of 7-chloro-8-methylalloxazine and 7,10-dimethyl-8-[(2-hydroxyethyl)thio]isoalloxazine. *J. Am. Chem. Soc.* **1986**, *108*, 490-496. <https://doi.org/10.1021/ja00263a022>
- 5 Alaerts, L.; Maes, M.; Giebel, L.; Jacobs, P.A.; Martens, J.A.; Denayer, J.F.M.; Kirschhock, C.E.A.; De Vos, D.E. Selective Adsorption and Separation of ortho-Substituted Alkylaromatics with the Microporous Aluminum Terephthalate MIL-53. *J. Am. Chem. Soc.* **2008**, *130*, 14170-14178. <https://doi.org/10.1021/ja802761z>
- 6 Loiseau, T.; Serre, C.; Huguenard, C.; Fink, G.; Taulelle, F.; Henry, M.; Bataille, T.; Férey, G. A Rationale for the Large Breathing of the Porous Aluminum Terephthalate (MIL-53) Upon Hydration *Chem. Eur. J.* **2004**, *10*, 1373-1382. <https://doi.org/10.1002/chem.200305413>
- 7 Han, S.; Wei, Y.; Valente, C.; Lagzi, I.; Gassensmith, J.J.; Coskun, A.; Stoddart, J.F.; Grzybowski, B.A. Chromatography in a Single Metal–Organic Framework (MOF) Crystal. *J. Am. Chem. Soc.* **2010**, *132*, 16358-16361. <https://doi.org/10.1021/ja1074322>
- 8 Eddaoudi, M.; Kim, J.; Rosi, N.; Vodak, D.; Wachter, J.; O’Keeffe, M.; Yaghi, O.M. Systematic Design of Pore Size and Functionality in Isoreticular MOFs and Their Application in Methane Storage. *Science* **2002**, *295*, 469-472. <https://doi.org/10.1126/science.1067208>
- 9 Brandenburg, K. *Diamond (Version 4.6), Crystal and Molecular Structure Visualization, Crystal Impact* – K. Brandenburg & H. Putz Gbr, Bonn, Germany, **2009-2022**.
- 10 Wang, M.; Fritchie Jr., C.J. Geometry of the Unperturbed Flavin Nucleus. The Crystal Structure of 10-Methylisoalloxazine. *Acta Cryst.* **1973**, *B29*, 2040-2045. <https://doi.org/10.1107/S0567740873006096>
- 11 Meilikhov, M.; Yusenko, K.; Fischer, R.A. The adsorbate structure of ferrocene inside [Al(OH)(bdc)]_x (MIL-53): a powder X-ray diffraction study. *Dalton Trans.* **2009**, 600-602. <https://doi.org/10.1039/B820882B>
- 12 Couck, S.; Gobechiya, E.; Kirschhock, C.E.A.; Serra-Crespo, P.; Juan-Alcañiz, J.; Martinez Joaristi, A.; Stavitski, E.; Gascon, J.; Kapteijn, F.; Baron, G.V.; Denayer, J.F.M. Adsorption and Separation of Light Gases on an Amino-Functionalized Metal–Organic Framework: An

-
- Adsorption and In Situ XRD Study. *ChemSusChem*, **2012**, *5*, 740-750. <https://doi.org/10.1002/cssc.201100378>
- 13 Rosenbach, N.J.; Jobic, H.; Ghoufi, A.; Salles, F.; Maurin, G.; Bourrelly, S.; Llewellyn, P.L.; Devic, T.; Serre, C.; Férey, G. Quasi-Elastic Neutron Scattering and Molecular Dynamics Study of Methane Diffusion in Metal Organic Frameworks MIL-47(V) and MIL-53(Cr). *Angew. Chem. Int. Ed.* **2008**, *47*, 6611-6615. <https://doi.org/10.1002/anie.200801748>
- 14 Salles, F.; Bourrelly, S.; Jobic, H.; Devic, T.; Guillerm, V.; Llewellyn, P.; Serre, C.; Férey, G.; Maurin, G. Molecular Insight into the Adsorption and Diffusion of Water in the Versatile Hydrophilic/Hydrophobic Flexible MIL-53(Cr) MOF. *J. Phys. Chem. C* **2011**, *115*, 21, 10764-10776. <https://doi.org/10.1021/jp202147m>
- 15 Bauer, S.; Serre, C.; Devic, T.; Horcajada, P.; Marrot, J.; Férey, G.; Stock, N. High-Throughput Assisted Rationalization of the Formation of Metal Organic Frameworks in the Iron(III) Aminoterephthalate Solvothermal System, *Inorg. Chem.* **2008**, *47*, 7568-7576. <https://doi.org/10.1021/ic800538r>
- 16 Serre, C.; Millange, F.; Thouvenot, C.; Noguès, M.; Marsolier, G.; Louër, D.; Férey, G. Very Large Breathing Effect in the First Nanoporous Chromium(III)-Based Solids: MIL-53 or $\text{Cr}^{\text{III}}(\text{OH})\cdot\{\text{O}_2\text{C}-\text{C}_6\text{H}_4-\text{CO}_2\}\cdot\{\text{HO}_2\text{C}-\text{C}_6\text{H}_4-\text{CO}_2\text{H}\}_x\cdot\text{H}_2\text{O}_y$. *J. Am. Chem. Soc.* **2002**, *124*, 13519-13526. <https://doi.org/10.1021/ja0276974>
- 17 Millange, F.; Serre, C.; Férey, G. Synthesis, structure determination and properties of MIL-53as and MIL-53ht: the first Cr^{III} hybrid inorganic-organic microporous solids: $\text{Cr}^{\text{III}}(\text{OH})\cdot\{\text{O}_2\text{C}-\text{C}_6\text{H}_4-\text{CO}_2\}\cdot\{\text{HO}_2\text{C}-\text{C}_6\text{H}_4-\text{CO}_2\text{H}\}_x$. *Chem. Commun.* **2002**, 822-823. <https://doi.org/10.1039/B201381A>
- 18 Millange, F.; Guillou, N.; Walton, R.I.; Grenèche, J.-M.; Margiolaki, I.; Férey, G. Effect of the nature of the metal on the breathing steps in MOFs with dynamic frameworks. *Chem. Commun.* **2008**, 4732-4734. <https://doi.org/10.1039/B809419E>
- 19 Li, H.; Eddaoudi, M.; O'Keeffe, M.; Yaghi, O.M. Design and synthesis of an exceptionally stable and highly porous metal-organic framework. *Nature* **1999**, *402*, 276-279. <https://doi.org/10.1038/46248>
- 20 Li, H.; Eddaoudi, M.; O'Keeffe, M.; Yaghi, O.M. *CCDC 256966: Experimental Crystal Structure Determination*, Cambridge Crystallographic Data Centre, **2005**. <https://doi.org/10.5517/cc8md7h>
- 21 Bailey, M.; Brown, C.J. The crystal structure of terephthalic acid. *Acta Crystallogr.* **1967**, *22*, 387-391. <https://doi.org/10.1107/s0365110x67000751>
- 22 Lock, N.; Wu, Y.; Christensen, M.; Cameron, L.J.; Peterson, V.K.; Bridgeman, A.J.; Kepert, C.J.; Iversen, B.B. Elucidating Negative Thermal Expansion in MOF-5. *J. Phys. Chem. C* **2010**, *114*, 16181-16186. <https://doi.org/10.1021/jp103212z>
- 23 Möckel, C.; Kubiak, J.; Schillinger, O.; Kühnemuth, R.; Della Corte, D.; Schröder, G.F.; Willbold, D.; Strodel, B.; Seidel, C.A.M.; Neudecker, P. Integrated NMR, fluorescence and MD benchmark

-
- study of protein mechanics and hydrodynamics. *J. Phys. Chem. B* **2019**, *123*, 1453-1480. <https://doi.org/10.1021/acs.jpcb.8b08903>
- 24 Giannozzi, P.; Baroni, S.; Bonini, N.; Calandra, M.; Car, R.; Cavazzoni, C.; Ceresoli, D.; Chiarotti, G.L.; Cococcioni, M.; Dabo, I.; Dal Corso, A.; de Gironcoli, S.; Fabris, S.; Fratesi, G.; Gebauer, R.; Gerstmann, U.; Gougoussis, C.; Kokalj, A.; Lazzeri, M.; Martin-Samos, L.; Marzari, N.; Mauri, F.; Mazzarello, R.; Paolini, S.; Pasquarello, A.; Paulatto, L.; Sbraccia, C.; Scandolo, S.; Sclauzero, G.; Seitsonen, A.P.; Smogunov, A.; Umari, P.; Wentzcovitch, R.M. QUANTUM ESPRESSO: a modular and open-source software project for quantum simulations of materials. *J. Phys.: Condens. Matter* **2009**, *21*, 395502. <https://doi.org/10.1088/0953-8984/21/39/395502>
- 25 Vanduyfhuys, L.; Vandenbrande, S.; Verstraelen, T.; Schmid, R.; Waroquier, M.; Van Speybroeck, V. QuickFF: A program for a quick and easy derivation of force fields for metal-organic frameworks from ab initio input. *J. Comput. Chem.* **2015**, *36*, 1015-1027. <https://doi.org/10.1002/jcc.23877>
- 26 Frisch, M.J.; Trucks, G.W.; Schlegel, H.B.; Scuseria, G.E.; Robb, M.A.; Cheeseman, J.R.; Scalmani, G.; Barone, V.; Petersson, G.A.; Nakatsuji, H.; et al. *Gaussian 16*, Revision C.01; Gaussian, Inc.: Wallingford, CT, USA, 2016.

PAPER

[View Article Online](#)
[View Journal](#) | [View Issue](#)Cite this: *J. Mater. Chem. C*, 2023, 11, 8982

Molecular design of phenazine-5,10-diyl-dibenzonitriles and the impact on their thermally activated delayed fluorescence properties†

Dietrich Püschel,^a Julia Wiefermann,^b Simon Hédé,^c Tobias Heinen,^a Leo Pfeifer,^a Oliver Weingart,^{id}*^c Markus Suta,^{id}*^a Thomas J. J. Müller^{id}*^b and Christoph Janiak^{id}*^a

The photoluminescence properties of the compounds 3,3'-(phenazine-5,10-diyl)dibenzonitrile (**mBN**) and 4',4'''-(phenazine-5,10-diyl)bis([1,1'-biphenyl]-4-carbonitrile) (**BPN**) are presented and compared to those of the known fluorophore 4,4'-(phenazine-5,10-diyl)dibenzonitrile (**pBN**), which has been reported to show thermally activated delayed fluorescence (TADF). In the solid state, **pBN** shows clear TADF properties. In contrast, TADF is only weakly pronounced in **mBN**, and **BPN** is a conventional fluorescent emitter. This is discussed in terms of the provided through-space overlap between donating phenazinediyl and accepting benzonitrile units in these three molecules, which is only effective in **pBN**. These compounds are only weakly luminescent in toluene, tetrahydrofuran (THF) or dichloromethane (CH₂Cl₂) solution, most intensively in toluene, with yellow (**pBN** and **mBN**) to orange (**BPN**) colors of the emission. The emission maxima $\lambda_{em,max}$ in toluene differ slightly between **pBN** (562 nm) and **mBN** (572 nm) and overlap in THF (634 nm) and CH₂Cl₂ (~660 nm), respectively. Their emission is broad-banded and strongly solvent-dependent and thus indicates a CT-type nature of the excited state. **BPN** shows weak solvent-dependent photoluminescence (604 nm in toluene, 589 nm in THF, and 587 nm in CH₂Cl₂) and together with an observable vibronic structure in the low temperature spectra of the powder, it can be concluded that emission in **BPN** occurs from a localized electronic (LE) state non-beneficial for TADF properties. This demonstrates that even tiny modifications in the molecular templating structure of the phenazines can significantly affect their TADF properties.

Received 7th April 2023,
Accepted 15th May 2023

DOI: 10.1039/d3tc01228j

rsc.li/materials-c

Introduction

The phenomenon of thermally activated delayed fluorescence (TADF) was first described in detail by Parker and Hatchard in 1961¹ and discovered even earlier by Perrin in 1929 on uranyl salts.^{2,3} After a long period of time without application, the concept has been re-introduced by Adachi *et al.* in the 2010s to

motivate the usage of new organic chromophores in organic light-emitting diodes (OLEDs) with the goal to replace common phosphorescent expensive noble-metal complex emitters.^{4,5} Since then, the field of organic TADF chromophores has received a lot of attention worldwide with vivid development over the last decade.^{6–13} A key advantage of TADF emitters in OLEDs is the high quantum efficiency based on harvesting of both spin singlet and triplet excitons, which formally allows achieving internal quantum efficiencies of ~100% and high external quantum efficiencies (EQEs) of up to ~40%.^{5,6,14–17} This high efficiency can be achieved because the lowest excited singlet state (S₁) and lowest excited triplet state (T₁) are energetically sufficiently close that reverse intersystem crossing (rISC) can be thermally triggered.^{18–23} The energy difference ΔE_{ST} of both energy levels is typically less than 0.1 eV for the current highly efficient organic TADF emitters.^{14,24–27} The smaller the energy gap ΔE_{ST} between S₁ and T₁ the higher the equilibrium population of the higher excited S₁ state, which governs up to 25% of the internal quantum efficiency in cases of electric injection of charge carriers.

^a Institute of Inorganic and Structural Chemistry, Heinrich Heine University Düsseldorf, Universitätsstraße 1, D-40225 Düsseldorf, Germany. E-mail: Markus.Suta@hhu.de, Janiak@uni-duesseldorf.de

^b Institute of Organic and Macromolecular Chemistry, Heinrich Heine University Düsseldorf, Universitätsstraße 1, D-40225 Düsseldorf, Germany. E-mail: ThomasJJ.Mueller@hhu.de

^c Institute for Theoretical Chemistry and Computational Chemistry, Heinrich-Heine-Universität Düsseldorf, Universitätsstraße 1, D-40225 Düsseldorf, Germany. E-mail: Oliver.Weingart@hhu.de

† Electronic supplementary information (ESI) available: Sources of chemicals, synthesis, crystal structure details, supramolecular interaction analysis, photophysical properties, and quantum chemical calculations. CCDC 2238744, 2222499 and 2222500. For ESI and crystallographic data in CIF or other electronic format see DOI: <https://doi.org/10.1039/d3tc01228j>

Small organic molecules such as TADF emitters have the advantage that they can be synthesized in high purity or can be optimally purified by recrystallisation and/or sublimation. In addition, the molecules can be modified and optimized in a large variety to lead to high luminous efficacies of light-emitting devices containing these compounds. Ideally, the emitters should have high color purity and narrow emission bands.^{24,28}

It has been shown that the photoluminescence (PL) efficiency of donor–acceptor TADF compounds can be controlled and optimized by the selective choice of specific donor and acceptor moieties.^{29–31} Furthermore, systems with donor–acceptor–donor (D–A–D)³² and acceptor–donor–acceptor type (A–D–A) topologies have proven to be a beneficial combination.^{33,34}

The phenazine-5,10-diyl molecule with two nitrogen atoms in the central 1,4-dihydrodiazine core is an excellent donor moiety.³⁵ By arylation of the 5 and 10 positions, 5,10-di-aryl derivatives are obtained. The variation of acceptor groups attached to the nitrogen atoms of phenazine-5,10-diyl has been well investigated in this symmetrical A–D–A system. Benzonitrile has been found to be the most effective acceptor in these designed TADF emitters.^{33,35} Compound 4,4'-(phenazine-5,10-diyl)dibenzonitrile (Fig. 1), which is derived from 5,10-dihydrophenazine (DHPZ) as the strong electron donor and two *para*-benzonitrile moieties as strong electron acceptor units, has an energy gap of $\Delta E_{ST} = 0.10$ eV and a photoluminescence quantum yield of 35.2% with the corresponding EQE of 5–8%. It is an established TADF emitter.³³

Here, we analyze the effect of a change in the nitrile substitution pattern from a *para* to *meta* configuration and an elongation of the phenyl to a biphenyl group on the photophysical properties with special emphasis on potential TADF properties. This offers the possibility of deriving structure–property relationships and to formulate molecular design rules to control desirable TADF parameters such as ΔE_{ST} by simple chemical inspection. Thus, we synthesized and investigated the luminescence properties of 3,3'-(phenazine-5,10-diyl)dibenzonitrile (**mBN**) and 4',4'''-(phenazine-5,10-diyl)bis([1,1'-biphenyl]-4-carbonitrile) (**BPN**) and compared them to those of the

literature-known TADF emitter 4,4'-(phenazine-5,10-diyl)dibenzonitrile (**pBN**) (Fig. 1). We analyzed the optical properties both in the solid state and in solution to identify the overall nature of the radiative transition and to verify if aggregation-induced effects in the powder lead to significant changes in the TADF properties. This is usually relevant for applications such as emitting materials in OLEDs, in which thin films are used rather than dissolved dyes. In particular, the presented dyes have high melting points (**mBN** = 284 °C, **pBN** and **BPN** > 300 °C) and can be even processed by sublimation, which is beneficial for applications.

Results and discussion

For the synthesis of the phenazine-5,10-diyl dibenzonitriles, phenazine was first reduced to dihydrophenazine following established literature procedures (see the ESI† for details).^{33,36} Then, Buchwald–Hartwig coupling with 4-bromobenzonitrile, 3-bromobenzonitrile, or 4'-bromo-[1,1'-biphenyl]-4-carbonitrile forms the products 4,4'-(phenazine-5,10-diyl)dibenzonitrile (**pBN**), 3,3'-(phenazine-5,10-diyl)dibenzonitrile (**mBN**) or 4',4'''-(phenazine-5,10-diyl)bis([1,1'-biphenyl]-4-carbonitrile) (**BPN**), respectively (Fig. 1). The dihydrophenazine derivatives are obtained in good to high yields of 65–78%. Their purity and identity were confirmed by ¹H NMR, mass spectrometry, combustion analysis and single-crystal structures.

The crystal structure of **pBN** was only published recently (α -polymorph, space group $P2_1$, no. 4)³⁷ and another β -polymorph (space group $P\bar{1}$, no. 2) has been determined in parallel in this work (see the ESI† for details). Both **pBN** polymorphs consist of two types of molecules, namely a 'linear' one and a *trans*-bent 'distorted one' (ratios 1 : 1 in β - and 1 : 2 in α -polymorph), with a characteristic non-linearity of the latter associated with the weak, but clearly distinguishable pyramidalicity at the N atoms of the phenazinediyl core (Fig. 2a). In both molecules of β -**pBN** and also in crystalline **mBN** (Fig. 2b), the center of the pyrazine ring coincides with an inversion center; hence, the pyrazine rings are planar by symmetry (see the ESI† for crystallographic details). The dihedral angles between the benzonitrile aryl group and the pyrazine core or phenazine plane are 75.08(5)° or 76.41(4)° in β -**pBN** molecule 1, 79.37(5)° or 79.93(4)° in β -**pBN** molecule 2, 86.67(5)° or 85.80(3)° in **mBN**, respectively. The fused benzo and pyrazine rings are almost coplanar with a small interplanar angle of 2.79(4)°, 1.07(5)° in β -**pBN** molecule 1,2 and 1.71(4)° in **mBN**.

Photophysical properties

Solution. UV-Vis absorption and emission spectra were recorded in solvents of different polarity. For each compound, the absorption maxima in the different solvents are located at around the same wavelengths (Table 1 and Fig. 3).

Compound **pBN** has the strongest absorption maximum at ~320 nm with a pronounced tailing shoulder at 371 nm and a weak one at 427 nm. In toluene, the absorption at 371 nm is a distinct band (Table 1 and Fig. 3a). In comparison to **pBN**, for **mBN** the strongest absorption bands are redshifted to

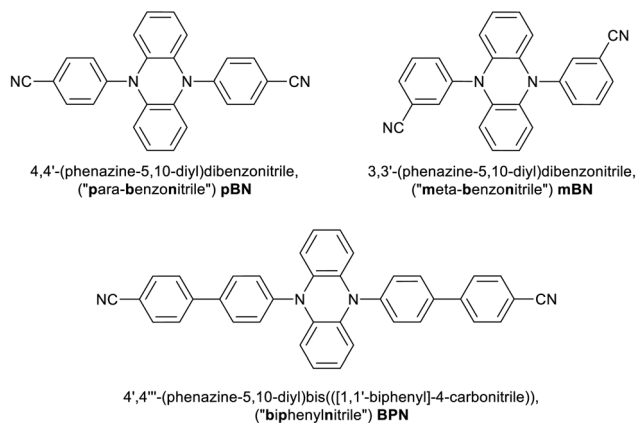


Fig. 1 Chemical formulae of the investigated phenazine-5,10-diyl dibenzonitriles in this work.



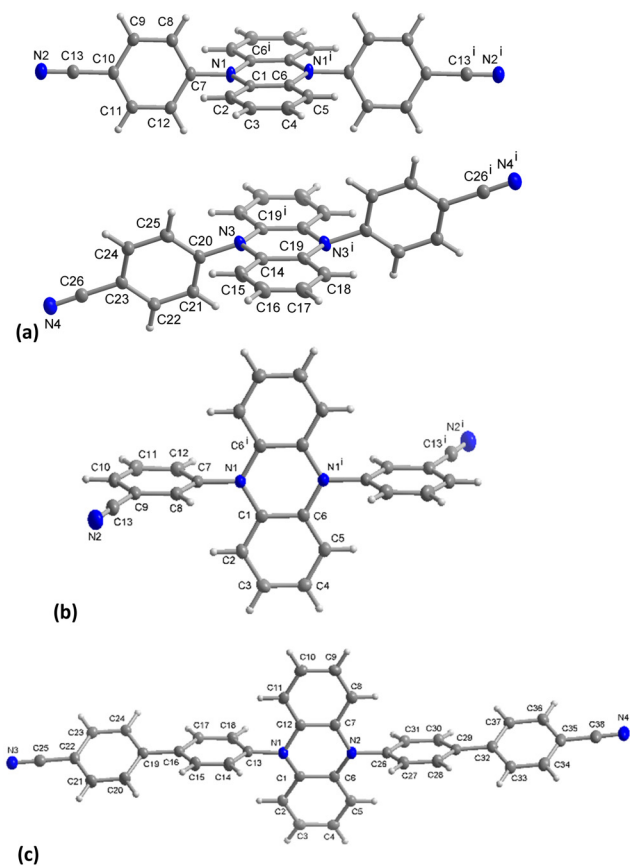


Fig. 2 Molecular structures of (a) **pBN** with linear molecule 1 and trans-bent molecule 2, (b) **mBN** and (c) **BPN** (CHCl_3 solvent molecule omitted) in the crystalline state (50% thermal ellipsoids, H atoms with arbitrary radii). Symmetry transformation in (a) $i = -x + 1, -y + 1, -z$; (b) $i = -x + 1, -y, -z + 2$.

~ 331 nm with a weak shoulder at ~ 380 nm. For **BPN**, an additional redshift of the strongest band to ~ 373 nm and the tailing shoulder to 427 nm is observed. This band and shoulder coincide with the two shoulders in **pBN**. The molar absorption coefficients of the strongest absorptions above 300 nm are relatively low and in the range of $6000\text{--}8000 \text{ L mol}^{-1} \text{ cm}^{-1}$ (and even lower for **pBN** in toluene and **BPN** in THF) (Table 1).

In toluene, the absorption spectra for **pBN** and **BPN** are very similar and the longest wavelength absorption maxima appear as incompletely resolved shoulders at 427 nm (Fig. 3a). The comparable lowest energetic absorption of **mBN** is located at 381 nm (Table 1). This can also be rationalized by DFT/MRCI calculations (see the Theoretical Calculations section).

The compounds are only weakly luminescent in solution, yet, most intensively in toluene. Unlike the absorption spectra, the emission bands of the three compounds recorded upon excitation at each absorption maximum ($\lambda_{\text{exc}} = \lambda_{\text{max,abs}}$) show a pronounced solvatochromicity. For **pBN** and **mBN**, the emission maxima differ by 10 nm in toluene with $\lambda_{\text{em}} = 562$ nm and 572 nm, respectively, but lie closely together in THF ($\lambda_{\text{em}} = 634$ nm) and CH_2Cl_2 ($\lambda_{\text{em}} = 660$ nm) (Table 1 and Fig. 3). The bathochromic shift from toluene to THF and CH_2Cl_2 of

the emission bands indicates a positive emission solvatochromism (see also Fig. S17 and S19, ESI †).³⁸

Compared to the **pBN** and **mBN** compounds, the emission maximum for **BPN** with its biphenyl π -system is bathochromically shifted to 604 nm in toluene but hypsochromically to 589 nm in THF and to 587 nm in CH_2Cl_2 . In CH_2Cl_2 , there is also a second emission band observable at 760 nm. For **BPN**, the hypsochromic emission shift from toluene to THF and CH_2Cl_2 represents a negative emission solvatochromism (see also Fig. S21, ESI †).

Compared to the solid-state (at 25 $^\circ\text{C}$), the λ_{max} values for **pBN** (558 nm) and **mBN** (551 nm) differ depending on the solvent. In the solid state, the emission maxima of **pBN** and **mBN** are located at similar wavelengths. The emission maximum of **BPN** (596 nm) is at a comparable wavelength to the values in solution and indicates limited solvatochromism.

The emission bands of the chromophores in toluene are narrow, with full width at half maximum (FWHM) values ranging from 0.44 to 0.47 eV (Table 1). The FWHM values only increase slightly for **pBN** and **mBN** from toluene to THF and CH_2Cl_2 (to 0.50–0.56 eV). Emission intensities are low for these molecules in toluene, and the CIE coordinates in toluene comply with the observable yellow (**pBN**, **mBN**) to orange (**BPN**) colors of the emission. In THF the CIE coordinates account for orange emission colors (Table 1 and Fig. S18, S20 and S22, ESI †). In CH_2Cl_2 , the CIE coordinates match the observable orange emission colors of all compounds (Table 1).

Luminescence decay times are in a typical range for fluorescent organic chromophores.³⁹ For **pBN** and **mBN**, the decay times decrease from toluene (5.7 ns and 8.9 ns) to THF (2.5 and 1.7 ns, respectively) and further to CH_2Cl_2 (1.0 and 1.6 ns, respectively) (Table 1). If the decay was purely radiative, the decay time should expectedly increase with redshifted emission wavelength based on the λ_{em}^3 dependence of the radiative decay time. On the other hand, the increasing refractive index of the solvents from toluene over THF to CH_2Cl_2 leads to a local field enhancement and thus compensates the pure wavelength dependence of the radiative decay time.⁴⁰ Finally, redshifted broad-band luminescence is more strongly prone to non-radiative relaxation and consequently lower quantum yields. The general decrease in emission brightness of **pBN/mBN** from toluene to CH_2Cl_2 indicates that it is the non-radiative pathway that is most relevant to the observed decrease of the photoluminescence decay time.

For **BPN**, the decay time first increases from toluene (6.7 ns) to THF (12.0 ns) along with the hypsochromic shift and then decreases again in CH_2Cl_2 (5.5/0.5 ns) in line with the lower intensity in emission which, however, is not visible anymore. The increase in decay time from toluene to THF is not readily expected given the slightly blue-shifted emission wavelength and similar photophysical properties such as FWHM and Stokes shift of **BPN** in THF compared to toluene (Table 1). However, the molar absorption coefficients in THF are lowered by a factor of almost 3 compared to those in toluene. If the difference in refractive indices between toluene and THF is considered, this could explain the difference in factor of almost



Table 1 Photophysical data for compounds **pBN**, **mBN**, and **BPN** in different solvents at room temperature

Compound	$\lambda_{\text{max,abs}}/\text{nm}$ ($\epsilon/\text{L mol}^{-1} \text{cm}^{-1}$)	$\lambda_{\text{em}}/\text{nm}$	τ/ns	Stokes shift ^a / cm^{-1}	FWHM ^b / cm^{-1} (eV)	CIE ^c
pBN						
Toluene	427sh (900) 371 (1800) 318 (2700)	562	5.7	5600	3624 (0.45)	0.450, 0.530
THF	427sh (1700) 370sh (3800) 318 (7200)	634	2.5	7600	4018 (0.50)	0.572, 0.422
Dichloromethane	427sh (2100) 372sh (4200) 321 (7700) 255 (42600) ^d	659	1.0	8200	4436 (0.55)	0.567, 0.418
mBN						
Toluene	381sh (2400) 331 (6800)	572	8.9	8800	3746 (0.47)	0.468, 0.513
THF	383sh (1900) 329 (5900)	634	1.7	10 300	4101 (0.51)	0.556, 0.422
Dichloromethane	384sh (2600) 332 (7400) 250 (54200) ^d	662	1.6	10 900	4517 (0.56)	0.561, 0.432
BPN						
Toluene	427sh (2800) 375 (6600)	604	6.7	6900	3564 (0.44)	0.544, 0.451
THF	428sh (1000) 373 (1900)	589	12.0	6400	3739 (0.46)	0.525, 0.446
Dichloromethane	427sh (2500) 373 (6500) 271sh (71900) 255 (98000) ^d	587 760	5.5 0.5	6400	6442 (0.8)	0.463, 0.449

^a $\Delta\tilde{\nu} = \frac{1}{\lambda_{\text{max,abs}}} - \frac{1}{\lambda_{\text{max,em}}}$. ^b FWHM = full width at half maximum. ^c Refers to a transparent solution of the respective compound, not an OLED device. ^d In toluene and THF, the absorption measurement starts above 285 nm because of solvent absorption below 285 nm.

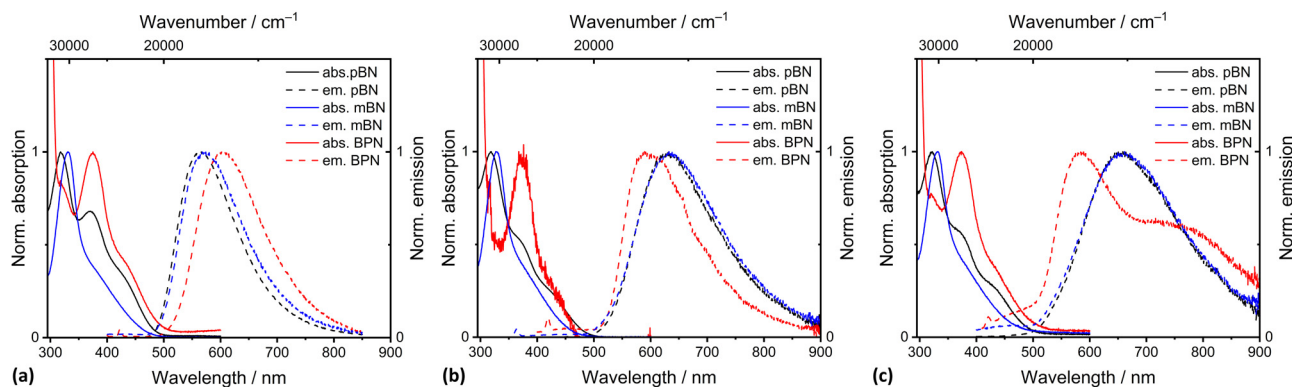


Fig. 3 Absorption and emission spectra ($\lambda_{\text{exc}} = \lambda_{\text{max,abs}}$) of **pBN**, **mBN** and **BPN** recorded in (a) toluene, (b) THF, and (c) dichloromethane. $c = 10^{-5} \text{ mol L}^{-1}$, $T = 293 \text{ K}$.

2 in the luminescence decay times of the luminescence of **BPN** in these two solvents.

In addition, all chromophores show a higher energy absorption maximum of around 250 nm (Fig. S17, S19, S21, ESI† and Table 1), which might be assigned to $\pi-\pi^*$ transitions. This absorption is only seen in dichloromethane because toluene and THF are not transparent at this wavelength. While the molar absorption coefficients of the longest wavelength absorption bands were low, the higher energy absorption bands are characterized by molar absorption coefficients of up to $98000 \text{ L mol}^{-1} \text{cm}^{-1}$. The spectral features of the ground state,

as reflected by the absorption characteristics, indicate that **pBN** and its phenylene expanded congener **BPN** are not only similar, but the ground state is largely insensitive to the change of polarity. Due to steric effects, a significant twist of the *N*-aryl substituents can be plausibly assumed in the ground state as is also indicated by single crystal structural data (Fig. 2). Yet, the electron-withdrawing nitrile substituent is positioned in conjugation with the phenazine-5,10-diyl nitrogen atoms. For **mBN**, this conjugative pathway is excluded due to the *meta*-positioning of the nitrile group, as indicated by the hypsochromic shift with respect to the maxima of the former two chromophores.



The spectral features of the excited states of the constitutional isomers **pBN** and **mBN** represented by the spectral ranges of their emission are mutually more similar than for the phenylene expanded system **BPN**. The positive emission solvatochromicity of the former indicates a polar excited state arising from a charge transfer from the phenazinediyl donor to the benzonitrile acceptor. The expansion of the π -system in **BPN** leads to negative emission solvatochromicity and hence to a less polar excited state. However, peculiar for the latter system is the occurrence of a second longer wavelength emission band at 760 nm in dichloromethane, which could either indicate a twisted intramolecular charge transfer (TICT) state^{41–44} or phosphorescence. Especially the latter type of transition should, however, be strongly prone to non-radiative relaxation in solution. **BPN** can be divided into a donor (phenazinediyl) and an acceptor (biaryl) moiety linked by a single bond. Upon excitation from the ground state, the locally excited (LE) state with a planar conformation can rapidly equilibrate with an intramolecular twisted charge transfer state of lower energy.⁴⁵ This often results in dual emission with a high energy band through relaxation of the LE state (587 nm) and a low energy band by relaxation of the TICT state (760 nm). In a less polar solvent, like THF, the LE state is slightly energetically increased, but due to lower solvent polarity, the TICT state cannot be stabilized. Only in dichloromethane can the twisted CT state be stabilized and therefore be observed. This might explain the recorded negative emission solvatochromicity. The phenomenon of TICT has previously been observed for biphenyls and terphenyls.^{46,47}

Solid state. The solid-state luminescence/emission spectra were measured as a function of temperature from 79 K to 473 K to investigate potential TADF properties. The luminescence intensity of all phenazinediyl derivatives decreases with increasing temperatures (see Fig. S11, ESI†). At 79 K, **pBN** shows a broad emission with a maximum at $\lambda_{\text{em}} \approx 565$ nm and a shoulder peak at around 590 nm (Fig. 4a). With higher temperatures, the emission band evolves into a more symmetric Gaussian band shape. An interesting peculiarity is that the emission maximum shows an initial thermally induced blue shift between 79 K and 273 K before it shows a red shift above 273 K. This observation indicates thermal occupation of

a higher excited emissive state already in the low-temperature domain before.

mBN features an emission maximum at $\lambda_{\text{em}} \approx 537$ nm with a shoulder at 522 nm upon excitation at $\lambda_{\text{exc}} = 420$ nm at 79 K. With increasing temperature, the shoulder is not resolved anymore due to vibronic broadening. The barycenter of the emission band becomes thermally redshifted (Fig. 4b) in the whole regarded temperature range. The location of the emission maximum at shorter wavelengths compared to **pBN** at 79 K is assigned to the *meta* position of the nitrile functionalities that limits effective linear charge transfer from the phenazinediyl unit mediated through the phenyl moieties and thus, should lead to expectedly less pronounced TADF properties.

The emission spectra of solid **BPN** at 79 K show a vibronic fine structure (Fig. 4c). The maximum is located at $\lambda_{\text{em}} \approx 583$ nm and is also redshifted with increasing temperature accompanied by a loss in the resolution of the vibronic fine structure. Together with the findings of nearly no solvatochromism of the respective emission of **BPN** in toluene, THF, and CH_2Cl_2 , the observation of vibronic structure in the powder luminescence spectra at low temperatures indicate emission from a LE state. Both this observation and the redshifted luminescence in **BPN** compared to **mBN/pBN** can be rationalized by the donor–acceptor distances in the molecule due to the presence of the additional phenylene moiety (see Fig. 1). Charge transfer interaction strength roughly scales inversely exponentially with the donor–acceptor distance, which should be expectedly weakened in the large **BPN** molecule.⁴⁸ In addition, the twisted configuration between the intermediate phenyl ring and the benzonitrile moiety additionally minimizes orbital overlap thereby localizing electron density.

Fig. 5 depicts the temperature-dependent time-resolved luminescence of the three phenazinediyl derivatives. **pBN** shows clear signatures of TADF such as a prompt component in the ns range ($\tau_{\text{p}}(79 \text{ K}) = 11 \text{ ns}$; $\tau_{\text{p}}(273 \text{ K}) = 6.2 \text{ ns}$) and delayed time component in the μs range ($\tau_{\text{d}}(79 \text{ K}) = 2.0 \mu\text{s}$; $\tau_{\text{d}}(273 \text{ K}) = 0.3 \mu\text{s}$) as well as a temperature-dependent amplitude ratio between the prompt and delayed component. This is in line with the observable thermally-assisted blueshift of the emission below 272 K (Fig. 4a). From the delayed components at low temperatures ($T < 220 \text{ K}$), an effective singlet–triplet gap of

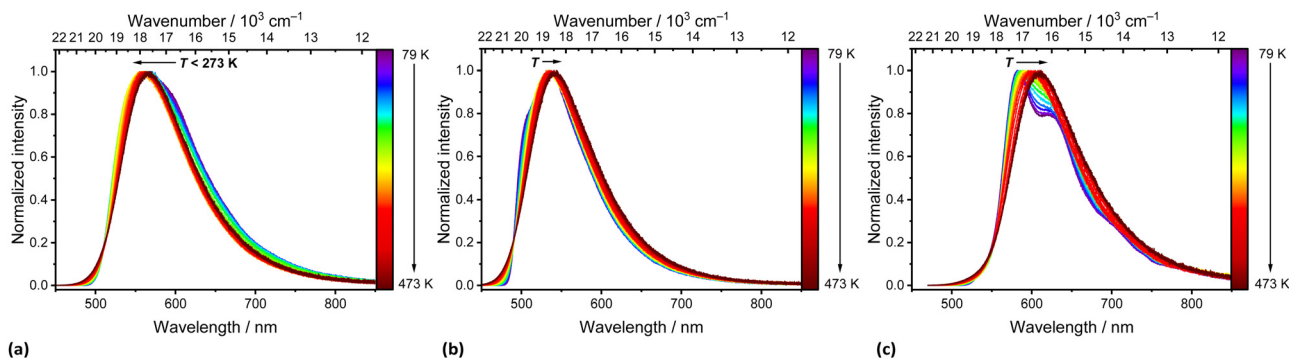


Fig. 4 Temperature-dependent emission spectra of solid (a) **pBN**, (b) **mBN**, and (c) **BPN** upon excitation at $\lambda_{\text{exc}} = 420$ nm (a, b) and 450 nm (c). Temperature intervals were $\Delta T = 25 \text{ K}$.



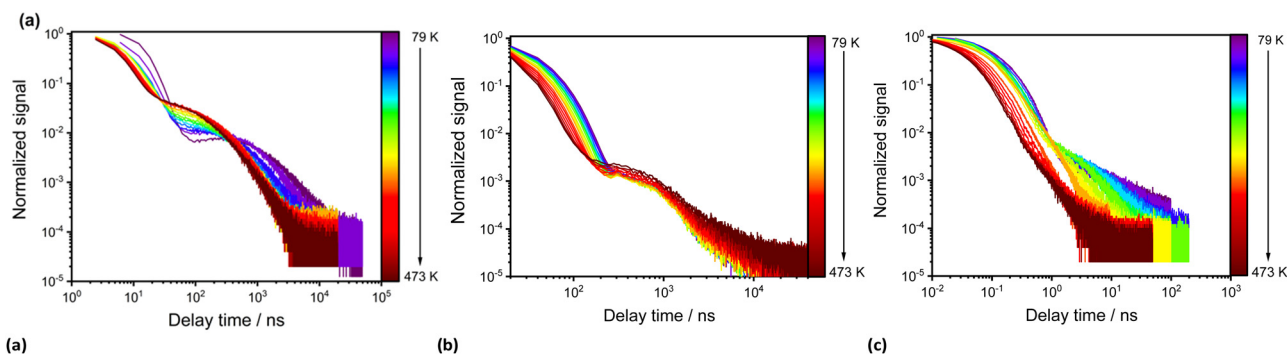


Fig. 5 Temperature-dependent time-resolved photoluminescence of solid (a) **pBN**, (b) **mBN** and (c) **BPN** upon excitation at $\lambda_{\text{exc}} = 450$ nm. Temperature intervals were $\Delta T = 25$ K.

$\Delta E_{\text{ST}} = (174 \pm 3) \text{ cm}^{-1} = (21.5 \pm 0.4) \text{ meV}$ was derived (Fig. S14, ESI[†]), which is in agreement with the spectroscopically deduced value of $\Delta E_{\text{ST}} \approx 200 \text{ cm}^{-1}$ (25 meV) based on the energy difference of the emission maxima at 79 K and 273 K of **pBN** (Fig. S16, ESI[†]). Our derived energy gap is lower than the literature-reported value of $\Delta E_{\text{ST}} = 806 \text{ cm}^{-1}$ (100 meV), which refers, however, to a 6 wt% **pBN**:*m*-CBP doped thin film and was solely estimated based on the energy difference between noisy spectra.³³ In a neat powder, additional intermolecular interactions and aggregate formation expectedly decrease the energy gap consistent with our finding. Another aspect that can affect the energy gap by means of the effective orbital overlap is the relative twisting angle of the benzonitrile moieties to the central dihydrophenazine residue. This angle is fixed in a crystalline solid and may differ from the respective angle upon doping into a thin film. In contrast, **mBN** (Fig. 4b) shows weak TADF properties with a more dominant prompt ($\tau_{\text{p}}(79 \text{ K}) = 33 \text{ ns}$; $\tau_{\text{p}}(273 \text{ K}) = 24 \text{ ns}$) and weakly defined delayed component ($\tau_{\text{d}}(79 \text{ K}) = 0.9 \mu\text{s}$; $\tau_{\text{d}}(273 \text{ K}) = 0.6 \mu\text{s}$) with an average singlet–triplet gap of $\Delta E_{\text{ST}} = (38 \pm 6) \text{ cm}^{-1} = (4.7 \pm 0.8) \text{ meV}$ (Fig. S15, ESI[†]). No TADF properties are observed for **BPN** (Fig. 4c) and it shows conventional fluorescence with decay times in the ns range ($\tau_{\text{p}}(79 \text{ K}) = 14 \text{ ns}$; $\tau_{\text{p}}(273 \text{ K}) = 8.6 \text{ ns}$). Unfortunately, no non-radiative intersystem crossing rates are readily accessible with our spectroscopic equipment that would allow a more detailed analysis of the TADF kinetics. It is, however, evident that only **pBN** is a potent TADF emitter with reasonable photoluminescence quantum yield ($\phi_{\text{PL}} = 35.8\%$) if doped into a thin film (as the literature-reported 6 wt% **pBN**:*m*-CBP doped film).³³ Its absolute quantum yield in powdered form is much lower ($\phi_{\text{PL}} = 1.00\%$), which is understandable given the close contacts between the molecules within the crystalline solid (see section S4 in the ESI[†]) and agrees with the significant quenching of the luminescence at room temperature (see Fig. S11, ESI[†]). A similar low quantum yield of only 3.3% was found for **pBN** in aerated toluene solution with no observation of any delayed fluorescence at all.³³ From the time-resolved photoluminescence of **pBN** at room temperature (see Fig. 5), we derive that the prompt and delayed components have almost equal contributions ($\phi_{\text{p}}(\text{pBN}) = 0.46\%$, $\phi_{\text{d}}(\text{pBN}) = 0.54\%$), also in agreement with the findings in a thin film.³³ Similarly, the absolute quantum yields of powdered **mBN** ($\phi_{\text{PL}} = 3.10\%$; $\phi_{\text{p}}(\text{mBN}) = 2.97\%$, $\phi_{\text{d}}(\text{mBN}) = 0.13\%$) are low and

dominantly stem from prompt fluorescence according to the time-resolved luminescence at room temperature (see Fig. 5). This again indicates that **mBN** is just at the boundary of being a TADF emitter. Finally, also the fluorescence of powdered **BPN** ($\phi_{\text{PL}} = 2.80\%$) is significantly quenched at room temperature, which makes these compounds not readily applicable organic emitters if used as neat powders and requires dilution or doping into thin films.

Theoretical calculations

The DFT/MRCI-computed vertical excitation energies to the HOMO–LUMO S_1 -state in **pBN**, **BPN** and **mBN** in a vacuum are 402, 415 and 401 nm, respectively. **BPN** and **pBN** have zero oscillator strength of the $S_0 \rightarrow S_1$ transition, and the computed value for f in **mBN** is weak (0.01) (Table S4, ESI[†]). This results from a lack of overlap between the participating orbitals (Fig. S31, ESI[†]). The first states with noticeable intensity are S_4 in **BPN** ($f = 0.10$) and in **pBN** ($f = 0.09$) and S_6 in **mBN** ($f = 0.14$) (Fig. 6). Similar findings hold true for the S_1 structures and the corresponding vertical emission from this state. In the S_1 geometry, the phenazine moiety flattens and becomes essentially planar (Fig. S26, ESI[†]).

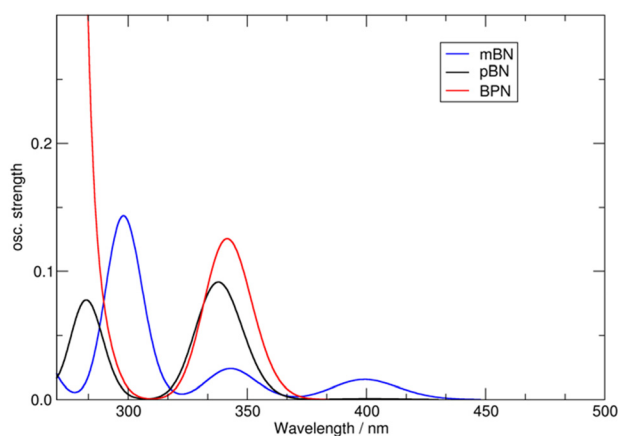


Fig. 6 DFT/MRCI computed static absorption spectra of **pBN**, **mBN** and **BPN** in vacuum.

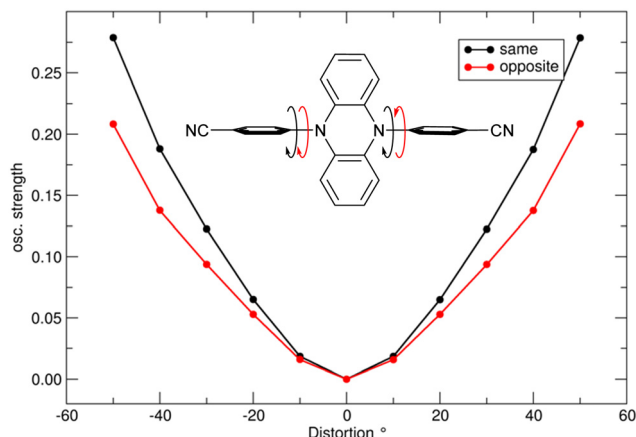


Fig. 7 Unrelaxed dihedral scan for phenyl-rotation in **pBN** showing oscillator strength (same and opposite directions of phenyl ring rotation, the starting point corresponds to the perpendicular arrangement (90°) of phenazine and phenyl rings); see also Fig. S26 (ESI †) for the energy profile.

Notably, the lowest triplet state at the S_0 geometry is not of HOMO–LUMO character but rather mixed in all models (Table S4, ESI †).

The oscillator strength of both S_1 absorption and emission are, however, tuned by motion of the phenyl rings with respect to the phenazine core as depicted in Fig. 7.

Hence, low-frequency normal mode vibrations ($\sim 21\text{ cm}^{-1}$, Fig. S28, ESI †) increase the absorption intensity and slightly shift the corresponding bands, which appear in our zero-point energy (ZPE) simulated absorption spectrum as shoulders at *ca.* 405 nm (**mBN**) and 415 nm (**pBN**) (Fig. 8).

Through ZPE sampling, we note only a slight enhancement in the emission intensity ($f < 0.002$, Fig. S29, ESI †). Here, the normal mode including torsion of the phenyl rings is shifted towards slightly higher frequencies ($34\text{ vs. }21\text{ cm}^{-1}$). The emission bands gain additional intensity ($f \sim 0.008$) after including temperature effects. In our simulation at 300 K the emission bands appear at 547 nm (**mBN**) and 573 nm (**pBN**). Thermal sampling at the S_0 geometry leads to unphysical

distortions indicating the limits of the harmonic approximation in this model.

Variations in phenyl torsions furthermore affect the singlet–triplet gap, this finding is visualized in Fig. S29 (ESI †). The effect is significantly stronger in **pBN**, where ΔE_{ST} decreases from 105 meV to 34 meV by rotation of one phenyl moiety by only -15° (left graph in Fig. S30, ESI †). Fixation in this position through an external force (such as exerted in a rigid crystal structure) may enable efficient tuning of its emission properties and offers an explanation for the difference between the originally reported value of $\Delta E_{ST} = 100\text{ meV}$ in the 6 wt% **mBN**:*m*-CBP doped thin film and our slightly smaller value (22 meV).³³

Conclusions

The investigated compounds 3,3'-(phenazine-5,10-diyl)dibenzonitrile (**mBN**) and 4',4'''-(phenazine-5,10-diyl)bis([1,1'-biphenyl]-4-carbonitrile) (**BPN**) do not show any evident TADF behavior compared to 4,4'-(phenazine-5,10-diyl)dibenzonitrile (**pBN**) known from the literature. This indicates that even slight changes in the molecular structure have a significant effect on the photophysical properties of the molecules. Thus, **pBN** exhibits unique TADF properties both in the solid state and in liquid solution. In the solid state, **pBN** exhibits a decay time that is in the microsecond range over the entire temperature range measured, along with a blue shift of the emission maximum at temperatures below 220 K. The effective singlet–triplet gap here is $\Delta E_{ST} = (174 \pm 3)\text{ cm}^{-1} = (21.5 \pm 0.4)\text{ meV}$ as derived from temperature-dependent time-resolved luminescence data. **mBN** only exhibits very weak TADF properties with an effective estimated exchange energy gap below 10 meV. We assign this marked difference between **pBN** and **mBN** in their TADF behavior to the minimized orbital overlap in the latter case given by the *meta*-substitution pattern of the nitrile functionalities. Apart from that, the two emitters are strongly related, which is reflected in their similar emission wavelengths and solvatochromism. The emission spectra are broad and featureless, which indicates a CT-like character of the electronic transition in both compounds. In contrast, **BPN** is a conventional fluorescent emitter and shows a vibronic fine structure indicating an emissive localized state. Their emission maxima are strongly dependent on the solvent, indicating a CT-like character of the excited state. Overall, it can be seen that TADF donor–acceptor-type emitters follow clear electronic guidelines that can be structurally controlled on a molecular scale and within the solid.

Materials and methods

The purity of the compounds was determined by NMR spectroscopy, elemental analysis, high-resolution mass spectrometry and single crystal structure analysis (for details, see the ESI †).

Solid state optical measurements were performed using an FLS1000 photoluminescence spectrometer from Edinburgh Instruments equipped with a 450 W Xe arc lamp as an excitation source, double excitation and emission monochromators

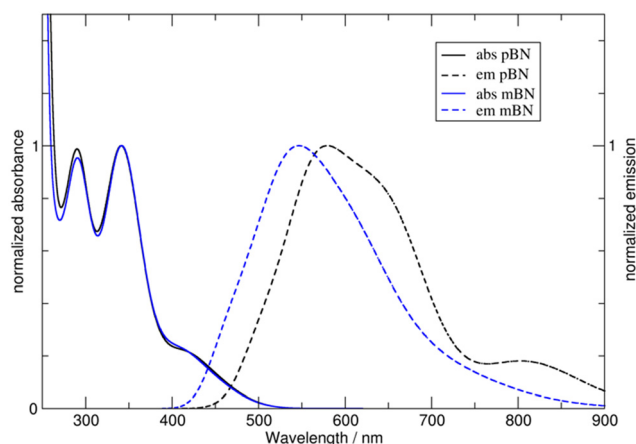


Fig. 8 Combined calculated absorption and emission spectra from vibrational sampling in toluene.



in Czerny–Turner configuration and a thermoelectrically cooled ($-20\text{ }^{\circ}\text{C}$) photomultiplier tube PMT-980 from Hamamatsu. The emission spectra were corrected with respect to the grating efficiency and PMT sensitivity, while excitation spectra were additionally corrected with respect to the lamp intensity. Time-resolved photoluminescence was excited with pulsed laser diodes EPL-450 (Edinburgh Instruments, temporal pulse width: 90 ps, 0.15 mW average incident peak power) or VPL-450 (Edinburgh Instruments, 90 mW average incident peak power in CW mode) with adjustable temporal pulse width (0.1 ms...1 ms) and variable trigger frequency (0.1 Hz...5 MHz) as pulsed excitation sources. The detection mode for the time-resolved measurements was time-correlated single photon counting. Absolute quantum yields at room temperature were measured with a BenFlect[®]-covered integrating sphere and excitation wavelength of 420 nm in all three regarded compounds.

Solution state absorption spectra were recorded in toluene, tetrahydrofuran and CH_2Cl_2 of high-performance liquid chromatography (HPLC) grade at 293 K on a PerkinElmer UV/Vis/NIR Lambda 19 spectrometer. For the determination of the molar extinction coefficients ϵ absorption measurements at five different concentrations were carried out. Emission spectra and fluorescence lifetimes were recorded in toluene, tetrahydrofuran and CH_2Cl_2 of HPLC grade at 293 K using an Edinburgh FS5 spectrometer. As light sources a 150 W xenon lamp as well as pulsed EPLED-320 (Edinburgh Instruments, 313.5 nm, temporal pulse width: 950 ps, 3 μW average incident peak power) and EPL-375 (Edinburgh Instruments, 372.2 nm, temporal pulse width: 76 ps, 0.15 mW average incident power) laser sources were used.

Computations

Single-molecule structures of **pBN**, **mBN** and **BPN** were geometry-optimized with Gaussian16,⁴⁹ taking the crystal structure data as input. Calculations were performed with the PBE0 functional,⁵⁰ the TZVP basis set⁵¹ and Grimme D3 dispersion corrections⁵² in vacuum and in toluene solvent applying the PCM model. TD-DFT was used for the excited S_1 and T_1 states. Vibrational analysis ensured that the obtained structures were true minima with no imaginary frequencies. For the computation of spectral properties, the optimized structures were recomputed at the BH-LYP/TZVP level of theory using Turbomole 7.5.⁵³ Solvation was considered with the COSMO model.⁵⁴ A DFT/MRCI computation was then performed with the R2022 Hamiltonian,⁵⁵ the tight parameter set and an energy selector of $0.8E_{\text{h}}$. The starting wavefunction was computed including eight orbitals and eight electrons with single and double excitations. An updated reference space was obtained by performing a second run with the same parameters to yield the final values for energies and oscillator strengths. Combined unrelaxed scans along the dihedral angles involving the phenyl rings were applied to document changes in ΔE_{ST} and oscillator strengths f .

Vibrational effects in emission and absorption data were considered by sampling the vibrational modes (zero-point-energy (ZPE) sampling) generating 200 structures for each molecule and state in **pBN** and **mBN**. Thermal sampling at a temperature of

300 K was performed in addition to the S_1 structures. After orbital computation with BH-LYP and the SV(P) basis, the resulting geometries were processed with DFT/MRCI and the R2016 Hamiltonian⁵⁶ using the same selector choices stated above. The final spectra with vibrational contributions were obtained by Gaussian broadening using a FWHM of 0.3 eV.

Author contributions

Conceptualization: D. P. and M. S.; methodology: D. P., J. W., T. H. and M. S.; validation: D. P.; formal analysis: D. P., J. W., T. H., L. P. and M. S.; investigation: D. P., J. W., T. H., L. P. and M. S.; resources: M. S., T. J. J. M. and C. J.; data curation: D. P., J. W., T. H. and M. S.; writing – original draft preparation: D. P. and J. W.; writing – review and editing: D. P., M. S., T. J. J. M. and C. J.; visualization: D. P., J. W. and C. J.; supervision: C. J.; project administration: C. J.; funding acquisition: M. S., T. J. J. M. and C. J.

Conflicts of interest

The authors declare that they have no known competing financial interests or personal relationship that could have appeared to influence the work reported in this paper.

Acknowledgements

D. P., J. W., T. J. J. M. and C. J. thank the Deutsche Forschungsgemeinschaft (DFG, German Research Foundation) for grant 396890929/GRK 2482 and grant Mu 1088/9-1. The Rigaku X-ray diffractometer was funded by the DFG through grant 440366605. M. S. gratefully acknowledges funding from a materials cost allowance of the Fonds der Chemischen Industrie e. V. and the “Junges Kolleg” of the North Rhine-Westphalian Academy of Sciences and Arts. The authors thank Dr István Boldog for his support in the supramolecular analysis of the single crystal structures of **pBN**. We also thank the Center for Molecular and Structural Analytics at Heinrich Heine University (CeMSA@HHU) for recording the mass spectrometric and NMR-spectrometric data.

References

- 1 C. A. Parker and G. G. Hatchard, *Trans. Faraday Soc.*, 1961, 57, 1894–1904, DOI: [10.1039/TF9615701894](https://doi.org/10.1039/TF9615701894).
- 2 R. Delorme and F. Perrin, *J. Phys. Radium*, 1929, 10, 177–186, DOI: [10.1051/jphysrad:01929001005017700](https://doi.org/10.1051/jphysrad:01929001005017700); J. Perrin and N. Choucroun, Fluorescence sensibilisée en milieu liquide (transfert d'activation par induction moléculaire), *Comptes Rendus*, 1929, 189, 1213–1216; F. Perrin and J. Perrin, Activation et deactivation par induction moléculaire, *Activation et structure des molécules: Rapports et discussions*, 1929, pp. 354–382.
- 3 M. N. Berberan-Santos, Pioneering Contributions of Jean and Francis Perrin to Molecular Luminescence, in *New*



- Trends in Fluorescence Spectroscopy*, ed. B. Valeur and J. C. Brochon, Springer Series on Fluorescence, Springer, Berlin, Heidelberg, 2001, vol. 1, DOI: [10.1007/978-3-642-56853-4_2](https://doi.org/10.1007/978-3-642-56853-4_2).
- 4 H. Uoyama, K. Goushi, K. Shizu, H. Nomura and C. Adachi, *Nature*, 2012, **492**, 234–238, DOI: [10.1038/nature11687](https://doi.org/10.1038/nature11687).
 - 5 A. Endo, K. Sato, K. Yoshimura, T. Kai, A. Kawada, H. Miyazaki and C. Adachi, *Appl. Phys. Lett.*, 2011, **98**, 42, DOI: [10.1063/1.3558906](https://doi.org/10.1063/1.3558906).
 - 6 M. Y. Wong and E. Zysman-Colman, *Adv. Mater.*, 2017, **29**, 1605444, DOI: [10.1002/adma.201605444](https://doi.org/10.1002/adma.201605444).
 - 7 M. K. Manna, S. Shokri, G. P. Wiederrecht, D. J. Gosztola and A. J.-L. Ayitou, *Chem. Commun.*, 2018, **54**, 5809–5818, DOI: [10.1039/C8CC01553H](https://doi.org/10.1039/C8CC01553H).
 - 8 T. Chatterjee and K.-T. Wong, *Adv. Opt. Mater.*, 2018, **7**, 1800565, DOI: [10.1002/adom.201800565](https://doi.org/10.1002/adom.201800565).
 - 9 X. Yin, Y. He, X. Wang, Z. Wu, E. Pang, J. Xu and J. Wang, *Front. Chem.*, 2020, **8**, 725, DOI: [10.3389/fchem.2020.00725](https://doi.org/10.3389/fchem.2020.00725).
 - 10 S. Achelle, M. Hodée, J. Massue, A. Fihey and C. Katan, *Dyes Pigm.*, 2022, **200**, 110157, DOI: [10.1016/j.dyepig.2022.110157](https://doi.org/10.1016/j.dyepig.2022.110157).
 - 11 X. Wang, S. Gao, M. Zhao and N. Marom, *Phys. Rev. Res.*, 2022, **4**, 033147, DOI: [10.1103/PhysRevResearch.4.033147](https://doi.org/10.1103/PhysRevResearch.4.033147).
 - 12 C. Li, A. K. Harrison, Y. Liu, Z. Zhao, C. Zeng, F. B. Dias, Z. Ren, S. Yan and M. R. Bryce, *Angew. Chem. Int. Ed.*, 2022, **61**, e20211540, DOI: [10.1002/anie.202115140](https://doi.org/10.1002/anie.202115140).
 - 13 L. Hua, Y. Liu, B. Liu, Z. Zhao, L. Zhang, S. Yan and Z. Ren, *Nat. Commun.*, 2022, **13**, 7828, DOI: [10.1038/s41467-022-35591-w](https://doi.org/10.1038/s41467-022-35591-w).
 - 14 T. Hosokai, H. Matsuzaki, H. Nakanotani, K. Tokumaru, T. Tsutsui, A. Furube, K. Nasu, H. Nomura, M. Yahiro and C. Adachi, *Sci. Adv.*, 2017, **3**, e1603282, DOI: [10.1126/sciadv.1603282](https://doi.org/10.1126/sciadv.1603282).
 - 15 Y. Yu, L. Ma, Z. Feng, B. Liu, H. Zhou, H. Qin, H. Li, J. Song, G. Zhou and Z. Wu, *J. Mater. Chem. C*, 2019, **7**, 5604–5614, DOI: [10.1039/C9TC00789J](https://doi.org/10.1039/C9TC00789J).
 - 16 T. B. Nguyen, H. Nakanotani, T. Hatakeyama and C. Adachi, *Adv. Mater.*, 2020, **32**, 1906614, DOI: [10.1002/adma.201906614](https://doi.org/10.1002/adma.201906614).
 - 17 J. Wiefermann, P. Schmeinck, C. Ganter and T. J. J. Müller, *Chem. – Eur. J.*, 2022, **28**, e202200576, DOI: [10.1002/chem.202200576](https://doi.org/10.1002/chem.202200576).
 - 18 T. J. Penfold, E. Gindensperger, C. Daniel and C. M. Marian, *Chem. Rev.*, 2018, **118**, 6975–7025, DOI: [10.1021/acs.chemrev.7b00617](https://doi.org/10.1021/acs.chemrev.7b00617).
 - 19 D. Hu, L. Yao, B. Yang and Y. Ma, *Philos. Trans. R. Soc., A*, 2015, **373**, 20140318, DOI: [10.1098/rsta.2014.0318](https://doi.org/10.1098/rsta.2014.0318).
 - 20 I. Lyskov and C. M. Marian, *J. Phys. Chem. C*, 2017, **121**, 21145–21153, DOI: [10.1021/acs.jpcc.7b06187](https://doi.org/10.1021/acs.jpcc.7b06187).
 - 21 J. Gibson, A. Monkman and T. Penfold, *Chem. Phys. Chem.*, 2016, **17**, 2956–2961, DOI: [10.1002/cphc.201600662](https://doi.org/10.1002/cphc.201600662).
 - 22 M. Inoue, T. Serevicius, H. Nakanotani, K. Yoshida, T. Matsushima, S. Jursenas and C. Adachi, *Chem. Phys. Lett.*, 2016, **644**, 62–67, DOI: [10.1016/j.cplett.2015.11.042](https://doi.org/10.1016/j.cplett.2015.11.042).
 - 23 J. Wiefermann, J. M. Kaminski, E. Pankert, D. Hertel, K. Meerholz, C. M. Marian and T. J. J. Müller, *ChemPhotoChem*, 2023, **7**, e202200265, DOI: [10.1002/cptc.202200265](https://doi.org/10.1002/cptc.202200265).
 - 24 Y. Liu, C. Li, Z. Ren, S. Yan and M. R. Bryce, *Nat. Rev. Mater.*, 2018, **3**, 18020, DOI: [10.1038/natrevmats.2018.20](https://doi.org/10.1038/natrevmats.2018.20).
 - 25 I. Marghad, D. H. Kim, X. Tian, F. Mathevet, C. Gosmini, J.-C. Ribierre and C. Adachi, *ACS Omega*, 2018, **3**, 2254–2260, DOI: [10.1021/acsomega.7b01570](https://doi.org/10.1021/acsomega.7b01570).
 - 26 R. K. Konidena, J. Lim and J. Y. Lee, *Chem. Eng. J.*, 2021, **416**, 129097, DOI: [10.1016/j.cej.2021.129097](https://doi.org/10.1016/j.cej.2021.129097).
 - 27 Z. Zhao, C. Zeng, X. Peng, Y. Liu, H. Zhao, L. Hua, S.-J. Su, S. Yan and Z. Ren, *Angew. Chem. Int. Ed.*, 2022, **61**, e202210864, DOI: [10.1002/anie.202210864](https://doi.org/10.1002/anie.202210864).
 - 28 F. Rodella, S. Bagnich, E. Duda, T. Meier, J. Kahle, S. Athanasopoulos, A. Köhler and P. Strohmriegl, *Front. Chem.*, 2020, **8**, 657, DOI: [10.3389/fchem.2020.00657](https://doi.org/10.3389/fchem.2020.00657).
 - 29 T. Matulaitis, P. Imbrasas, N. A. Kukhta, P. Baronas, T. Bučiūnas, D. Banevičius, K. Kazlauskas, J. V. Gražulevičius and S. Juršėnas, *J. Phys. Chem. C*, 2017, **121**, 23618–23625, DOI: [10.1021/acs.jpcc.7b08034](https://doi.org/10.1021/acs.jpcc.7b08034).
 - 30 E. V. Verbitskiy, R. M. Gadirov, L. G. Samsonova, K. M. Degtyarenko, A. E. Kurtcevic, E. V. Sapozhnikova, M. V. Medvedeva, T. S. Svalova, A. N. Kozitsina, G. L. Rusinov and V. N. Charushin, *Dyes Pigm.*, 2022, **207**, 110716, DOI: [10.1016/j.dyepig.2022.110716](https://doi.org/10.1016/j.dyepig.2022.110716).
 - 31 D. Gudeikaa, O. Bezikonnyia, D. Volyniuka and J. V. Gražuleviciusa, *Dyes Pigm.*, 2020, **172**, 107789, DOI: [10.1016/j.dyepig.2019.107789](https://doi.org/10.1016/j.dyepig.2019.107789).
 - 32 J. Lee, K. Shizu, H. Tanaka, H. Nomura, T. Yasuda and C. Adachi, *J. Mater. Chem. C*, 2013, **1**, 4599–4604, DOI: [10.1039/C3TC30699B](https://doi.org/10.1039/C3TC30699B).
 - 33 J. Lee, K. Shizu, H. Tanaka, H. Nakanotani, T. Yasuda, H. Kaji and C. Adachi, *J. Mater. Chem. C*, 2015, **3**, 2175–2181, DOI: [10.1039/c4tc02530j](https://doi.org/10.1039/c4tc02530j).
 - 34 S.-J. Woo, Y. Kim, M.-J. Kim, J. Y. Baek, S.-K. Kwon, Y.-H. Kim and J.-J. Kim, *Chem. Mater.*, 2018, **30**, 857–863, DOI: [10.1021/acs.chemmater.7b04437](https://doi.org/10.1021/acs.chemmater.7b04437).
 - 35 Y. Im, M. Kim, Y. J. Cho, J.-A. Seo, K. S. Yook and J. Y. Lee, *Chem. Mater.*, 2017, **29**, 1946–1963, DOI: [10.1021/acs.chemmater.6b05324](https://doi.org/10.1021/acs.chemmater.6b05324).
 - 36 J. C. Theriot, C.-H. Lim, H. Yang, M. D. Ryan, C. B. Musgrave and G. M. Miyake, *Science*, 2016, **352**, 1082–1086, DOI: [10.1126/science.aaf3935](https://doi.org/10.1126/science.aaf3935).
 - 37 Q. Wan, Y. Li, K. Ding, Y. Xie, J. Fan, J. Tong, Z. Zeng, Y. Li, C. Zhao, Z. Wang and B. Z. Tang, *J. Am. Chem. Soc.*, 2023, **145**, 1607–1616, DOI: [10.1021/jacs.2c09210](https://doi.org/10.1021/jacs.2c09210).
 - 38 M. J. Kamlet, J. L. Abboud and R. W. Taft, *J. Am. Chem. Soc.*, 1977, **99**, 6027–6038, DOI: [10.1021/ja00460a031](https://doi.org/10.1021/ja00460a031).
 - 39 *Principles of Fluorescence Spectroscopy*, ed. J. R. Lakowicz, Springer US, Boston, MA, 2006.
 - 40 D. Toptygin, *J. Fluoresc.*, 2003, **13**, 201–219, DOI: [10.1023/A:1025033731377](https://doi.org/10.1023/A:1025033731377).
 - 41 W. Rettig and M. Zander, *Chem. Phys. Lett.*, 1982, **87**, 229–234, DOI: [10.1016/0009-2614\(82\)83131-X](https://doi.org/10.1016/0009-2614(82)83131-X).
 - 42 Z. R. Grabowski and J. Dobkowski, *Pure Appl. Chem.*, 1983, **55**, 245–252, DOI: [10.1351/pac198855020245](https://doi.org/10.1351/pac198855020245).
 - 43 C. Wang, W. Chi, Q. Qiao, D. Tan, Z. Xu and X. Liu, *Chem. Soc. Rev.*, 2021, **50**, 12656–12678, DOI: [10.1039/D1CS00239B](https://doi.org/10.1039/D1CS00239B).



- 44 A. M. El-Zohry, E. A. Orabi, M. Karlsson and B. Zietz, *J. Phys. Chem. A*, 2021, **125**, 2885–2894, DOI: [10.1021/acs.jpca.1c00629](https://doi.org/10.1021/acs.jpca.1c00629).
- 45 S. Sasaki, G. P. C. Drummen and G. Konishi, *J. Mater. Chem. C*, 2016, **4**, 2731–2743, DOI: [10.1039/C5TC03933A](https://doi.org/10.1039/C5TC03933A).
- 46 S. Delmond, J.-F. Létard, R. Lapouyade and W. Rettig, *J. Photochem. Photobiol., A*, 1997, **105**, 135–148, DOI: [10.1016/S1010-6030\(96\)04544-3](https://doi.org/10.1016/S1010-6030(96)04544-3).
- 47 S. Sharm, Z. Wei, T. C. Grozema and S. Sengupta, *Phys. Chem. Chem. Phys.*, 2020, **22**, 25514–25521, DOI: [10.1039/d0cp04579a](https://doi.org/10.1039/d0cp04579a).
- 48 D. L. Dexter, A Theory of Sensitized Luminescence in Solids, *J. Chem. Phys.*, 1953, **21**, 836–850, DOI: [10.1063/1.1699044](https://doi.org/10.1063/1.1699044).
- 49 M. J. Frisch, G. W. Trucks, H. B. Schlegel, G. E. Scuseria, M. A. Robb, J. R. Cheeseman, G. Scalmani, V. Barone, G. A. Petersson, H. Nakatsuji, X. Li, M. Caricato, A. V. Marenich, J. Bloino, B. G. Janesko, R. Gomperts, B. Mennucci, H. P. Hratchian, J. V. Ortiz, A. F. Izmaylov, J. L. Sonnenberg, D. Williams-Young, F. Ding, F. Lipparini, F. Egidi, J. Goings, B. Peng, A. Petrone, T. Henderson, D. Ranasinghe, V. G. Zakrzewski, J. Gao, N. Rega, G. Zheng, W. Liang, M. Hada, M. Ehara, K. Toyota, R. Fukuda, J. Hasegawa, M. Ishida, T. Nakajima, Y. Honda, O. Kitao, H. Nakai, T. Vreven, K. Throssell, J. A. Montgomery, Jr., J. E. Peralta, F. Ogliaro, M. J. Bearpark, J. J. Heyd, E. N. Brothers, K. N. Kudin, V. N. Staroverov, T. A. Keith, R. Kobayashi, J. Normand, K. Raghavachari, A. P. Rendell, J. C. Burant, S. S. Iyengar, J. Tomasi, M. Cossi, J. M. Millam, M. Klene, C. Adamo, R. Cammi, J. W. Ochterski, R. L. Martin, K. Morokuma, O. Farkas, J. B. Foresman and D. J. Fox, *Gaussian 16, Revision C.01*, Gaussian, Inc., Wallingford CT, 2016.
- 50 C. Adamo and G. E. Scuseria, *J. Chem. Phys.*, 1999, **111**, 2889–2899, DOI: [10.1063/1.479571](https://doi.org/10.1063/1.479571).
- 51 F. Weigend and R. Ahlrichs, *Phys. Chem. Chem. Phys.*, 2005, **7**, 3297–3305, DOI: [10.1039/B508541A](https://doi.org/10.1039/B508541A).
- 52 S. Grimme, J. Antony, S. Ehrlich and H. Krieg, *J. Chem. Phys.*, 2010, **132**, 154104, DOI: [10.1063/1.3382344](https://doi.org/10.1063/1.3382344).
- 53 S. G. Balasubramani, G. P. Chen, S. Coriani, M. Diedenhofen, M. S. Frank, Y. J. Franzke, F. Furche, R. Grotjahn, M. E. Harding, C. Hättig, A. Hellweg, B. Helmich-Paris, C. Holzer, U. Huniar, M. Kaupp, A. Marefat Khah, S. Karbalaee Khani, T. Müller, F. Mack, B. D. Nguyen, S. M. Parker, E. Perlt, D. Rappoport, K. Reiter, S. Roy, M. Rückert, G. Schmitz, M. Sierka, E. Tapavicza, D. P. Tew, C. van Wüllen, V. K. Voora, F. Weigend, A. Wodyński and J. M. Yu, Turbomole: Modular program suite for ab initio quantum-chemical and condensed-matter simulations, *J. Chem. Phys.*, 2020, **152**, 184107, DOI: [10.1063/5.0004635](https://doi.org/10.1063/5.0004635).
- 54 A. Klamt and G. Schüürmann, *J. Chem. Soc., Perkin Trans. 2*, 1993, 799–805, DOI: [10.1039/P29930000799](https://doi.org/10.1039/P29930000799).
- 55 D. R. Dombrowski, T. Schulz, M. Kleinschmidt and C. M. Marian, *J. Chem. Phys. A*, 2023, **127**, 2011–2025, DOI: [10.1021/acs.jpca.2c07951](https://doi.org/10.1021/acs.jpca.2c07951).
- 56 I. Lyskov, M. Kleinschmidt and C. M. Marian, *J. Chem. Phys.*, 2016, **144**, 034104, DOI: [10.1063/1.4940036](https://doi.org/10.1063/1.4940036).



Electronic Supplementary Information (ESI)

Molecular design of thermally activated delayed fluorescence properties of phenazine-5,10-diyl-dibenzonitriles†

Dietrich Püschel,¹ Julia Wiefermann,² Simon Hédé,³ Tobias Heinen,¹ Leo Pfeifer,¹ Oliver Weingart,^{3,*} Markus Suta,^{1,*} Thomas J. J. Müller,^{2,*} Christoph Janiak^{1,*}

1 Institut für Anorganische Chemie und Strukturchemie, Heinrich-Heine-Universität Düsseldorf, Universitätsstraße 1, D-40225 Düsseldorf, Germany

E-Mail: Markus.Suta@hhu.de, Janiak@uni-duesseldorf.de

2 Institut für Organische Chemie und Makromolekulare Chemie, Heinrich-Heine-Universität Düsseldorf, Universitätsstraße 1, D-40225 Düsseldorf, Germany

E-Mail: ThomasJJ.Mueller@hhu.de

3 Institute for Theoretical Chemistry and Computational Chemistry, Heinrich-Heine-Universität Düsseldorf, Universitätsstraße 1, D-40225 Düsseldorf, Germany

E-mail: Oliver.Weingart@hhu.de

Emails: dietrich.pueschel@hhu.de, julia.wiefermann@hhu.de, hede@hhu.de, t.heinen@hhu.de, leo.pfeifer@hhu.de, Oliver.Weingart@hhu.de, markus.suta@hhu.de, thomasJJ.Mueller@hhu.de, janiak@hhu.de

Content

- S1 Sources of chemicals**
- S2 Synthesis**
- S3 Crystal structure details**
- S4 Supramolecular interaction analysis**
- S5 Photophysical properties**
- S6 Quantum chemical calculations**

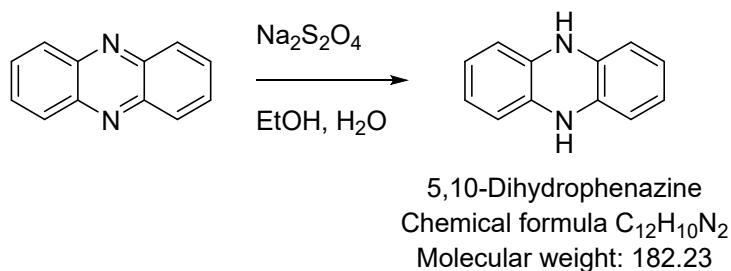
S1 Sources of chemicals

Commercially available reagents were used without further purification.

Items	Manufacturer
Phenazine, 97 %	BLDpharm
3-Bromobenzonitrile	BLDpharm
4-Bromobenzonitrile	fluorochem
4'-Bromo-[1,1'-biphenyl]-4-carbonitrile, 95 %	BLDpharm
Palladium(II) acetate, 98 %	Sigma-Aldrich
Tri- <i>tert</i> -butyl-phosphine	Sigma-Aldrich
Sodium dithionite	VWR Chemicals
Sodium chloride, ≥ 99.5 %	Sigma-Aldrich
Magnesium sulfate	VWR Chemicals
Potassium carbonate	Riedel-de Haen
Toluene, ≥ 99.7 %	Sigma-Aldrich
Ethanol, ≥ 99.8 %	Honeywell
Dichloromethane, ≥ 99.9 %	Sigma-Aldrich
Chloroform, ≥ 99.8 %	Fisher Chemical
n-Hexane, ≥ 99.0 %	VWR Chemicals
Cyclohexane, ≥ 99.8 %	Fisher Chemical

S2 Synthesis

S2.1 5,10-Dihydrophenazine

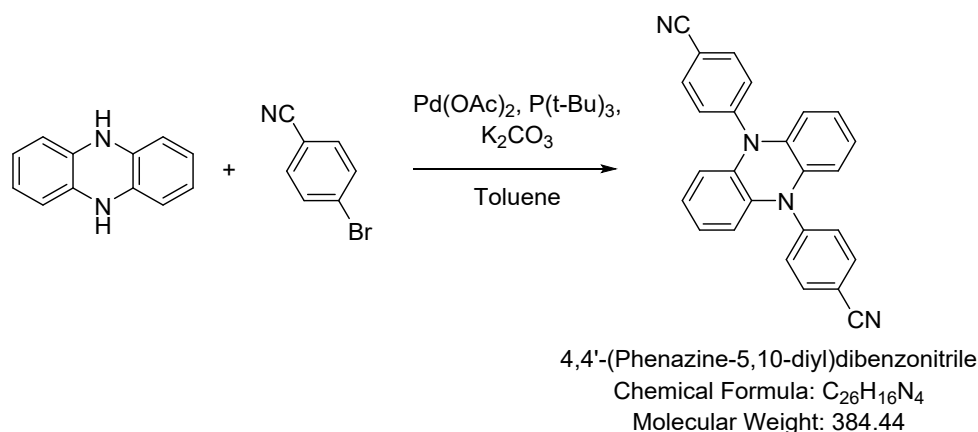


Starting materials	$M / \text{g} \cdot \text{mol}^{-1}$	$\rho / \text{g} \cdot \text{cm}^{-3}$	eq	n / mmol	m / g	V / mL
Phenazine	180.21	-	1.0	27.7	5.00	-
Sodium dithionite	174.11	2.38	10.0	277.0	48.2	-

Following literature procedures,^{1,2} phenazine was dissolved in ethanol (125 mL), sodium dithionite in de-ionized water (500 mL) and both solutions were combined and heated under stirring and reflux for three hours or overnight. The precipitate was filtered off and washed three times with deionized water. Finally, the solid was dried at 20 °C in vacuum (1×10^{-3} mbar) for 16 h. The product (yield 4.75 g, 94 %) was obtained as a light green solid and was used without further purification. Important: The dihydrophenazine solid must be stored under a protective gas atmosphere (nitrogen or argon), otherwise it re-oxidizes which is evidenced by slowly turning dark blue and then black.

[¹H NMR] (600 MHz, CDCl₃) δ = 8.27 (dd, J = 6.8, 3.5 Hz, 1H), 7.86 (dd, J = 6.8, 3.4 Hz, 1H), 6.12 (s, 2H), 1.57 (s, 3H).

S2.2 4,4'-(Phenazine-5,10-diyl)dibenzonitrile (pBN)



Starting materials	<i>M</i> / g·mol ⁻¹	<i>ρ</i> / g·cm ⁻³	eq	<i>n</i> / mmol	<i>m</i> / g	<i>V</i> / mL
5,10-Dihydrophenazine	182.22	-	1.00	5.49	1.00	-
4-Bromobenzonitrile	182.02	-	2.20	12.1	2.20	-
Potassium carbonate	138.20	2.43	6.00	32.9	4.55	-
Palladium(II) acetate	224.51	-	5 mol%		0.061	-
Tri- <i>tert</i> -butyl-phosphine	202.32	0.83	10 mol%		0.111	134

Following literature procedures,^{1,2} 5,10-dihydrophenazine, 4-bromobenzonitrile and potassium carbonate were dissolved in degassed toluene (20 mL). Palladium(II) acetate and tri-*tert*-butylphosphine were dissolved in degassed toluene (20 mL). Both solutions were combined under stirring. Under nitrogen inert gas the reaction mixture was heated with stirring to reflux for 24 hours. After cooling to room temperature, water (60 mL) was added to the reaction mixture and the water/toluene mixture extracted three times with chloroform (3 x 200 mL). The organic phases were combined, washed with a brine, dried over magnesium sulfate (5 min) and concentrated using a rotary evaporator. After addition of n-hexane (20 mL), a golden yellow insoluble precipitate was formed. The precipitated raw product was filtered off and washed three times with 60 mL each of a mixture of n-hexane/chloroform (2:1) and dried at 20 °C under vacuum (1x10⁻³ mbar) for 16 h. The product was obtained as a golden yellow crystalline solid (yield 1.6 g, 76 %). Ideally, the product occurs as small yellow-gold crystals. To increase the yield, the crystallisation solution can be concentrated and purified by column chromatography (dichloromethane/cyclohexane 10:1).



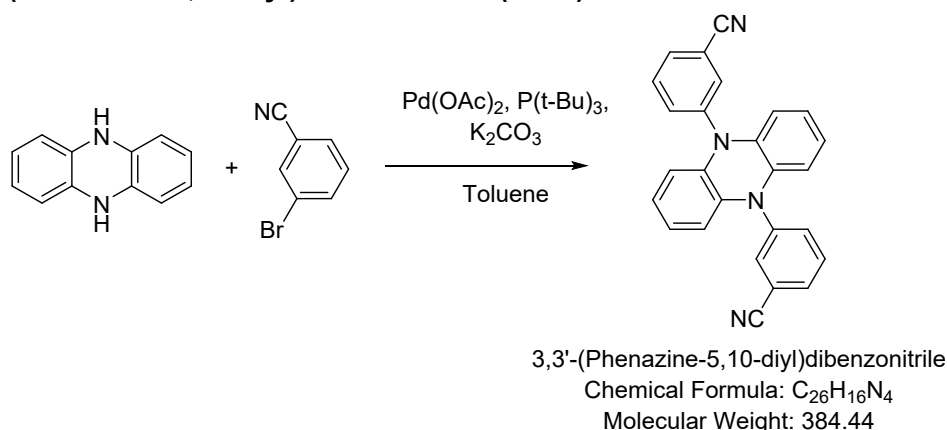
[¹H NMR] (600 MHz, C₆D₆) δ = 6.96 (d, *J* = 8.2 Hz, 4H), 6.71 (d, *J* = 8.2 Hz, 4H), 6.41 – 6.37 (m, 4H), 5.69 (dt, *J* = 7.9, 3.9 Hz, 4H).

[HR-ESI-MS] (*m/z*): Calc. for [M⁺]: 384.1375 – found: 384.1370

[EA] Calc. for C₂₆H₁₆N₄: C 81.20, H 4.20, N 14.57 – found: C 80.7, H 4.21, N 14.39 %

[M.p] > 300 °C

S2.3 3,3'-(Phenazine-5,10-diyl)dibenzonitrile (mBN)



Starting materials	<i>M</i> / g·mol ⁻¹	<i>ρ</i> / g·cm ⁻³	eq	<i>n</i> / mmol	<i>m</i> / g	<i>V</i> / mL
5,10-Dihydrophenazine	182.22	-	1.00	5.49	1.00	-
3-Bromobenzonitrile	182.02	-	2.20	12.1	2.20	-
Potassium carbonate	138.20	2.43	6.00	32.9	4.55	-
Palladium(II) acetate	224.51	-	5 mol%		0.061	-
Tri- <i>tert</i> -butylphosphine	202.32	0.83	10 mol%		0.111	134

Following the procedure in S2.2 the starting materials 5,10-dihydrophenazine, 3-bromobenzonitrile and potassium carbonate were dissolved in toluene (20 mL). Palladium(II) acetate and tri-*tert*-butylphosphine were dissolved in toluene (20 mL). Both solutions were combined under stirring. Under nitrogen inert gas the reaction mixture was heated with stirring to reflux for 24 hours.³ After cooling to room temperature, water (60 mL) was added to the reaction mixture and the water/toluene mixture extracted three times with chloroform (3 x 200 mL). The organic phases were combined, washed with a saturated aqueous NaCl solution (~ 25 %), dried over magnesium sulfate (5 min) and concentrated using a rotary evaporator. After 3 d and slow evaporation of the solvent, yellow crystals precipitated. The precipitated raw product was filtered off and washed three times with 60 mL each of a mixture of n-hexane/chloroform (2:1) and dried at 20 °C under vacuum (1x10⁻³ mbar) for 16 h. The product was obtained as small yellow crystals (yield 1.67 g, 79 %). To increase the yield, the crystallization solution can be concentrated and purified by column chromatography (dichloromethane/cyclohexane 10:1).



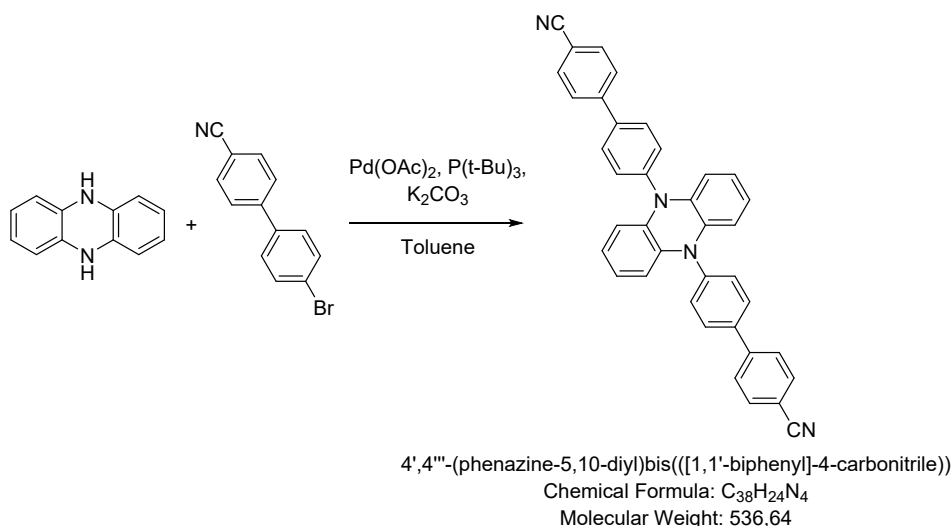
[¹H NMR] (300 MHz, C₆D₆) δ = 7.47 (s, 2H), 7.45 – 7.30 (m, 6H), 6.53 - 6.47 (m, 4H), 5.80 - 5.73 (m, 4H)

[HR-ESI-MS] (m/z): Calc. for [M⁺]: 384.1375 – found: 384.1367

[EA] Calc. for C₂₆H₁₆N₄: C 81.20, H 4.20, N 14.57 – found: C 81.41, H 4.27, N 14.51 %

[M.p] 284 °C

S2.4 4',4'''-(Phenazine-5,10-diyl)bis(((1,1'-biphenyl)-4-carbonitrile)) (BPN)



Starting materials	<i>M</i> / g·mol ⁻¹	<i>ρ</i> / g·cm ⁻³	eq	<i>n</i> / mmol	<i>m</i> / g	<i>V</i> / mL
5,10-Dihydrophenazine	182.22	-	1.00	5.49	1.00	-
4'-Bromo-[1,1'-biphenyl]-4-carbonitrile	258.12	-	2.20	12.0	3.10	-
Potassium carbonate	138.20	2.43	6.00	32.9	4.55	-
Palladium(II) acetate	224.51	-	8 mol%		0.098	-
Tri- <i>tert</i> -butylphosphine	202.32	-	16 mol%		0.178	-

Following the procedure in S2.2 the starting materials 5,10-dihydrophenazine, 4'-bromo-[1,1'-biphenyl]-4-carbonitrile, and potassium carbonate were dissolved in degassed toluene (20 mL). Palladium(II) acetate and tri-*tert*-butylphosphine were dissolved in degassed toluene (20 mL). Both solutions were combined under stirring. Under nitrogen inert gas the reaction mixture was heated with stirring to reflux for 48 hours. The solvent toluene was removed by rotary evaporator. The crude product (dark orange/brown to black) was dissolved and resuspended in hot chloroform and filtered using a short (10 cm) filter column (silica). The filter cake was washed with hot chloroform until the filtrate became colorless (approximately 250 mg of product dissolves in 1 L of hot chloroform). The chloroform filtrates were combined and the solvent concentrated to about 200 mL using a rotary evaporator. The crystallized product was filtered and washed three times with chloroform (20 mL). The product was obtained as fine orange crystals (yield 2.06 g, 70 %).



[¹H NMR] (600 MHz, C₆D₆) δ = 7.54 – 7.49 (m, 1H), 7.32 – 7.25 (m, 2H), 7.24 – 7.19 (m, 1H), 7.14 – 7.10 (m, 25H), 7.10 – 7.05 (m, 1H), 7.03 – 6.97 (m, 1H).

[HR-ESI-MS] (*m/z*): Calc. for [M⁺]: 536.2001 – found: 536.1998

[EA] Calc. for C₃₈H₂₄N₄: C 85.05, H 4.51, N 10.44 – found: C 85.67, H 4.43, N 10.52 %

[M.p] > 300 °C

S3 Crystal structure details

The sample of **β -pBN** crystallized via slow evaporation of a CHCl_3 solution as yellow elongated blocks/needles with a nearly rectangular (rather trapeze) cross section. A suitable crystal was mounted on a microloop in a drop of immersion oil. For 4,4'-(phenazine-5,10-diyl)dibenzonitrile (**pBN**, β -polymorph) the data was collected using ϕ and ω -scans on a Bruker Kappa APEX 2 CCD X-ray diffractometer with a microfocus sealed tube, Mo- $K\alpha$ radiation ($\lambda = 0.71073 \text{ \AA}$), and a multi-layer mirror monochromator. For the compounds 3,3'-(phenazine-5,10-diyl)dibenzonitrile (**mBN**) and 4',4'''-(phenazine-5,10-diyl)bis([1,1'-biphenyl]-4-carbonitrile) (**BPN**) the single-crystal diffraction data was collected using ω -scans on a Rigaku XtaLAB Synergy S four-circle diffractometer with a Hybrid Pixel Array Detector and a PhotonJet X-ray source for Cu- $K\alpha$ radiation ($\lambda = 1.54184 \text{ \AA}$) with a multilayer mirror monochromator. The data were collected under a cold nitrogen gas-stream (Oxford Cryostream liquid nitrogen cooling system) at 140 K (**β -pBN**) or 100 K (**mBN**, **BPN**). Data reduction and absorption correction were performed with APEX2,⁴ SAINT⁵ and SADABS on the Bruker device and by CrysAlisPro on the Rigaku diffractometer [6]. Structures were solved by direct methods with SHELX-2018 and refined with full-matrix least squares refinements on F^2 using SHELXL [7] in OLEX2 [8]. Crystal data and details on the structure refinement are given in Table S1 and Table S2. All hydrogen atoms were positioned geometrically and refined using riding models with $U_{\text{iso}}(\text{H}) = 1.2 \cdot U_{\text{eq}}$. For structure **BPN** the chloroform solvent molecule was disordered over two positions and refined in a 66:34 ratio. Graphics were drawn with the program Diamond.⁹

Table S1. Crystal data and structure refinement for α - and β -polymorph of **pBN**.

	α-pBN reported previously ¹⁰	β-pBN reported here
Identification code	wq_2_2	mo_th_dp_paralinker_0m_a
CCDC number	2156760	2238744
Empirical formula	$\text{C}_{26}\text{H}_{16}\text{N}_4$	$\text{C}_{26}\text{H}_{16}\text{N}_4$
Formula weight / g mol^{-1}	384.43	384.43
Temperature / K	149.99(10)	140.0(10)
Crystal system	Monoclinic	Triclinic
Space group	$P2_1$ (no. 4)	$P\bar{1}$ (no. 2)
$a / \text{\AA}$	9.16980(10)	9.2154(7)
$b / \text{\AA}$	25.87320(10)	9.8882(8)
$c / \text{\AA}$	13.00690(10)	11.5256(9)
$\alpha / ^\circ$	110.2310(10) $^\circ$	105.439(4)
$\beta / ^\circ$	90	100.122(4)
$\gamma / ^\circ$	90	104.034(4)
Volume / \AA^3	2895.53(4)	949.16(13)
Z	6	2
$\rho_{\text{calc}} / \text{g cm}^{-3}$	1.323	1.345
μ / mm^{-1}	0.630	0.082
$F(000)$	1200	400
Crystal size / mm^3	$0.08 \times 0.07 \times 0.05$	$0.24 \times 0.15 \times 0.1$
Radiation	Cu $K\alpha$ ($\lambda = 1.54184 \text{ \AA}$)	Mo $K\alpha$ ($\lambda = 0.71073 \text{ \AA}$)
2θ range for data collection / $^\circ$	3.416 to 67.080	1.90 to 30.51
Index ranges	$-10 \leq h \leq 10, -30 \leq k \leq 30, -15 \leq l \leq 13, -14 \leq k \leq 14, -16 \leq l \leq 15$	$-16 \leq h \leq 16, -14 \leq k \leq 14, -16 \leq l \leq 16$
Reflections collected	77636	19393
Independent reflections	10131 ($R_{\text{int}} = 0.0284$)	5723 ($R_{\text{int}} = 0.0304$)

Data/restraints/parameters	10131 / 1 / 812	5723 / 0 / 271
Final R indexes [$I \geq 2\sigma(I)$] ^a	$R_1 = 0.0281$, $wR_2 = 0.0751$	$R_1 = 0.0508$, $wR_2 = 0.1257$
Final R indexes [all data] ^a	$R_1 = 0.0288$, $wR_2 = 0.0757$	$R_1 = 0.0760$, $wR_2 = 0.1398$
Goodness-of-fit on F^2 ^b	1.043	1.060
Largest diff. peak/hole / e Å ⁻³	0.114 and -0.229	0.326 and -0.263
Absolute structure parameter	0.2(3)	

^a Full-matrix least-square refinement on F^2 as implemented in SHELX. $R_1 = [\Sigma(\|F_o\| - \|F_c\|) / \Sigma \|F_o\|]$; $wR_2 = [\Sigma[w(F_o^2 - F_c^2)^2] / \Sigma[w(F_o^2)^2]]^{1/2}$ where $w^{-1} = [\sigma^2(F_o^2) + (aP)^2 + bP]$, $P = [2F_c^2 + \text{Max}(F_o^2, 0)] / 3$, a and b are refined parameters. ^b Goodness-of-fit $S = [\Sigma[w(F_o^2 - F_c^2)^2] / (n - p)]^{1/2}$.

Table S2. Crystallographic details for structures **mBN** and **BPN** · CHCl₃.

	mBN	BPN · CHCl ₃
Identification code	DP-metaLinker	DP-LinkerA2
CCDC number	2222499	2222500
Empirical formula	C ₂₆ H ₁₆ N ₄	C ₃₉ H ₂₅ Cl ₃ N ₄
Formula weight / g mol ⁻¹	384.43	655.98
Temperature / K	100.0(1)	100.0(1)
Crystal system	monoclinic	triclinic
Space group	$P2_1/c$ (no. 14)	$P\bar{1}$ (no. 2)
a / Å	12.7220(4)	9.4403(2)
b / Å	7.6706(2)	12.0125(2)
c / Å	11.0125(3)	14.3830(3)
α / °	90	80.303(2)
β / °	113.828(4)	82.611(2)
γ / °	90	78.921(2)
Volume / Å ³	983.06(6)	1569.97(6)
Z	2	2
ρ_{calc} / g cm ⁻³	1.299	1.388
μ / mm ⁻¹	0.618	2.922
$F(000)$	400.0	676.0
Crystal size / mm ³	0.64 × 0.39 × 0.2	0.18 × 0.06 × 0.04
Radiation	Cu $K\alpha$ ($\lambda = 1.54184$ Å)	Cu $K\alpha$ ($\lambda = 1.54184$ Å)
2θ range for data collection/°	3.798 to 78.680	3.133 to 79.754
Index ranges	-13 ≤ h ≤ 16, -9 ≤ k ≤ 7, -13 ≤ l ≤ 13 -12 ≤ h ≤ 11, -14 ≤ k ≤ 15, -17 ≤ l ≤ 17	
Reflections collected	11223	45762
Independent reflections	2024 [$R_{\text{int}} = 0.0229$, $R_{\text{sigma}} = 0.0143$]	6294 [$R_{\text{int}} = 0.0476$, $R_{\text{sigma}} = 0.0257$]
Data/restraints/parameters	2024/0/136	6294/0/460
Final R indexes [$I \geq 2\sigma(I)$] ^a	$R_1 = 0.0360$, $wR_2 = 0.0950$	$R_1 = 0.0418$, $wR_2 = 0.1000$
Final R indexes [all data] ^a	$R_1 = 0.0377$, $wR_2 = 0.0963$	$R_1 = 0.0526$, $wR_2 = 0.1037$
Goodness-of-fit on F^2 ^b	1.047	1.057
Largest diff. peak/hole / e Å ⁻³	0.14/-0.21	0.20/-0.28

^a Full-matrix least-square refinement on F^2 as implemented in SHELX. $R_1 = [\Sigma(\|F_o\| - \|F_c\|) / \Sigma \|F_o\|]$; $wR_2 = [\Sigma[w(F_o^2 - F_c^2)^2] / \Sigma[w(F_o^2)^2]]^{1/2}$ where $w^{-1} = [\sigma^2(F_o^2) + (aP)^2 + bP]$, $P = [2F_c^2 + \text{Max}(F_o^2, 0)] / 3$, a and b are refined parameters. ^b Goodness-of-fit $S = [\Sigma[w(F_o^2 - F_c^2)^2] / (n - p)]^{1/2}$.

Comparison of α - and β -polymorph of pBN

Both polymorphs consist of two type of molecules, namely the ‘linear’ one and the ‘distorted one’ (ratios 1:1 in **β-pBN** and 1:2 in **α-pBN**), with a characteristic non-planarity of the latter associated with the weak, but clearly distinguishable, pyramidalicity of the N atoms (Table S3), constituting the dihydrophenazine core (Figure S1 and Figure 2 in the main text).

Table S3. Listing of angular distortions of the independent **pBN** molecules constituting the structures of the two known α - and β -polymorphs expressed as the sum of the C-N-C angles at the N atoms of the phenazinediyl core.

α-pBN (reported earlier)		β-pBN (reported here)	
Molecule 1, ('linear')	$\Sigma(\angle\text{CNC}) / ^\circ \text{ }^a$	Molecule 1, (linear)	$\Sigma(\angle\text{CNC}) / ^\circ \text{ }^a$
N(1)	360.0	N(1)	359.8
N(2)	359.3	N(2)	359.8
Molecule 2, ('distorted')	$\Sigma(\angle\text{CNC}) / ^\circ \text{ }^{a,b}$	Molecule 2, ('distorted')	$\Sigma(\angle\text{CNC}) / ^\circ \text{ }^{a,b}$
N(1)	356.5	N(1)	355.8
N(2)	358.7	N(2)	355.8
Molecule 3, ('distorted')	$\Sigma(\angle\text{CNC}), ^\circ \text{ }^{a,b}$		
N(1)	359.9 ^a		
N(2)	357.3		

^a $\Sigma(\angle\text{CNC}) = \angle\text{C1NC2} + \angle\text{C2NC3} + \angle\text{C3NC2}$, i.e. the sum of all angles between bonded atoms, with N atoms serving a vertex of the angles; a measure of non-planarity, with 360° corresponding to a planar case.

^b Due to the significant distortion of the phenazine moiety the geometry of the N-atom environment is nearly planar, but the direction of the N-C_{Ph} bond is still significantly off the least squares plane for atoms constituting the phenazinediyl plane, i.e. the molecule is notwithstanding characteristically non-linear.

The α - and β -polymorphs could be rationalized as being both constituted from layers of molecules of the same type, following the ABBABB... and ABAB... patterns (Figure S1a,b), where A and B are the layers consisting of ‘linear’ and ‘disordered’ molecules, respectively only. The packing efficiency is only slightly better in the β -polymorph compared to the α -polymorph, with the respective densities being 1.345 vs. 1.323 g cm⁻³ (Table S1).

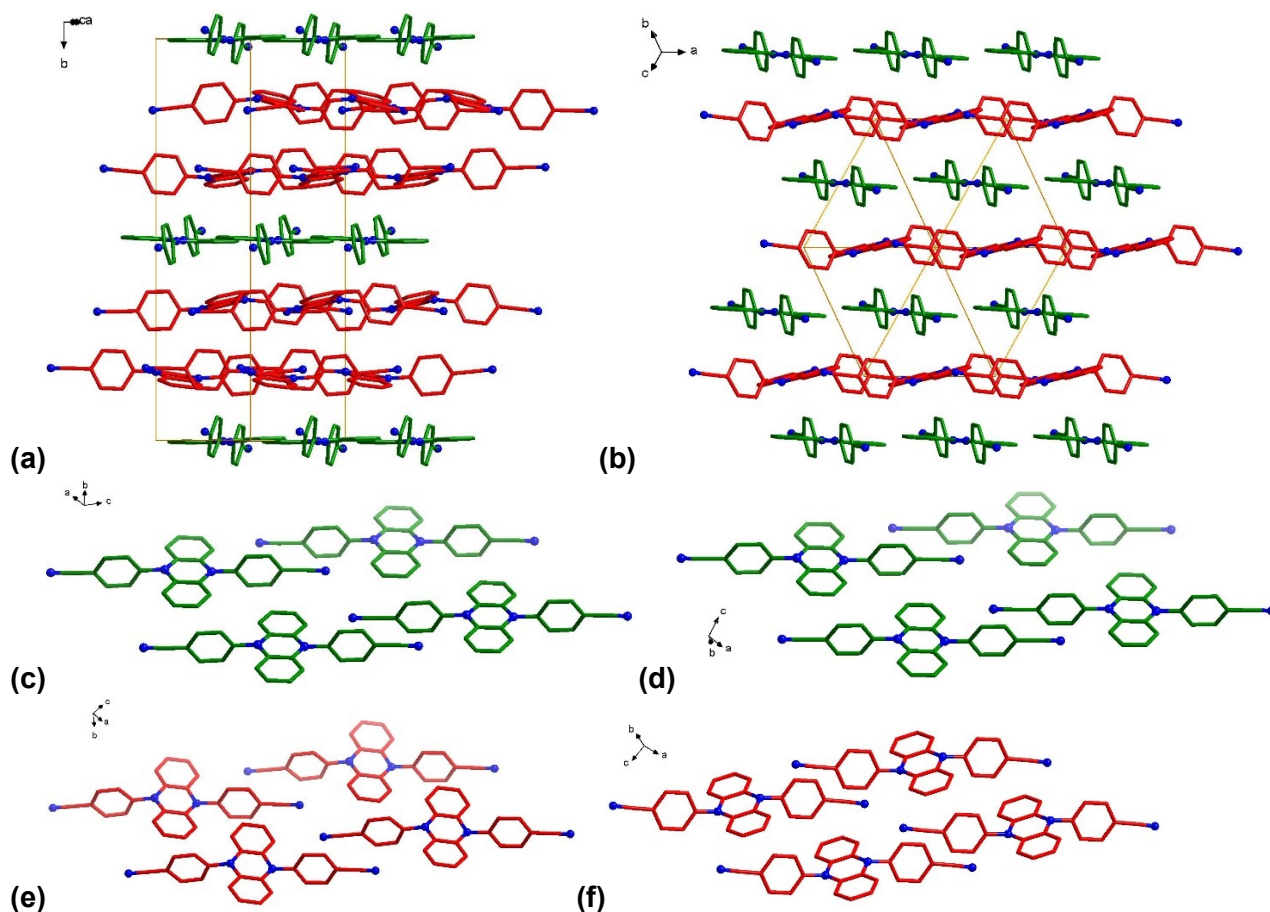


Figure S1. Comparison of the packing diagrams in the structures of **pBN**.

The previously reported polymorph **α-pBN**¹⁰ (monoclinic, $P2_1$ (no. 4), $Z' = 3$; crystallization by slow evaporation of a hexane/dichloromethane solution) left panes: **(a)**, **(c)**, **(e)**.

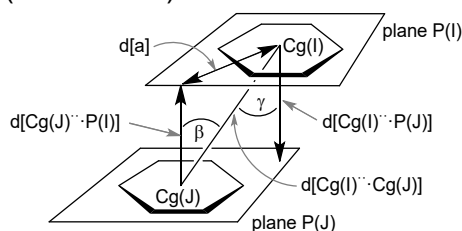
The **β-pBN** reported here (triclinic, $P\bar{1}$ (no. 2), $Z' = 1$; crystallization by slow evaporation of a solution in CHCl_3) right panes: **(b)**, **(d)**, **(f)**.

The linear molecules are depicted in green, the distorted ones in red.

S4 Supramolecular interaction analysis

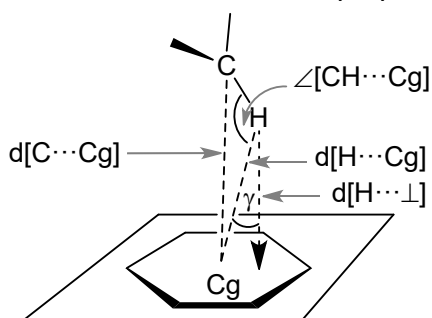
The supramolecular packing interactions have been analyzed for compounds **β-pBN**, **mBN** and **BPN** with PLATON.^{11,12,13}

The PLATON-listing "Analysis of Short Ring-Interactions" for possible π -stacking interactions yielded no π - π -stacking interactions in **β-pBN** or **mBN** and only one in **BPN**. π -Stacking, especially significant π -stacking would mean rather short centroid-centroid contacts ($< 3.8 \text{ \AA}$), near parallel ring planes ($\alpha < 10^\circ$ to $\sim 0^\circ$ or even exactly 0° by symmetry), small slip angles ($\beta, \gamma < 25^\circ$) and vertical displacements (slippage $< 1.5 \text{ \AA}$) which translate into a sizable overlap of the aryl-plane areas (Scheme S1).^{14,15}



Scheme S1. Graphical presentation of the parameters used for the description of π - π stacking.

However, from the "Analysis of X-H...Cg(Pi-Ring) Interactions ($H...Cg < 3.0 \text{ \AA} - \gamma < 30.0^\circ$) significant intermolecular C-H... π contacts were found in **mBN**, which start around 2.57 \AA for the (C-)H...ring centroid distances with H-perp starting below 2.5 \AA and C-H...Cg $> 135^\circ$ (Scheme S2) [16].



Scheme S2. Graphical presentation of the parameters used for the description of CH- π interactions.

Furthermore, there are C-H...N contacts in the solid-state packing arrangements of all three compounds.

Compound β -pBN:

Figure S2 gives an approximate view along the N...N axis in **β -pBN** to illustrate the planar nature of the pyrazine ring in both the linear and distorted molecule of **β -pBN** and shows the packing diagram.

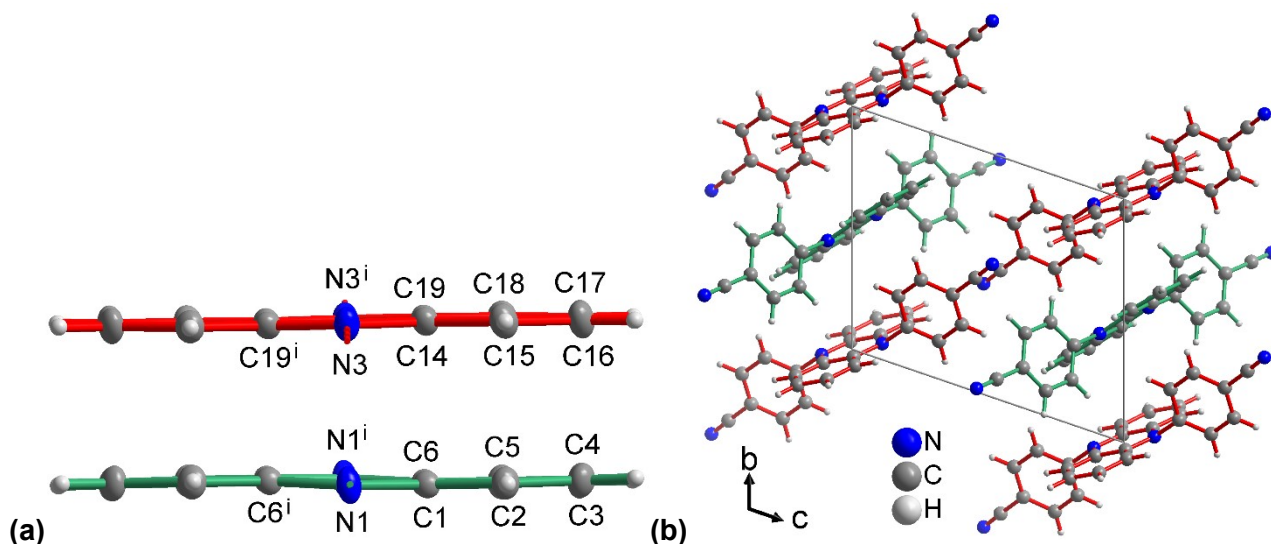


Figure S2. (a) Approximate view along the N...N axis in the linear (green) and distorted (red) molecules of **β -pBN** and (b) packing diagram. The linear molecules are depicted with green bonds, the distorted ones with red bonds.

Intermolecular C-H... π contacts in the packing of **β -pBN** (shown in Figure S3):

Analysis of X-H...Cg(Pi-Ring) Interactions ($H...Cg < 3.0 \text{ \AA}$ - $\text{Gamma} < 30.0 \text{ Deg}$)

===== Cg(J)

= Center of gravity of ring J (Plane number above)

- H-Perp = Perpendicular distance of H to ring plane J

- Gamma = Angle between Cg-H vector and ring J normal

- X-H...Cg = X-H-Cg angle (degrees)

- X...Cg = Distance of X to Cg (Angstrom)

- X-H, Pi = Angle of the X-H bond with the Pi-plane (i.e.' Perpendicular = 90 degrees, Parallel = 0 degrees)

X--H(I)	Res(I)	Cg(J)	[ARU(J)]	H..Cg	H-Perp	Gamma	X-H..Cg	X..Cg	X-H,Pi
C4 -H4	[1] -> Cg3	[1455.01]	2.85	2.83	7.02	154	3.7317(18)	59	
C12 -H12	[1] -> Cg8	[2676.02]	2.89	2.84	10.84	145	3.7073(17)	63	
C21 -H21	[2] -> Cg1	[2666.01]	2.64	2.55	14.71	138	3.4020(17)	56	

C21	-H21	[2] -> Cg4	[2666.01]	2.80	2.55	24.51	120	3.3799(17)	55
C21	-H21	[2] -> Cg6	[2666.01]	2.64	2.55	14.36	138	3.4020(16)	54
C22	-H22	[2] -> Cg2	[2666.01]	2.50	2.50	3.24	144	3.3203(17)	58
C22	-H22	[2] -> Cg4	[2666.01]	2.81	2.49	27.47	119	3.3798(16)	57

[1455] = -1+X,Y,Z
[2676] = 1-X,2-Y,1-Z
[2666] = 1-X,1-Y,1-Z

Cg(1) = centroid of N1-C1-C6-N1i-C1i-C6i
Cg(2) = centroid of C1-C2-C3-C4-C5-C6
Cg(3) = centroid of C7-C8-C9-C10-C11-C12
Cg(4) = centroid of N1-C1-C2-C3-C4-C5-C6-N1i-C1i-C6i
Cg(6) = centroid of N1-C1-C2-C3-C4-C5-C6-N1i-C1i-C2i-C3i-C4i-C5i-C6i = corresponds to Cg(1)
Cg(8) = centroid of C14-C15-C16-C17-C18-C19

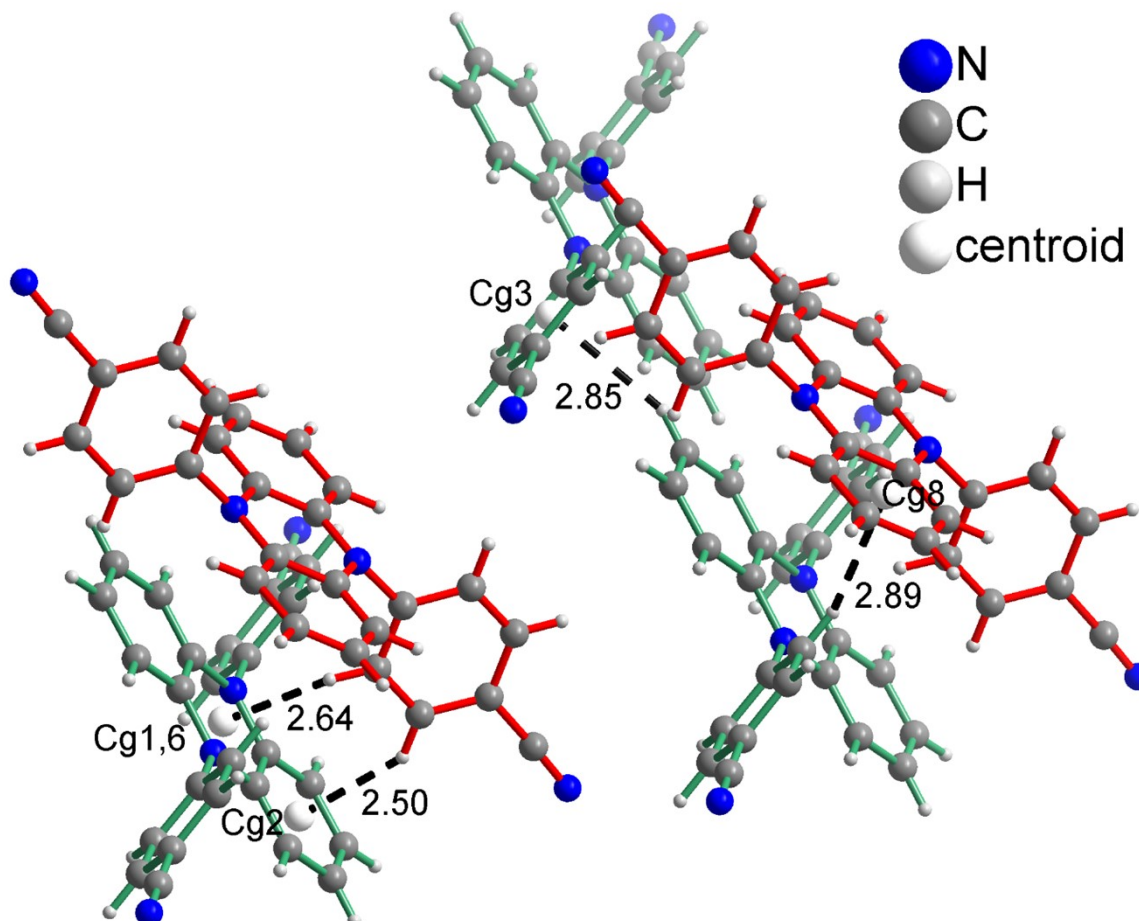


Figure S3. Intermolecular C-H \cdots π contacts in **β -pBN**. Cg = ring centroids and distances (in Å) according to the Table above. The linear molecules are depicted with green bonds, the distorted ones with red bonds.

Intermolecular C-H \cdots N contacts in the packing of **β -pBN** (shown in Figure S4)

Analysis of Potential Hydrogen Bonds and Schemes with $d(D\cdots A) < R(D)+R(A)+0.50$, $d(H\cdots A) < R(H)+R(A)-0.12$ Ang., $D-H\cdots A > 100.0$ Deg

Nr	Typ	Res	Donor	H...Acceptor	[ARU]	D - H	H...A	D...A	D - H...A
1	1	C2	--H2	..N2	[2776.01]	0.95	2.55	3.363(2)	143
2	2	C15	--H15	..N4	[2666.02]	0.95	2.59	3.441(2)	150

[2776.] = [2_776] = 2-x,2-y,1-z
[2666.] = [2_666] = 1-x,1-y,1-z

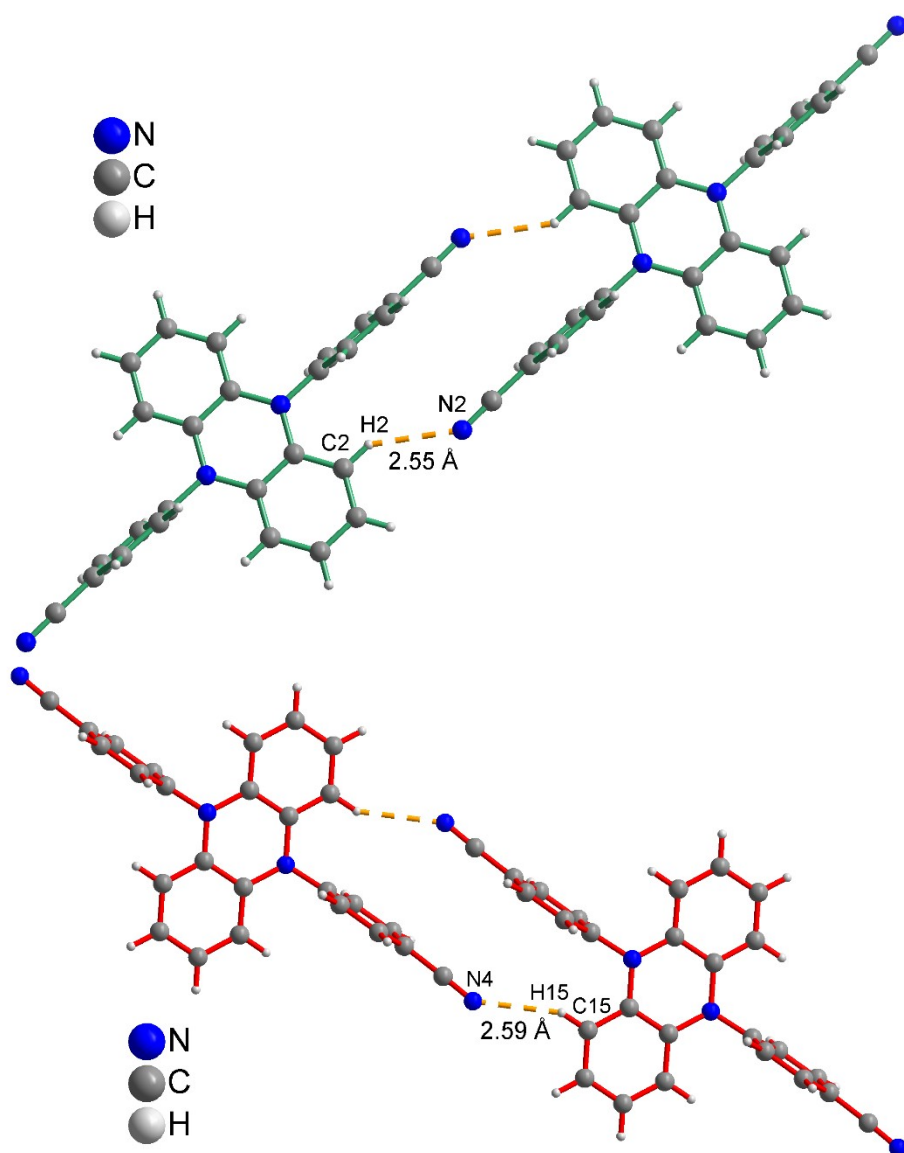


Figure S4. Intermolecular C-H...N contacts in β -pBN according to the Table above. The linear molecules are depicted with green bonds, the distorted ones with red bonds.

Compound mBN:

Figure S5 gives an approximate view along the N···N axis in **mBN** to illustrate the planar nature of the pyrazine ring in **mBN** and shows the packing diagram.

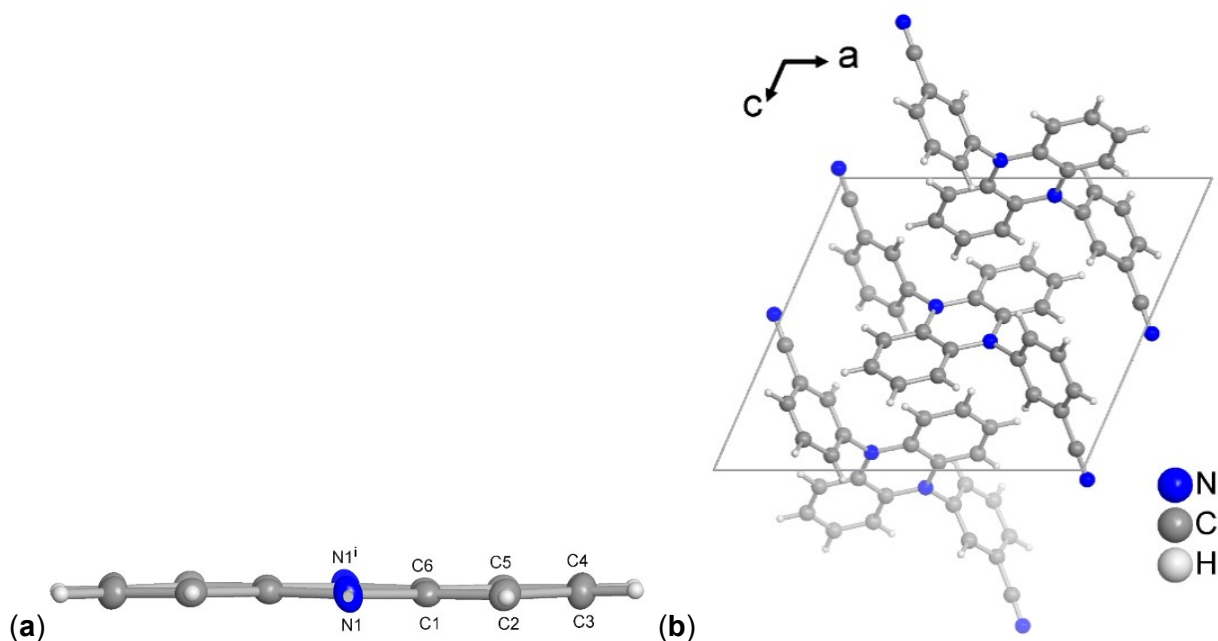


Figure S5. (a) Approximate view along the N···N axis in **mBN** and (b) packing diagram.

Intermolecular C-H··· π contacts in the packing of **mBN** (shown in Figure S6):

Analysis of X-H...Cg(Pi-Ring) Interactions (H...Cg < 3.0 Å, - Gamma < 30.0 Deg)

===== Cg(J)

= Center of gravity of ring J (Plane number above)

- H-Perp = Perpendicular distance of H to ring plane J

- Gamma = Angle between Cg-H vector and ring J normal

- X-H...Cg = X-H-Cg angle (degrees)

- X...Cg = Distance of X to Cg (Å)

- X-H, Pi = Angle of the X-H bond with the Pi-plane (i.e. Perpendicular = 90 degrees, Parallel = 0 degrees)

X-H(I)	Res(I)	Cg(J) [ARU(J)]	H...Cg	H-Perp	Gamma	X-H...Cg	X...Cg	X-H, Pi
C(2) -H(2) [1] -> Cg(2) [2656.01]			2.95	2.82	16.89	135	3.6779(11)	52
C(3) -H(3) [1] -> Cg(1) [2656.01]			2.57	2.49	15.07	148	3.4194(12)	67
C(3) -H(3) [1] -> Cg(4) [2656.01]			2.66	2.48	21.65	136	3.4142(11)	67
C(3) -H(3) [1] -> Cg(6) [2656.01]			2.57	2.48	15.80	148	3.4194(11)	67

[2656] = 1-X, 1/2+Y, 3/2-Z

[4554] = X, 1/2-Y, -1/2+Z

Cg(1) = centroid of N1-C1-C6-N1i-C1i-C6i

Cg(2) = centroid of C1-C2-C3-C4-C5-C6

Cg(4) = centroid of N1-C1-C2-C3-C4-C5-C6-N1i-C1i-C6i

Cg(6) = centroid of N1-C1-C2-C3-C4-C5-C6- N1i-C1i-C2i-C3i-C4i-C5i-C6i = corresponds to Cg(1)

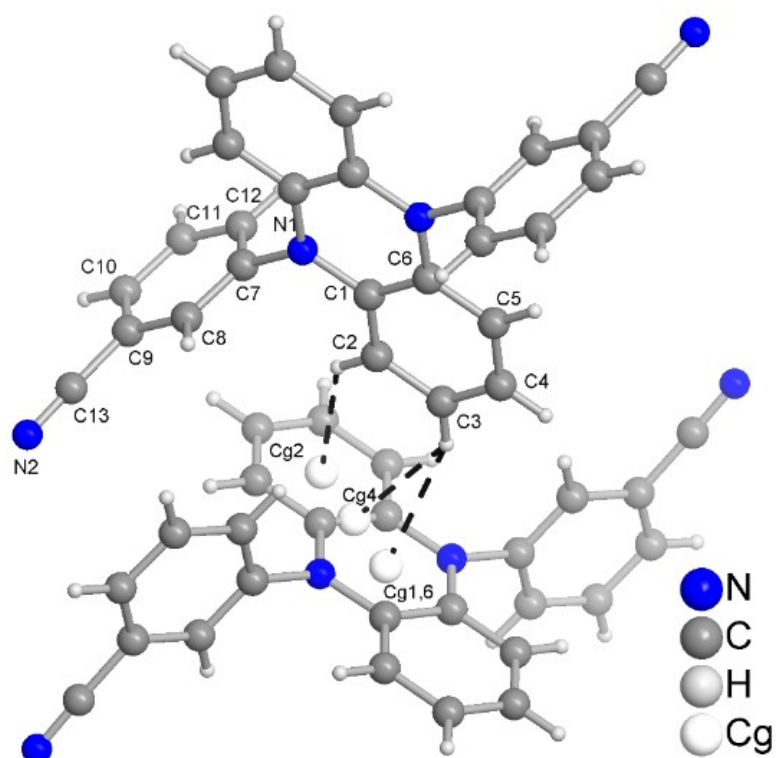


Figure S6. Intermolecular C-H \cdots π contacts in **mBN**. Symmetry transformation $i = -x+1, -y, -z+2$. Cg = ring centroids according to the Table above.

Intermolecular C-H \cdots N contacts in the packing of **mBN** (shown in Figure S7)

Analysis of Potential Hydrogen Bonds and Schemes with $d(D\cdots A) < R(D)+R(A)+0.50$, $d(H\cdots A) < R(H)+R(A)-0.12$ Ang., $D-H\cdots A > 100.0$ Deg

Nr	Typ	Res Donor	H...Acceptor	[ARU]	D - H	H...A	D...A	D - H...A
1	1	C(4)	-H(4) ..N(2)	[4655.01]	0.95	2.61	3.3597(17)	136

[4655.] = [4_666] = $1+x, 1/2-y, 1/2+z$

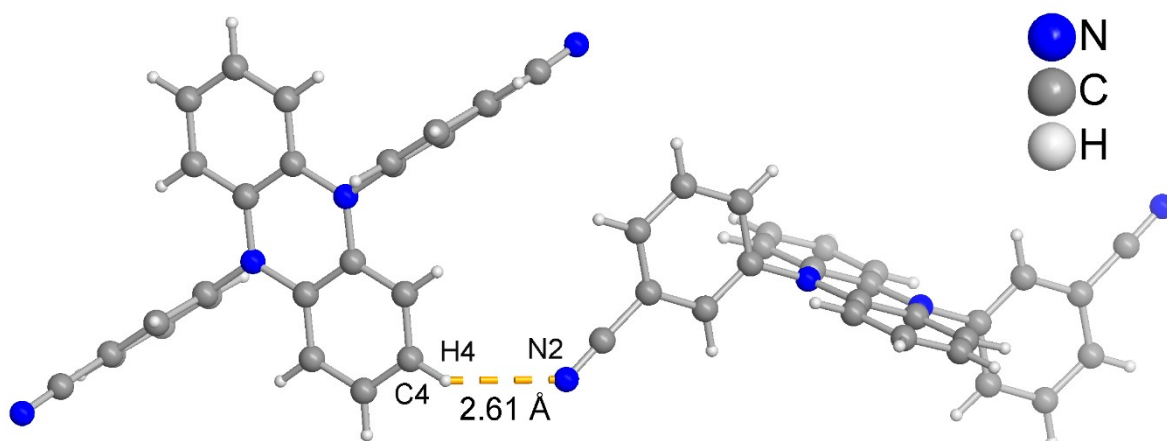


Figure S7. Intermolecular C-H \cdots N contact in **mBN** according to the Table above.

Compound BPN:

Figure S8 depicts the molecular structure of **BPN** with the chloroform solvent of crystallization, gives an approximate view along the N···N axis in **BPN** to illustrate the bending and shows the packing diagram.

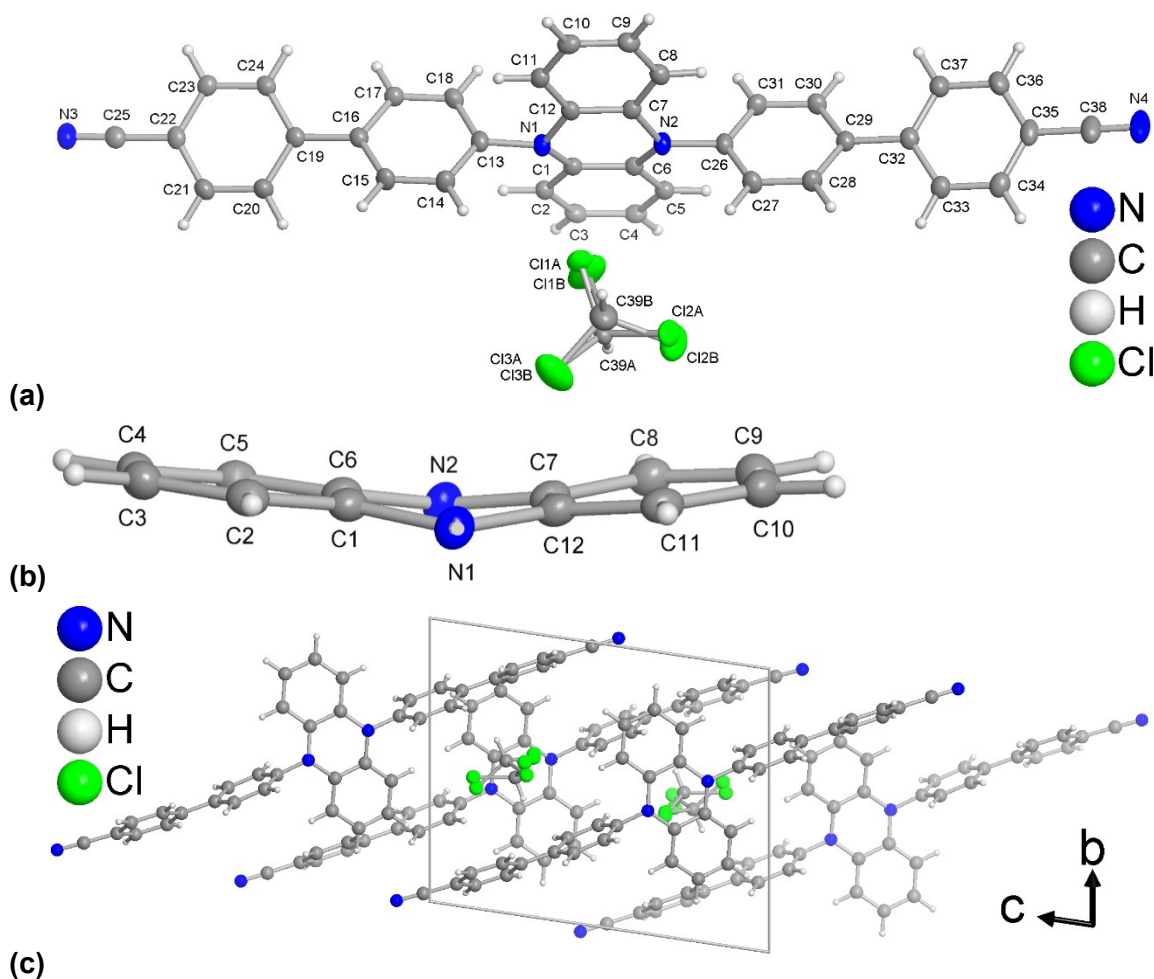


Figure S8. (a) Molecular structure of **BPN** showing also the disordered CHCl₃ solvent molecule in the crystalline state (50% thermal ellipsoids, H atoms with arbitrary radii). (b) Approximate view along the N···N axis in **BPN** to illustrate the bending by 16.00° of the two pyrazine halves in **BPN**. The angles in **BPN** between the benzene ring planes and the anellated half of the pyrazine ring are 2.71° (C1-C6) and 1.19° (C7-C12). (c) Section of the packing diagram.

Intermolecular π - π -Stacking interactions in the packing of **BPN** (shown in Figure S9a):

Analysis of Short Ring-Interactions with Cg-Cg Distances < 6.0 Å, Alpha < 20.000 Deg. and Beta < 60.0 Deg.

- Cg(I) = Plane number I (= ring number in () above)
- Alpha = Dihedral Angle between Planes I and J (Deg)
- Beta = Angle Cg(I)→Cg(J) or Cg(I)→Me vector and normal to plane I (Deg)
- Gamma = Angle Cg(I)→Cg(J) vector and normal to plane J (Deg)
- Cg-Cg = Distance between ring Centroids (Å)
- CgI_Perp = Perpendicular distance of Cg(I) on ring J (Å)
- CgJ_Perp = Perpendicular distance of Cg(J) on ring I (Å)
- Slippage = Distance between Cg(I) and Perpendicular Projection of Cg(J) on Ring I (Å)
- P,Q,R,S = J-Plane Parameters for Carth. Coord. (Xo, Yo, Zo)

Cg(I)	Res(I)	Cg(J)	[ARU(J)]	Cg-Cg	Alpha	Beta	Gamma	CgI_Perp	CgJ_Perp	Slippage
Cg(5)	[1]	-> Cg(7)	[1564.01]	3.7043(10)	5.87(8)	28.3	22.4	3.4247(7)	3.2626(7)	1.754
Cg(7)	[1]	-> Cg(5)	[1546.01]	3.7041(10)	5.87(8)	22.4	28.3	3.2625(7)	3.4246(7)	1.412

(Cg-Cg contacts above 4.9 Å have been omitted.)

[1564] = X,1+Y,-1+Z

[1546] = X,-1+Y,1+Z

Cg(5) = centroid of C19-C20-C21-C22-C23-C24

Cg(7) = centroid of C32-C33-C34-C35-C36-C37

Intermolecular C-H... π contacts in the packing of **BPN** (shown in Figure S9b):

Analysis of X-H...Cg(Pi-Ring) Interactions (H...Cg < 3.0 Ang. - Gamma < 30.0 Deg)

===== Cg(J)

= Center of gravity of ring J (Plane number above)

- H-Perp = Perpendicular distance of H to ring plane J

- Gamma = Angle between Cg-H vector and ring J normal

- X-H...Cg = X-H-Cg angle (degrees)

- X...Cg = Distance of X to Cg (Angstrom)

- X-H, Pi = Angle of the X-H bond with the Pi-plane (i.e.' Perpendicular = 90 degrees, Parallel = 0 degrees)

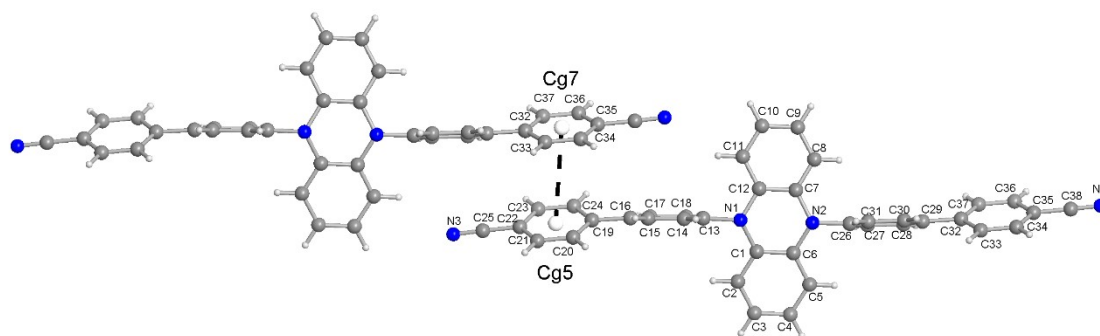
X-H(I)	Res(I)	Cg(J)	[ARU(J)]	H...Cg	H-Perp	Gamma	X-H...Cg	X...Cg	X-H,Pi
C(17) -H(17)	[1] -> Cg(2)	[2666.01]		2.71	2.69	6.49	154	3.5831(18)	62
C(28) -H(28)	[1] -> Cg(3)	[2567.01]		2.80	2.68	17.19	169	3.7406(19)	64

[2666] = 1-X,1-Y,1-Z

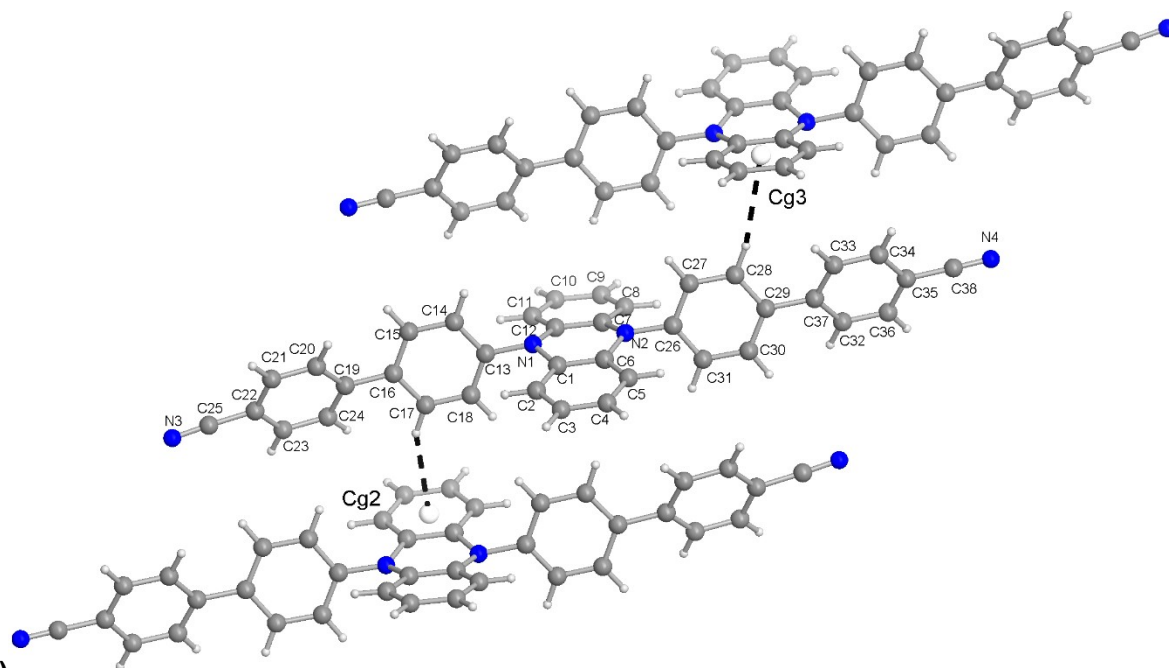
[2567] = -X,1-Y,2-Z

Cg(2) = centroid of C1-C2-C3-C4-C5-C6

Cg(3) = centroid of C7-C8-C9-C10-C11-C12



(a)



(b)

Figure S9. (a) π - π -Stacking interactions and (b) intermolecular C-H \cdots π contacts in **BPN. Cg = ring centroids according to the Table above.**

Intermolecular C-H \cdots N contacts in the packing of **BPN** (shown in Figure S10)

Analysis of Potential Hydrogen Bonds and Schemes with $d(D\cdots A) < R(D)+R(A)+0.50$, $d(H\cdots A) < R(H)+R(A)-0.12$ Ang., $D-H\cdots A > 100.0$ Deg

Nr	Typ	Res	Donor	H....Acceptor [ARU]	D - H	H...A	D...A	D - H...A
1	1	C(5)	--H(5)	..N(3) [1546.01]	0.95	2.55	3.395(2)	149
3	1	C(11)	--H(11)	..N(4) [1564.01]	0.95	2.53	3.365(2)	147

[1564.] = [1_564] = x,1+y,-1+z
[1546.] = [1_546] = x,-1+y,1+z

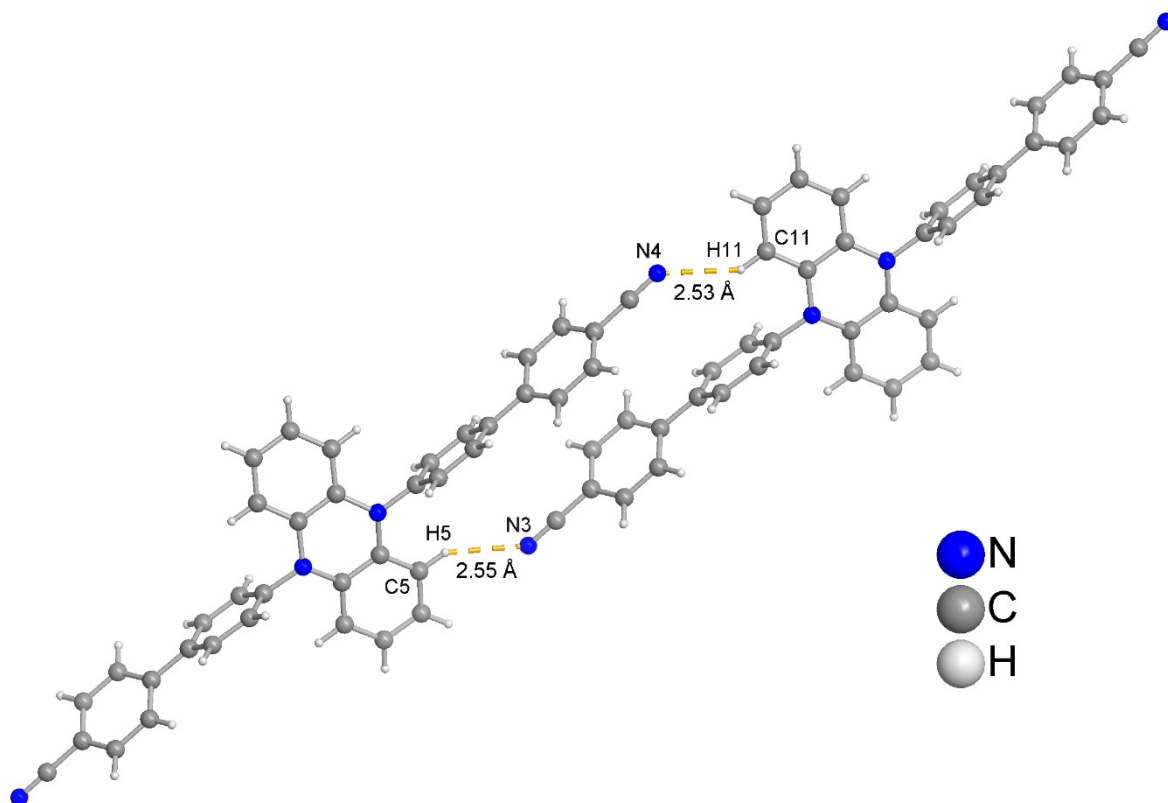


Figure S10. Intermolecular C-H \cdots N contacts in **BPN** according to the Table above.

S5 Photophysical properties

Emission spectra (Solid state)

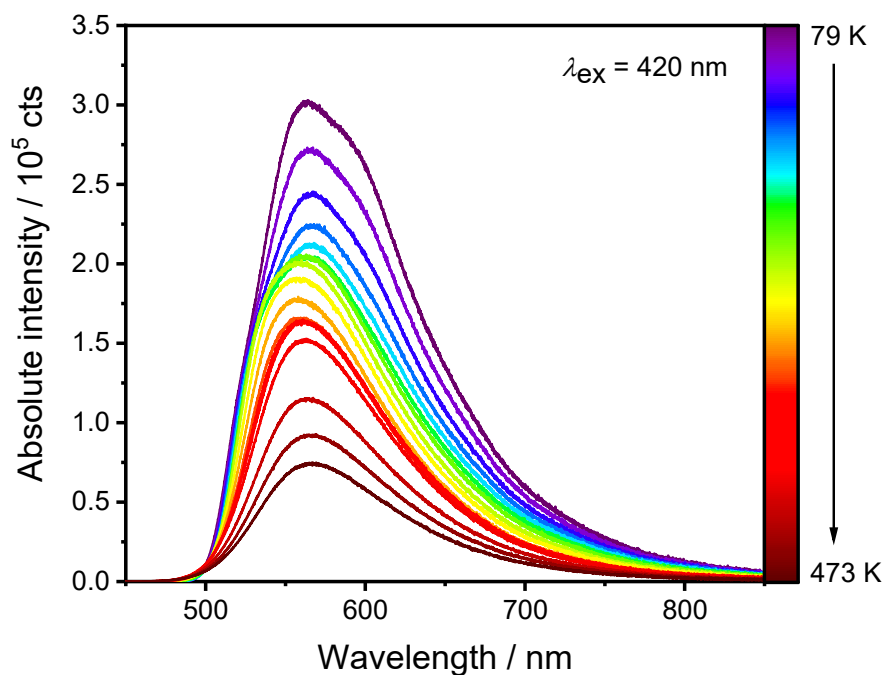


Figure S11. Temperature-dependent emission spectrum of powdered **pBN**. Excitation wavelength is indicated. Temperature intervals were $\Delta T = 25$ K.

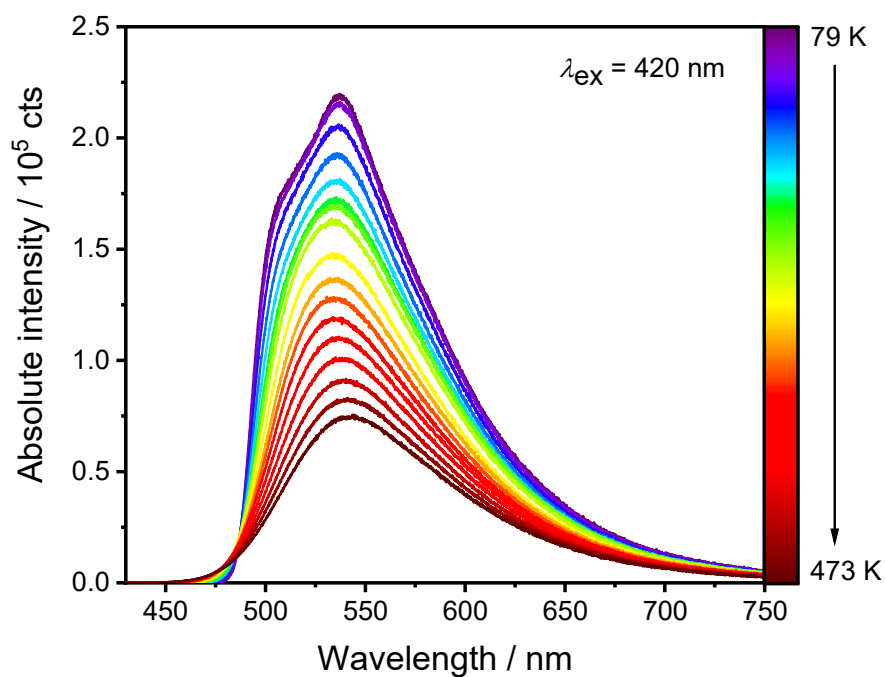


Figure S12. Temperature-dependent emission spectrum of powdered **mBN**. Excitation wavelength is indicated. Temperature intervals were $\Delta T = 25$ K.

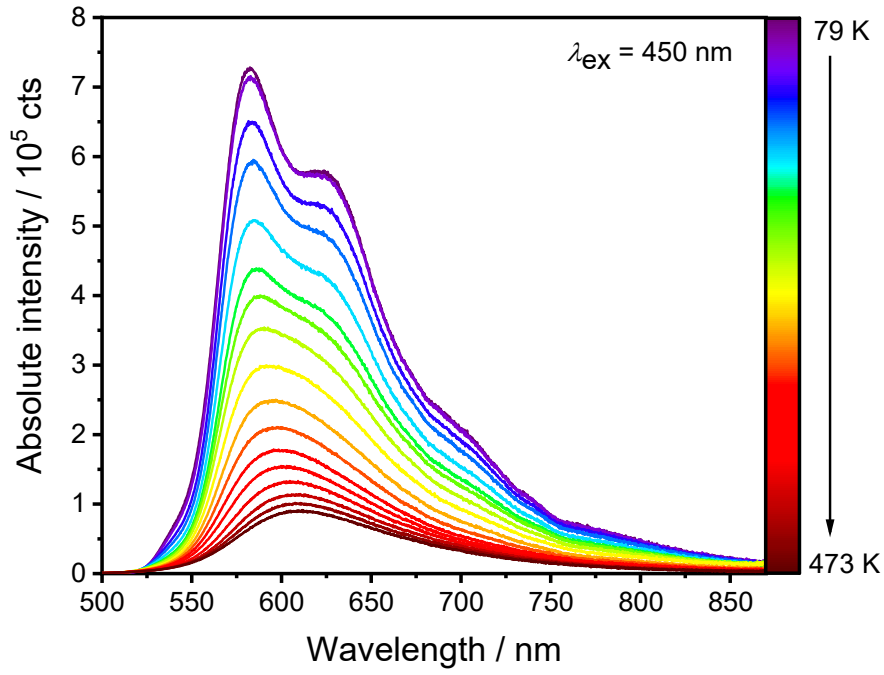


Figure S13. Temperature-dependent emission spectrum of powdered **BPN**. Excitation wavelength is indicated. Temperature intervals were $\Delta T = 25$ K.

Arrhenius plots (Solid state)

The temperature-dependent delayed components were fitted to an Arrhenius law in the low temperature range:

$$k_{\text{delayed}}(T) = k_{d0} \exp \left(- \frac{\Delta E_{ST}}{k_B T} \right) \quad (1)$$

with k_{d0} as a pre-factor, ΔE_{ST} as the effective singlet-triplet energy gap, k_B as the Boltzmann constant and T as the absolute temperature. In the cases of **pBN** and **mBN**, the prompt and delayed components were obtained from the time-resolved luminescence by biexponential fits over the whole dynamic range,

$$I(t, T) = A_{\text{prompt}} \exp(-k_{\text{prompt}}(T) \cdot t) + A_{\text{delayed}} \exp(-k_{\text{delayed}}(T) \cdot t) \quad (2)$$

with $I(t, T)$ as the time-dependent intensity at a given temperature T , A_{prompt} and A_{delayed} as the amplitudes of the prompt and delayed component, respectively, and $k_{\text{prompt}}(T)$ and $k_{\text{delayed}}(T)$ as the (eventually temperature-dependent) decay rate constants of the prompt and delayed fluorescence, respectively.

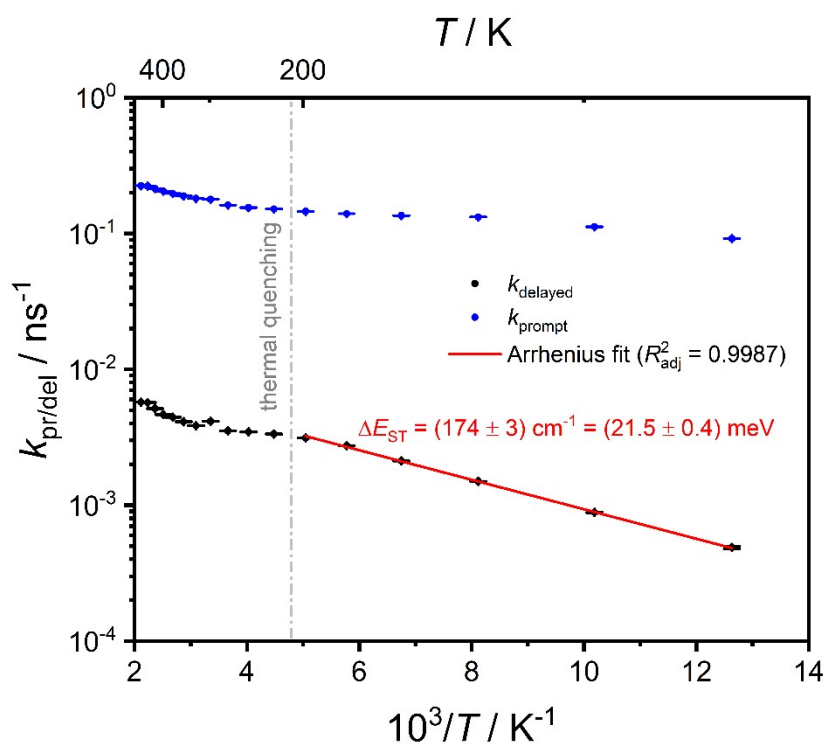


Figure S14. Arrhenius plot of the temperature-dependent time-resolved luminescence data of pBN.

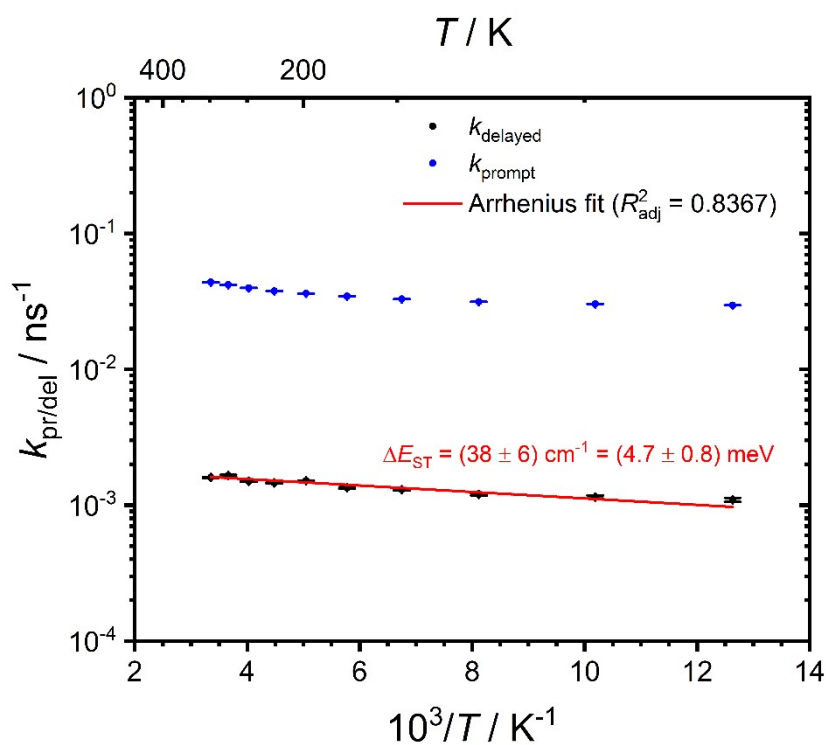


Figure S15. Arrhenius plot of the temperature-dependent time-resolved luminescence data of mBN.

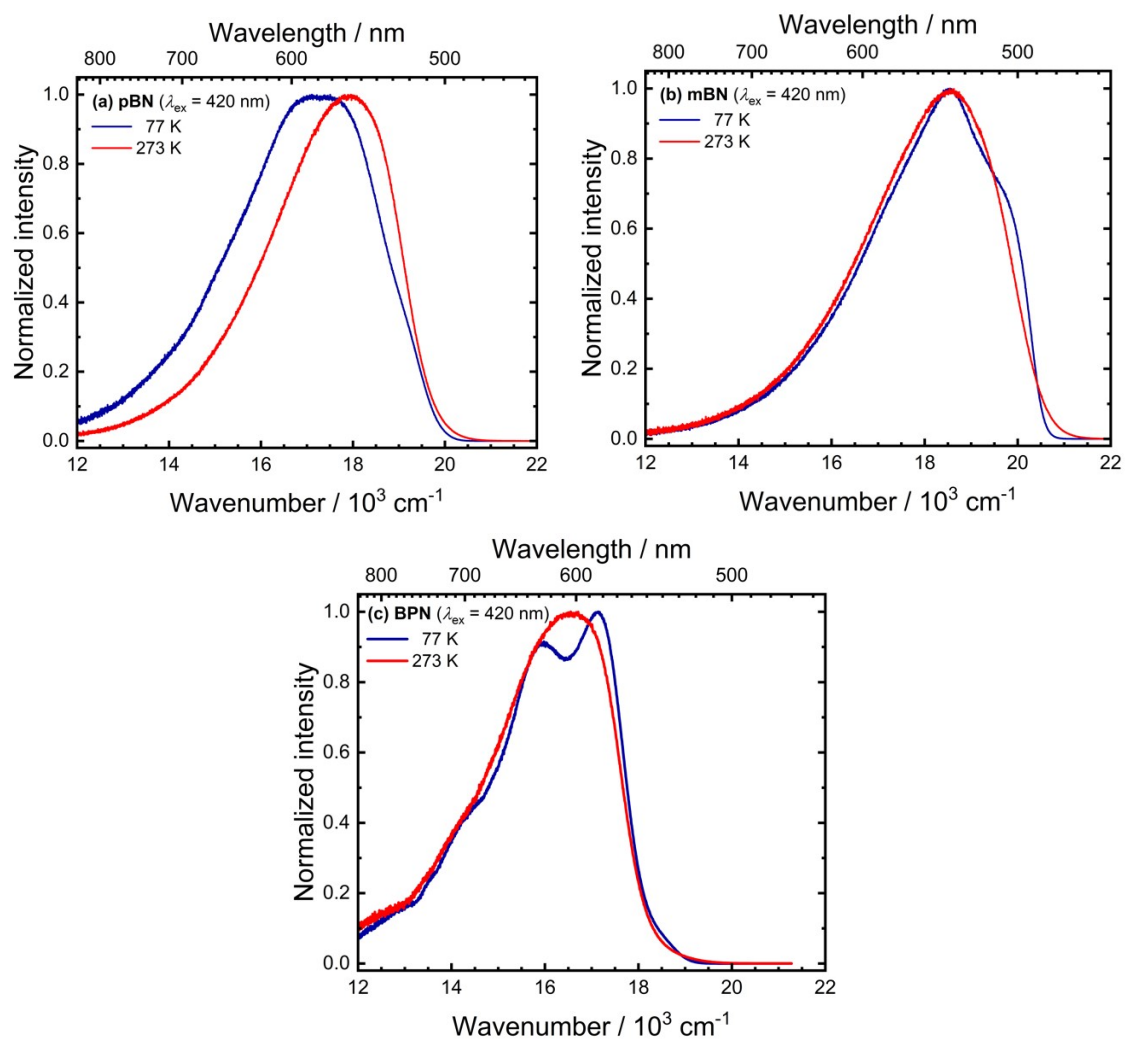


Figure S16. Photoluminescence spectra in wavenumber scale (including Jacobian λ^2 intensity correction) for (a) pBN, (b) mBN, and (c) BPN at 77 K (blue) and 273 K (red).

Absorption and emission spectra (solution state)

Compound **pBN**:

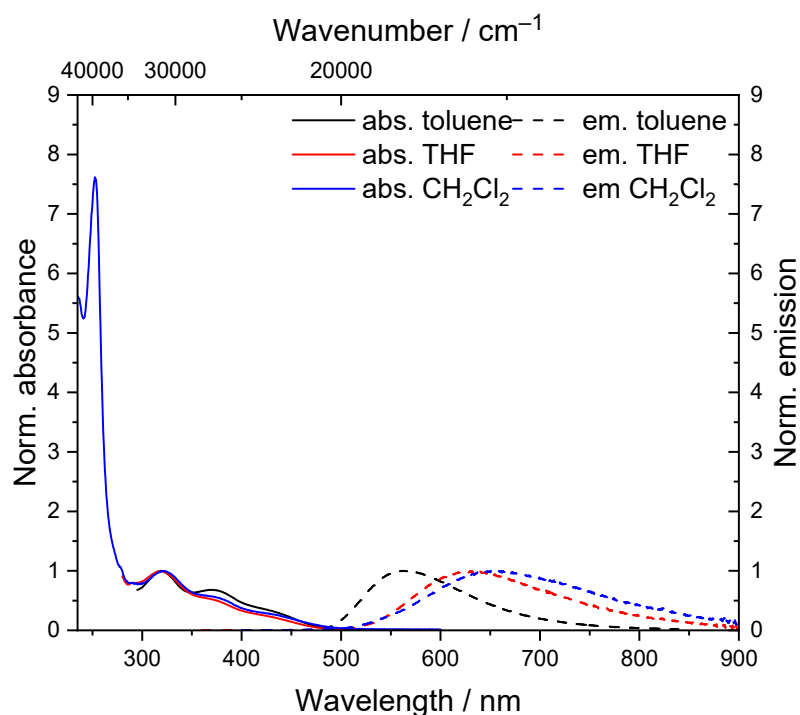


Figure S17. Absorbance and emission spectra of **pBN** recorded in solvents with different polarity ($c = 10^{-5}$ mol/L, $T = 293$ K).

Compound **pBN** possesses in toluene (318 nm, $\varepsilon = 2700$ L mol $^{-1}$ cm $^{-1}$), THF (318 nm, $\varepsilon = 7200$ L mol $^{-1}$ cm $^{-1}$) and dichloromethane (321 nm, $\varepsilon = 7700$ L mol $^{-1}$ cm $^{-1}$) one distinct absorption maximum, which is accompanied by two shoulders around 370 nm and 427 nm with weaker intensity (Figure S17, Table 1). In dichloromethane a maximum at higher energy at 255 nm with a molar absorption coefficient of 42600 L mol $^{-1}$ cm $^{-1}$ is detected (Table 1).

While the absorbance spectra are almost indifferent to the change of solvent polarity regarding their absorption maxima, the emission is strongly affected by solvent polarity and a distinct positive emission solvatochromicity can be observed in solvents of higher polarity (Table 1).¹⁷ The broad emission bands (full width at half maximum (FWHM) from 3624 cm $^{-1}$ (0.45 eV) to 4426 cm $^{-1}$ (0.55 eV) are redshifted from toluene (562 nm) over THF (634 nm) to dichloromethane (659 nm) and a pronounced increase of the Stokes shifts from 9200 to 16000 cm $^{-1}$ can be determined. The bathochromic emission shift with increasing solvent polarity indicates a significant charge transfer character of the excited state. CIE coordinates reveal yellow to orange emission colors (Figure S18). Emission is not intense and hardly visible to the eye in THF and dichloromethane. Luminescence lifetimes are in a typical range for organic chromophores¹⁸, and decrease with increasing solvent polarity from toluene ($\tau = 5.7$ ns) over THF ($\tau = 2.5$ ns) to dichloromethane ($\tau = 1.0$ ns). This observation indicates high non-radiative rate constants in each solvent.

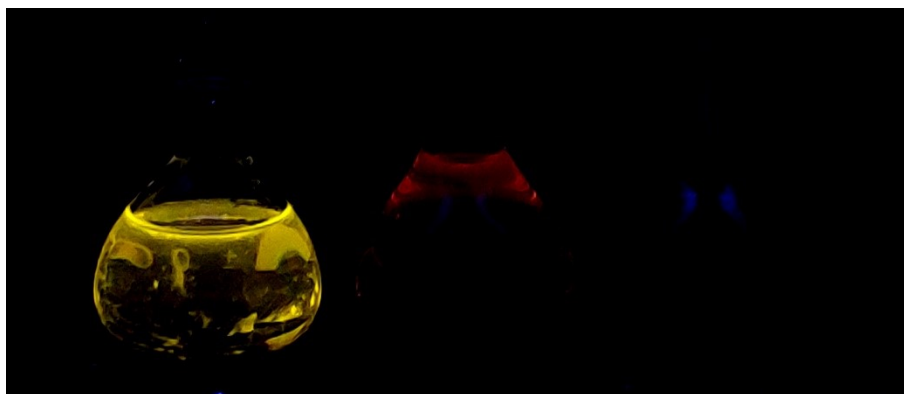


Figure S18. Emission of **pBN** in toluene, THF and dichloromethane (from left to right) ($c = 10^{-4}$ mol/L, $\lambda_{exc} = 365$ nm).

Compound mBN:

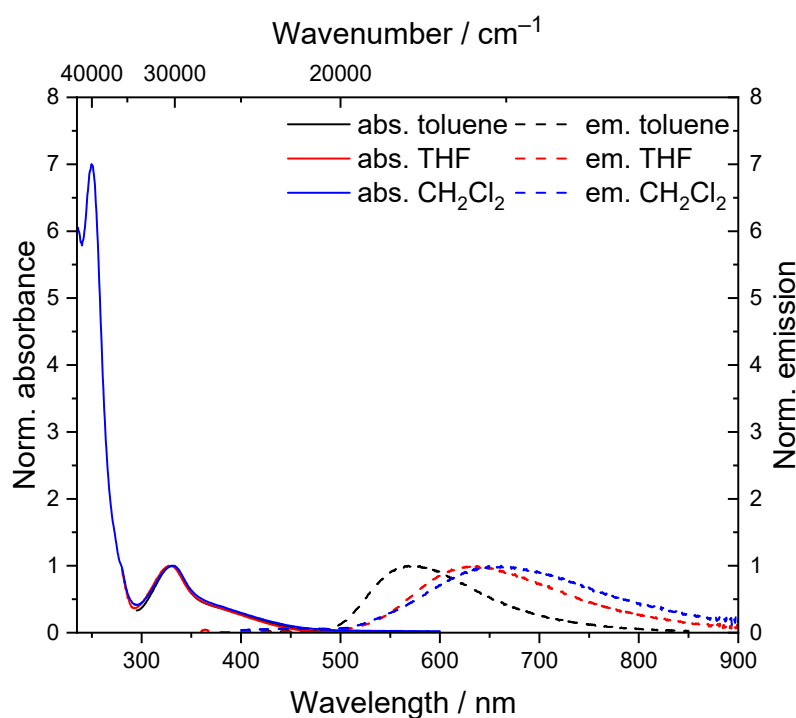


Figure S19. Absorbance and emission spectra of **mBN** recorded in solvents with different polarity ($c = 10^{-5}$ mol/L, $T = 293$ K).

Compound **mBN** possesses in toluene (331 nm, $\varepsilon = 6800$ L mol $^{-1}$ cm $^{-1}$) and THF (329 nm, $\varepsilon = 5900$ L mol $^{-1}$ cm $^{-1}$) a distinct longest wavelength absorption maximum that is accompanied by broad tailing shoulder around 380 nm with weaker intensity (Figure S19, Table 1). In dichloromethane, the higher energy absorption band at 250 nm with a molar absorption coefficient of 54200 L mol $^{-1}$ cm $^{-1}$ is found (Table 1). Also, in dichloromethane a shoulder around 380 nm can be identified.

While the absorption spectra are almost indifferent to the change of solvent polarity, the emission is strongly affected by solvent polarity and a distinct positive emission solvatochromism can be

observed in solvents of higher polarity (Table 1).¹⁷ The broad emission bands (full width at half maximum (FWHM) from 3746 cm⁻¹ (0.47 eV) to 4517 cm⁻¹ (0.56 eV) are redshifted from toluene (572 nm) over THF (634 nm) to dichloromethane (662 nm) and a pronounced increase of the Stokes shifts from 12700 to 15000 cm⁻¹ can be determined. The bathochromic emission shift with increasing solvent polarity indicates a significant charge transfer character of the excited state. CIE coordinates indicate an orangish-yellow color in emission (Figure S20, Table 1). Emission intensity strongly decreases with increasing solvent polarity. Already in toluene the emission is very weak, being not visible to the eye in THF and dichloromethane (Figure S20). Furthermore, the luminescence lifetimes fall into the typical range for organic chromophores,¹⁸ and the lifetimes decrease from toluene (τ = 8.9 ns) over THF (τ = 1.7 ns) to dichloromethane (τ = 1.6 ns). These observations indicate high non-radiative rate constants in each solvent.



Figure S20. Emission of **mBN** in toluene, THF and dichloromethane (from left to right) ($c = 10^{-4}$ mol/L, $\lambda_{exc} = 365$ nm).

Compound BPN:

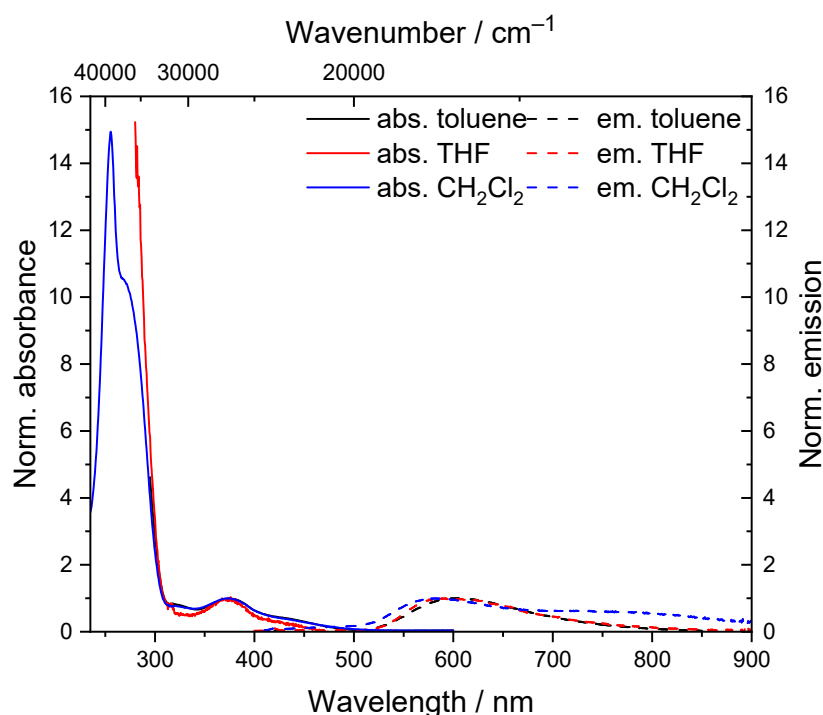


Figure S21. Absorbance and emission spectra of **BPN** recorded in solvents with different polarity ($c = 10^{-5}$ mol/L, $T = 293$ K).

Compound **BPN** possesses in toluene (375 nm, $\varepsilon = 6600$ L mol⁻¹ cm⁻¹) and THF (373 nm, $\varepsilon = 1900$ L mol⁻¹ cm⁻¹) a distinct longest wavelength absorption maximum that is accompanied by tailing shoulder around 427 nm with weaker intensity (Figure S21, Table 1). In dichloromethane, the higher energy absorption band at 255 nm with a molar absorption coefficient of 98000 L mol⁻¹ cm⁻¹ is found (Table 1). Also, in dichloromethane a shoulder around 427 nm and 271 nm can be identified.

While the absorbance spectra are almost indifferent to the change of solvent polarity, the emission is strongly affected by solvent polarity and a distinct negative emission solvatochromism can be observed in solvents of higher polarity (Table 1).¹⁷ The broad emission bands (full width at half maximum (FWHM) from 3564 cm⁻¹ (0.44 eV) to 6442 cm⁻¹ (0.88 eV) are blueshifted from toluene (604 nm) over THF (589 nm) to dichloromethane (587 nm) and a decrease of the Stokes shifts from 10100 to 9800 cm⁻¹ can be determined. The hypsochromic emission shift with increasing solvent polarity indicates a stabilization of the excited state in apolar solvents. Dual emission in dichloromethane might be caused by a twisted intramolecular charge transfer (TICT) state.¹⁹ Upon photonic excitation the LE state equilibrates rapidly with the TICT state at lower energy.²⁰ This results in two emission maxima, one at higher energy (587 nm, emission from the LE state) and one at lower energy (760 nm, emission from the TICT state). The CIE coordinates clearly indicate orange emission colors (Figure S22). The intensity of the emission is low in THF and dichloromethane, in toluene it is stronger, but not that intense (Figure S22). Furthermore, the luminescence lifetimes fall

into the typical range for organic chromophores,¹⁸ and range from 5.5 ns (toluene) to 12.0 ns (THF).



Figure S22. Emission of **BPN** in toluene, THF and dichloromethane (from left to right) ($c = 10^{-4}$ mol/L, $\lambda_{exc} = 365$ nm).

Luminescence decay times (Solution state)

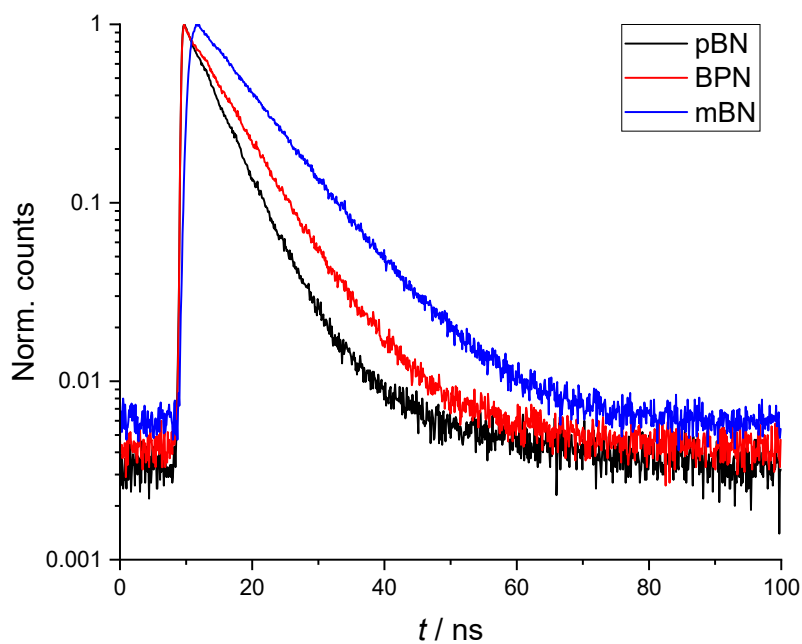


Figure S23. Photoluminescence decays for **pBN**, **mBN** and **BPN** recorded in toluene ($c = 10^{-4}$ mol/L, $T = 293$ K).

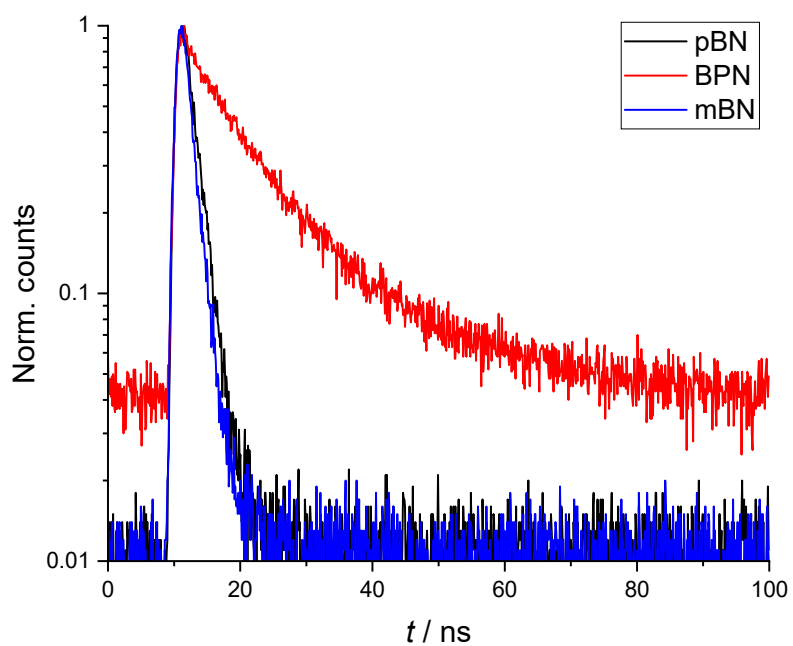


Figure S24. Photoluminescence decays for **pBN**, **mBN** and **BPN** recorded in THF ($c = 10^{-4}$ mol/L, $T = 293$ K).

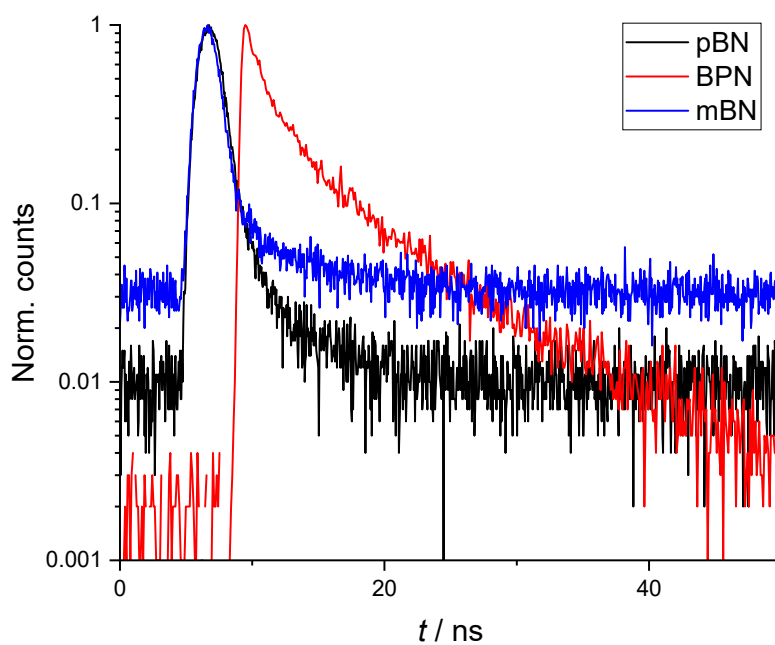


Figure S25. Photoluminescence decays for **pBN**, **mBN** and **BPN** recorded in dichloromethane ($c = 10^{-4}$ mol/L, $T = 293$ K).

S6 Data of quantum chemical calculations

Table S4. Computed absorption and emission data for **BPN**, **mBN** and **pBN** in vacuum. Oscillator strengths f are only given when > 0 , adiabatic energies are given in bold italics.

Molec.	Geom.	State	Spectral line / nm	Energy / eV	Composition
BPN	S₀	S ₀	-	0.00	92% GS
		S ₁	415	2.98	81% H-L
		S ₂	412	2.00	81% H-(L+1)
		S ₃	362	2.42	42% H-(L+2), 30% H-(L+4), 17% H-
		S ₄	343 $f = 0.10$	3.61	42% H-(L+3), 35% H-(L+5)
		T ₁	-	2.92	64% H-(L+2), 26% H-(L+7), 20% H-
		T ₂	-	2.95	53% H-L, 12% H-(L+8)
	S₁	S ₀	-	0.00	91% GS
		S ₁	544	2.28 2.49	84% H-L
		T ₁	-	2.34	84% H-L
	T₁	S ₀	-	0.00	91% GS
		S ₁	-	2.28	84% H-L
		T ₁	-	2.24 2.44	84% H-L
pBN	S₀	S ₀	-	0.00	94% GS
		S ₁	401	3.09	88% H-L
		S ₂	398	3.11	87% H-(L+1)
		S ₃	351	3.53	71% H-(L+2), 18% H-(L+4)
		S ₄	338 $f = 0.09$	3.67	77% H-(L+3)
		T ₁	-	3.01	41% H-(L+2), 38% H-(L+4)
		T ₂	-	3.06	80% H-L
	S₁	S ₀	-	0.00	93% GS
		S ₁	-	2.57 2.70	89% H-L
		T ₁	-	2.54	89% H-L
	T₁	S ₀	-	0.00	93% GS
		S ₁	-	2.58	89% H-L
		T ₁	-	2.54 2.67	89% H-L
mBN	S₀	S ₀	-	0.00	94% GS
		S ₁	402 $f = 0.01$	3.08	78% H-L
		S ₂	398 $f = 0.01$	3.11	78% H-(L+1)
		S ₃	351 $f = 0.01$	3.54	73% H-(L+2)
		S ₄	344 $f = 0.01$	3.60	73% H-(L+3), 11% H-(L+2)
		S ₅	310	4.00	80% H-(L+4)
		S ₆	296 $f = 0.14$	4.20	82% H-(L+5)
		T ₁	-	2.89	37% H-(L+1), 26% H-(L+4), 20%
		T ₂	-	3.01	59% H-L, 24% H-(L+1)
	S₁	S ₀	-	0.00	93% GS
		S ₁	497	2.49 2.68	89% H-L
		T ₁	-	2.41	81% H-L
	T₁	S ₀	-	0.00	93% GS
		S ₁	-	2.51	89% H-L
		T ₁	-	2.41 2.59	79% H-L

	S_0	S_1
BPN	8.78°	0.01°
mBN	10.95°	1.49°
pBN	11.43°	0.01°

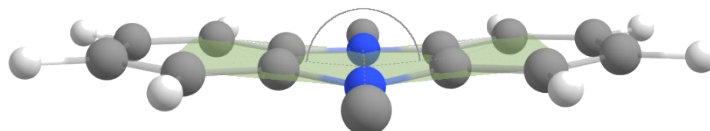
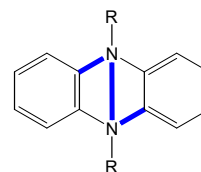


Figure S26. Phenazine-core planarization. Table entries denote the C-N-N-C dihedral angle in S_0 and S_1 geometries computed at the (TD)-DFT PBE0 level of theory.

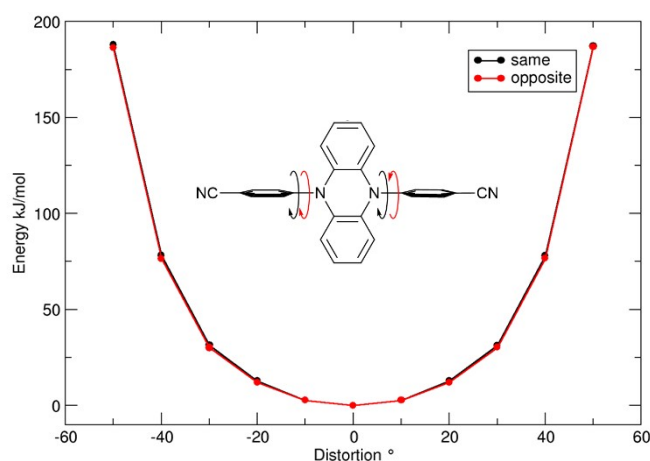


Figure S27. Unrelaxed dihedral scan for phenyl-rotation in **pBN** showing the energy profile (same and opposite directions phenyl rotation, the starting point corresponds to the perpendicular arrangement (90°) of phenazine and phenyl rings).

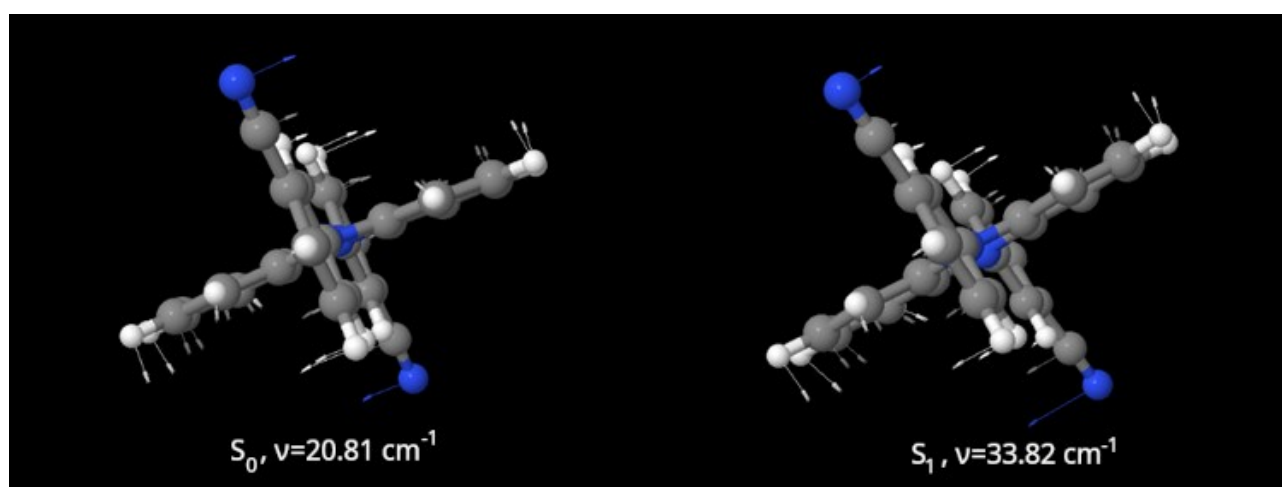


Figure S28. Normal mode vibrations including phenyl torsions in **mBN** (same direction) in S_0 (left) and S_1 (right) geometries.

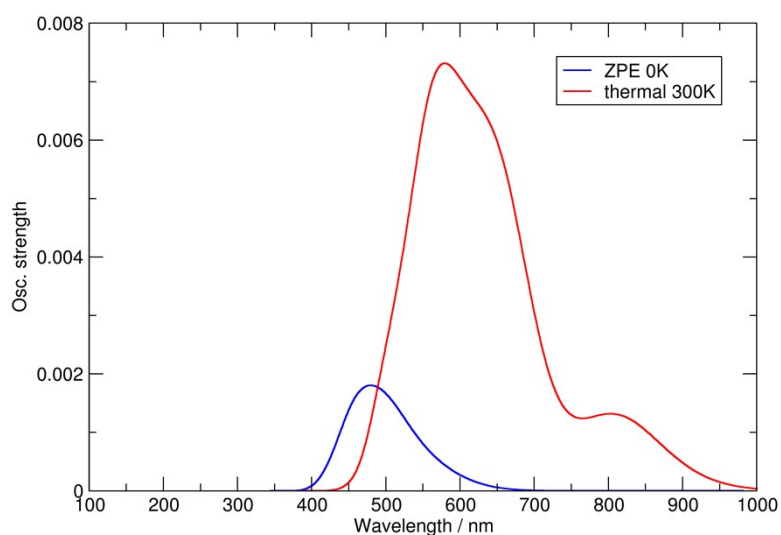


Figure S29. Computed emission in **pBN** at 0 K and 300 K (vacuum).

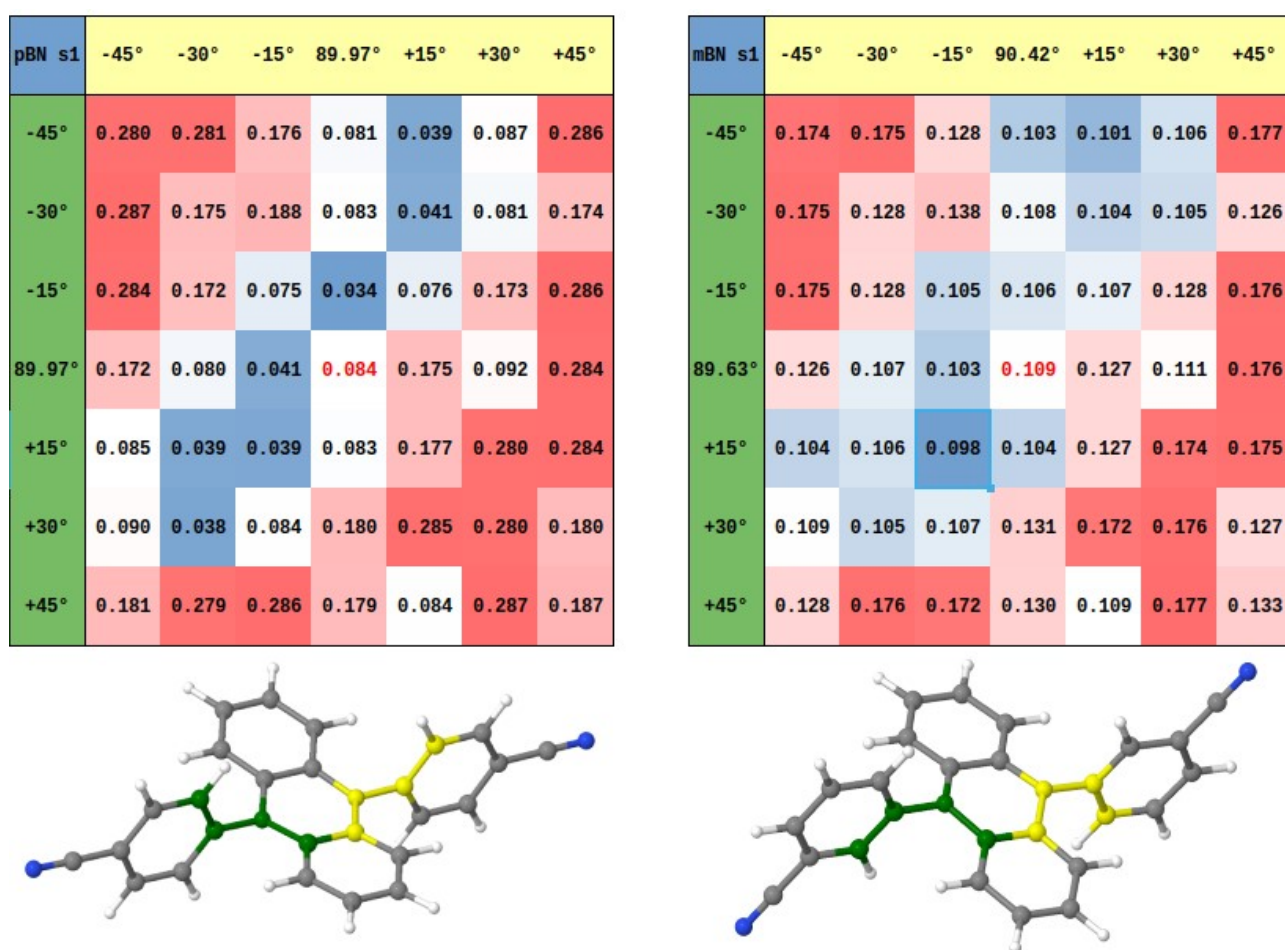


Figure S30. Modulation of ΔE_{ST} in **mBN** and **pBN**.

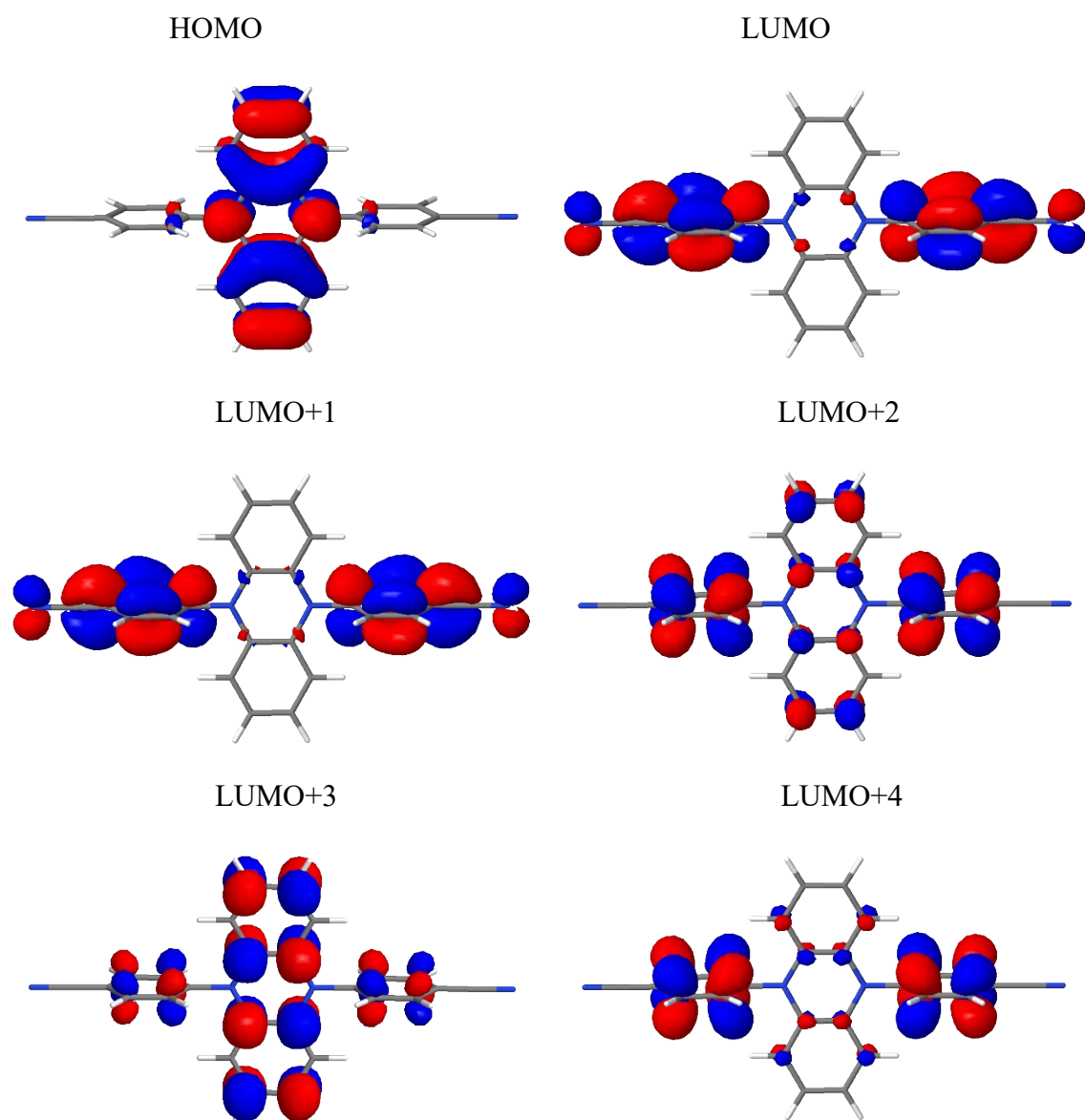


Figure S31. BH-LYP-computed orbitals involved in **pBN** excitations.

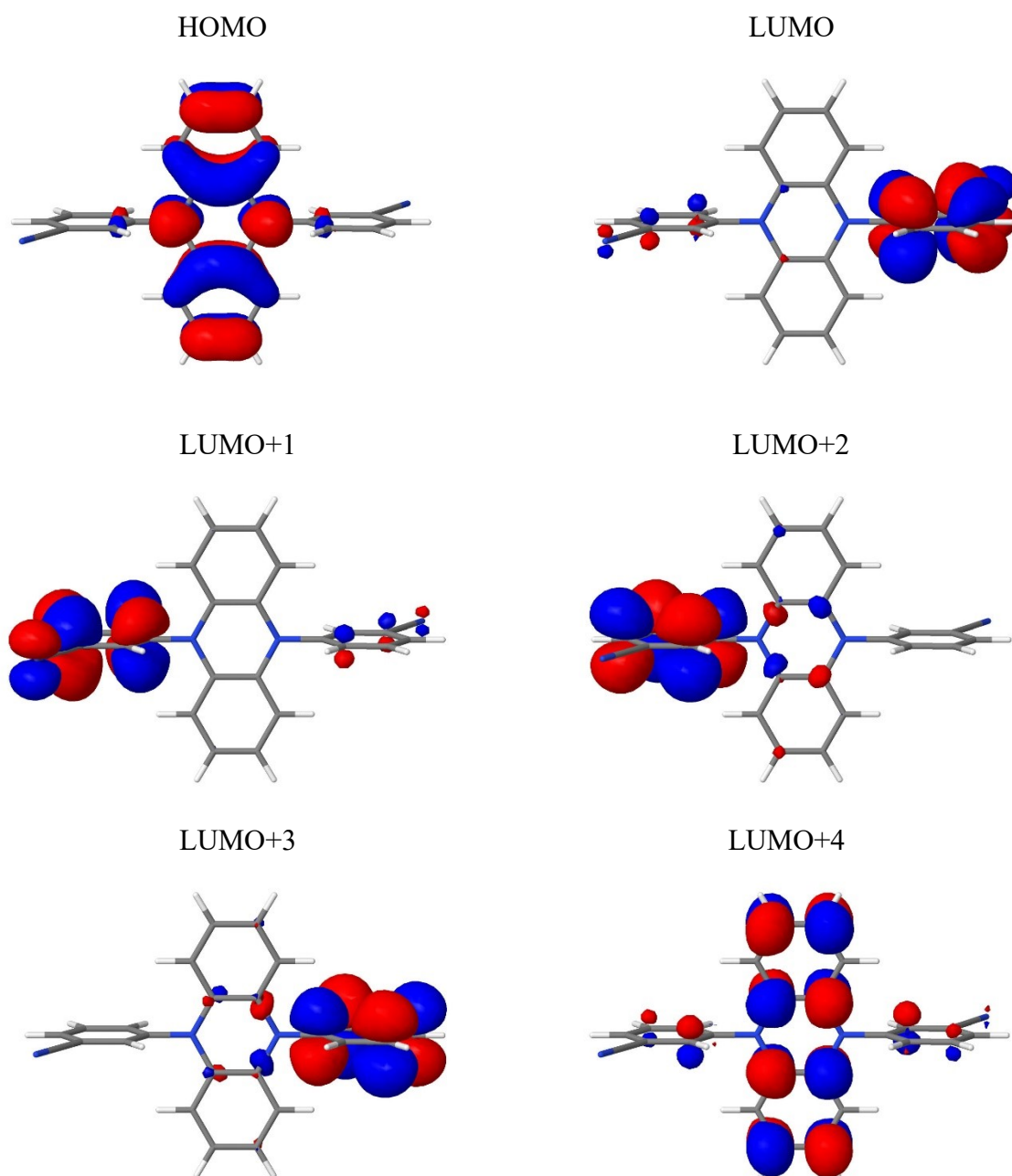


Figure S32. BH-LYP-computed orbitals involved in **mBN** excitations.

References

1. Lee, J.; Shizu, K.; Tanaka, H.; Nakanotani, H.; Yasuda, T.; Kaji, H.; Adachi, C. Controlled emission colors and singlet–triplet energy gaps of dihydrophenazine-based thermally activated delayed fluorescence emitters. *J. Mater. Chem. C* **2015**, *3*, 2175–2181. <https://doi.org/10.1039/c4tc02530j>
2. Theriot, J.C.; Lim, C.-H.; Yang, H.; Ryan, M.D.; Musgrave, C.B.; Miyake, G.M. Organocatalyzed atom transfer radical polymerization driven by visible light. *Science* **2016**, *352*, 1082–1086. <https://doi.org/10.1126/science.aaf3935>
3. WO 2014/18922 A1
4. APEX2, data collection program for the CCD area-detector system, Version 2.1-0, Bruker Analytical X-ray Systems, Madison (WI), USA, 1997–2014.
5. SAINT, data reduction and frame integration program for the CCD area-detector system, Bruker Analytical X-ray Systems, Madison (WI), USA, 1997–2014.
6. CrysAlis^{Pro}, Rigaku Oxford Diffraction/Agilent Technologies UK Ltd, Yarnton, Great Britain, release 1.171.40.103a, **2021**.
7. Sheldrick, G.M. Crystal structure refinement with SHELXL. *Acta Crystallogr. Sect. C Cryst. Struct. Commun.* **2015**, *C71*, 3–8. <https://doi.org/10.1107/S2053229614024218>.
8. Dolomanov, O.V.; Bourhis, L.J.; Gildea, R.J.; Howard, J.A.K.; Puschmann, H. OLEX2: A complete structure solution, refinement and analysis program. *J. Appl. Crystallogr.* **2009**, *42*, 339–341. <https://doi.org/10.1107/S0021889808042726>.
9. Brandenburg, K. Diamond 4.6, Crystal and Molecular Structure Visualization. Copyright 1997–2022 Crystal Impact GbR, Bonn, Germany. Available online: <https://www.crystalimpact.com/diamond/> (accessed on 10 August 2022).
10. Q. Wan, Y. Li, K. Ding, Y. Xie, J. Fan, J. Tong, Z. Zeng, Y. Li, C. Zhao, Z. Wang, B. Z. Tang. Aggregation Effect on Multiperformance Improvement in Aryl-Armed Phenazine-Based Emitters. *J. Am. Chem. Soc.* **2023**, *145*, 1607–1616. <https://doi.org/10.1021/jacs.2c09210>
11. Spek, A.L. Structure validation in chemical crystallography. *Acta Crystallogr. D Biol. Crystallogr.* **2009**, *65*, 148–155, doi:10.1107/S090744490804362X.
12. Spek, A.L. *PLATON—A Multipurpose Crystallographic Tool*; Utrecht University: Utrecht, The Netherlands, 2008.
13. Farrugia, L.J. *Platon – Windows Implementation*; Version 270519; University of Glasgow: Scotland, UK, 2019.
14. Janiak, C. A critical account on π – π stacking in metal complexes with aromatic nitrogen-containing ligands. *J. Chem. Soc. Dalton Trans.* **2000**, 3885–3896. <https://doi.org/10.1039/b003010o>.
15. Yang, X.-J.; Drepper, F.; Wu, B.; Sun, W.-H.; Haehnel, W.; Janiak, C. From model compounds to protein binding: Syntheses, characterizations and fluorescence studies of $[\text{Ru}^{\text{II}}(\text{bipy})(\text{terpy})\text{L}]^{2+}$ complexes (bipy = 2,2'-bipyridine; terpy = 2,2':6',2''-terpyridine; L = imidazole, pyrazole and derivatives, cytochrome c). *Dalton Trans.*, **2005**, 256–267. <http://dx.doi.org/10.1039/b414999h>.
16. Nishio, M. The CH/ π hydrogen bond in chemistry. Conformation, supramolecules, optical resolution and interactions involving carbohydrates. *Phys. Chem. Chem. Phys.* **2011**, *13*, 13873–13900. <https://doi.org/10.1039/C1CP20404A>.
17. Kamlet, M.J.; Abboud, J.L.; Taft, R.W. The Solvatochromic Comparison Method. 6. The π^* Scale of Solvent Polarities. *J. Am. Chem. Soc.* **1977**, *99*, 6027–6038. <https://doi.org/10.1021/ja00460a031>
18. Lakowicz, J.R. (Ed.) *Principles of Fluorescence Spectroscopy*; Springer US, Boston, MA, **2006**.
19. Grabowski, Z.R.; Dobkowski, J. Twisted intramolecular charge transfer (TICT) excited states: energy and molecular structure. *Pure Appl. Chem.* **1983**, *55*, 245–252. <https://doi.org/10.1351/pac198855020245>
20. Sasaki, S.; Drummen, G.P.C.; Konishi, G. Recent advances in twisted intramolecular charge transfer (TICT) fluorescence and related phenomena in materials chemistry. *J. Mater. Chem. C* **2016**, *4*, 2731–2743. <https://doi.org/10.1039/C5TC03933A>

RESEARCH ARTICLE | APRIL 10 2024

Multiexcitonic and optically bright states in subunits of pentacene crystals: A hybrid DFT/MRCI and molecular mechanics study

Timo Schulz ; Simon Hédé ; Oliver Weingart ; Christel M. Marian  

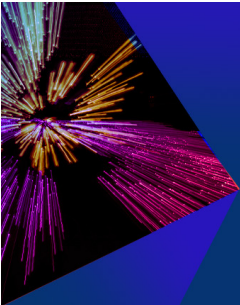


J. Chem. Phys. 160, 144114 (2024)


<https://doi.org/10.1063/5.0203006>



25 July 2024 10:41:47




The Journal of Chemical Physics



**Special Topic: Festschrift in
honor of Yuen-Ron Shen**

Submit Today



Multiexcitonic and optically bright states in subunits of pentacene crystals: A hybrid DFT/MRCI and molecular mechanics study

Cite as: J. Chem. Phys. 160, 144114 (2024); doi: 10.1063/5.0203006

Submitted: 8 February 2024 • Accepted: 22 March 2024 •

Published Online: 10 April 2024



Timo Schulz,^{a)} Simon Hédé,^{b)} Oliver Weingart,^{c)} and Christel M. Marian^{d)}

AFFILIATIONS

Institute of Theoretical and Computational Chemistry, Faculty of Mathematics and Natural Sciences, Heinrich Heine University Düsseldorf, Düsseldorf, Germany

^{a)}Electronic mail: timo.schulz@hhu.de

^{b)}Electronic mail: simon.hede@hhu.de

^{c)}Electronic mail: weingart@hhu.de. Present address: Center for Information and Media Technology, Heinrich Heine University Düsseldorf, Düsseldorf, Germany.

^{d)}Author to whom correspondence should be addressed: christel.marian@hhu.de

ABSTRACT

A hybrid quantum mechanics/molecular mechanics setup was used to model electronically excited pentacene in the crystal phase. Particularly interesting in the context of singlet fission (SF) is the energetic location of the antiferromagnetically coupled multiexcitonic singlet state, $^1(TT)$, and the ferromagnetically coupled analog in relation to the optically bright singlet state. To provide photophysical properties of the accessible spin manifold, combined density functional theory and multi-reference configuration interaction calculations were performed on pentacene dimers and a trimer, electrostatically embedded in the crystal. The likelihood of a quintet intermediate in the SF process was estimated by computing singlet–quintet electron spin–spin couplings employing the Breit–Pauli Hamiltonian. The performance of the applied methods was assessed on the pentacene monomer. The character of the optically bright state and the energetic location of the $^1(TT)$ state depend strongly on the relative orientation of the pentacene units. In the V-shaped dimers and in the trimer, the optically bright state is dominated by local and charge transfer (CT) excitations, with admixtures of doubly excited configurations. The CT excitations gain weight upon geometry relaxation, thus supporting a CT-mediated SF mechanism as the primary step of the SF process. For the slip-stacked dimer, the energetic order of the bright and the $^1(TT)$ states swaps upon geometry relaxation, indicating strong nonadiabatic coupling close to the Franck–Condon region—a prerequisite for a coherent SF process. The multiexcitonic singlet, triplet, and quintet states are energetically too far apart and their spin–spin couplings are too small to bring about a noteworthy multiplicity mixing.

Published under an exclusive license by AIP Publishing. <https://doi.org/10.1063/5.0203006>

I. INTRODUCTION

Oligoacenes have stirred the interest of experimental and computational chemists alike, as they have remarkable photophysical and electrical properties. Prominent in recent research is the process of singlet fission (SF) due to its potential to lead to efficient third generation solar cells.^{1,2} In this process, a singlet excited state (or singlet exciton) evolves into two triplet states on very short time scales and can thus address wavelength regions of the solar radiation spectrum that are otherwise unusable for generating electric current in photovoltaic (PV) devices. In this way, the Shockley–Queisser limit³ of 33.7% efficiency for an ideal single-junction solar cell can

be overcome.⁴ Comprehensive reviews on the topic were given by Casanova,⁵ Monahan and Zhu,⁶ and Smith and Michl.^{7,8}

While there is agreement on the basic mechanism, which involves an optically bright singlet excited state as well as a dark, spatially confined singlet-coupled bitriplet exciton, $^1(TT)$, losing spatial-, but retaining spin-coherence,^{9,10} details have been heavily debated. Whether the initial step forming the $^1(TT)$ state is a coherent process¹¹ or follows a stepwise charge transfer (CT)-mediated mechanism^{12–15} has been controversially discussed. Very recently, the authors of the work of Neef *et al.*^{16,17} presented clear experimental evidence supporting the CT-mediated route in pentacene crystals. It remains unclear, however, how the antiferromagnetically

coupled triplet pair evolves into free triplets. Mechanisms involving a ferromagnetically coupled triplet pair, $^5(T \dots T)$, seem to be a plausible variant.¹⁸ Experimental indications for the formation of an intermediate quintet state come from transient electron paramagnetic resonance (EPR) spectroscopy of pentacene films¹⁹ and covalently linked pentacene dimers.^{20–22}

Although pentacene dimers have been extensively studied computationally,^{23–28} very few computational studies have investigated the full spin manifold, i.e., singlet, triplet, and quintet states, possibly involved in the SF process. One of the main problems has been the quality of the electronic structure methods that are applicable to dimers or even trimers: Accurate *ab initio* methods that can handle double excitations, such as equation-of-motion coupled cluster singles and doubles (EOM-CCSD) or complete active space self-consistent field methods with perturbative second-order correlation corrections (CASSCF/MRPT2), are prohibitively expensive; cheaper methods such as linear response time-dependent density functional theory (TDDFT) are limited to single excitations and hence miss the biexcitonic states completely. Our group recently presented a cost-efficient approach²⁹ to reliably compute doubly excited states containing open-shell configurations in the framework of combined density functional theory and multi-reference configuration interaction (DFT/MRCI), which has proven to be a robust and fast method in the computation of excited states of varying character.^{30,31} In this work, we apply the DFT/MRCI method in a hybrid QM/MM (quantum mechanics/molecular mechanics) setup to model pentacene in the crystal phase and to investigate the full spin manifold, accessible to an entangled triplet pair, and analyze their interactions.

II. COMPUTATIONAL DETAILS

A. Gas-phase geometries

The ground, quintet, and excited state geometries of pentacene were optimized using the Gaussian 16 program suite. Ground state geometries were obtained with Kohn–Sham density functional theory (KS-DFT).³² Excited singlet state geometries were optimized using time-dependent density functional theory.^{33,34} In triplet state computations, the Tamm–Dancoff approximation (TDA)³⁵ was employed. The minima of lowest quintet states were determined with unrestricted KS-DFT. In all cases, PBE0^{36–40} was used as an approximation to the exchange–correlation functional. All centers were equipped with a def2-SV(P)⁴¹ basis set. Grimme’s D3 dispersion correction⁴² with Becke–Johnson damping⁴³ (D3-BJ) was used throughout.

B. QM/MM methodology

The crystal structure of pentacene (CCDC no./Refcode PEN-CEN04/170187)⁴⁴ was taken from the CCDC website. The unit cell was then refined through Quantum Espresso⁴⁵ using the generalized gradient approximation with PBE exchange–correlation⁴⁰ and RRKJ pseudopotentials.⁴⁶ Additionally, the D3-BJ dispersion correction was employed. The periodic boundary calculations were performed only at the gamma point and using a kinetic energy cutoff of 40 eV, with the cell size fixed to the experimental values. To create the bulk from the optimized unit cell, a $4 \times 4 \times 4$ supercell was generated and all molecules whose centroids were located strictly inside

the supercell were kept, resulting in a bulk of 7380 atoms in total. Atomic partial charges, to be employed in subsequent QM/MM calculations, were computed using restricted Hartree–Fock, the 6-31G* basis set, and the Merz–Kollmann scheme⁴⁷ for a nuclear arrangement extracted from the pentacene crystal. Force-field parameters were obtained from the Generalized Amber Force Field (GAFF), the parameters for nonbonding interactions (van der Waals parameters) were taken from the third set in the work of Singh and Kollman.⁴⁷ QM/MM geometry optimizations were performed with the COBRAMM2.0⁴⁸ package using Gaussian16 for the QM part and AMBER16 for the MM part. The geometries of the states in the QM layer, consisting of one, two, or three pentacene molecules, respectively, were optimized employing the same methods and technical parameters as in the gas-phase calculations. Vibrational analyses were performed in order to validate that the obtained structures were true minima for all S_0 and Q_1 states and for the S_1 and T_1 states of pentacene monomers and dimers. A vibrational frequency calculation was not performed for pentacene trimers due to the high demand on computational resources.

C. DFT/MRCI setup

DFT/MRCI^{30,49} is a semiempirical electronic structure method for computing the properties of electronically excited states in large molecular systems. It employs KS-DFT orbitals and orbital energies of a closed-shell anchor configuration in combination with a multi-reference configuration interaction (MRCI) expansion of the wavefunction. The idea behind this approach is to use the dynamical correlation, included in DFT by construction, to efficiently truncate the otherwise necessary large MRCI expansion. To avoid double counting of electron correlation, the approach makes use of extensive configuration selection and inserts scaling parameters and damping functions into the MRCI Hamiltonian. The R2022 ansatz²⁹ improves a description of doubly excited and degenerate states with respect to former DFT/MRCI parametrizations. In particular, good agreement with experimental trends for the low-lying excited states of polyacenes, β -carotenoids, and *para*-oligophenylenes was achieved with the R2022 approach.^{29,50} Unless noted otherwise, an energy selection threshold of $0.8 E_h$ and the *tight* parameter set optimized for this threshold was used in the present calculations. The one-particle basis was generated using the BH-LYP^{37,39,51–53} functional, again with a def2-SV(P) basis and an integration grid of 5, as implemented in the TURBOMOLE program suite.^{54,55} The MM surrounding was incorporated through point charges generated by COBRAMM2.0 in the previous step. Convergence criteria were met when the energy was converged to $10^{-7} E_h$ and the density to 10^{-7} . The frozen orbital approximation was employed in the DFT/MRCI calculations. Orbitals with an energy less than $-10 E_h$ and higher than $2 E_h$ were excluded from the correlation treatment. All DFT/MRCI calculations were carried out using a revised implementation of the program, which uses the OpenMP implementation of multithreading, instead of message passing as specified Message Passing Interface standard. Performance benchmarks and technical details of the OpenMP implementation will be published elsewhere. For the monomer, we calculated 21, 20, and 16 roots for the singlet, triplet, and quintet multiplicity, respectively. In the dimer cases, these numbers were reduced to 11 singlets, 10 triplets, and 5 quintets. Due to high demands on the computational resources, the

number of CI vectors was further reduced in the trimer case to 6 singlets, 7 triplets, and 2 quintets. The energy of the highest root in the reference space has an impact on the effective configuration selection threshold (tsel) in the DFT/MRCI method.⁴⁹ To obtain DFT/MRCI energies of comparable quality for the dimers and the trimer, the selection parameter was chosen such that an effective tsel value of $\approx 0.93 E_h$ resulted in both cases. Further information from the DFT/MRCI wavefunctions were extracted by means of the TheoDOR program.⁵⁶ In this context, molecular fragments were auto-generated using the interface to Open Babel⁵⁷ and transition densities were computed using ORBKIT.⁵⁸ All plots of molecular orbitals and densities were created with Jmol.⁵⁹

D. Electronic spin-spin coupling

Electron spin-spin dipole coupling (SSC) calculations were performed at the DFT/MRCI level using an OpenMP implementation of the SPOCK.SISTR⁶⁰ program, employing spin-spin integrals computed in the resolution-of-the-identity framework⁶¹ in a def2-SV(P) basis set. Second-order spin-orbit coupling (SOC) effects were evaluated perturbationally with SPOCK⁶² in the atomic mean-field approximation⁶³ of the Breit–Pauli Hamiltonian. SSC and SOC matrix elements were calculated for the five, ten, and eleven lowest quintet, triplet, and singlet states, respectively. The SSC Hamiltonian has the power to couple states of singlet and quintet spin multiplicity directly, thus enabling transitions between an antiferromagnetically (singlet) and ferromagnetically (quintet) coupled triplet pair states. Unlike SOC, SSC leads to first-order zero-field splitting (ZFS) of triplet and quintet states, even if they are orbitally nondegenerate as in the present case of pentacene. The same effect can be brought about by second-order SOC interactions. Experimentally, these two effects can be hardly told apart because both exhibit the same tensorial structure. For this reason, typically two fine structure parameters, D and E , are used to define an effective dipolar electron spin magnetic interaction Hamiltonian in spin multiplets.^{64–66} To avoid any possibility of confusion with symbols employed for doubly excited states or energy, we will use D_T and E_T in conjunction with the ZFS in triplet states and D_Q and E_Q for quintets, respectively. Due to symmetry selection rules, only the diagonal elements of the second-rank tensor contribute to the ZFS in D_{2h} molecular point groups.⁶⁵

III. RESULTS

To begin this section, we wish to introduce the nomenclature used in the following subsections. Commonly, the excited states of oligoacenes are labeled according to the nomenclature introduced by Platt,⁶⁷ which was derived for a simple perimeter model. However, as we deal not only with monomeric systems but also with dimers (and trimers) in which the situation is rather complex and the states have mixed character, we decided not to transfer this nomenclature as it would be too inflexible. Instead, we equipped all labels with a super- and a subscript encoding the leading configurations of the state, similar to the notation of excited determinants or configuration state functions in the context of configuration interaction. Singly excited states are labeled according to their spin multiplicity as S for singlets and T for triplets, as is common practice. A singlet excited state dominated by a single substitution in the highest

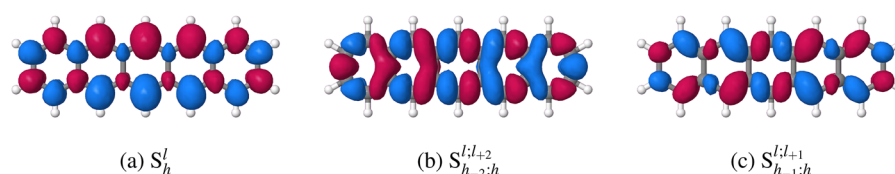
occupied molecular orbital (HOMO) and the lowest unoccupied orbital (LUMO) would be denoted as S_h^l , the corresponding triplet state as T_h^l in this nomenclature. $S_{h-1,h}^{l,l+1}$ denotes a singlet state featuring two singly excited configurations as leading terms, i.e., HOMO-1 to LUMO and HOMO to LUMO+1. Doubly excited states are differentiated by the number of open shells in their spatial configurations. Configurations with zero, two, or four open shells are denoted as N, Z, and V, based on the German words Null, Zwei, and Vier, respectively. A doubly substituted closed-shell spatial configuration involving an excitation from the HOMO to the LUMO, for example, would be denominated N_h^l , a double excitation from the HOMO to the LUMO and LUMO+1 with two open shells would be called $Z_h^{l,l-1}$, and finally a double excitation from the HOMO-1 and HOMO to LUMO and LUMO+1 featuring four open shells would be denoted as $V_{h-1,h}^{l,l+1}$.

A. Monomers

To assess the performance of the theoretical methods, we first discuss the excited states of the pentacene monomer. The four lowest excited singlet and triplet states are of interest to us, in the quintet manifold we will focus on the lowest electronic state only. It is commonly accepted that the lowest singlet excited transition S_h^l (1L_a , B_{2u}) of pentacene is polarized along the short molecular axis,⁶⁷ has ionic character,^{68–70} and is governed by a configuration constructed from a single substitution from the HOMO to the LUMO.^{25,71} Moreover, it is established that the long-axis transition $S_{h-2,h}^{l,l+2}$ (1L_b , B_{3u}) is located above the S_h^l and has a much weaker oscillator strength f . A third, yet less often discussed singlet state, $S_{h-1,h}^{l,l+1}$ (B_{1g}), is located close to the $S_{h-2,h}^{l,l+2}$ state and is dipole forbidden. Lastly, a doubly excited singlet state of A_g symmetry owing multiconfiguration character has been discussed in the vicinity of these two states due to its potential role in the SF mechanism.^{23,26} In Table I, this state is listed as N_h^l according to its leading configuration in our calculations. In the triplet manifold, the T_1 state (T_h^l , 3L_a , B_{2u}) has been studied by various experimental^{72,73} and theoretical methods.^{25,74–77} The T_2 state transforms according to the B_{1g} irreducible representation and is denoted here as $T_{h-1,h}^{l,l+1}$. Energetically, it is located far above T_h^l [$\Delta E(T_2 - T_1) \approx 1.4$ eV].⁷⁷ The second triplet state of B_{1g} symmetry is composed of the same leading terms as T_2 but exhibits a much higher oscillator strength in the triplet absorption spectrum and is therefore experimentally well known,⁷⁸ in contrast to the $T_{h-2,h}^{l,l+2}$ state (3L_b , B_{3u}), which cannot be reached from the T_1 state by a dipole-allowed transition. For a meaningful comparison of our results with literature data, it is mandatory to recognize whether the cited excitation energies refer to vertical, adiabatic, or 0–0 transition energies. For this reason, we annotated the literature data in Table I by specifying the experimental or computational method, respectively. Our calculations reproduce the state energies and their characters well, as can be seen from Table I. The crystal environment stabilizes the monomer by 0.46 eV in the electronic ground state but appears to have a minor impact on its excitation energies and oscillator strengths. The transition densities, displayed in Fig. 1, confirm that the $S_0 \rightarrow S_h^l$ (1L_a) transition dipole is oriented along the short molecular axes, whereas it points in the

TABLE I. Calculated vertical energies at the S_0 ($E_{\text{vert.}}$) and T_1 geometries ($E_{\text{vert.}}^a$) as well as adiabatic ($E_{\text{ad.}}$) energies of selected states of a pentacene monomer in crystal and gas-phase environments in comparison to literature values. All energies in eV. Oscillator strengths f of singlet transitions refer to the S_0 geometry, those of triplet transitions to the T_1 geometry.

State		$E_{\text{ad.}}$		$E_{\text{vert.}} (f)$		$E_{\text{vert.}} (f)^a$		Literature	
		Crystal	Gas	Crystal	Gas	Crystal	Gas	Experiments	Computations
1^3B_{2u}	T_h^l	0.89	0.88	1.10	1.09	0.00	0.00	0.86, ^b 0.95 ^c	0.98, ^d 1.07 ^e 0.87, ^f 0.72 ^g
1^3B_{1g}	$T_{h-1;h}^{l,l+1}$...	2.00	2.19	2.15	1.28 (0.0009)	1.25 (0.0017)	1.4 ^h	1.24, ⁱ 1.37, ^j 1.41 ^g
1^3B_{3u}	$T_{h-2;h}^{l,l+2}$	3.19	3.11	2.34	2.27
2^3B_{1g}	$T_{h-1;h}^{l,l+1}$	3.57	3.54	2.60 (1.0322)	2.58 (0.9948)	2.46 ^k	2.53, ^d 2.67 ^g
1^1B_{2u}	S_h	2.21	2.20	2.34 (0.1100)	2.34 (0.1087)			2.21, ^l 2.31 ^m	2.34, ⁿ 2.31, ^o 2.31 ^e
2^1A_g	N_h^l	2.97	2.94			...	2.63, ^e 2.52, ^d 2.88 ^o
1^1B_{3u}	$S_{h-2;h}^{l,l+2}$	3.22 (0.0000)	3.16 (0.0086)			2.94 ^l	3.29, ⁿ 3.14 ^o
1^1B_{1g}	$S_{h-1;h}^{l,l+1}$	3.30	3.24		
1^5A_g	$V_{h-1;h}^{l,l+1}$	4.24	4.19	4.78	4.70		

^a $T_1 \rightarrow T_n$.^bExtracted from kinetic data in crystal.⁷³^cIn cyclohexane, UV-vis absorption.⁷²^dVertical/pp-RPA.⁶⁹^eVertical/SS-CAS(12 π ,12)SCF+MRMP2, S_0 geometry.²⁶^fAdiabatic/SS-CAS(12 π ,12)SCF+MRMP2.²⁶^gVertical/RI-CC2, T_1 geometry.⁸³^hTransient triplet absorption in crystal.⁸⁰ⁱVertical/CAS(12,12)SCF+MRMP2.²³^jVertical/EOM-CCSD, S_0 geometry.⁷⁷^kFlash photolysis in benzene, lowest energy band of triplet absorption.⁷⁸^lIn argon matrix at 10 K, lowest energy band within a system.⁸¹^mSupersonic beam, band origin.⁸²ⁿVertical/CC2, S_0 geometry.⁸⁴^oVertical/SA-CAS(14,14)SCF+CASPT2.²⁵**FIG. 1.** Transition densities of the $S_0 \rightarrow S_h^l$, $S_{h-2;h}^{l,l+2}$, and $S_{h-1;h}^{l,l+1}$ excitations of monomeric pentacene. Isosurfaces were plotted with an absolute cutoff of 0.0004. Positive values are colored red and negative values blue.

direction of the long molecular axis in case of the $S_0 \rightarrow S_{h-2;h}^{l,l+2}$ (1L_b) excitation.

The singlet and triplet states of pentacene originating from $\pi\pi^*$ single excitations follow a principle introduced by Klán and Wirz⁷⁹ that relates the size of the singlet–triplet energy gap ΔE_{ST} to the overlap of the electron densities of the orbitals involved in the transition. The electron densities of HOMO and LUMO strongly overlap (see Fig. 2), with the result that the singlet–triplet splitting of the S_h^l and T_h^l states is very large, as required for efficient SF. In contrast, the ΔE_{ST} value of the $S_{h-2;h}^{l,l+2}$ and $T_{h-2;h}^{l,l+2}$ states is very small. The $S_{h-2;h}^{l,l+2}$ and

$T_{h-2;h}^{l,l+2}$ wavefunctions are composed of nearly equal contributions of HOMO-2 \rightarrow LUMO and HOMO \rightarrow LUMO+2 excitations. Klán and Wirz show that very small singlet–triplet splittings cannot only be achieved when donor and acceptor orbitals are spatially far apart but also in cases where the local electron densities in the orbitals involved in the electronic transition peak at different atoms.⁷⁹

Considering the 2^1A_g state of pentacene, we find dominant contributions of the doubly excited $(h)^0(l)^2$ and the ground state $(h)^2(l)^0$ configurations. While the former dominates with a weight of $\approx 70\%$, the ground state configuration contributes $\approx 5\%$

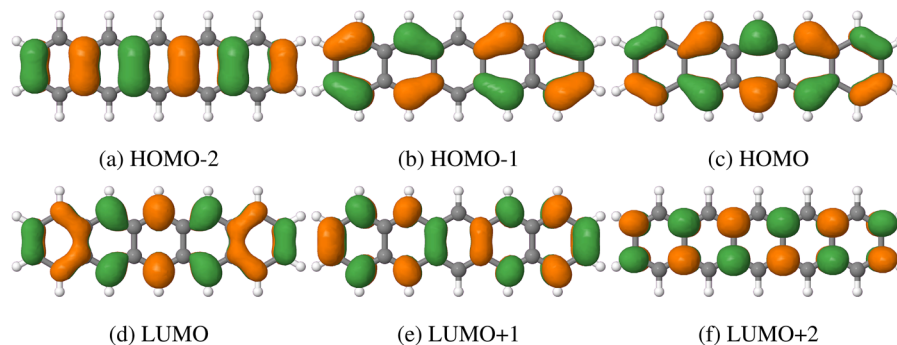


FIG. 2. Selected molecular orbitals in the ground state geometry of pentacene. Isosurfaces were plotted with a cutoff of 0.03. The electron densities of HOMO and LUMO strongly overlap, resulting in a large ΔE_{ST} value of the S_h^l and T_h^l states ($1^1B_{2u}-1^3B_{2u}$). In contrast, the electron density of HOMO-2 and LUMO and those of HOMO and LUMO+2 overlaps only slightly, explaining the tiny energy gap between the $S_{h-2,h}^{l/2}$ and $T_{h-2,h}^{l/2}$ states ($1^1B_{3u}-1^3B_{3u}$). The energetic splitting of the $S_{h-1,h}^{l/2}$ and $T_{h-1,h}^{l/2}$ states ($1^1B_{1g}-1^3B_{1g}$) is in-between.

to the wavefunction. 2^1A_g is likely the state labeled D by Zimmerman, Zhang, and Musgrave²³ using multi-reference perturbation theory (MRMP). They found the ground state configuration to contribute with 7% and report large amplitudes of doubly excited configurations involving HOMO-1, HOMO, LUMO, and LUMO+1. Unfortunately, the authors do not state whether their computed configurations are of closed- or open-shell character. The extra ordinarily low energetic position of their D state of 1.95 eV (lying below the bright S_h^l state in their calculation) is likely due to an intruder state problem, as discussed by Zeng, Hoffmann, and Ananth.²⁶ The latter authors determined the D state's energy at 2.63 eV, which is much closer to our computed value of 2.94 eV.

As a general trend, the C–C bonds perpendicular to the main molecular axis shorten upon electronic excitation (see Sec. S1.4 of the supplementary material). In the S_1 state, the C–C bonds at angles of $\pm 60^\circ$ with respect to this axis widen in the central ring while elongations and shortenings alternate in the neighboring rings. These atomic displacements clearly shape the first absorption band of pentacene (see below). Similar trends are seen for excitation to the T_1 state. Because the high-spin coupled electrons in the open shells tend to avoid each other, the shift in electron density away from the center toward the terminal rings is more pronounced in comparison to S_1 , thus resulting in stronger C–C bond elongations in the central ring. The Q_1 state is dominated by a double excitation involving the HOMO-1, HOMO, LUMO, and LUMO+1 orbitals (see Table I). Here, the Fermi correlation effect on the molecular geometry is even more pronounced than in the triplet states. As a consequence, its minimum nuclear arrangement shows extreme deformations of the terminal rings with displacements of the carbon centers by up to ± 5.4 pm.

The Franck–Condon (FC) spectrum of the $S_0 \rightarrow S_1$ absorption in the gas phase (Fig. 3) is dominated by a C–C stretch mode of the pentacene core with a progression of 1495 cm^{-1} , which fits the experimental results of 1514 cm^{-1} measured in a Ne matrix⁸⁵ very well. The second clearly visible structure peaking at 756 cm^{-1} to the blue-side of the 0–0 maximum matches the structure found by the authors of the work of Halasinski *et al.*⁸⁵ at 734 cm^{-1} . It is assigned to

a C–C concertina-like motion with a computed energy of 772 cm^{-1} in the electronic ground state. The shoulder at about 1200 cm^{-1} can be attributed to the A_g in-plane C–H bending vibration, which was measured by the same authors⁸⁵ at 1181 cm^{-1} and in the work of He *et al.*⁸⁶ at 1177 cm^{-1} in resonance Raman experiments. We identified it as mode 60 in pentacene. Figure S4 shows vectors of normal modes with a non-negligible dimensionless displacement in the Duschinsky transformation.

Before turning our attention to the pentacene dimers and the trimer, we want to present ZFS parameters of the T_1 state of

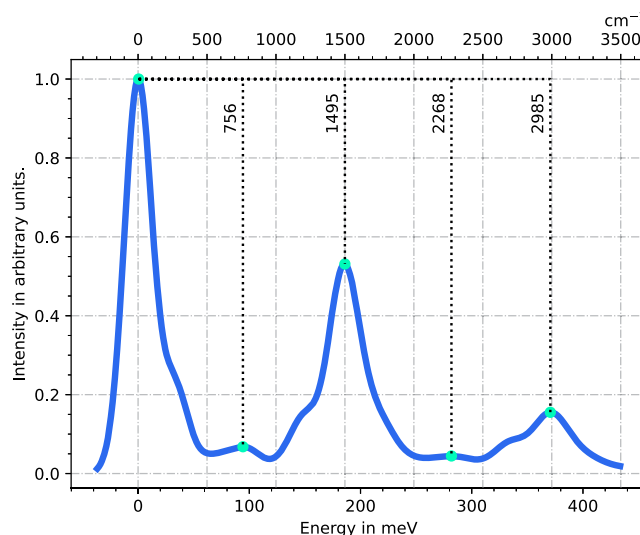
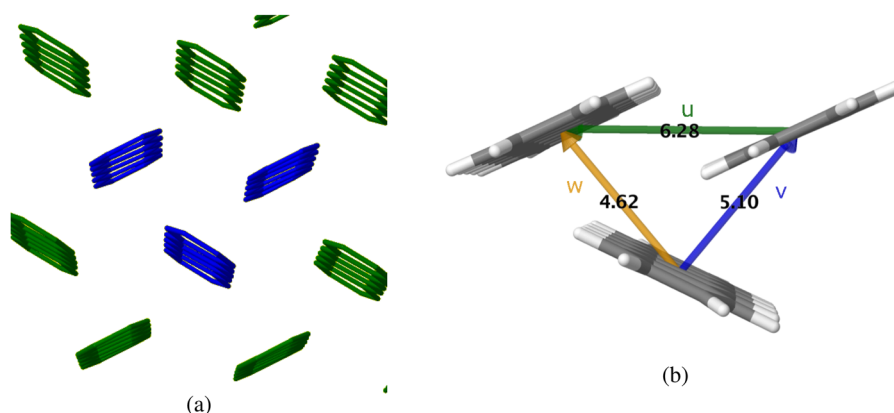


FIG. 3. Simulated Franck–Condon spectrum of the $S_0 \rightarrow S_1$ absorption of pentacene for a temperature of 10 K. Peak maxima are marked by green dots and their distances to the maximum of the largest peak are given in cm^{-1} . The correlation function was damped with a Gaussian of 100 cm^{-1} full width at half maximum before Fourier transformation. The numerical integration was performed for a time interval of 3000 fs and 262 144 grid points.

TABLE II. Comparison of calculated zero-field splitting parameters D_T and E_T of the T_1 state of monomeric pentacene at the optimized T_1 geometry with literature values. All values are given in cm^{-1} .

	This work		Other calculations				Experiments
D_T	0.032 126	0.0303 ^a	0.0305 ^b	0.0600 ^c	0.0327 ^d	0.046 510 ^e	0.046 519 ^f
E_T	0.001 237	0.0111 ^a	0.0079 ^b	−0.0042 ^c	−0.0008 ^d	0.001 823 ^e	0.001 778 ^f

^aROHF@TZVPP.⁶¹^bROHF@DZP.⁸⁷^cDDCI@TZVPP.⁶¹^dDFT/MRCI(original)@def2-SV(P).⁶¹^ePulsed EPR free induction decay (FID) after laser excitation of pentacene- h_{14} in benzoic acid.⁸⁸^fPulsed EPR free induction decay (FID) after laser excitation of pentacene- h_{14} in *p*-terphenyl crystals.⁸⁸**FIG. 4.** (a) Herringbone structure of the pentacene crystal. The trimer is marked in blue. (b) Definition of the dimer interaction patterns *u*, *v*, and *w*. The distances between the molecular centroids are given in Å.

the monomer computed with a newly developed OpenMP parallel version of our group's spin-spin coupling program, employing DFT/MRCI(R2022) vectors.

In the absence of an external field, the triplet spin of a nonlinear molecule is quantized in the direction of the principal axes of the spin-spin dipolar tensor *x*, *y*, *z*. In D_{2h} -symmetric molecules, these axes coincide with the C_2 symmetry axes of the point group. The model spin Hamiltonian in a zero field can then be written as⁶⁶

$$\hat{\mathcal{H}}_{SS} = -(X\hat{\mathcal{I}}_x^2 + Y\hat{\mathcal{I}}_y^2 + Z\hat{\mathcal{I}}_z^2), \quad (1)$$

where *X*, *Y*, and *Z* are the energies of the triplet sublevels arising from the ZFS. For the triplet ZFS parameters, one then obtains

$$D_T = \frac{1}{2}(X + Y) - Z = -\frac{3}{2}Z, \quad (2)$$

$$E_T = \frac{1}{2}(Y - X). \quad (3)$$

As can be seen from Table II, the agreement of the computed and experimental values is very good. Especially, the better agreement of the E_T value compared to the value computed with the original Hamiltonian is noteworthy. Second-order SOC contributions to the ZFS were found to be negligible.

B. Trimer and dimer subpatterns

In the crystalline phase, the pentacene molecules are arranged in a herringbone structure [Fig. 4(a)]. The authors of the work of Nagami *et al.*⁸⁹ identified three distinct interaction patterns, *u*, *v*, and *w*, in dimer subsets of herringbone pentacene structures [Fig. 4(b)].

1. Geometries and binding energies

The S_0 interaction energies of the respective subpatterns at the optimized ground state are given in Table III. Each value was computed as the difference between twice (or three times) the S_0 energy of a monomer in the crystalline environment E_{mon} and the S_0 state energy of the subpattern E_{pat} , i.e., $E_{int} = n \times E_{mon} - E_{pat}$, where $n = 2$ (dimers) or $n = 3$ (trimer). While the interaction energies

TABLE III. Ground state interaction energy E_{int} of the subpatterns in the crystal. All values in eV.

Pattern	Trimer	u	v	w
Geometry				
S_0	−0.55	0.14	−0.16	−0.23

of the **v** and **w** patterns are fairly similar, the **u** energy differs substantially. Furthermore, it is noteworthy that the interaction energy of the trimer differs from the sum of the pair interaction energies. The positive, i.e., repulsive interaction of the monomers in the **u**-pattern at the ground state geometry may be traced back to the slip-stacked orientation of the monomeric units and the electrostatic repulsion of their negatively charged π -electron systems. The attractive interactions of the **v** and **w** subpatterns are readily explained with a small overlap of the π -systems of the subunits and the proximity between the negatively charged π -electron cloud of one pentacene and the partially positive hydrogen atoms of the other, as can be seen exemplarily from the highest occupied molecular orbitals at the respective nuclear arrangements (Fig. 5). Illustrations of other molecular orbitals can be found in Figs. S7, S10, and S14.

A view along the long and short molecular axes of a reference pentacene (Fig. 6) reveals why the interaction energy is somewhat larger in the **w** than in the **v** pattern. The onset of the long axes in the **v** subpattern is slightly shifted with respect to the onset of the reference long axis, while the onsets of the long axes in the **w** configuration are almost congruent, leading to a larger interaction surface in the **w** pattern.

Comparing the electronic structures of the **u**-dimer at the ground, S_1 , T_1 , and Q_1 state minima, we notice that the MOs localize on the individual pentacenes in the S_1 and T_1 minimum nuclear arrangements (Fig. 7). Nevertheless, the excitation is delocalized over both pentacene molecules in the bright singlet state. The unidirectional polarization of the transition dipoles [Fig. 8(a)] effectuates a reduction of the monomer repulsion energy and leads to a slight decrease in the intermolecular separation between the slip-stacked

units (see Sec. II B). C–C bond elongations and shortenings in the individual pentacene units follow the same pattern as in the monomer S_1 state, but they are less pronounced. In the T_1 state, the excitation localizes on one of the pentacene molecules while the other acts as a spectator. The C–C bond length alterations in the Q_1 state of the **u**-dimer are indicative of a high-spin coupled triplet excitation on two adjacent pentacene units, hence featuring less drastic atomic displacements than the Q_1 state of the monomer and a similar distortion pattern as in the T_1 state in both units. The intermolecular separation of the pentacenes at the T_1 and Q_1 minima is nearly unaltered with respect to the electronic ground state configuration. Similar trends are observed for the geometry changes upon electronic excitation of the **v**- and **w**-dimers, but the trend of the exciton to localize or delocalize is less distinctive here.

2. Absorption in the Franck-Condon region

Investigating the transition densities of the lowest bright singlet excitation of the dimers at their ground state geometries (Fig. 8), we find short-axis transitions on the individual subunits, in agreement with expectations. Accordingly, the lowest transition in the full trimer is a combination of short-axis transitions on the three monomers, as shown in Fig. 8(d). Although the transitions have similar characters, their oscillator strengths f vary significantly among the different subpatterns (Table IV). Comparing with the oscillator strength of the monomer $S_0 \rightarrow S_1^f$ transition (Table I), it is clear that the subunits do not behave independently. While the oscillator strength of the first bright transition almost triples in the **u**-pattern, it decreases in the **w** and **v** patterns, respectively.

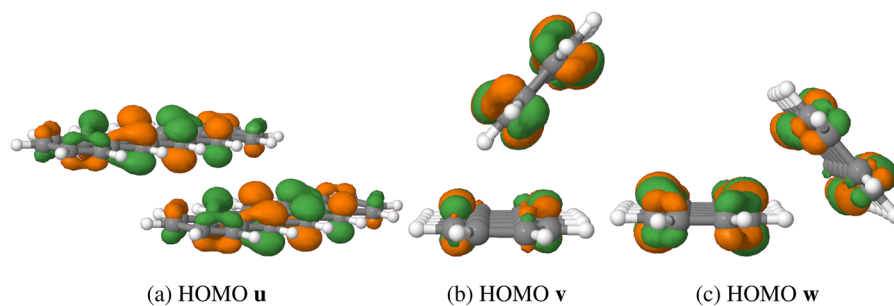


FIG. 5. The highest occupied molecular orbital of the subpatterns at their respective optimized ground state geometries. Isosurfaces were plotted with an absolute cutoff of 0.03.

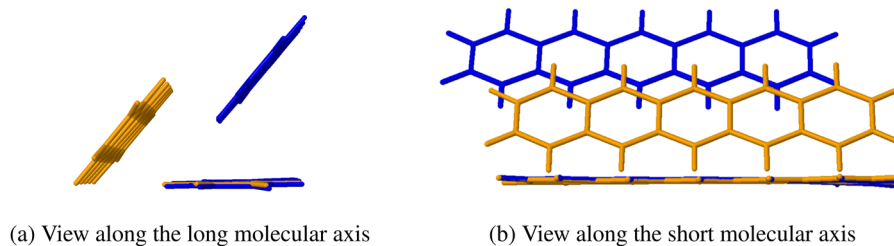


FIG. 6. Views along the (a) long and (b) short molecular axes of a reference pentacene in a trimer. The **v**-dimer is drawn in blue, the **w**-dimer in gold.

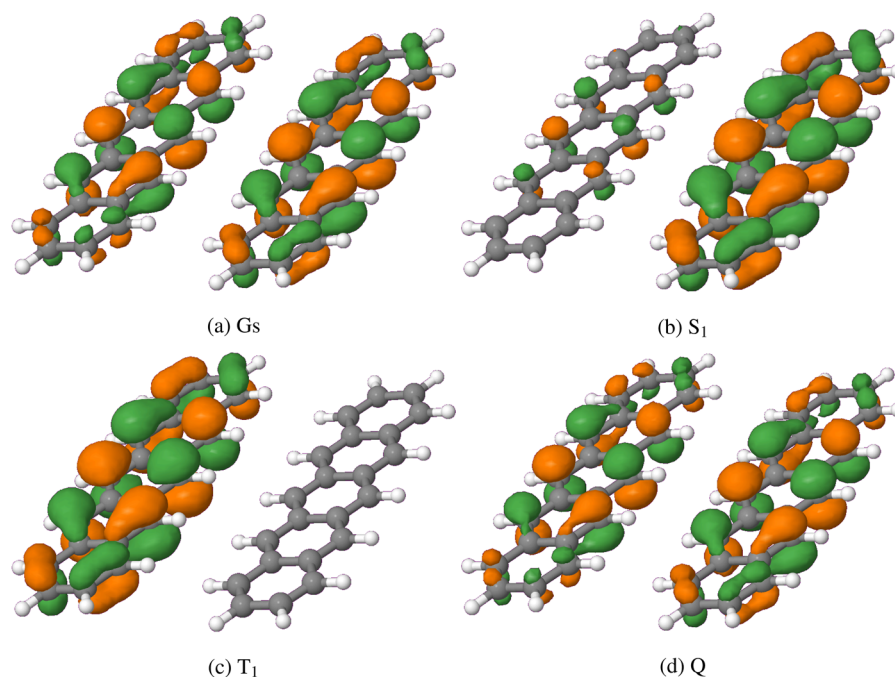


FIG. 7. Highest occupied molecular orbital at different optimized geometries of the **u** subpattern. Isosurfaces were plotted with a cutoff of 0.03.

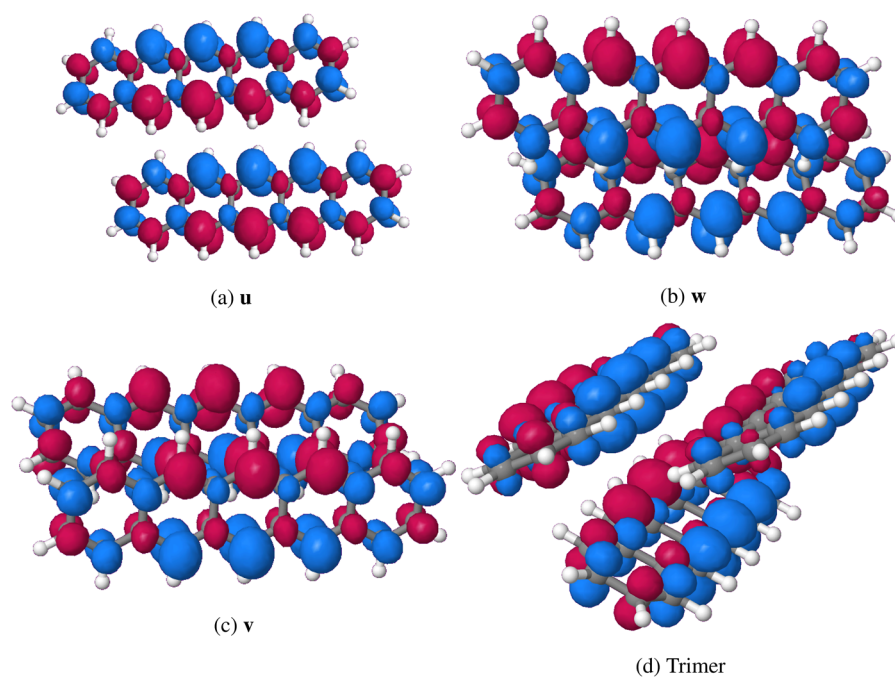


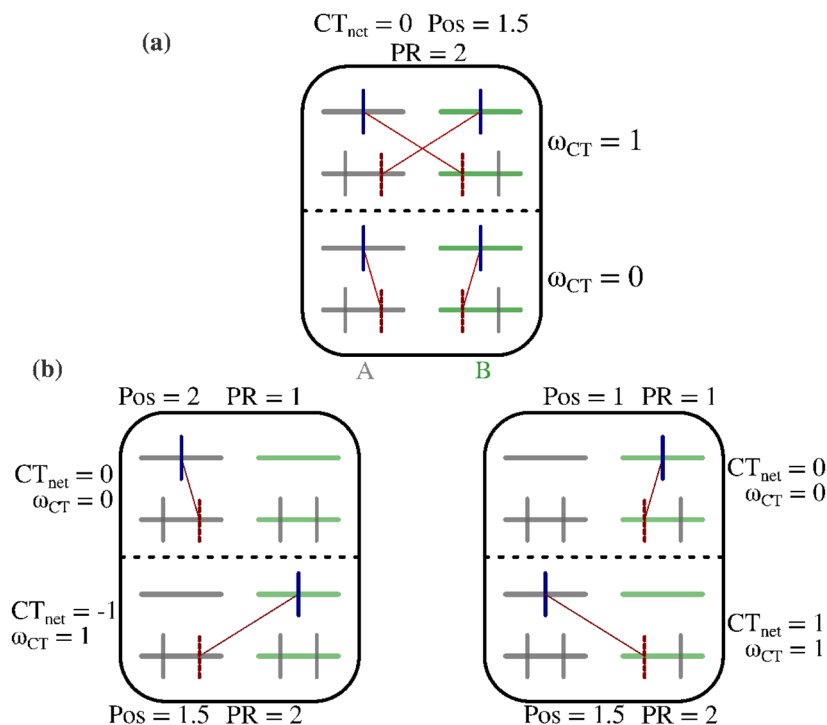
FIG. 8. Plots of the transition densities of the $S_0 \rightarrow S_1^h$ transition at the ground state geometries of the **u**, **v**, and **w** subpatterns and the trimer.

TABLE IV. Vertical energies at the respective geometries $E_{\text{vert.}}$, adiabatic energies $E_{\text{ad.}}$, oscillator strength f , and characterization of the singlet excited states with an oscillator strength larger than 0.05. All energies in eV. States are characterized as delocalized (DL), locally excited (LE), charge-resonance (CR), or charge transfer (CT) excitation.

Subpattern	u		v			w			Trimer			
Exc. state no.	1	2	1	1	2	1	1	2	1	3	1	5
At geometry	S_0	S_1	S_0	S_1		S_0	S_1		S_0		S_1	
$E_{\text{vert.}}$	2.31	2.14	2.25	2.02	2.09	2.21	1.99	2.07	2.24	2.37	2.14	2.44
f	0.2733	0.2486	0.1708	0.0533	0.1042	0.1664	0.0779	0.0732	0.2414	0.0921	0.1694	0.1599
Character	DL	LE + CR	CT + LE	CT	CT + LE	CT	CT	CT + LE	(DL + CR) _w	DL _v + CT _{A→v}	(CT + LE) _w	LE _B + CT _{C→B}
Assignment	$S_{h-1;l}^{l_{+1;l}}$	$S_{h;l-1}^{l_{+1;l+1}}$	S_h^l	S_h^l	$S_{h;l-1}^{l_{+1;l+1}}$	S_h^l	S_h^l	$S_{h;l-1}^l/N_h^l$	S_h^l	$S_{h-1;l;l-2}^{l_{+1;l}}$	S_h^l	$S_{h-1;l}^{l_{+1;l+2}}$

In the **u**-dimer, the subunits obviously form a J-type aggregate with singlet excitation energies of 2.31 and 2.37 eV, respectively, at the ground state geometry compared to 2.34 eV for the monomer in the crystal environment. The transition dipoles of the lower of the Davydov-split excitonic states lie parallel and hence increase the transition strength whereas they are antiparallel in the upper one and nearly cancel. As is evident from Table IV and Fig. 8, the transition dipoles of the $S_0 \rightarrow S_1$ excitations form acute angles in the **v** and **w** substructures, thus leading to a mild increase in the oscillator

strength compared to the S_h^l monomer absorption. The obtuse angle of the $S_0 \rightarrow S_2$ transition dipoles does not lead to a complete cancellation but a significant reduction of the electric dipole oscillator strength. In the trimer, the first bright absorption mainly involves local excitations on the A and C building blocks [Fig. 8(d)]. The situation therefore resembles the picture in the **w** subpattern. However, smaller contributions from an L_a -type transition on the B building block add to the transition dipole vector and enhance the oscillator strength compared to **w**. The $S_0 \rightarrow S_2$ transition of the trimer

**FIG. 9.** Types of single excitations on two predefined fragments A and B and the resulting descriptors. Red vertical lines depict holes, blue vertical lines electrons. Red connectors symbolize the direction of the excitation. Part (a) shows the usefulness of the ω_{CT} value if one needs to distinguish a charge-resonance configuration (upper panel) from an excitonic-resonance state (lower panel). Part (b) shows the idealized cases of pure local (upper panels) vs pure charge transfer excitations (lower panel) on the respective fragments.

(Fig. S30) resembles the corresponding transition of the **u**-dimer at the ground state geometry where the transition dipoles largely cancel. The transition dipole vector of the $S_0 \rightarrow S_3$ trimer excitation can be thought of as a positive linear combination of the individual vectors on the parallel A and B units, diminished by the transition vector of the C building block forming an obtuse angle with the former two.

3. Emission/photoexcitation decay

Due the pronounced multiconfiguration character of the excited state wavefunctions, an analysis based on the hole (donor) and particle (acceptor) MOs involved in the transition is elusive. First, we computed the difference densities⁹⁰ with respect to the ground state density, but this diagnostic is not suitable in all cases. For example, it does not allow us to distinguish a charge resonance (CR) transition, i.e., two simultaneous CT excitations from fragment 1 to fragment 2 and from fragment 2 to fragment 1, from two local excitations (LEs) on the fragments. To further characterize the states,

we employed additional descriptors deduced from a fragment analysis of the one-particle transition density matrix (1-TDM).^{56,91–93} A full list of the computed descriptors can be found in Tables S4–S6 for selected states. The most important ones for our interpretation of the electronic structures are the Frobenius norm Ω of the 1-TDM, the signed net charge transfer length CT_{net} , the CT-ratio ω_{CT} , the mean position of the electron-hole pair (exciton), Pos., and the participation ratio of the individual fragments, PR. The Frobenius norm Ω is a measure of the single excitation character of the transition and can vary between 0 (pure double and higher excitations) and 1 (pure single excitation). A value of $CT_{net} = 0$ in combination with $\omega_{CT} = 0$ means that no charge displacement took place upon excitation whereas $CT_{net} = 0$ in combination with $\omega_{CT} \gg 0$ indicates a charge resonance. A value of $CT_{net} = 1$ would imply a transfer of one electron from fragment 1 to fragment 2, a value of $CT_{net} = -1$ a transfer in the opposite direction. Pos. contains information about the final mean position of the particle and the initial mean position of the hole. The PR value measures how many fragments are involved in the transition. Detailed explanations of the

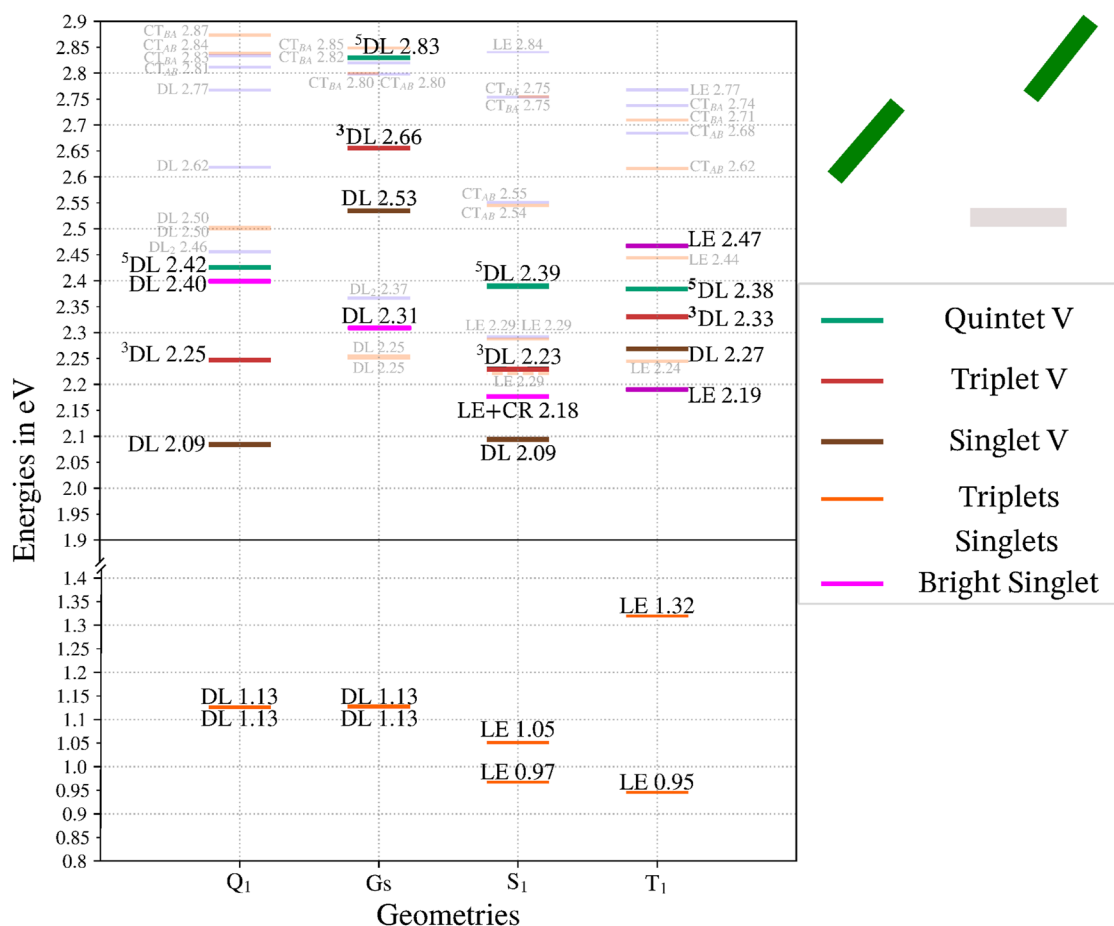


FIG. 10. Energy level scheme of the **u** subpattern. In the upper right corner, the position of the **u**-dimer within the trimer is indicated by thick green bars. All energies are given in eV and are calculated with respect to the ground state energy of this subpattern. States are characterized as either delocalized (DL), locally excited (LE), charge-resonance (CR), or as a charge transfer (CT) excitation.

mentioned quantities can be found in Refs. 56 and 91–93. To exemplify the usefulness of these descriptors, especially in the case of delocalized orbitals, we sketched possible situations for two fragments in Fig. 9.

a. Bright state. Although the MOs localize at the TDDFT-optimized S_1 geometry of the **u**-dimer (Fig. 7), the net charge transfer (-0.025) is very small in the bright state and the excitation remains delocalized over both units. Correspondingly, the oscillator strength remains high. With an interlayer spacing of >6 Å, the interaction between the two pentacenes in the **u**-dimer is significantly smaller (computed Davydov splitting of the $S_{h-1,h}^{hl+1}$ excitation $0.06/0.11$ eV at the S_0/S_1 geometry) than in films with more than 10% pentacene concentration where an interlayer spacing of ≈ 3.5 Å was assumed.¹⁹ Note, however, that a state with predominant double excitation character forms the lowest excited singlet state at the optimized $S_{h-1,h}^{hl+1}$ geometry according to the DFT/MRCI calculations (Fig. 10). The nonequivalence of the two pentacene subunits at this geometry is evident from the energetic splitting of the corresponding triplet states, which is small [$\Delta E(T_2 - T_1) = 0.08$ eV] at this nuclear arrangement.

For the **v** pattern, the bright singlet excited state S_h^l contains minor CT contributions in addition to local or charge resonance configurations, as indicated by the difference density plotted in Fig. 14(c) as well as the CT_{net} and ω_{CT} descriptors in Table S4. At the TDDFT-optimized S_1 geometry, we find a noticeable increase in the CT character for the S_h^l state as well as a mixing with the second excited state, which itself consists of $\approx 22\%$ doubly excited configurations. Out of these double excitations, 16% are of type N_h^l/N_{h-1}^l , while the remaining 6% can be attributed to the $V_{h,h-1}^{hl+1}$ configuration. This admixture is also seen clearly in the diagnostics. The PR drops from 1.928 at the S_0 geometry to 1.450 at the S_1 geometry while the CT_{net} greatly increases. The Frobenius norm Ω of the first excited singlet state value drops from 0.880 at the ground state geometry, indicating a dominantly single excitation character in the FC region, to 0.501 at the relaxed S_h^l geometry. Concomitantly, the oscillator strength is reduced from 0.1708 to 0.0533. The largest oscillator strength (0.1042) is found for the S_2 wavefunction at the S_1 minimum geometry. Similar trends are observed for the **w** pattern, but the single excitation character

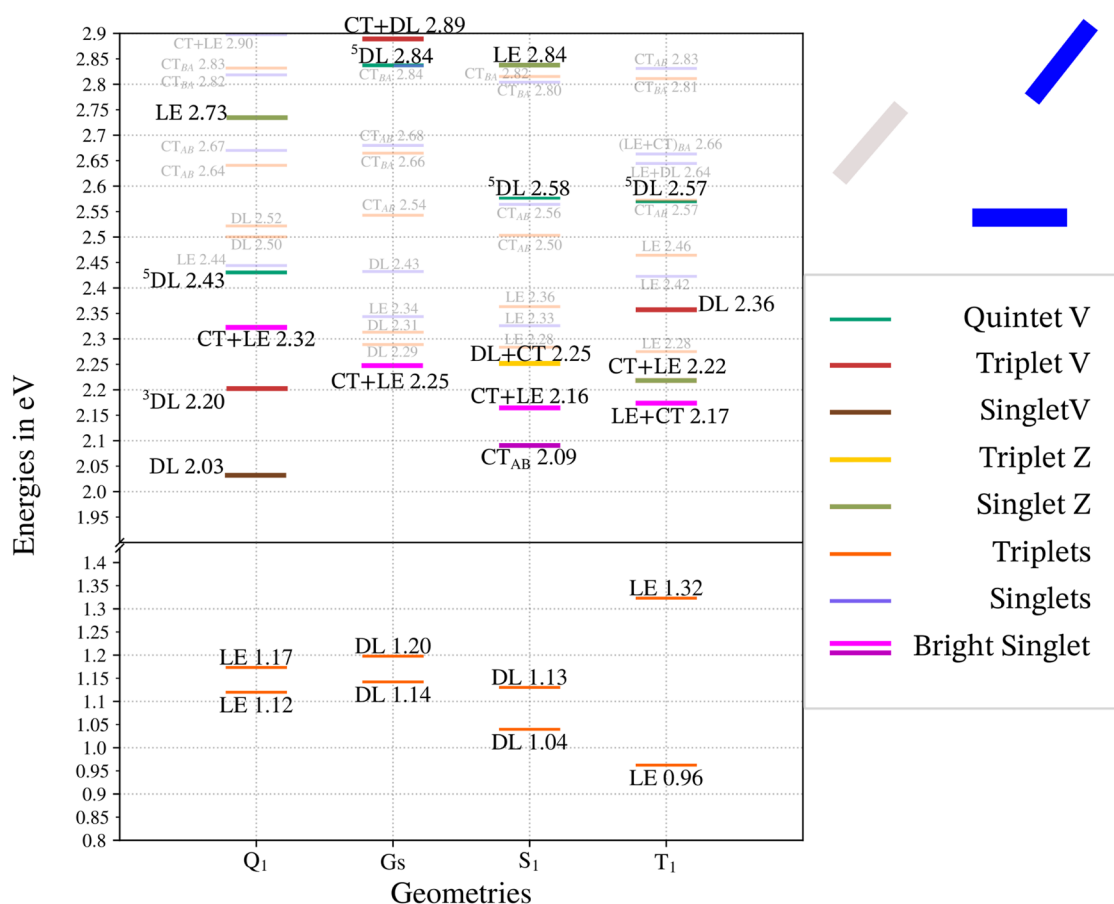


FIG. 11. Energy level scheme of the **v** subpattern. In the upper right corner, the position of the **v**-dimer within the trimer is indicated by thick blue bars. All energies are given in eV and are calculated with respect to the ground state energy of this subpattern.

remains dominant in the lowest excited singlet state, as exemplified by an Ω value of 0.631 and an oscillator strength of 0.0779 (Table S4). In this case, the second excited singlet state carries more double excitation character. The S_1 state of the trimer is also the brightest among the low-lying excited singlet states. At the S_1 geometry, it mainly involves the A and C units, similar to the w subpattern, and may be characterized as CT + LE. This state localizes on the C unit at the optimized T_1 geometry without changing the adiabatic excitation energy significantly. In all considered cases, the adiabatic excitation energy of the brightest singlet state ($E_{ad,dimer,trimer} \approx 2.15$ eV) (cp. Figs. 10–13) is somewhat lower than the corresponding monomer energy ($E_{ad,mono} = 2.21$ eV), i.e., the S_h^l state is stabilized by the delocalization of the excitation.

b. Doubly excited singlet state. As already mentioned, a singlet composed predominantly of double substitutions in the HOMO-1, HOMO, LUMO, and LUMO+1, as shown in Table V, becomes the lowest singlet state at the S_1 geometry of the u -dimer. We

associate this state with the singlet entangled bi-triplet exciton. This state is of utmost importance for the fission of the singlet exciton to independent triplets as it shares the same spatial occupation as two antiferromagnetically coupled triplet states. At first sight, the S_h^l state does not mix with this doubly excited state in the u -dimer, neither at the S_0 nor at the S_1 geometry. Note, however, that a conical intersection between the optically bright and the dark multiexcitonic singlet state must occur on the pathway between the absorption region and the minimum of S_h^l state (Fig. 10), thus providing the strong electronic coupling between the two singlet states that is required for a coherent mechanism as postulated in the work of Chan *et al.*¹¹ Figure 14(d) suggests that the excitation is completely delocalized over the two adjacent pentacene units in the dark state. However, the PR of 1.751 and the Frobenius norm of 0.348 indicate the participation of further configurations at the S_1 geometry. Remembering that the MO pairs HOMO/LUMO+1 and HOMO-1/LUMO of the u -dimer are mainly localized on one of the pentacene building units at the S_1 geometry, it is evident that the configurations number 3–7

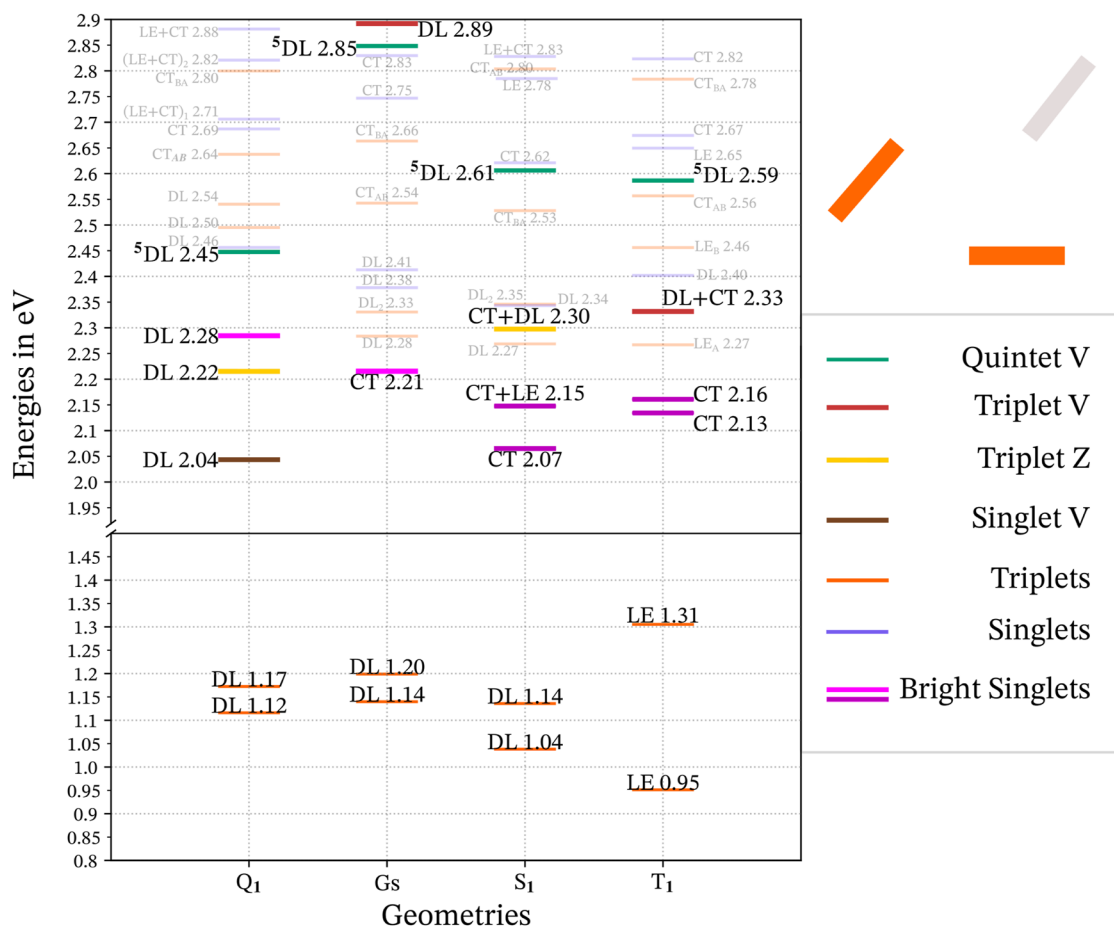


FIG. 12. Energy level scheme of the w subpattern. In the upper right corner, the position of the w -dimer within the trimer is indicated by thick orange bars. All energies are given in eV and are calculated with respect to the ground state energy of this subpattern. States are characterized as delocalized (DL), locally excited (LE), charge-resonance (CR), or as a charge transfer (CT) excitation.

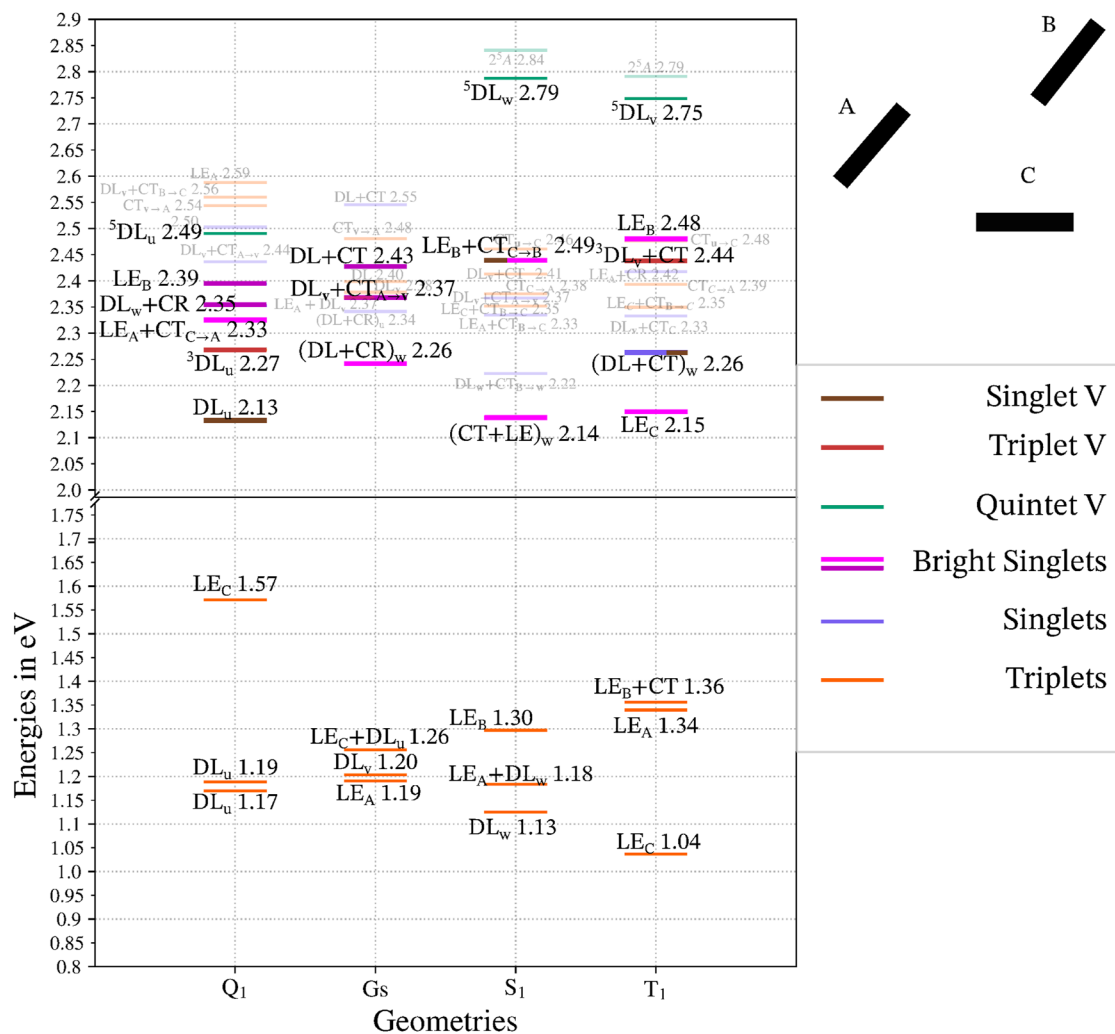


FIG. 13. Energy level scheme of the trimer. The position of the monomers A, B, and C within the trimer is indicated in the upper right corner. All energies are given in eV and are calculated with respect to the ground state energy. States are characterized as delocalized (DL), locally excited (LE), charge-resonance (CR) character, or as a charge transfer (CT) excitation.

in Table V all have an ionic component, i.e., are of CT or CR type, respectively. The CT_{net} value is found to be -0.377 at this geometry.

At the Q_1 geometry, which corresponds to the minimum of two ferromagnetically coupled triplet states and is our closest proxy for the minimum of the singlet-coupled triplet pair state, $^1(TT)$, the Ω value reduces to 0.018 as ought to be expected for a dominantly doubly excited state. With a value of 1.995 , the PR is close to its maximum (2.0) for a completely delocalized dimer state and the net CT reduces to 0.050 . Interestingly, the adiabatic energy of the $^1(TT)$ state (2.09 eV) hardly changes when moving from the S_1 to the Q_1 geometry.

Considering the already discussed CT states at the v and w patterns, we find noteworthy admixtures of the $V_{h-1,h}^{kl+1}$ configuration and a double excitation of type N_h^l (Table V). These findings

support the experimental results presented in the work of Neef *et al.*,¹⁶ which point toward a CT-mediated mechanism with a hybridization of Frenkel and CT states in the primary step of the SF process in single-crystal pentacene.

In the trimer, the optically bright singlet state and the $^1(TT)$ state are adiabatically degenerate, but they localize on different subpatterns. As described above, the bright state is dominated by excitations on the A and C units [Fig. 14(h)], thus resembling the excitation of the w -dimer. Its minimum geometry appears to be unfavorable for the triplet pair states (Fig. 13). The first singlet state with noteworthy contributions from $V_{h-1,h}^{kl+1}$ configurations is S_5 with an energy of 2.49 eV at this geometry. In contrast, the $^1(TT)$ forms the lowest excited state at the Q_1 geometry [Fig. 14(i)] where the excitation is delocalized over the A and B units, just like in the case of the u -dimer.

TABLE V. Composition, label, adiabatic energy $E_{ad.}$ (eV), coefficient, and weight in the CI vector of the lowest state with a double excitation character larger than 10% at the optimized S_1 geometry. The place in the energetic order is also given.

Subpattern	Order	$E_{ad.}$	No.	CSF	Composition	Coeff.	Weight	Label
u	1	2.09	1	1	$(h_{-1})^1(h)^1(l)^1(l_{+1})^1$	-0.3750	14.1	$V_{h_{-1};h}^{l,l_{+1}}$
			2	2	$(h_{-1})^1(h)^1(l)^1(l_{+1})^1$	0.3654	13.3	$V_{h_{-1};h}^{l,l_{+1}}$
			3	1	$(h)^0(l)^1(l_{+1})^1$	-0.3213	10.3	$Z_h^{l,l_{+1}}$
			4	1	$(h_{-1})^1(h)^1(l)^2$	0.3097	9.6	$Z_{h_{-1};h}^l$
			5	1	$(h_{-1})^0(l)^1(l_{+1})^1$	0.2729	7.4	$Z_{h_{-1}}^{l,l_{+1}}$
			6	1	$(h)^0(l)^2$	-0.2596	6.7	N_h^l
			7	1	$(h_{-1})^1(h)^1(l_{+1})^2$	-0.2447	6.0	$Z_{h_{-1}}^l$
			8	1	$(h)^1(l)^1$	0.1809	3.3	S_h^l
v	1	2.09	1	1	$(h)^1(l)^1$	0.6521	42.5	S_h^l
			2	1	$(h)^0(l)^2$	-0.3080	9.5	N_h^l
			3	1	$(h_{-1})^1(h)^1(l)^1(l_{+1})^1$	0.2410	5.8	$V_{h_{-1};h}^{l,l_{+1}}$
			4	1	$(h_{-1})^1(l)^1$	-0.2026	4.1	$S_{h_{-1}}^l$
w	1	2.07	1	1	$(h)^1(l)^1$	-0.7532	56.7	S_h^l
			2	1	$(h)^0(l)^2$	-0.2861	8.2	N_h^l
			3	1	$(h_{-1})^1(h)^1(l)^1(l_{+1})^1$	-0.1908	3.6	$V_{h_{-1};h}^{l,l_{+1}}$
Trimer	2	2.22	1	1	$(h)^1(l)^1$	0.5677	32.2	$S_{h_{+1}}^l$
			2	1	$(h)^0(l)^2$	-0.2966	8.8	N_h^l
			3	1	$(h)^1(l)^1$	0.2206	4.9	S_h^l

c. Triplet states. The two lowest states in the triplet manifold, T_h^l and $T_{h_{-1};h}^{l,l_{+1}}$, exhibit negligible CT character (Table S6). Energetically, they are almost degenerate at the ground state and the quintet geometries in all subpatterns and the excitations are delocalized. At the minimum geometries of the bright singlet states, the energetic splitting between the T_1 and T_2 states is still small, ranging from 0.08 eV in the **u**-dimer to 0.10 eV in the **w**-dimer as can be seen from the energy level plots shown in Figs. 10–12. More importantly, however, the requirement for an exothermal SF process, namely that the energy of the optically bright singlet state is larger than the sum of the two triplet energies, is fulfilled for the **u**-dimer. For the other two dimers, this process is slightly endothermic according to our calculations. In the **u**-dimer, the exothermicity of the SF holds true even for the multiexcitonic singlet state, i.e., $E(^1(TT)) > E(T_1) + E(T_2)$.

Upon geometry relaxation, the triplet excitations localize, as is evident from the energy schemes in Figs. 10–12 and the descriptors in Table S6. The adiabatic T_1 dimer excitation energy ($E_{ad.dimer} \approx 0.95$ eV) is somewhat higher than the corresponding monomer value ($E_{ad.mono} = 0.89$ eV) in the crystal surrounding. This might have technical reasons caused by slightly different effective configuration selection thresholds in the DFT/MRCI runs of the monomer and the dimers, but we note that the trend is opposite to what is found for the bright singlet. In the **u**-dimer, the T_1 is represented by a LE on fragment 1, i.e., the A unit. While the localization has a minor stabilization effect on T_1 with respect to the S_1 geometry (ΔE

$= -0.02$ eV), it causes a marked upshift of the T_2 excitation energy that localizes on fragment 2, i.e., unit B. The relaxation effect is somewhat larger in the **v** (0.08 eV, LE on B) and **w** patterns (0.09 eV, LE on C), but even in these dimers the sum of the T_1 and T_2 excitation energies is higher than at the relaxed geometry of the bright singlet state (cp. Figs. 10–12). In the trimer, the T_1 excitation localizes on unit C while the T_2 (LE on A) and T_3 (LE on B) states are almost uniformly upshifted. Hence, there seems to be a small driving force for a spatial separation of the two triplet excitons. We did not carry out dynamics simulations, but it appears plausible that the localization promotes the disentanglement of the triplet pair.

Particularly interesting in the context of SF is the energetic location of the triplet analog of the multiexcitonic singlet state, characterized by the $^3V_{h_{-1};h}^{l,l_{+1}}$ configuration. At the Q_1 geometries of the **u**- and **v**-dimers and of the trimer, we find a triplet state with this electronic structure in the energetic vicinity of the primary absorption transition. In contrast, a doubly excited triplet state with merely two open shells is observed in the **w**-dimer. Remarkably, the multi-excitonic state of the trimer seems to favor the **u** arrangement in all three possible spin manifolds, i.e., singlet, triplet, and quintet.

d. Quintet states. The quintet manifold allows for a compact discussion, as the situation for every subpattern is clear. A state dominated by a $V_{h_{-1};h}^{l,l_{+1}}$ spatial configuration constitutes the lowest quintet, as ought to be expected. Adiabatically, it is located between

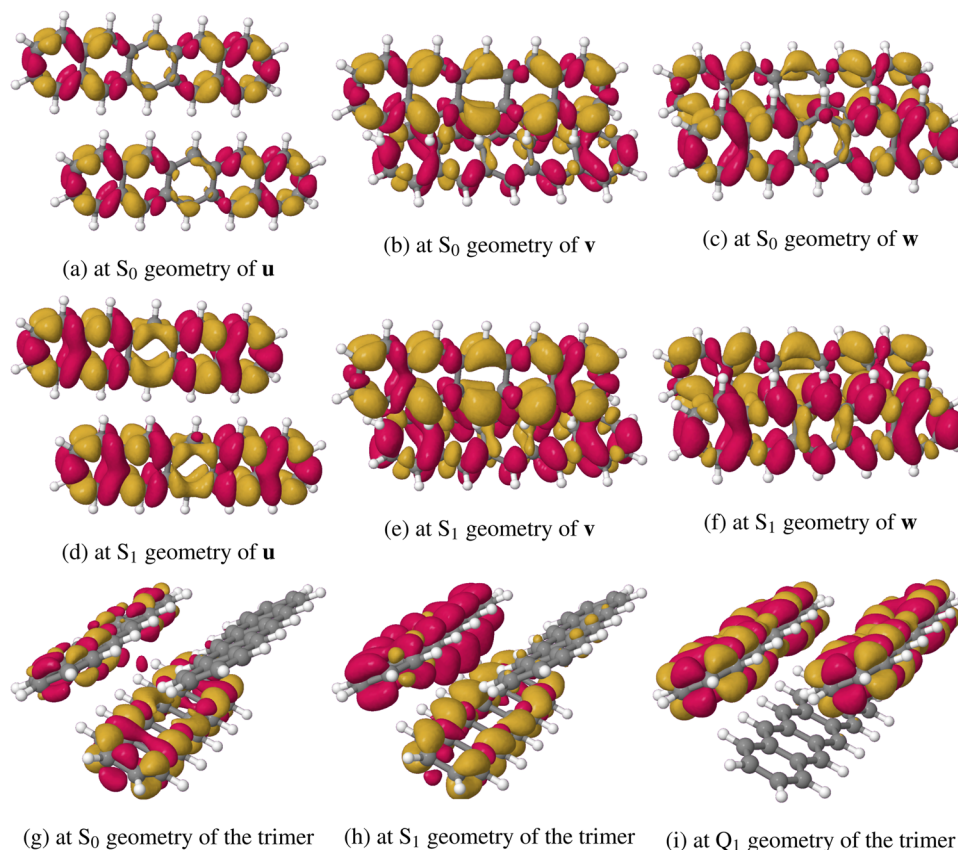


FIG. 14. Difference densities with respect to the ground state density (isovalue 0.0004) for the lowest singlet excited states at different geometries of the subpatterns.

2.42 and 2.45 eV above the electronic ground state in the dimers (Figs. 10–12) and at 2.49 eV in the trimer (Fig. 13). The gap to the next quintet state is larger than 1.1 eV in all investigated cases, ruling out the participation of any other quintet state than the lowest one. A look at the level schemes further reveals that a direct involvement of the Q_1 state in the SF process, as discussed in the work of Lubert-Perquel *et al.*¹⁹ for dilute pentacene films, is unlikely in spatially confined dimers composed of adjacent pentacene molecules. The energy separations of the $^1(\text{TT})$ and $^5(\text{TT})$ states are substantial in the **u**-, **v**-, and **w**-dimers as well as in the trimer. For the **u** subpattern, exhibiting the smallest energy gap (0.31 eV) among the dimers, we explicitly computed the spin–spin coupling matrix elements. In the limiting case of a large electrostatic energy splitting, the couplings between the spin pair functions are expected to be weak, but the spin multiplets split individually due to the fine structure interaction.⁶⁵ The computed off-diagonal SSC matrix elements are negligible ($\leq 10^{-6} \text{ cm}^{-1}$), indeed, and no singlet–quintet multiplicity mixing is apparent in the perturbed wavefunctions. As the coordinate axes do not coincide with the symmetry axes of the dimer, a transformation of the fine structure tensor to principal axes (x'' , y'' , z'') is required to express the calculated ZFSs in terms of the effective SSC parameters D_Q and E_Q .⁶⁵

$$\begin{aligned} E(Q_{1z''}) &= 2D_Q\sqrt{1 + 3E_Q^2/D_Q^2}, & E(Q_{2z''}) &= 2D_Q, \\ E(Q_{x''}) &= -D_Q + 3E_Q, & E(Q_{y''}) &= -D_Q - 3E_Q, \\ E(Q_{x''y''}) &= -2D_Q\sqrt{1 + 3E_Q^2/D_Q^2}. \end{aligned} \quad (4)$$

Here, $E(Q_{j''})$ denotes the energy of the quintet fine structure level $Q_{j''}$ with respect to the energy of the unperturbed quintet state. Comparing our computed energies of the $^5V_{h-1,h}^{l,l+1}$ sublevels with the expressions in Eq. (4), we arrive at ZFS parameters of $V_{h-1,h}^{l,l+1}$ of $D_Q = 0.00928 \text{ cm}^{-1}$ and $E_Q = 0.00511 \text{ cm}^{-1}$. The $^3(\text{TT})$ state of the **u**-dimer is located energetically about halfway between the $^1(\text{TT})$ and $^5(\text{TT})$ states but does not play a role in the spin multiplicity mixing either. Interestingly, its ZFS parameters ($D_{\text{TV}} = 0.02928 \text{ cm}^{-1}$, $E_{\text{TV}} = 0.00261 \text{ cm}^{-1}$) have similar magnitudes as those of the monomer T_1 state (Table II) and dimer ($D_{\text{T1}} = 0.03067 \text{ cm}^{-1}$, $E_{\text{T1}} = 0.00172 \text{ cm}^{-1}$) T_1 states although the excitation is delocalized over both pentacene molecules at the Q_1 geometry.

IV. CONCLUSION

In this work, we performed combined density functional theory and multi-reference configuration interaction (DFT/MRCI)

calculations on the energetics and photophysical properties of the low-lying electronic states of a pentacene monomer, three dimers, and a trimer structure, electrostatically embedded in a crystal surrounding. The quantum chemically treated dimer and trimer models are chosen such that they represent different spatially confined sub-patterns of the herringbone crystal structure of pentacene. While the **u**-dimer consists of adjacent, parallelly arranged pentacene molecules, the constituting pentacene units form an acute angle in the **v**- and **w**-dimers. To evaluate the likelihood of a quintet intermediate in the disentanglement of the triplet pair state, electron spin–spin coupling calculations were carried out on the **u**-dimer. The performance of the applied methods was assessed on the pentacene monomer where numerous theoretical and experimental reference values are at hand.

In the **u**-dimer, the optically bright $S_{h-1,h}^{l,l+1}$ and the multiexcitonic $^1(TT)$ states are clearly separated at the ground state and optimized $S_{h-1,h}^{l,l+1}$ geometries. Their wavefunctions show no apparent mixing in the absorption and emission regions, but their energetic order swaps. Hence, a conical intersection between the $S_{h-1,h}^{l,l+1}$ and $^1(TT)$ potential energy surfaces must have occurred upon geometry relaxation of the primarily excited singlet state. In the other dimers and in the trimer, this is not the case. Strong nonadiabatic coupling of the optically bright state and the dark multiexcitonic states close to the absorption region is a prerequisite for a coherent process. Consequently, we postulate that the **u**-pattern plays a fundamental role in the direct SF mechanism. A parallel orientation of the molecules in the spirit of the **u**-pattern is observed in 6,13-bis-(triisopropylsilyl)ethynyl-pentacene (TIPS-pentacene) crystals that exhibit a brickwork structure⁹⁴ and is imaginable in pentacene films and covalently linked pentacene dimers as well. The results of our calculations do not support, however, the involvement of a ferromagnetically coupled triplet pair state in the SF process: The multiexcitonic singlet, triplet, and quintet states on spatially confined dimers, consisting of adjacent pentacene molecules, are energetically too far apart and their off-diagonal spin–spin couplings are too small to bring about a noteworthy multiplicity mixing observed in transient EPR spectroscopies of films with high pentacene concentrations.¹⁹

A pattern, reminiscent of the **w**-dimer, hosts the lowest excited singlet state in the trimer. Here and in the **w**-dimer, the two lowest excited singlet states are mixtures of $S_{h-1,h}^{l,l+1}$ and $^1(TT)$ configurations. The folded nuclear arrangement of the two pentacene units facilitates CT excitations, which are relatively small in the absorption region but increase markedly upon geometry relaxation in the S_1 state. Excitation of the **w**-dimer therefore supports a CT-mediated SF mechanism with a hybridization of Frenkel and CT states in the primary step of the SF process in pentacene crystals, as postulated in the work of Neef *et al.*¹⁷ on the basis of their time- and angle-resolved photoemission spectroscopy investigations of single-crystal pentacene.

SUPPLEMENTARY MATERIAL

See the supplementary material for more information on molecular orbitals, selected geometry parameters and normal mode displacements, transition densities, difference densities, state

descriptors, and wavefunction composition of states with substantial double excitation character.

ACKNOWLEDGMENTS

This research was funded by the Deutsche Forschungsgemeinschaft (DFG, German Research Foundation)—Grant Nos. MA-1051/20-1 and 396890929/GRK 2482. Parts of the calculations were carried out on the central HPC system “HILBERT” at the Heinrich Heine University Düsseldorf.

AUTHOR DECLARATIONS

Conflict of Interest

The authors have no conflicts to disclose.

Author Contributions

Timo Schulz: Conceptualization (lead); Data curation (equal); Software (lead); Visualization (lead); Writing – original draft (lead); Writing – review & editing (supporting). **Simon Hédé:** Data curation (equal); Software (supporting); Visualization (supporting); Writing – original draft (supporting). **Oliver Weingart:** Funding acquisition (supporting); Supervision (supporting). **Christel M. Marian:** Conceptualization (supporting); Funding acquisition (lead); Supervision (lead); Writing – review & editing (lead).

DATA AVAILABILITY

The data that support the findings of this study are available within this article and its supplementary material. Additional data are available from the corresponding author upon reasonable request.

REFERENCES

- 1 N. Shah, A. A. Shah, P. K. Leung, S. Khan, K. Sun, X. Zhu, and Q. Liao, *Processes* **11**, 1852 (2023).
- 2 D. N. Congreve, J. Lee, N. J. Thompson, E. Hontz, S. R. Yost, P. D. Reuswig, M. E. Bahlke, S. Reineke, T. Van Voorhis, and M. A. Baldo, *Science* **340**, 334 (2013).
- 3 W. Shockley and H. J. Queisser, *J. Appl. Phys.* **32**, 510 (1961).
- 4 M. C. Hanna and A. J. Nozik, *J. Appl. Phys.* **100**, 074510 (2006).
- 5 D. Casanova, *Chem. Rev.* **118**, 7164 (2018).
- 6 N. Monahan and X.-Y. Zhu, *Annu. Rev. Phys. Chem.* **66**, 601 (2015).
- 7 M. B. Smith and J. Michl, *Chem. Rev.* **110**, 6891 (2010).
- 8 M. B. Smith and J. Michl, *Annu. Rev. Phys. Chem.* **64**, 361 (2013).
- 9 R. D. Pensack, E. E. Ostroumov, A. J. Tilley, S. Mazza, C. Grieco, K. J. Thorley, J. B. Asbury, D. S. Seferos, J. E. Anthony, and G. D. Scholes, *J. Phys. Chem. Lett.* **7**, 2370 (2016).
- 10 C. K. Yong, A. J. Musser, S. L. Bayliss, S. Lukman, H. Tamura, O. Bubnova, R. K. Hallani, A. Meneau, R. Resel, M. Maruyama, S. Hotta, L. M. Herz, D. Beljonne, J. E. Anthony, J. Clark, and H. Sirringhaus, *Nat. Commun.* **8**, 15953 (2017).
- 11 W.-L. Chan, T. C. Berkelbach, M. R. Provorse, N. R. Monahan, J. R. Tritsch, M. S. Hybertsen, D. R. Reichman, J. Gao, and X.-Y. Zhu, *Acc. Chem. Res.* **46**, 1321 (2013).
- 12 S. M. Hart, W. R. Silva, and R. R. Frontiera, *Chem. Sci.* **9**, 1242 (2018).
- 13 T. C. Berkelbach, M. S. Hybertsen, and D. R. Reichman, *J. Chem. Phys.* **138**, 114102 (2013).

- ¹⁴T. C. Berkelbach, M. S. Hybertsen, and D. R. Reichman, *J. Chem. Phys.* **138**, 114103 (2013).
- ¹⁵T. C. Berkelbach, M. S. Hybertsen, and D. R. Reichman, *J. Chem. Phys.* **141**, 074705 (2014).
- ¹⁶A. Neef, S. Beaulieu, S. Hammer, S. Dong, J. Maklar, T. Pincelli, R. P. Xian, M. Wolf, L. Rettig, J. Pflaum, and R. Ernstorfer, *Nature* **616**, 275 (2023).
- ¹⁷A. Neef, M. Rossi, M. Wolf, R. Ernstorfer, and H. Seiler, *Phys. Status Solidi A* **221**, 2300304 (2024).
- ¹⁸M. I. Collins, F. Campaioli, M. J. Tayebjee, J. H. Cole, and D. R. McCamey, *Commun. Phys.* **6**, 64 (2023).
- ¹⁹D. Lubert-Perquel, E. Salvadori, M. Dyson, P. N. Stavrinou, R. Montis, H. Nagashima, Y. Kobori, S. Heutz, and C. W. M. Kay, *Nat. Commun.* **9**, 4222 (2018).
- ²⁰B. S. Basel, J. Zirzmeier, C. Hetzer, B. T. Phelan, M. D. Krzyaniak, S. R. Reddy, P. B. Coto, N. E. Horwitz, R. M. Young, F. J. White, F. Hampel, T. Clark, M. Thoss, R. R. Tykwinski, M. R. Wasielewski, and D. M. Guldi, *Nat. Commun.* **8**, 15171 (2017).
- ²¹M. J. Y. Tayebjee, S. N. Sanders, E. Kumarasamy, L. M. Campos, M. Y. Sfeir, and D. R. McCamey, *Nat. Phys.* **13**, 182 (2017).
- ²²H. Sakai, R. Inaya, H. Nagashima, S. Nakamura, Y. Kobori, N. V. Tkachenko, and T. Hasobe, *J. Phys. Chem. Lett.* **9**, 3354 (2018).
- ²³P. M. Zimmerman, Z. Zhang, and C. B. Musgrave, *Nat. Chem.* **2**, 648 (2010).
- ²⁴P. M. Zimmerman, F. Bell, D. Casanova, and M. Head-Gordon, *J. Am. Chem. Soc.* **133**, 19944 (2011).
- ²⁵P. B. Coto, S. Sharifzadeh, J. B. Neaton, and M. Thoss, *J. Chem. Theory Comput.* **11**, 147 (2014).
- ²⁶T. Zeng, R. Hoffmann, and N. Ananth, *J. Am. Chem. Soc.* **136**, 5755 (2014).
- ²⁷P. Petelenz, M. Snamina, and G. Mazur, *J. Phys. Chem. C* **119**, 14338 (2015).
- ²⁸P. Petelenz and M. Snamina, *J. Phys. Chem. C* **119**, 28570 (2015).
- ²⁹D. R. Dombrowski, T. Schulz, M. Kleinschmidt, and C. M. Marian, *J. Phys. Chem. A* **127**, 2011 (2023).
- ³⁰C. M. Marian, A. Heil, and M. Kleinschmidt, *Wiley Interdiscip. Rev.: Comput. Mol. Sci.* **9**, e1394 (2019).
- ³¹D. C. A. Valente, M. T. do Casal, M. Barbatti, T. A. Niehaus, A. J. A. Aquino, H. Lischka, and T. M. Cardozo, *J. Chem. Phys.* **154**, 044306 (2021).
- ³²W. Kohn and L. J. Sham, *Phys. Rev.* **140**, A1133 (1965).
- ³³E. Runge and E. K. U. Gross, *Phys. Rev. Lett.* **52**, 997 (1984).
- ³⁴E. K. U. Gross and W. Kohn, *Phys. Rev. Lett.* **55**, 2850 (1985).
- ³⁵S. Hirata and M. Head-Gordon, *Chem. Phys. Lett.* **314**, 291 (1999).
- ³⁶J. P. Perdew and Y. Wang, *Phys. Rev. B* **45**, 13244 (1992).
- ³⁷J. C. Slater, *Phys. Rev.* **81**, 385 (1951).
- ³⁸J. P. Perdew, K. Burke, and M. Ernzerhof, *Phys. Rev. Lett.* **77**, 3865 (1996).
- ³⁹P. A. M. Dirac *Proc. R. Soc. London, Ser. A* **123**, 714 (1929).
- ⁴⁰J. P. Perdew, M. Ernzerhof, and K. Burke, *J. Chem. Phys.* **105**, 9982 (1996).
- ⁴¹F. Weigend and R. Ahlrichs, *Phys. Chem. Chem. Phys.* **7**, 3297 (2005).
- ⁴²S. Grimme, J. Antony, S. Ehrlich, and H. Krieg, *J. Chem. Phys.* **132**, 154104 (2010).
- ⁴³S. Grimme, S. Ehrlich, and L. Goerigk, *J. Comput. Chem.* **32**, 1456 (2011).
- ⁴⁴C. Mattheus, A. Dros, J. Baas, A. Meetsma, J. De Boer, and T. Palstra, "CCDC 170187: Experimental crystal structure determination," *Acta Cryst. C* **57**, 939 (2001).
- ⁴⁵P. Giannozzi, S. Baroni, N. Bonini, M. Calandra, R. Car, C. Cavazzoni, D. Ceresoli, G. L. Chiarotti, M. Cococcioni, I. Dabo, A. D. Corso, S. de Gironcoli, S. Fabris, G. Fratesi, R. Gebauer, U. Gerstmann, C. Gougoussis, A. Kokalj, M. Lazzeri, L. Martin-Samos, N. Marzari, F. Mauri, R. Mazzarello, S. Paolini, A. Pasquarello, L. Paulatto, C. Sbraccia, S. Scandolo, G. Sclauzero, A. P. Seitsonen, A. Smogunov, P. Umari, and R. M. Wentzcovitch, *J. Phys.: Condens. Matter* **21**, 395502 (2009).
- ⁴⁶A. M. Rappe, K. M. Rabe, E. Kaxiras, and J. D. Joannopoulos, *Phys. Rev. B* **41**, 1227 (1990).
- ⁴⁷U. C. Singh and P. A. Kollman, *J. Comput. Chem.* **5**, 129 (1984).
- ⁴⁸O. Weingart, A. Nenov, P. Altoè, I. Rivalta, J. Segarra-Martí, I. Dokukina, and M. Garavelli, *J. Mol. Model.* **24**, 271 (2018).
- ⁴⁹S. Grimme and M. Waletzke, *J. Chem. Phys.* **111**, 5645 (1999).
- ⁵⁰T. Schulz, P. Konieczny, D. R. Dombrowski, S. Metz, C. M. Marian, and R. Weinkauff, *Phys. Chem. Chem. Phys.* **25**, 29850 (2023).
- ⁵¹A. D. Becke, *J. Chem. Phys.* **98**, 1372 (1993).
- ⁵²A. D. Becke, *Phys. Rev. A* **38**, 3098 (1988).
- ⁵³C. Lee, W. Yang, and R. G. Parr, *Phys. Rev. B* **37**, 785 (1988).
- ⁵⁴TURBOMOLE V7.5.1 2021, a development of University of Karlsruhe and Forschungszentrum Karlsruhe GmbH, 1989–2007, TURBOMOLE GmbH, since 2007; available at <https://www.turbomole.org>.
- ⁵⁵S. G. Balasubramani, G. P. Chen, S. Coriani, M. Diedenhofen, M. S. Frank, Y. J. Franzke, F. Furche, R. Grotjahn, M. E. Harding, C. Hättig, A. Hellweg, B. Helmich-Paris, C. Holzer, U. Huniar, M. Kaupp, A. M. Khah, S. K. Khani, T. Müller, F. Mack, B. D. Nguyen, S. M. Parker, E. Perlt, D. Rappoport, K. Reiter, S. Roy, M. Rückert, G. Schmitz, M. Sierka, E. Tapavicza, D. P. Tew, C. van Wüllen, V. K. Voora, F. Weigend, A. Wodyński, and J. M. Yu, *J. Chem. Phys.* **152**, 184107 (2020).
- ⁵⁶F. Plasser, *J. Chem. Phys.* **152**, 084108 (2020).
- ⁵⁷N. M. O'Boyle, M. Banck, C. A. James, C. Morley, T. Vandermeersch, and G. R. Hutchison, *J. Cheminf.* **3**, 33 (2011).
- ⁵⁸G. Hermann, V. Pohl, J. C. Tremblay, B. Paulus, H. Hege, and A. Schild, *J. Comput. Chem.* **37**, 1511 (2016).
- ⁵⁹See <http://www.jmol.org/> for Jmol: An open-source java viewer for chemical structures in 3D.
- ⁶⁰N. Gilka, P. R. Taylor, and C. M. Marian, *J. Chem. Phys.* **129**, 044102 (2008).
- ⁶¹D. Ganyushin, N. Gilka, P. R. Taylor, C. M. Marian, and F. Neese, *J. Chem. Phys.* **132**, 144111 (2010).
- ⁶²M. Kleinschmidt, J. Tatchen, and C. M. Marian, *J. Chem. Phys.* **124**, 124101 (2006).
- ⁶³AMFI is an atomic spin-orbit integral program written by B. Schimmelpfennig, University of Stockholm, 1996.
- ⁶⁴A. McLachlan, *Mol. Phys.* **6**, 441 (1963).
- ⁶⁵H. Benk and H. Sixl, *Mol. Phys.* **42**, 779 (1981).
- ⁶⁶J. van der Waals, *Appl. Magn. Reson.* **20**, 545–561 (2001).
- ⁶⁷J. R. Platt, *J. Chem. Phys.* **17**, 484 (1949).
- ⁶⁸M. Parac and S. Grimme, *Chem. Phys.* **292**, 11 (2003).
- ⁶⁹Y. Yang, E. R. Davidson, and W. Yang, *Proc. Natl. Acad. Sci. U. S. A.* **113**, E5098 (2016).
- ⁷⁰L. Salem and C. Rowland, *Angew. Chem., Int. Ed. Engl.* **11**, 92 (1972).
- ⁷¹C. M. Marian and N. Gilka, *J. Chem. Theory Comput.* **4**, 1501 (2008).
- ⁷²N. Nijegorodov, V. Ramachandran, and D. Winkoun, *Spectrochim. Acta, Part A* **53**, 1813 (1997).
- ⁷³J. Burgos, M. Pope, C. E. Swenberg, and R. R. Alfano, *Phys. Status Solidi B* **83**, 249 (1977).
- ⁷⁴E. S. Kadantsev, M. J. Stott, and A. Rubio, *J. Chem. Phys.* **124**, 134901 (2006).
- ⁷⁵H. Chakraborty and A. Shukla, *J. Chem. Phys.* **141**, 164301 (2014).
- ⁷⁶J. Hachmann, J. J. Dorando, M. Avilés, and G. K.-L. Chan, *J. Chem. Phys.* **127**, 134309 (2007).
- ⁷⁷Y. Y. Pan, J. Huang, Z. Wang, D. W. Yu, B. Yang, and Y. G. Ma, *RSC Adv.* **7**, 26697 (2017).
- ⁷⁸C. Hellner, L. Lindqvist, and P. C. Roberge, *J. Chem. Soc., Faraday Trans. 2* **68**, 1928 (1972).
- ⁷⁹P. Klán and J. Wirz, *Photochemistry of Organic Compounds* (John Wiley & Sons, Ltd., 2009).
- ⁸⁰V. K. Thorsmølle, R. D. Averitt, J. Demsar, D. L. Smith, S. Tretiak, R. L. Martin, X. Chi, B. K. Crone, A. P. Ramirez, and A. J. Taylor, *Phys. Rev. Lett.* **102**, 017401 (2009).
- ⁸¹R. Mondal, C. Tönshoff, D. Khon, D. C. Neckers, and H. F. Bettinger, *J. Am. Chem. Soc.* **131**, 14281 (2009).
- ⁸²E. Heinecke, D. Hartmann, R. Müller, and A. Hese, *J. Chem. Phys.* **109**, 906 (1998).
- ⁸³M. Pabst and A. Köhn, *J. Chem. Phys.* **129**, 214101 (2008).
- ⁸⁴I. Benkyi, E. Tapavicza, H. Fliegl, and D. Sundholm, *Phys. Chem. Chem. Phys.* **21**, 21094 (2019).
- ⁸⁵T. M. Halasinski, D. M. Hudgins, F. Salama, L. J. Allamandola, and T. Bally, *J. Phys. Chem. A* **104**, 7484 (2000).

- ⁸⁶R. He, N. G. Tassi, G. B. Blanchet, and A. Pinczuk, *Phys. Rev. B* **83**, 115452 (2011).
- ⁸⁷O. Loboda, B. Minaev, O. Vahtras, B. Schimmelpfennig, H. Ågren, K. Ruud, and D. Jonsson, *Chem. Phys.* **286**, 127 (2003).
- ⁸⁸T.-C. Yang, D. J. Sloop, S. I. Weissman, and T.-S. Lin, *J. Chem. Phys.* **113**, 11194 (2000).
- ⁸⁹T. Nagami, H. Miyamoto, R. Sakai, and M. Nakano, *J. Phys. Chem. C* **125**, 2264 (2021).
- ⁹⁰K. B. Wiberg, C. M. Hadad, J. B. Foresman, and W. A. Chupka, *J. Phys. Chem.* **96**, 10756 (1992).
- ⁹¹F. Plasser and H. Lischka, *J. Chem. Theory Comput.* **8**, 2777 (2012).
- ⁹²F. Plasser, S. A. Bäppler, M. Wormit, and A. Dreuw, *J. Chem. Phys.* **141**, 024107 (2014).
- ⁹³F. Plasser, M. Wormit, and A. Dreuw, *J. Chem. Phys.* **141**, 024106 (2014).
- ⁹⁴J. Anthony, J. Brooks, D. Eaton, and S. Parkin, "CCDC 172476: Experimental crystal structure determination," *J. Am. Chem. Soc.* **123**, 9482 (2001).

Supplemental Material for

Multiexcitonic and optically bright states in subunits of pentacene crystals: A hybrid DFT/MRCI and molecular mechanics study

Timo Schulz,¹ Simon Hédé,¹ O. Weingart,^{1, a)} and Christel M. Marian¹

Institute of Theoretical and Computational Chemistry, Faculty of Mathematics and Natural Sciences, Heinrich Heine University Düsseldorf

(*Electronic mail: christel.marian@hhu.de)

(*Electronic mail: weingart@hhu.de)

(*Electronic mail: simonh@hhu.de)

(*Electronic mail: timo.schulz@hhu.de)

(Dated: 8 February 2024)

Contents

S1 Monomer	S2
S1.1 Energy Level Plots at different Geometries	S2
S1.2 Molecular Orbitals at Ground State Geometry	S2
S1.3 Computed Normal Modes for the Monomer in vacuum	S5
S1.4 C-C Distances at different Geometries of the Monomer	S5
S2 Dimer sub-patterns	S7
S2.1 Molecular Orbitals	S7
S2.2 Distances at different geometries of the sub-patterns	S18
S2.3 Selected states of u , v and w	S21
S2.4 Transition densities at singlet Geometries of u , v , w	S48
S2.5 Transition densities at singlet Geometries of the Trimer	S52
S2.6 Difference densities at singlet Geometries of u , v , w	S53
S2.7 Difference densities at singlet Geometries of the Trimer	S57
S2.8 Descriptors for Charge Transfer States and Multi-Configuration Character	S58
S2.9 States with profound double excitation character	S70

S1 Monomer

S1.1 Energy Level Plots at different Geometries

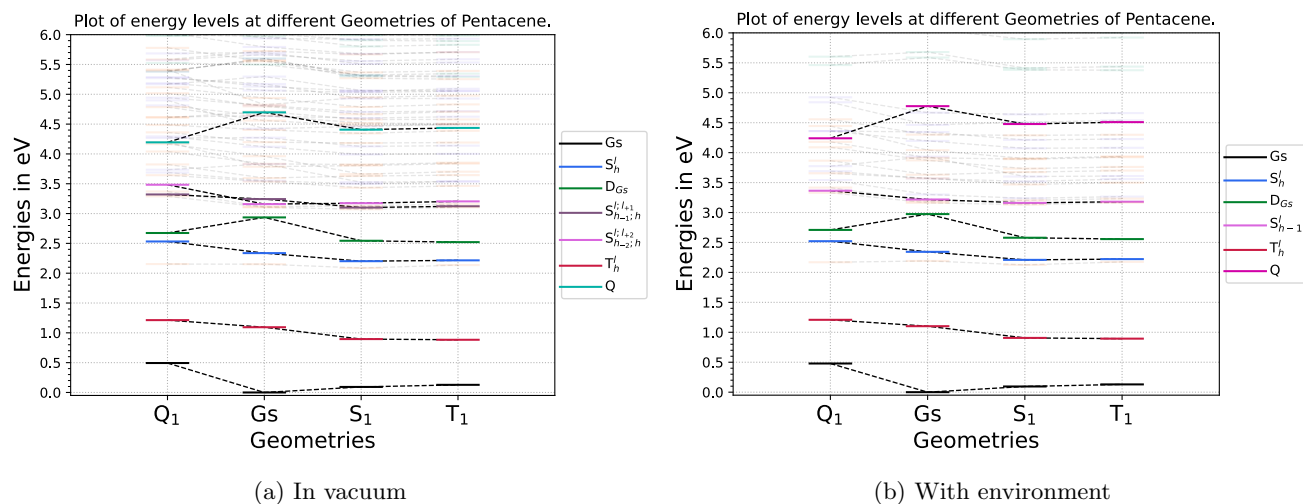


Figure S1: Energy Level Plots of Pentacene monomers *in vacuo* and in a crystalline environment

S1.2 Molecular Orbitals at Ground State Geometry

Figure S2: Molecular Orbitals involved in the construction of spatial configurations with a weight larger than 1% in the CI-Vectors at the ground state geometry. All plots were generated with an absolute cutoff off 0.03.

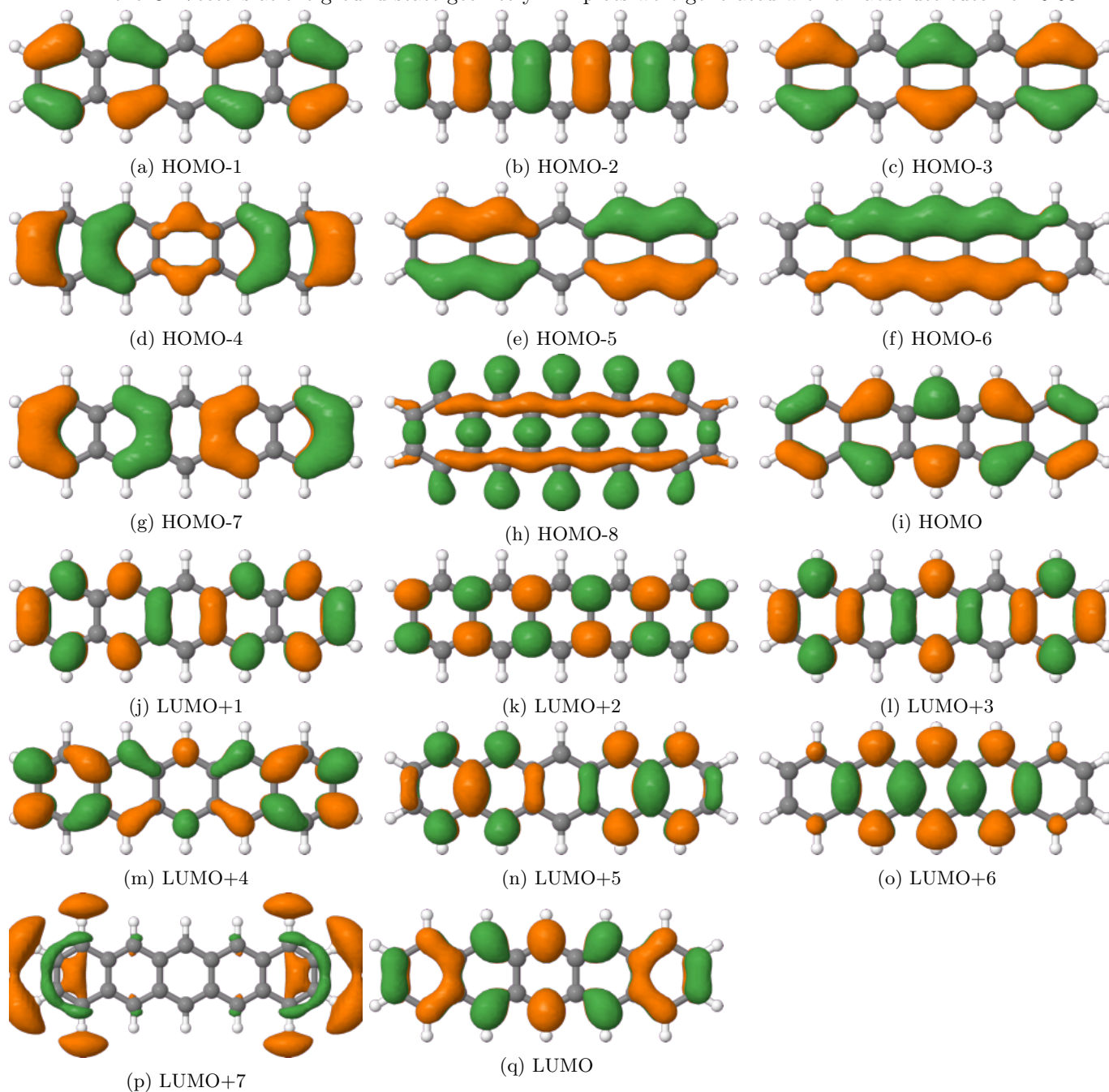
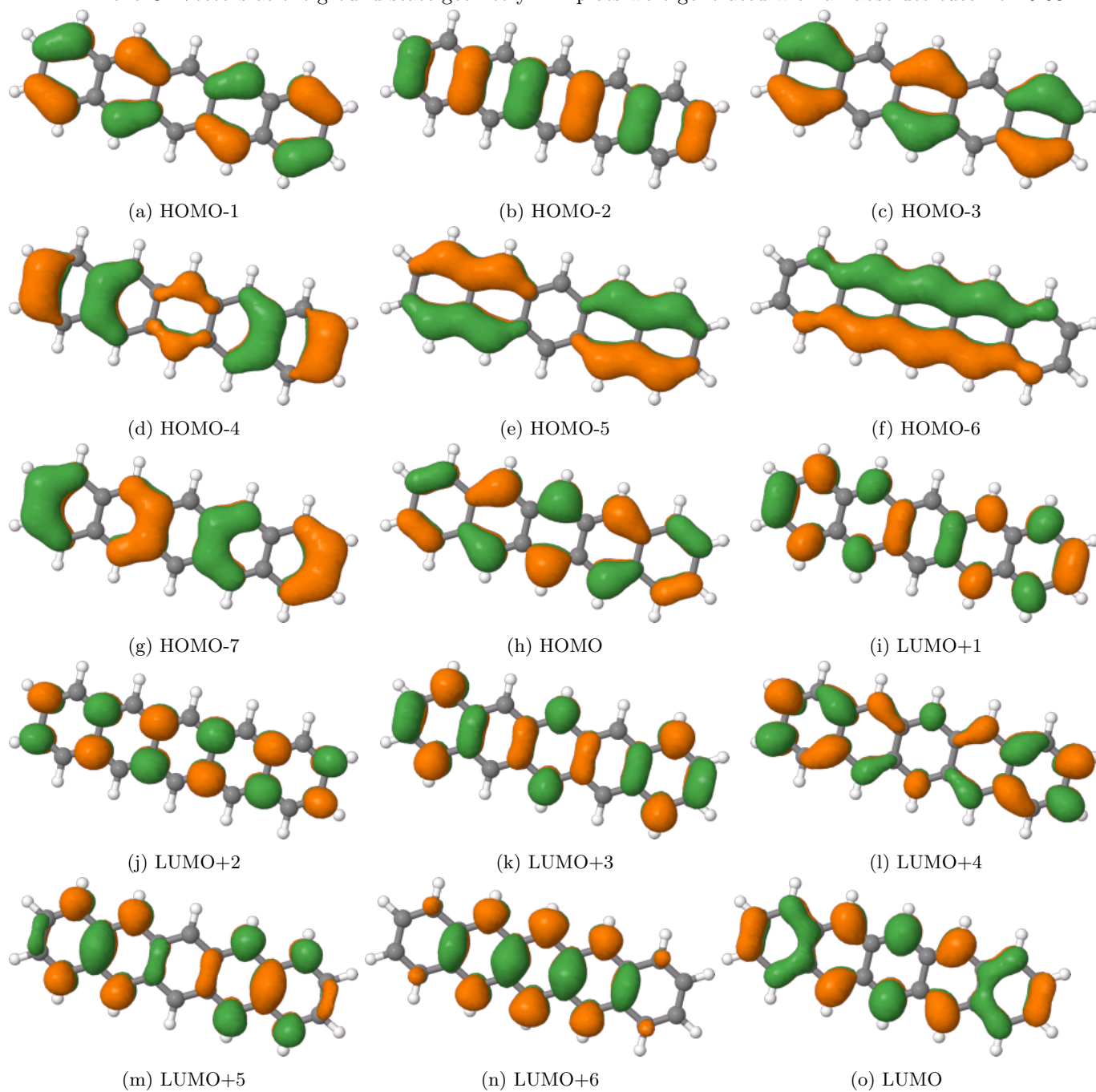


Figure S3: Molecular Orbitals involved in the construction of spatial configurations with a weight larger than 1% in the CI-Vectors at the ground state geometry. All plots were generated with an absolute cutoff off 0.03.



S1.3 Computed Normal Modes for the Monomer in vacuum

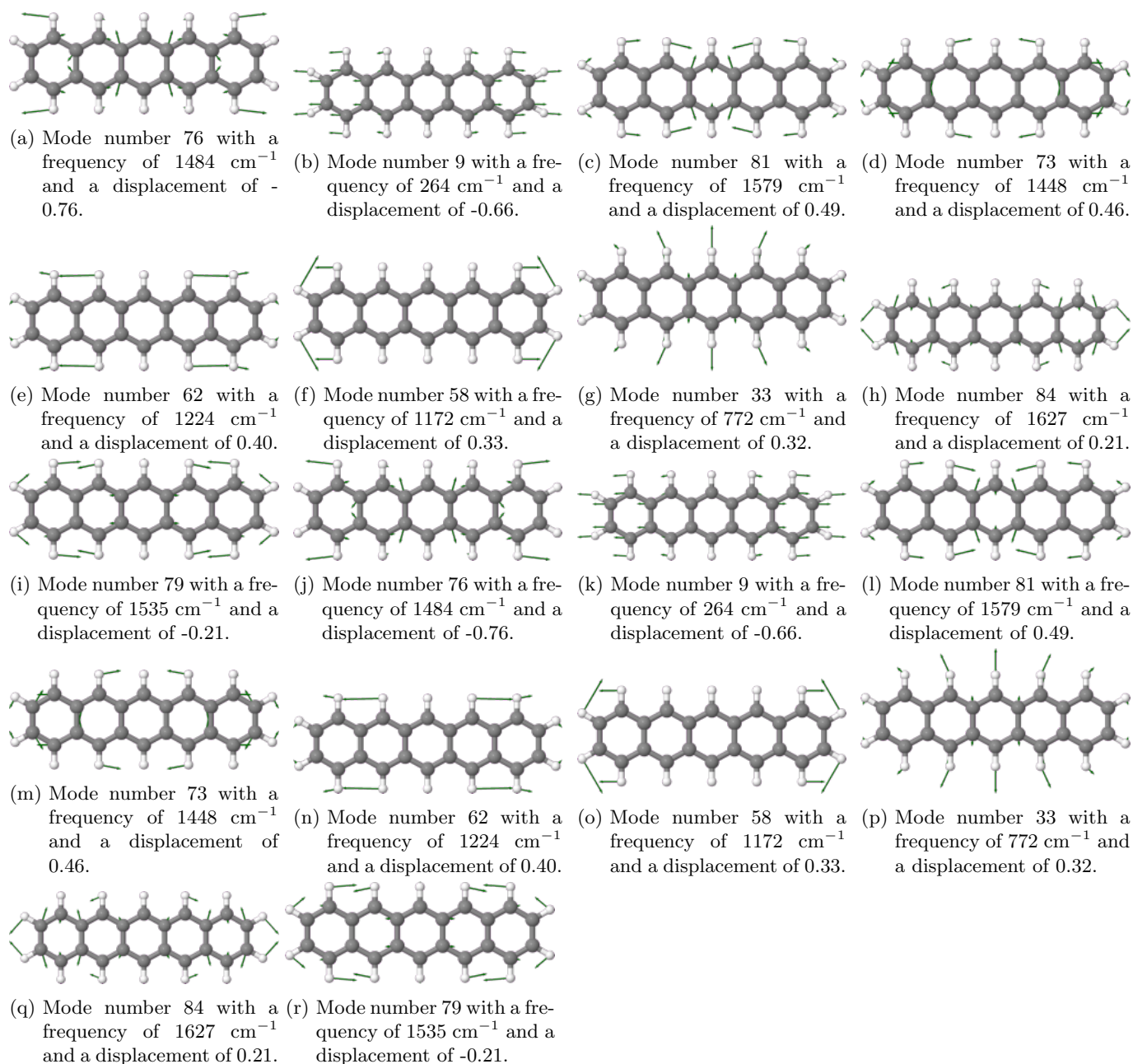


Figure S4: Displacement vectors of normal modes at the S_1 geometry of Pentacene scaled by a factor of 5. Their displacement in the Duschinsky transformation is given in the sub-captions.

S1.4 C–C Distances at different Geometries of the Monomer

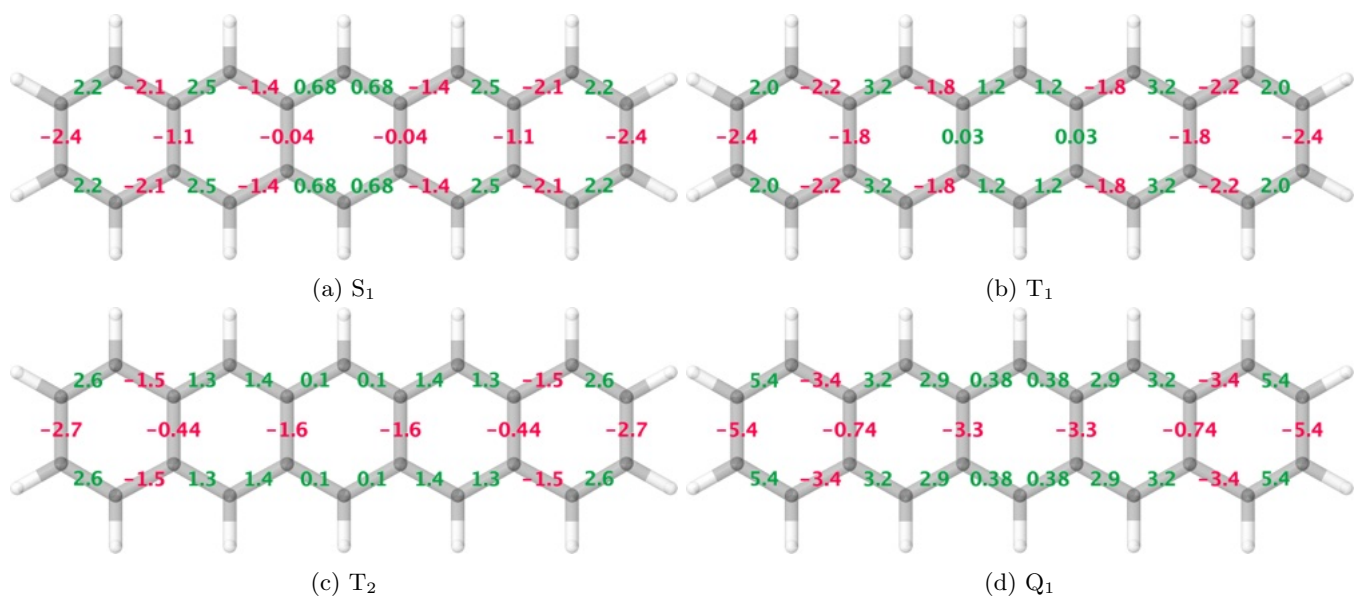


Figure S5: Change of C-C distances w.r.t. the ground state geometry of the pentacene monomer in vacuum. All values given in pm.

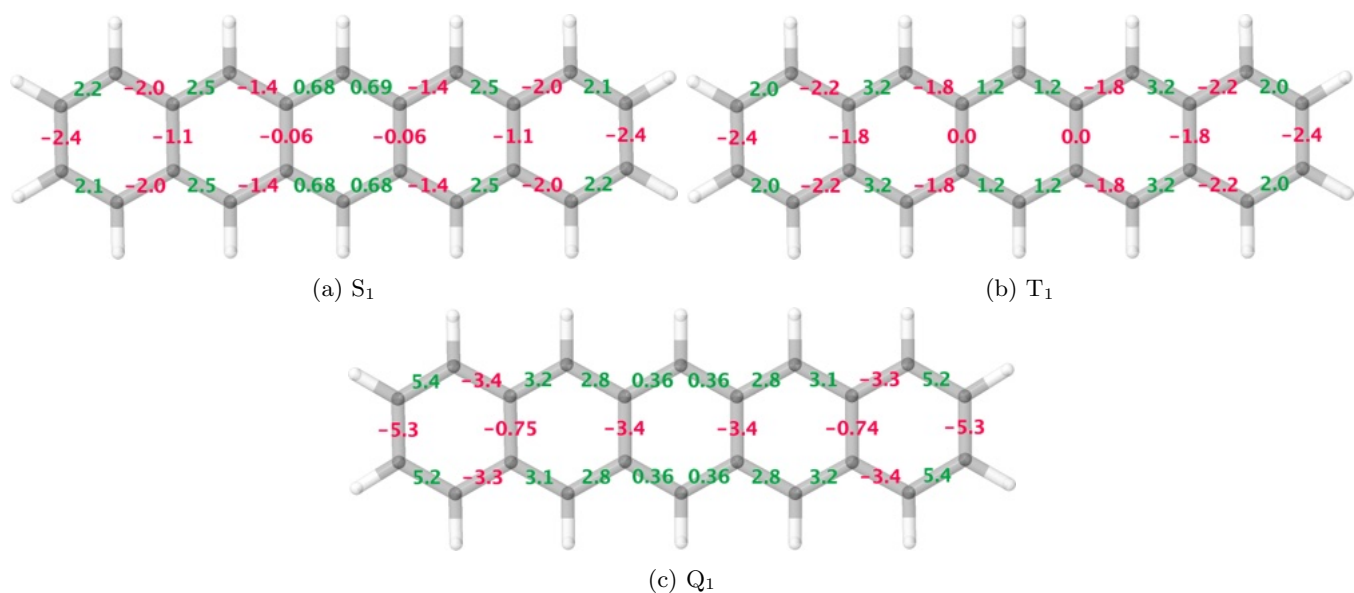


Figure S6: Change of C-C distances w.r.t. the ground state geometry of the pentacene monomer in crystalline environment. All values given in pm.

S2 Dimer sub-patterns

S2.1 Molecular Orbitals

u-sub-pattern

Figure S7: Molecular Orbitals involved in the construction of spatial configurations with a weight larger than 1% in the CI-Vectors at the ground state geometry. All plots generated with an absolute cutoff of 0.03

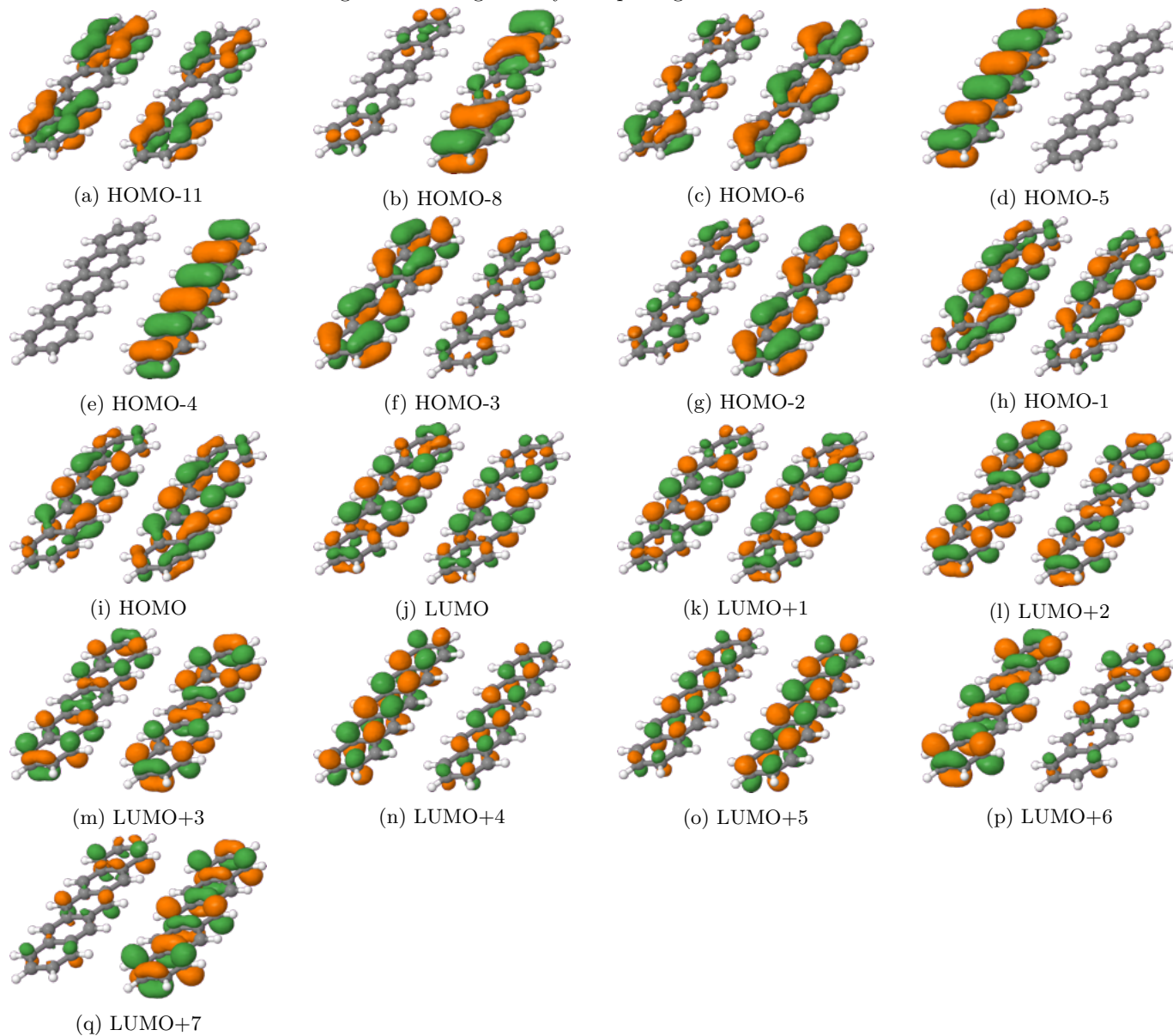


Figure S8: Molecular Orbitals involved in the construction of spatial configurations with a weight larger than 1% in the CI-Vectors at the S_1 geometry. All plots generated with an absolute cutoff of 0.03

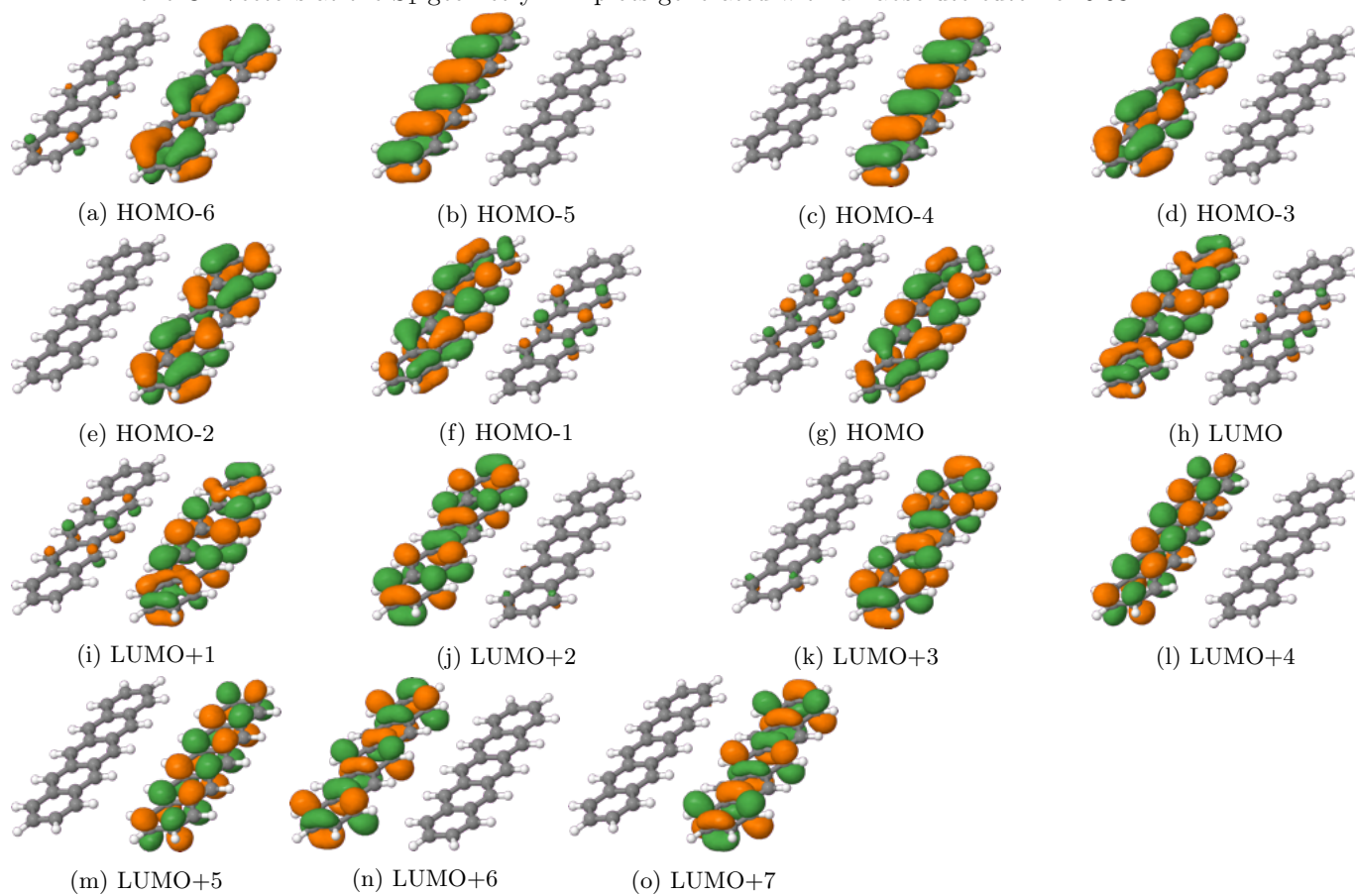
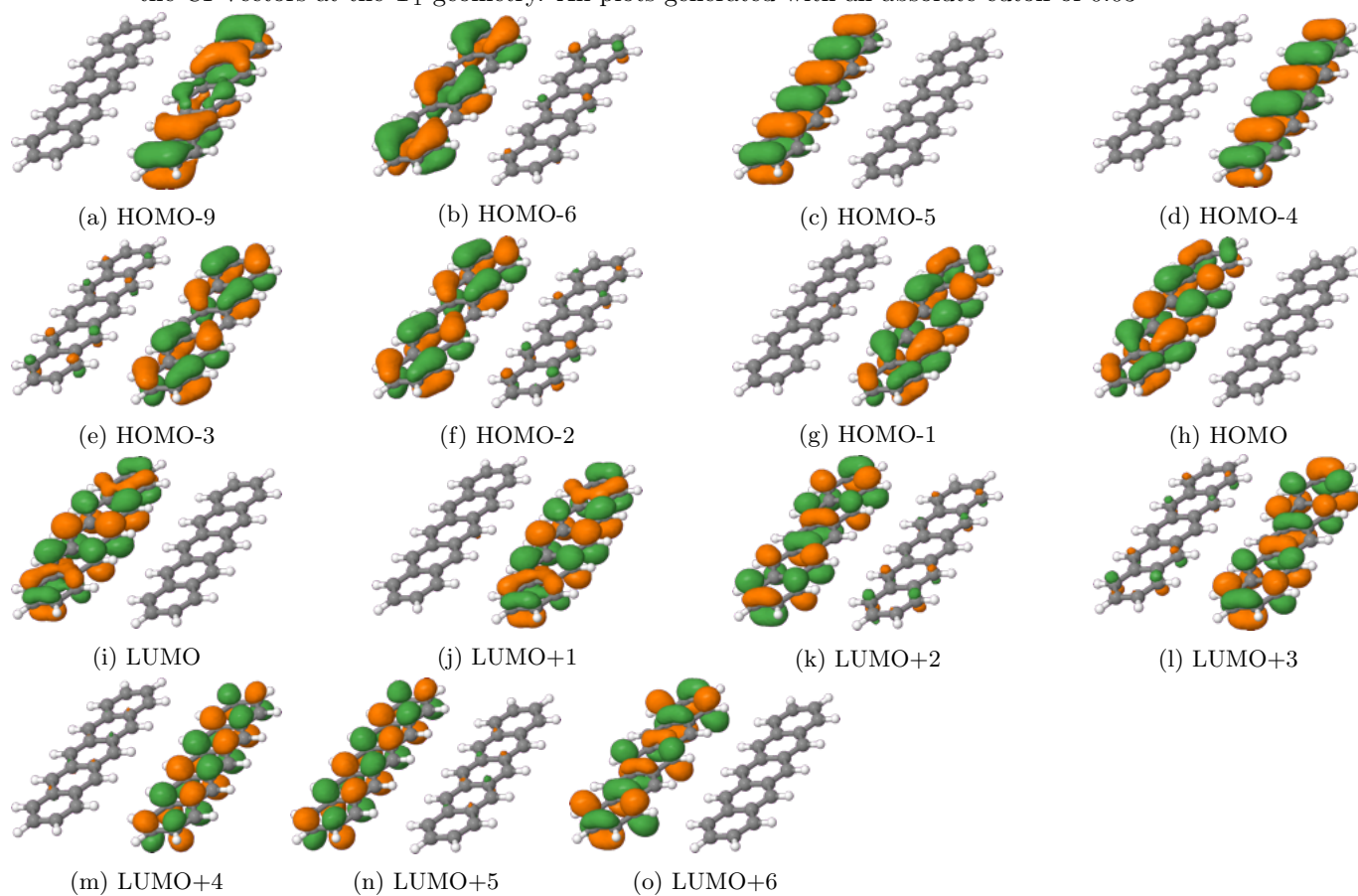


Figure S9: Molecular Orbitals involved in the construction of spatial configurations with a weight larger than 1% in the CI-Vectors at the T_1 geometry. All plots generated with an absolute cutoff of 0.03



v-sub-pattern

Figure S10: Molecular Orbitals involved in the construction of spatial configurations with a weight larger than 1% in the CI-Vectors at the ground state geometry. All plots generated with an absolute cutoff of 0.03

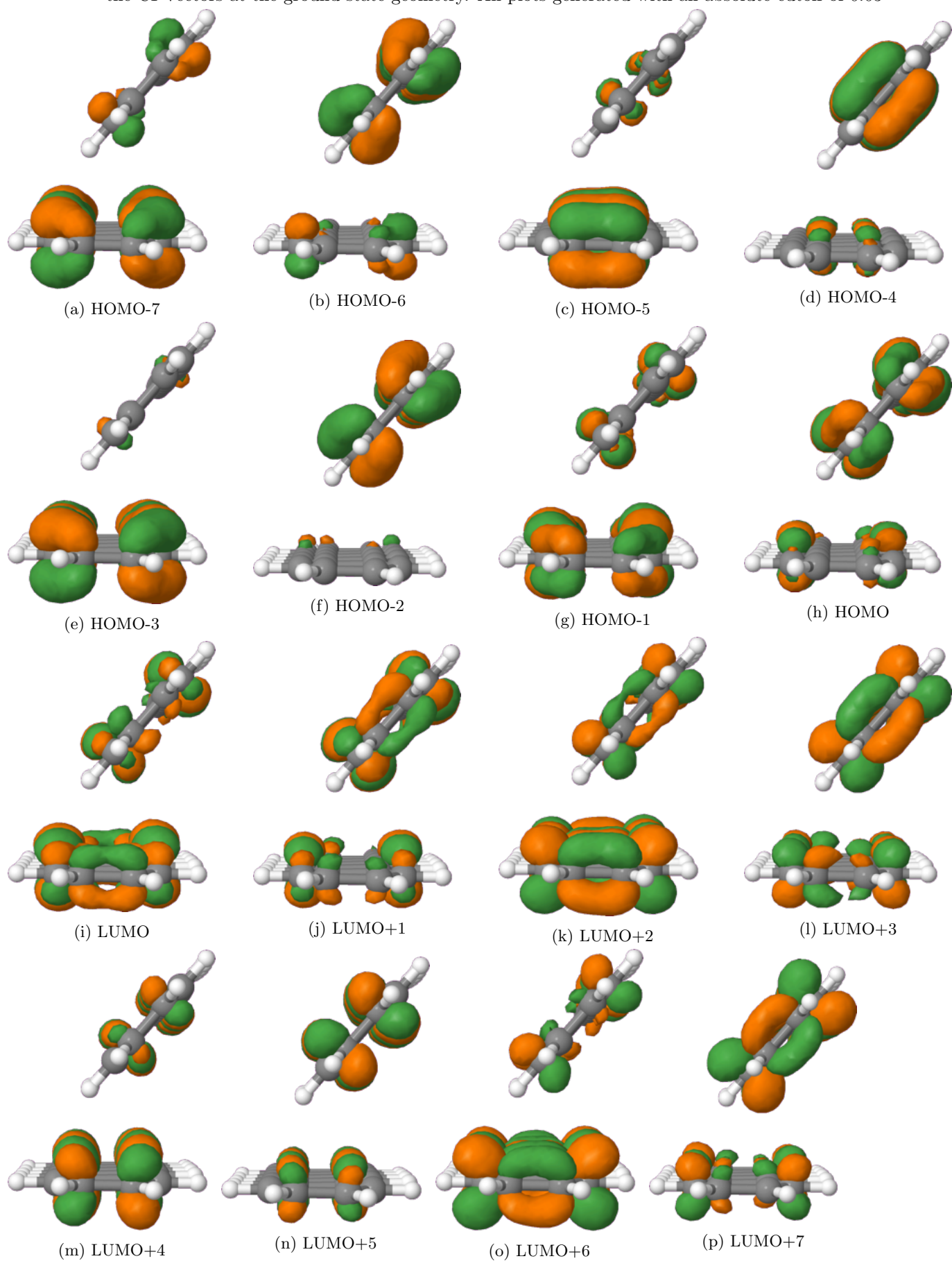


Figure S11: Molecular Orbitals involved in the construction of spatial configurations with a weight larger than 1% in the CI-Vectors at the S_1 geometry. All plots generated with an absolute cutoff of 0.03

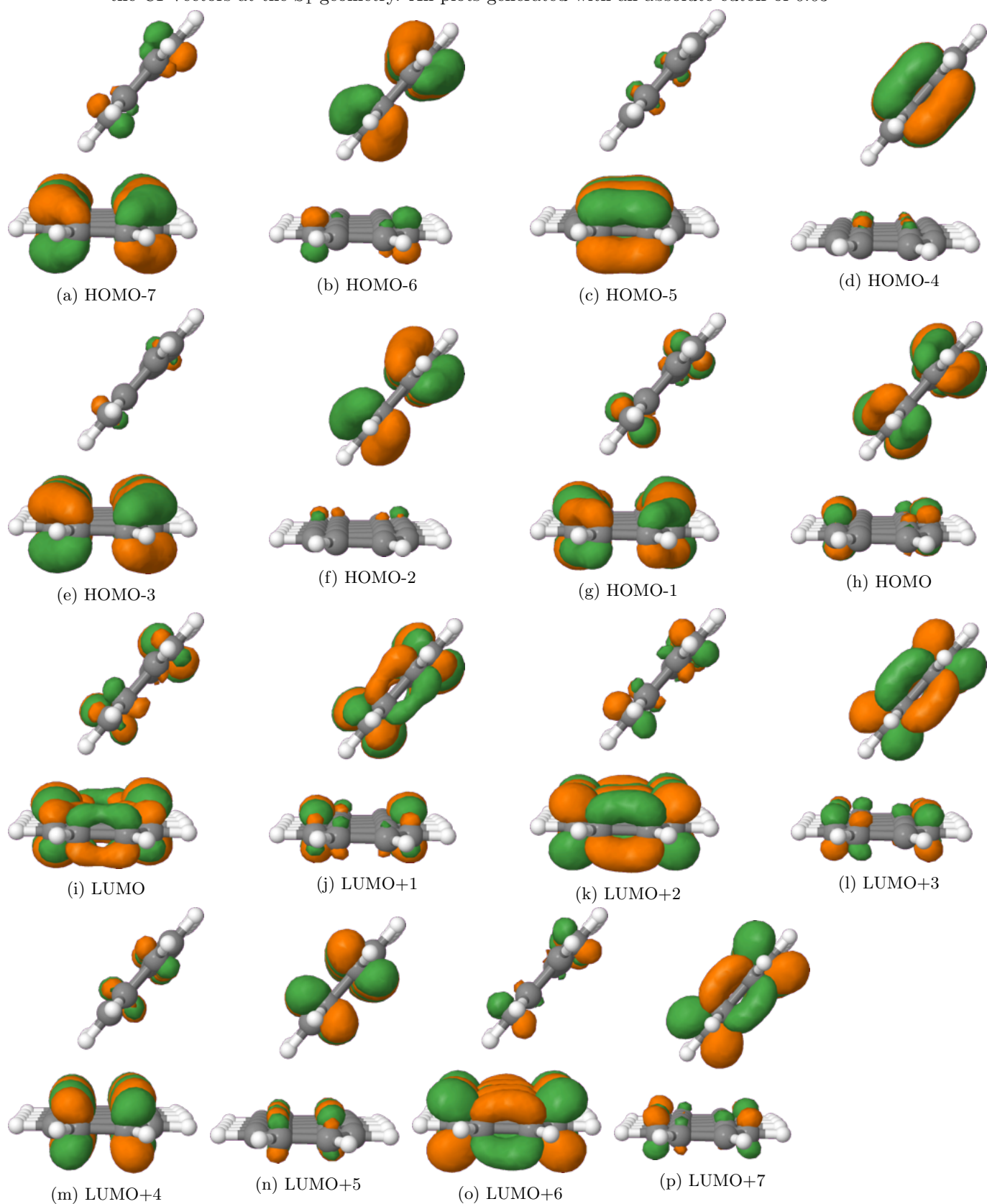


Figure S12: Molecular Orbitals involved in the construction of spatial configurations with a weight larger than 1% in the CI-Vectors at the T_1 geometry. All plots generated with an absolute cutoff of 0.03

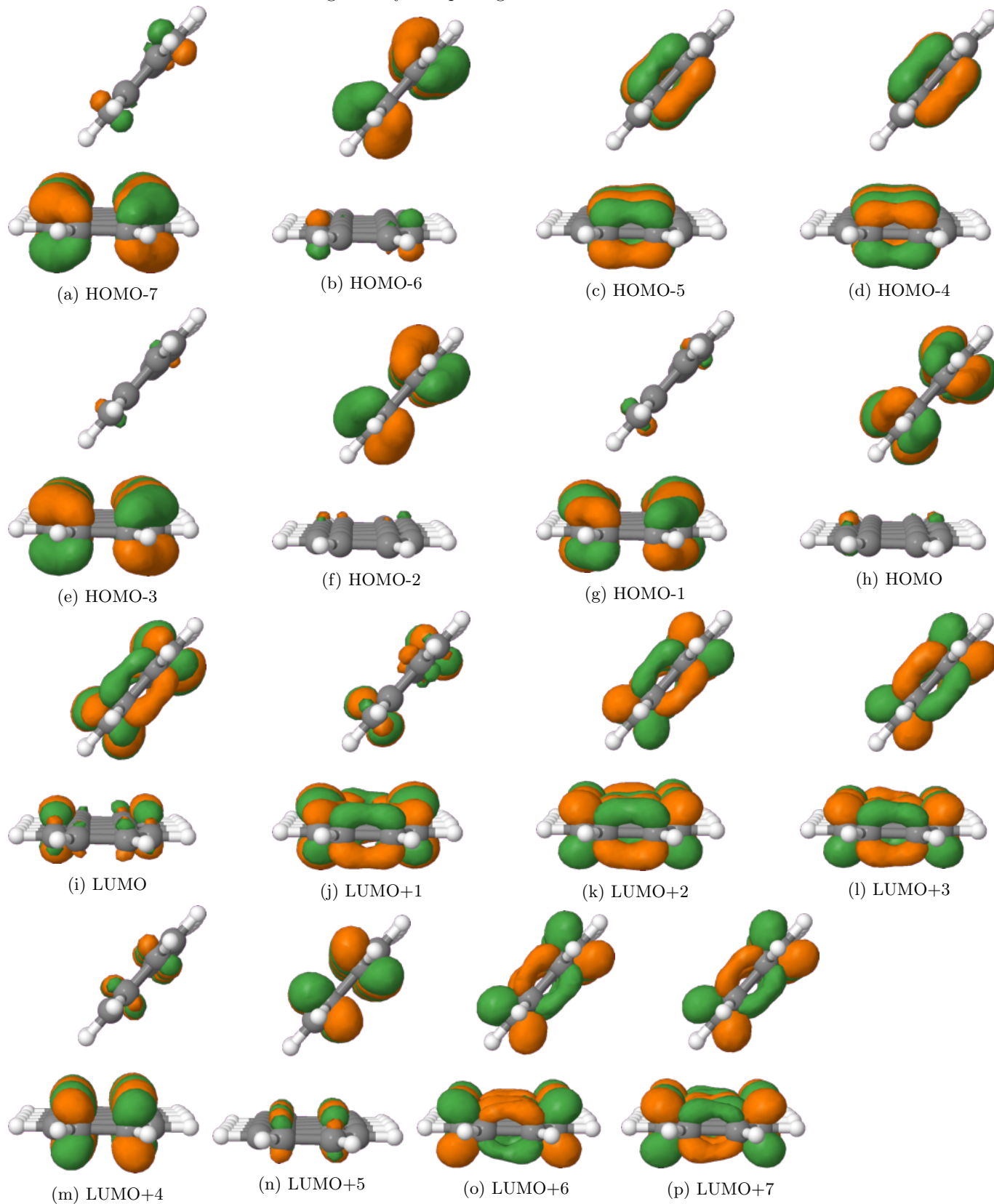


Figure S13: Molecular Orbitals involved in the construction of spatial configurations with a weight larger than 1% in the CI-Vectors at the Q_1 geometry. All plots generated with an absolute cutoff of 0.03

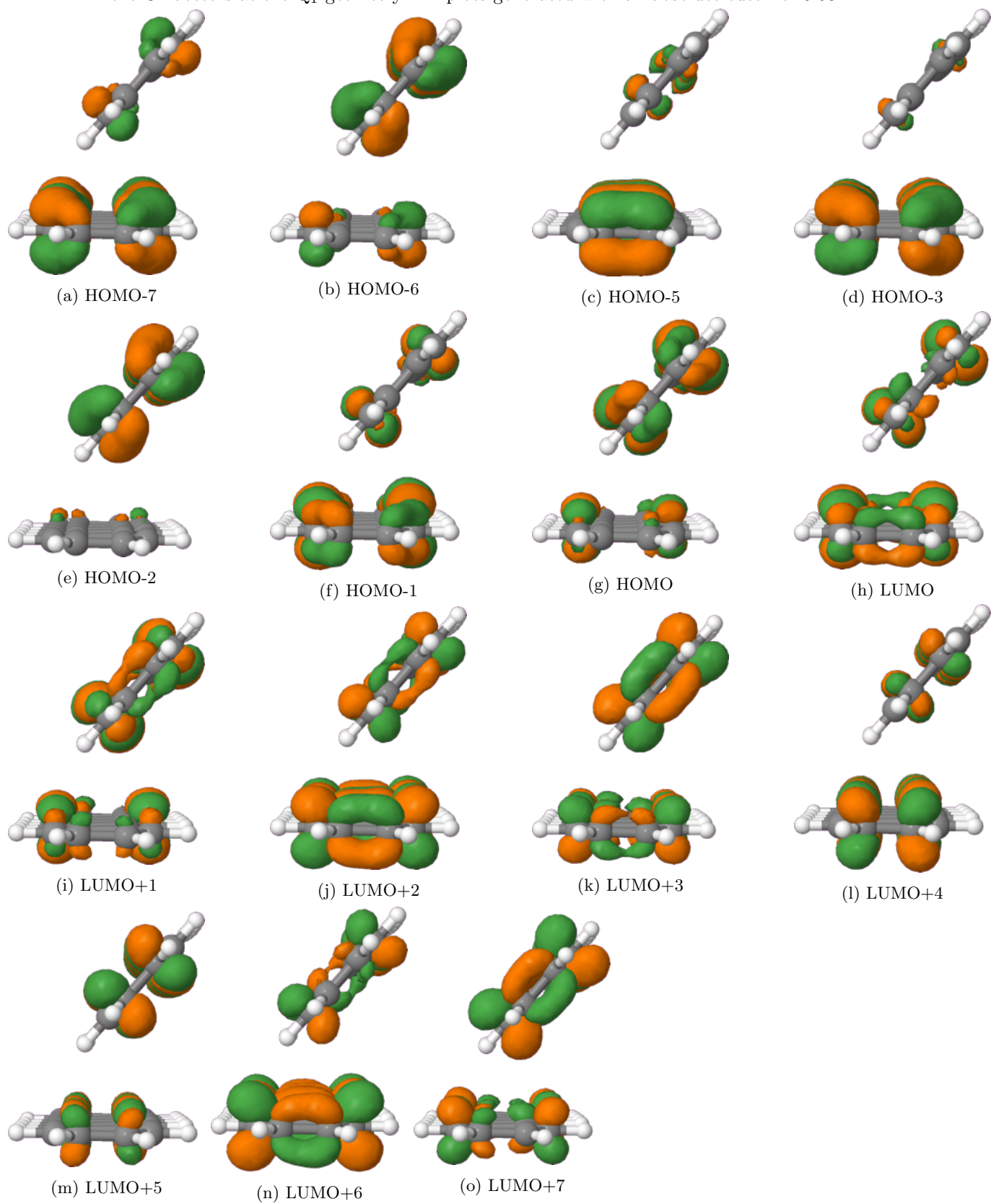


Figure S14: Molecular Orbitals involved in the construction of spatial configurations with a weight larger than 1% in the CI-Vectors at the ground state geometry. All plots generated with an absolute cutoff of 0.03

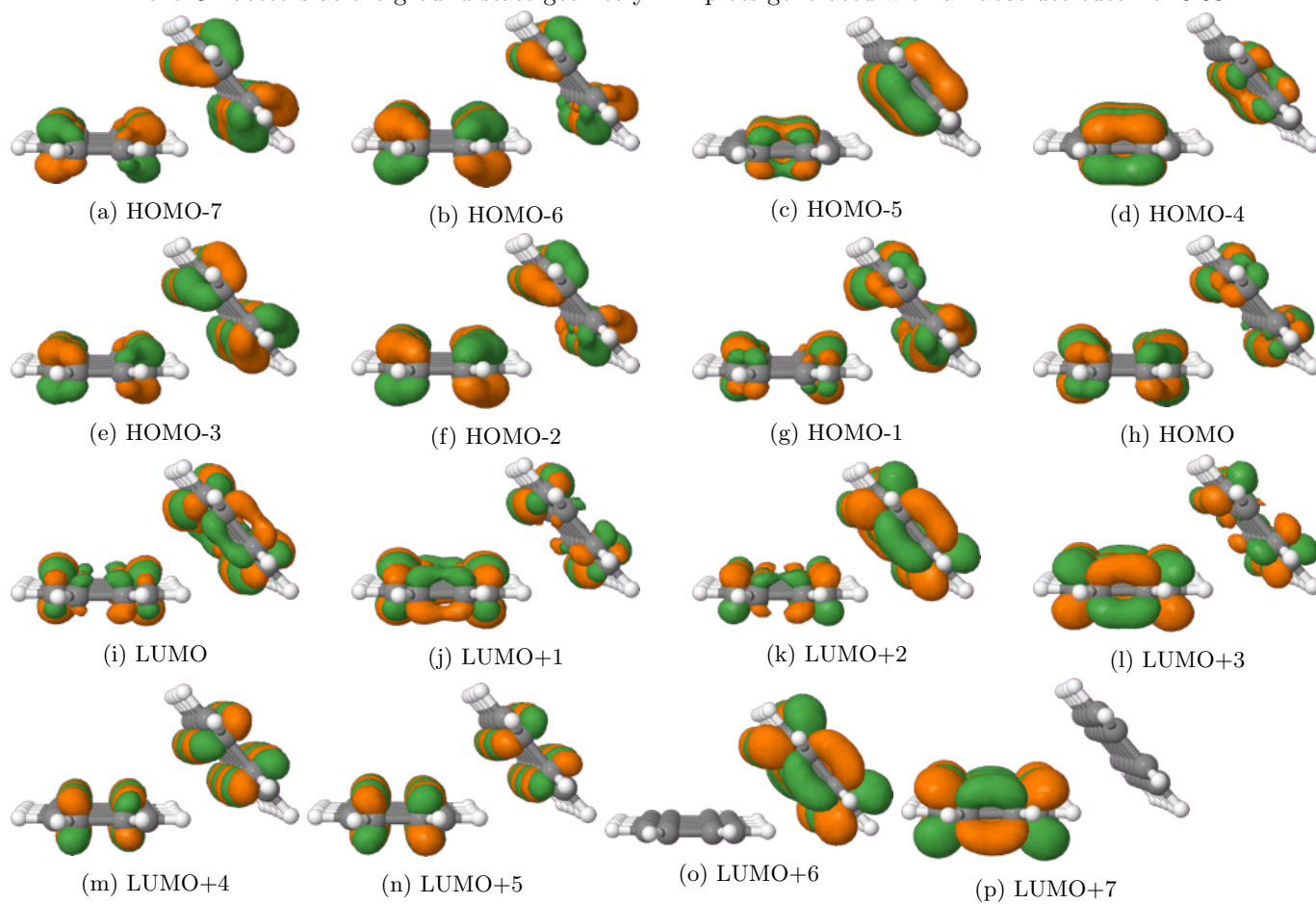


Figure S15: Molecular Orbitals involved in the construction of spatial configurations with a weight larger than 1% in the CI-Vectors at the S_1 geometry. All plots generated with an absolute cutoff of 0.03

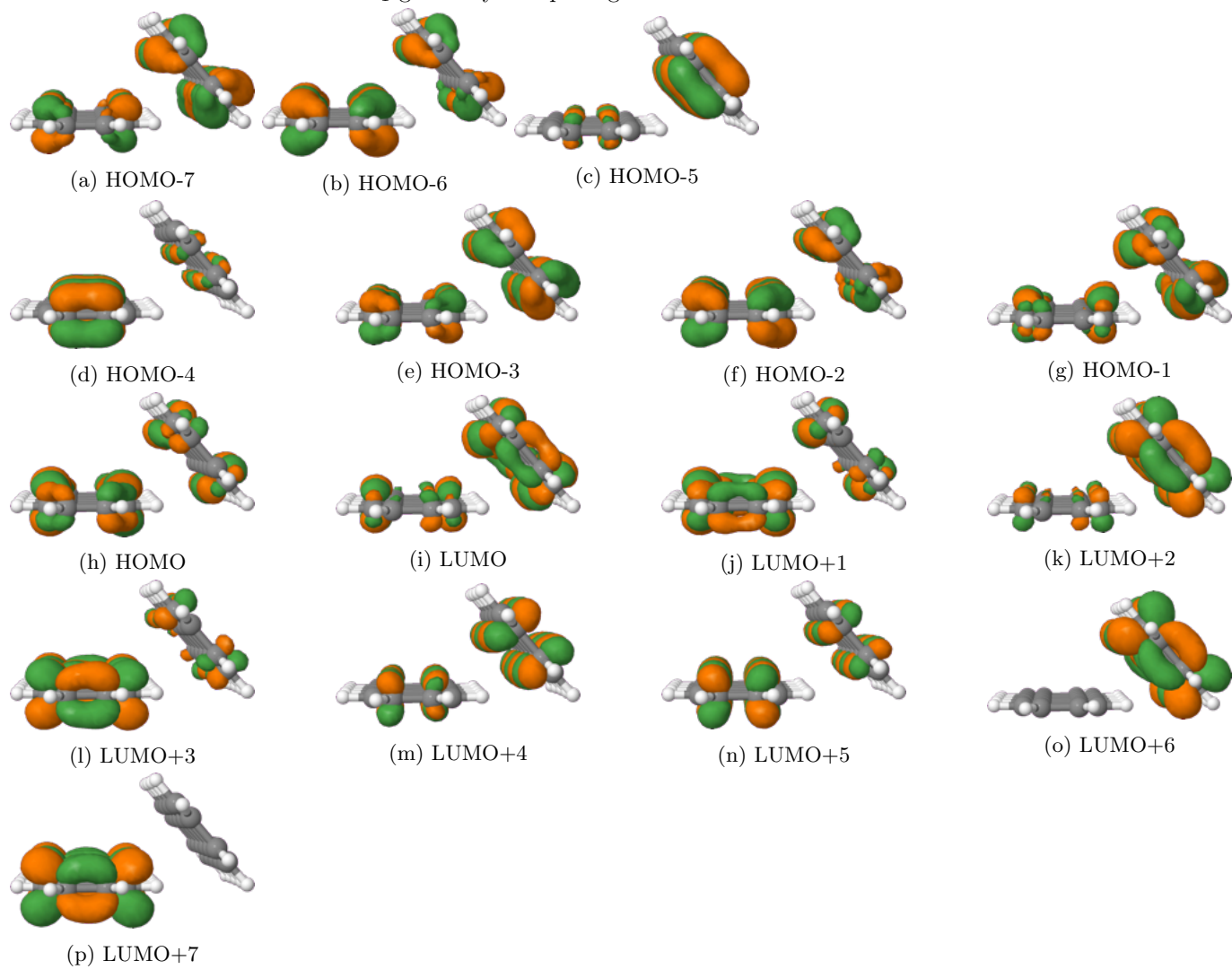


Figure S16: Molecular Orbitals involved in the construction of spatial configurations with a weight larger than 1% in the CI-Vectors at the T_1 geometry. All plots generated with an absolute cutoff of 0.03

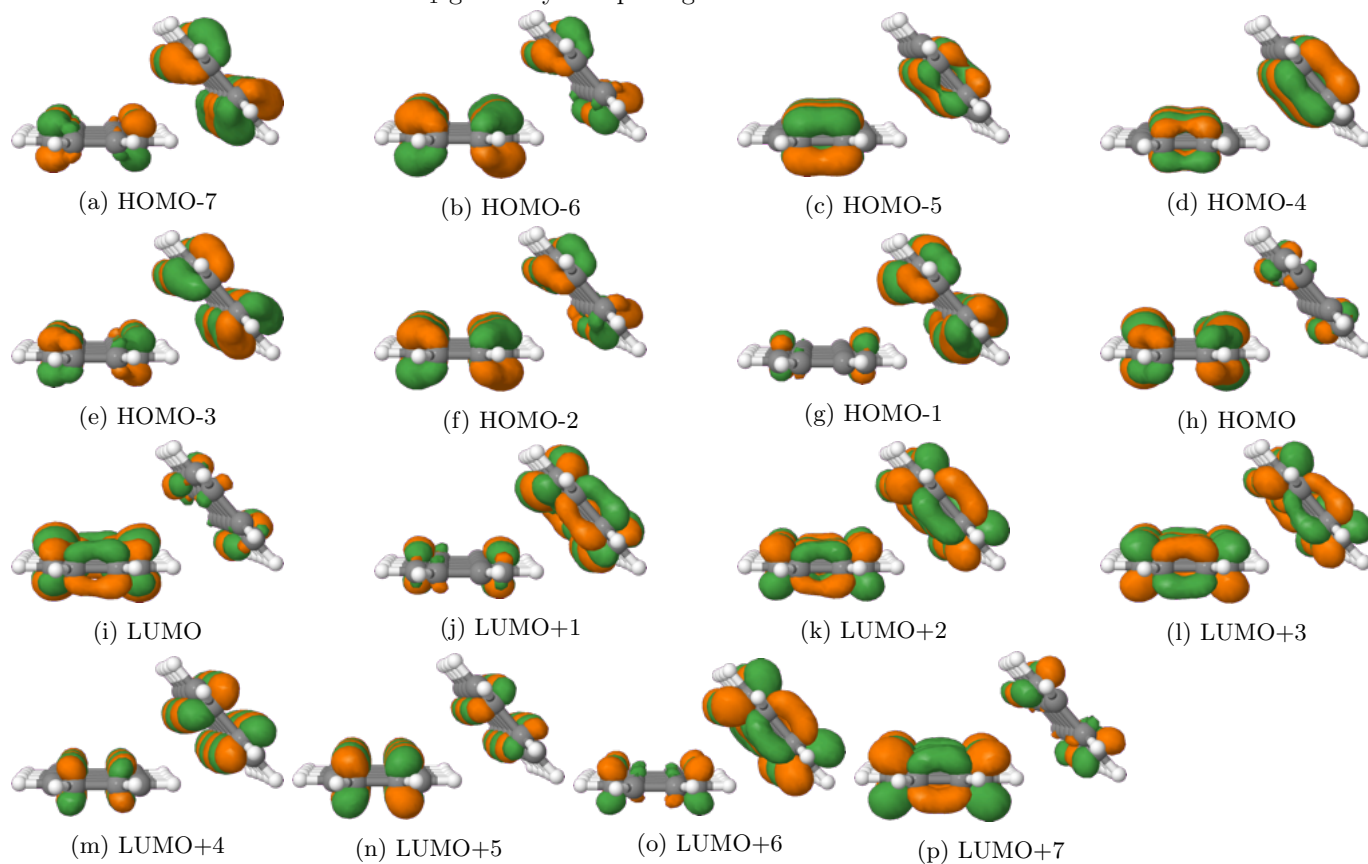
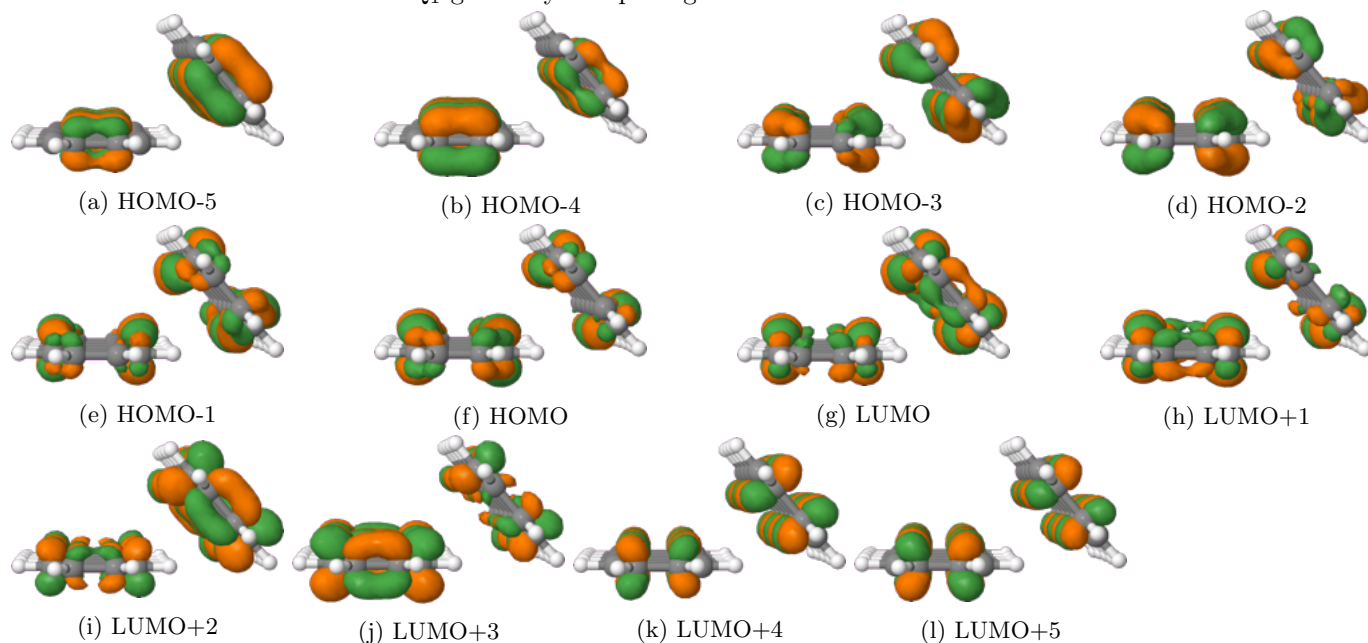


Figure S17: Molecular Orbitals involved in the construction of spatial configurations with a weight larger than 1% in the CI-Vectors at the Q_1 geometry. All plots generated with an absolute cutoff of 0.03



S2.2 Distances at different geometries of the sub-patterns

Figure S18: Distance between centre of masses of the pentacene building units in the **u**-sub-pattern. All values given in Ångstroem.

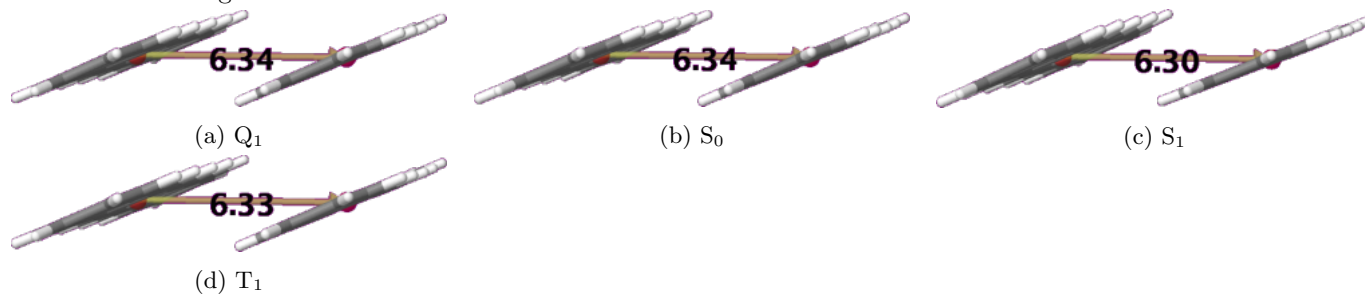


Figure S19: Distance between centre of masses of the pentacene building units in the **v**-sub-pattern. All values given in Ångstroem.

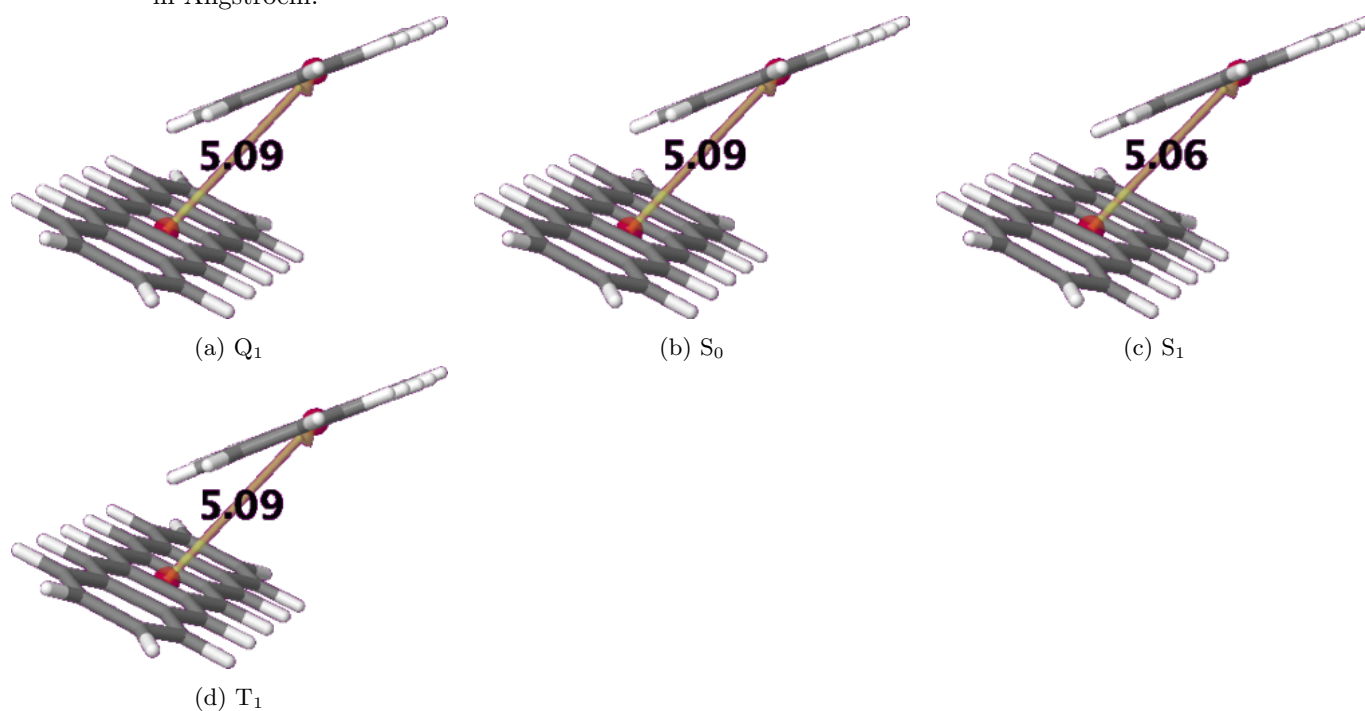


Figure S20: Distance between centre of masses of the pentacene building units in the **w**-sub-pattern. All values given in Ångstrom.

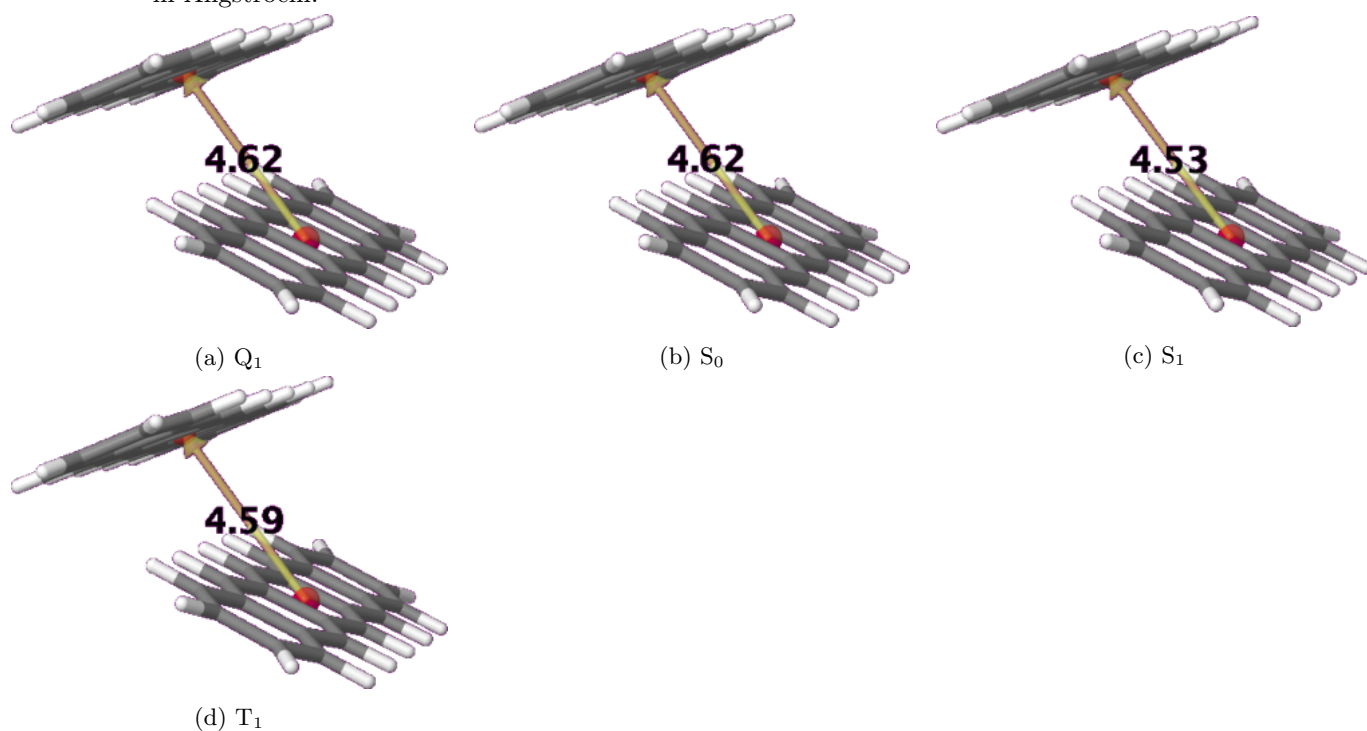


Figure S21: Change of C-C distances w.r.t. the ground state geometry of the pentacene building units in the **u**-sub-pattern. All values given in pm.

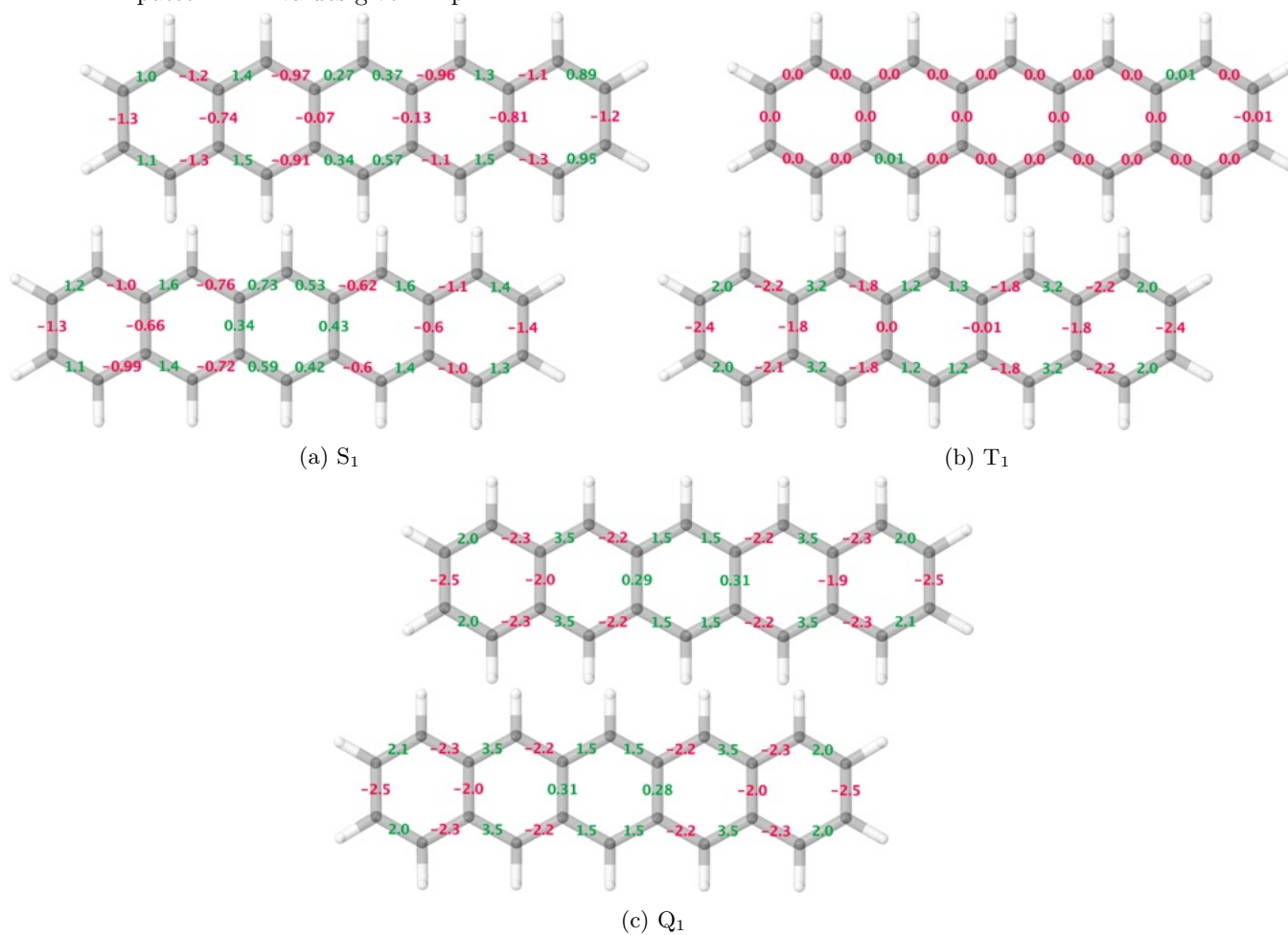


Figure S22: Change of C-C distances w.r.t. the ground state geometry of the pentacene building units in the **v**-sub-pattern. All values given in pm.

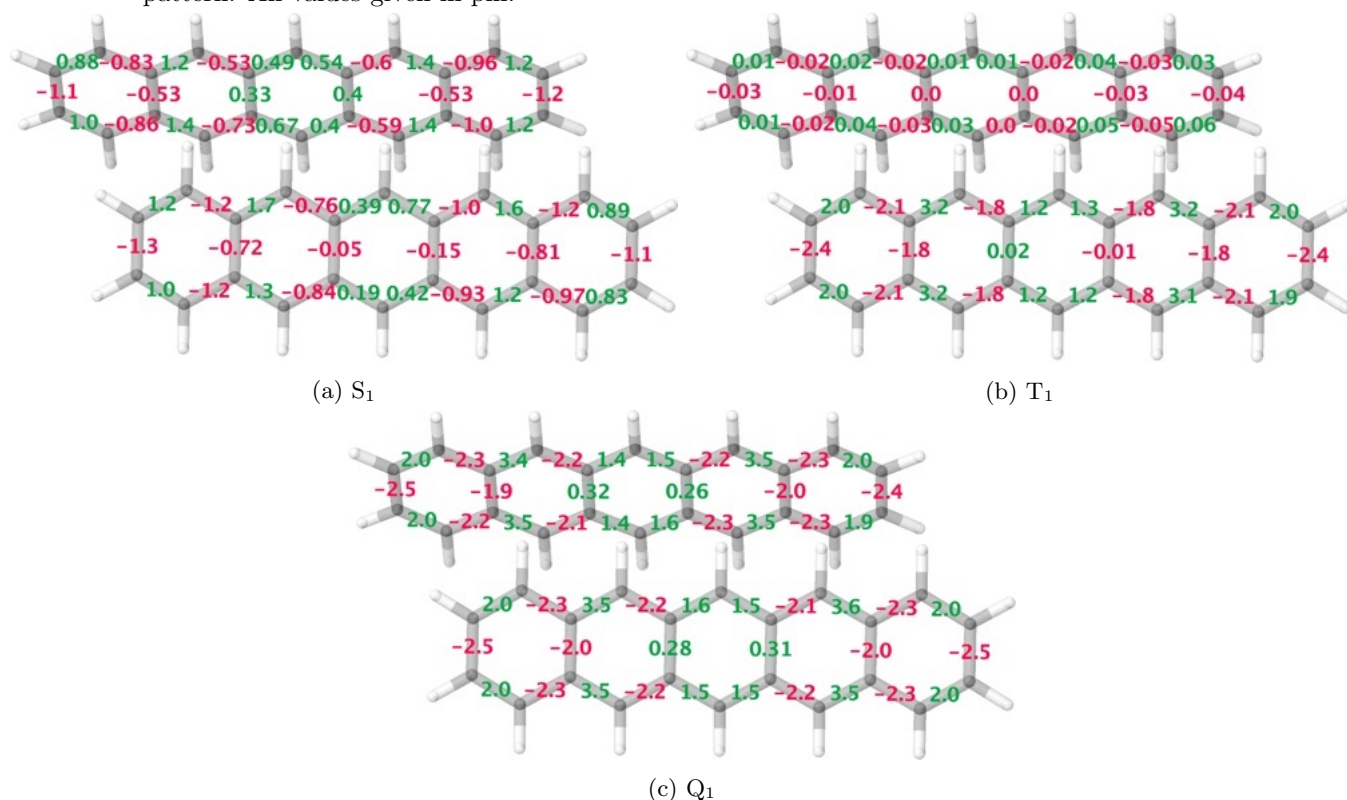
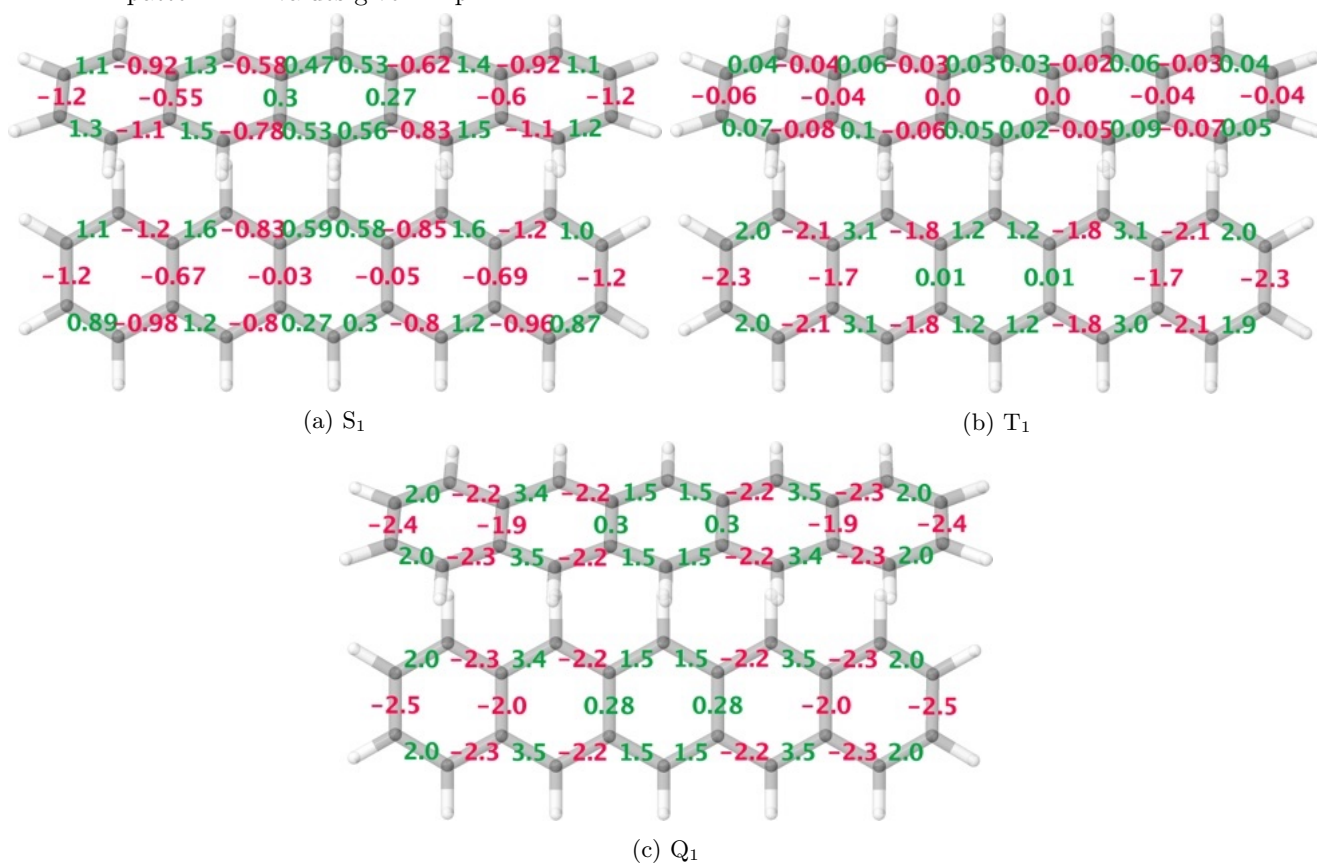


Figure S23: Change of C-C distances w.r.t. the ground state geometry of the pentacene building units in the **w**-sub-pattern. All values given in pm.



S2.3 Selected states of **u**, **v** and **w**

Table S1: Adiabatic energies, state assignments, coefficients, weights and spatial configurations at different geometries of the **u**-sub-pattern

Geometry	State	Order	$E_{ad.}$	f	No.	c_i	$ c_i ^2$	Composition
S_0	Gs	1_0	0.00	0.0000	$\frac{1}{2}$	0.91 -0.16	0.82 0.02	$(h)^2(l)^0$ $(h_{-1})^1(h)^1(l)^1(l_{+1})^1$
Q_1	Gs	1_0	0.33	0.0000	$\frac{1}{2}$	-0.87 0.22	0.76 0.05	$(h)^2(l)^0$ $(h_{-1})^1(h)^1(l)^1(l_{+1})^1$
S_1	Gs	1_0	0.03	0.0000	$\frac{1}{2}$	0.90 -0.12	0.80 0.02	$(h)^2(l)^0$ $(h_{-1})^0(l)^2$
T_1	Gs	1_0	0.11	0.0000	$\frac{1}{2}$	-0.90 0.18	0.80 0.03	$(h)^2(l)^0$ $(h)^0(l)^2$
Q_1	DL; $N_h^l/N_{h-1}^l/N_{h-1}^{l+1}/N_h^{l+1}/V_{h-1;h}^{l;l+1}$	1_1	2.09	0.0000	$\frac{1}{2}$	0.43	0.19	$(h)^0(l)^2$
					$\frac{2}{2}$	-0.40	0.16	$(h_{-1})^0(l)^2$
					$\frac{3}{4}$	0.40	0.16	$(h_{-1})^1(h)^1(l)^1(l_{+1})^1$
					$\frac{4}{5}$	-0.39	0.15	$(h)^0(l_{+1})^2$
					$\frac{5}{6}$	0.35	0.12	$(h_{-1})^0(l_{+1})^2$
S_0	DL; $N_h^l/N_{h-1}^l/N_{h-1}^{l+1}/N_h^{l+1}/V_{h-1;h}^{l;l+1}$	1_3	2.53	0.0000	$\frac{6}{7}$	0.10	0.01	$(h_{-1})^1(l)^1$
					$\frac{1}{2}$	-0.42	0.18	$(h)^0(l)^2$
					$\frac{2}{3}$	0.38	0.14	$(h_{-1})^0(l)^2$
					$\frac{3}{4}$	-0.37	0.14	$(h_{-1})^1(h)^1(l)^1(l_{+1})^1$
					$\frac{4}{5}$	0.36	0.13	$(h)^0(l_{+1})^2$
S_1	DL; $Z_h^{l;l+1}/V_{h-1;h}^{l;l+1}/V_{h-1;h}^{l;l+1}$	1_1	2.09	0.0033	$\frac{5}{6}$	-0.32	0.10	$(h_{-1})^0(l_{+1})^2$
					$\frac{6}{7}$	-0.23	0.05	$(h)^1(l_{+1})^1$
					$\frac{7}{8}$	-0.20	0.04	$(h_{-1})^1(l)^1$
					$\frac{1}{2}$	-0.38	0.14	$(h_{-1})^1(h)^1(l)^1(l_{+1})^1$
					$\frac{2}{3}$	0.37	0.13	$(h_{-1})^1(h)^1(l)^1(l_{+1})^1$
S_1	DL; $Z_h^{l;l+1}/V_{h-1;h}^{l;l+1}/V_{h-1;h}^{l;l+1}$	1_1	2.09	0.0033	$\frac{3}{4}$	-0.32	0.10	$(h)^0(l)^1(l_{+1})^1$
					$\frac{4}{5}$	0.31	0.10	$(h_{-1})^1(h)^1(l)^2$
					$\frac{5}{6}$	0.27	0.07	$(h_{-1})^0(l)^1(l_{+1})^1$
					$\frac{6}{7}$	-0.26	0.07	$(h)^0(l)^2$
					$\frac{7}{8}$	-0.24	0.06	$(h_{-1})^1(h)^1(l_{+1})^2$
S_1	DL; $Z_h^{l;l+1}/V_{h-1;h}^{l;l+1}/V_{h-1;h}^{l;l+1}$	1_1	2.09	0.0033	$\frac{8}{8}$	0.18	0.03	$(h)^1(l)^1$

Continued on next page

Table S1: Adiabatic energies, state assignments, coefficients, weights and spatial configurations at different geometries of the **u**-sub-pattern

Geometry	State	Order	$E_{ad.}$	f	No.	c_i	$ c_i ^2$	Composition
T_1	DL; $V_{h-1;h}^{l;l+1}/V_{h-1;h}^{l;l+1}$	1_2	2.27	0.0002	1	-0.62	0.39	$(h_{-1})^1(h)^1(l)^1(l_{+1})^1$
					2	-0.41	0.17	$(h_{-1})^1(h)^1(l)^1(l_{+1})^1$
					3	-0.26	0.07	$(h_{-1})^1(h)^1(l)^2$
					4	0.24	0.06	$(h)^0(l)^1(l_{+1})^1$
					5	0.18	0.03	$(h_{-1})^1(h)^1(l_{+1})^2$
	LE; S_h^l	1_1	2.19	0.1460	1	-0.89	0.80	$(h)^1(l)^1$
					2	0.13	0.02	$(h_{-1})^1(l)^1$
S_1	LE+CR; $S_{h;h-1}^{l;l+1}$	1_2	2.18	0.2486	1	0.61	0.37	$(h)^1(l)^1$
					2	0.51	0.26	$(h_{-1})^1(l)^1$
					3	-0.33	0.11	$(h_{-1})^1(l_{+1})^1$
					4	0.31	0.09	$(h)^1(l_{+1})^1$
					5	-0.07	0.01	$(h_{-1})^1(h)^0(l)^1(l_{+1})^2$
S_0	DL; $S_{h-1;h}^{l+1;l}$	1_1	2.31	0.2733	1	-0.75	0.56	$(h)^1(l)^1$
					2	0.53	0.28	$(h_{-1})^1(l_{+1})^1$
					3	-0.07	0.01	$(h_{-1})^1(h)^0(l)^2(l_{+1})^1$
Q_1	DL; $S_{h-1;h}^{l+1;l}$	1_2	2.40	0.2317	1	-0.75	0.56	$(h)^1(l)^1$
					2	0.50	0.25	$(h_{-1})^1(l_{+1})^1$
					3	-0.10	0.01	$(h_{-1})^1(h)^0(l)^2(l_{+1})^1$
S_1	LE; $S_{h-1;h}^{l;l+1}$	1_3	2.29	0.0068	1	-0.68	0.46	$(h)^1(l_{+1})^1$
					2	0.59	0.35	$(h_{-1})^1(l)^1$
					3	-0.11	0.01	$(h)^1(l)^1$
T_1	LE; $S_{h-1;h-1;h}^{l+1;l;l+1}$	1_3	2.47	0.1183	1	-0.71	0.50	$(h_{-1})^1(l_{+1})^1$
					2	-0.44	0.20	$(h_{-1})^1(l)^1$
					3	-0.35	0.13	$(h)^1(l_{+1})^1$
					4	0.14	0.02	$(h_{-1})^1(h)^0(l)^2(l_{+1})^1$
S_0	DL ₂ ; $S_{h-1;h}^{l;l+1}$	1_2	2.37	0.0000	1	-0.67	0.45	$(h_{-1})^1(l)^1$
					2	0.62	0.39	$(h)^1(l_{+1})^1$
					3	-0.08	0.01	$(h_{-1})^0(h)^1(l)^2(l_{+1})^1$
Q_1	DL ₂ ; $S_{h-1;h}^{l;l+1}$	1_3	2.46	0.0000	1	-0.66	0.43	$(h_{-1})^1(l)^1$
					2	0.62	0.38	$(h)^1(l_{+1})^1$
					3	0.12	0.01	$(h_{-1})^1(h)^0(l)^1(l_{+1})^2$

Continued on next page

Table S1: Adiabatic energies, state assignments, coefficients, weights and spatial configurations at different geometries of the **u**-sub-pattern

Geometry	State	Order	E_{ad}	f	No.	c_i	$ c_i ^2$	Composition
Q_1	DL; $Z_{h-1}^l/Z_h^{l;l+1}/Z_{h-1}^{l;l+1}/Z_{h-1}^{l+1};h$	1_4	2.62	0.0012	1	0.46	0.22	$(h_{-1})^1(h)^1(l)^2$
					2	0.45	0.21	$(h)^0(l)^1(l_{+1})^1$
					3	0.40	0.16	$(h_{-1})^0(l)^1(l_{+1})^1$
					4	0.39	0.15	$(h_{-1})^1(h)^1(l_{+1})^2$
					5	0.10	0.01	$(h)^1(l_{+8})^1$
S_0	DL; $Z_{h-1}^l/Z_h^{l;l+1}/Z_{h-1}^{l;l+1}/Z_{h-1}^{l+1};h$	1_6	2.91	0.0001	1	0.45	0.21	$(h_{-1})^1(h)^1(l)^2$
					2	0.45	0.20	$(h)^0(l)^1(l_{+1})^1$
					3	0.39	0.15	$(h_{-1})^0(l)^1(l_{+1})^1$
					4	0.39	0.15	$(h_{-1})^1(h)^1(l_{+1})^2$
					5	-0.12	0.01	$(h_{-8})^1(l)^1$
S_0	$CT_{AB}; S_{h-1}^{l+1;l;l+1;l};h;h;h_{-1}$	1_4	2.80	0.0011	1	-0.55	0.31	$(h_{-1})^1(l_{+1})^1$
					2	-0.46	0.21	$(h)^1(l)^1$
					3	0.40	0.16	$(h)^1(l_{+1})^1$
					4	0.36	0.13	$(h_{-1})^1(l)^1$
					5	-0.10	0.01	$(h_{-1})^0(l_{+1})^2$
Q_1	$CT_{AB}; S_{h-1}^{l+1;l;l+1;l};h;h;h_{-1}$	1_6	2.81	0.0006	1	0.51	0.26	$(h)^1(l_{+1})^1$
					2	0.49	0.24	$(h_{-1})^1(l)^1$
					3	-0.38	0.15	$(h_{-1})^1(l_{+1})^1$
					4	-0.33	0.11	$(h)^1(l)^1$
					5	0.16	0.02	$(h_{-1})^1(h)^1(l)^1(l_{+1})^1$
S_1	$CT_{AB}; S_{h-1}^{l+1;l;l+1;l};h;h;h_{-1}$	1_4	2.55	0.0052	1	-0.65	0.43	$(h)^1(l)^1$
					2	0.40	0.16	$(h)^1(l_{+1})^1$
					3	0.37	0.14	$(h_{-1})^1(l)^1$
					4	-0.29	0.09	$(h_{-1})^1(l_{+1})^1$
					5	0.10	0.01	$(h_{-1})^1(h)^1(l)^1(l_{+1})^1$
T_1	$CT_{AB}; S_{h-1}^{l+1;l;l+1;l};h;h;h_{-1}$	1_4	2.68	0.0035	1	0.74	0.55	$(h_{-1})^1(l)^1$
					2	-0.39	0.16	$(h)^1(l_{+1})^1$
					3	-0.28	0.08	$(h_{-1})^1(l_{+1})^1$
					4	-0.16	0.03	$(h_{-1})^1(h)^1(l)^1(l_{+1})^1$
S_0	$CT_{BA}; S_{h-1}^{l+1;l;l+1;l};h;h_{-1}$	1_5	2.82	0.0006	1	0.50	0.25	$(h_{-1})^1(l_{+1})^1$
					2	0.48	0.23	$(h)^1(l_{+1})^1$
					3	0.47	0.22	$(h_{-1})^1(l)^1$
					4	0.28	0.08	$(h)^1(l)^1$

Continued on next page

Table S1: Adiabatic energies, state assignments, coefficients, weights and spatial configurations at different geometries of the **u**-sub-pattern

Geometry	State	Order	$E_{ad.}$	f	No.	c_i	$ c_i ^2$	Composition
Q ₁	CT _{BA} ; S _{$h_{-1};h;h_{-1}$} ^{$l_{+1};l_{+1};l$}	1 ₇	2.83	0.0014	5	-0.15	0.02	$(h_{-1})^0(l_{+1})^2$
					1	0.65	0.42	$(h_{-1})^1(l_{+1})^1$
					2	0.39	0.15	$(h)^1(l)^1$
					3	0.34	0.11	$(h)^1(l_{+1})^1$
					4	0.34	0.11	$(h_{-1})^1(l)^1$
S ₁	CT _{BA} ; S _{$h_{-1};h;h_{-1}$} ^{$l_{+1};l_{+1};l$}	1 ₅	2.75	0.0007	5	0.09	0.01	$(h)^0(l_{+1})^2$
					1	-0.79	0.62	$(h_{-1})^1(l_{+1})^1$
					2	-0.33	0.11	$(h)^1(l_{+1})^1$
					3	-0.28	0.08	$(h_{-1})^1(l)^1$
T ₁	CT _{BA} ; S _{$h_{-1};h;h_{-1}$} ^{$l_{+1};l_{+1};l$}	1 ₅	2.74	0.0068	4	0.09	0.01	$(h_{-1})^1(h)^1(l_{+1})^2$
					1	0.72	0.52	$(h)^1(l_{+1})^1$
					2	-0.49	0.24	$(h_{-1})^1(l_{+1})^1$
					3	0.20	0.04	$(h_{-1})^1(l)^1$
S ₁	LE; N _{h_{-1}} ^{l} /Z _{h} ^{$l;l_{+1}$}	1 ₆	2.77	0.0002	1	0.77	0.59	$(h)^0(l)^2$
					2	-0.21	0.04	$(h)^0(l)^1(l_{+1})^1$
					1	0.51	0.26	$(h_{-1})^0(l)^2$
					2	-0.42	0.18	$(h_{-1})^1(h)^1(l)^2$
S ₁	LE; N _{h_{-1}} ^{l} /Z _{$h;h_{-1}$} ^{l}	1 ₆	2.84	0.0002	3	-0.30	0.09	$(h_{-1})^0(l)^1(l_{+1})^1$
					4	-0.26	0.07	$(h)^0(l)^1(l_{+1})^1$
					5	-0.22	0.05	$(h_{-1})^1(h)^1(l_{+1})^2$
					6	-0.22	0.05	$(h)^0(l_{+1})^2$
S ₁	LE; N _{h} ^{l_{+1}} /V _{$h;h_{-1}$} ^{$l;l_{+1}$}	1 ₇	2.94	0.0000	1	0.51	0.26	$(h)^0(l_{+1})^2$
					2	0.34	0.12	$(h_{-1})^1(h)^1(l)^1(l_{+1})^1$
					3	0.30	0.09	$(h)^0(l)^1(l_{+1})^1$
					4	0.25	0.06	$(h_{-1})^1(h)^1(l_{+1})^2$
					5	0.25	0.06	$(h_{-1})^0(l)^2$
					6	0.22	0.05	$(h)^2(l)^0$
Q ₁	DL; V _{$h_{-1};h$} ^{$l;l_{+1}$}	1 ₅	2.77	0.0000	1	-0.55	0.31	$(h_{-1})^1(h)^1(l)^1(l_{+1})^1$
					2	-0.29	0.09	$(h)^2(l)^0$
					3	-0.29	0.08	$(h)^0(l)^2$
					4	-0.26	0.07	$(h_{-1})^0(l_{+1})^2$
					5	0.24	0.06	$(h)^1(l_{+1})^1$
					6	-0.23	0.05	$(h_{-1})^0(l)^2$

Continued on next page

Table S1: Adiabatic energies, state assignments, coefficients, weights and spatial configurations at different geometries of the **u**-sub-pattern

Geometry	State	Order	$E_{ad.}$	f	No.	c_i	$ c_i ^2$	Composition
S ₀	DL; $S_{h-1;h}^{l;l+1}$	1 ₇	3.00	0.0000	<u>7</u>	-0.23	0.05	$(h)^0(l_{+1})^2$
					8	0.16	0.03	$(h_{-1})^1(l)^1$
					<u>1</u>	-0.59	0.35	$(h_{-1})^1(h)^1(l)^1(l_{+1})^1$
					<u>2</u>	-0.31	0.10	$(h)^0(l)^2$
					<u>3</u>	-0.28	0.08	$(h_{-1})^0(l)^2$
					<u>4</u>	-0.27	0.07	$(h)^0(l_{+1})^2$
					<u>5</u>	-0.23	0.05	$(h_{-1})^0(l_{+1})^2$
					<u>6</u>	-0.22	0.05	$(h)^2(l)^0$
					<u>1</u>	-0.68	0.46	$(h_{-1})^0(l_{+1})^2$
					<u>2</u>	-0.30	0.09	$(h_{-1})^0(l)^1(l_{+1})^1$
					<u>3</u>	0.28	0.08	$(h_{-1})^1(h)^1(l_{+1})^2$
					<u>4</u>	0.18	0.03	$(h_{-9})^1(l_{+1})^1$
T ₁	LE; $N_{h-1}^{l+1}/Z_{h-1}^{l;l+1}/Z_{h-1}^{l+1;h}$	1 ₉	3.43	0.0000	<u>1</u>	-0.68	0.46	$(h_{-1})^0(l_{+1})^2$
					<u>2</u>	-0.30	0.09	$(h_{-1})^0(l)^1(l_{+1})^1$
					<u>3</u>	0.28	0.08	$(h_{-1})^1(h)^1(l_{+1})^2$
Q ₁	DL; $T_{h-1;h}^{l;l+1;l}$	3 ₀	1.13	0.0000	<u>1</u>	0.66	0.44	$(h)^1(l)^1$
					<u>2</u>	-0.60	0.36	$(h_{-1})^1(l_{+1})^1$
					<u>3</u>	0.11	0.01	$(h_{-1})^1(h)^0(l)^2(l_{+1})^1$
S ₀	DL; $T_{h-1;h}^{l;l+1;l}$	3 ₀	1.13	0.0000	<u>1</u>	-0.67	0.44	$(h)^1(l)^1$
					<u>2</u>	0.60	0.36	$(h_{-1})^1(l_{+1})^1$
					<u>3</u>	-0.11	0.01	$(h_{-2})^1(l_{+2})^1$
T ₁	LE; T_h^l	3 ₀	0.95	0.0000	<u>1</u>	-0.86	0.74	$(h)^1(l)^1$
					<u>2</u>	0.20	0.04	$(h)^1(l_{+1})^1$
S ₁	LE; $T_{h-1;h}^{l;l+1;l}$	3 ₀	0.97	0.0000	<u>1</u>	-0.53	0.29	$(h_{-1})^1(l)^1$
					<u>2</u>	-0.50	0.25	$(h)^1(l)^1$
					<u>3</u>	0.42	0.18	$(h_{-1})^1(l_{+1})^1$
					<u>4</u>	-0.31	0.10	$(h)^1(l_{+1})^1$
					<u>5</u>	0.11	0.01	$(h_{-3})^1(l_{+2})^1$
Q ₁	DL; $T_{h-1;h}^{l;l+1}$	3 ₁	1.13	0.0000	<u>1</u>	-0.64	0.40	$(h_{-1})^1(l)^1$
					<u>2</u>	0.63	0.40	$(h)^1(l_{+1})^1$
					<u>3</u>	-0.11	0.01	$(h_{-1})^0(h)^1(l)^2(l_{+1})^1$
S ₀	DL; $T_{h-1;h}^{l;l+1}$	3 ₁	1.13	0.0000	<u>1</u>	0.64	0.41	$(h_{-1})^1(l)^1$
					<u>2</u>	-0.64	0.40	$(h)^1(l_{+1})^1$
					<u>3</u>	-0.12	0.01	$(h_{-2})^1(l_{+3})^1$
S ₁	LE; $T_{h-1;h}^{l;l+1}$	3 ₁	1.05	0.0000	<u>1</u>	-0.70	0.49	$(h)^1(l_{+1})^1$

Continued on next page

Table S1: Adiabatic energies, state assignments, coefficients, weights and spatial configurations at different geometries of the **u**-sub-pattern

Geometry	State	Order	$E_{ad.}$	f	No.	c_i	$ c_i ^2$	Composition
T ₁	LE; T _{<i>h</i>-1} ^{<i>l</i>+1}	3 ₁	1.32	0.0000	2	0.55	0.31	$(h_{-1})^1(l)^1$
					3	-0.12	0.01	$(h_{-2})^1(l_{+3})^1$
					1	0.83	0.69	$(h_{-1})^1(l_{+1})^1$
					2	0.23	0.05	$(h_{-1})^1(l)^1$
					3	0.21	0.05	$(h)^1(l_{+1})^1$
					1	0.46	0.22	$(h_{-2})^1(l)^1$
					2	-0.44	0.20	$(h_{-3})^1(l_{+1})^1$
					3	0.43	0.19	$(h)^1(l_{+2})^1$
					4	-0.40	0.16	$(h_{-1})^1(l_{+3})^1$
					5	0.15	0.02	$(h_{-3})^1(l)^1$
					1	-0.46	0.21	$(h_{-2})^1(l)^1$
					2	0.45	0.20	$(h_{-3})^1(l_{+1})^1$
Q ₁	(LE+CR) ₁ ; T	3 ₃	2.50	0.0011	3	-0.44	0.19	$(h)^1(l_{+2})^1$
					4	0.41	0.17	$(h_{-1})^1(l_{+3})^1$
					5	-0.16	0.03	$(h_{-3})^1(l)^1$
					1	-0.48	0.23	$(h_{-3})^1(l)^1$
					2	0.40	0.16	$(h_{-1})^1(l_{+2})^1$
S ₀	(LE+CR) ₁ ; T	3 ₂	2.25	0.0007	3	0.26	0.07	$(h)^1(l_{+2})^1$
					4	0.23	0.05	$(h_{-3})^1(l_{+1})^1$
					5	-0.20	0.04	$(h_{-1})^1(h)^1(l)^1(l_{+1})^1$
					1	-0.59	0.35	$(h_{-2})^1(l)^1$
					2	0.53	0.28	$(h)^1(l_{+2})^1$
T ₁	(LE+CR) ₁ ; T	3 ₂	2.24	0.0007	3	0.27	0.07	$(h_{-3})^1(l)^1$
					4	0.24	0.06	$(h)^1(l_{+3})^1$
					5	0.15	0.02	$(h_{-2})^1(l_{+1})^1$
					1	-0.46	0.22	$(h_{-3})^1(l)^1$
					2	0.45	0.21	$(h_{-2})^1(l_{+1})^1$
Q ₁	(LE+CR) ₂ ; T	3 ₄	2.50	0.0000	3	0.42	0.18	$(h)^1(l_{+3})^1$
					4	-0.41	0.17	$(h_{-1})^1(l_{+2})^1$
					5	0.11	0.01	$(h_{-2})^1(l)^1$
					1	-0.47	0.22	$(h_{-3})^1(l)^1$
					2	0.46	0.21	$(h_{-2})^1(l_{+1})^1$
S ₀	(LE+CR) ₂ ; T	3 ₃	2.25	0.0000	3	0.43	0.18	$(h)^1(l_{+3})^1$

Continued on next page

Table S1: Adiabatic energies, state assignments, coefficients, weights and spatial configurations at different geometries of the **u**-sub-pattern

Geometry	State	Order	$E_{ad.}$	f	No.	c_i	$ c_i ^2$	Composition
					<u>4</u>	-0.42	0.18	$(h_{-1})^1(l_{+2})^1$
					<u>5</u>	0.12	0.02	$(h_{-2})^1(l)^1$
S_1	$(LE+CR)_2; T$	3_4	2.29	0.0001	<u>1</u>	0.54	0.30	$(h_{-2})^1(l_{+1})^1$
					<u>2</u>	0.50	0.25	$(h)^1(l_{+3})^1$
					<u>3</u>	-0.29	0.09	$(h_{-3})^1(l)^1$
					<u>4</u>	0.27	0.07	$(h_{-1})^1(l_{+2})^1$
					<u>5</u>	0.20	0.04	$(h_{-2})^1(l)^1$
T_1	$(LE+CR)_2; T$	3_4	2.44	0.0000	<u>1</u>	0.59	0.35	$(h_{-3})^1(l_{+1})^1$
					<u>2</u>	0.53	0.28	$(h_{-1})^1(l_{+3})^1$
					<u>3</u>	0.23	0.05	$(h_{-2})^1(l_{+1})^1$
					<u>4</u>	-0.22	0.05	$(h_{-1})^1(l_{+2})^1$
T_1	${}^3DL; {}_3V_{h_{-1};h}^{l;l+1}$	3_3	2.33	0.0000	<u>1</u>	0.55	0.31	$(h_{-1})^1(h)^1(l)^1(l_{+1})^1$
					<u>2</u>	-0.45	0.20	$(h_{-1})^1(h)^1(l)^1(l_{+1})^1$
					<u>3</u>	0.32	0.10	$(h_{-1})^1(h)^1(l)^1(l_{+1})^1$
					<u>4</u>	-0.22	0.05	$(h_{-1})^1(h)^1(l)^2$
S_1	${}^3DL; {}_3V_{h_{-1};h}^{l;l+1}/Z_{h_{-1};h}^l/Z_h^{l;l+1}/Z_{h_{-1}}^{l;l+1}/Z_{h_{-1};h}^{l+1}$	3_3	2.23	0.0004	<u>1</u>	-0.36	0.13	$(h_{-1})^1(h)^1(l)^1(l_{+1})^1$
					<u>2</u>	-0.30	0.09	$(h_{-1})^1(h)^1(l)^1(l_{+1})^1$
					<u>3</u>	0.29	0.08	$(h)^0(l)^1(l_{+1})^1$
					<u>4</u>	-0.28	0.08	$(h_{-1})^1(h)^1(l)^2$
					<u>5</u>	-0.24	0.06	$(h_{-1})^0(l)^1(l_{+1})^1$
					<u>6</u>	0.23	0.05	$(h_{-1})^1(h)^1(l_{+1})^2$
					<u>7</u>	0.23	0.05	$(h_{-3})^1(l)^1$
					<u>8</u>	0.21	0.05	$(h_{-1})^1(h)^1(l)^1(l_{+1})^1$
S_0	${}^3DL; {}_3V_{h_{-1};h}^{l;l+1}/Z_{h_{-1};h}^l/Z_h^{l;l+1}/Z_{h_{-1}}^{l;l+1}/Z_{h_{-1};h}^{l+1}$	3_4	2.66	0.0000	<u>1</u>	0.43	0.19	$(h_{-1})^1(h)^1(l)^2$
					<u>2</u>	-0.43	0.18	$(h)^0(l)^1(l_{+1})^1$
					<u>3</u>	0.37	0.14	$(h_{-1})^0(l)^1(l_{+1})^1$
					<u>4</u>	-0.37	0.13	$(h_{-1})^1(h)^1(l_{+1})^2$
					<u>5</u>	-0.28	0.08	$(h_{-1})^1(l_{+1})^1$
					<u>6</u>	-0.26	0.07	$(h)^1(l)^1$
					<u>7</u>	0.07	0.01	$(h_{-1})^1(h)^1(l)^1(l_{+1})^1$
Q_1	${}^3DL; {}_3V_{h_{-1};h}^{l;l+1}/Z_{h_{-1};h}^l/Z_h^{l;l+1}/Z_{h_{-1}}^{l;l+1}/Z_{h_{-1};h}^{l+1}$	3_2	2.25	0.0000	<u>1</u>	-0.47	0.22	$(h_{-1})^1(h)^1(l)^2$
					<u>2</u>	0.46	0.21	$(h)^0(l)^1(l_{+1})^1$
					<u>3</u>	-0.42	0.18	$(h_{-1})^0(l)^1(l_{+1})^1$

Continued on next page

Table S1: Adiabatic energies, state assignments, coefficients, weights and spatial configurations at different geometries of the **u**-sub-pattern

Geometry	State	Order	$E_{ad.}$	f	No.	c_i	$ c_i ^2$	Composition
					$\frac{4}{5}$	0.41 0.10	0.17 0.01	$(h_{-1})^1(h)^1(l_{+1})^2$ $(h_{-1})^1(l_{+1})^1$
					$\frac{1}{2}$	-0.77 0.49	0.59 0.24	$(h_{-1})^1(l)^1$ $(h)^1(l_{+1})^1$
					$\frac{3}{3}$	0.09	0.01	$(h_{-1})^1(l_{+1})^1$
T ₁	${}^3\text{CT}_{AB}; \text{T}_{h_{-1};h;h_{-1}}^{l_{+1};l;l_{+1};l}$	3 ₅	2.62	0.0001	$\frac{1}{2}$	-0.77 0.49	0.59 0.24	$(h_{-1})^1(l)^1$ $(h)^1(l_{+1})^1$
					$\frac{3}{3}$	0.09	0.01	$(h_{-1})^1(l_{+1})^1$
					$\frac{1}{2}$	-0.77 0.49	0.59 0.24	$(h_{-1})^1(l)^1$ $(h)^1(l_{+1})^1$
Q ₁	${}^3\text{CT}_{AB}; \text{T}_{h_{-1};h;h_{-1}}^{l_{+1};l;l_{+1};l}$	3 ₅	2.84	0.0164	$\frac{1}{2}$	0.62 0.61	0.38 0.37	$(h)^1(l_{+1})^1$ $(h_{-1})^1(l)^1$
					$\frac{3}{3}$	-0.24	0.06	$(h)^1(l)^1$
					$\frac{4}{4}$	-0.14	0.02	$(h_{-1})^1(l_{+1})^1$
S ₁	${}^3\text{CT}_{AB}; \text{T}_{h_{-1};h}^l$	3 ₅	2.54	0.0225	$\frac{1}{2}$	0.73 -0.32	0.54 0.10	$(h)^1(l)^1$ $(h_{-1})^1(l)^1$
					$\frac{3}{3}$	-0.30	0.09	$(h)^1(l_{+1})^1$
					$\frac{4}{5}$	0.23 0.13	0.05 0.02	$(h_{-1})^1(l_{+1})^1$ $(h_{-1})^1(h)^1(l)^1(l_{+1})^1$
S ₀	${}^3\text{CT}_{BA}; \text{T}_{h_{-1};h}^{l;l_{+1}}$	3 ₅	2.80	0.0156	$\frac{1}{2}$	0.64 0.63	0.41 0.40	$(h)^1(l_{+1})^1$ $(h_{-1})^1(l)^1$
					$\frac{3}{3}$	-0.18	0.03	$(h)^1(l)^1$
					$\frac{1}{2}$	0.71 0.37	0.50 0.14	$(h)^1(l_{+1})^1$ $(h_{-1})^1(l)^1$
T ₁	${}^3\text{CT}_{BA}; \text{T}_{h_{-1};h;h_{-1}}^{l_{+1};l;l_{+1};l}$	3 ₆	2.71	0.0001	$\frac{3}{3}$	-0.31	0.09	$(h_{-1})^1(l_{+1})^1$
					$\frac{4}{5}$	0.24 0.13	0.06 0.02	$(h)^1(l)^1$ $(h_{-1})^1(h)^1(l)^1(l_{+1})^1$
					$\frac{1}{2}$	0.71 0.37	0.50 0.14	$(h)^1(l_{+1})^1$ $(h_{-1})^1(l)^1$
Q ₁	${}^3\text{CT}_{BA}; \text{T}_{h_{-1};h;h_{-1}}^{l_{+1};l;l_{+1};l}$	3 ₆	2.87	0.0017	$\frac{1}{2}$	0.65 0.56	0.42 0.32	$(h_{-1})^1(l_{+1})^1$ $(h)^1(l)^1$
					$\frac{3}{3}$	0.19	0.04	$(h_{-1})^1(l)^1$
					$\frac{1}{2}$	0.75 0.37	0.57 0.14	$(h_{-1})^1(l_{+1})^1$ $(h)^1(l_{+1})^1$
S ₁	${}^3\text{CT}_{BA}; \text{T}_{h_{-1};h;h_{-1}}^{l_{+1};l;l}$	3 ₆	2.75	0.0055	$\frac{3}{3}$	0.35	0.12	$(h_{-1})^1(l)^1$
					$\frac{4}{4}$	-0.08	0.01	$(h_{-1})^1(h)^1(l_{+1})^2$
					$\frac{1}{2}$	0.75 0.37	0.57 0.14	$(h_{-1})^1(l_{+1})^1$ $(h)^1(l_{+1})^1$
S ₀	${}^3\text{CT}_{BA}; \text{T}_{h_{-1};h}^{l_{+1};l;l}$	3 ₆	2.85	0.0008	$\frac{1}{2}$	0.62 0.54	0.38 0.29	$(h_{-1})^1(l_{+1})^1$ $(h)^1(l)^1$
					$\frac{3}{3}$	0.20	0.04	$(h_{-1})^0(l)^1(l_{+1})^1$
					$\frac{1}{2}$	0.75 0.37	0.57 0.14	$(h_{-1})^1(l_{+1})^1$ $(h)^1(l_{+1})^1$

Continued on next page

Table S1: Adiabatic energies, state assignments, coefficients, weights and spatial configurations at different geometries of the **u**-sub-pattern

Geometry	State	Order	$E_{ad.}$	f	No.	c_i	$ c_i ^2$	Composition
Q ₁	${}^3\text{DL}_2; Z_{h-1;h}^l/Z_h^{l;l+1}/Z_{h-1}^{l;l+1}/Z_{h-1;h}^{l+1}$	3 ₈	3.59	0.0002	1	0.50	0.25	$(h_{-1})^1(h)^1(l)^2$
					2	0.49	0.24	$(h)^0(l)^1(l_{+1})^1$
					3	-0.40	0.16	$(h_{-1})^0(l)^1(l_{+1})^1$
					4	-0.40	0.16	$(h_{-1})^1(h)^1(l_{+1})^2$
					5	-0.09	0.01	$(h_{-1})^1(h)^1(l)^1(l_{+1})^1$
S ₁	${}^3\text{DL}_2; {}_3V_{h-1;h}^{l;l+1}/Z_{h-1;h}^l/Z_h^{l;l+1}/Z_{h-1}^{l;l+1}/Z_{h-1;h}^{l+1}$	3 ₉	3.51	0.0062	1	0.42	0.18	$(h_{-1})^1(h)^1(l)^1(l_{+1})^1$
					2	-0.38	0.15	$(h_{-1})^1(h)^1(l)^2$
					3	-0.37	0.14	$(h)^0(l)^1(l_{+1})^1$
					4	-0.35	0.12	$(h_{-1})^1(h)^1(l)^1(l_{+1})^1$
					5	0.28	0.08	$(h_{-1})^0(l)^1(l_{+1})^1$
					6	0.27	0.07	$(h_{-1})^1(h)^1(l)^1(l_{+1})^1$
					7	0.26	0.07	$(h_{-1})^1(h)^1(l_{+1})^2$
					8	-0.09	0.01	$(h_{-1})^1(l_{+2})^1$
S ₀	${}^5\text{DL}; V_{h-1;h}^{l;l+1}$	5 ₀	2.83	0.0000	1	0.89	0.78	$(h_{-1})^1(h)^1(l)^1(l_{+1})^1$
					2	-0.09	0.01	$(h_{-3})^1(h)^1(l_{+1})^1(l_{+2})^1$
Q ₁	${}^5\text{DL}; V_{h-1;h}^{l;l+1}$	5 ₀	2.42	0.0000	1	-0.89	0.80	$(h_{-1})^1(h)^1(l)^1(l_{+1})^1$
					2	-0.08	0.01	$(h_{-1})^1(h)^1(l)^1(l_{+4})^1$
S ₁	${}^5\text{DL}; V_{h-1;h}^{l;l+1}$	5 ₀	2.39	0.0000	1	-0.89	0.79	$(h_{-1})^1(h)^1(l)^1(l_{+1})^1$
					2	-0.13	0.02	$(h_{-3})^1(h)^1(l_{+1})^1(l_{+2})^1$
T ₁	${}^5\text{DL}; V_{h-1;h}^{l;l+1}$	5 ₀	2.38	0.0000	1	-0.89	0.80	$(h_{-1})^1(h)^1(l)^1(l_{+1})^1$
					2	-0.13	0.02	$(h_{-3})^1(h)^1(l)^1(l_{+3})^1$

Table S2: Adiabatic energies, state assignments, coefficients, weights and spatial configurations at different geometries of the **v**-sub-pattern

Geometry	State	Order	$E_{ad.}$	f	No.	c_i	$ c_i ^2$	Composition
S ₀	Gs	1 ₀	0.00	0.0000	1	0.91	0.82	$(h)^2(l)^0$
					2	0.13	0.02	$(h_{-1})^1(h)^1(l)^1(l_{+1})^1$
Q ₁	Gs	1 ₀	0.33	0.0000	1	-0.88	0.77	$(h)^2(l)^0$
					2	-0.19	0.04	$(h_{-1})^1(h)^1(l)^1(l_{+1})^1$

Continued on next page

Table S2: Adiabatic energies, state assignments, coefficients, weights and spatial configurations at different geometries of the \mathbf{v} -sub-pattern

Geometry	State	Order	E_{ad}	f	No.	c_i	$ c_i ^2$	Composition
S ₁	Gs	1 ₀	0.07	0.0000	$\frac{1}{2}$	-0.90 -0.13	0.80 0.02	$(h)^2(l)^0$ $(h_{-1})^1(h)^1(l)^1(l_{+1})^1$
T ₁	Gs	1 ₀	0.14	0.0000	$\frac{1}{2}$	-0.89 0.14	0.80 0.02	$(h)^2(l)^0$ $(h)^0(l)^2$
S ₁	CT _{AB} ; S _h ^l	1 ₁	2.09	0.0533	$\frac{1}{2}$ $\frac{3}{4}$	0.65 -0.31 0.24 -0.20	0.43 0.09 0.06 0.04	$(h)^1(l)^1$ $(h)^0(l)^2$ $(h_{-1})^1(h)^1(l)^1(l_{+1})^1$ $(h_{-1})^1(l)^1$
S ₀	CT+LE; S _h ^l	1 ₁	2.25	0.1708	$\frac{1}{2}$	-0.89 -0.20	0.78 0.04	$(h)^1(l)^1$ $(h_{-1})^1(l_{+1})^1$
Q ₁	DL; N _h ^l /V _{h-1;h} ^{l;l+1}	1 ₁	2.03	0.0003	$\frac{1}{2}$ $\frac{2}{3}$ $\frac{4}{5}$ $\frac{6}{7}$ $\frac{8}{8}$	-0.89 -0.15 -0.44 0.36 0.33 0.30 0.26 -0.25 -0.24 -0.18	0.80 0.02 0.19 0.13 0.11 0.09 0.07 0.06 0.06 0.03	$(h)^1(l)^1$ $(h_{-1})^1(l_{+1})^1$ $(h)^0(l)^2$ $(h_{-1})^1(h)^1(l)^1(l_{+1})^1$ $(h_{-1})^0(l)^2$ $(h)^0(l_{+1})^2$ $(h_{-1})^1(h)^1(l)^2$ $(h_{-1})^1(l)^1$ $(h_{-1})^0(l_{+1})^2$ $(h_{-1})^1(h)^1(l_{+1})^2$
T ₁	LE+CT; S _h ^l	1 ₁	2.17	0.1108	$\frac{1}{2}$	0.84 -0.19	0.70 0.04	$(h)^1(l)^1$ $(h_{-1})^1(l)^1$
S ₁	CT+LE; S _{h;h-1} ^{l;l+1}	1 ₂	2.16	0.1042	$\frac{1}{2}$ $\frac{3}{4}$ $\frac{5}{5}$	0.62 0.37 0.24 -0.23 -0.22	0.38 0.14 0.06 0.05 0.05	$(h)^1(l)^1$ $(h_{-1})^1(l)^1$ $(h)^0(l)^2$ $(h)^1(l_{+1})^1$ $(h_{-1})^1(h)^1(l)^2$
S ₀	LE; S _{h-1} ^l	1 ₂	2.34	0.0342	$\frac{1}{2}$ $\frac{2}{3}$ $\frac{3}{3}$	0.82 0.30 0.15	0.67 0.09 0.02	$(h_{-1})^1(l)^1$ $(h)^1(l_{+1})^1$ $(h)^0(l)^2$
T ₁	CT+LE; S _h ^{l;l+1} /Z _{h;h-1} ^l	1 ₂	2.22	0.0299				

Continued on next page

Table S2: Adiabatic energies, state assignments, coefficients, weights and spatial configurations at different geometries of the \mathbf{v} -sub-pattern

Geometry	State	Order	$E_{ad.}$	f	No.	c_i	$ c_i ^2$	Composition
S ₁	LE; $S_{h-1;h}^{l;l+1}$	1 ₃	2.33	0.0402	3	-0.33	0.11	$(h)^1(l)^1$
					4	0.31	0.10	$(h_{-1})^1(h)^1(l)^1(l_{+1})^1$
					5	-0.30	0.09	$(h_{-1})^1(l)^1$
					6	-0.26	0.07	$(h_{-1})^1(h)^1(l_{+1})^2$
					7	-0.23	0.05	$(h)^0(l)^2$
					8	0.20	0.04	$(h_{-1})^1(h)^1(l)^1(l_{+1})^1$
					1	-0.66	0.44	$(h_{-1})^1(l)^1$
					2	-0.61	0.37	$(h)^1(l_{+1})^1$
Q ₁	LE; $S_{h-1;h}^{l;l+1}$	1 ₃	2.44	0.0347	3	0.09	0.01	$(h_{-1})^1(h)^0(l)^1(l_{+1})^2$
					1	0.73	0.53	$(h_{-1})^1(l)^1$
					2	0.52	0.27	$(h)^1(l_{+1})^1$
S ₀	DL; S_h^{l+1}/N_h^l	1 ₃	2.43	0.0098	3	-0.11	0.01	$(h_{-1})^1(h)^0(l)^1(l_{+1})^2$
					1	-0.65	0.43	$(h)^1(l_{+1})^1$
					2	0.34	0.11	$(h)^0(l)^2$
					3	-0.27	0.07	$(h_{-1})^1(h)^1(l)^1(l_{+1})^1$
T ₁	LE; $S_{h-1;h}^{l;l+1}$	1 ₃	2.42	0.0427	4	-0.22	0.05	$(h_{-1})^0(l)^2$
					1	-0.64	0.40	$(h_{-1})^1(l)^1$
					2	-0.56	0.31	$(h)^1(l_{+1})^1$
					3	-0.30	0.09	$(h_{-1})^1(l_{+1})^1$
S ₀	CT _{AB} ; $S_{h-1;h}^{l+1}$	1 ₄	2.68	0.0297	4	-0.12	0.02	$(h)^1(l)^1$
					1	0.57	0.33	$(h_{-1})^1(l_{+1})^1$
					2	-0.45	0.20	$(h)^1(l_{+1})^1$
					3	0.28	0.08	$(h_{-1})^1(l)^1$
					4	-0.23	0.05	$(h)^1(l)^1$
T ₁	LE+DL; $N_h^l/S_h^{l+1}/Z_h^{l;l+1}$	1 ₄	2.64	0.0118	5	0.19	0.03	$(h_{-1})^1(h)^1(l)^2$
					1	-0.48	0.23	$(h)^0(l)^2$
					2	-0.44	0.19	$(h)^1(l_{+1})^1$
					3	0.33	0.11	$(h)^0(l)^1(l_{+1})^1$
					4	0.27	0.07	$(h_{-1})^1(l)^1$
					5	0.23	0.05	$(h_{-1})^1(l_{+1})^1$
S ₁	CT _{AB} ; $S_{h-1;h;h-1}^{l;l+1;l+1}$	1 ₄	2.56	0.0359	6	0.20	0.04	$(h_{-1})^1(h)^1(l)^1(l_{+1})^1$
					1	-0.58	0.34	$(h)^1(l_{+1})^1$
					2	0.41	0.17	$(h_{-1})^1(l)^1$

Continued on next page

Table S2: Adiabatic energies, state assignments, coefficients, weights and spatial configurations at different geometries of the \mathbf{v} -sub-pattern

Geometry	State	Order	$E_{ad.}$	f	No.	c_i	$ c_i ^2$	Composition
Q ₁	$CT_{AB}; S_{h_{-1};h;h_{-1}}^{l;l+1;l+1}$	1 ₄	2.67	0.0218	3	0.39	0.15	$(h_{-1})^1(l_{+1})^1$
					4	0.20	0.04	$(h_{-1})^1(h)^1(l)^2$
					1	0.65	0.42	$(h)^1(l_{+1})^1$
					2	-0.41	0.17	$(h_{-1})^1(l)^1$
					3	-0.35	0.12	$(h_{-1})^1(l_{+1})^1$
					4	-0.22	0.05	$(h_{-1})^1(h)^1(l)^2$
					1	-0.67	0.45	$(h_{-1})^1(l_{+1})^1$
					2	-0.33	0.11	$(h)^1(l_{+1})^1$
					3	0.30	0.09	$(h_{-1})^1(l)^1$
					4	-0.23	0.05	$(h)^0(l)^2$
					5	0.16	0.02	$(h_{-1})^1(h)^1(l)^1(l_{+1})^1$
					1	0.47	0.22	$(h)^1(l_{+1})^1$
T ₁	$(LE+CT)_{BA}; S_h^{l+1}/Z_h^{l;l+1}/N_h^l$	1 ₅	2.66	0.0110	2	0.36	0.13	$(h)^0(l)^1(l_{+1})^1$
					3	-0.36	0.13	$(h)^0(l)^2$
					4	-0.30	0.09	$(h_{-1})^1(h)^1(l)^2$
					5	-0.28	0.08	$(h_{-1})^1(l)^1$
					6	-0.23	0.05	$(h_{-1})^1(l_{+1})^1$
					7	-0.17	0.03	$(h)^0(l_{+1})^2$
					1	0.79	0.62	$(h_{-1})^1(l_{+1})^1$
T ₁	$CT_{AB}; S_{h_{-1}}^{l+1;l}$	1 ₆	2.83	0.0410	2	-0.39	0.15	$(h_{-1})^1(l)^1$
					3	-0.13	0.02	$(h_{-1})^1(h)^1(l)^1(l_{+1})^1$
					1	-0.78	0.60	$(h_{-1})^1(l_{+1})^1$
S ₁	$CT_{BA}; S_{h_{-1}}^{l+1}$	1 ₅	2.80	0.0193	2	-0.22	0.05	$(h)^0(l)^2$
					1	0.71	0.50	$(h_{-1})^1(l_{+1})^1$
					2	-0.31	0.10	$(h_{-1})^1(h)^1(l)^1(l_{+1})^1$
					3	0.25	0.06	$(h)^0(l)^2$
					4	-0.16	0.03	$(h_{-1})^1(l)^1$
Q ₁	$CT_{BA}; S_{h_{-1}}^{l+1}$	1 ₆	2.82	0.0196	1	-0.51	0.26	$(h)^0(l)^1(l_{+1})^1$
					2	0.45	0.20	$(h_{-1})^1(h)^1(l)^2$
					3	-0.30	0.09	$(h_{-1})^0(l)^1(l_{+1})^1$
					4	0.28	0.08	$(h_{-1})^1(h)^1(l_{+1})^2$
					5	0.20	0.04	$(h)^0(l_{+1})^2$

Continued on next page

Table S2: Adiabatic energies, state assignments, coefficients, weights and spatial configurations at different geometries of the \mathbf{v} -sub-pattern

Geometry	State	Order	E_{ad}	f	No.	c_i	$ c_i ^2$	Composition
S_1	$LE; Z_{h-1}^{l;l+1}/Z_{h-1;h}^l$	1_6	2.84	0.0000	1	-0.53	0.28	$(h)^0(l)^1(l_{+1})^1$
					2	0.44	0.19	$(h_{-1})^1(h)^1(l)^2$
					3	0.27	0.07	$(h)^0(l_{+1})^2$
					4	-0.26	0.07	$(h_{-1})^0(l)^1(l_{+1})^1$
					5	0.24	0.06	$(h_{-1})^1(h)^1(l_{+1})^2$
					6	-0.15	0.02	$(h_{-1})^0(l)^2$
Q_1	$LE; Z_{h-1}^{l;l+1}/Z_{h-1;h}^l$	1_5	2.73	0.0005	1	0.51	0.26	$(h)^0(l)^1(l_{+1})^1$
					2	-0.45	0.20	$(h_{-1})^1(h)^1(l)^2$
					3	0.31	0.09	$(h_{-1})^0(l)^1(l_{+1})^1$
					4	-0.29	0.09	$(h_{-1})^1(h)^1(l_{+1})^2$
					5	-0.17	0.03	$(h)^0(l_{+1})^2$
T_1	$LE; Z_{h-1}^{l;l+1}/N_{h-1}^l/N_{h-1}^{l+1}$	1_7	3.25	0.0001	1	-0.52	0.27	$(h_{-1})^0(l)^1(l_{+1})^1$
					2	-0.35	0.12	$(h_{-1})^0(l)^2$
					3	-0.33	0.11	$(h_{-1})^0(l_{+1})^2$
					4	0.29	0.08	$(h_{-1})^1(h)^1(l)^1(l_{+1})^1$
					5	0.22	0.05	$(h_{-1})^1(h)^1(l_{+1})^2$
S_1	$LE+CT; N_{h-1}^l/V_{h-1;h}^{l;l+1}$	1_7	2.96	0.0014	1	0.46	0.21	$(h_{-1})^1(h)^1(l)^1(l_{+1})^1$
					2	-0.43	0.18	$(h_{-1})^0(l)^2$
					3	-0.28	0.08	$(h)^0(l_{+1})^2$
					4	-0.24	0.06	$(h)^0(l)^2$
					5	0.23	0.05	$(h_{-1})^1(l_{+1})^1$
					6	-0.20	0.04	$(h)^2(l)^0$
S_0	$LE+CT; N_{h-1}^l/V_{h-1;h}^{l;l+1}$	1_7	3.11	0.0002	1	-0.51	0.27	$(h_{-1})^1(h)^1(l)^1(l_{+1})^1$
					2	0.40	0.16	$(h_{-1})^0(l)^2$
					3	0.27	0.07	$(h)^0(l)^2$
					4	0.27	0.07	$(h)^0(l_{+1})^2$
					5	0.20	0.04	$(h)^2(l)^0$
Q_1	$CT+LE; N_{h-1}^l/S_{h-1}^{l+1}/V_{h-1;h}^{l;l+1}$	1_7	2.90	0.0060	1	0.42	0.17	$(h_{-1})^1(h)^1(l)^1(l_{+1})^1$
					2	0.40	0.16	$(h_{-1})^1(l_{+1})^1$
					3	-0.36	0.13	$(h_{-1})^0(l)^2$
					4	-0.26	0.07	$(h)^0(l_{+1})^2$
					5	-0.23	0.05	$(h)^2(l)^0$
					6	0.22	0.05	$(h)^1(l_{+1})^1$

Continued on next page

Table S2: Adiabatic energies, state assignments, coefficients, weights and spatial configurations at different geometries of the \mathbf{v} -sub-pattern

Geometry	State	Order	$E_{ad.}$	f	No.	c_i	$ c_i ^2$	Composition
S_0	DL; $T_{h;h-1}^{l;l+1}$	3_0	1.14	0.0000	1	-0.69	0.48	$(h)^1(l)^1$
					2	-0.49	0.24	$(h_{-1})^1(l_{+1})^1$
					3	0.25	0.06	$(h)^1(l_{+1})^1$
					4	-0.17	0.03	$(h_{-1})^1(l)^1$
T_1	LE; $T_h^{l;l+1}$	3_0	0.96	0.0000	1	-0.77	0.59	$(h)^1(l)^1$
					2	0.43	0.18	$(h)^1(l_{+1})^1$
					3	0.21	0.04	$(h_{-1})^1(l)^1$
S_1	CR+LE; $T_{h;h-1;h}^{l;l+1}$	3_0	1.04	0.0000	1	-0.68	0.46	$(h)^1(l)^1$
					2	-0.44	0.19	$(h_{-1})^1(l_{+1})^1$
					3	0.32	0.11	$(h)^1(l_{+1})^1$
					4	-0.23	0.05	$(h_{-1})^1(l)^1$
					5	0.08	0.01	$(h_{-2})^1(l_{+3})^1$
Q_1	CR+LE; $T_{h;h-1}^{l;l+1}$	3_0	1.12	0.0000	1	0.69	0.48	$(h)^1(l)^1$
					2	0.49	0.24	$(h_{-1})^1(l_{+1})^1$
					3	-0.28	0.08	$(h)^1(l_{+1})^1$
					4	-0.10	0.01	$(h_{-1})^1(h)^0(l)^2(l_{+1})^1$
S_0	DL; $T_{h;h-1}^{l+1;l}$	3_1	1.20	0.0000	1	-0.67	0.45	$(h_{-1})^1(l)^1$
					2	-0.59	0.35	$(h)^1(l_{+1})^1$
					3	-0.12	0.01	$(h_{-3})^1(l_{+2})^1$
S_1	LE; $T_{h;h-1}^{l+1;l}$	3_1	1.13	0.0000	1	-0.67	0.45	$(h_{-1})^1(l)^1$
					2	-0.59	0.35	$(h)^1(l_{+1})^1$
					3	-0.11	0.01	$(h_{-3})^1(l_{+2})^1$
T_1	LE; $T_{h-1}^{l;l+1}$	3_1	1.32	0.0000	1	0.64	0.41	$(h_{-1})^1(l_{+1})^1$
					2	0.54	0.29	$(h_{-1})^1(l)^1$
					3	0.26	0.07	$(h)^1(l_{+1})^1$
					4	0.21	0.04	$(h)^1(l)^1$
Q_1	LE; $T_{h;h-1}^{l+1;l}$	3_1	1.17	0.0000	1	0.67	0.45	$(h_{-1})^1(l)^1$
					2	0.57	0.33	$(h)^1(l_{+1})^1$
					3	0.15	0.02	$(h_{-1})^1(l_{+1})^1$
S_0	DL; T	3_2	2.29	0.0014	1	0.44	0.19	$(h_{-2})^1(l)^1$
					2	-0.43	0.18	$(h)^1(l_{+2})^1$
					3	0.34	0.11	$(h_{-1})^1(l_{+3})^1$

Continued on next page

Table S2: Adiabatic energies, state assignments, coefficients, weights and spatial configurations at different geometries of the **v**-sub-pattern

Geometry	State	Order	$E_{ad.}$	f	No.	c_i	$ c_i ^2$	Composition
T_1	LE; T	3_2	2.28	0.0006	4	-0.32	0.10	$(h_{-3})^1(l_{+1})^1$
					5	-0.30	0.09	$(h_{-2})^1(l_{+1})^1$
					6	-0.24	0.06	$(h_{-3})^1(l)^1$
					7	-0.21	0.04	$(h)^1(l_{+3})^1$
					1	-0.54	0.29	$(h_{-2})^1(l)^1$
					2	-0.40	0.16	$(h)^1(l_{+3})^1$
					3	0.39	0.15	$(h)^1(l_{+2})^1$
					4	0.30	0.09	$(h_{-2})^1(l_{+1})^1$
					5	-0.15	0.02	$(h_{-1})^1(l_{+1})^1$
					1	-0.47	0.22	$(h_{-1})^1(h)^1(l)^2$
Q_1	DL; Z/T/V	3_2	2.20	0.0000	2	-0.42	0.18	$(h)^0(l)^1(l_{+1})^1$
					3	0.34	0.11	$(h_{-1})^1(h)^1(l_{+1})^2$
					4	0.33	0.11	$(h_{-1})^0(l)^1(l_{+1})^1$
					5	-0.27	0.07	$(h_{-1})^1(l_{+1})^1$
					6	0.25	0.06	$(h_{-1})^1(h)^1(l)^1(l_{+1})^1$
					7	0.18	0.03	$(h)^1(l)^1$
					1	-0.38	0.15	$(h)^1(l)^1$
S_1	DL; T/Z	3_2	2.25	0.0087	2	0.37	0.13	$(h_{-1})^1(l_{+1})^1$
					3	0.31	0.10	$(h_{-3})^1(l)^1$
					4	0.26	0.07	$(h_{-1})^1(h)^1(l)^2$
					5	0.25	0.06	$(h)^0(l)^1(l_{+1})^1$
					6	0.24	0.06	$(h_{-1})^1(l_{+2})^1$
					7	-0.23	0.05	$(h)^1(l_{+1})^1$
					8	-0.17	0.03	$(h_{-1})^1(h)^1(l_{+1})^2$
					1	0.48	0.23	$(h_{-3})^1(l)^1$
S_0	DL ₂ ; T	3_3	2.31	0.0002	2	0.42	0.18	$(h_{-1})^1(l_{+2})^1$
					3	-0.39	0.15	$(h)^1(l_{+3})^1$
					4	-0.36	0.13	$(h_{-2})^1(l_{+1})^1$
					5	0.20	0.04	$(h_{-3})^1(l_{+1})^1$
					1	0.40	0.16	$(h_{-1})^1(h)^1(l)^2$
T_1	CR+DL; V/Z/T	3_3	2.36	0.0008	2	-0.39	0.15	$(h_{-1})^1(h)^1(l)^1(l_{+1})^1$
					3	-0.28	0.08	$(h)^1(l_{+1})^1$
					4	-0.27	0.07	$(h_{-1})^1(h)^1(l_{+1})^2$
					5	0.27	0.07	$(h)^0(l)^1(l_{+1})^1$

Continued on next page

Table S2: Adiabatic energies, state assignments, coefficients, weights and spatial configurations at different geometries of the **v**-sub-pattern

Geometry	State	Order	$E_{ad.}$	f	No.	c_i	$ c_i ^2$	Composition
S ₁	LE+CR; T	3 ₃	2.28	0.0012	6	0.26	0.07	$(h_{-1})^1(l_{+1})^1$
					7	-0.21	0.04	$(h)^1(l)^1$
					1	0.43	0.19	$(h_{-2})^1(l)^1$
					2	-0.38	0.15	$(h)^1(l_{+2})^1$
					3	-0.33	0.11	$(h_{-2})^1(l_{+1})^1$
					4	-0.29	0.08	$(h)^1(l_{+3})^1$
					5	0.29	0.08	$(h_{-1})^1(l_{+3})^1$
					6	-0.28	0.08	$(h_{-3})^1(l_{+1})^1$
					7	-0.22	0.05	$(h_{-3})^1(l)^1$
					1	0.44	0.19	$(h_{-3})^1(l)^1$
					2	-0.38	0.15	$(h)^1(l_{+3})^1$
					3	0.38	0.15	$(h_{-1})^1(l_{+2})^1$
					4	-0.36	0.13	$(h_{-2})^1(l_{+1})^1$
					5	-0.20	0.04	$(h)^1(l)^1$
S ₀	${}^3\text{CT}_{AB}; \text{T}_{h;h-1;h}^{l;l+1}$	3 ₄	2.54	0.0142	1	0.50	0.25	$(h)^1(l)^1$
					2	-0.42	0.18	$(h_{-1})^1(l_{+1})^1$
					3	0.36	0.13	$(h)^1(l_{+1})^1$
					4	-0.24	0.06	$(h_{-1})^1(l)^1$
					5	-0.23	0.05	$(h_{-1})^1(h)^1(l)^2$
					6	-0.23	0.05	$(h)^0(l)^1(l_{+1})^1$
					7	0.16	0.03	$(h_{-1})^1(h)^1(l_{+1})^2$
T ₁	LE+CR; T	3 ₄	2.46	0.0009	1	-0.46	0.21	$(h_{-3})^1(l_{+1})^1$
					2	-0.40	0.16	$(h_{-1})^1(l_{+2})^1$
					3	-0.37	0.14	$(h_{-3})^1(l)^1$
					4	-0.31	0.10	$(h_{-1})^1(l_{+3})^1$
					5	0.20	0.04	$(h)^1(l_{+1})^1$
S ₁	(LE+CR) ₂ ; T	3 ₄	2.36	0.0015	1	0.40	0.16	$(h_{-3})^1(l)^1$
					2	0.36	0.13	$(h_{-1})^1(l_{+2})^1$
					3	-0.35	0.13	$(h_{-2})^1(l_{+1})^1$
					4	-0.34	0.11	$(h)^1(l_{+3})^1$
					5	-0.24	0.06	$(h_{-1})^1(h)^1(l)^2$
					6	-0.23	0.05	$(h)^0(l)^1(l_{+1})^1$
					7	0.17	0.03	$(h_{-1})^1(h)^1(l)^1(l_{+1})^1$

Continued on next page

Table S2: Adiabatic energies, state assignments, coefficients, weights and spatial configurations at different geometries of the **v**-sub-pattern

Geometry	State	Order	E_{ad}	f	No.	c_i	$ c_i ^2$	Composition
Q ₁	${}^3\text{CT}_{AB}; \text{T}_{h_{-1};h;h_{-1}}^{l_{+1};l}$	3 ₅	2.64	0.0401	1	0.55	0.31	$(h)^1(l_{+1})^1$
					2	-0.46	0.21	$(h_{-1})^1(l)^1$
					3	0.40	0.16	$(h)^1(l)^1$
					4	0.20	0.04	$(h_{-3})^1(l)^1$
S ₀	${}^3\text{CT}_{BA}; \text{T}_{h_{-1};h}^{l_{+1};l}$	3 ₅	2.66	0.0390	1	-0.50	0.25	$(h)^1(l_{+1})^1$
					2	0.49	0.24	$(h_{-1})^1(l)^1$
					3	-0.29	0.09	$(h_{-1})^1(l_{+1})^1$
					4	-0.28	0.08	$(h_{-1})^1(h)^1(l)^2$
T ₁	${}^3\text{CT}_{AB}; \text{T}_{h_{-1};h}^{l;l_{+1}}$	3 ₅	2.57	0.0178	1	-0.67	0.45	$(h)^1(l_{+1})^1$
					2	0.44	0.19	$(h_{-1})^1(l)^1$
					3	-0.26	0.07	$(h)^1(l)^1$
					4	-0.15	0.02	$(h_{-3})^1(l_{+1})^1$
S ₁	${}^3\text{CT}_{AB}; \text{T}_{h;h_{-1};h}^{l_{+1};l}$	3 ₅	2.50	0.0580	1	0.50	0.25	$(h)^1(l_{+1})^1$
					2	-0.44	0.19	$(h_{-1})^1(l)^1$
					3	0.38	0.15	$(h)^1(l)^1$
					4	0.25	0.06	$(h_{-1})^1(h)^1(l)^2$
S ₀	CR+DL; T/V/Z	3 ₆	2.89	0.0070	5	-0.21	0.04	$(h_{-1})^1(h)^1(l)^1(l_{+1})^1$
					1	-0.52	0.27	$(h_{-1})^1(l_{+1})^1$
					2	0.33	0.11	$(h_{-1})^1(h)^1(l)^2$
					3	0.29	0.09	$(h)^0(l)^1(l_{+1})^1$
					4	0.28	0.08	$(h)^1(l)^1$
					5	-0.27	0.07	$(h_{-1})^1(h)^1(l_{+1})^2$
					6	-0.25	0.06	$(h_{-1})^0(l)^1(l_{+1})^1$
					7	0.23	0.05	$(h_{-1})^1(l)^1$
T ₁	${}^3\text{CT}_{BA}; \text{T}_{h_{-1};h}^{l_{+1};l}$	3 ₆	2.81	0.0018	8	-0.21	0.04	$(h_{-1})^1(h)^1(l)^1(l_{+1})^1$
					1	-0.55	0.30	$(h_{-1})^1(l_{+1})^1$
					2	0.52	0.27	$(h_{-1})^1(l)^1$
					3	0.29	0.08	$(h)^1(l)^1$
S ₁	${}^3\text{CT}_{BA}; \text{T}_{h_{-1}}^{l_{+1}}$	3 ₆	2.82	0.0203	4	-0.21	0.05	$(h_{-1})^1(h)^1(l)^1(l_{+1})^1$
					1	-0.67	0.46	$(h_{-1})^1(l_{+1})^1$
					2	0.31	0.09	$(h_{-1})^1(l)^1$
					3	0.25	0.06	$(h)^1(l)^1$

Continued on next page

Table S2: Adiabatic energies, state assignments, coefficients, weights and spatial configurations at different geometries of the **v**-sub-pattern

Geometry	State	Order	$E_{ad.}$	f	No.	c_i	$ c_i ^2$	Composition
Q ₁	${}^3\text{CT}_{BA}; \text{T}_{h_{-1};h;h_{-1}}^{l_{+1};l}$	3 ₆	2.83	0.0143	4	-0.23	0.05	$(h)^1(l_{+1})^1$
					5	0.19	0.04	$(h_{-1})^1(h)^1(l)^2$
					1	-0.65	0.43	$(h_{-1})^1(l_{+1})^1$
					2	0.34	0.12	$(h)^1(l)^1$
					3	0.34	0.12	$(h_{-1})^1(l)^1$
					4	-0.25	0.06	$(h)^1(l_{+1})^1$
					5	-0.14	0.02	$(h_{-1})^1(h)^1(l_{+1})^2$
					1	0.59	0.34	$(h_{-1})^1(h)^1(l)^2$
					2	-0.48	0.23	$(h)^0(l)^1(l_{+1})^1$
					3	0.29	0.08	$(h_{-1})^1(h)^1(l)^1(l_{+1})^1$
Q ₁	DL ₂ ; Z/T/V	3 ₇	3.53	0.0273	4	0.28	0.08	$(h_{-1})^0(l)^1(l_{+1})^1$
					5	-0.23	0.06	$(h_{-1})^1(h)^1(l_{+1})^2$
					6	-0.11	0.01	$(h_{-1})^1(h)^1(l)^1(l_{+1})^1$
					1	-0.89	0.79	$(h_{-1})^1(h)^1(l)^1(l_{+1})^1$
					2	0.10	0.01	$(h_{-2})^1(h_{-1})^1(l)^1(l_{+3})^1$
Q ₁	${}^5\text{DL}; \text{V}_{h_{-1};h}^{l;l_{+1}}$	5 ₀	2.43	0.0000	1	0.90	0.80	$(h_{-1})^1(h)^1(l)^1(l_{+1})^1$
					2	-0.08	0.01	$(h_{-2})^1(h_{-1})^1(l)^1(l_{+3})^1$
S ₁	${}^5\text{DL}; \text{V}_{h_{-1};h}^{l;l_{+1}}$	5 ₀	2.58	0.0000	1	0.89	0.80	$(h_{-1})^1(h)^1(l)^1(l_{+1})^1$
					2	-0.10	0.01	$(h_{-3})^1(h)^1(l_{+1})^1(l_{+2})^1$
T ₁	${}^5\text{DL}; \text{V}_{h_{-1};h}^{l;l_{+1}}$	5 ₀	2.57	0.0000	1	0.89	0.80	$(h_{-1})^1(h)^1(l)^1(l_{+1})^1$
					2	0.09	0.01	$(h_{-3})^1(h)^1(l)^1(l_{+3})^1$

Table S3: Adiabatic energies, state assignments, coefficients, weights and spatial configurations at different geometries of the **w**-sub-pattern

Geometry	State	Order	$E_{ad.}$	f	No.	c_i	$ c_i ^2$	Composition
S ₀	Gs	1 ₀	0.00	0.0000	1	-0.91	0.82	$(h)^2(l)^0$
					2	0.14	0.02	$(h_{-1})^1(h)^1(l)^1(l_{+1})^1$
Q ₁	Gs	1 ₀	0.33	0.0000	1	-0.87	0.76	$(h)^2(l)^0$
					2	0.21	0.04	$(h_{-1})^1(h)^1(l)^1(l_{+1})^1$

Continued on next page

Table S3: Adiabatic energies, state assignments, coefficients, weights and spatial configurations at different geometries of the **w**-sub-pattern

Geometry	State	Order	$E_{ad.}$	f	No.	c_i	$ c_i ^2$	Composition
S ₁	Gs	1 ₀	0.08	0.0000	$\frac{1}{2}$	0.90 -0.15	0.80 0.02	$(h)^2(l)^0$ $(h_{-1})^1(h)^1(l)^1(l_{+1})^1$
T ₁	Gs	1 ₀	0.13	0.0000	$\frac{1}{2}$	-0.89 0.14	0.80 0.02	$(h)^2(l)^0$ $(h)^0(l)^2$
Q ₁	DL; S _{<i>h</i>} ^{<i>l</i>}	1 ₂	2.28	0.1391	$\frac{1}{2}$	-0.90 0.12	0.81 0.02	$(h)^1(l)^1$ $(h_{-1})^1(l_{+1})^1$
S ₀	CT; S _{<i>h</i>} ^{<i>l</i>}	1 ₁	2.21	0.1664	$\frac{1}{2}$	-0.90 0.18	0.81 0.03	$(h)^1(l)^1$ $(h_{-1})^1(l_{+1})^1$
S ₁	CT; S _{<i>h</i>} ^{<i>l</i>}	1 ₁	2.07	0.0779	$\frac{1}{2}$ $\frac{3}{3}$	-0.75 -0.29 -0.19	0.57 0.08 0.04	$(h)^1(l)^1$ $(h)^0(l)^2$ $(h_{-1})^1(h)^1(l)^1(l_{+1})^1$
T ₁	CT; S _{<i>h</i>} ^{<i>l</i>}	1 ₁	2.13	0.0731	$\frac{1}{2}$ $\frac{3}{4}$ $\frac{5}{5}$	0.67 0.24 -0.23 0.23 -0.21	0.45 0.06 0.05 0.05 0.04	$(h)^1(l)^1$ $(h)^0(l)^2$ $(h_{-1})^1(l)^1$ $(h_{-1})^1(h)^1(l)^1(l_{+1})^1$ $(h_{-1})^1(h)^1(l)^2$
S ₁	CT+LE; S _{<i>h;h</i>-1} ^{<i>l</i>} /N _{<i>h</i>} ^{<i>l</i>}	1 ₂	2.15	0.0732	$\frac{1}{2}$ $\frac{3}{4}$ $\frac{5}{6}$	-0.51 0.35 -0.33 -0.32 0.25 -0.21	0.26 0.12 0.11 0.10 0.06 0.04	$(h)^1(l)^1$ $(h)^0(l)^2$ $(h_{-1})^1(l)^1$ $(h)^1(l_{+1})^1$ $(h_{-1})^1(h)^1(l)^1(l_{+1})^1$ $(h_{-1})^0(l)^2$
S ₀	DL; S _{<i>h;h</i>-1} ^{<i>l</i>} /N _{<i>h</i>} ^{<i>l</i>}	1 ₂	2.38	0.0435	$\frac{1}{2}$ $\frac{3}{3}$	-0.67 0.63 0.08	0.45 0.39 0.01	$(h_{-1})^1(l)^1$ $(h)^1(l_{+1})^1$ $(h_{-1})^1(h)^0(l)^1(l_{+1})^2$
Q ₁	DL; S _{<i>h;h</i>-1} ^{<i>l</i>} /N _{<i>h</i>} ^{<i>l</i>}	1 ₃	2.46	0.0373	$\frac{1}{2}$ $\frac{3}{3}$	-0.64 0.64 0.11	0.41 0.41 0.01	$(h_{-1})^1(l)^1$ $(h)^1(l_{+1})^1$ $(h_{-1})^1(h)^0(l)^1(l_{+1})^2$
T ₁	CT; S _{<i>h;h</i>-1} ^{<i>l</i>} /N _{<i>h</i>} ^{<i>l</i>}	1 ₂	2.16	0.0746	$\frac{1}{2}$ $\frac{3}{4}$	-0.61 -0.32 -0.25 0.24	0.37 0.10 0.06 0.06	$(h)^1(l)^1$ $(h)^1(l_{+1})^1$ $(h_{-1})^1(h)^1(l)^2$ $(h)^0(l)^2$

Continued on next page

Table S3: Adiabatic energies, state assignments, coefficients, weights and spatial configurations at different geometries of the **w**-sub-pattern

Geometry	State	Order	$E_{ad.}$	f	No.	c_i	$ c_i ^2$	Composition
S_0	DL; $S_{h;h-1}^{l+1;l}/N_h^l$	1_3	2.41	0.0043	5	0.24	0.06	$(h_{-1})^1(h)^1(l)^1(l_{+1})^1$
					6	-0.18	0.03	$(h)^0(l_{+1})^2$
					1	0.48	0.23	$(h)^1(l_{+1})^1$
					2	0.43	0.18	$(h_{-1})^1(l)^1$
					3	-0.40	0.16	$(h)^0(l)^2$
					4	-0.27	0.08	$(h_{-1})^1(h)^1(l)^1(l_{+1})^1$
					5	0.25	0.06	$(h)^0(l_{+1})^2$
					6	0.24	0.06	$(h_{-1})^0(l)^2$
					7	-0.17	0.03	$(h_{-1})^0(l_{+1})^2$
					1	0.47	0.22	$(h_{-1})^1(l)^1$
					2	0.43	0.19	$(h)^1(l_{+1})^1$
					3	-0.40	0.16	$(h_{-1})^1(h)^1(l)^2$
					4	-0.30	0.09	$(h)^0(l)^1(l_{+1})^1$
					5	-0.20	0.04	$(h_{-1})^0(l)^1(l_{+1})^1$
S_1	DL; $S_{h;h-1}^{l;l+1}$	1_3	2.34	0.0447	1	-0.66	0.44	$(h)^1(l_{+1})^1$
					2	0.63	0.39	$(h_{-1})^1(l)^1$
					3	0.09	0.01	$(h_{-1})^0(h)^1(l)^2(l_{+1})^1$
	DL; $S_{h;h-1}^{l;l+1}$	1_3	2.40	0.0314	1	0.63	0.39	$(h)^1(l_{+1})^1$
					2	-0.62	0.38	$(h_{-1})^1(l)^1$
					3	0.21	0.04	$(h_{-1})^1(l_{+1})^1$
T_1	LE; $N_h^l/Z_h^{l;l+1}$	1_4	2.65	0.0010	1	0.58	0.34	$(h)^0(l)^2$
					2	0.41	0.17	$(h)^0(l)^1(l_{+1})^1$
					3	0.26	0.07	$(h_{-1})^1(h)^1(l)^2$
					4	0.21	0.04	$(h_{-1})^1(h)^1(l)^1(l_{+1})^1$
	CT; $S_{h-1;h}^{l;l+1}$	1_5	2.67	0.0073	1	0.54	0.30	$(h)^1(l_{+1})^1$
					2	0.53	0.28	$(h_{-1})^1(l)^1$
					3	-0.26	0.07	$(h_{-1})^1(h)^1(l)^2$
					4	-0.22	0.05	$(h)^0(l)^1(l_{+1})^1$
S_1	CT; $S_{h-1;h}^{l;l+1}$	1_4	2.62	0.0230	1	-0.53	0.28	$(h_{-1})^1(l)^1$
					2	-0.47	0.22	$(h)^1(l_{+1})^1$
					3	0.31	0.09	$(h_{-1})^1(l_{+1})^1$
					4	-0.29	0.08	$(h)^0(l)^2$

Continued on next page

Table S3: Adiabatic energies, state assignments, coefficients, weights and spatial configurations at different geometries of the **w**-sub-pattern

Geometry	State	Order	$E_{ad.}$	f	No.	c_i	$ c_i ^2$	Composition
S_0	CT; $S_{h-1;h}^{l;l+1}$	1_4	2.75	0.0253	5	0.19	0.04	$(h_{-1})^1(h)^1(l)^2$
					1	-0.54	0.30	$(h_{-1})^1(l_{+1})^1$
					2	0.36	0.13	$(h_{-1})^1(l)^1$
					3	0.35	0.13	$(h)^1(l_{+1})^1$
					4	0.28	0.08	$(h)^0(l)^2$
					5	0.20	0.04	$(h_{-1})^1(h)^1(l)^1(l_{+1})^1$
S_1	LE; $S_{h-1}^{l+1}/Z_h^{l;l+1}/Z_{h;h-1}^l$	1_5	2.78	0.0097	1	-0.46	0.21	$(h_{-1})^1(l_{+1})^1$
					2	0.45	0.20	$(h_{-1})^1(h)^1(l)^2$
					3	0.43	0.18	$(h)^0(l)^1(l_{+1})^1$
					4	0.21	0.05	$(h_{-1})^0(l)^1(l_{+1})^1$
S_0	DL; $Z_{h;h-1}^l/Z_h^{l+1}$	1_6	3.00	0.0001	1	-0.52	0.27	$(h)^0(l)^1(l_{+1})^1$
					2	-0.50	0.25	$(h_{-1})^1(h)^1(l)^2$
					3	-0.31	0.09	$(h_{-1})^1(h)^1(l_{+1})^2$
					4	-0.29	0.08	$(h_{-1})^0(l)^1(l_{+1})^1$
					5	0.14	0.02	$(h_{-7})^1(l)^1$
S_1	LE+CT; $S_{h-1}^{l+1}/Z_{h;h-1}^l$	1_6	2.83	0.0211	1	0.67	0.44	$(h_{-1})^1(l_{+1})^1$
					2	0.33	0.11	$(h)^0(l)^1(l_{+1})^1$
					3	0.26	0.07	$(h_{-1})^1(h)^1(l)^2$
					4	0.19	0.04	$(h_{-1})^1(h)^1(l_{+1})^2$
Q_1	$(LE+CT)_1; S_h^{l+1}/Z_{h;h-1}^l/Z_h^{l;l+1}$	1_5	2.71	0.0045	1	0.44	0.20	$(h)^0(l)^1(l_{+1})^1$
					2	0.35	0.13	$(h)^1(l_{+1})^1$
					3	0.34	0.11	$(h_{-1})^1(h)^1(l)^2$
					4	0.32	0.10	$(h_{-1})^1(l)^1$
					5	0.29	0.08	$(h_{-1})^1(h)^1(l_{+1})^2$
					6	0.22	0.05	$(h_{-1})^0(l)^1(l_{+1})^1$
Q_1	$(LE+CT)_2; S_{h-1}^{l+1}/V_{h;h-1}^{l;l+1}$	1_6	2.82	0.0308	1	-0.74	0.55	$(h_{-1})^1(l_{+1})^1$
					2	-0.33	0.11	$(h_{-1})^1(h)^1(l)^1(l_{+1})^1$
					3	-0.23	0.05	$(h)^0(l)^2$
					4	-0.16	0.03	$(h)^2(l)^0$
T_1	CT; S_{h-1}^{l+1}	1_6	2.82	0.0592	1	-0.86	0.73	$(h_{-1})^1(l_{+1})^1$
					2	-0.27	0.08	$(h_{-1})^1(l)^1$
					3	-0.10	0.01	$(h)^1(l)^1$

Continued on next page

Table S3: Adiabatic energies, state assignments, coefficients, weights and spatial configurations at different geometries of the **w**-sub-pattern

Geometry	State	Order	$E_{ad.}$	f	No.	c_i	$ c_i ^2$	Composition
S_0	CT; S_{h-1}^{l+1}	1_5	2.83	0.0233	1	-0.71	0.51	$(h_{-1})^1(l_{+1})^1$
					2	-0.30	0.09	$(h)^1(l_{+1})^1$
					3	-0.28	0.08	$(h_{-1})^1(l)^1$
					4	-0.24	0.06	$(h)^0(l)^2$
					5	0.16	0.02	$(h)^0(l_{+1})^2$
S_1	DL; $V_{h-1;h}^{l+1;l}/Z_h^{l;l+1}/Z_{h;h-1}^l$	1_7	2.94	0.0026	1	-0.49	0.24	$(h_{-1})^1(h)^1(l)^1(l_{+1})^1$
					2	-0.38	0.14	$(h)^0(l_{+1})^2$
					3	-0.34	0.12	$(h_{-1})^0(l)^2$
					4	0.27	0.07	$(h_{-1})^1(l_{+1})^1$
					5	-0.24	0.06	$(h)^0(l)^2$
					6	-0.20	0.04	$(h)^2(l)^0$
S_0	DL; $V_{h-1;h}^{l+1;l}/N_h^{l+1}/N_{h-1}^l$	1_7	3.10	0.0001	1	0.57	0.32	$(h_{-1})^1(h)^1(l)^1(l_{+1})^1$
					2	0.34	0.12	$(h_{-1})^0(l)^2$
					3	0.34	0.11	$(h)^0(l_{+1})^2$
					4	0.30	0.09	$(h)^0(l)^2$
					5	0.20	0.04	$(h)^2(l)^0$
Q_1	LE+CT; $S_{h-1}^{l+1}/V_{h;h-1}^{l;l+1}$	1_7	2.88	0.0103	1	-0.46	0.21	$(h_{-1})^1(l_{+1})^1$
					2	0.42	0.18	$(h_{-1})^1(h)^1(l)^1(l_{+1})^1$
					3	0.30	0.09	$(h)^0(l_{+1})^2$
					4	0.29	0.09	$(h_{-1})^0(l)^2$
					5	-0.23	0.05	$(h)^1(l_{+1})^1$
					6	0.22	0.05	$(h)^2(l)^0$
T_1	LE; $V_{h-1;h}^{l+1;l}/Z_h^{l;l+1}/Z_{h;h-1}^l$	1_7	3.23	0.0001	1	0.40	0.16	$(h_{-1})^1(h)^1(l)^1(l_{+1})^1$
					2	-0.40	0.16	$(h_{-1})^0(l)^1(l_{+1})^1$
					3	-0.34	0.11	$(h_{-1})^1(h)^1(l_{+1})^2$
					4	0.28	0.08	$(h_{-1})^0(l)^2$
					5	0.26	0.07	$(h_{-1})^0(l_{+1})^2$
					6	0.20	0.04	$(h)^0(l_{+1})^2$
T_1	LE; $T_h^{l;l+1}$	3_0	0.95	0.0000	1	0.75	0.57	$(h)^1(l)^1$
					2	0.39	0.15	$(h)^1(l_{+1})^1$
					3	-0.29	0.08	$(h_{-1})^1(l)^1$
					4	-0.15	0.02	$(h_{-1})^1(l_{+1})^1$
					1	0.59	0.34	$(h_{-1})^1(l_{+1})^1$
T_1	LE; $T_{h-1;h}^{l+1;l;l+1}$	3_1	1.31	0.0000	Continued on next page			

Table S3: Adiabatic energies, state assignments, coefficients, weights and spatial configurations at different geometries of the **w**-sub-pattern

Geometry	State	Order	$E_{ad.}$	f	No.	c_i	$ c_i ^2$	Composition
					2	-0.48	0.23	$(h_{-1})^1(l)^1$
					3	0.40	0.16	$(h)^1(l_{+1})^1$
					4	-0.27	0.07	$(h)^1(l)^1$
					5	-0.12	0.01	$(h_{-1})^1(h)^0(l)^2(l_{+1})^1$
					1	-0.73	0.54	$(h)^1(l)^1$
S ₀	DL; T _{$h;h_{-1}$} ^{$l;l_{+1}$}	3 ₀	1.14	0.0000	2	0.50	0.25	$(h_{-1})^1(l_{+1})^1$
					3	-0.15	0.02	$(h)^1(l_{+1})^1$
					1	0.74	0.54	$(h)^1(l)^1$
S ₁	DL; T _{$h;h_{-1}$} ^{$l;l_{+1}$}	3 ₀	1.04	0.0000	2	-0.45	0.20	$(h_{-1})^1(l_{+1})^1$
					3	0.22	0.05	$(h_{-1})^1(l)^1$
					1	-0.73	0.53	$(h)^1(l)^1$
Q ₁	DL; T _{$h;h_{-1}$} ^{$l;l_{+1}$}	3 ₀	1.12	0.0000	2	0.50	0.25	$(h_{-1})^1(l_{+1})^1$
					3	-0.16	0.02	$(h)^1(l_{+1})^1$
					1	-0.64	0.41	$(h_{-1})^1(l)^1$
S ₀	DL; T _{$h_{-1};h$} ^{$l;l_{+1}$}	3 ₁	1.20	0.0000	2	0.64	0.41	$(h)^1(l_{+1})^1$
					3	-0.12	0.01	$(h_{-2})^1(l_{+3})^1$
					1	-0.65	0.43	$(h)^1(l_{+1})^1$
S ₁	DL; T _{$h_{-1};h$} ^{$l;l_{+1}$}	3 ₁	1.14	0.0000	2	0.62	0.38	$(h_{-1})^1(l)^1$
					3	0.11	0.01	$(h_{-2})^1(l_{+3})^1$
					1	-0.64	0.41	$(h_{-1})^1(l)^1$
Q ₁	DL; T _{$h_{-1};h$} ^{$l;l_{+1}$}	3 ₁	1.17	0.0000	2	0.63	0.39	$(h)^1(l_{+1})^1$
					3	0.11	0.01	$(h_{-1})^1(h)^0(l)^1(l_{+1})^2$
					1	0.53	0.28	$(h_{-2})^1(l)^1$
T ₁	LE _A ; T	3 ₂	2.27	0.0010	2	0.40	0.16	$(h)^1(l_{+2})^1$
					3	-0.39	0.15	$(h)^1(l_{+3})^1$
					4	0.29	0.08	$(h_{-3})^1(l)^1$
					5	0.24	0.06	$(h_{-2})^1(l_{+1})^1$
					6	0.19	0.03	$(h_{-3})^1(l_{+1})^1$
					1	0.54	0.29	$(h_{-2})^1(l)^1$
S ₀	DL; T	3 ₂	2.28	0.0011	2	0.45	0.20	$(h)^1(l_{+2})^1$
					3	0.39	0.15	$(h_{-3})^1(l_{+1})^1$
					4	0.35	0.12	$(h_{-1})^1(l_{+3})^1$

Continued on next page

Table S3: Adiabatic energies, state assignments, coefficients, weights and spatial configurations at different geometries of the **w**-sub-pattern

Geometry	State	Order	$E_{ad.}$	f	No.	c_i	$ c_i ^2$	Composition
S ₁	DL; T	3 ₂	2.27	0.0013	5	-0.15	0.02	$(h)^1(l_{+3})^1$
					1	-0.54	0.29	$(h_{-2})^1(l)^1$
					2	-0.44	0.20	$(h)^1(l_{+2})^1$
					3	-0.35	0.12	$(h_{-3})^1(l_{+1})^1$
					4	-0.29	0.09	$(h_{-1})^1(l_{+3})^1$
					5	-0.22	0.05	$(h_{-1})^1(l_{+2})^1$
					6	0.20	0.04	$(h_{-3})^1(l)^1$
Q ₁	DL; T	3 ₃	2.50	0.0016	1	0.54	0.29	$(h_{-2})^1(l)^1$
					2	0.44	0.19	$(h)^1(l_{+2})^1$
					3	0.38	0.14	$(h_{-3})^1(l_{+1})^1$
					4	0.35	0.12	$(h_{-1})^1(l_{+3})^1$
					5	-0.15	0.02	$(h)^1(l_{+3})^1$
Q ₁	DL; Z/T	3 ₂	2.22	0.0001	1	-0.47	0.22	$(h)^0(l)^1(l_{+1})^1$
					2	0.47	0.22	$(h_{-1})^1(h)^1(l)^2$
					3	-0.34	0.12	$(h_{-1})^1(h)^1(l_{+1})^2$
					4	0.34	0.12	$(h_{-1})^0(l)^1(l_{+1})^1$
					5	0.29	0.09	$(h_{-1})^1(l_{+1})^1$
					6	0.19	0.03	$(h)^1(l)^1$
T ₁	DL+CT; Z/V/T	3 ₃	2.33	0.0003	1	0.41	0.16	$(h_{-1})^1(h)^1(l)^2$
					2	-0.38	0.15	$(h)^0(l)^1(l_{+1})^1$
					3	0.33	0.11	$(h_{-1})^1(l_{+1})^1$
					4	0.33	0.11	$(h_{-1})^1(h)^1(l)^1(l_{+1})^1$
					5	-0.27	0.07	$(h_{-1})^1(h)^1(l_{+1})^2$
					6	-0.24	0.06	$(h)^1(l_{+1})^1$
					7	0.23	0.05	$(h_{-1})^0(l)^1(l_{+1})^1$
					8	0.20	0.04	$(h)^1(l)^1$
S ₁	CT+DL; T/Z	3 ₃	2.30	0.0099	1	0.43	0.18	$(h_{-1})^1(l_{+1})^1$
					2	-0.39	0.15	$(h)^0(l)^1(l_{+1})^1$
					3	0.36	0.13	$(h_{-1})^1(h)^1(l)^2$
					4	0.35	0.12	$(h)^1(l)^1$
					5	-0.24	0.06	$(h_{-1})^1(h)^1(l_{+1})^2$
					6	0.23	0.05	$(h_{-1})^0(l)^1(l_{+1})^1$
					7	-0.22	0.05	$(h_{-1})^1(l)^1$

Continued on next page

Table S3: Adiabatic energies, state assignments, coefficients, weights and spatial configurations at different geometries of the **w**-sub-pattern

Geometry	State	Order	$E_{ad.}$	f	No.	c_i	$ c_i ^2$	Composition
S_0	$DL_2; T$	3_3	2.33	0.0000	1	-0.48	0.23	$(h_{-2})^1(l_{+1})^1$
					2	-0.47	0.22	$(h_{-3})^1(l)^1$
					3	0.43	0.19	$(h)^1(l_{+3})^1$
					4	0.41	0.17	$(h_{-1})^1(l_{+2})^1$
					5	0.08	0.01	$(h_{-6})^1(l_{+3})^1$
S_1	$DL_2; T$	3_4	2.35	0.0000	1	0.50	0.25	$(h_{-2})^1(l_{+1})^1$
					2	-0.46	0.21	$(h)^1(l_{+3})^1$
					3	0.44	0.20	$(h_{-3})^1(l)^1$
					4	-0.37	0.14	$(h_{-1})^1(l_{+2})^1$
					5	0.11	0.01	$(h_{-1})^1(l_{+3})^1$
Q_1	$DL_2; T$	3_4	2.54	0.0000	1	-0.47	0.22	$(h_{-3})^1(l)^1$
					2	-0.47	0.22	$(h_{-2})^1(l_{+1})^1$
					3	0.42	0.18	$(h)^1(l_{+3})^1$
					4	0.41	0.17	$(h_{-1})^1(l_{+2})^1$
					5	0.08	0.01	$(h)^1(l_{+2})^1$
T_1	$LE_B; T$	3_4	2.46	0.0001	1	-0.41	0.17	$(h_{-1})^1(l_{+2})^1$
					2	0.38	0.15	$(h_{-2})^1(l_{+1})^1$
					3	-0.38	0.14	$(h_{-3})^1(l_{+1})^1$
					4	0.33	0.11	$(h_{-3})^1(l)^1$
					5	-0.30	0.09	$(h_{-1})^1(l_{+3})^1$
					6	-0.23	0.05	$(h)^1(l_{+3})^1$
					7	-0.21	0.04	$(h_{-2})^1(l)^1$
T_1	$CT_{AB}; T_{h;h_{-1}}^{l;l_{+1}}$	3_5	2.56	0.0270	1	-0.67	0.44	$(h)^1(l_{+1})^1$
					2	-0.58	0.34	$(h_{-1})^1(l)^1$
					3	-0.14	0.02	$(h_{-1})^1(h)^1(l)^2$
S_0	$CT_{AB}; T_{h;h_{-1}}^{l;l_{+1}}$	3_4	2.54	0.0160	1	0.51	0.26	$(h_{-1})^1(l_{+1})^1$
					2	0.45	0.20	$(h)^1(l)^1$
					3	-0.31	0.10	$(h)^1(l_{+1})^1$
					4	-0.31	0.09	$(h_{-1})^1(l)^1$
					5	-0.27	0.07	$(h)^0(l)^1(l_{+1})^1$
					6	0.24	0.06	$(h_{-1})^1(h)^1(l)^2$
					7	-0.17	0.03	$(h_{-1})^1(h)^1(l_{+1})^2$
					1	-0.66	0.43	$(h_{-1})^1(l_{+1})^1$
Continued on next page								
S_1	$CT_{AB}; T_{h;h_{-1}}^{l;l_{+1}}$	3_6	2.80	0.0139				

Table S3: Adiabatic energies, state assignments, coefficients, weights and spatial configurations at different geometries of the **w**-sub-pattern

Geometry	State	Order	$E_{ad.}$	f	No.	c_i	$ c_i ^2$	Composition
					2	-0.33	0.11	$(h)^1(l)^1$
					3	-0.25	0.06	$(h)^0(l)^1(l_{+1})^1$
					4	-0.23	0.05	$(h)^1(l_{+1})^1$
					5	0.23	0.05	$(h_{-1})^1(h)^1(l)^2$
					6	-0.21	0.05	$(h_{-1})^1(l)^1$
					1	0.60	0.36	$(h)^1(l_{+1})^1$
Q ₁	CT _{AB} ; T _{<i>h</i>; <i>h</i>-1} ^{<i>l</i>; <i>l</i>+1}	3 ₅	2.64	0.0625	2	0.60	0.36	$(h_{-1})^1(l)^1$
					3	-0.27	0.07	$(h)^1(l)^1$
					4	-0.14	0.02	$(h_{-1})^1(l_{+1})^1$
					1	-0.58	0.34	$(h_{-1})^1(l_{+1})^1$
T ₁	CT _{BA} ; T _{<i>h</i>; <i>h</i>-1; <i>h</i>} ^{<i>l</i>+1; <i>l</i>}	3 ₆	2.78	0.0024	2	-0.42	0.17	$(h_{-1})^1(l)^1$
					3	-0.37	0.14	$(h)^1(l)^1$
					4	0.20	0.04	$(h_{-1})^1(h)^1(l)^1(l_{+1})^1$
					1	-0.56	0.31	$(h_{-1})^1(l)^1$
S ₀	CT _{BA} ; T _{<i>h</i>; <i>h</i>-1; <i>h</i>} ^{<i>l</i>+1; <i>l</i>}	3 ₅	2.66	0.0559	2	-0.55	0.30	$(h)^1(l_{+1})^1$
					3	-0.32	0.10	$(h_{-1})^1(l_{+1})^1$
					4	-0.22	0.05	$(h_{-1})^1(h)^1(l)^2$
					1	0.55	0.30	$(h_{-1})^1(l)^1$
S ₁	CT _{BA} ; T _{<i>h</i>; <i>h</i>-1; <i>h</i>} ^{<i>l</i>+1; <i>l</i>}	3 ₅	2.53	0.0811	2	0.53	0.28	$(h)^1(l_{+1})^1$
					3	-0.26	0.07	$(h)^1(l)^1$
					4	0.25	0.06	$(h_{-1})^1(h)^1(l)^2$
					5	-0.21	0.04	$(h)^0(l)^1(l_{+1})^1$
					1	-0.67	0.45	$(h_{-1})^1(l_{+1})^1$
Q ₁	CT _{BA} ; T _{<i>h</i>; <i>h</i>-1; <i>h</i>} ^{<i>l</i>+1; <i>l</i>}	3 ₆	2.80	0.0091	2	-0.44	0.20	$(h)^1(l)^1$
					3	-0.23	0.05	$(h_{-1})^1(l)^1$
					4	-0.20	0.04	$(h)^1(l_{+1})^1$
					1	0.47	0.22	$(h_{-1})^1(l_{+1})^1$
S ₀	DL; V/Z/T	3 ₆	2.89	0.0018	2	0.39	0.15	$(h)^0(l)^1(l_{+1})^1$
					3	-0.37	0.14	$(h_{-1})^1(h)^1(l)^2$
					4	0.32	0.10	$(h)^1(l)^1$
					5	0.29	0.09	$(h_{-1})^1(h)^1(l_{+1})^2$
					6	-0.29	0.08	$(h_{-1})^0(l)^1(l_{+1})^1$
					7	-0.12	0.01	$(h_{-1})^1(h)^1(l)^1(l_{+1})^1$

Continued on next page

Table S3: Adiabatic energies, state assignments, coefficients, weights and spatial configurations at different geometries of the **w**-sub-pattern

Geometry	State	Order	$E_{ad.}$	f	No.	c_i	$ c_i ^2$	Composition
Q ₁	DL; Z	3 ₇	3.54	0.0234	1	0.57	0.32	$(h_{-1})^1(h)^1(l)^2$
					2	0.55	0.31	$(h)^0(l)^1(l_{+1})^1$
					3	-0.24	0.06	$(h_{-1})^1(h)^1(l_{+1})^2$
					4	-0.23	0.05	$(h_{-1})^0(l)^1(l_{+1})^1$
					5	-0.15	0.02	$(h_{-4})^1(l)^1$

S2.4 Transition densities at singlet Geometries of u, v, w

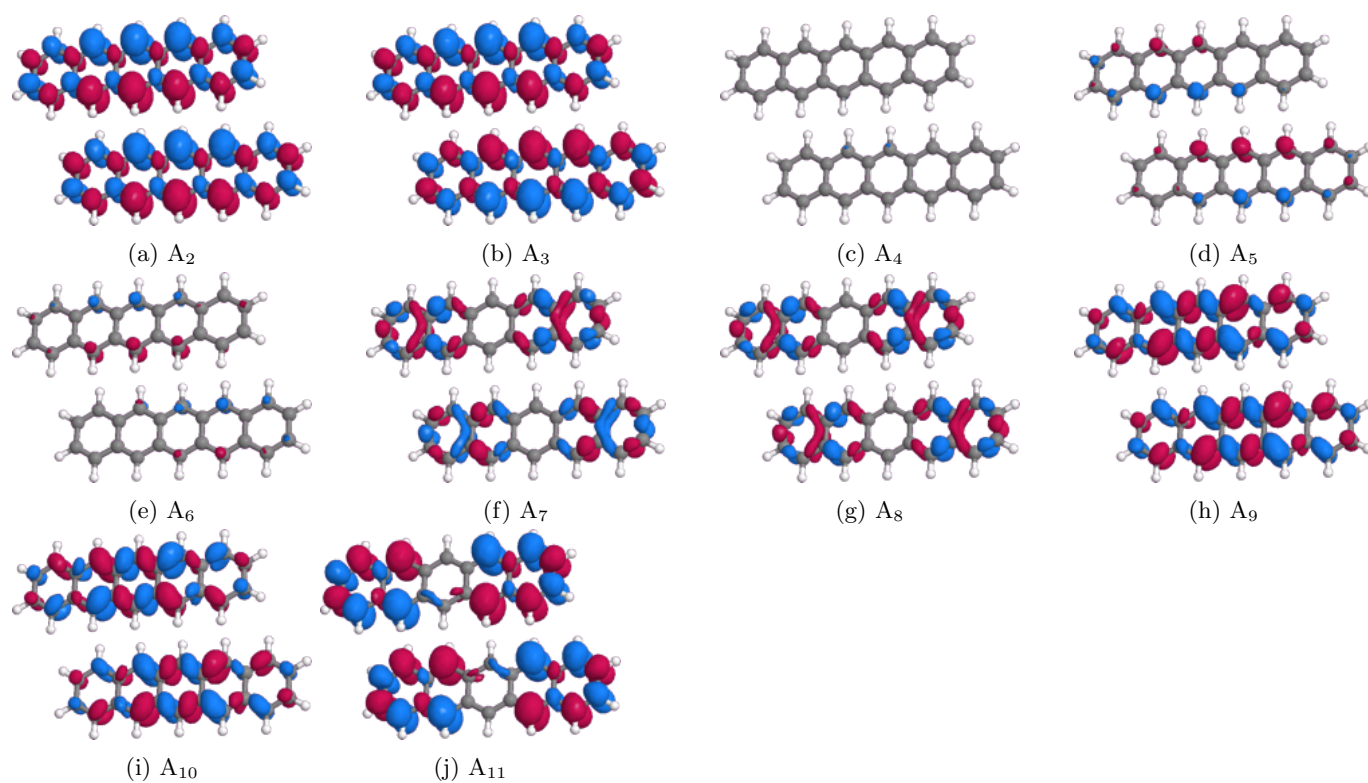


Figure S24: Transition densities for the $S_0 \rightarrow S_n$ transitions at the ground states geometry. Plotted with an absolute isovalue of 0.0004

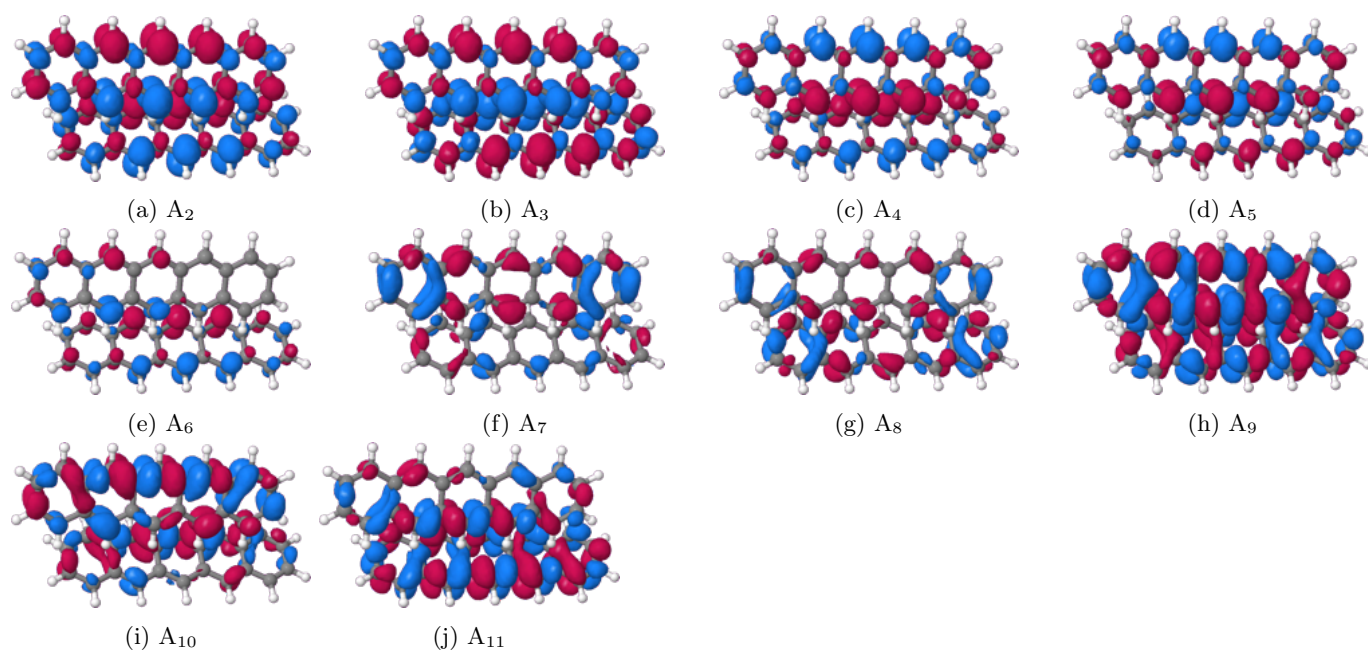


Figure S25: Transition densities for the $S_0 \rightarrow S_n$ transitions at the G_s geometry. Plotted with an isovalue of 0.0004

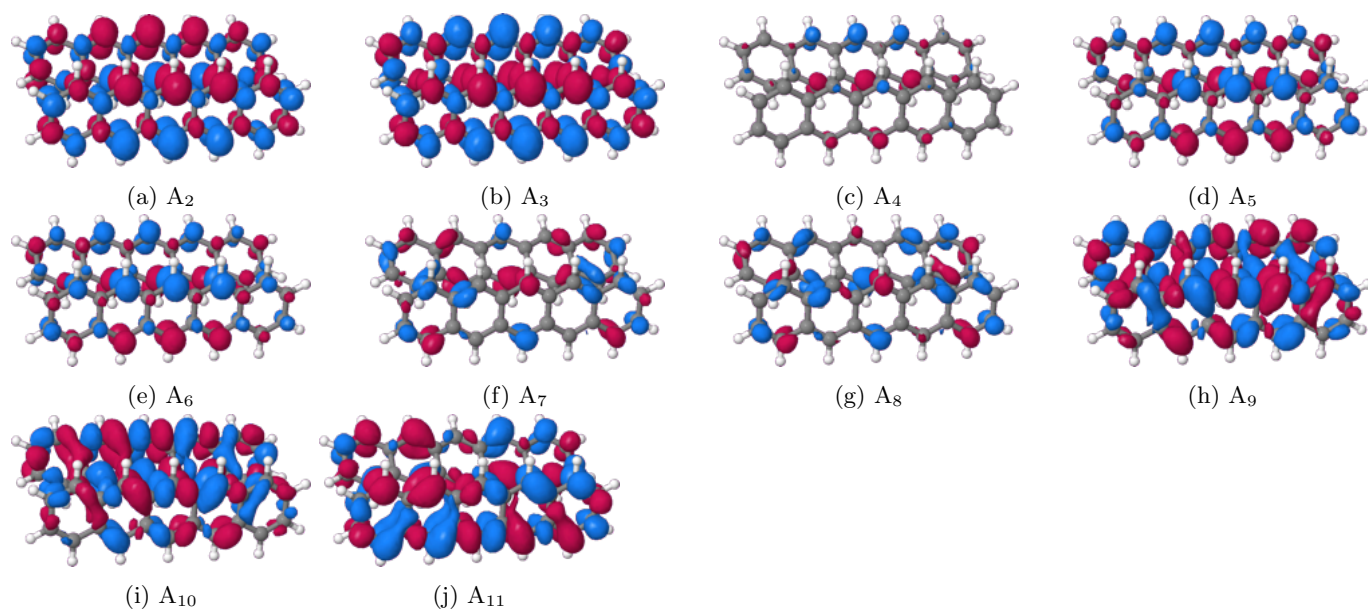


Figure S26: Transition densities for the $S_0 \rightarrow S_n$ transitions at the ground state geometry. Plotted with an isovalue of 0.0004

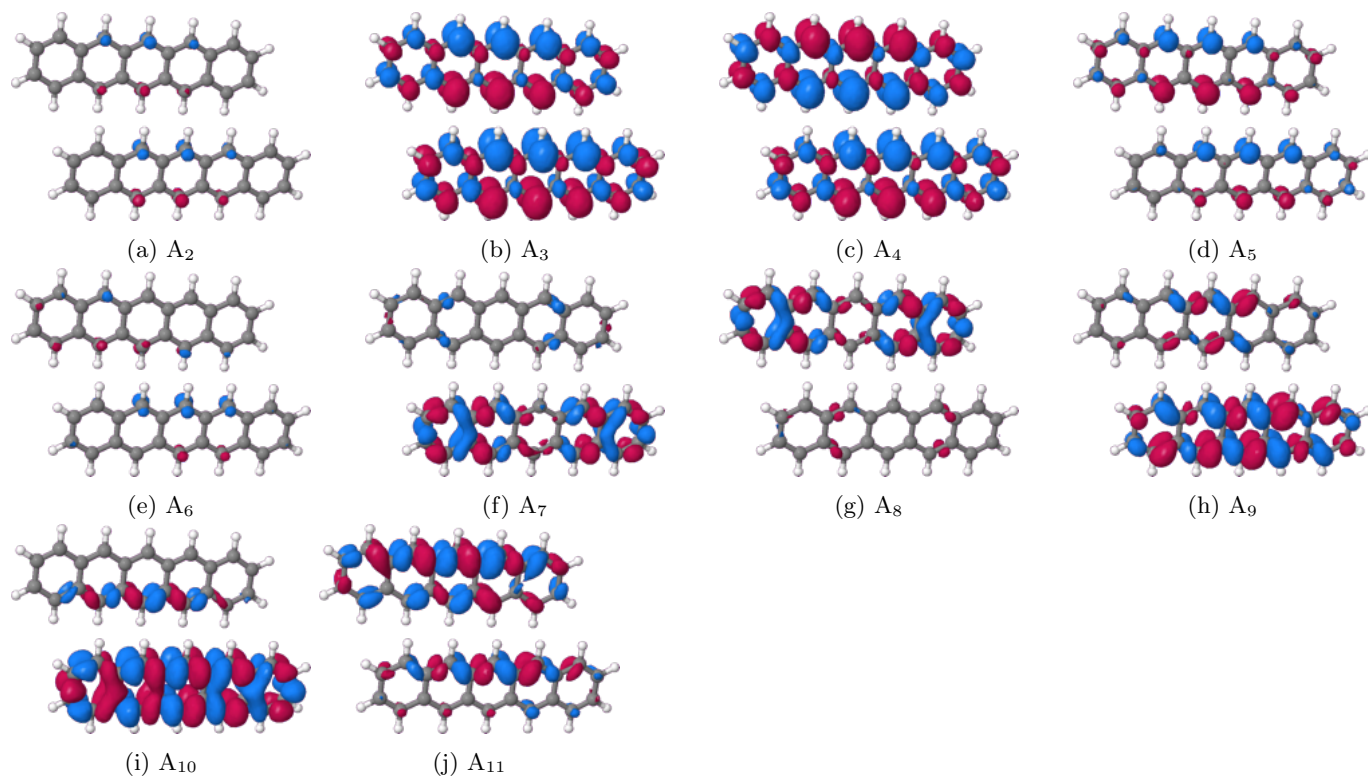


Figure S27: Transition densities for the $S_0 \rightarrow S_n$ transitions at the S_1 geometry. Plotted with an absolute isovalue of 0.0004

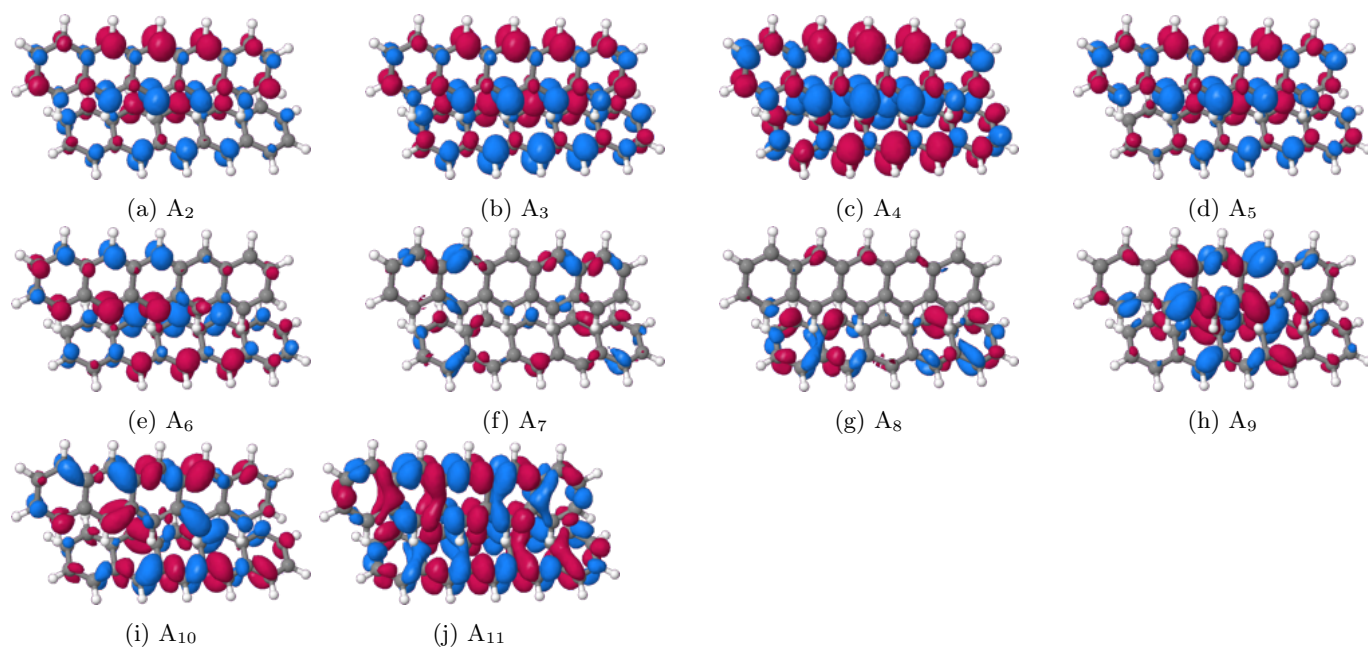


Figure S28: Transition densities for the $S_0 \rightarrow S_n$ transitions at the S_1 geometry. Plotted with an isovalue of 0.0004

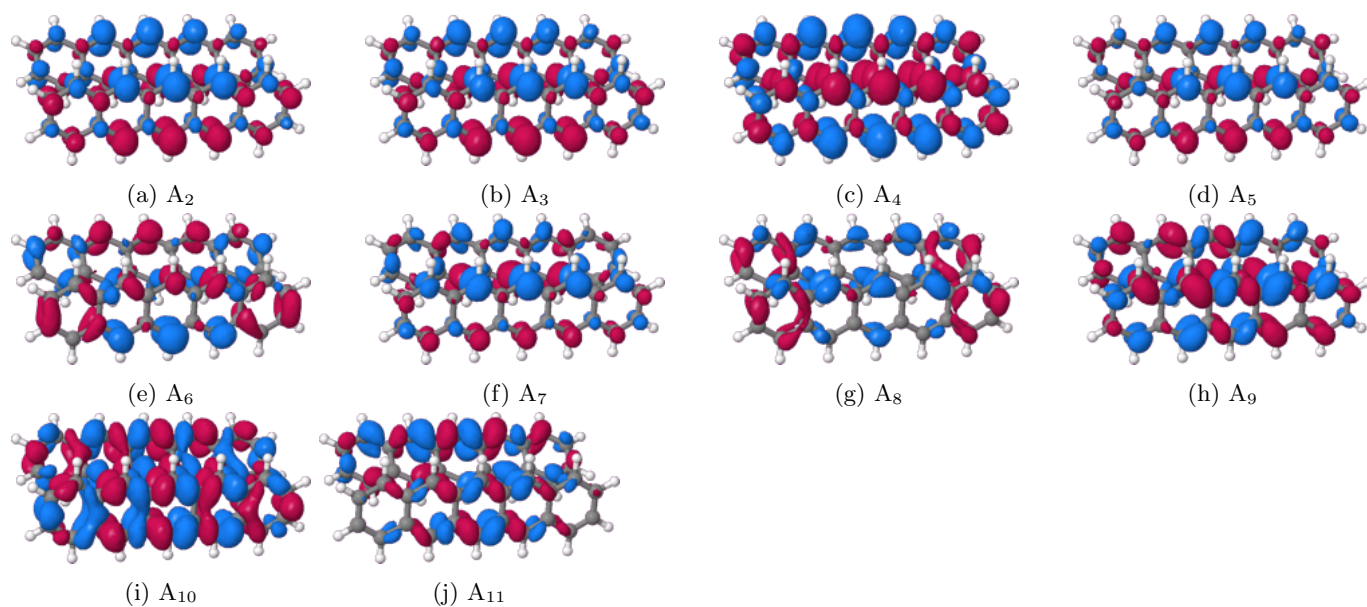


Figure S29: Transition densities for the $S_0 \rightarrow S_n$ transitions at the S_1 geometry. Plotted with an isovalue of 0.0004

S2.5 Transition densities at singlet Geometries of the Trimer

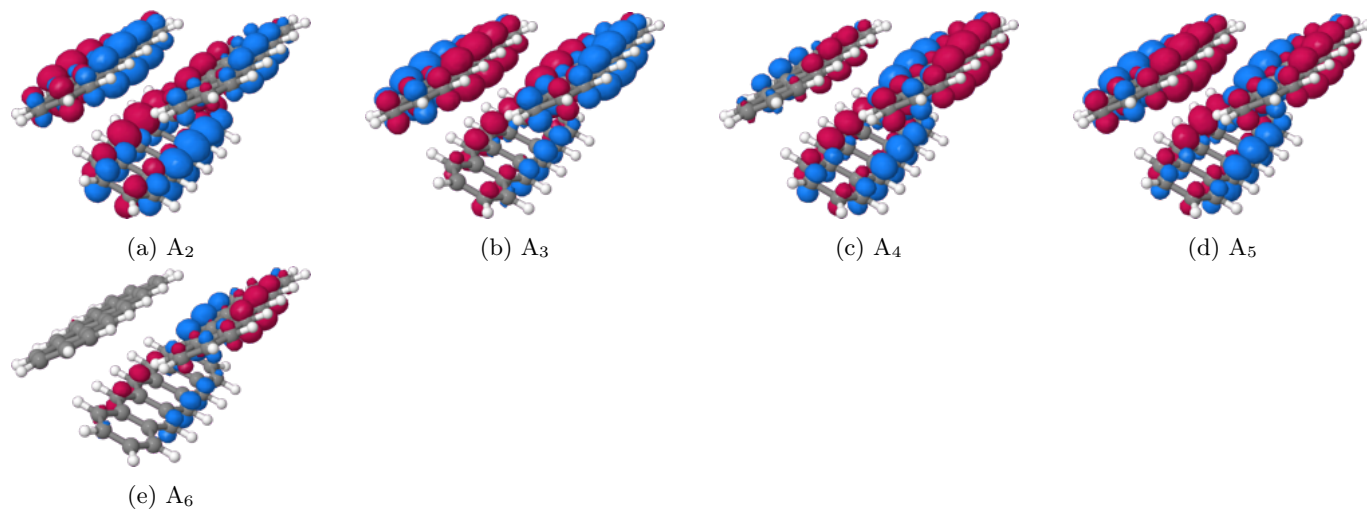


Figure S30: Transition densities for the $S_0 \rightarrow S_n$ transitions at the ground state geometry. Plotted with an isovalue of 0.0004

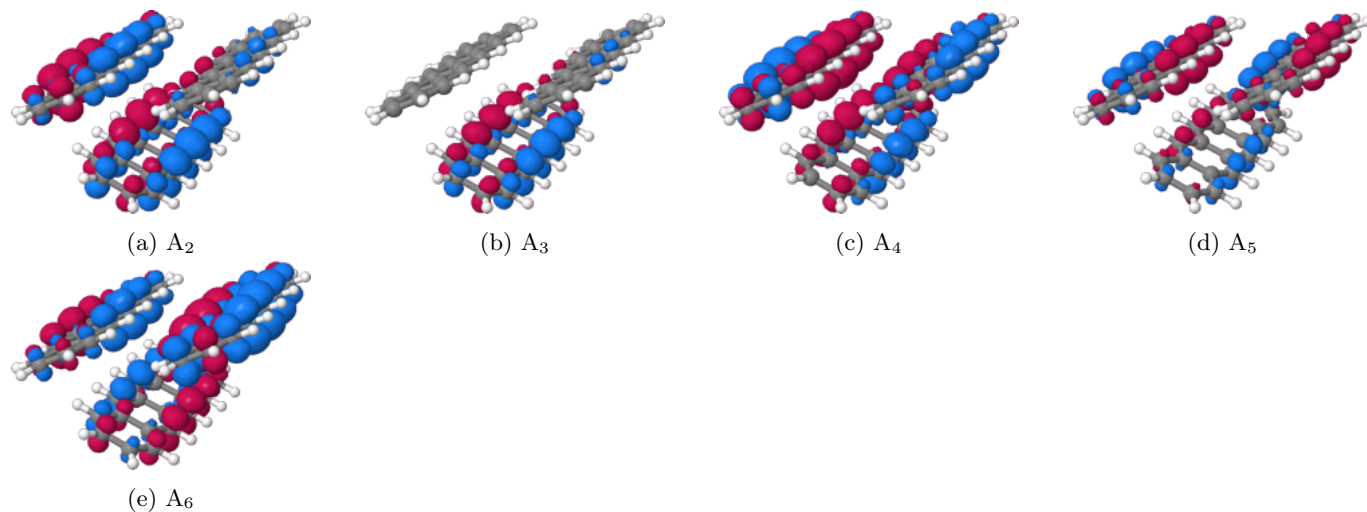


Figure S31: Transition densities for the $S_0 \rightarrow S_n$ transitions at the S_1 geometry. Plotted with an isovalue of 0.0004

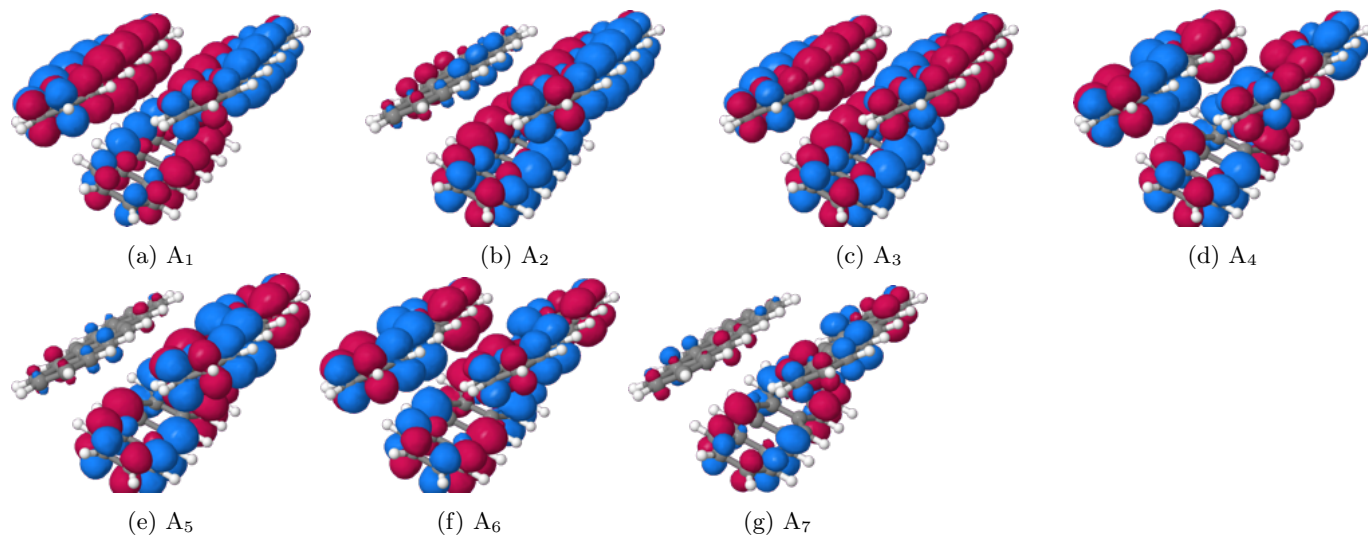


Figure S32: Transition densities for the $S_0 \rightarrow T_n$ transitions at the ground states geometry. Plotted with an isovalue of 0.0004

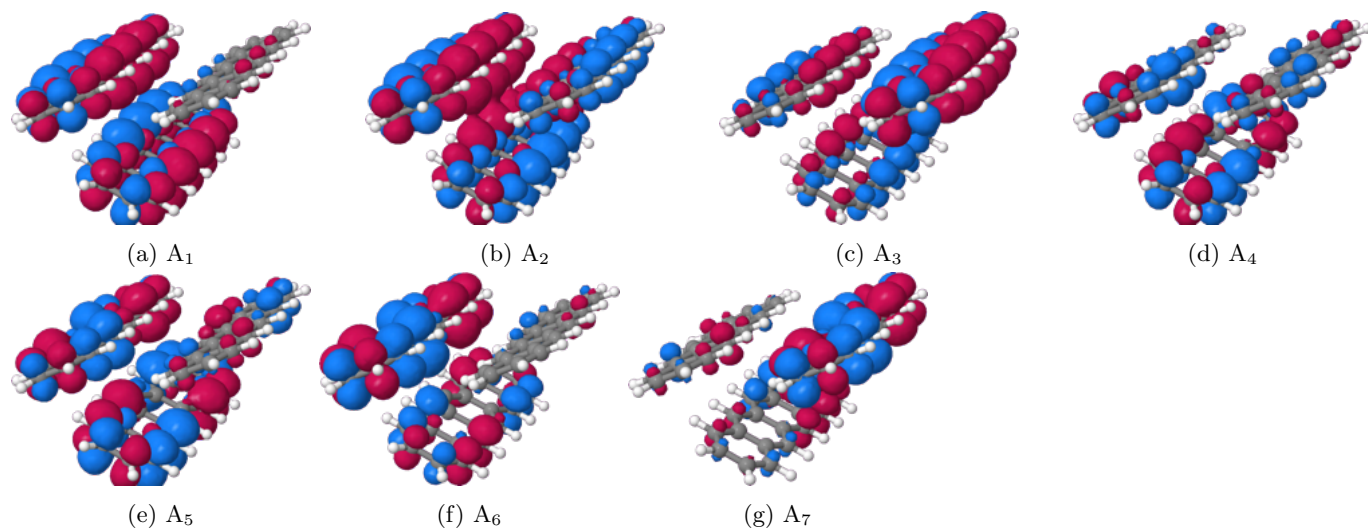


Figure S33: Transition densities for the $S_0 \rightarrow T_n$ transitions at the S_1 geometry. Plotted with an isovalue of 0.0004

S2.6 Difference densities at singlet Geometries of u, v, w

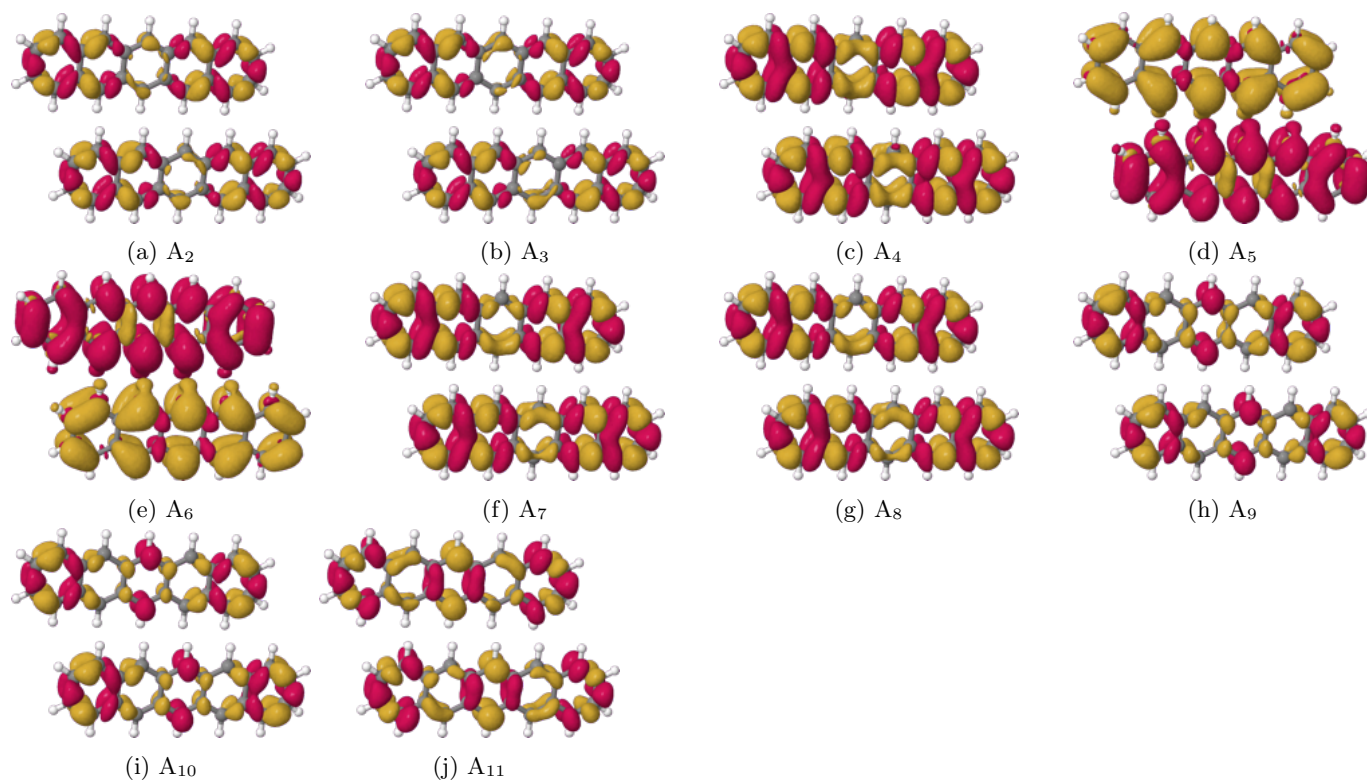


Figure S34: Difference densities w.r.t. the ground state density at the ground state geometry of the **u**-pattern. Plotted with an isovalue of 0.0004.

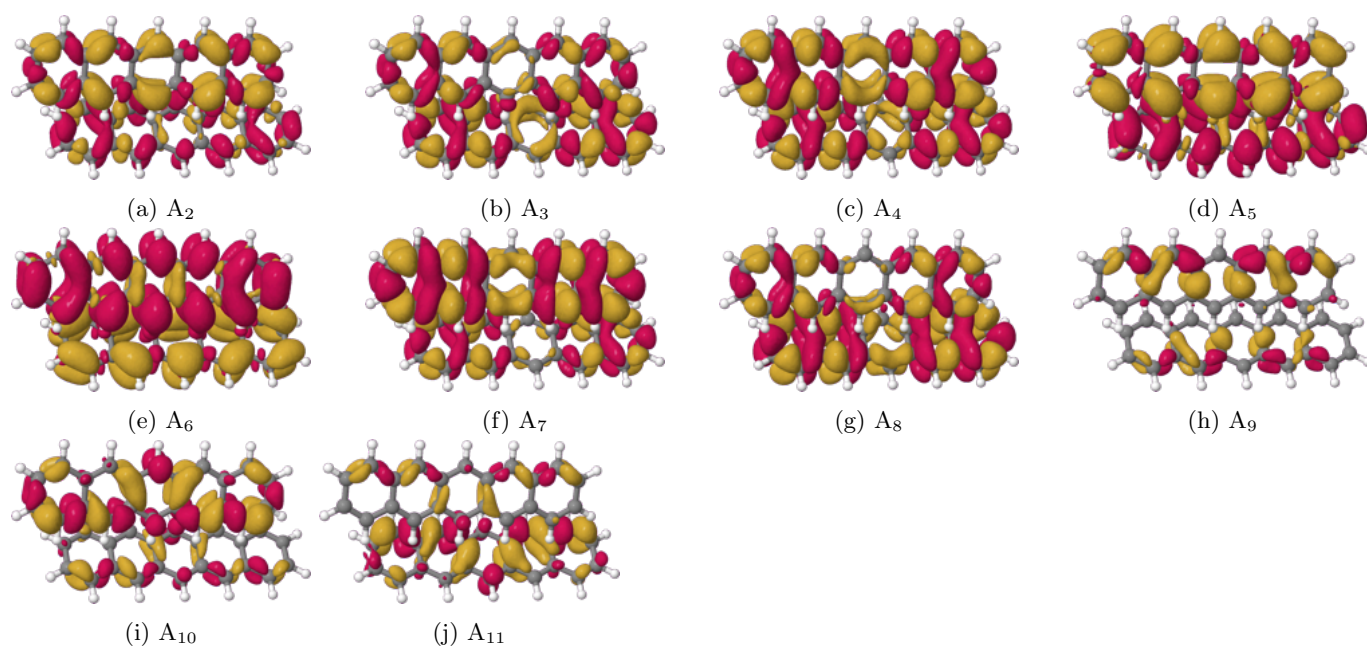


Figure S35: Difference densities w.r.t. the ground state density at the ground state geometry of the **v**-pattern. Plotted with an isovalue of 0.0004.

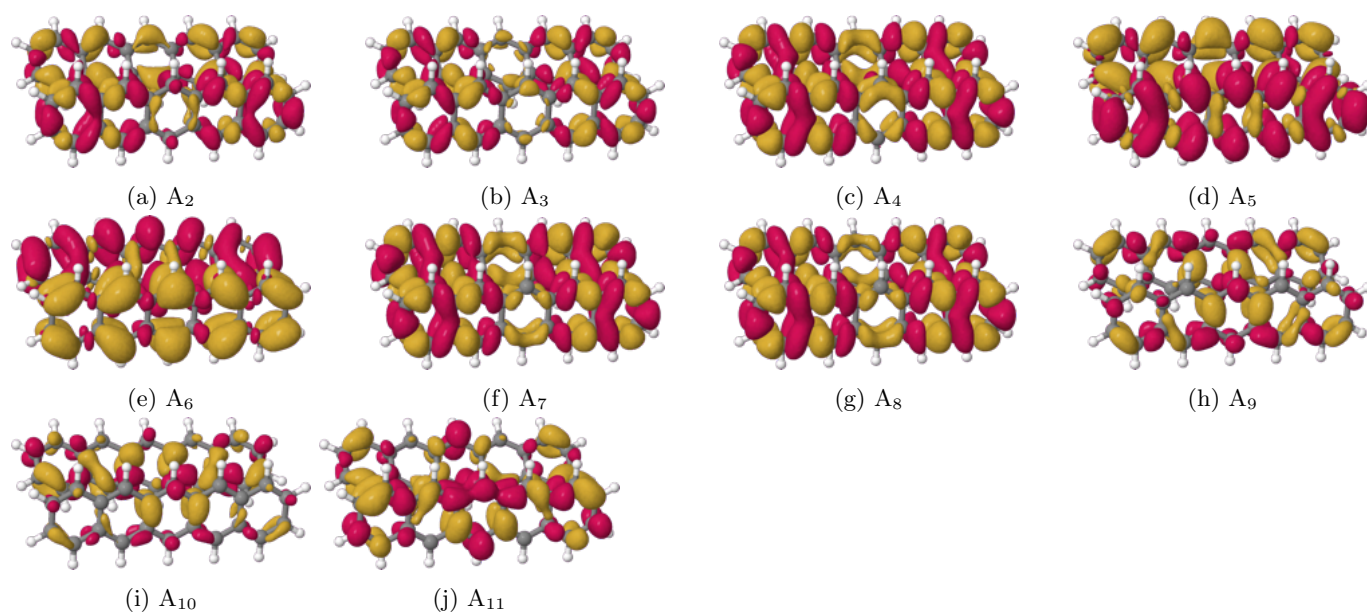


Figure S36: Difference densities w.r.t. the ground state density at the ground state geometry of the **w**-pattern. Plotted with an isovalue of 0.0004.

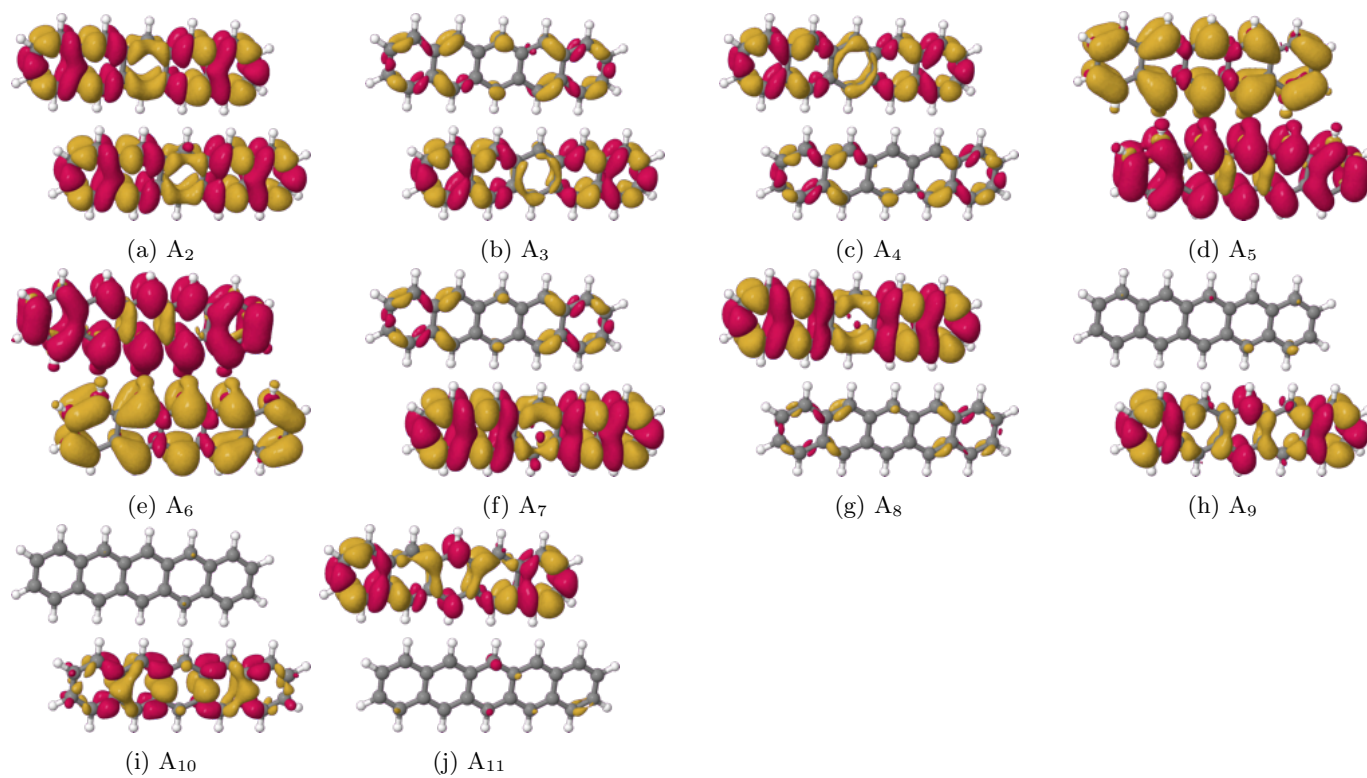


Figure S37: Difference densities w.r.t. the ground state density at the S_1 geometry. Plotted with an isovalue of 0.0004.

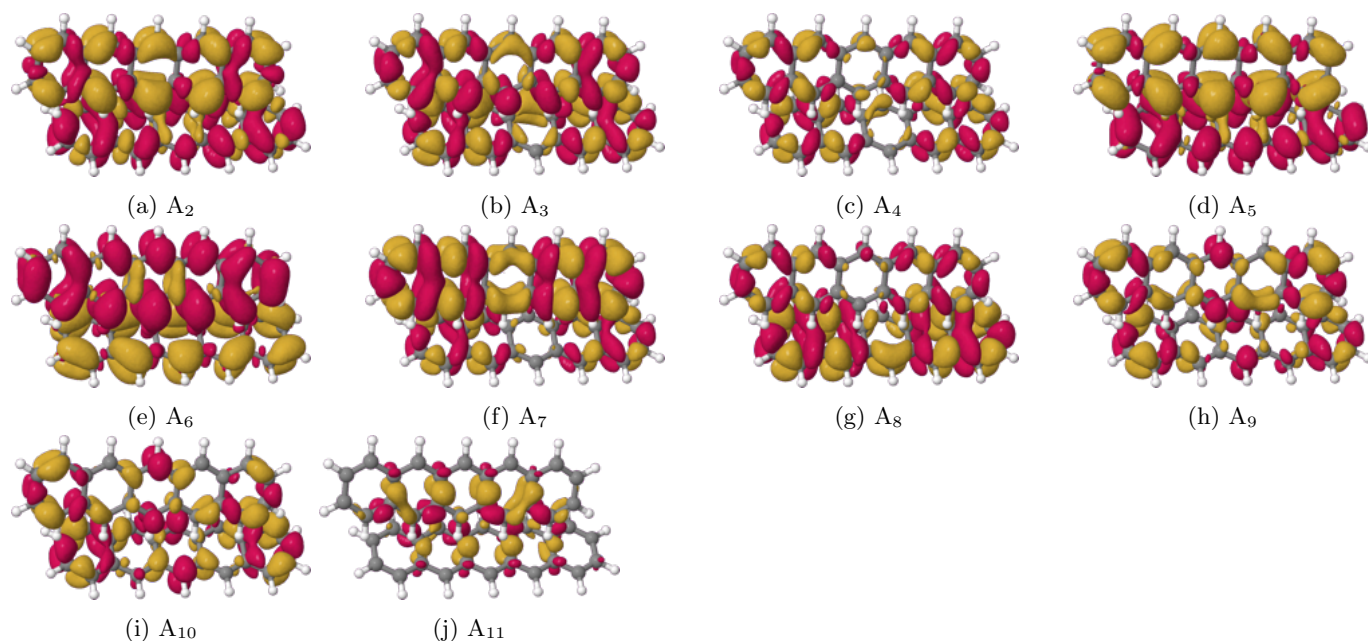


Figure S38: Difference densities w.r.t. the ground state density at the S_1 geometry. Plotted with an isovalue of 0.0004.

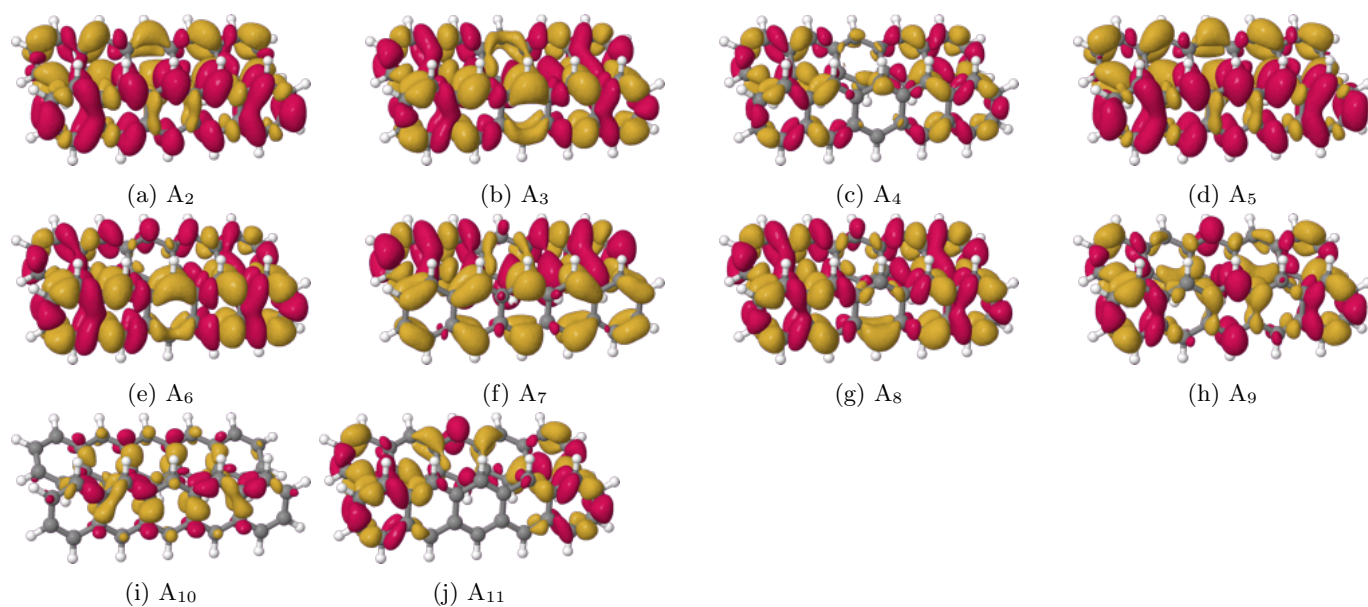


Figure S39: Difference densities w.r.t. the ground state density at the S_1 geometry. Plotted with an isovalue of 0.0004.

S2.7 Difference densities at singlet Geometries of the Trimer

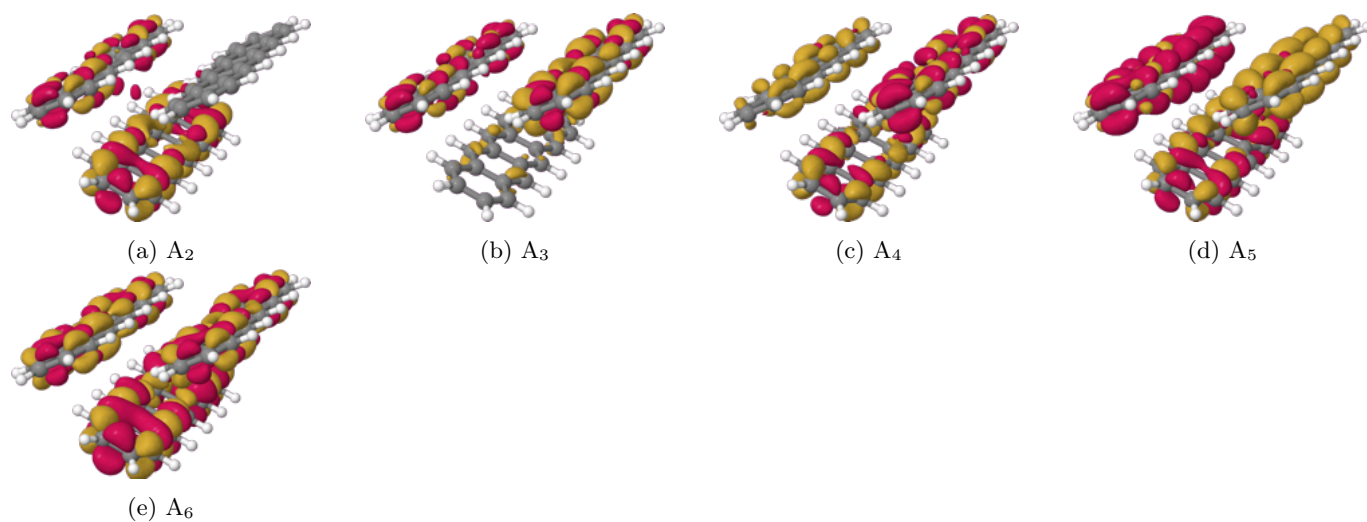


Figure S40: Difference densities w.r.t. the ground state density at the ground state geometry. Plotted with an isovalue of 0.0004.

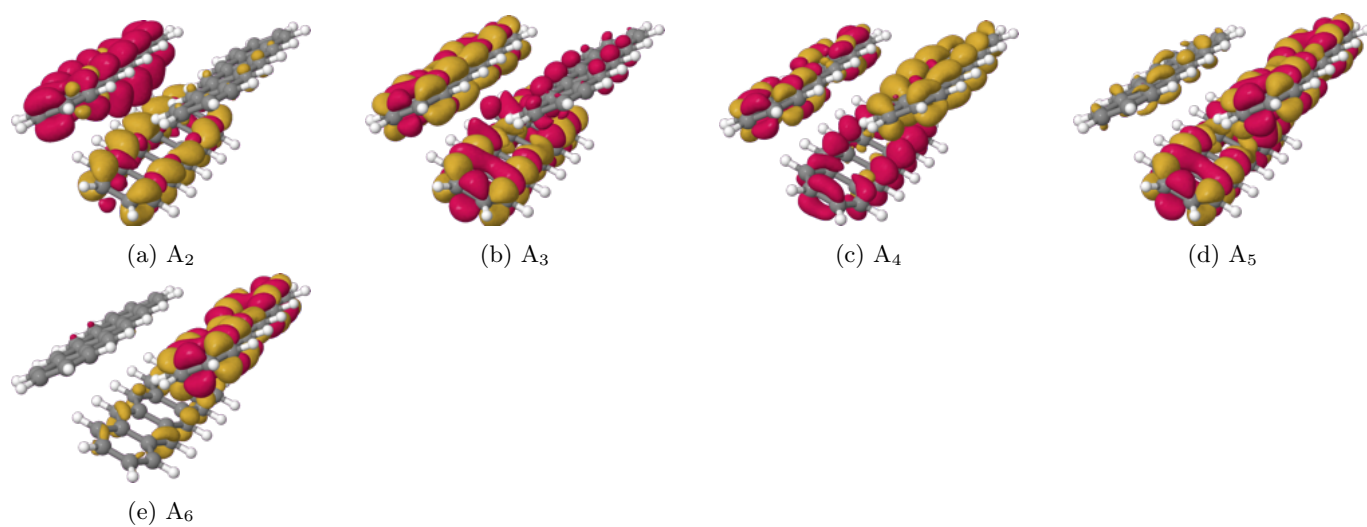


Figure S41: Difference densities w.r.t. the ground state density at the S_1 geometry. Plotted with an isovalue of 0.0004.

S2.8 Descriptors for Charge Transfer States and Multi-Configuration Character

Table S4: Vertical- $E_{vert.}$ and adiabatic-energy $E_{ad.}$ as well as oscillator strength f , squared Frobenius-Norm of the 1-TDM Ω , the participation ratio PR, averaged position of the exciton Pos., CT ratio ω_{CT} , particle-hole coherence length $\omega_{Coh.}$ and netto CT length CT_{net} , for the $S_0 \rightarrow S_n$ transitions of the **u**, **v** and **w** sub-patterns and the Trimer **t** in the given geometries.

Pattern	Geometry	State	$E_{vert.}$	f	$E_{ad.}$	Ω	PR	Pos.	ω_{CT}	$\omega_{Coh.}$	CT_{net}	Assigned
u	S_0	A ₂	2.31	0.2733	2.31	0.893	2.000	1.500	0.030	1.063	0.000	DL; $S_{h-1;h}^{l+1;l}$
		A ₃	2.37	0.0000	2.37	0.900	2.000	1.499	0.006	1.012	-0.000	DL ₂ ; $S_{h-1;h}^{l;l+1}$
		A ₄	2.53	0.0000	2.53	0.094	2.000	1.500	0.988	1.024	-0.009	DL; $N_h^l/N_{h-1}^l/N_{h-1}^{l+1}/N_h^{l+1}/V_{h-1;h}^{l;l+1}$
		A ₅	2.80	0.0011	2.80	0.786	1.075	1.502	0.971	1.031	-0.927	CT _{AB} ; $S_{h-1;h;h-1}^{l+1;l;l+1;l}$
		A ₆	2.82	0.0006	2.82	0.763	1.045	1.498	0.979	1.022	0.956	CT _{BA} ; $S_{h-1;h;h-1}^{l+1;l;l+1;l}$
	S_0	A ₇	2.91	0.0001	2.91	0.158	2.000	1.496	0.015	1.031	0.002	DL; $Z_{h-1;h}^l/Z_h^{l;l+1}/Z_{h-1}^{l;l+1}/Z_{h-1;h}^{l+1}$
		A ₈	3.00	0.0000	3.00	0.154	2.000	1.504	0.009	1.018	0.002	DL; $S_{h-1;h}^{l;l+1}$
	Q_1	A ₂	1.75	0.0000	2.09	0.018	1.995	1.500	0.993	1.014	0.050	DL; $N_h^l/N_{h-1}^l/N_{h-1}^{l+1}/N_h^{l+1}/V_{h-1;h}^{l;l+1}$
		A ₃	2.06	0.2317	2.40	0.873	2.000	1.502	0.036	1.075	-0.000	DL; $S_{h-1;h}^{l+1;l}$
		A ₄	2.12	0.0000	2.46	0.886	2.000	1.497	0.006	1.011	-0.000	DL ₂ ; $S_{h-1;h}^{l;l+1}$
		A ₅	2.28	0.0012	2.62	0.241	2.000	1.501	0.010	1.019	-0.001	DL; $Z_{h-1;h}^l/Z_h^{l;l+1}/Z_{h-1}^{l;l+1}/Z_{h-1;h}^{l+1}$
		A ₆	2.43	0.0000	2.77	0.271	1.997	1.502	0.291	1.701	-0.041	DL; $V_{h-1;h}^{l;l+1}$
	Q_1	A ₇	2.48	0.0006	2.81	0.707	1.103	1.500	0.948	1.057	-0.902	CT _{AB} ; $S_{h-1;h;h-1}^{l+1;l;l+1;l}$
		A ₈	2.50	0.0014	2.83	0.737	1.128	1.500	0.953	1.054	0.879	CT _{BA} ; $S_{h-1;h;h-1}^{l+1;l;l+1;l}$
	T_1	A ₂	2.08	0.1460	2.19	0.891	1.024	1.012	0.012	1.013	0.001	LE; S_h^l
		A ₃	2.16	0.0002	2.27	0.050	1.951	1.497	0.975	1.050	-0.159	DL; $V_{h-1;h}^{l;l+1}/V_{h-1;h}^{l;l+1}$
		A ₄	2.36	0.1183	2.47	0.889	1.160	1.926	0.126	1.144	-0.042	LE; $S_{h-1;h-1}^{l+1;l;l+1}$
		A ₅	2.58	0.0035	2.68	0.766	1.400	1.525	0.939	1.085	-0.655	CT _{AB} ; $S_{h-1;h;h-1}^{l+1;l;l+1;l}$
		A ₆	2.63	0.0068	2.74	0.810	1.371	1.551	0.887	1.147	0.679	CT _{BA} ; $S_{h-1;h;h-1}^{l+1;l;l+1;l}$
v	T_1	A ₇	2.66	0.0002	2.77	0.208	1.031	1.015	0.026	1.027	-0.015	LE; $N_{h-1}^l/Z_h^{l;l+1}$
		1A ₀	3.32	0.0000	3.43	0.163	1.067	1.968	0.015	1.016	-0.002	LE; $N_{h-1}^{l+1}/Z_{h-1}^{l;l+1}/Z_{h-1;h}^{l+1}$
	S_1	A ₂	2.06	0.0033	2.09	0.049	1.751	1.487	0.761	1.467	-0.377	DL; $Z_h^{l;l+1}/V_{h-1;h}^{l;l+1}/V_{h-1;h}^{l;l+1}$
		A ₃	2.14	0.2486	2.18	0.875	1.827	1.346	0.052	1.098	-0.025	LE+CR; $S_{h;h-1}^{l;l+1}$
		A ₄	2.26	0.0068	2.29	0.896	1.847	1.644	0.011	1.021	-0.005	LE; $S_{h-1;h}^{l;l+1}$

Continued on next page

Table S4: Vertical- $E_{vert.}$ and adiabatic-energy $E_{ad.}$ as well as oscillator strength f , squared Frobenius-Norm of the 1-TDM Ω , the participation ratio PR, averaged position of the exciton Pos., CT ratio ω_{CT} , particle-hole coherence length $\omega_{Coh.}$ and netto CT length CT_{net} , for the $S_0 \rightarrow S_n$ transitions of the **u**, **v** and **w** sub-patterns and the Trimer **t** in the given geometries.

Pattern	Geometry	State	$E_{vert.}$	f	$E_{ad.}$	Ω	PR	Pos.	ω_{CT}	$\omega_{Coh.}$	CT_{net}	Assigned
	S_1	A ₅	2.52	0.0052	2.55	0.791	1.085	1.511	0.931	1.075	-0.918	CT _{AB} ; $S_{h-1}^{l+1;l;l+1;l}$
		A ₆	2.72	0.0007	2.75	0.787	1.030	1.500	0.982	1.019	0.971	CT _{BA} ; $S_{h-1}^{l+1;l+1;l}$
		A ₇	2.81	0.0002	2.84	0.175	1.428	1.184	0.013	1.018	0.000	LE; $N_{h-1}^l/Z_{h;h-1}^l$
		A ₈	2.90	0.0000	2.94	0.174	1.425	1.818	0.047	1.068	0.033	LE; $N_h^{l+1}/V_{h;h-1}^{l;l+1}$
	S_0	A ₂	2.25	0.1708	2.25	0.880	1.928	1.566	0.281	1.634	-0.146	CT+LE; S_h^l
		A ₃	2.34	0.0342	2.34	0.799	1.869	1.368	0.153	1.319	0.029	LE; S_{h-1}^l
		A ₄	2.43	0.0098	2.43	0.445	1.920	1.599	0.493	1.921	-0.059	DL; S_h^{l+1}/N_h^l
		A ₅	2.68	0.0297	2.68	0.668	1.404	1.537	0.707	1.401	-0.652	CT _{AB} ; S_{h-1}^{l+1}
	S_0	A ₆	2.84	0.0129	2.84	0.662	1.143	1.479	0.874	1.142	0.867	CT _{BA} ; S_{h-1}^{l+1}
		A ₇	3.02	0.0000	3.02	0.152	1.812	1.659	0.137	1.271	-0.059	LE; $Z_h^{l;l+1}/Z_{h-1}^{l;l+1}$
		A ₈	3.11	0.0002	3.11	0.157	1.771	1.321	0.165	1.320	0.046	LE+CT; $N_{h-1}^l/V_{h-1}^{l;l+1}$
v	Q_1	A ₂	1.70	0.0003	2.03	0.099	1.943	1.491	0.935	1.134	0.170	DL; $N_h^l/V_{h-1}^{l;l+1}$
		A ₃	1.99	0.1469	2.32	0.851	1.934	1.558	0.316	1.715	-0.147	CT+LE; S_h^l
		A ₄	2.11	0.0347	2.44	0.867	1.951	1.421	0.033	1.067	0.013	LE; $S_{h-1}^{l;l+1}$
		A ₅	2.33	0.0218	2.67	0.715	1.461	1.570	0.739	1.364	-0.608	CT _{AB} ; $S_{h-1}^{l;l+1;l+1}$
	Q_1	A ₆	2.40	0.0005	2.73	0.233	1.827	1.648	0.158	1.316	-0.103	LE; $Z_{h-1}^{l;l+1}/Z_{h-1}^{l;l+1}$
		A ₇	2.48	0.0196	2.82	0.604	1.428	1.462	0.719	1.396	0.634	CT _{BA} ; S_{h-1}^{l+1}
		A ₈	2.56	0.0060	2.90	0.370	1.594	1.410	0.534	1.604	0.497	CT+LE; $N_{h-1}^l/S_{h-1}^{l+1}/V_{h-1}^{l;l+1}$
	T_1	A ₂	2.03	0.1108	2.17	0.771	1.284	1.879	0.219	1.222	-0.203	LE+CT; S_h^l
		A ₃	2.08	0.0299	2.22	0.305	1.646	1.688	0.503	1.570	0.363	CT+LE; $S_h^{l;l+1}/Z_{h;h-1}^l$
		A ₄	2.28	0.0427	2.42	0.865	1.546	1.229	0.232	1.380	-0.027	LE; $S_{h-1}^{l;l+1}$
		A ₅	2.50	0.0118	2.64	0.426	1.632	1.563	0.641	1.578	-0.470	LE+DL; $N_h^l/S_h^{l+1}/Z_h^{l;l+1}$
	T_1	A ₆	2.52	0.0110	2.66	0.449	1.592	1.577	0.643	1.540	-0.502	(LE+CT) _{BA} ; $S_h^{l+1}/Z_h^{l;l+1}/N_h^l$
		A ₇	2.69	0.0410	2.83	0.783	1.415	1.391	0.691	1.357	0.648	CT _{AB} ; $S_{h-1}^{l+1;l}$
		A ₈	3.11	0.0001	3.25	0.161	1.528	1.222	0.255	1.401	-0.072	LE; $Z_{h-1}^{l;l+1}/N_{h-1}^l/N_{h-1}^{l+1}$
	S_1	A ₂	2.02	0.0533	2.09	0.501	1.450	1.571	0.656	1.451	-0.617	CT _{AB} ; S_h^l
		A ₃	2.09	0.1042	2.16	0.593	1.903	1.440	0.319	1.698	0.196	CT+LE; $S_{h;h-1}^{l;l+1}$

Continued on next page

Table S4: Vertical- $E_{vert.}$ and adiabatic-energy $E_{ad.}$ as well as oscillator strength f , squared Frobenius-Norm of the 1-TDM Ω , the participation ratio PR, averaged position of the exciton Pos., CT ratio ω_{CT} , particle-hole coherence length $\omega_{Coh.}$ and netto CT length CT_{net} , for the $S_0 \rightarrow S_n$ transitions of the **u**, **v** and **w** sub-patterns and the Trimer **t** in the given geometries.

Pattern	Geometry	State	$E_{vert.}$	f	$E_{ad.}$	Ω	PR	Pos.	ω_{CT}	$\omega_{Coh.}$	CT_{net}	Assigned
	S_1	A ₄	2.25	0.0402	2.33	0.869	1.997	1.480	0.020	1.042	0.005	LE; $S_{h-1}^{l;l+1}$
		A ₅	2.49	0.0359	2.56	0.691	1.466	1.558	0.645	1.482	-0.604	CT _{AB} ; $S_{h-1}^{l;l+1;l+1}$
		A ₆	2.73	0.0193	2.80	0.706	1.226	1.484	0.815	1.225	0.795	CT _{BA} ; S_{h-1}^{l+1}
		A ₇	2.77	0.0000	2.84	0.164	1.794	1.669	0.213	1.429	0.046	LE; $Z_{h-1}^{l;l+1}/Z_{h-1}^l$
		A ₈	2.89	0.0014	2.96	0.216	1.800	1.377	0.438	1.756	0.253	LE+CT; $N_{h-1}^l/V_{h-1}^{l;l+1}$
	S_0	A ₂	2.21	0.1664	2.21	0.879	1.975	1.508	0.308	1.726	0.111	CT; S_h^l
		A ₃	2.38	0.0435	2.38	0.898	1.998	1.485	0.013	1.027	-0.004	DL; $S_{h;h-1}^l/N_h^l$
		A ₄	2.41	0.0043	2.41	0.410	1.994	1.484	0.931	1.148	0.047	DL; $S_{h;h-1}^{l+1;l}/N_h^l$
		A ₅	2.75	0.0253	2.75	0.582	1.303	1.504	0.745	1.328	0.731	CT; $S_{h-1}^{l;l+1}$
	S_0	A ₆	2.83	0.0233	2.83	0.686	1.227	1.506	0.810	1.233	-0.794	CT; S_{h-1}^{l+1}
		A ₇	3.00	0.0001	3.00	0.144	1.991	1.466	0.233	1.553	-0.002	DL; $Z_{h;h-1}^l/Z_h^{l+1}$
		A ₈	3.10	0.0001	3.10	0.138	1.980	1.547	0.235	1.554	-0.037	DL; $V_{h-1}^{l+1;l}/N_h^{l+1}/N_{h-1}^l$
w	Q_1	A ₂	1.71	0.0001	2.04	0.119	1.984	1.497	0.959	1.084	0.091	DL; $N_h^l/V_{h;h-1}^{l;l+1}/Z_h^{l;l+1}/Z_{h-1}^{l;l+1}$
		A ₃	1.95	0.1391	2.28	0.848	1.991	1.510	0.332	1.792	0.064	DL; S_h^l
		A ₄	2.13	0.0373	2.46	0.880	1.992	1.469	0.011	1.022	-0.004	DL; $S_{h;h-1}^l/N_h^l$
		A ₅	2.36	0.0043	2.69	0.478	1.855	1.527	0.786	1.453	0.276	CT; $S_{h;h-1}^{l+1;l}/Z_{h;h-1}^l$
	Q_1	A ₆	2.38	0.0045	2.71	0.391	1.733	1.432	0.585	1.703	0.380	(LE+CT) ₁ ; $S_h^{l+1}/Z_{h;h-1}^l/Z_h^{l;l+1}$
		A ₇	2.49	0.0308	2.82	0.614	1.894	1.504	0.582	1.854	-0.237	(LE+CT) ₂ ; $S_{h-1}^{l+1}/V_{h;h-1}^{l;l+1}$
		A ₈	2.55	0.0103	2.88	0.409	1.586	1.557	0.532	1.630	-0.509	LE+CT; $S_{h-1}^{l+1}/V_{h;h-1}^{l;l+1}$
	T_1	A ₂	2.00	0.0731	2.13	0.544	1.544	1.247	0.397	1.403	0.382	CT; S_h^l
		A ₃	2.03	0.0746	2.16	0.522	1.448	1.190	0.298	1.320	-0.283	CT; $S_{h;h-1}^l/N_h^l$
		A ₄	2.27	0.0314	2.40	0.869	1.716	1.703	0.188	1.354	0.022	DL; $S_{h;h-1}^{l;l+1}$
		A ₅	2.52	0.0010	2.65	0.232	1.482	1.204	0.339	1.481	0.096	LE; $N_h^l/Z_h^{l;l+1}$
	T_1	A ₆	2.54	0.0073	2.67	0.606	1.804	1.509	0.889	1.217	0.330	CT; $S_{h-1}^{l;l+1}$
		A ₇	2.69	0.0592	2.82	0.825	1.705	1.627	0.604	1.620	-0.371	CT; S_{h-1}^{l+1}
		A ₈	3.10	0.0001	3.23	0.145	1.429	1.816	0.315	1.442	-0.048	LE; $V_{h-1}^{l+1;l}/Z_h^{l;l+1}/Z_{h;h-1}^l$
	S_1	A ₂	1.99	0.0779	2.07	0.631	1.552	1.530	0.560	1.613	0.537	CT; S_h^l

Continued on next page

Table S4: Vertical- $E_{vert.}$ and adiabatic-energy $E_{ad.}$ as well as oscillator strength f , squared Frobenius-Norm of the 1-TDM Ω , the participation ratio PR, averaged position of the exciton Pos., CT ratio ω_{CT} , particle-hole coherence length $\omega_{Coh.}$ and netto CT length CT_{net} , for the $S_0 \rightarrow S_n$ transitions of the **u**, **v** and **w** sub-patterns and the Trimer **t** in the given geometries.

Pattern	Geometry	State	$E_{vert.}$	f	$E_{ad.}$	Ω	PR	Pos.	ω_{CT}	$\omega_{Coh.}$	CT_{net}	Assigned
	S_1	A ₃	2.07	0.0732	2.15	0.481	1.735	1.521	0.413	1.723	-0.390	CT+LE; $S_{h;h-1}^l/N_h^l$
		A ₄	2.27	0.0447	2.34	0.889	1.979	1.449	0.015	1.030	-0.005	DL; $S_{h;h-1}^{l;l+1}$
		A ₅	2.54	0.0230	2.62	0.612	1.495	1.517	0.768	1.361	0.581	CT; $S_{h-1;h}^{l;l+1}$
		A ₆	2.71	0.0097	2.78	0.336	1.788	1.548	0.484	1.796	-0.336	LE; $S_{h-1}^{l+1}/Z_h^{l;l+1}/Z_{h;h-1}^l$
		A ₇	2.75	0.0211	2.83	0.546	1.491	1.472	0.669	1.488	-0.584	LE+CT; $S_{h-1}^{l+1}/Z_{h;h-1}^l$
		A ₈	2.86	0.0026	2.94	0.240	1.789	1.494	0.390	1.741	-0.343	DL; $V_{h-1;h}^{l+1;l}/Z_h^{l;l+1}/Z_{h;h-1}^l$
	S_0	A ₂	2.22	0.2414	2.24	0.887	2.282	1.545	0.329	1.805	0.092	(DL+CR) w ; S_h^l
		A ₃	2.32	0.0174	2.34	0.861	2.760	2.181	0.323	1.575	0.163	(DL+CR) u ; $S_{h-1;h}^{l;l+1}$
		A ₄	2.33	0.0921	2.37	0.693	2.391	2.204	0.471	2.051	-0.148	DL v +CT _{A→v} ; $S_{h-1;h;h-2}^{l+1;l}$
	S_0	A ₅	2.38	0.0461	2.43	0.737	2.794	2.030	0.341	1.948	-0.159	DL+CT; $S_{h-1;h}^{l;l+1}$
		A ₆	2.42	0.0005	2.55	0.282	2.750	1.915	0.790	1.915	-0.078	DL+CT; $S_{h-2;h}^{l;l+2}$
t	Q_1	A ₂	1.82	0.0000	2.13	0.014	2.117	2.452	0.984	1.108	-0.107	DL u ; $V_{h;h-1}^{l;l+1}$
		A ₃	2.02	0.1536	2.33	0.695	2.126	1.964	0.353	1.456	0.158	LE _A +CT _{C→A} ; $S_{h;h-1;h-1}^{l;l+1}$
		A ₄	2.04	0.0976	2.35	0.508	2.639	1.972	0.500	1.925	0.017	DL _w +CR; $S_{h;h-1}^{l;l+1}$
	Q_1	A ₅	2.08	0.0431	2.39	0.849	1.770	2.627	0.199	1.213	-0.205	LE _B ; $S_{h-1;h}^{l;l+1}$
		A ₆	2.12	0.0005	2.44	0.272	2.241	1.990	0.699	1.525	0.889	DL v +CT _{A→v} ; $S_{h-2;h-1;h}^{l;l+1;l}$
	T_1	A ₂	2.01	0.1570	2.15	0.884	1.440	1.243	0.268	1.381	0.097	LE _C ; S_h^l
		A ₃	2.13	0.0032	2.26	0.388	2.327	1.695	0.947	1.486	0.322	(DL+CT) w ; $S_{h;h-1}^{l+1;l}/V_{h;h-1}^{l;l+1}$
		A ₄	2.20	0.0072	2.33	0.271	2.081	1.998	0.903	1.392	-0.652	DL v +CT _C ; $Z_{h;h-1}^l/S_{h-1}^l/S_h^{l_2}$
	T_1	A ₅	2.28	0.0078	2.42	0.838	2.576	1.965	0.466	1.751	-0.092	LE _A +CR; $S_{h;h-1;h-2}^{l+1;l}$
		A ₆	2.34	0.2030	2.48	0.858	2.200	2.462	0.105	1.178	-0.043	LE _B ; $S_{h-1;h-2;h}^{l+1;l;l+2}$
	S_1	A ₂	2.04	0.1694	2.14	0.827	1.961	1.515	0.467	1.905	0.282	(CT+LE) w ; S_h^l
		A ₃	2.12	0.0313	2.22	0.521	2.168	1.532	0.715	2.015	0.204	DL w +CT _{B→w} ; S_h^{l+1}
		A ₄	2.23	0.0020	2.33	0.846	2.631	1.991	0.372	1.598	-0.444	LE _A +CT _{B→C} ; $S_{h-1;h}^{l;l+1}$
	S_1	A ₅	2.27	0.0285	2.37	0.414	2.754	2.072	0.685	1.705	-0.051	DL v +CT _{A→v} ; $S_{h-2;h-1}^{l;l+1}/V_{h;h-1}^{l;l+1}$
		A ₆	2.34	0.1599	2.44	0.812	1.815	2.554	0.138	1.204	0.074	LE _B +CT _{C→B} ; $S_{h-1;h}^{l+1;l;l+2}$

Table S5: Vertical- $E_{vert.}$ and adiabatic-energy $E_{ad.}$ as well as oscillator strength f , squared Frobenius-Norm of the 1-TDM Ω , the participation ratio PR, averaged position of the exciton Pos., CT ratio ω_{CT} , particle-hole coherence length $\omega_{Coh.}$ and netto CT length CT_{net} , for the $T_1 \rightarrow T_n$ transitions of the **u**, **v** and **w** sub-patterns and the Trimer **t** in the given geometries.

Pattern	Geometry	State	$E_{vert.}$	f	$E_{ad.}$	Ω	PR	Pos.	ω_{CT}	$\omega_{Coh.}$	CT_{net}	Assigned
u	S ₀	A ₂	0.00	0.0000	1.13	0.401	2.000	1.500	0.013	1.027	0.000	DL; $T_{h-1;h}^{l;l+1}$
		A ₃	1.12	0.0007	2.25	0.214	1.958	1.427	0.031	1.063	0.000	DL; T
		A ₄	1.13	0.0000	2.25	0.212	1.992	1.533	0.038	1.078	0.001	DL; T
	S ₀	A ₅	1.53	0.0000	2.66	0.078	1.995	1.500	0.988	1.024	-0.052	³ DL; $3V_{h-1;h}^{l;l+1}/Z_{h-1;h}^l/Z_h^{l;l+1}/Z_{h-1}^{l;l+1}/Z_{h-1;h}^{l+1}$
		A ₆	1.67	0.0156	2.80	0.416	1.781	1.500	0.984	1.029	-0.350	CT _{BA} ; $T_{h-1;h}^{l;l+1}$
		A ₇	1.72	0.0008	2.85	0.343	1.678	1.499	0.990	1.016	0.438	CT _{BA} ; $T_{h-1;h}^{l+1;l}$
	Q ₁	A ₂	0.00	0.0000	1.13	0.384	2.000	1.500	0.018	1.036	-0.000	DL; $T_{h-1;h}^{l;l+1}$
		A ₃	1.12	0.0000	2.25	0.014	1.987	1.500	0.980	1.040	0.081	³ DL; $3V_{h-1;h}^{l;l+1}/Z_{h-1;h}^l/Z_h^{l;l+1}/Z_{h-1}^{l;l+1}/Z_{h-1;h}^{l+1}$
		A ₄	1.37	0.0011	2.50	0.215	1.967	1.435	0.035	1.072	-0.003	DL; T
		A ₅	1.38	0.0000	2.50	0.214	2.000	1.504	0.050	1.105	-0.007	DL; T
		A ₆	1.71	0.0164	2.84	0.417	1.550	1.501	0.979	1.032	-0.539	CT _{AB} ; $T_{h-1;h;h-1}^{l+1;l;l+1;l}$
		A ₇	1.75	0.0017	2.87	0.401	1.522	1.500	0.987	1.020	0.560	CT _{BA} ; $T_{h-1;h;h-1}^{l+1;l;l+1;l}$
		A ₉	2.46	0.0002	3.59	0.445	1.994	1.528	0.012	1.025	-0.000	³ DL ₂ ; $Z_{h-1;h}^l/Z_h^{l;l+1}/Z_{h-1}^{l;l+1}/Z_{h-1;h}^{l+1}$
	T ₁	A ₂	0.37	0.0000	1.32	0.007	1.983	1.499	0.402	1.911	-0.093	LE; T_{h-1}^{l+1}
		A ₃	1.30	0.0007	2.24	0.416	1.036	1.018	0.034	1.035	0.002	LE; T
		A ₄	1.39	0.0000	2.33	0.026	1.937	1.436	0.864	1.294	-0.131	³ DL; $3V_{h-1;h}^{l;l+1}$
		A ₅	1.50	0.0000	2.44	0.012	1.628	1.266	0.332	1.520	0.182	LE; T
		A ₆	1.67	0.0001	2.62	0.417	1.639	1.502	0.983	1.028	-0.470	CT _{AB} ; $T_{h-1;h;h-1}^{l+1;l;l+1;l}$
		A ₇	1.76	0.0001	2.71	0.394	1.587	1.499	0.990	1.016	0.510	CT _{BA} ; $T_{h-1;h;h-1}^{l+1;l;l+1;l}$
v	S ₁	A ₂	0.08	0.0000	1.05	0.348	2.000	1.501	0.015	1.030	0.005	LE; $T_{h-1;h}^{l;l+1}$
		A ₃	1.25	0.0009	2.22	0.218	1.201	1.092	0.085	1.102	-0.027	LE; T
		A ₄	1.26	0.0004	2.23	0.088	1.805	1.336	0.292	1.594	-0.036	³ DL; $3V_{h-1;h}^{l;l+1}/Z_{h-1;h}^l/Z_h^{l;l+1}/Z_{h-1}^{l;l+1}/Z_{h-1;h}^{l+1}$
		A ₅	1.32	0.0001	2.29	0.161	1.734	1.696	0.043	1.076	-0.008	LE; T
		A ₆	1.58	0.0225	2.54	0.391	1.041	1.500	0.976	1.025	-0.960	CT _{AB} ; $T_{h-1;h}^l$
	S ₁	A ₇	1.79	0.0055	2.75	0.410	1.048	1.501	0.985	1.016	0.954	CT _{BA} ; $T_{h-1;h;h-1}^{l+1;l}$
		1A ₀	2.54	0.0062	3.51	0.435	1.845	1.645	0.013	1.024	-0.001	³ DL ₂ ; $3V_{h-1;h}^{l;l+1}/Z_{h-1;h}^l/Z_h^{l;l+1}/Z_{h-1}^{l;l+1}/Z_{h-1;h}^{l+1}$
	S ₀	A ₂	0.06	0.0000	1.20	0.394	2.000	1.501	0.032	1.066	0.007	DL; $T_{h;h-1}^{l+1;l}$
		A ₃	1.15	0.0014	2.29	0.234	1.797	1.668	0.083	1.158	-0.005	DL; T
	T ₁	A ₂	0.37	0.0000	1.32	0.007	1.983	1.499	0.402	1.911	-0.093	LE; T_{h-1}^{l+1}
		A ₃	1.30	0.0007	2.24	0.416	1.036	1.018	0.034	1.035	0.002	LE; T

Continued on next page

Table S5: Vertical- $E_{vert.}$ and adiabatic-energy $E_{ad.}$ as well as oscillator strength f , squared Frobenius-Norm of the 1-TDM Ω , the participation ratio PR, averaged position of the exciton Pos., CT ratio ω_{CT} , particle-hole coherence length $\omega_{Coh.}$ and netto CT length CT_{net} , for the $T_1 \rightarrow T_n$ transitions of the **u**, **v** and **w** sub-patterns and the Trimer **t** in the given geometries.

Pattern	Geometry	State	$E_{vert.}$	f	$E_{ad.}$	Ω	PR	Pos.	ω_{CT}	$\omega_{Coh.}$	CT_{net}	Assigned
	S_0	A ₄	1.17	0.0002	2.31	0.221	1.993	1.475	0.145	1.328	-0.036	DL; T
		A ₅	1.40	0.0142	2.54	0.310	1.196	1.495	0.945	1.067	-0.820	CT _{AB} ; $T_{h;h-1}^{l;l+1}$
		A ₆	1.52	0.0390	2.66	0.302	1.782	1.502	0.940	1.112	0.350	CT _{BA} ; $T_{h-1;h}^{l+1;l}$
		A ₇	1.75	0.0070	2.89	0.209	1.231	1.504	0.968	1.040	0.790	CT+DL; T/Z/V
	Q_1	A ₂	0.05	0.0000	1.17	0.349	2.000	1.498	0.049	1.103	0.010	LE; $T_{h;h-1}^{l+1;l}$
		A ₃	1.08	0.0000	2.20	0.079	1.971	1.500	0.957	1.088	0.121	DL; Z/T/V
		A ₄	1.38	0.0045	2.50	0.246	1.740	1.693	0.150	1.284	-0.037	DL; T
		A ₅	1.40	0.0020	2.52	0.229	1.885	1.600	0.228	1.488	-0.158	DL; T
	Q_1	A ₆	1.52	0.0401	2.64	0.365	1.321	1.474	0.893	1.141	-0.718	CT _{AB} ; $T_{h-1;h;h-1}^{l+1;l}$
		A ₇	1.71	0.0143	2.83	0.351	1.158	1.503	0.932	1.079	0.852	CT _{BA} ; $T_{h-1;h;h-1}^{l+1;l}$
		A ₈	2.41	0.0273	3.53	0.426	1.862	1.364	0.040	1.076	0.011	DL ₂ ; Z/T/V
	T_1	A ₂	0.36	0.0000	1.32	0.021	1.741	1.504	0.977	1.041	0.385	LE; $T_{h-1}^{l;l+1}$
		A ₃	1.31	0.0006	2.28	0.408	1.055	1.973	0.052	1.054	0.025	LE; T
		A ₄	1.40	0.0008	2.36	0.131	1.715	1.596	0.784	1.379	-0.384	DL; V/Z/T
		A ₅	1.50	0.0009	2.46	0.039	1.808	1.499	0.942	1.109	-0.326	LE; T
	T_1	A ₆	1.61	0.0178	2.57	0.363	1.612	1.497	0.944	1.093	-0.491	CT _{AB} ; $T_{h-1;h}^{l;l+1}$
		A ₇	1.85	0.0018	2.81	0.330	1.348	1.507	0.964	1.049	0.695	CT _{BA} ; $T_{h-1;h}^{l+1;l}$
	S_1	A ₂	0.09	0.0000	1.13	0.386	2.000	1.501	0.047	1.097	0.014	DL; $T_{h;h-1}^{l+1;l}$
		A ₃	1.21	0.0087	2.25	0.236	1.614	1.419	0.728	1.436	-0.482	DL+CT; T/Z
		A ₄	1.24	0.0012	2.28	0.241	1.694	1.712	0.128	1.233	0.035	LE; T
		A ₅	1.32	0.0015	2.36	0.179	1.970	1.548	0.237	1.552	-0.078	LE; T
	S_1	A ₆	1.46	0.0580	2.50	0.310	1.634	1.490	0.903	1.167	-0.473	CT _{AB} ; $T_{h;h-1;h}^{l+1;l}$
		A ₇	1.78	0.0203	2.82	0.316	1.121	1.506	0.946	1.061	0.886	CT _{BA} ; T_{h-1}^{l+1}
	S_0	A ₂	0.06	0.0000	1.20	0.401	2.000	1.499	0.038	1.079	-0.003	DL; $T_{h-1;h}^{l;l+1}$
		A ₃	1.14	0.0011	2.28	0.235	1.960	1.428	0.096	1.204	0.000	DL; T
		A ₄	1.19	0.0000	2.33	0.212	1.999	1.487	0.041	1.085	-0.001	DL ₂ ; T
		A ₅	1.40	0.0160	2.54	0.312	1.172	1.499	0.972	1.033	0.840	CT _{AB} ; $T_{h;h-1}^{l;l+1}$
	S_0	A ₆	1.52	0.0559	2.66	0.361	1.558	1.501	0.944	1.089	-0.533	CT _{BA} ; $T_{h;h-1;h}^{l+1;l}$

Continued on next page

Table S5: Vertical- $E_{vert.}$ and adiabatic-energy $E_{ad.}$ as well as oscillator strength f , squared Frobenius-Norm of the 1-TDM Ω , the participation ratio PR, averaged position of the exciton Pos., CT ratio ω_{CT} , particle-hole coherence length $\omega_{Coh.}$ and netto CT length CT_{net} , for the $T_1 \rightarrow T_n$ transitions of the **u**, **v** and **w** sub-patterns and the Trimer **t** in the given geometries.

Pattern	Geometry	State	$E_{vert.}$	f	$E_{ad.}$	Ω	PR	Pos.	ω_{CT}	$\omega_{Coh.}$	CT_{net}	Assigned
		A ₇	1.75	0.0018	2.89	0.167	1.644	1.498	0.982	1.030	-0.465	DL; V/Z/T
	Q ₁	A ₂	0.06	0.0000	1.17	0.375	2.000	1.499	0.051	1.107	-0.003	DL; $T_{h-1;h}^{l;l+1}$
		A ₃	1.10	0.0001	2.22	0.095	1.997	1.501	0.977	1.047	0.038	DL; Z/T
		A ₄	1.38	0.0016	2.50	0.240	1.850	1.358	0.120	1.242	-0.001	DL; T
		A ₅	1.42	0.0000	2.54	0.208	1.998	1.483	0.065	1.139	0.002	DL ₂ ; T
		A ₆	1.52	0.0625	2.64	0.405	1.542	1.502	0.925	1.119	0.545	CT _{AB} ; $T_{h;h-1}^{l;l+1}$
	Q ₁	A ₇	1.68	0.0091	2.80	0.332	1.353	1.500	0.973	1.036	-0.691	CT _{BA} ; $T_{h;h-1;h}^{l+1;l}$
		A ₈	2.42	0.0234	3.54	0.404	1.968	1.564	0.033	1.066	0.001	DL; Z
	T ₁	A ₂	0.35	0.0000	1.31	0.031	1.986	1.500	0.979	1.043	0.083	LE; $T_{h-1;h}^{l+1;l;l+1}$
		A ₃	1.32	0.0010	2.27	0.423	1.034	1.017	0.032	1.033	0.001	LE; T
		A ₄	1.38	0.0003	2.33	0.114	1.699	1.505	0.968	1.055	0.421	DL+CT; Z/V/T
		A ₅	1.50	0.0001	2.46	0.016	1.934	1.408	0.787	1.479	0.018	LE; T
	T ₁	A ₆	1.60	0.0270	2.56	0.405	1.886	1.508	0.942	1.114	0.246	CT _{AB} ; $T_{h;h-1}^{l;l+1}$
		A ₇	1.83	0.0024	2.78	0.316	1.646	1.498	0.976	1.041	-0.464	CT _{BA} ; $T_{h;h-1;h}^{l+1;l}$
	S ₁	A ₂	0.10	0.0000	1.14	0.395	2.000	1.497	0.058	1.122	-0.011	DL; $T_{h-1;h}^{l;l+1}$
		A ₃	1.23	0.0013	2.27	0.250	1.836	1.649	0.135	1.273	0.003	DL; T
		A ₄	1.26	0.0099	2.30	0.212	1.467	1.499	0.964	1.054	0.603	CT+DL; T/Z
		A ₅	1.31	0.0000	2.35	0.209	1.949	1.419	0.063	1.129	-0.008	DL ₂ ; T
	S ₁	A ₆	1.49	0.0811	2.53	0.340	1.898	1.500	0.903	1.198	0.232	CT _{BA} ; $T_{h;h-1;h}^{l+1;l}$
		A ₇	1.77	0.0139	2.80	0.284	1.238	1.500	0.965	1.043	-0.784	CT _{AB} ; $T_{h;h-1}^{l;l+1}$
	S ₀	A ₂	0.01	0.0000	1.20	0.140	2.253	2.212	0.133	1.167	-0.010	DL _v ; $T_{h-1;h}^{l+1;l}$
		A ₃	0.07	0.0000	1.26	0.251	2.065	1.987	0.064	1.104	-0.001	LEC+DL _u ; $T_{h-2;h-1;h}^{l;l+1;l+2}$
		A ₄	1.18	0.0008	2.37	0.204	1.494	1.979	0.102	1.123	-0.011	LE _A +DL _v ; T_{h-3}^l
		A ₅	1.19	0.0008	2.38	0.090	2.347	2.250	0.344	1.558	-0.008	DL _v ; T_{h-4}^l
	S ₀	A ₆	1.21	0.0002	2.40	0.186	1.636	2.003	0.145	1.153	-0.109	DL; T_{h-5}^l
		A ₇	1.29	0.0152	2.48	0.291	2.347	1.943	0.953	1.764	0.118	CT _{v→A} ; $T_{h;h-1}^l$
	Q ₁	A ₂	0.02	0.0000	1.19	0.393	2.069	2.477	0.048	1.066	-0.001	DL _u ; $T_{h-1;h}^{l;l+1}$
		A ₃	0.40	0.0000	1.57	0.036	2.533	1.674	0.828	1.985	0.150	LE _C ; $T_{h-2;h;h-2}^{l+2;l}$

Continued on next page

Table S5: Vertical- $E_{vert.}$ and adiabatic-energy $E_{ad.}$ as well as oscillator strength f , squared Frobenius-Norm of the 1-TDM Ω , the participation ratio PR, averaged position of the exciton Pos., CT ratio ω_{CT} , particle-hole coherence length $\omega_{Coh.}$ and netto CT length CT_{net} , for the $T_1 \rightarrow T_n$ transitions of the **u**, **v** and **w** sub-patterns and the Trimer **t** in the given geometries.

Pattern	Geometry	State	$E_{vert.}$	f	$E_{ad.}$	Ω	PR	Pos.	ω_{CT}	$\omega_{Coh.}$	CT_{net}	Assigned
	Q ₁	A ₄	1.10	0.0000	2.27	0.010	1.965	2.453	0.962	1.148	-0.286	³ DL _u ; $V_{h;h_{-1}}^{l;l+1}$
		A ₅	1.37	0.0013	2.54	0.196	2.043	2.123	0.843	1.837	-0.064	CT _{v→A} ; $T_{h;h_{-2}}^{l;l+1}$
		A ₆	1.39	0.0003	2.56	0.177	2.236	2.275	0.868	1.708	-0.641	DL _v +CT _{B→C} ; $T_{h;h_{-1}}^l$
		A ₇	1.42	0.0005	2.59	0.221	1.213	2.002	0.141	1.147	-0.019	LE _A ; $T_{h-3;h_{-1};h_{-5}}^{l;l+3;l}$
	T ₁	A ₂	0.30	0.0000	1.34	0.034	2.302	1.622	0.957	1.312	0.111	LE _A ; $T_{h-2;h;h_{-1}}^{l+1;l+1;l+2;l}$
		A ₃	0.32	0.0000	1.36	0.021	2.092	1.908	0.902	1.371	-0.638	LE _B +CT; $T_{h_{-1}}^{l+1;l+2}$
		A ₄	1.31	0.0031	2.35	0.400	1.222	1.173	0.183	1.203	-0.234	LE _C +CT _{B→C} ; $T_{h-3;h;h_{-1}}^{l;l+3;l}$
	T ₁	A ₅	1.36	0.0072	2.39	0.218	1.705	1.607	0.903	1.414	0.965	CT _{C→A} ; $T_{h;h_{-2}}^{l+1}/V_{h_{-1};h}^{l;l+1}$
		A ₆	1.40	0.0078	2.44	0.154	2.267	1.676	0.784	2.114	0.144	³ DL _v +CT; $V_{h_{-1};h}^{l;l+1}/Z_h^{l;l+1}/T_{h;h_{-2};h;h_{-2}}^{l+2;l}$
		A ₇	1.44	0.0034	2.48	0.361	2.439	1.697	0.870	1.865	-0.484	CT _{u→C} ; $T_{h;h_{-1}}^{l+1;l}$
	S ₁	A ₂	0.06	0.0000	1.18	0.359	2.069	1.538	0.098	1.182	-0.001	LE _A +DL _w ; $T_{h-2;h;h_{-1}}^{l;l+1;l+2;l}$
		A ₃	0.17	0.0000	1.30	0.040	2.326	1.603	0.315	1.567	-0.257	LE _B ; $T_{h_{-1}}^{l+1;l+2}$
		A ₄	1.23	0.0174	2.35	0.301	1.650	1.596	0.837	1.492	0.438	LE _C +CT _{B→C} ; $T_{h;h_{-1};h}^{l+1;l}$
	S ₁	A ₅	1.25	0.0015	2.38	0.252	1.823	1.360	0.364	1.712	0.019	CT _{C→A} ; $T_{h-3;h}^{l;l+3}$
		A ₆	1.29	0.0001	2.41	0.190	1.975	1.892	0.344	1.400	-0.322	DL _v +CT; $T_{h_{-5}}^l$
		A ₇	1.34	0.0031	2.46	0.126	2.055	1.903	0.928	1.500	0.843	CT _{u→C} ; T

Table S6: Adiabatic energy $E_{ad.}$ as well as squared Frobenius-Norm of the 1-TDM Ω , the participation ratio PR, averaged position of the exciton Pos., CT ratio ω_{CT} , particle-hole coherence length $\omega_{Coh.}$ and netto CT length CT_{net} , for the $S_0 \rightarrow T_n$ transitions of the **u**, **v** and **w** sub-patterns and the Trimer **t** in the given geometries.

Pattern	Geometry	State	$E_{ad.}$	Ω	PR	Pos.	ω_{CT}	$\omega_{Coh.}$	CT_{net}	Assigned
u	S ₀	A ₁	1.13	0.845	1.995	1.475	0.022	1.045	0.003	DL; $T_{h_{-1};h}^{l+1;l}$
		A ₂	1.13	0.844	1.998	1.515	0.020	1.041	0.004	DL; $T_{h_{-1};h}^{l;l+1}$
		A ₃	2.25	0.820	1.975	1.444	0.034	1.070	0.004	DL; T
		A ₄	2.25	0.819	1.981	1.549	0.036	1.073	0.007	DL; T

Continued on next page

Table S6: Adiabatic energy $E_{ad.}$ as well as squared Frobenius-Norm of the 1-TDM Ω , the participation ratio PR, averaged position of the exciton Pos., CT ratio ω_{CT} , particle-hole coherence length $\omega_{Coh.}$ and netto CT length CT_{net} , for the $S_0 \rightarrow T_n$ transitions of the **u**, **v** and **w** sub-patterns Trimer **t** in the given geometries.

Pattern	Geometry	State	$E_{ad.}$	Ω	PR	Pos.	ω_{CT}	$\omega_{Coh.}$	CT_{net}	Assigned
	S_0	A ₅	2.66	0.130	1.991	1.500	0.982	1.037	-0.067	${}^3DL; {}_3V_{h-1;h}^{l;l+1}/Z_{h-1;h}^l/Z_h^{l;l+1}/Z_{h-1}^{l;l+1}/Z_{h-1;h}^{l+1}$
		A ₆	2.80	0.738	1.775	1.500	0.990	1.017	-0.356	$CT_{BA}; T_{h-1;h}^{l;l+1}$
		A ₇	2.85	0.625	1.682	1.500	0.987	1.022	0.435	$CT_{BA}; T_{h-1;h}^{l+1;l}$
	Q_1	A ₁	1.13	0.795	1.993	1.470	0.026	1.053	-0.001	$DL; T_{h-1;h}^{l+1;l}$
		A ₂	1.13	0.793	1.994	1.528	0.023	1.048	-0.002	$DL; T_{h-1;h}^{l;l+1}$
		A ₃	2.25	0.015	1.999	1.500	0.962	1.078	0.027	${}^3DL; {}_3V_{h-1;h}^{l;l+1}/Z_{h-1;h}^l/Z_h^{l;l+1}/Z_{h-1}^{l;l+1}/Z_{h-1;h}^{l+1}$
		A ₄	2.50	0.742	1.991	1.467	0.044	1.091	0.002	$DL; T$
	Q_1	A ₅	2.50	0.740	1.990	1.535	0.049	1.101	-0.001	$DL; T$
A ₆		2.84	0.656	1.538	1.499	0.990	1.015	-0.548	$CT_{AB}; T_{h-1;h;h;h-1}^{l+1;l;l+1;l}$	
A ₇		2.87	0.649	1.530	1.501	0.982	1.028	0.554	$CT_{BA}; T_{h-1;h;h-1}^{l+1;l+1;l}$	
A ₉		3.59	0.011	1.997	1.494	0.106	1.234	0.039	${}^3DL_2; Z_{h-1;h}^l/Z_h^{l;l+1}/Z_{h-1}^{l;l+1}/Z_{h-1;h}^{l+1}$	
		T_1	A ₁	0.95	0.826	1.042	1.021	0.027	1.028	-0.011
	A ₂		1.32	0.814	1.045	1.978	0.032	1.034	0.008	$LE; T_{h-1}^{l+1}$
	A ₃		2.24	0.778	1.100	1.048	0.052	1.057	-0.023	$LE; T$
	A ₄		2.33	0.044	1.956	1.453	0.820	1.404	-0.118	${}^3DL; {}_3V_{h-1;h}^{l;l+1}$
	T_1	A ₅	2.44	0.792	1.085	1.959	0.046	1.049	0.019	$LE; T$
		A ₆	2.62	0.709	1.635	1.499	0.989	1.018	-0.473	$CT_{AB}; T_{h-1;h;h;h-1}^{l+1;l;l+1;l}$
		A ₇	2.71	0.683	1.601	1.508	0.973	1.044	0.499	$CT_{BA}; T_{h-1;h;h-1}^{l+1;l+1;l}$
	S_1	A ₁	0.97	0.819	1.793	1.330	0.017	1.031	-0.004	$LE; T_{h-1;h}^{l;l+1;l}$
		A ₂	1.05	0.817	1.791	1.671	0.013	1.023	-0.000	$LE; T_{h-1;h}^{l;l+1}$
		A ₃	2.22	0.610	1.289	1.128	0.057	1.074	-0.018	$LE; T$
		A ₄	2.23	0.254	1.964	1.435	0.145	1.322	-0.038	${}^3DL; {}_3V_{h-1;h}^{l;l+1}/Z_{h-1;h}^l/Z_h^{l;l+1}/Z_{h-1}^{l;l+1}/Z_{h-1;h}^{l+1}$
	S_1	A ₅	2.29	0.760	1.413	1.822	0.024	1.034	-0.002	$LE; T$
		A ₆	2.54	0.680	1.049	1.500	0.970	1.031	-0.952	$CT_{AB}; T_{h-1;h}^l$
		A ₇	2.75	0.706	1.044	1.502	0.988	1.013	0.957	$CT_{BA}; T_{h-1;h;h-1}^{l+1;l}$
		1A ₀	3.51	0.026	1.992	1.469	0.046	1.097	-0.005	${}^3DL_2; {}_3V_{h-1;h}^{l;l+1}/Z_{h-1;h}^l/Z_h^{l;l+1}/Z_{h-1}^{l;l+1}/Z_{h-1;h}^{l+1}$
	S_0	A ₁	1.14	0.878	1.952	1.578	0.033	1.067	-0.002	$DL; T_{h;h-1}^{l;l+1}$
		A ₂	1.20	0.877	1.952	1.422	0.019	1.037	0.004	$DL; T_{h;h-1}^{l+1;l}$
v		Continued on next page								

Table S6: Adiabatic energy $E_{ad.}$ as well as squared Frobenius-Norm of the 1-TDM Ω , the participation ratio PR, averaged position of the exciton Pos., CT ratio ω_{CT} , particle-hole coherence length $\omega_{Coh.}$ and netto CT length CT_{net} , for the $S_0 \rightarrow T_n$ transitions of the **u**, **v** and **w** sub-patterns Trimer **t** in the given geometries.

Pattern	Geometry	State	$E_{ad.}$	Ω	PR	Pos.	ω_{CT}	$\omega_{Coh.}$	CT_{net}	Assigned
		A ₃	2.29	0.855	1.907	1.611	0.037	1.072	0.001	DL; T
		A ₄	2.31	0.849	1.925	1.401	0.068	1.140	-0.011	DL; T
	S ₀	A ₅	2.54	0.619	1.235	1.485	0.889	1.138	-0.788	CT _{AB} ; T ^{<i>l;l+1</i>} _{<i>h;h-1;h</i>}
		A ₆	2.66	0.548	1.797	1.504	0.962	1.071	0.336	CT _{BA} ; T ^{<i>l+1;l</i>} _{<i>h-1;h</i>}
		A ₇	2.89	0.409	1.217	1.505	0.953	1.057	0.802	CT+DL; T/Z/V
		A ₁	1.12	0.800	1.826	1.654	0.040	1.076	0.000	LE; T ^{<i>l;l+1</i>} _{<i>h;h-1</i>}
	Q ₁	A ₂	1.17	0.794	1.835	1.350	0.030	1.056	0.000	LE; T ^{<i>l+1;l</i>} _{<i>h;h-1</i>}
		A ₃	2.20	0.089	1.986	1.507	0.897	1.225	0.082	DL; Z/T/V
		A ₄	2.50	0.745	1.947	1.582	0.089	1.188	-0.020	DL; T
	Q ₁	A ₅	2.52	0.721	1.979	1.477	0.131	1.291	-0.092	DL; T
		A ₆	2.64	0.671	1.364	1.434	0.832	1.213	-0.686	CT _{AB} ; T ^{<i>l+1;l</i>} _{<i>h-1;h;h-1</i>}
		A ₇	2.83	0.620	1.159	1.513	0.935	1.075	0.852	CT _{BA} ; T ^{<i>l+1;l</i>} _{<i>h-1;h;h-1</i>}
		A ₈	3.53	0.020	1.925	1.446	0.470	1.916	0.170	DL ₂ ; Z/T/V
		A ₁	0.96	0.868	1.018	1.991	0.015	1.016	-0.001	LE; T ^{<i>l;l+1</i>} _{<i>h</i>}
	T ₁	A ₂	1.32	0.864	1.035	1.017	0.034	1.035	0.011	LE; T ^{<i>l;l+1</i>} _{<i>h-1</i>}
		A ₃	2.28	0.789	1.056	1.973	0.046	1.048	0.021	LE; T
		A ₄	2.36	0.262	1.799	1.515	0.620	1.734	-0.334	DL; V/Z/T
	Q ₁	A ₅	2.46	0.757	1.092	1.044	0.083	1.090	-0.023	LE; T
	T ₁	A ₆	2.57	0.733	1.655	1.444	0.852	1.252	-0.452	CT _{AB} ; T ^{<i>l;l+1</i>} _{<i>h-1;h</i>}
		A ₇	2.81	0.627	1.375	1.495	0.934	1.092	0.674	CT _{BA} ; T ^{<i>l+1;l</i>} _{<i>h-1;h</i>}
		A ₁	1.04	0.849	1.936	1.591	0.049	1.099	-0.008	DL; T ^{<i>l;l+1</i>} _{<i>h;h-1;h</i>}
	S ₁	A ₂	1.13	0.843	1.941	1.413	0.027	1.053	0.006	DL; T ^{<i>l+1;l</i>} _{<i>h;h-1</i>}
		A ₃	2.25	0.552	1.669	1.332	0.507	1.604	-0.366	DL+CT; T/Z
		A ₄	2.28	0.789	1.822	1.656	0.061	1.116	0.011	LE; T
	Q ₁	A ₅	2.36	0.602	1.988	1.472	0.103	1.225	-0.051	LE; T
		A ₆	2.50	0.558	1.527	1.479	0.916	1.131	-0.557	CT _{AB} ; T ^{<i>l+1;l</i>} _{<i>h;h-1;h</i>}
		A ₇	2.82	0.618	1.120	1.509	0.939	1.068	0.886	CT _{BA} ; T ^{<i>l+1</i>} _{<i>h-1</i>}
		A ₁	1.14	0.866	1.984	1.455	0.037	1.076	0.001	DL; T ^{<i>l;l+1</i>} _{<i>h;h-1</i>}
	S ₀	A ₂	1.20	0.866	1.985	1.544	0.013	1.025	-0.002	DL; T ^{<i>l;l+1</i>} _{<i>h-1;h</i>}
		A ₃	2.28	0.844	1.991	1.466	0.029	1.059	0.001	DL; T
w										
Continued on next page										

Continued on next page

Table S6: Adiabatic energy $E_{ad.}$ as well as squared Frobenius-Norm of the 1-TDM Ω , the participation ratio PR, averaged position of the exciton Pos., CT ratio ω_{CT} , particle-hole coherence length $\omega_{Coh.}$ and netto CT length CT_{net} , for the $S_0 \rightarrow T_n$ transitions of the **u**, **v** and **w** sub-patterns Trimer **t** in the given geometries.

Pattern	Geometry	State	$E_{ad.}$	Ω	PR	Pos.	ω_{CT}	$\omega_{Coh.}$	CT_{net}	Assigned
	S_0	A ₄	2.33	0.845	1.992	1.532	0.010	1.020	-0.001	DL ₂ ; T
		A ₅	2.54	0.594	1.161	1.498	0.950	1.058	0.850	CT _{AB} ; $T_{h;h-1}^{l;l+1}$
		A ₆	2.66	0.647	1.531	1.499	0.983	1.026	-0.553	CT _{BA} ; $T_{h;h-1;h}^{l+1;l}$
		A ₇	2.89	0.312	1.600	1.498	0.959	1.067	-0.500	DL; V/Z/T
	Q_1	A ₁	1.12	0.804	1.942	1.413	0.048	1.097	-0.002	DL; $T_{h;h-1}^{l;l+1}$
		A ₂	1.17	0.798	1.942	1.586	0.032	1.065	-0.000	DL; $T_{h-1;h}^{l;l+1}$
		A ₃	2.22	0.099	1.975	1.498	0.916	1.178	0.113	DL; Z/T
		A ₄	2.50	0.751	1.963	1.431	0.074	1.155	0.000	DL; T
	Q_1	A ₅	2.54	0.754	1.962	1.569	0.056	1.115	0.001	DL ₂ ; T
		A ₆	2.64	0.657	1.477	1.499	0.970	1.044	0.595	CT _{AB} ; $T_{h;h-1}^{l;l+1}$
		A ₇	2.80	0.602	1.367	1.498	0.964	1.050	-0.680	CT _{BA} ; $T_{h;h-1;h}^{l+1;l}$
		A ₈	3.54	0.073	1.991	1.467	0.551	1.971	0.013	DL; Z
	T_1	A ₁	0.95	0.847	1.032	1.016	0.028	1.029	0.005	LE; $T_h^{l;l+1}$
		A ₂	1.31	0.841	1.050	1.976	0.045	1.047	-0.007	LE; $T_{h-1;h}^{l+1;l+1}$
		A ₃	2.27	0.801	1.051	1.025	0.037	1.039	0.014	LE; T
		A ₄	2.33	0.185	1.690	1.513	0.918	1.145	0.428	DL+CT; Z/V/T
	T_1	A ₅	2.46	0.821	1.059	1.971	0.041	1.043	-0.011	LE; T
		A ₆	2.56	0.701	1.873	1.501	0.974	1.049	0.260	CT _{AB} ; $T_{h;h-1}^{l;l+1}$
		A ₇	2.78	0.590	1.658	1.505	0.950	1.086	-0.454	CT _{BA} ; $T_{h;h-1;h}^{l+1;l}$
	S_1	A ₁	1.04	0.878	1.981	1.548	0.054	1.112	0.006	DL; $T_{h;h-1}^{l;l+1}$
		A ₂	1.14	0.874	1.980	1.449	0.017	1.035	-0.003	DL; $T_{h-1;h}^{l;l+1}$
		A ₃	2.27	0.845	1.877	1.628	0.043	1.083	0.008	DL; T
		A ₄	2.30	0.365	1.336	1.499	0.908	1.125	0.705	CT+DL; T/Z
	S_1	A ₅	2.35	0.847	1.873	1.370	0.012	1.023	-0.003	DL ₂ ; T
		A ₆	2.53	0.590	1.808	1.498	0.973	1.050	0.326	CT _{BA} ; $T_{h;h-1;h}^{l+1;l}$
		A ₇	2.80	0.587	1.228	1.497	0.952	1.059	-0.793	CT _{AB} ; $T_{h;h-1}^{l;l+1}$
t	S_0	A ₁	1.19	0.847	1.878	2.049	0.046	1.067	0.008	LE _A ; $T_{h-1;h;h-2;h}^{l;l+1}$
		A ₂	1.20	0.846	2.050	2.094	0.052	1.093	0.010	DL _v ; $T_{h-1;h}^{l+1;l}$
		A ₃	1.26	0.844	2.878	1.854	0.031	1.065	0.009	LEC+DL _u ; $T_{h-2;h-1;h}^{l;l+1;l+2}$
		A ₄	2.37	0.818	2.558	1.952	0.066	1.115	-0.014	LE _A +DL _v ; T_{h-3}^l

Continued on next page

Table S6: Adiabatic energy $E_{ad.}$ as well as squared Frobenius-Norm of the 1-TDM Ω , the participation ratio PR, averaged position of the exciton Pos., CT ratio ω_{CT} , particle-hole coherence length $\omega_{Coh.}$ and netto CT length CT_{net} , for the $S_0 \rightarrow T_n$ transitions of the **u**, **v** and **w** sub-patterns Trimer **t** in the given geometries.

Pattern	Geometry	State	$E_{ad.}$	Ω	PR	Pos.	ω_{CT}	$\omega_{Coh.}$	CT_{net}	Assigned
	S_0	A ₅	2.38	0.816	2.024	2.215	0.118	1.195	0.016	DL _v ; T_{h-4}^l
		A ₆	2.40	0.810	2.718	1.890	0.107	1.184	-0.085	DL; T_{h-5}^l
		A ₇	2.48	0.753	2.486	1.882	0.885	2.123	0.145	CT _{v→A} ; $T_{h;h-1}^l$
	Q_1	A ₁	1.17	0.802	2.090	2.452	0.050	1.068	0.004	DL _u ; $T_{h-1;h;h-1;h}^{l;l+1}$
		A ₂	1.19	0.800	2.073	2.489	0.045	1.060	0.005	DL _u ; $T_{h-1;h}^{l;l+1}$
		A ₃	1.57	0.789	1.112	1.074	0.080	1.085	0.031	LE _C ; $T_{h-2;h;h-2}^{l+2;l}$
		A ₄	2.27	0.011	2.120	2.423	0.968	1.142	-0.196	³ DL _u ; $V_{h;h-1}^{l;l+1}$
	Q_1	A ₅	2.54	0.472	2.240	2.055	0.769	2.003	0.163	CT _{v→A} ; $T_{h;h-2}^{l;l+1}$
		A ₆	2.56	0.433	2.440	2.192	0.776	1.958	-0.544	DL _v +CT _{B→C} ; $T_{h;h-1}^l$
		A ₇	2.59	0.741	1.233	1.971	0.119	1.125	-0.005	LE _A ; $T_{h-3;h-1;h-5}^{l;l+3;l}$
	T_1	A ₁	1.04	0.823	1.063	1.046	0.057	1.061	-0.008	LE _C ; T_h^l
		A ₂	1.34	0.811	1.495	2.154	0.059	1.066	0.004	LE _A ; $T_{h-2;h;h-1}^{l+1;l+1;l+2;l}$
		A ₃	1.36	0.813	1.480	2.783	0.046	1.055	0.008	LE _B +CT; $T_{h-1}^{l+1;l+2}$
		A ₄	2.35	0.732	1.261	1.191	0.185	1.202	-0.229	LE _C +CT _{B→C} ; $T_{h-3;h;h-1}^{l;l+3;l}$
	T_1	A ₅	2.39	0.406	1.860	1.705	0.830	1.583	0.857	CT _{C→A} ; $T_{h;h-2}^{l+1}/V_{h-1;h}^{l;l+1}$
		A ₆	2.44	0.285	2.514	1.812	0.691	2.494	0.134	³ DL _v +CT; $V_{h-1;h;l;l+2}/Z_h^{l;l+1}/T_{h;h-2;h;h-2}^{l+2;l}$
		A ₇	2.48	0.677	2.608	1.798	0.891	2.140	-0.456	CT _{u→C} ; $T_{h;h-1}^{l+1;l}$
	S_1	A ₁	1.13	0.846	1.921	1.391	0.076	1.138	0.009	DL _w ; T_h^l
		A ₂	1.18	0.844	2.124	1.737	0.050	1.076	0.005	LE _A +DL _w ; $T_{h-2;h;h-1}^{l;l+1;l+2;l}$
		A ₃	1.30	0.847	1.193	2.863	0.042	1.046	0.015	LE _B ; $T_{h-1}^{l+1;l+2}$
		A ₄	2.35	0.628	1.769	1.646	0.775	1.743	0.345	LE _C +CT _{B→C} ; $T_{h;h-1;h}^{l+1;l}$
	S_1	A ₅	2.38	0.713	1.990	1.425	0.237	1.478	0.004	CT _{C→A} ; $T_{h-3;h}^{l;l+3}$
		A ₆	2.41	0.767	1.549	1.939	0.185	1.145	-0.175	DL _v +CT; T_{h-5}^l
		A ₇	2.46	0.586	1.818	2.511	0.401	1.446	0.463	CT _{u→C} ; T

S2.9 States with profound double excitation character

Table S7: Composition, coefficient and weight in % for states with contributions of doubly excited configurations of at least 10% and adiabatic energy less than 3 eV for the **u** sub-pattern. Spatial configurations of $V_{h-1;h}^{l;l+1}$ excited character are highlighted green.

Geometry	Exc. State No.	$E_{ad.}$	No.	CSF	Composition	Coeff.	Weight	N_{opn}
1₁		2.09	1	1	$(h)^0(l)^2$	0.4331	18.8	0
			2	1	$(h_{-1})^0(l)^2$	-0.3958	15.7	0
			3	1	$(h_{-1})^1(h)^1(l)^1(l_{+1})^1$	0.3954	15.6	4
			4	1	$(h)^0(l_{+1})^2$	-0.3887	15.1	0
			5	1	$(h_{-1})^0(l_{+1})^2$	0.3500	12.2	0
			6	1	$(h_{-1})^1(l)^1$	0.1012	1.0	2
1₄		2.62	1	1	$(h_{-1})^1(h)^1(l)^2$	0.4650	21.6	2
			2	1	$(h)^0(l)^1(l_{+1})^1$	0.4539	20.6	2
			3	1	$(h_{-1})^0(l)^1(l_{+1})^1$	0.4031	16.2	2
			4	1	$(h_{-1})^1(h)^1(l_{+1})^2$	0.3935	15.5	2
			5	1	$(h)^1(l_{+8})^1$	0.1014	1.0	2
Q₁	1₅	2.77	1	2	$(h_{-1})^1(h)^1(l)^1(l_{+1})^1$	-0.5528	30.6	4
			2	0	$(h)^2(l)^0$	-0.2923	8.5	0
			3	1	$(h)^0(l)^2$	-0.2881	8.3	0
			4	1	$(h_{-1})^0(l_{+1})^2$	-0.2605	6.8	0
			5	1	$(h)^1(l_{+1})^1$	0.2356	5.5	2
			6	1	$(h_{-1})^0(l)^2$	-0.2321	5.4	0
			7	1	$(h)^0(l_{+1})^2$	-0.2258	5.1	0
			8	1	$(h_{-1})^1(l)^1$	0.1587	2.5	2
3₂		2.25	1	1	$(h_{-1})^1(h)^1(l)^2$	-0.4652	21.6	2
			2	1	$(h)^0(l)^1(l_{+1})^1$	0.4634	21.5	2
			3	1	$(h_{-1})^0(l)^1(l_{+1})^1$	-0.4204	17.7	2
			4	1	$(h_{-1})^1(h)^1(l_{+1})^2$	0.4148	17.2	2
			5	1	$(h_{-1})^1(l_{+1})^1$	0.1039	1.1	2
1₃		2.53	1	1	$(h)^0(l)^2$	-0.4204	17.7	0
			2	1	$(h_{-1})^0(l)^2$	0.3752	14.1	0
			3	1	$(h_{-1})^1(h)^1(l)^1(l_{+1})^1$	-0.3704	13.7	4
			4	1	$(h)^0(l_{+1})^2$	0.3645	13.3	0
			5	1	$(h_{-1})^0(l_{+1})^2$	-0.3177	10.1	0
			6	1	$(h)^1(l_{+1})^1$	-0.2334	5.4	2
			7	1	$(h_{-1})^1(l)^1$	-0.2023	4.1	2
S₀	1₆	2.91	1	1	$(h_{-1})^1(h)^1(l)^2$	0.4530	20.5	2
			2	1	$(h)^0(l)^1(l_{+1})^1$	0.4506	20.3	2
			3	1	$(h_{-1})^0(l)^1(l_{+1})^1$	0.3924	15.4	2
			4	1	$(h_{-1})^1(h)^1(l_{+1})^2$	0.3887	15.1	2
			5	1	$(h_{-8})^1(l)^1$	-0.1169	1.4	2
3₄		2.66	1	1	$(h_{-1})^1(h)^1(l)^2$	0.4327	18.7	2
			2	1	$(h)^0(l)^1(l_{+1})^1$	-0.4294	18.4	2
			3	1	$(h_{-1})^0(l)^1(l_{+1})^1$	0.3736	14.0	2
			4	1	$(h_{-1})^1(h)^1(l_{+1})^2$	-0.3660	13.4	2
			5	1	$(h_{-1})^1(l_{+1})^1$	-0.2821	8.0	2
			6	1	$(h)^1(l)^1$	-0.2574	6.6	2
			7	3	$(h_{-1})^1(h)^1(l)^1(l_{+1})^1$	0.0716	0.5	4
1₁		2.09	1	1	$(h_{-1})^1(h)^1(l)^1(l_{+1})^1$	-0.3750	14.1	4
			2	2	$(h_{-1})^1(h)^1(l)^1(l_{+1})^1$	0.3654	13.3	4
			3	1	$(h)^0(l)^1(l_{+1})^1$	-0.3213	10.3	2
			4	1	$(h_{-1})^1(h)^1(l)^2$	0.3097	9.6	2
			5	1	$(h_{-1})^0(l)^1(l_{+1})^1$	0.2729	7.4	2

Continued on next page

Table S7: Composition, coefficient and weight in % for states with contributions of doubly excited configurations of at least 10% and adiabatic energy less than 3 eV for the **u** sub-pattern. Spatial configurations of $V_{h-1;h}^{l;l+1}$ excited character are highlighted green.

Geometry	Exc. State No.	E_{ad}	No.	CSF	Composition	Coeff.	Weight	N_{opn}
			6	1	$(h)^0(l)^2$	-0.2596	6.7	0
			7	1	$(h_{-1})^1(h)^1(l_{+1})^2$	-0.2447	6.0	2
			8	1	$(h)^1(l)^1$	0.1809	3.3	2
1₆		2.84	1	1	$(h_{-1})^0(l)^2$	0.5058	25.6	0
			2	1	$(h_{-1})^1(h)^1(l)^2$	-0.4203	17.7	2
			3	1	$(h_{-1})^0(l)^1(l_{+1})^1$	-0.2997	9.0	2
			4	1	$(h)^0(l)^1(l_{+1})^1$	-0.2645	7.0	2
			5	1	$(h_{-1})^1(h)^1(l_{+1})^2$	-0.2241	5.0	2
			6	1	$(h)^0(l_{+1})^2$	-0.2174	4.7	0
1₇		2.94	1	1	$(h)^0(l_{+1})^2$	0.5126	26.3	0
			2	2	$(h_{-1})^1(h)^1(l)^1(l_{+1})^1$	0.3393	11.5	4
			3	1	$(h)^0(l)^1(l_{+1})^1$	0.3048	9.3	2
			4	1	$(h_{-1})^1(h)^1(l_{+1})^2$	0.2523	6.4	2
			5	1	$(h_{-1})^0(l)^2$	0.2480	6.1	0
			6	0	$(h)^2(l)^0$	0.2173	4.7	0
3₃		2.23	1	3	$(h_{-1})^1(h)^1(l)^1(l_{+1})^1$	-0.3608	13.0	4
			2	1	$(h_{-1})^1(h)^1(l)^1(l_{+1})^1$	-0.3021	9.1	4
			3	1	$(h)^0(l)^1(l_{+1})^1$	0.2897	8.4	2
			4	1	$(h_{-1})^1(h)^1(l)^2$	-0.2813	7.9	2
			5	1	$(h_{-1})^0(l)^1(l_{+1})^1$	-0.2446	6.0	2
			6	1	$(h_{-1})^1(h)^1(l_{+1})^2$	0.2277	5.2	2
			7	1	$(h_{-3})^1(l)^1$	0.2251	5.1	2
			8	2	$(h_{-1})^1(h)^1(l)^1(l_{+1})^1$	0.2130	4.5	4
1₂		2.27	1	2	$(h_{-1})^1(h)^1(l)^1(l_{+1})^1$	-0.6205	38.5	4
			2	1	$(h_{-1})^1(h)^1(l)^1(l_{+1})^1$	-0.4078	16.6	4
			3	1	$(h_{-1})^1(h)^1(l)^2$	-0.2566	6.6	2
			4	1	$(h)^0(l)^1(l_{+1})^1$	0.2397	5.7	2
			5	1	$(h_{-1})^1(h)^1(l_{+1})^2$	0.1804	3.3	2
T₁	1₆	2.77	1	1	$(h)^0(l)^2$	0.7653	58.6	0
			2	1	$(h)^0(l)^1(l_{+1})^1$	-0.2094	4.4	2
3₃		2.33	1	3	$(h_{-1})^1(h)^1(l)^1(l_{+1})^1$	0.5549	30.8	4
			2	1	$(h_{-1})^1(h)^1(l)^1(l_{+1})^1$	-0.4500	20.2	4
			3	2	$(h_{-1})^1(h)^1(l)^1(l_{+1})^1$	0.3178	10.1	4
			4	1	$(h_{-1})^1(h)^1(l)^2$	-0.2233	5.0	2

Table S8: Composition, coefficient and weight in % for states with contributions of doubly excited configurations of at least 10% and adiabatic energy less than 3 eV for the **v** sub-pattern. Spatial configurations of $V_{h-1;h}^{l;l+1}$ excited character are highlighted green.

Geometry	Exc. State No.	E_{ad}	No.	CSF	Composition	Coeff.	Weight	N_{opn}
1₁		2.03	1	1	$(h)^0(l)^2$	-0.4365	19.1	0
			2	1	$(h_{-1})^1(h)^1(l)^1(l_{+1})^1$	0.3647	13.3	4
			3	1	$(h_{-1})^0(l)^2$	0.3284	10.8	0
			4	1	$(h)^0(l_{+1})^2$	0.2950	8.7	0
			5	1	$(h_{-1})^1(h)^1(l)^2$	0.2618	6.9	2
			6	1	$(h_{-1})^1(l)^1$	-0.2545	6.5	2
			7	1	$(h_{-1})^0(l_{+1})^2$	-0.2435	5.9	0

Continued on next page

Table S8: Composition, coefficient and weight in % for states with contributions of doubly excited configurations of at least 10% and adiabatic energy less than 3 eV for the \mathbf{v} sub-pattern. Spatial configurations of $V_{h-1;h}^{l;l+1}$ excited character are highlighted green.

Geometry	Exc. State No.	E_{ad}	No.	CSF	Composition	Coeff.	Weight	N_{opn}
	$\mathbf{1}_5$	2.73	8	1	$(h_{-1})^1(h)^1(l_{+1})^2$	-0.1826	3.3	2
			1	1	$(h)^0(l)^1(l_{+1})^1$	0.5148	26.5	2
			2	1	$(h_{-1})^1(h)^1(l)^2$	-0.4512	20.4	2
			3	1	$(h_{-1})^0(l)^1(l_{+1})^1$	0.3055	9.3	2
			4	1	$(h_{-1})^1(h)^1(l_{+1})^2$	-0.2936	8.6	2
	$\mathbf{1}_6$	2.82	5	1	$(h)^0(l_{+1})^2$	-0.1706	2.9	0
			1	1	$(h_{-1})^1(l_{+1})^1$	0.7054	49.8	2
			2	2	$(h_{-1})^1(h)^1(l)^1(l_{+1})^1$	-0.3127	9.8	4
			3	1	$(h)^0(l)^2$	0.2521	6.4	0
			4	1	$(h_{-1})^1(l)^1$	-0.1644	2.7	2
	$\mathbf{1}_7$	2.90	1	2	$(h_{-1})^1(h)^1(l)^1(l_{+1})^1$	0.4171	17.4	4
			2	1	$(h_{-1})^1(l_{+1})^1$	0.4026	16.2	2
			3	1	$(h_{-1})^0(l)^2$	-0.3555	12.6	0
			4	1	$(h)^0(l_{+1})^2$	-0.2604	6.8	0
			5	0	$(h)^2(l)^0$	-0.2257	5.1	0
			6	1	$(h)^1(l_{+1})^1$	0.2205	4.9	2
	$\mathbf{3}_2$	2.20	1	1	$(h_{-1})^1(h)^1(l)^2$	-0.4707	22.2	2
			2	1	$(h)^0(l)^1(l_{+1})^1$	-0.4184	17.5	2
			3	1	$(h_{-1})^1(h)^1(l_{+1})^2$	0.3387	11.5	2
			4	1	$(h_{-1})^0(l)^1(l_{+1})^1$	0.3325	11.1	2
			5	1	$(h_{-1})^1(l_{+1})^1$	-0.2718	7.4	2
			6	3	$(h_{-1})^1(h)^1(l)^1(l_{+1})^1$	0.2512	6.3	4
			7	1	$(h)^1(l)^1$	0.1820	3.3	2
	$\mathbf{1}_3$	2.43	1	1	$(h)^1(l_{+1})^1$	-0.6530	42.6	2
			2	1	$(h)^0(l)^2$	0.3364	11.3	0
			3	1	$(h_{-1})^1(h)^1(l)^1(l_{+1})^1$	-0.2689	7.2	4
			4	1	$(h_{-1})^0(l)^2$	-0.2206	4.9	0
	$\mathbf{1}_5$	2.84	1	1	$(h_{-1})^1(l_{+1})^1$	-0.6737	45.4	2
			2	1	$(h)^1(l_{+1})^1$	-0.3293	10.8	2
			3	1	$(h_{-1})^1(l)^1$	0.3025	9.2	2
			4	1	$(h)^0(l)^2$	-0.2299	5.3	0
			5	1	$(h_{-1})^1(h)^1(l)^1(l_{+1})^1$	0.1573	2.5	4
\mathbf{S}_0	$\mathbf{3}_4$	2.54	1	1	$(h)^1(l)^1$	0.4986	24.9	2
			2	1	$(h_{-1})^1(l_{+1})^1$	-0.4228	17.9	2
			3	1	$(h)^1(l_{+1})^1$	0.3558	12.7	2
			4	1	$(h_{-1})^1(l)^1$	-0.2354	5.5	2
			5	1	$(h_{-1})^1(h)^1(l)^2$	-0.2341	5.5	2
			6	1	$(h)^0(l)^1(l_{+1})^1$	-0.2340	5.5	2
			7	1	$(h_{-1})^1(h)^1(l_{+1})^2$	0.1593	2.5	2
	$\mathbf{3}_5$	2.66	1	1	$(h)^1(l_{+1})^1$	-0.4992	24.9	2
			2	1	$(h_{-1})^1(l)^1$	0.4855	23.6	2
			3	1	$(h_{-1})^1(l_{+1})^1$	-0.2924	8.5	2
			4	1	$(h_{-1})^1(h)^1(l)^2$	-0.2842	8.1	2
			5	1	$(h)^0(l)^1(l_{+1})^1$	-0.2139	4.6	2
	$\mathbf{3}_6$	2.89	1	1	$(h_{-1})^1(l_{+1})^1$	-0.5218	27.2	2
			2	1	$(h_{-1})^1(h)^1(l)^2$	0.3340	11.2	2
			3	1	$(h)^0(l)^1(l_{+1})^1$	0.2945	8.7	2
			4	1	$(h)^1(l)^1$	0.2832	8.0	2
			5	1	$(h_{-1})^1(h)^1(l_{+1})^2$	-0.2676	7.2	2

Continued on next page

Table S8: Composition, coefficient and weight in % for states with contributions of doubly excited configurations of at least 10% and adiabatic energy less than 3 eV for the \mathbf{v} sub-pattern. Spatial configurations of $V_{h-1;h}^{l;l+1}$ excited character are highlighted green.

Geometry	Exc. State No.	E_{ad}	No.	CSF	Composition	Coeff.	Weight	N_{opn}
S_1			6	1	$(h_{-1})^0(l)^1(l_{+1})^1$	-0.2506	6.3	2
			7	1	$(h_{-1})^1(l)^1$	0.2294	5.3	2
			8	3	$(h_{-1})^1(h)^1(l)^1(l_{+1})^1$	-0.2081	4.3	4
	1_1	2.09	1	1	$(h)^1(l)^1$	0.6521	42.5	2
			2	1	$(h)^0(l)^2$	-0.3080	9.5	0
			3	1	$(h_{-1})^1(h)^1(l)^1(l_{+1})^1$	0.2410	5.8	4
			4	1	$(h_{-1})^1(l)^1$	-0.2026	4.1	2
	1_2	2.16	1	1	$(h)^1(l)^1$	0.6150	37.8	2
			2	1	$(h_{-1})^1(l)^1$	0.3680	13.5	2
			3	1	$(h)^0(l)^2$	0.2431	5.9	0
			4	1	$(h)^1(l_{+1})^1$	-0.2342	5.5	2
			5	1	$(h_{-1})^1(h)^1(l)^2$	-0.2184	4.8	2
	1_6	2.84	1	1	$(h)^0(l)^1(l_{+1})^1$	-0.5289	28.0	2
			2	1	$(h_{-1})^1(h)^1(l)^2$	0.4404	19.4	2
			3	1	$(h)^0(l_{+1})^2$	0.2708	7.3	0
			4	1	$(h_{-1})^0(l)^1(l_{+1})^1$	-0.2569	6.6	2
			5	1	$(h_{-1})^1(h)^1(l_{+1})^2$	0.2374	5.6	2
			6	1	$(h_{-1})^0(l)^2$	-0.1532	2.3	0
S_1	1_7	2.96	1	2	$(h_{-1})^1(h)^1(l)^1(l_{+1})^1$	0.4622	21.4	4
			2	1	$(h_{-1})^0(l)^2$	-0.4286	18.4	0
			3	1	$(h)^0(l_{+1})^2$	-0.2773	7.7	0
			4	1	$(h)^0(l)^2$	-0.2352	5.5	0
			5	1	$(h_{-1})^1(l_{+1})^1$	0.2287	5.2	2
			6	0	$(h)^2(l)^0$	-0.2044	4.2	0
	3_2	2.25	1	1	$(h)^1(l)^1$	-0.3838	14.7	2
			2	1	$(h_{-1})^1(l_{+1})^1$	0.3657	13.4	2
			3	1	$(h_{-3})^1(l)^1$	0.3146	9.9	2
			4	1	$(h_{-1})^1(h)^1(l)^2$	0.2647	7.0	2
			5	1	$(h)^0(l)^1(l_{+1})^1$	0.2511	6.3	2
			6	1	$(h_{-1})^1(l_{+2})^1$	0.2401	5.8	2
			7	1	$(h)^1(l_{+1})^1$	-0.2295	5.3	2
			8	1	$(h_{-1})^1(h)^1(l_{+1})^2$	-0.1704	2.9	2
	3_4	2.36	1	1	$(h_{-3})^1(l)^1$	0.4000	16.0	2
			2	1	$(h_{-1})^1(l_{+2})^1$	0.3619	13.1	2
			3	1	$(h_{-2})^1(l_{+1})^1$	-0.3539	12.5	2
			4	1	$(h)^1(l_{+3})^1$	-0.3391	11.5	2
			5	1	$(h_{-1})^1(h)^1(l)^2$	-0.2418	5.8	2
			6	1	$(h)^0(l)^1(l_{+1})^1$	-0.2260	5.1	2
			7	3	$(h_{-1})^1(h)^1(l)^1(l_{+1})^1$	0.1717	2.9	4
	3_5	2.50	1	1	$(h)^1(l_{+1})^1$	0.4997	25.0	2
			2	1	$(h_{-1})^1(l)^1$	-0.4395	19.3	2
			3	1	$(h)^1(l)^1$	0.3838	14.7	2
			4	1	$(h_{-1})^1(h)^1(l)^2$	0.2521	6.4	2
			5	3	$(h_{-1})^1(h)^1(l)^1(l_{+1})^1$	-0.2092	4.4	4
1_2		2.22	1	1	$(h_{-1})^1(h)^1(l)^2$	0.3945	15.6	2
			2	1	$(h)^1(l_{+1})^1$	0.3255	10.6	2
			3	1	$(h)^1(l)^1$	-0.3252	10.6	2
			4	1	$(h_{-1})^1(h)^1(l)^1(l_{+1})^1$	0.3141	9.9	4
			5	1	$(h_{-1})^1(l)^1$	-0.3029	9.2	2
			6	1	$(h_{-1})^1(h)^1(l_{+1})^2$	-0.2603	6.8	2

Continued on next page

Table S8: Composition, coefficient and weight in % for states with contributions of doubly excited configurations of at least 10% and adiabatic energy less than 3 eV for the **v** sub-pattern. Spatial configurations of $V_{h-1;h}^{l;l+1}$ excited character are highlighted green.

Geometry	Exc. State No.	$E_{ad.}$	No.	CSF	Composition	Coeff.	Weight	N_{opn}
1₄			7	1	$(h)^0(l)^2$	-0.2325	5.4	0
			8	2	$(h_{-1})^1(h)^1(l)^1(l_{+1})^1$	0.2025	4.1	4
	2.64		1	1	$(h)^0(l)^2$	-0.4818	23.2	0
			2	1	$(h)^1(l_{+1})^1$	-0.4386	19.2	2
			3	1	$(h)^0(l)^1(l_{+1})^1$	0.3287	10.8	2
			4	1	$(h_{-1})^1(l)^1$	0.2718	7.4	2
			5	1	$(h_{-1})^1(l_{+1})^1$	0.2285	5.2	2
			6	2	$(h_{-1})^1(h)^1(l)^1(l_{+1})^1$	0.1991	4.0	4
	1₅	2.66	1	1	$(h)^1(l_{+1})^1$	0.4659	21.7	2
			2	1	$(h)^0(l)^1(l_{+1})^1$	0.3648	13.3	2
			3	1	$(h)^0(l)^2$	-0.3612	13.0	0
			4	1	$(h_{-1})^1(h)^1(l)^2$	-0.3029	9.2	2
			5	1	$(h_{-1})^1(l)^1$	-0.2775	7.7	2
			6	1	$(h_{-1})^1(l_{+1})^1$	-0.2300	5.3	2
			7	1	$(h)^0(l_{+1})^2$	-0.1674	2.8	0
3₃		2.36	1	1	$(h_{-1})^1(h)^1(l)^2$	0.4006	16.0	2
			2	3	$(h_{-1})^1(h)^1(l)^1(l_{+1})^1$	-0.3925	15.4	4
			3	1	$(h)^1(l_{+1})^1$	-0.2794	7.8	2
			4	1	$(h_{-1})^1(h)^1(l_{+1})^2$	-0.2701	7.3	2
			5	1	$(h)^0(l)^1(l_{+1})^1$	0.2670	7.1	2
			6	1	$(h_{-1})^1(l_{+1})^1$	0.2568	6.6	2
			7	1	$(h)^1(l)^1$	-0.2054	4.2	2

Table S9: Composition, coefficient and weight in % for states with contributions of doubly excited configurations of at least 10% and adiabatic energy less than 3 eV for the **w** sub-pattern. Spatial configurations of $V_{h-1;h}^{l;l+1}$ excited character are highlighted green.

Geometry	Exc. State No.	$E_{ad.}$	No.	CSF	Composition	Coeff.	Weight	N_{opn}
1₁		2.04	1	1	$(h)^0(l)^2$	0.4888	23.9	0
			2	1	$(h_{-1})^1(h)^1(l)^1(l_{+1})^1$	0.3603	13.0	4
			3	1	$(h)^0(l_{+1})^2$	-0.3372	11.4	0
			4	1	$(h_{-1})^0(l)^2$	-0.3352	11.2	0
			5	1	$(h_{-1})^1(l)^1$	-0.2495	6.2	2
			6	1	$(h_{-1})^0(l_{+1})^2$	0.2473	6.1	0
			7	1	$(h)^1(l_{+1})^1$	-0.2443	6.0	2
			8	1	$(h_{-1})^1(h)^1(l)^2$	-0.1111	1.2	2
Q₁	1₄	2.69	1	1	$(h_{-1})^1(l)^1$	0.4679	21.9	2
			2	1	$(h)^1(l_{+1})^1$	0.4301	18.5	2
			3	1	$(h_{-1})^1(h)^1(l)^2$	-0.3996	16.0	2
			4	1	$(h)^0(l)^1(l_{+1})^1$	-0.3019	9.1	2
			5	1	$(h_{-1})^0(l)^1(l_{+1})^1$	-0.1970	3.9	2
	1₅	2.71	1	1	$(h)^0(l)^1(l_{+1})^1$	0.4444	19.8	2
			2	1	$(h)^1(l_{+1})^1$	0.3545	12.6	2
			3	1	$(h_{-1})^1(h)^1(l)^2$	0.3380	11.4	2
			4	1	$(h_{-1})^1(l)^1$	0.3153	9.9	2
			5	1	$(h_{-1})^1(h)^1(l_{+1})^2$	0.2911	8.5	2
			6	1	$(h_{-1})^0(l)^1(l_{+1})^1$	0.2183	4.8	2
	1₆	2.82	1	1	$(h_{-1})^1(l_{+1})^1$	-0.7402	54.8	2
						Continued on next page		

Table S9: Composition, coefficient and weight in % for states with contributions of doubly excited configurations of at least 10% and adiabatic energy less than 3 eV for the **w** sub-pattern. Spatial configurations of $V_{h-1;h}^{l;l+1}$ excited character are highlighted green.

Geometry	Exc. State No.	E_{ad}	No.	CSF	Composition	Coeff.	Weight	N_{opn}
			2	2	$(h_{-1})^1(h)^1(l)^1(l_{+1})^1$	-0.3345	11.2	4
			3	1	$(h)^0(l)^2$	-0.2259	5.1	0
			4	0	$(h)^2(l)^0$	-0.1647	2.7	0
1₇		2.88	1	1	$(h_{-1})^1(l_{+1})^1$	-0.4566	20.8	2
			2	2	$(h_{-1})^1(h)^1(l)^1(l_{+1})^1$	0.4201	17.6	4
			3	1	$(h)^0(l_{+1})^2$	0.3040	9.2	0
			4	1	$(h_{-1})^0(l)^2$	0.2919	8.5	0
			5	1	$(h)^1(l_{+1})^1$	-0.2266	5.1	2
			6	0	$(h)^2(l)^0$	0.2170	4.7	0
3₂		2.22	1	1	$(h)^0(l)^1(l_{+1})^1$	-0.4724	22.3	2
			2	1	$(h_{-1})^1(h)^1(l)^2$	0.4684	21.9	2
			3	1	$(h_{-1})^1(h)^1(l_{+1})^2$	-0.3403	11.6	2
			4	1	$(h_{-1})^0(l)^1(l_{+1})^1$	0.3393	11.5	2
			5	1	$(h_{-1})^1(l_{+1})^1$	0.2929	8.6	2
			6	1	$(h)^1(l)^1$	0.1855	3.4	2
1₃		2.41	1	1	$(h)^1(l_{+1})^1$	0.4839	23.4	2
			2	1	$(h_{-1})^1(l)^1$	0.4275	18.3	2
			3	1	$(h)^0(l)^2$	-0.3966	15.7	0
			4	1	$(h_{-1})^1(h)^1(l)^1(l_{+1})^1$	-0.2749	7.6	4
			5	1	$(h)^0(l_{+1})^2$	0.2464	6.1	0
			6	1	$(h_{-1})^0(l)^2$	0.2413	5.8	0
			7	1	$(h_{-1})^0(l_{+1})^2$	-0.1704	2.9	0
1₄		2.75	1	1	$(h_{-1})^1(l_{+1})^1$	-0.5440	29.6	2
			2	1	$(h_{-1})^1(l)^1$	0.3633	13.2	2
			3	1	$(h)^1(l_{+1})^1$	0.3539	12.5	2
			4	1	$(h)^0(l)^2$	0.2825	8.0	0
			5	1	$(h_{-1})^1(h)^1(l)^1(l_{+1})^1$	0.2033	4.1	4
1₅		2.83	1	1	$(h_{-1})^1(l_{+1})^1$	-0.7118	50.7	2
			2	1	$(h)^1(l_{+1})^1$	-0.2969	8.8	2
			3	1	$(h_{-1})^1(l)^1$	-0.2847	8.1	2
			4	1	$(h)^0(l)^2$	-0.2446	6.0	0
			5	1	$(h)^0(l_{+1})^2$	0.1557	2.4	0
1₆		3.00	1	1	$(h)^0(l)^1(l_{+1})^1$	-0.5232	27.4	2
			2	1	$(h_{-1})^1(h)^1(l)^2$	-0.5025	25.2	2
			3	1	$(h_{-1})^1(h)^1(l_{+1})^2$	-0.3056	9.3	2
			4	1	$(h_{-1})^0(l)^1(l_{+1})^1$	-0.2893	8.4	2
			5	1	$(h_{-7})^1(l)^1$	0.1350	1.8	2
3₄		2.54	1	1	$(h_{-1})^1(l_{+1})^1$	0.5058	25.6	2
			2	1	$(h)^1(l)^1$	0.4511	20.3	2
			3	1	$(h)^1(l_{+1})^1$	-0.3117	9.7	2
			4	1	$(h_{-1})^1(l)^1$	-0.3066	9.4	2
			5	1	$(h)^0(l)^1(l_{+1})^1$	-0.2693	7.3	2
			6	1	$(h_{-1})^1(h)^1(l)^2$	0.2447	6.0	2
			7	1	$(h_{-1})^1(h)^1(l_{+1})^2$	-0.1694	2.9	2
3₆		2.89	1	1	$(h_{-1})^1(l_{+1})^1$	0.4687	22.0	2
			2	1	$(h)^0(l)^1(l_{+1})^1$	0.3857	14.9	2
			3	1	$(h_{-1})^1(h)^1(l)^2$	-0.3749	14.1	2
			4	1	$(h)^1(l)^1$	0.3189	10.2	2
			5	1	$(h_{-1})^1(h)^1(l_{+1})^2$	0.2945	8.7	2
			6	1	$(h_{-1})^0(l)^1(l_{+1})^1$	-0.2901	8.4	2

Continued on next page

Table S9: Composition, coefficient and weight in % for states with contributions of doubly excited configurations of at least 10% and adiabatic energy less than 3 eV for the **w** sub-pattern. Spatial configurations of $V_{h-1;h}^{l;l+1}$ excited character are highlighted green.

Geometry	Exc. State No.	E_{ad}	No.	CSF	Composition	Coeff.	Weight	N_{opn}
S₁	1₁	2.07	7	3	$(h_{-1})^1(h)^1(l)^1(l_{+1})^1$	-0.1181	1.4	4
			1	1	$(h)^1(l)^1$	-0.7532	56.7	2
			2	1	$(h)^0(l)^2$	-0.2861	8.2	0
	1₂	2.15	3	1	$(h_{-1})^1(h)^1(l)^1(l_{+1})^1$	-0.1908	3.6	4
			1	1	$(h)^1(l)^1$	-0.5063	25.6	2
			2	1	$(h)^0(l)^2$	0.3520	12.4	0
			3	1	$(h_{-1})^1(l)^1$	-0.3329	11.1	2
			4	1	$(h)^1(l_{+1})^1$	-0.3154	9.9	2
			5	1	$(h_{-1})^1(h)^1(l)^1(l_{+1})^1$	0.2491	6.2	4
			6	1	$(h_{-1})^0(l)^2$	-0.2064	4.3	0
	1₄	2.62	1	1	$(h_{-1})^1(l)^1$	-0.5302	28.1	2
			2	1	$(h)^1(l_{+1})^1$	-0.4717	22.3	2
			3	1	$(h_{-1})^1(l_{+1})^1$	0.3060	9.4	2
			4	1	$(h)^0(l)^2$	-0.2874	8.3	0
			5	1	$(h_{-1})^1(h)^1(l)^2$	0.1903	3.6	2
	1₅	2.78	1	1	$(h_{-1})^1(l_{+1})^1$	-0.4598	21.1	2
			2	1	$(h_{-1})^1(h)^1(l)^2$	0.4502	20.3	2
			3	1	$(h)^0(l)^1(l_{+1})^1$	0.4255	18.1	2
			4	1	$(h_{-1})^0(l)^1(l_{+1})^1$	0.2136	4.6	2
	1₆	2.83	1	1	$(h_{-1})^1(l_{+1})^1$	0.6652	44.3	2
			2	1	$(h)^0(l)^1(l_{+1})^1$	0.3275	10.7	2
			3	1	$(h_{-1})^1(h)^1(l)^2$	0.2561	6.6	2
			4	1	$(h_{-1})^1(h)^1(l_{+1})^2$	0.1884	3.6	2
	1₇	2.94	1	2	$(h_{-1})^1(h)^1(l)^1(l_{+1})^1$	-0.4896	24.0	4
			2	1	$(h)^0(l_{+1})^2$	-0.3758	14.1	0
			3	1	$(h_{-1})^0(l)^2$	-0.3396	11.5	0
			4	1	$(h_{-1})^1(l_{+1})^1$	0.2676	7.2	2
			5	1	$(h)^0(l)^2$	-0.2382	5.7	0
			6	0	$(h)^2(l)^0$	-0.2039	4.2	0
	3₃	2.30	1	1	$(h_{-1})^1(l_{+1})^1$	0.4255	18.1	2
			2	1	$(h)^0(l)^1(l_{+1})^1$	-0.3902	15.2	2
			3	1	$(h_{-1})^1(h)^1(l)^2$	0.3556	12.6	2
			4	1	$(h)^1(l)^1$	0.3534	12.5	2
			5	1	$(h_{-1})^1(h)^1(l_{+1})^2$	-0.2352	5.5	2
			6	1	$(h_{-1})^0(l)^1(l_{+1})^1$	0.2324	5.4	2
			7	1	$(h_{-1})^1(l)^1$	-0.2231	5.0	2
	3₅	2.53	1	1	$(h_{-1})^1(l)^1$	0.5487	30.1	2
			2	1	$(h)^1(l_{+1})^1$	0.5281	27.9	2
			3	1	$(h)^1(l)^1$	-0.2583	6.7	2
			4	1	$(h_{-1})^1(h)^1(l)^2$	0.2460	6.1	2
			5	1	$(h)^0(l)^1(l_{+1})^1$	-0.2072	4.3	2
	3₆	2.80	1	1	$(h_{-1})^1(l_{+1})^1$	-0.6578	43.3	2
			2	1	$(h)^1(l)^1$	-0.3296	10.9	2
			3	1	$(h)^0(l)^1(l_{+1})^1$	-0.2529	6.4	2
			4	1	$(h)^1(l_{+1})^1$	-0.2327	5.4	2
			5	1	$(h_{-1})^1(h)^1(l)^2$	0.2270	5.2	2
			6	1	$(h_{-1})^1(l)^1$	-0.2147	4.6	2
I₁		2.13	1	1	$(h)^1(l)^1$	0.6700	44.9	2
			2	1	$(h)^0(l)^2$	0.2404	5.8	0

Continued on next page

Table S9: Composition, coefficient and weight in % for states with contributions of doubly excited configurations of at least 10% and adiabatic energy less than 3 eV for the **w** sub-pattern. Spatial configurations of $V_{h-1;h}^{l;l+1}$ excited character are highlighted green.

Geometry	Exc. State No.	E_{ad}	No.	CSF	Composition	Coeff.	Weight	N_{opn}
			3	1	$(h_{-1})^1(l)^1$	-0.2300	5.3	2
			4	1	$(h_{-1})^1(h)^1(l)^1(l_{+1})^1$	0.2295	5.3	4
			5	1	$(h_{-1})^1(h)^1(l)^2$	-0.2116	4.5	2
1₂		2.16	1	1	$(h)^1(l)^1$	-0.6122	37.5	2
			2	1	$(h)^1(l_{+1})^1$	-0.3214	10.3	2
			3	1	$(h_{-1})^1(h)^1(l)^2$	-0.2496	6.2	2
			4	1	$(h)^0(l)^2$	0.2428	5.9	0
			5	1	$(h_{-1})^1(h)^1(l)^1(l_{+1})^1$	0.2413	5.8	4
			6	1	$(h)^0(l_{+1})^2$	-0.1813	3.3	0
1₄		2.65	1	1	$(h)^0(l)^2$	0.5840	34.1	0
			2	1	$(h)^0(l)^1(l_{+1})^1$	0.4111	16.9	2
			3	1	$(h_{-1})^1(h)^1(l)^2$	0.2640	7.0	2
			4	2	$(h_{-1})^1(h)^1(l)^1(l_{+1})^1$	0.2073	4.3	4
1₅		2.67	1	1	$(h)^1(l_{+1})^1$	0.5436	29.5	2
			2	1	$(h_{-1})^1(l)^1$	0.5296	28.1	2
			3	1	$(h_{-1})^1(h)^1(l)^2$	-0.2603	6.8	2
			4	1	$(h)^0(l)^1(l_{+1})^1$	-0.2197	4.8	2
3₃		2.33	1	1	$(h_{-1})^1(h)^1(l)^2$	0.4055	16.4	2
			2	1	$(h)^0(l)^1(l_{+1})^1$	-0.3818	14.6	2
			3	1	$(h_{-1})^1(l_{+1})^1$	0.3302	10.9	2
			4	3	$(h_{-1})^1(h)^1(l)^1(l_{+1})^1$	0.3288	10.8	4
			5	1	$(h_{-1})^1(h)^1(l_{+1})^2$	-0.2725	7.4	2
			6	1	$(h)^1(l_{+1})^1$	-0.2357	5.6	2
			7	1	$(h_{-1})^0(l)^1(l_{+1})^1$	0.2298	5.3	2
			8	1	$(h)^1(l)^1$	0.2017	4.1	2

Trimer

Table S10: Composition, coefficient and weight in % for states with contributions of doubly excited configurations of at least 10% and adiabatic energy less than 3 eV for the **t** sub-pattern. Spatial configurations of $V_{h-1;h}^{l;l+1}$ excited character are highlighted green.

Geometry	Exc. State No.	E_{ad}	No.	CSF	Composition	Coeff.	Weight	N_{opn}
$\mathbf{1_1}$		2.13	1	1	$(h_{-1})^0(l)^1(l_{+1})^1$	-0.3998	16.0	2
			2	1	$(h_{-1})^1(h)^1(l)^1(l_{+1})^1$	-0.3165	10.0	4
			3	1	$(h)^0(l)^1(l_{+1})^1$	0.3022	9.1	2
			4	2	$(h_{-2})^1(h)^1(l)^1(l_{+1})^1$	0.2538	6.4	4
			5	2	$(h_{-1})^1(h)^1(l)^1(l_{+1})^1$	0.2257	5.1	4
			6	1	$(h_{-1})^0(l_{+1})^2$	0.2141	4.6	0
$\mathbf{1_{10}}$		2.88	1	1	$(h_{-1})^1(h)^1(l)^2$	0.3468	12.0	2
			2	1	$(h_{-1})^1(l_{+2})^1$	0.3323	11.0	2
			3	1	$(h_{-1})^0(l)^2$	0.2977	8.9	0
			4	1	$(h_{-1})^1(h)^1(l_{+1})^2$	0.2514	6.3	2
			5	1	$(h)^1(l_{+2})^1$	-0.2079	4.3	2
$\mathbf{Q_1}$	$\mathbf{1_5}$	2.44	1	1	$(h)^1(l_{+1})^1$	0.2818	7.9	2
			2	1	$(h_{-2})^1(l)^1$	0.2731	7.5	2
			3	1	$(h)^0(l_{+1})^1(l_{+2})^1$	0.2233	5.0	2
			1	1	$(h_{-1})^0(l)^1(l_{+1})^1$	0.3770	14.2	2
Continued on next page								
$\mathbf{3_3}$		2.27						

Table S10: Composition, coefficient and weight in % for states with contributions of doubly excited configurations of at least 10% and adiabatic energy less than 3 eV for the **t** sub-pattern. Spatial configurations of $V_{h-1;h}^{l;l+1}$ excited character are highlighted green.

Geometry	Exc. State No.	E_{ad}	No.	CSF	Composition	Coeff.	Weight	N_{opn}
			2	1	$(h_{-1})^1(h)^1(l)^1(l_{+1})^1$	-0.3482	12.1	4
			3	1	$(h)^0(l)^1(l_{+1})^1$	-0.2857	8.2	2
			4	2	$(h_{-1})^1(h)^1(l)^1(l_{+1})^1$	0.2494	6.2	4
			5	3	$(h_{-2})^1(h)^1(l)^1(l_{+1})^1$	-0.2356	5.6	4
			6	3	$(h_{-1})^1(h)^1(l)^1(l_{+1})^1$	-0.2113	4.5	4
S₀	3₅	2.56	1	1	$(h)^1(l)^1$	-0.3731	13.9	2
			2	1	$(h_{-1})^1(l)^1$	-0.3092	9.6	2
			3	1	$(h_{-1})^1(l_{+2})^1$	-0.2786	7.8	2
			4	1	$(h)^0(l_{+1})^1(l_{+2})^1$	0.1892	3.6	2
S₀	1₅	2.55	1	1	$(h_{-2})^1(l)^1$	0.4390	19.3	2
			2	1	$(h)^1(l_{+2})^1$	0.4382	19.2	2
			3	1	$(h_{-1})^1(h)^1(l)^2$	0.2820	8.0	2
			4	1	$(h)^0(l)^1(l_{+1})^1$	0.2540	6.4	2
			5	1	$(h)^0(l_{+1})^1(l_{+2})^1$	0.1841	3.4	2
S₁	1₂	2.22	1	1	$(h)^1(l_{+1})^1$	0.5677	32.2	2
			2	1	$(h)^0(l)^2$	-0.2966	8.8	0
			3	1	$(h)^1(l)^1$	0.2206	4.9	2
S₁	1₄	2.37	1	1	$(h_{-2})^1(l)^1$	-0.4053	16.4	2
			2	1	$(h_{-1})^1(l_{+1})^1$	0.2797	7.8	2
			3	2	$(h_{-1})^1(h)^1(l)^1(l_{+1})^1$	-0.2454	6.0	4
			4	1	$(h)^1(l_{+1})^1$	0.2417	5.8	2
			5	1	$(h_{-1})^1(h)^1(l)^2$	-0.2244	5.0	2
			6	1	$(h_{-1})^1(l)^1$	0.1994	4.0	2
T₁	1₂	2.26	1	1	$(h)^1(l_{+1})^1$	-0.4921	24.2	2
			2	1	$(h_{-1})^1(l)^1$	0.3069	9.4	2
			3	2	$(h_{-1})^1(h)^1(l)^1(l_{+1})^1$	0.2927	8.6	4
			4	1	$(h)^0(l)^2$	-0.2222	4.9	0
T₁	1₃	2.33	1	1	$(h_{-1})^1(h)^1(l)^2$	0.3200	10.2	2
			2	1	$(h_{-1})^1(l)^1$	0.3051	9.3	2
			3	1	$(h)^1(l_{+2})^1$	0.2921	8.5	2
			4	1	$(h)^0(l)^1(l_{+1})^1$	-0.2812	7.9	2
			5	1	$(h_{-2})^1(l)^1$	-0.2712	7.4	2
			6	2	$(h_{-1})^1(h)^1(l)^1(l_{+2})^1$	-0.2234	5.0	4
T₁	3₄	2.39	1	1	$(h)^1(l_{+1})^1$	0.5020	25.2	2
			2	1	$(h_{-2})^1(l_{+1})^1$	0.3060	9.4	2
			3	3	$(h_{-1})^1(h)^1(l)^1(l_{+1})^1$	-0.2280	5.2	4
			4	1	$(h_{-2})^1(h)^1(l)^2$	-0.2087	4.4	2
T₁	3₅	2.44	1	3	$(h_{-1})^1(h)^1(l)^1(l_{+2})^1$	-0.3077	9.5	4
			2	1	$(h_{-1})^1(h)^1(l)^2$	-0.2578	6.6	2
			3	1	$(h)^1(l_{+2})^1$	0.2511	6.3	2
			4	1	$(h)^0(l)^1(l_{+1})^1$	-0.2387	5.7	2
			5	1	$(h_{-2})^1(h)^1(l)^1(l_{+1})^1$	0.2239	5.0	4
			6	1	$(h)^1(l)^1$	-0.2201	4.8	2